PB80-187487

Proceedings: Advances in Particle Sampling and Measurement (Daytona Beach, FL, October 1979)

Southern Research Inst.
Birmingham, AL

Prepared for

Industrial Environmental Research Lab.
Research Triangle Park, NC

Jan 80

U.S. Department of Commerce
National Technical Information Service
NTIS

United States
Environmental Protection
Agency

Industrial Environmental Research
Laboratory
Research Triangle Park NC 27711

EPA-600/9-80-004
January 1980

PB80-187487

EPA

Proceedings: Advances in Particle Sampling and Measurement (Daytona Beach, FL, October 1979)

Interagency Energy/Environment R&D Program Report

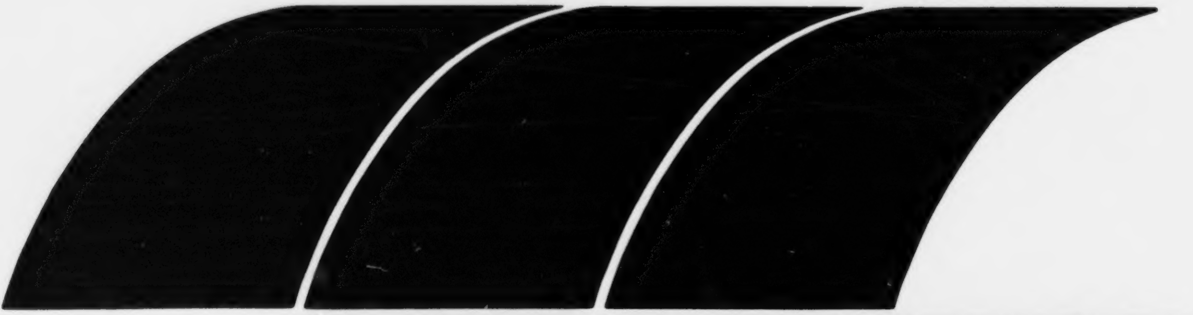

REPRODUCED BY
NATIONAL TECHNICAL
INFORMATION SERVICE
U.S. DEPARTMENT OF COMMERCE
SPRINGFIELD, VA 22161

RESEARCH REPORTING SERIES

Research reports of the Office of Research and Development, U.S. Environmental Protection Agency, have been grouped into nine series. These nine broad categories were established to facilitate further development and application of environmental technology. Elimination of traditional grouping was consciously planned to foster technology transfer and a maximum interface in related fields. The nine series are:

1. Environmental Health Effects Research
2. Environmental Protection Technology
3. Ecological Research
4. Environmental Monitoring
5. Socioeconomic Environmental Studies
6. Scientific and Technical Assessment Reports (STAR)
7. Interagency Energy-Environment Research and Development
8. "Special" Reports
9. Miscellaneous Reports

This report has been assigned to the INTERAGENCY ENERGY-ENVIRONMENT RESEARCH AND DEVELOPMENT series. Reports in this series result from the effort funded under the 17-agency Federal Energy/Environment Research and Development Program. These studies relate to EPA's mission to protect the public health and welfare from adverse effects of pollutants associated with energy systems. The goal of the Program is to assure the rapid development of domestic energy supplies in an environmentally-compatible manner by providing the necessary environmental data and control technology. Investigations include analyses of the transport of energy-related pollutants and their health and ecological effects; assessments of, and development of, control technologies for energy systems; and integrated assessments of a wide range of energy-related environmental issues.

EPA REVIEW NOTICE

This report has been reviewed by the participating Federal Agencies, and approved for publication. Approval does not signify that the contents necessarily reflect the views and policies of the Government, nor does mention of trade names or commercial products constitute endorsement or recommendation for use.

This document is available to the public through the National Technical Information Service, Springfield, Virginia 22161.

TECHNICAL REPORT DATA
(Please read Instructions on the reverse before completing)

1. REPORT NO. EPA-600/9-80-004	2.	3. RECIPIENT'S ACCESSION NO. PB80 187487
4. TITLE AND SUBTITLE Proceedings: Advances in Particle Sampling and Measurement (Daytona Beach, FL, October 1979)		5. REPORT DATE January 1980 6. PERFORMING ORGANIZATION CODE
7. AUTHOR(S) W.B. Smith, Editor		8. PERFORMING ORGANIZATION REPORT NO.
9. PERFORMING ORGANIZATION NAME AND ADDRESS Southern Research Institute 2000 Ninth Avenue, South Birmingham, Alabama 35205		10. PROGRAM ELEMENT NO. EHE624 11. CONTRACT/GRANT NO. 68-02-3118
12. SPONSORING AGENCY NAME AND ADDRESS EPA, Office of Research and Development Industrial Environmental Research Laboratory Research Triangle Park, NC 27711		13. TYPE OF REPORT AND PERIOD COVERED Proceedings; 4-11/79 14. SPONSORING AGENCY CODE EPA/600/13

15. SUPPLEMENTARY NOTES IERL-RTP project officer is D. Bruce Harris, Mail Drop 62, 919/541-2557.

16. ABSTRACT

The proceedings consist of 20 reports of research on equipment and techniques for sampling and characterizing particulate emissions and other aerosols. The inhalable particle size range (up to 15 micrometers) is emphasized, and the basis for selecting this range as a standard is discussed. Novel or improved equipment includes: virtual impactors; impactors for sampling high dust loadings; an impactor/quartz-crystal-microbalance combination used to sample stratospheric aerosols; a tapered-element oscillating microbalance for monitoring particulate emissions and aerosols; an automated piezoelectric microbalance for monitoring atmospheric aerosols; a hot-wire probe for measuring liquid droplets; sampling systems that are improvements on EPA Method 5 equipment for measuring mass emissions; and more efficient sampling probe inlets. New or improved techniques include: measurement of aerodynamic diameter by laser/doppler velocimetry of particles accelerated in a converging nozzle; automation of diffusion-battery/condensation nucleus counter systems; sampling inhalable particles in fugitive aerosols; particle-size spectrometry for characterizing inhalation toxicity; computer extrapolation of particle-size ranges; and the identification of impactor errors due to non-ideal behavior to particle deposition in sampling probe nozzles.

17. KEY WORDS AND DOCUMENT ANALYSIS

a. DESCRIPTORS		b. IDENTIFIERS/OPEN ENDED TERMS	c. COSATI Field/Group
Pollution	Analyzing	Pollution Control	13B
Dust		Stationary Sources	11G
Aerosols		Particulate	07D
Measurement		Characterizing	14B
Sampling			
Properties			

18. DISTRIBUTION STATEMENT Release to Public	19. SECURITY CLASS *(This Report)* Unclassified	21. NO. OF PAGES
	20. SECURITY CLASS *(This page)* Unclassified	22. PRICE

EPA Form 2220-1 (9-73)

EPA-600/9-80-004

January 1980

Proceedings:
Advances in Particle Sampling and Measurement
(Daytona Beach, FL, October 1979)

W.B. Smith, Editor

Southern Research Institute
2000 Ninth Avenue, South
Birmingham, Alabama 35205

Contract No. 68-02-3118
Program Element No. EHE624

EPA Project Officer: D. Bruce Harris

Industrial Environmental Research Laboratory
Office of Environmental Engineering and Technology
Research Triangle Park, NC 27711

Prepared for

U.S. ENVIRONMENTAL PROTECTION AGENCY
Office of Research and Development
Washington, DC 20460

i. a

PREFACE

The symposium was sponsored by the Process Measurements Branch, Industrial Environmental Research Laboratory, U.S. Environmental Protection Agency. D. Bruce Harris, EPA, served as chairman. Session chairmen were Robert Carr (Electric Power Research Institute), W.B. Kuykendal (EPA), Benjamin Y.H. Liu (University of Minnesota), Otto Raabe (University of California-Davis), and Herbert Spencer, III (Joy Manufacturing Co.). A.B. Craig, Director of the Industrial Processes Division of EPA, delivered a welcoming address.

A list of reports on the research supported by the Process Measurements Branch can be obtained from Mrs. Judy Ford, MD-62, Process Measurements Branch, Industrial Environmental Research Laboratory, U.S. Environmental Protection Agency, Research Triangle Park, NC 27711.

CONTENTS

Preface iii
Speakers and Chairmen vii

Paper 1. An Experimental Study of Virtual Impactors
Thomas J. Yule and Christopher G. Broniarek 1

Paper 2. A Theoretical Study of Virtual Impactors
Virgil A. Marple and Chung M. Chien 22

Paper 3. A Heavy Grain-Loading Impactor
Dale A. Lundgren, Ernest R. Cerini and Michael L. Smith 54

Paper 4. Velocimetric Determination of Aerodynamic Diameter in the Range from 0.1 μm to 15 μm
James C. Wilson and Benjamin Y.H. Liu 67

Paper 5. A Prototype Particulate Stack Sampler with Single-Cut Nozzle and Microcomputer Calculating/Display System
John C. Elder, Larry G. Littlefield, and Marvin I. Tillery. . . . 83

Paper 6. The Effects of Nozzle Losses on Impactor Sampling
Kenneth T. Knapp. 101

Paper 7. Dilution Source Sampling System
Robert J. Heinsohn, John W. Davis, and Kenneth T. Knapp 107

Paper 8. Aerosol Characterization with a Quartz Crystal Microbalance Cascade Impactor
David C. Woods and Raymond L. Chuan 130

Paper 9. Extending Precision in a Computer-Based Cascade Impactor Data Reduction System
Jean W. Johnson, B. E. Pyle, and Wallace B. Smith 146

Paper 10. Implementing CIDRS - A Programmer's Perspective
Clinton E. Tatsch 167

Paper 11. Numerical Simulation Studies and Data Reduction for Size Classifying Measurement Techniques
H. Fissan and C. Helsper. 180

Paper 12. Non-Ideal Behavior in Cascade Impactors
Joseph D. McCain and James E. McCormack. 201

Paper 13. Field Testing of Automatic Piezoelectric Microbalances for Outdoor Aerosol Mass Concentration Measurements
Kazuo Tsurubayashi and Hajime Kano 217

Paper 14. A New Real-Time Isokinetic Dust Mass Monitoring System
James C.F. Wang. 242

Paper 15. A New Real-Time Mass Monitoring Instrument: The TEOM
Harvey Patashnick and Georg Rupprecht. 264

Paper 16. New Automated Diffusion Battery/Condensation Nucleus Counter Submicron Sizing System: Description and Comparison with an Electrical Aerosol Analyzer
Gilmore J. Sem, Jugal K. Agarwal, and Charles E. McManus 276

Paper 17. An In-Situ Liquid Droplet Sizing System
Daniel E. Magnus and David S. Mahler 302

Paper 18. Some Aerodynamic Methods for Sampling Inhalable Particles
Wallace B. Smith, Kenneth M. Cushing, M. Christine Thomas, and Rufus R. Wilson, Jr. 316

Paper 19. Deposition of Inhaled Particles and Possible Sampling Methods
Vittorio Prodi, Giuseppe Tarroni, and Carlo Melandri 348

Paper 20. Aerosol Sampling Inlets and Inhalable Particles
Benjamin Y.H. Liu and David Y.H. Pui 382

SPEAKERS AND CHAIRMEN

Robert Carr
Electric Power Research Institute
P.O. Box 10402
Palo Alto, CA 94304
Phone: 415/855-2422 ext. 137

Raymond L. Chuan
Defense Division
Brunswick Corporation
3333 Harbor Boulevard
Costa Mesa, CA 92626
Phone: 714/546-8030

A.B. Craig
Director, Industrial Processes Division
Environmental Protection Agency
Research Triangle Park, NC 27711

Dennis Drehmel
Environmental Protection Agency
Particulate Technology Branch
Utilities & Industrial Power Division
Research Triangle Park, NC 27711

John C. Elder
Aerosol Studies Section
Industrial Hygiene Group
University of California
Los Alamos Scientific Laboratory
P.O. Box 1663
Los Alamos, NM 87545

H. Fissan
Gesamthochschule Duisburg
Aerosolmesstechnik
4100 Duisburg
Bismarckstrasse, 81
Federal Republic of Germany
Phone: 0203 392 202

D. Bruce Harris
Environmental Protection Agency
Industrial Environmental Research Laboratory
Mail Stop MD-62
Research Triangle Park, NC 27711
Phone: 919/541-2557

Robert J. Heinsohn
Pennsylvania State University
Mechanical Engineering Department
University Park, PA 16802
Phone: 814/865-8281

Jean W. Johnson
Southern Research Institute
2000 Ninth Avenue, South
Birmingham, AL 35205
Phone: 205/323-6592 ext. 547

Kenneth T. Knapp
Particulate Emissions Research Section
Environmental Sciences Research Laboratory
Environmental Protection Agency
Environmental Research Center
Mail Stop MD-46
Research Triangle Park, NC 27711
Phone: 919/541-3085

W.B. Kuykendal
Environmental Protection Agency
Industrial Environmental Research Laboratory
Mail Stop MD-62
Research Triangle Park, NC 27711
Phone: 919/541-2557

Benjamin Y.H. Liu
University of Minnesota
Department of Mechanical Engineering
125 Mechanical Engineering
111 Church Street S.E.
Minneapolis, MN 55455
Phone: 612/373-3043

Dale A. Lundgren
University of Florida
Department of Environmental Engineering Sciences
A.P. Black Hall
Gainesville, FL 32611
Phone: 904/392-0846

Dan Magnus
KLD Associates, Inc.
300 Broadway
Huntington Station, NY 11746
Phone: 561/549-9803

Virgil A. Marple
University of Minnesota
Mechanical Engineering Department
111 Church Street S.E.
Minneapolis, MN 55455
Phone: 612/373-9984

Joseph D. McCain
Southern Research Institute
2000 Ninth Avenue, South
Birmingham, AL 35205
Phone: 205/323-6952 ext. 278

Harvey Patashnick
Rupprecht and Patashnick Company
255 Hackett Boulevard
Albany, NY 12208
Phone: 518/438-5569

Vittorio Prodi
Comitato Nazionale per L'Energia
Nucleare
Centro di Calcolo
Laboratorio Fisica Sanitaria
Bologna
Via Massini, 2 - Cap 40138
Italy

Otto Raabe
Laboratory of Radiobiology
University of California - Davis
Davis, CA 95616
Phone: 916/752-7754

Gilmore Sem
TSI Incorporated
500 Cardigan Road
P.O. Box 3394
St. Paul, MN 55165
Phone: 612/483-0900

Wallace B. Smith
Southern Research Institute
2000 Ninth Avenue, South
Birmingham, AL 35205
Phone: 205/323-6592 ext. 520

Herbert Spencer, III
Western Precipitators Division
Joy Manufacturing Company
565 Colorado Boulevard
P.O. Box 2744, Terminal Annex
Los Angeles, CA 90051
Phone: 213/240-2300

C.E. Tatsch
Research Triangle Institute
P.O. Box 12194
Research Triangle Park, NC 27709
Phone: 919/541-6000

Kazuo Tsurubayashi
Nihon Kagaku Kogyo Co., Ltd.
Head Office, 2-1
Shimizu, Suita
Osaka
Japan

James C.F. Wang
Combustion Research Division
Sandia Laboratories
Livermore, CA 94550

James C. Wilson
University of Minnesota
Department of Mechanical
Engineering
125 Mechanical Engineering
111 Church Street S.E.
Minneapolis, MN 55455
Phone: 612/373-9984

David C. Woods
NASA Langley Research Center
Hampton, VA 23665

Thomas J. Yule
Applied Physics Division
Argonne National Laboratory
9700 South Cass Avenue
Argonne, IL 60439
Phone: 312/739-7711

PAPER 1

AN EXPERIMENTAL STUDY OF VIRTUAL IMPACTORS

THOMAS J. YULE
ARGONNE NATIONAL LABORATORY

AND

CHRISTOPHER G. BRONIAREK
RENSSELAER POLYTECHNIC INSTITUTE

ABSTRACT

Virtual impactors are currently being used in a number of instruments to separate an aerosol into different size ranges. The virtual impactor is a variation of the standard impactor in which the impaction surface is replaced by an orifice into which particles can pass and be collected or counted. We have made an experimental study of the collection characteristics of virtual impactors. The parameters varied included: acceleration nozzle-to-collection probe distance, the ratio of the collection probe-to-acceleration nozzle diameters, and the ratio of collection probe-to-inlet flows. Measurements were also made with different collection probe geometries. It was found that it is possible to parameterize much of the data by introduction of the Stokes number and an effective minor flow collection efficiency. One disadvantage of the virtual impactor is that in the transition region particles are collected on the inside walls of the collection probe near the probe tip. The amount that is collected is a sensitive function of the probe geometry.

INTRODUCTION

Virtual impactors are currently being used in a number of instruments to separate an aerosol into different size ranges. The virtual impactor is a variation of the standard impactor in which the impaction surface is replaced by a collection probe into which large particles will pass and then be collected or counted. Figure 1 is a schematic illustrating the operation of a virtual impactor. The aerosol stream is drawn through the acceleration nozzle where the velocity of the particles is increased. A collection probe is located at a short distance below

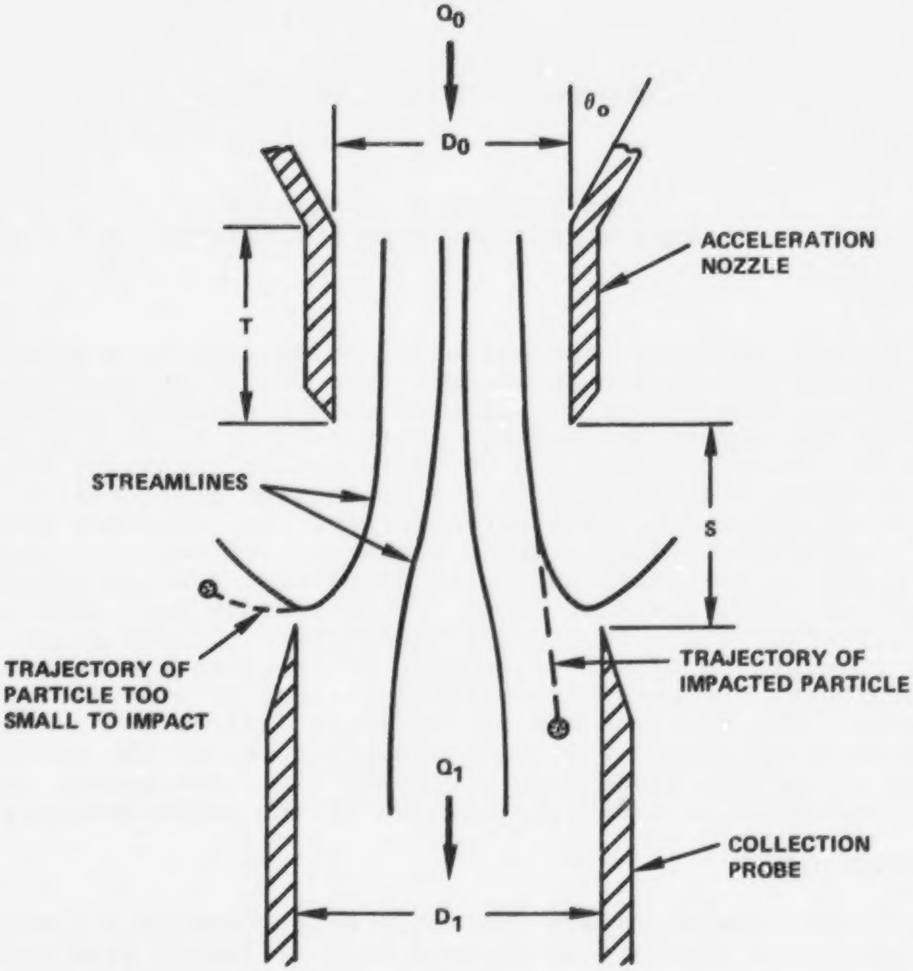
Q0
θo
D0
ACCELERATION NOZZLE
T
STREAMLINES
S
TRAJECTORY OF PARTICLE TOO SMALL TO IMPACT
TRAJECTORY OF IMPACTED PARTICLE
Q1
COLLECTION PROBE
D1

Figure 1. Schematic view of a virtual impactor showing representative streamlines and particle trajectories.

the acceleration nozzle. Flow conditions are maintained such that the flow in the collection probe is a fixed fraction of the inlet flow. A few representative streamlines are shown on the figure.

In order to understand the principle of operation, consider particles that exit from the acceleration nozzle near streamlines which do not pass through the collection probe. Small particles follow the streamlines and remain in the flow that does not pass through the collection probe; large particles are unable to follow the streamlines in regions of rapidly changing curvature and become caught up in the flow that passes through the collection probe. The flow in the collection probe, Q_1, is referred to as the minor flow. The ratio Q_1/Q_0, where Q_0 is the inlet flow, ranges in value from 0.03 to 0.25 in present designs. For zero particle size a fraction of the particles equal to Q_1/Q_0 follow the streamlines of the minor flow and pass through the collection probe. The small particles that enter the collection probe along with the large particles introduce cross contamination. The flow which does not enter the collection probe is referred to as the major flow; it contains most of the small particles.

Virtual impactors possess a number of advantages over standard impactors. These are: the size and placement of the size-separated sample can be optimized for the analysis system, particle bounce and reentrainment are minimized, and significant amounts of a sample can be collected without serious loading problems and without change in collection efficiency. There are also disadvantages. These are: the slope of the efficiency curve is less steep than that for a well-designed standard impactor, there is always some cross contamination, and some of the sample is collected on the inside walls of the collection probe.

The method of virtual impaction was introduced by Hounam and Sherwood[1] in 1965. They designed and constructed a multistage device called a cascade centripeter, which had cutpoints of 1.2, 3.5, and 12 micrometers. Flat orifice plates were used instead of acceleration nozzles. Their device had considerable wall losses. Shortly afterward, Conner[2] investigated the collection efficiency of a single-stage virtual impactor as a function of operating parameters.

More recently, interest in virtual impactors has been heightened by the U.S. Environmental Protection Agency's desire for a device which collects size-segregated ambient aerosol samples for large-scale monitoring applications. The device, which is referred to as a dichotomous sampler, separately collects fine (<2.5 micrometer) and coarse (>2.5 micrometer) airborne particles. An early design, which has two stages, is described by Dzubay and Stevens[3] and Loo, et al.[4] A second generation sampler, which has only a single stage and very low internal losses, has been developed by Loo, et al.[5] Virtual impactors have also appeared in other devices. McFarland, et al.[6] have developed a sampler that was used to collect large quantities of particulate matter from the stack of a coal-fired power plant. Kotrappa, et al.[7] and Yule[8] have used virtual impactors to size segregate radioactive aerosols in radiation detection instruments.

To aid in the development of the devices described above, various experimental studies on virtual impactors were undertaken. The most extensive studies are those by Loo, et al.[4] and by McFarland, et al.[9] Both studies were aimed at determining the optimum parameters for attaining sharp cutoffs with minimum internal losses for particular systems. The study reported here is somewhat broader in scope. It was undertaken to provide sufficient information to determine the cutoff size and collection characteristics for a wide range of system parameters. The study was patterned after the study on standard impactors by Marple and Liu.[10]

There have also been some theoretical studies of virtual impactors by Marple and Chien[11] and by Hassan, et al.[12] In general, these studies have given insight into the separation characteristics, but the agreement between measured and predicted data is not as good as that for the standard impactor.

EXPERIMENTAL METHODS

The collection characteristics of virtual impactors were studied using monodisperse aerosols. Most of the measurements were made with dioctyl phthalate (DOP) droplets, which contained trace amounts of uranine (the sodium salt of fluorescein) dye as a tracer. Aerosols with sizes from 1 to 10 micrometers were generated with a Berglund-Liu vibrating-orifice aerosol generator. Some measurements were also made with polystyrene latex (PSL) aerosols. The PSL aerosol generator consisted of a nebulizer, diluter, diffusion dryer, and Kr-85 charge neutralizer. The collection characteristics for the two aerosols are expected to be different since one is a liquid droplet which will stick on contacting a surface, while the other is an elastic sphere which can rebound from a surface. The results obtained with the DOP aerosols represent an upper limit for collection on surfaces of the virtual impactor and are easier to compare with calculated results, because one can assume any droplet that comes in contact with a surface will stick to that surface.

Figure 2 is a schematic view of the single-stage virtual-impactor test assembly that was used for the measurements. The assembly allows one to easily change the acceleration nozzle and collection probe geometries. For measurements with the DOP aerosols the quality of the aerosols was monitored with an optical particle counter that had the probe located in a region

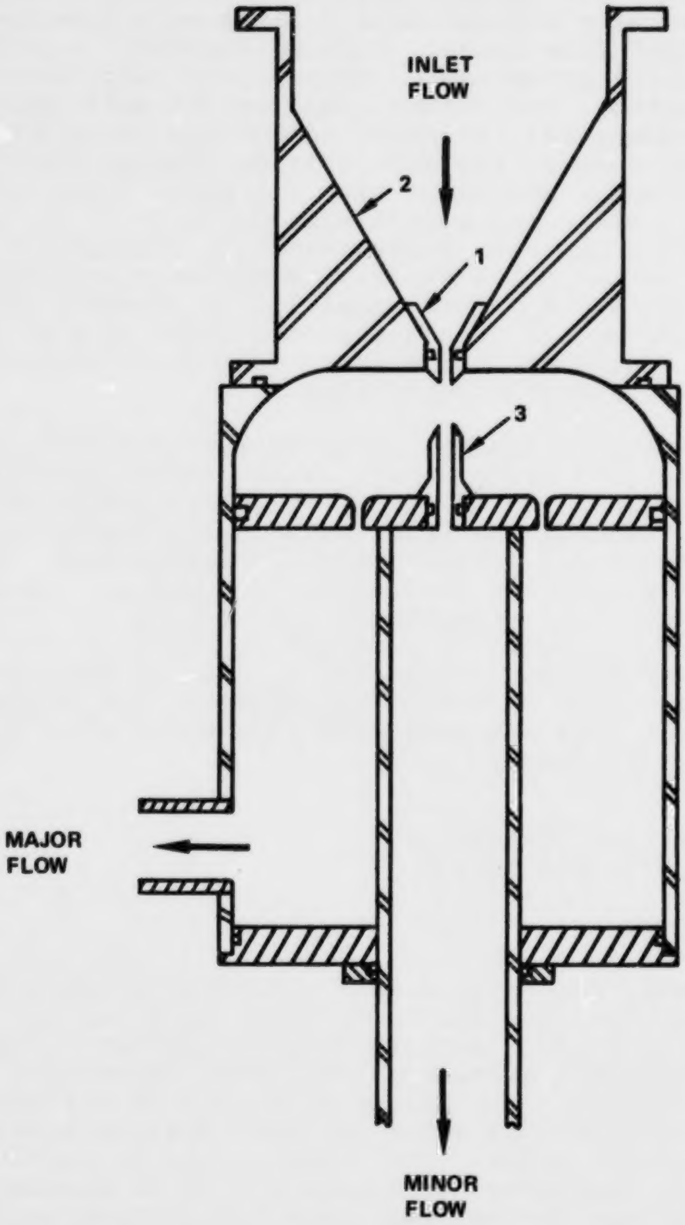
INLET FLOW
2
1
3
MAJOR FLOW
MINOR FLOW

Figure 2. Apparatus for measuring the collection characteristics of virtual impactors. Some of the key components are indicated: 1. acceleration nozzle, 2. flow transition cone, and 3. collection probe.

above the inlet. A Bausch and Lomb 40-1A counter was used with a modified flow system, as described by Marple, et al.,[13] and with interface electronics that allows pulse-height analysis with a multichannel analyzer. Such a monitor is very useful in determining whether the aerosol generator is operating properly. For the measurements with DOP aerosols filters were inserted in the minor and major flow lines. Flow measurements were made with pressure-corrected rotameters. Measurement times were on the order of 15 minutes. The aerosol depositions were determined on various components: the underside of the piece supporting the acceleration nozzle, the acceleration nozzle, the collection probe, and the major and minor flow filters. These are the only areas where there are significant deposits. The deposits were determined by washing the pieces or filters in measured amounts of a buffer solution (0.05 M Na_2HPO_4) and using fluorescence techniques. A Turner Model 110 fluorometer was used; calibration curves had been determined which relate the absorption to the uranine concentration. Concentrations as low as 0.005 μg/ml can be reliably determined.

For measurements with the PSL aerosols two aerosol sizes were used: 1.10 and 2.02 micrometers. The optical particle counter probe was placed in a region below the collection probe. For these measurements only the fraction of the incoming aerosol that passed through the collection probe was determined. For a given particle size and flow conditions, the aerosol concentrations before and after each measurement were determined by setting the major flow, Q_2, equal to zero and Q_0 equal to the nominal value of Q_1. The average concentration, $\bar{C}_{Q_2=0}$, was determined. With the nominal values of Q_0 and Q_2 established, the concentration, C, in the minor flow was measured. The minor flow collection efficiency, E_m, is simply

$$E_m = \frac{C}{(Q_0/Q_1)\ \bar{C}_{Q_2=0}} . \qquad (1)$$

RESULTS AND DISCUSSION

A series of measurements were made with DOP aerosols in which various geometrical and flow conditions were varied. A virtual impactor with geometrical and flow parameters listed in Table 1 was chosen as a standard; individual parameters were varied about these values. A value of $D_1/D_0 = 1.28$ was chosen for the standard, because this value results in minimum wall losses in the collection probe. The shape of the collection probe is the same as that shown in Figure 1. As is discussed below, this shape is not the optimum shape for minimum collection on the interior walls of the collection probe; however, it is a shape that has been used in a number of devices and is easy to treat analytically. Figure 3 shows the collection characteristics for the standard. Since the deposits in the acceleration nozzle and on the underside of the piece supporting the

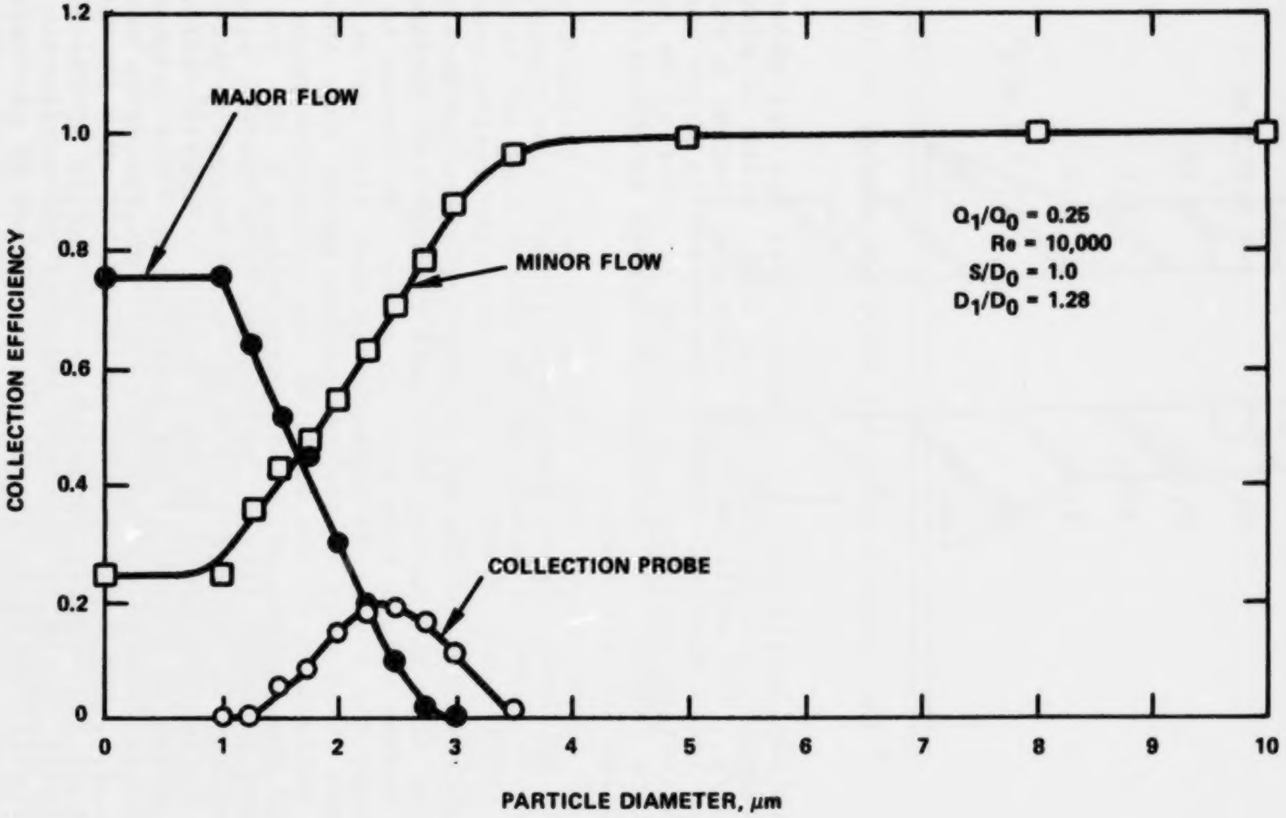

Figure 3. Collection efficiencies for the standard virtual impactor.

TABLE 1. GEOMETRICAL AND FLOW PARAMETERS FOR THE STANDARD VIRTUAL IMPACTOR

Parameter	Value
D_0	3.912 mm
D_1/D_0	1.28
S/D_0	1.0
T/D_0	2.0
Q_0	27.7 ℓ/min[a]
Q_1/Q_0	0.25

[a] Corresponds to a jet Reynolds number of 10,000.

acceleration nozzle were very small, they are not shown. The minor flow collection efficiency is 0.25, which is simply the ratio Q_1/Q_0, for small particle sizes and reaches a value of 1.00 for large particle sizes. The region in which the minor flow collection efficiency is varying is referred to as the transition region. It is useful to define an effective minor flow collection efficiency, E_m',

$$E_m' = \frac{E_m - Q_1/Q_0}{1 - Q_1/Q_0} , \qquad (2)$$

which corresponds to the efficiency for removing particles from the major flow and having them pass through the collection probe. E_m' may assume values from zero to unity. We choose to define the cutoff for a virtual impactor as that size for which $E_m' = 0.5$. Note that it is only in the transition region that there is significant collection on the walls of the collection probe. For the standard the maximum value is approximately 0.20. For aerosols that have a probability of rebounding from contact with a wall, this maximum is reduced. In order to investigate the wall losses in the collection probe in more detail, a special collection probe, shown in Figure 4, was constructed. The thickness of the annular inserts was one-third D_0. Measurements were made with 2, 2.5, and 3 micrometer DOP aerosols. For all sizes close to 100% of the deposit appeared on the inside of the top ring. This result indicates that the shape of the collection probe could significantly influence the magnitude of the wall losses in the transition region.

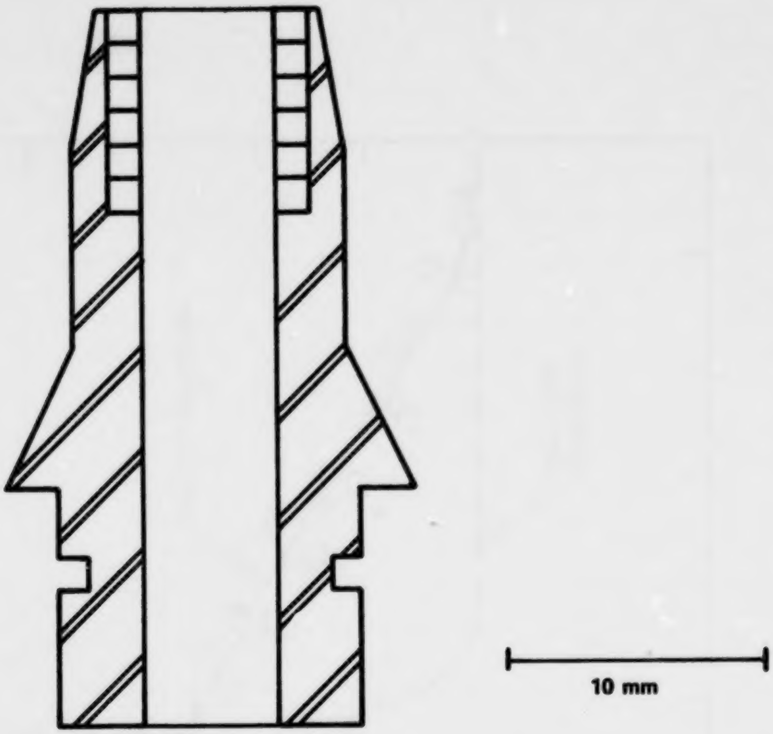

Figure 4. Modified collection probe with annular inserts.

For standard impactors it has been found useful to show the characteristic impaction curves with the abscissa expressed in units of the square root of the Stokes number, $\sqrt{St}$, which is a dimensionless particle size.[10] The Stokes number, as defined by Fuchs,[14] is the ratio of the particle stopping distance to the radius of the impactor throat,

$$St = \frac{\rho_p \; C \; V_0 \; D_p^{\,2}/18\mu}{D_0/2} \; , \tag{3}$$

where ρ_p is the particle density, C is the Cunningham slip correction factor, V_0 is the mean velocity in the throat, D_p is the particle diameter, μ is the fluid viscosity, and D_0 is the diameter of the throat. When plotted in this fashion, it has been found that the impaction curves are only slowly varying functions of S/D, the Reynolds number, and T/D. (See Figure 1 for definitions of S and T.) A similar representation is useful for showing the collection curves for virtual impactors. Figure 5 shows E_m as a function of $\sqrt{St}$ for measurements for which Q_1/Q_0, S/D_0, D_1/D_0, and T/D_0 were held constant and D_0, D_p, and Q_0 were varied. Two values of D_0 were used; 0.3048 and the standard 0.3912 cm. For a particular data set either Q_0 was

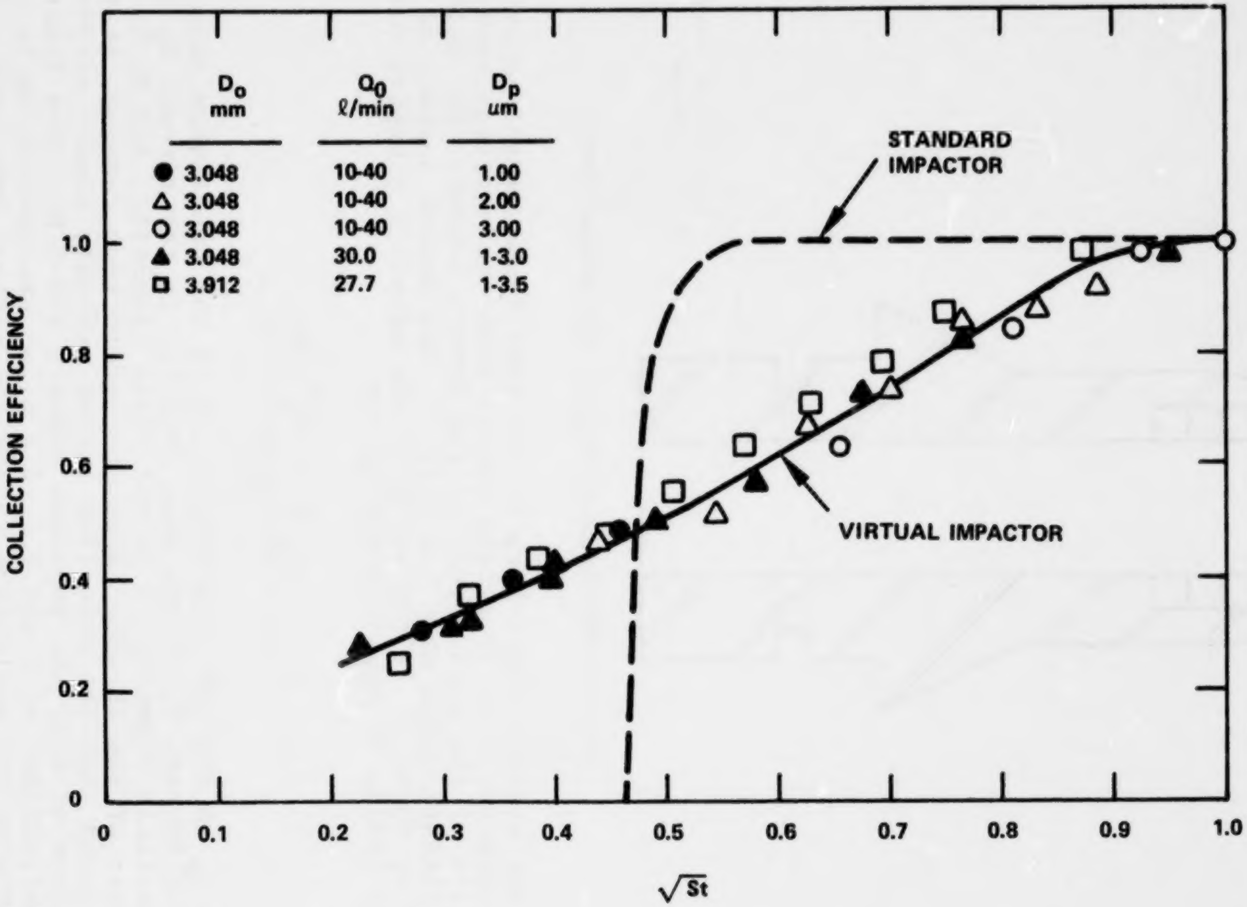

Figure 5. Minor flow collection efficiencies for virtual impactors having $Q_1/Q_0 = 0.25$, $S/D_0 = 1.0$, and $D_1/D_0 = 1.28$, and for which D_0, Q_0, and D_p were varied. The dashed curve shows the collection efficiency for a well-designed standard impactor.

varied and D_p kept constant, or D_p was varied and Q_0 kept constant. For the former, this corresponds to a variation in Reynolds number, Re, of a factor of four. In general, all the data for D_0 = 0.3048 cm fall on a single curve, while those for D_0 = 0.3912 cm lie slightly above the curve. This small variation is almost entirely due to different finishes on the inside walls of the collection probes. The inside wall of the larger probe was polished and had a maximum collection of 0.20, whereas the other one had a rougher surface and had a maximum collection of 0.25. A typical collection curve for a standard impactor is also shown on the figure; it is significantly steeper.

The collection characteristics of virtual impactors as a function of S/D_0, D_1/D_0, and Q_1/Q_0 were determined. The variation with T/D_0 was not determined. The analytical studies indicate that it should be small for T/D_0 values greater than one-half. Studies were not made of the variation in collection characteristics for wide ranges of Reynolds numbers, since the analytical studies indicate that to see a significant deviation, it would be necessary to go to very low values of the Reynolds number. Such measurements would have been quite interesting, but would have required a complete redesign of the experimental apparatus. Figure 6 shows the variation in the collection characteristics for 2-micrometer size particles as a function of S/D_0, with all other parameters fixed at those of the standard. This variation with S/D_0 is significantly greater than that seen for a standard impactor and is related to the divergence of the jet as S/D_0 increases. Figure 7 shows the variation in the collection characteristics for 2 and 10-micrometer size particles as a function of D_1/D_0. For the 2-micrometer size particles the collection on the walls of the probe significantly increases for D_1/D_0 greater than 1.6. Studies by Loo, et al.[4] with solid particles show similar results and also indicate that a minimum occurs at about D_1/D_0 = 1.3. For the 10-micrometer size particles increased wall losses in the collection probe begin at D_1/D_0 greater than 1.4.

The ratio Q_1/Q_0 was also varied. Figure 8 shows the results for Q_1/Q_0 = 0.10. The transition region is moved to larger particle sizes. The peak of the collection-probe wall-losses curve stays at around 0.20. There is also a small amount collected on the underside of the acceleration nozzle and on the acceleration nozzle support structure. Figure 9 shows the results for Q_1/Q_0 = 0.03. The transition region is moved to even larger particle sizes. The peak of the collection-probe wall-losses curve increases to about 0.30. In order to parameterize these results it is convenient to use the effective minor flow collection efficiency, E'_m, which was previously defined. Figure 10 shows E'_m versus $\sqrt{St}$ for various values of Q_1/Q_0. It is seen that over a significant portion of the transition region the

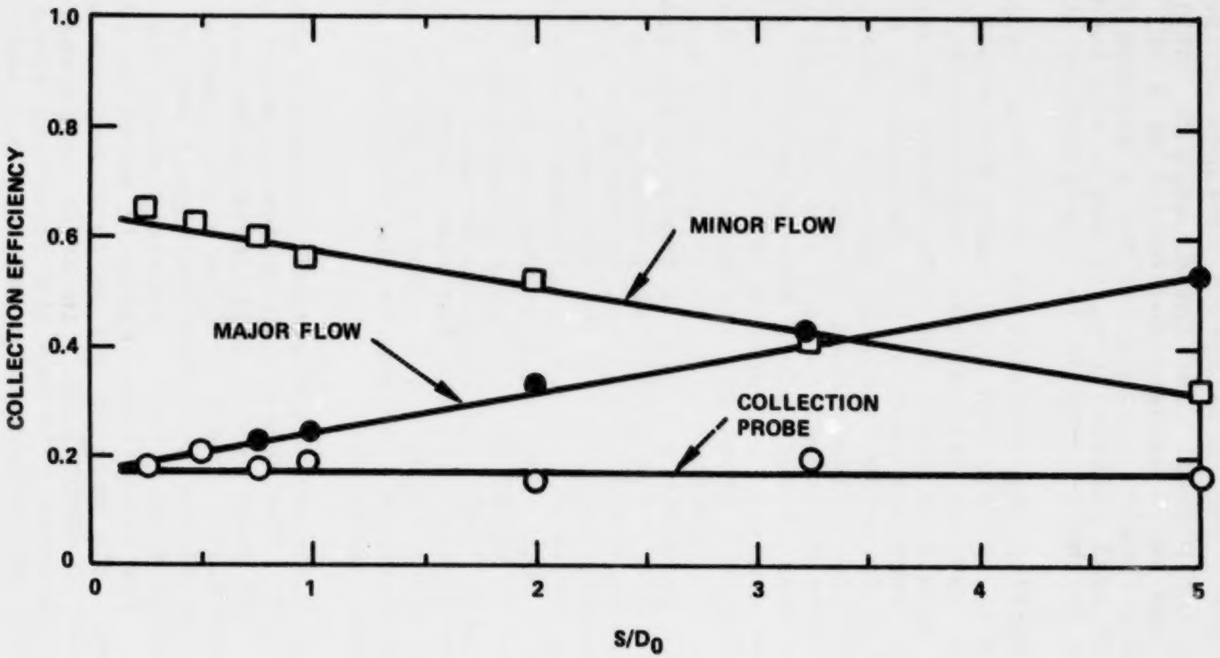

Figure 6. Variation in the collection efficiencies for 2-micrometer size particles as a function of S/D_0.

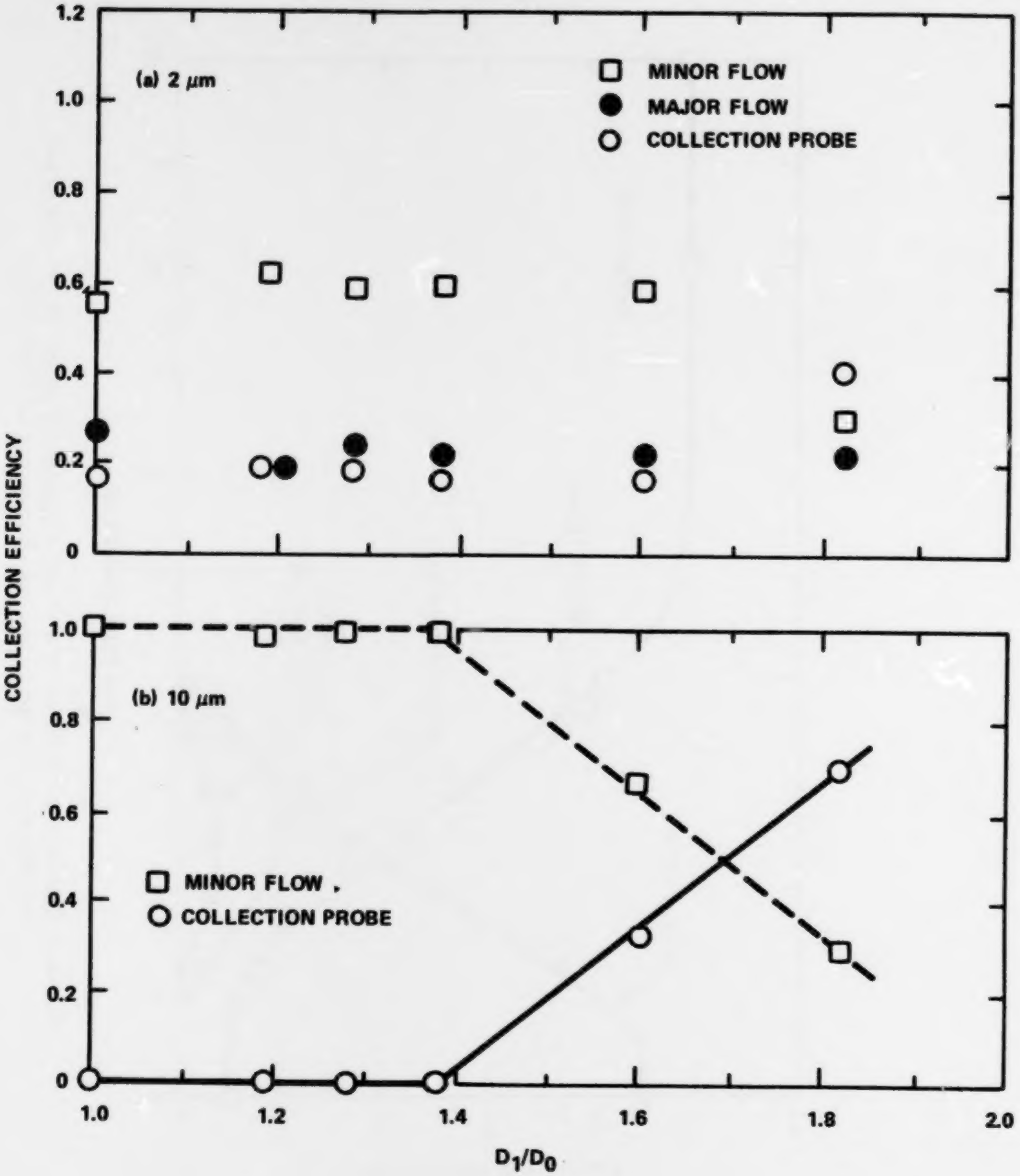

Figure 7. Variation in the collection efficiencies for 2 and 10-micrometer size particles as a function of D_1/D_0.

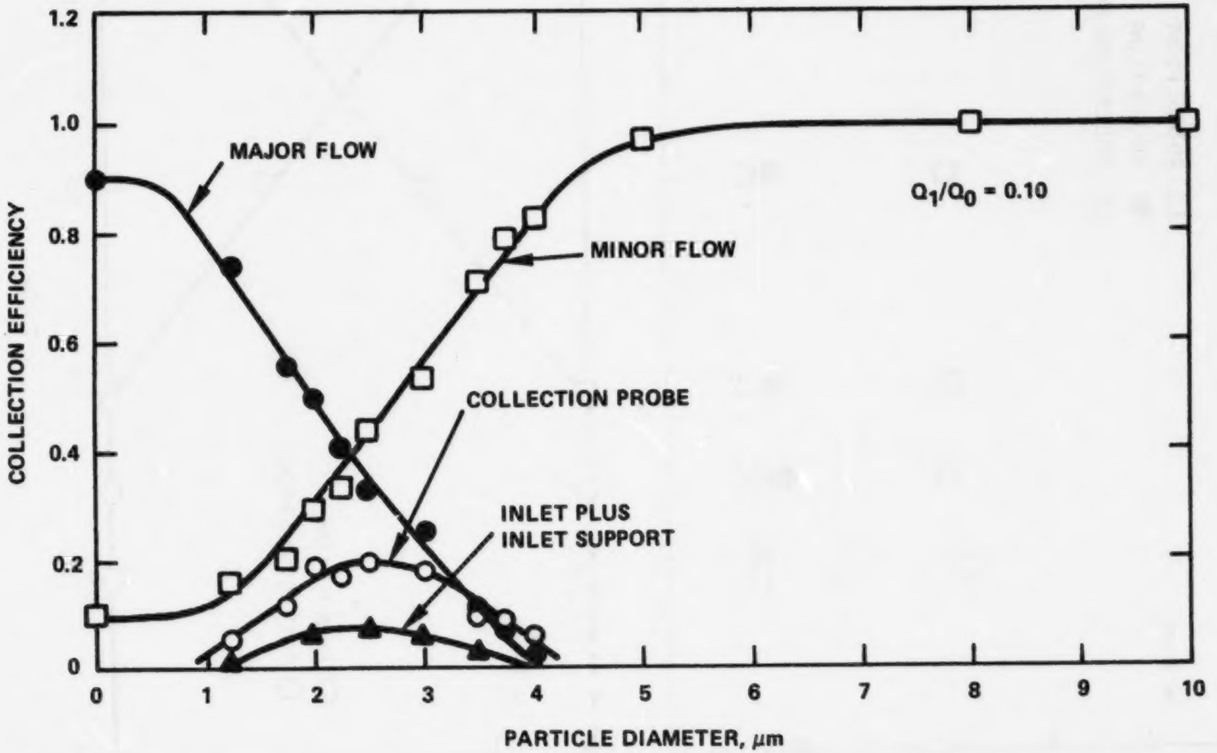

Figure 8. Collection efficiencies for a virtual impactor for which all the parameters are the same as those for the standard except $Q_1/Q_0 = 0.10$.

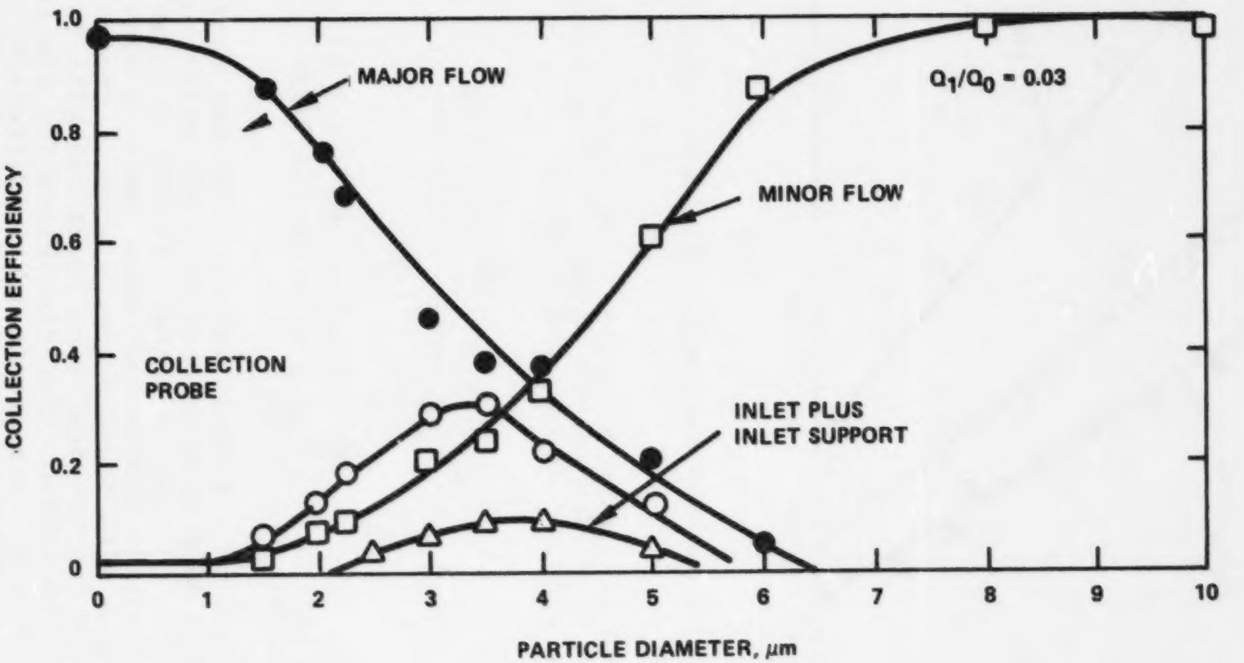

Figure 9. Collection efficiencies for a virtual impactor for which all the parameters are the same as those for the standard except $Q_1/Q_0 = 0.03$.

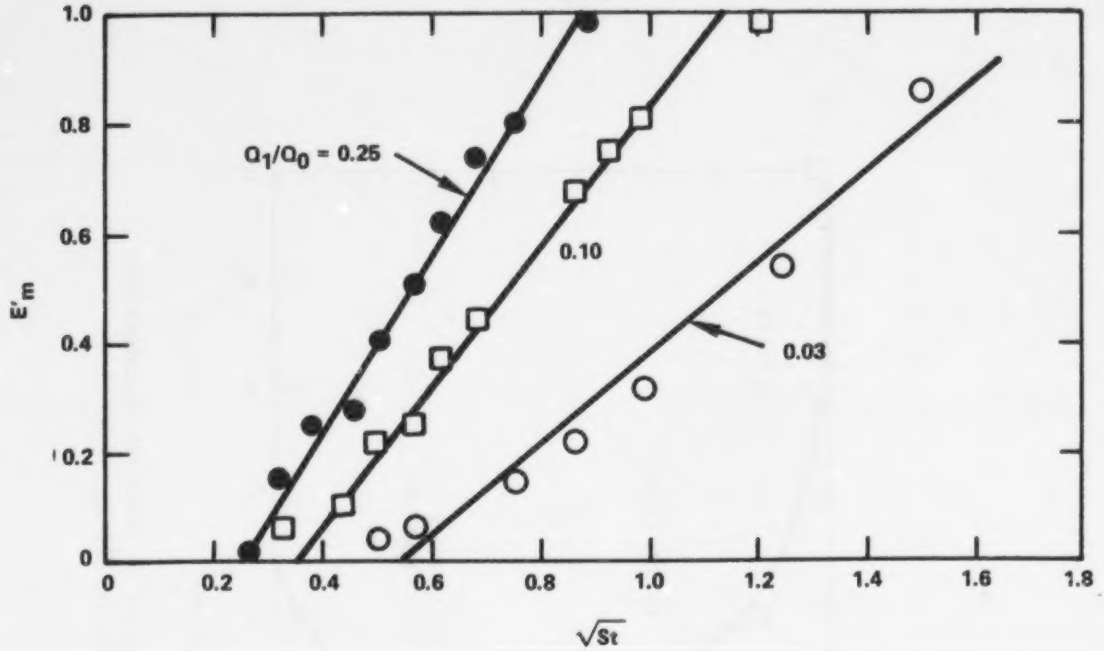

Figure 10. Effective minor flow collection efficiencies for various values of Q_1/Q_0.

data is fitted by a straight line. The line may be characterized by specifying the value of $\sqrt{St}$ at $E'_m = 0.50$ and the rate of change of the line, R, which is defined as

$$R = \frac{\sqrt{St}_{E'_m = 0.80} - \sqrt{St}_{E'_m = 0.20}}{\sqrt{St}_{E'_m = 0.50}} , \qquad (4)$$

where the subscript on $\sqrt{St}$ indicates the value of E'_m. Figure 11 shows the variation of $\sqrt{St}_{E'_m = 0.50}$ versus Q_1/Q_0. R remained constant at a value of 0.65.

In addition to the measurements described above, a number of measurements were made to determine the effect of changing the shape of the collection probe. Figure 12 shows two different shapes of collection probes that were used: a disc with a hole in it and a tube with rounded inside edges. The collection characteristics for the disc were identical with those for the standard. The collection characteristics for the tube with rounded inside edges were significantly different. The collection-probe wall-losses curve had approximately the same shape as that for the standard, but the magnitude was decreased by about 35%. There was a corresponding change in the collection curve for the major flow, while the collection curve for the

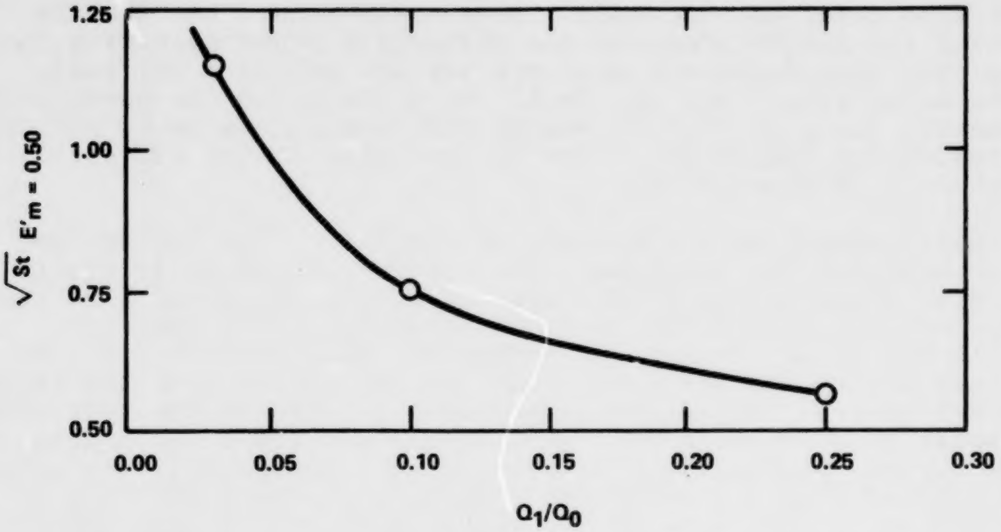

Figure 11. The variation in $\sqrt{St}$ at which the effective minor flow collection efficiency is 0.50 as a function of Q_1/Q_0.

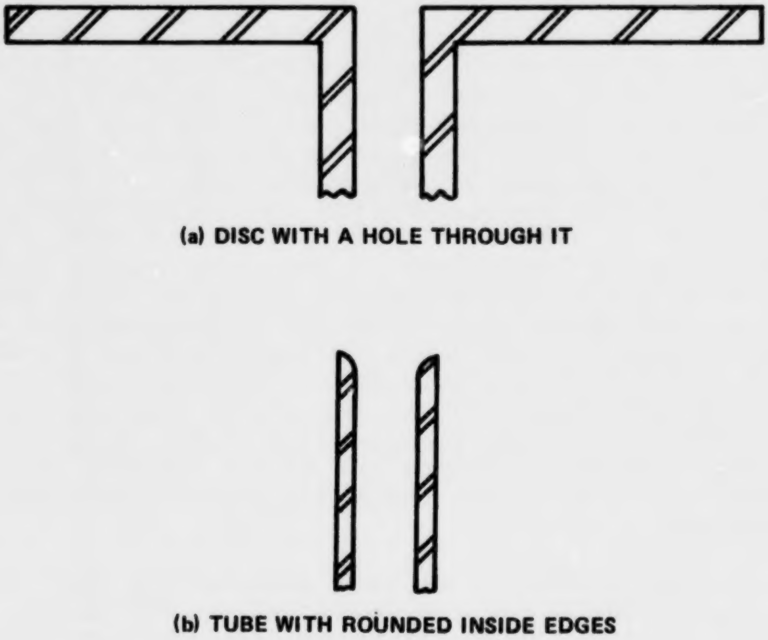
(a) DISC WITH A HOLE THROUGH IT

(b) TUBE WITH ROUNDED INSIDE EDGES

Figure 12. Modified collection probes.

minor flow remained unchanged. This result indicates that by rounding the inside edges of the collection probe particles that would have been deposited near the top are now able to remain in the major flow. Loo and Cork[15] have optimized the geometrical parameters for a particular design and have been able to reduce the losses for liquid particles to less than 1% for all particle sizes up to 20 micrometers.

Measurements were also made of the minor flow collection efficiency with PSL aerosols. The results are shown in Figure 13. Also shown on the figure are the curves for minor flow and receiving tube collection with DOP aerosols. Note that the results are quite similar for values of $\sqrt{St}$ less than 0.5, but that the DOP values are lower than the PSL values over the range from 0.5 to 0.9. The differences are explained by the fact that a droplet on striking a wall will stick, whereas a PSL sphere has a certain probability for rebounding. Apparently, the spheres that rebound from the walls can either enter the minor flow or be swept out of the tube in the major flow. The former appears to be much more likely for spheres with values of $\sqrt{St}$ near 0.8, the latter for those with values less than 0.5. Loo, et al.[4] found that with solid aerosols of uranine the maximum collection in the receiving tube with this geometry was only a few percent.

CONCLUSIONS

The purpose of this study was twofold: 1) to provide data that is useful in designing systems which employ virtual impactors, and 2) to develop an improved understanding of the principles of operation of virtual impactors. It was found that it is possible to parameterize much of the data by the introduction of the Stokes number and an effective minor flow collection efficiency. For given Q_1/Q_0, D_1/D_0, and S/D_0, there is a single curve which represents the minor flow collection efficiency as a function of $\sqrt{St}$. Analytical studies indicate that the curve should apply to quite low values of Reynolds number.[11] For different values of Q_1/Q_0, E_m' versus $\sqrt{St}$ is rather well represented by a straight line whose rate of change stays constant and for which $\sqrt{St}_{E_m' = 0.50}$ is a smoothly decreasing function of Q_1/Q_0. Thus, Figures 10 and 11 can be used to determine effective minor flow collection efficiency curves for a wide range of system parameters. The study also indicated that the collection efficiencies for virtual impactors are more dependent on S/D_0 for values greater than one, than the collection efficiency for a standard impactor.

One disadvantage of the virtual impactor is that in the transition region particles are collected on the inside walls of the collection probe near the probe tip. It was found in this study and in the study by Loo, et al.[4] that this collection is minimized if D_1/D_0 is kept at a value of about 1.3. Furthermore, the amount that is collected is a sensitive function of

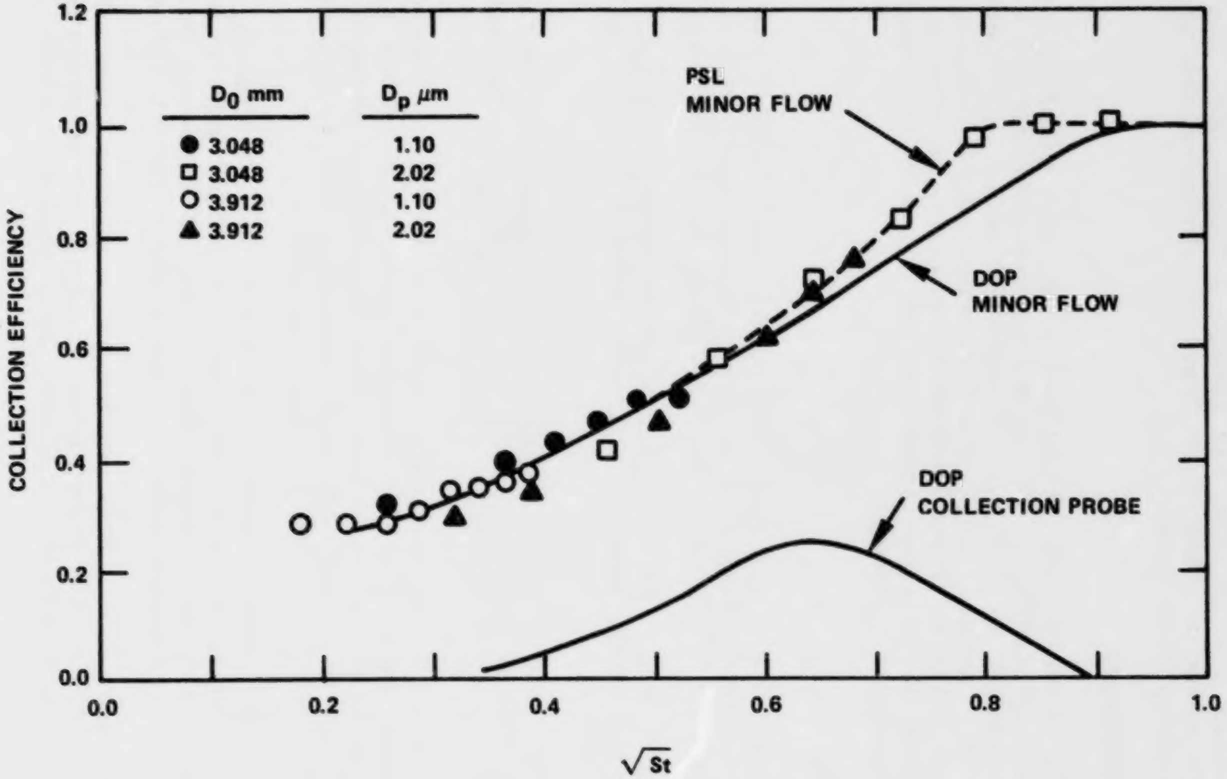

Figure 13. Collection efficiencies for virtual impactors for which $Q_1/Q_0 = 0.25$, $S/D_0 = 1.0$, and $D_1/D_0 = 1.28$ for PSL and DOP aerosols.

the probe geometry. Rounding the inside of the probe tip, polishing this surface, and maintaining good alignment between the acceleration nozzle and collection probe minimizes the amount collected. Using trial-and-error methods, Loo and Cork[15] have been able to minimize the collection peak to less than 1% for a particular set of flow and geometry conditions. At this time it is not known whether such dramatic improvements are possible for arbitrary flow conditions.

ACKNOWLEDGEMENT

This research was performed under the auspices of the U.S. Department of Energy. The submitted manuscript has been authored by a contractor of the U.S. Government under contract No. W-31-109-ENG-38. Accordingly, the U.S. Government retains a nonexclusive, royalty-free license to publish or reproduce the published form of this contribution, or allow others to do so, for U.S. Government purposes.

REFERENCES

1. Hounam, R.F., and R.J. Sherwood. The Cascade Centripeter: A Device for Determining the Concentration and Size Distribution of Aerosols. Am. Ind. Hyg. J. 26:122-131, 1965.

2. Conner, W.D. An Inertial-Type Particle Separator for Collecting Large Samples. J. Air Pollut. Control Assoc. 16(1):35-38, 1966.

3. Dzubay, T.G., and R.K. Stevens. Ambient Air Analysis with Dichotomous Sampler and X-Ray Fluorescence Spectrometer. Environ. Sci. Technol. 9(7):663-668, 1975.

4. Loo, B.W., J.M. Jaklevic, and F.S. Goulding. Dichotomous Virtual Impactors for Large-Scale Monitoring of Airborne Particulate Matter. In: Fine Particles: Aerosol Generation, Measurement, Sampling, and Analysis, B.Y.H. Liu, ed. Academic Press, New York, 1976. pp. 311-350.

5. Loo, B.W., R.S. Adachi, C.P. Cork, F.S. Goulding, J.M. Jaklevic, D.A. Landis, and W.L. Searles. A Second Generation Dichotomous Sampler for Large-Scale Monitoring of Airborne Particulate Matter. Lawrence Berkeley Laboratory Report LBL-8725, 1979.

6. McFarland, A.R., R.W. Bertch, G.L. Fisher, and B.A. Prentice. Fractionator for Size Classification of Aerosolized Solid Particulate Matter. Environ. Sci. Technol. 11(8):781-784, 1977.

7. Kotrappa, P., D.P. Bhanti, S.K. Dua, and P.P. Joshi. A Single Stage Centripeter for Rapid Analysis of Long-Lived Alpha Emitters in Air. Health Phys. 27:103-108, 1974.

8. Yule, T.J. An On-Line Monitor for Alpha-Emitting Aerosols. IEEE Trans. Nucl. Sci. NS-25(1):762-766, 1978.

9. McFarland, A.R., C.A. Ortiz, and R.W. Bertch, Jr. Particle Collection Characteristics of a Single-Stage Dichotomous Sampler. Environ. Sci. Technol. 12(6):679-682, 1978.

10. Marple, V.A., and B.Y.H. Liu. Characteristics of Laminar Jet Impactors. Environ. Sci. Technol. 8(7):648-654, 1974.

11. Marple, V.A., and C.M. Chien. A Theoretical Study of Virtual Impactors. University of Minnesota, Particle Technology Laboratory Publication 378, 1978. Submitted to Environ. Sci. Technol.

12. Hassan, Y.A., B.G. Jones, and T.J. Yule. An Analytical Study of Virtual Impactor Aerosol Separators. To be published in Trans. Am. Nucl. Soc., San Francisco Meeting, 1979.

13. Marple, V.A., N.J. Barsic, and K.T. Whitby. Instruments and Techniques for Dynamic Particle Size Measurements of Coal Dust. University of Minnesota, Particle Technology Laboratory Publication 215, 1974.

14. Fuchs, N.A. The Mechanics of Aerosols. Pergamon Press, New York, 1964.

15. Loo, B.W., and C.P. Cork. High-Efficiency Virtual Impactors. Submitted to Environ. Sci. Technol.

PAPER 2

A THEORETICAL STUDY OF VIRTUAL IMPACTORS

VIRGIL A. MARPLE
CHUNG M. CHIEN
PARTICLE TECHNOLOGY LABORATORY
MECHANICAL ENGINEERING DEPARTMENT
UNIVERSITY OF MINNESOTA

ABSTRACT

The characteristics of virtual impactors have been determined by the numerical solution of the Navier-Stokes equations and of the equations of motion of the particles. The effect of the nozzle Reynolds number, the fraction of flow passing through the collection probe, collection probe diameter, nozzle throat length, nozzle-to-collection probe distance, and collection probe inlet design on the small and large particle collection efficiencies has been studied. In addition, it was found that some particles would impact on the inner surface of the collection probe. The results show that most parameters, with the exception of the nozzle Reynolds number, have little effect on the large particle collection efficiency. However, the effect on the small particle collection efficiency and collection probe losses was significant for many of these parameters.

INTRODUCTION

The virtual impactor is a device used for the inertial separation of airborne particles.[1,2] In this impactor, shown schematically in Figure 1a, a jet of particle-laden air is directed at a collection probe which is slightly larger in diameter than the acceleration nozzle. The large particles cross the air streamlines and enter the collection probe, while the small particles follow the air streamlines into the side passage. To remove the large particles from the collection probe, a fraction of the total flow passing through the nozzle of the virtual impactor is allowed to pass through the collection probe. This flow will be referred to as the minor flow, while the flow through the side passage will be referred to as the major flow.

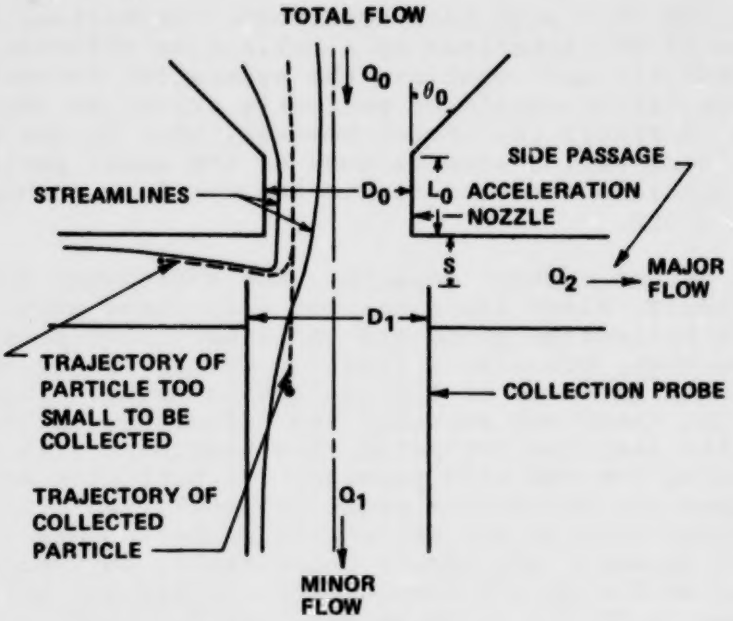
TOTAL FLOW
Q_0
θ_0
SIDE PASSAGE
STREAMLINES
D_0
L_0
ACCELERATION NOZZLE
S
Q_2
MAJOR FLOW
D_1
TRAJECTORY OF PARTICLE TOO SMALL TO BE COLLECTED
COLLECTION PROBE
TRAJECTORY OF COLLECTED PARTICLE
Q_1
MINOR FLOW

(a) VIRTUAL IMPACTOR

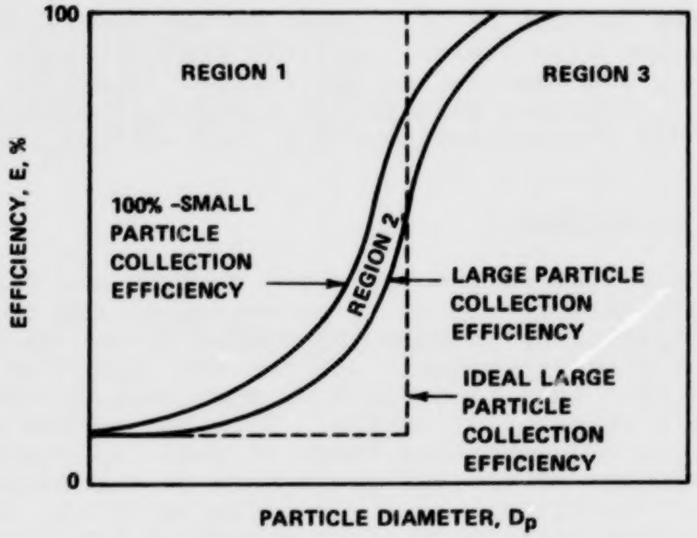

REGION 1 - PARTICLES IN THE MAJOR FLOW
REGION 2 - PARTICLES IMPACTED ON COLLECTION PROBE
REGION 3 - PARTICLES IN THE MINOR FLOW

(b) COLLECTION EFFICIENCY CURVES

Figure 1. Nomenclature, streamlines, particle trajectories, and efficiency curves for a virtual impactor.

As is the case with real impactors, the virtual impactor's performance is characterized by a collection efficiency curve. For the ideal virtual impactor, the separation between the large and small particles should be perfectly sharp, as shown for the ideal case in Figure 1b. Note, however, that in the virtual impactor, there will always be some of the small particles in the large particle fraction due to the air flow through the collection probe.

In an actual virtual impactor, the efficiency curve is not quite so simple, since there are not only large particles passing through the collection probe and small particles passing through the side passage, but also a fraction of the particles impacting upon the inner surfaces of the collection probe. Thus, as shown in Figure 1b, there are actually two efficiency curves separating the particles into the following three regions: (1) small particles passing out the side passage, (2) particles which are impacted upon the collection probe (losses), and (3) large particles passing through the collection probe. Since losses in the virtual impactor are highly undesirable, an impactor should be designed such that the displacement of the two efficiency curves shown in Figure 1b is as small as possible, with the two efficiency curves coinciding for the desirable case of a virtual impactor with no losses.

It is the purpose of this paper to use numerical methods to determine the flow fields, particle trajectories, and finally, the efficiency and loss curves for virtual impactors operating at different conditions of Reynolds numbers, fraction of flow passing through the collection probe, and virtual impactor design.

THEORETICAL TECHNIQUES

The method used to theoretically analyze the performance of the virtual impactor is to first determine the flow field within the impactor by solving the Navier-Stokes equations using numerical analysis techniques, and then to solve for the particle trajectory within this flow field by numerically integrating the particle's equation of motion. This method has been used successfully in a fundamental study of real impactors to determine the influence of various parameters on the characteristic collection efficiency curves.[3] Comparisons of the theoretical efficiency curves with those of experimental investigations[4-8] have shown that the agreement is good if the impactor inlet conditions, shapes, and Reynolds numbers are similar. Since the flow field and particle trajectories are similar in real and virtual impactors, this theoretical technique should be equally successful in determining the efficiency curves of virtual impactors.

The general method of solution of the flow field is to first express the Navier-Stokes equations in terms of the vorticity and the stream function. The resulting differential equations are then made dimensionless, with the radial, r, and axial, z, dimensions being in units of the nozzle throat diameter, D_0. The Reynolds number,

$$Re = \frac{\rho \, D_0 \, V_0}{\mu} \tag{1}$$

where ρ is the fluid density, V_0 is the mean fluid velocity at the nozzle throat, and μ is the absolute viscosity of the fluid, will be a parameter in these equations. The dimensionless differential equations are next expressed in a finite difference form and solved by the method of relaxation over a grid of node points covering the field of interest, as shown in Figure 2a. (Note that the flow is symmetrical about the centerline.) Although the solution is the determination of the vorticity and stream function values at each node point, the values of the velocity components at the node points can be calculated from the stream function values. For details on the derivation of the finite difference equations, boundary conditions, and relaxation technique, the reader is referred to a previous paper by Marple et al.[9]

After the flow field has been determined, it is then necessary to follow particle trajectories through the virtual impactor. To accomplish this, the particle's equations of motion in the r and z directions are made dimensionless by again expressing the r and z dimensions in units of D_0. For these equations, the Stokes number, St, defined by Fuchs[10] as the ratio of the particle stopping distance to $D_0/2$, will be a parameter. The Stokes number is thus expressed as

$$St = \frac{\rho_p \, V_0 \, C \, D_p^2}{9 \, \mu \, D_0} \tag{2}$$

where ρ_p is the particle density, C is the Cunningham slip correction, and D_p is the particle diameter. Since St is dimensionless, Equation 2 indicates that $\sqrt{St}$ is a measure of the dimensionless particle diameter. The dimensionless equations of motion are next put in finite difference form and integrated numerically through the area of interest. This technique, which is described in detail by Marple and Liu,[4] is capable of describing the particle's trajectory once the particle's initial position and velocity have been given.

The integration process is started by first assigning a specific value of $\sqrt{St}$ to a particle, and giving the particle an initial velocity equal to the local fluid velocity at a position near the entrance. By use of the Runge-Kutta integration method, the movement of the particle, Δz and Δr, during a small increment of time, Δt, is determined. This gives the position of the particle at the end of the time increment. This process is then repeated, and the movement of the particle through the impactor is followed until the particle either exits through the collection probe, exits to the side of the virtual impactor, or impacts upon the wall of the collection probe.

The particle is considered impacted when the center of the particle comes within one particle radius, r_p, of a surface. Since all dimensions of the virtual impactor are in units of the nozzle diameter, D_0, the particle radius must also be expressed in units of D_0. Thus, from Equations 1 and 2,

$$\frac{R_p}{D_0} = \sqrt{\frac{4.5\ \rho\ St}{\rho_p\ Re}} \tag{3}$$

A detailed description of the numerical procedure and the computer program used has been given by Marple.[3]

RESULTS

As described above, the flow fields, particle trajectories, and corresponding efficiency curves of a virtual impactor will depend on the parameters Re and Q_1/Q_0 and the physical design. Referring to Figure 1, the design can be specified by the values of D_1/D_0, L_0/D_0, S/D_0, and θ_0, and the shape of the entrance to the collection probe.

To initiate the parametric study, a set of base values for the parameters were chosen and are listed in the "boxed in" portion of Table 1. The other values of the parameters in Table 1 were then varied one at a time to the values listed, while the remaining parameters remained at the base values. Following is a discussion of the results for the base case, and then discussions of the effects of the various parameters.

Base Case

The grid used for the base case, corresponding to the parameters in Table 1, is shown in Figure 2a. A thin-walled tube collection probe, which simulates a collection probe with its wall tapered to a sharp edge at the entrance, was chosen, since this design introduces no new variables such as wall thickness, or radius of curvature of the probe entrance.

The flow field streamlines for the base case are shown in Figure 2b for streamlines corresponding to 5%, 10%, 20%, 40%, 80%, and 100% of the flow inside that streamline. Note that the 0% streamline is at the centerline, the 10% streamline intersects the collection probe (Q_1/Q_0 = 10%), and the 100% streamline corresponds to the nozzle wall. Also note that the free streamline emitted from the nozzle reattaches to the surface defining the nozzle exit plane, forming a recirculation between that surface and the free streamline. A second recirculation region is formed between the air flowing out the side passage and the lower surface, causing a 5% streamline to be indicated in this region.

In Figure 3a, the particle trajectories for five particles with different values of $\sqrt{St}$, all starting at the 50% streamline, are shown. These five particle trajectories include the three cases where particles (1) pass through the collection probe, (2) are impacted on the collection probe inner surface, and (3) pass through the side passage. Also included are the two critical trajectories between these three cases. For example, if the value of $\sqrt{St}$ of a particle is greater than 0.881, the particle will pass through the collection probe; if it is less than 0.677, the particle will pass through the side exit; and if it is between these two critical values, the particle will impact on the collection probe inner surface.

TABLE 1. VALUES OF DESIGN PARAMETERS USED IN STUDY

Re	Q_1/Q_0	D_1/D_0	L_0/D_0	S/D_0	Θ_0	Collection probe[a]	
1							
10						(B) 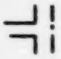	
100						(C) 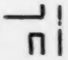	
500							
1,000	0.05	1.16	0.013	0.25	30°	(D) 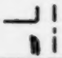	
5,000	0.10	1.33	2.5	1	45°	(A) 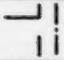	b
15,000	0.15	1.49		2			
	0.25						

[a] Collection probe A - thin wall
Collection probe B - infinite wall thickness
Collection probe C - finite wall thickness
Collection probe D - finite wall thickness with taper
(Collection probe designs are shown in Figure 18.)

[b] Base values from which parameters are varied.

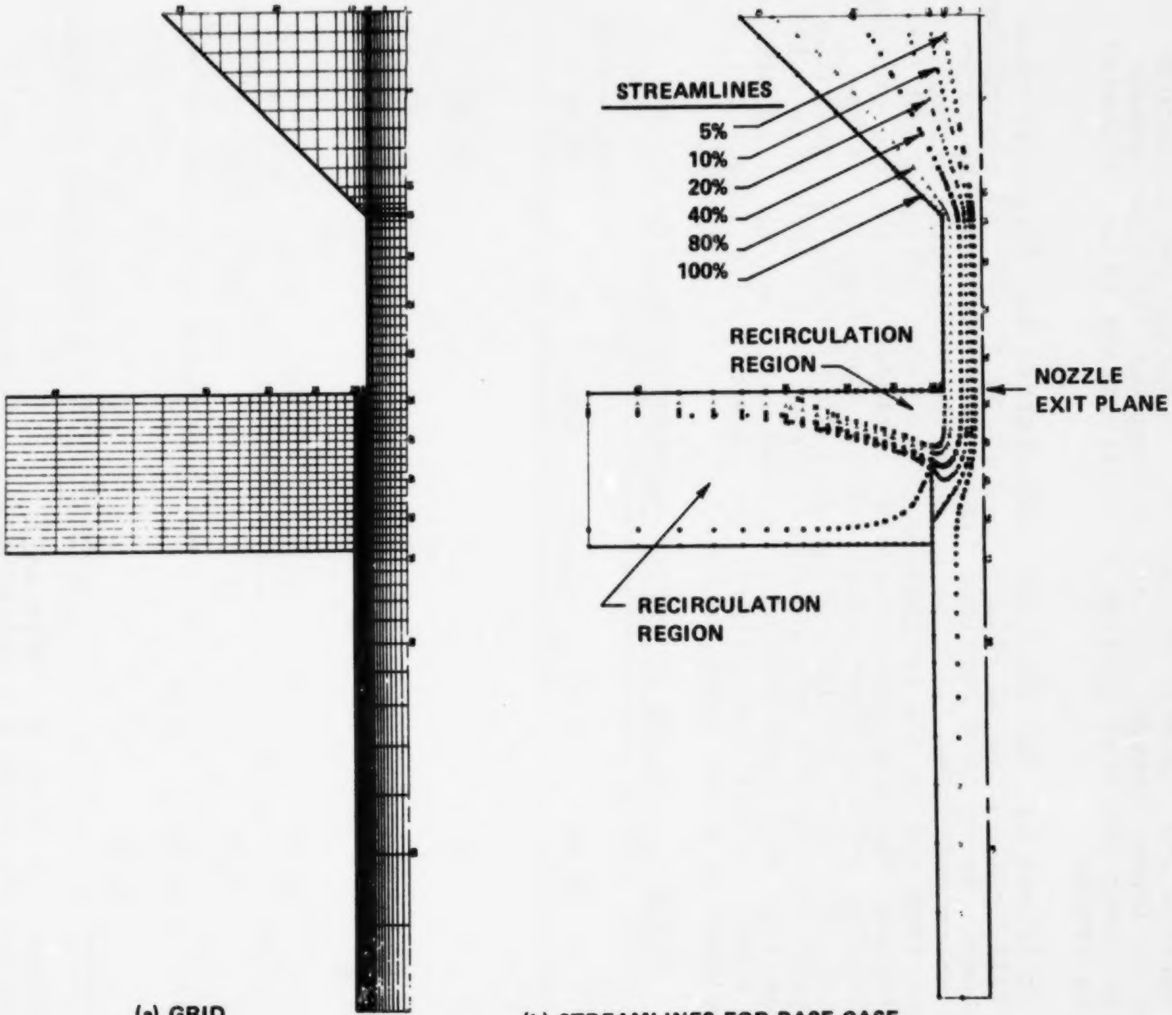
STREAMLINES
5%
10%
20%
40%
80%
100%
RECIRCULATION REGION
NOZZLE EXIT PLANE
RECIRCULATION REGION

(a) GRID

(b) STREAMLINES FOR BASE CASE

Figure 2. Grid and flow field for virtual impactor at base case conditions.

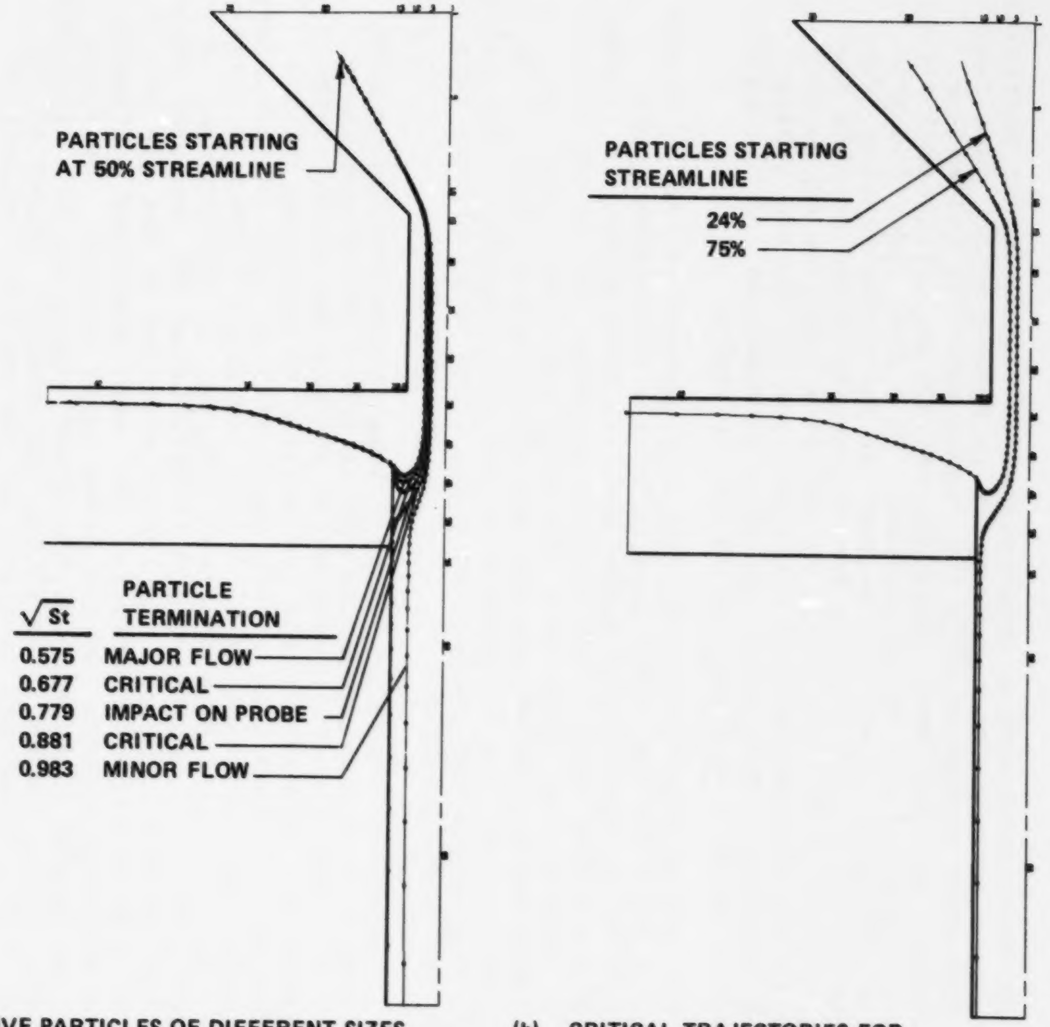
PARTICLES STARTING AT 50% STREAMLINE
$\sqrt{St}$
PARTICLE TERMINATION
0.575 MAJOR FLOW
0.677 CRITICAL
0.779 IMPACT ON PROBE
0.881 CRITICAL
0.983 MINOR FLOW
PARTICLES STARTING STREAMLINE
24%
75%

(a) FIVE PARTICLES OF DIFFERENT SIZES STARTING AT THE SAME POINT

(b) CRITICAL TRAJECTORIES FOR PARTICLES OF SIZE $\sqrt{St} = 0.5$

Figure 3. Particle trajectories at base conditions.

Another method by which the critical values of $\sqrt{St}$ can be determined is to keep $\sqrt{St}$ constant while varying the inlet starting position of the particle, as shown in Figure 3b. This shows that particles with $\sqrt{St} = 0.5$ starting between the 24% streamline and the centerline will pass through the collection probe, those starting between the 24% and 75% streamlines will impact on the collection probe, and those starting at streamlines greater than 75% will pass out the side exit.

By using data such as represented in Figure 3a for particles starting at several positions, or as in Figure 3b for particles with different values of $\sqrt{St}$, the "large particle collection efficiency" and the "small particle collection efficiency" curves shown in Figure 4 can be determined. In either case, the collection efficiencies are the percent of particles issuing from the nozzle which pass through the collection probe or side passage, respectively. The value of $\sqrt{St}$ as a function of these efficiencies is presented as the base case in the two tables of the Appendix. Also note that this information for all cases listed in Table 1 is presented in the Appendix.

For the purpose of determining the percent of the particles being impacted on the inner surface of the collection probe, referred to as "collection probe loss" in this paper, it is best to construct the curve "100% - small particle collection efficiency". This curve, along with the large particle collection efficiency curve, represents the two efficiency curves in Figure 1b. As stated before, the difference in the efficiencies at any value of $\sqrt{St}$ represents the collection probe loss, and thus the loss curve can be constructed.

It should be noted in Figure 4 that the collection characteristics of a virtual impactor can be specified by the large particle collection efficiency curve and any one of the other three curves. However, since the collection probe losses are of considerable importance, this curve will be used in this paper. Also note that the quantity of collection probe losses is quite large, being greater than has been reported in experimental investigations.[11,12] However, investigations of the computer outputs indicated that nearly all losses occurred at the tip of the collection probe by particles that were traveling vertically upward directly adjacent to the probe inner surface. As shown later, by proper contouring of the probe entrance, it is possible to reduce these losses. Therefore, the absolute values of the losses in this paper may be high, but the relative effects of the various parameters on these losses are of interest.

Although the contour of the collection probe entrance affects the probe losses, it has little effect on the large particle collection efficiency curve. Thus, this curve should be considered as the most significant characteristic curve for virtual impactors, and it is the curve by which virtual impactors will be characterized in this paper.

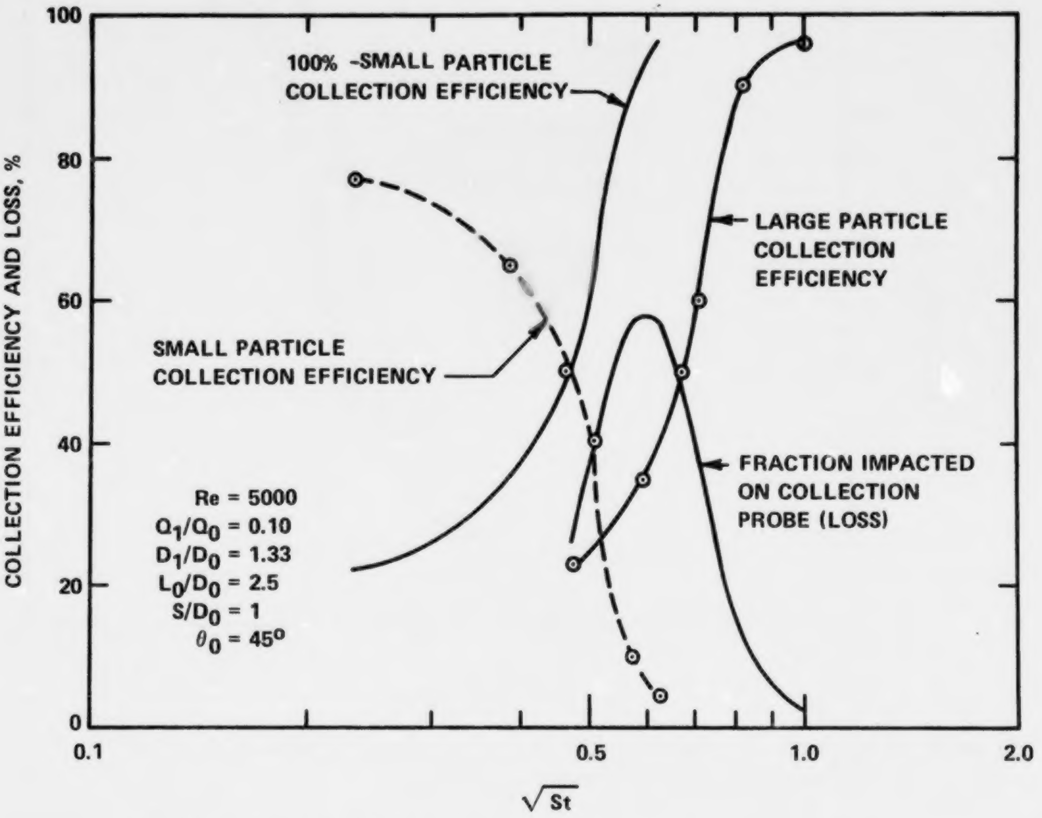

Figure 4. Collection efficiency and loss curves for base conditions.

It is of interest to compare the large particle collection efficiency curve determined theoretically to experimental curves by other investigators in Figure 5. The values of the parameters listed in Figure 5 for each curve indicate that the virtual impactors are similar. The comparison shows that the theory agrees well with the experimental curves of Loo[11] and McFarland et al.[12] The theoretical curve is nearly identical to Loo's experimental curve, with the experimental curve of McFarland et al. having approximately 20% lower values of $\sqrt{St}$.

Influence of Reynolds Number

To determine the influence of the Reynolds number, cases were run for the different values of Re listed in Table 1, while the other parameters were held constant at base values. The flow fields are shown in Figure 6 for Re = 1, 10, 100, 500, 1,000, and 15,000, and in Figure 2b for Re = 5,000. In Figure 6, only the portions of the flow fields in the vicinity of the collection probe are shown, since the flow fields in other portions of the impactors are very similar to those in Figure 2b. It should be noted that the flow may not be laminar for Re = 15,000, but is presented as a limiting case.

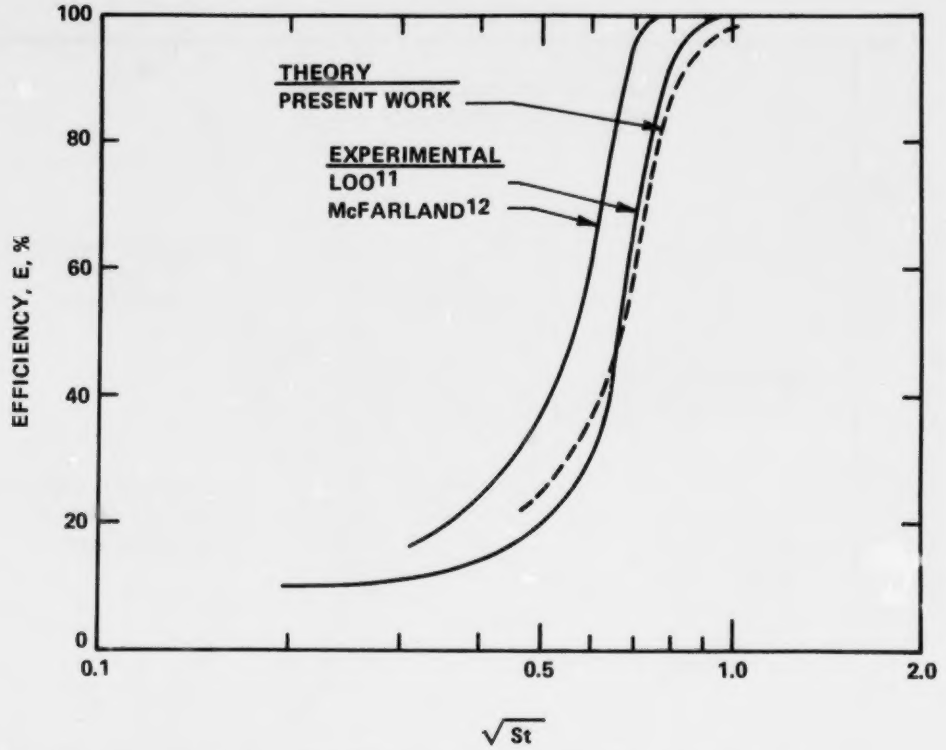

Figure 5. Comparison of theoretical and experimental large particle collection efficiency curves at the following conditions:

	Re	*Q_1/Q_0*	*S/D_0*	*D_1/D_0*	*L_0/D_0*	*θ_0*
Present theory	*5000*	*0.1*	*1.0*	*1.33*	*2.5*	*45°*
Loo[11]	*6000*	*0.1*	*0.8*	*1.38*	*0.8*	*45°*
McFarland[12]	*4500*	*0.1*	*0.9*	*1.31*	-	-

Since the large particle collection efficiency curves are of primary interest, the flow fields within the collection probe are of most importance. It is in this region where we observe the unexpected result that the penetration of the 10% and 20% streamlines into the collection probe is greater for the cases of Re = 100 and 500 instead of for the higher values of Re, where the inertial effects of the flow should be larger. The reason for this can be seen by inspecting the velocity profiles at the nozzle exit plane shown in Figure 7. At high values of Re (Re = 5,000 and 15,000), the velocity profile is relatively uniform across much of the nozzle, making it difficult for any portion of the flow to penetrate into the air in the collection probe. For the cases of Re = 500 and 100, the velocity profile is more parabolic, and the relatively high velocity near the centerline makes it possible for the jet to penetrate farther into the collection probe. However, if the value of Re is small (Re = 10), there is insufficient inertia in the jet to penetrate into the

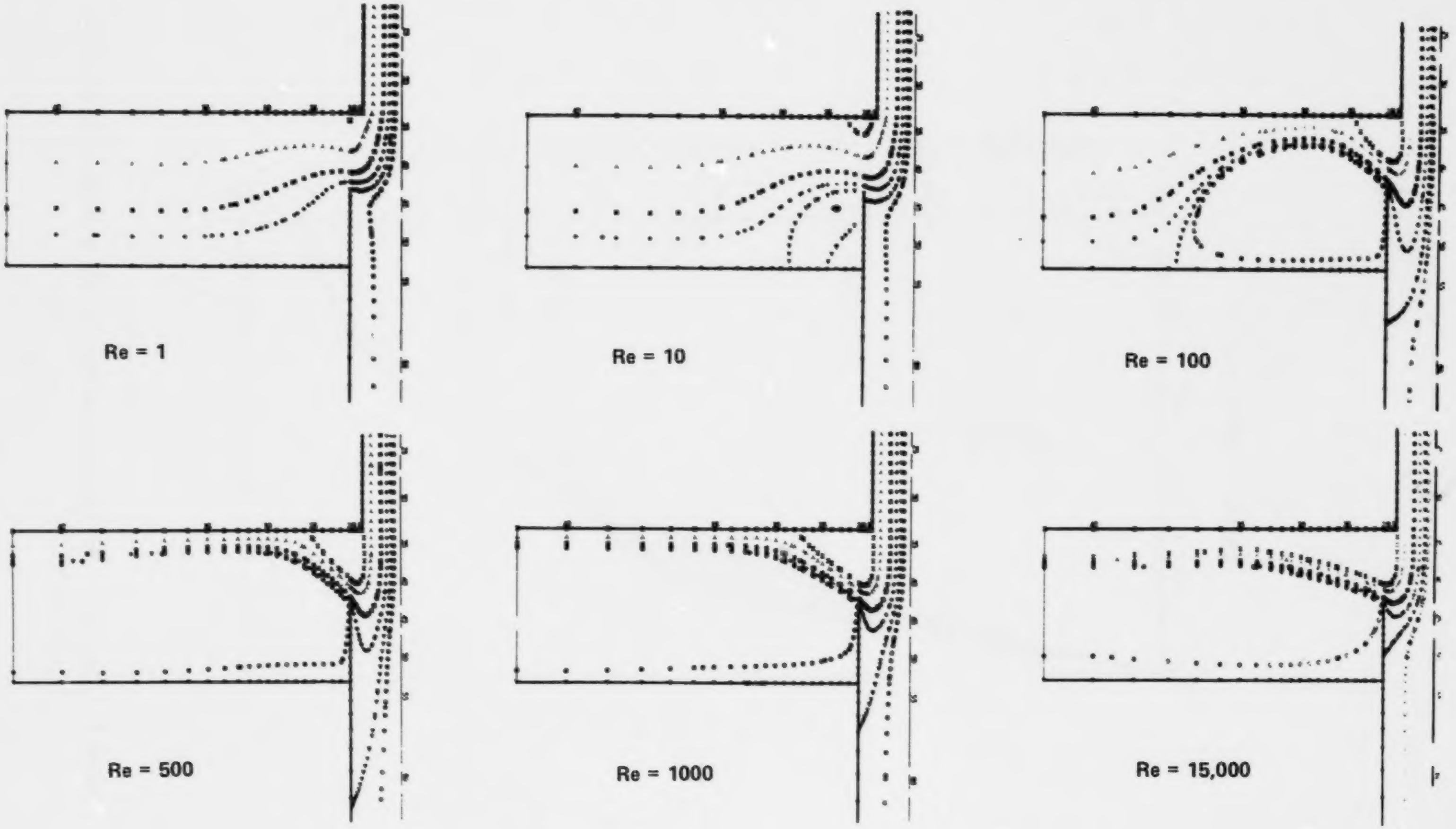

Re = 1

Re = 10

Re = 100

Re = 500

Re = 1000

Re = 15,000

Figure 6. Theoretical streamlines at the specified values of Re
($Q_1/Q_0 = 0.1$, $D_1/D_0 = 1.33$, $L_0/D_0 = 2.5$, $S/D_0 = 1$, and $\theta_0 = 45^o$).

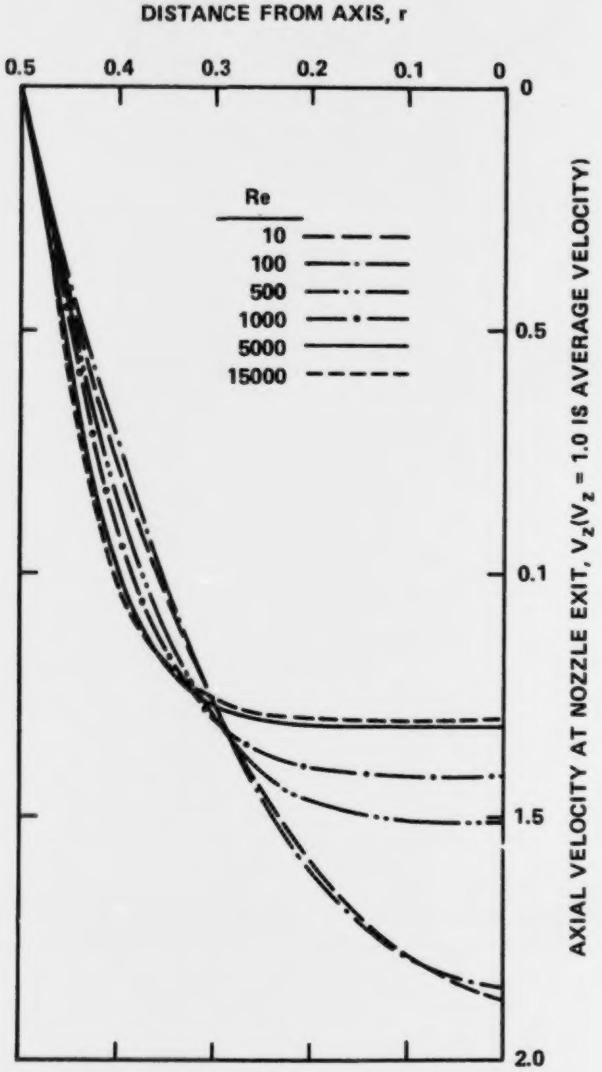

Figure 7. Influence of the Reynolds number on the axial velocity profile at the nozzle exit.

viscous air in the collection probe. Thus, Re in the range of 100 to 500 is the correct combination of nozzle velocity profile and inertia to obtain maximum penetration of the 10% and 20% streamline into the collection probe.

The large particle collection efficiency curves and loss curves are shown in Figure 8 with Re as a parameter. The influence of the flow penetration into the collection probe can be seen in the position of the large particle collection efficiency curves in Figure 8a. For the cases where the flow penetration into the collection probe is largest (Re = 100 and 500), the particle Stokes numbers must be larger in order for the particles to penetrate into the minor flow, since the Stokes number is defined as the ratio of the particle stopping distance to the radius of the nozzle. Where the flow penetration into the collection probe is small, the required distance that the particle must travel, and thus the value of the Stokes number, will be smaller.

It is of interest to note in Figure 8a that the efficiency curves are nearly identical for the cases of Re = 1 and 10, and for Re = 5,000 and 15,000, indicating that lower or higher Reynolds numbers than those listed should have little effect on these curves. It is also interesting to note that the slopes of the penetration curves are greater for the larger values of Re, indicating better cut-off characteristics. However, this effect is small, which is different from real impactors, where the cut-off characteristics are much poorer for low values of Re than for large values.[4]

Concerning the influence of Re on the losses, Figure 8b shows that the influence is large. In general, the losses increase from a minimum of about 10% at low values of Re to about 60% at high values of Re, with the maximum losses occurring at the value of $\sqrt{St}$ corresponding to 50% efficiency.

Influence of Q_1/Q_0

The flow fields corresponding to Q_1/Q_0 values of 0.05, 0.15, and 0.25 are shown in Figure 9, and should be compared to the base case of Q_1/Q_0 = 0.10 in Figure 2b. As can be seen from these figures, more streamlines pass through the collection probe for large values of Q_1/Q_0 and the small amount of flow in the side passage leaves more room for recirculation in this area. The flow field for Q_1/Q_0 = 0.05 shows reattachment to the lower surface of the side passage, much like the flow at Re = 100 in Figure 6. Whether or not the flow field in this region is correct is uncertain. However, since the flow in the region has no effect on the flow field in the important area within the collection probe, a more detailed investigation of the flow in this region was not made.

The corresponding large particle collection efficiency curves and loss curves are shown in Figure 10. The large particle collection efficiency curves indicate that a "sharper" cut between

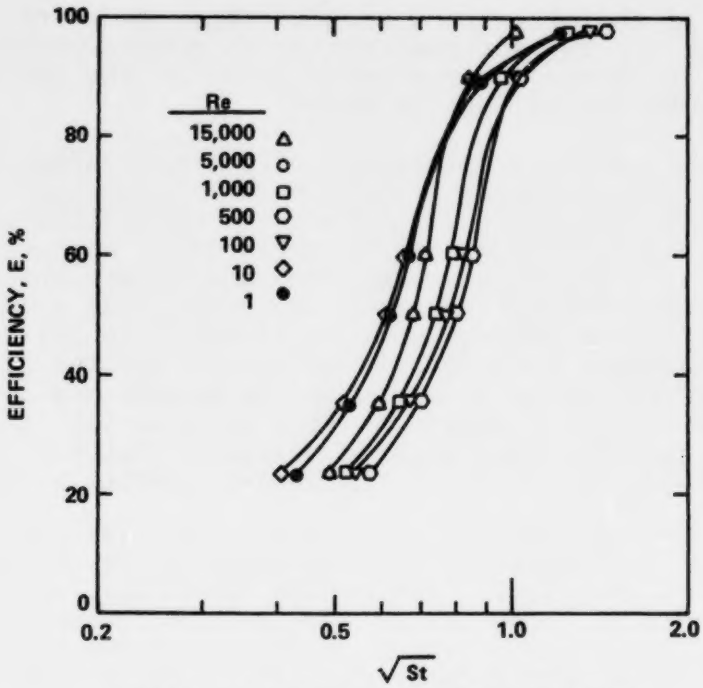

(a) LARGE PARTICLE COLLECTION EFFICIENCY

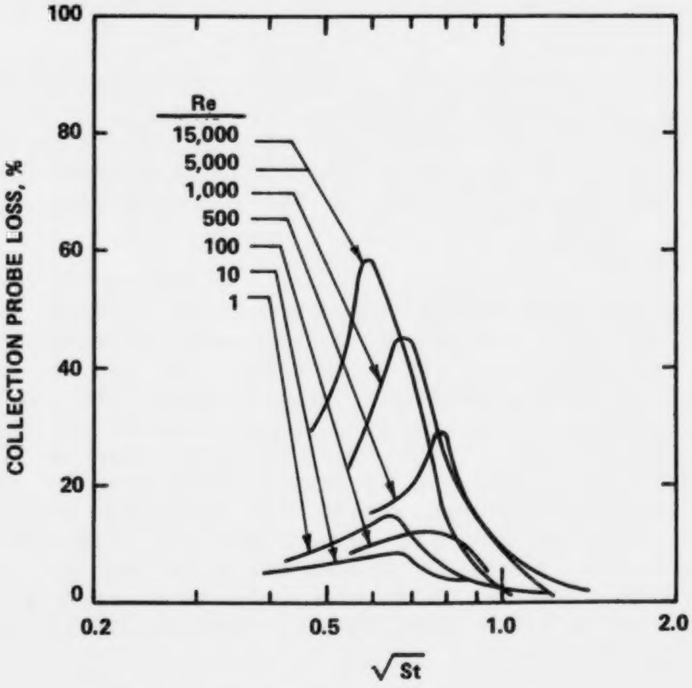

(b) COLLECTION PROBE LOSS

Figure 8. Large particle collection efficiency and collection probe loss curves at the specified values of Re ($Q_1/Q_0 = 0.1$, $D_1/D_0 = 1.33$, $L_0/D_o = 2.5$, $S/D_0 = 1$, and $\theta_o = 45^o$).

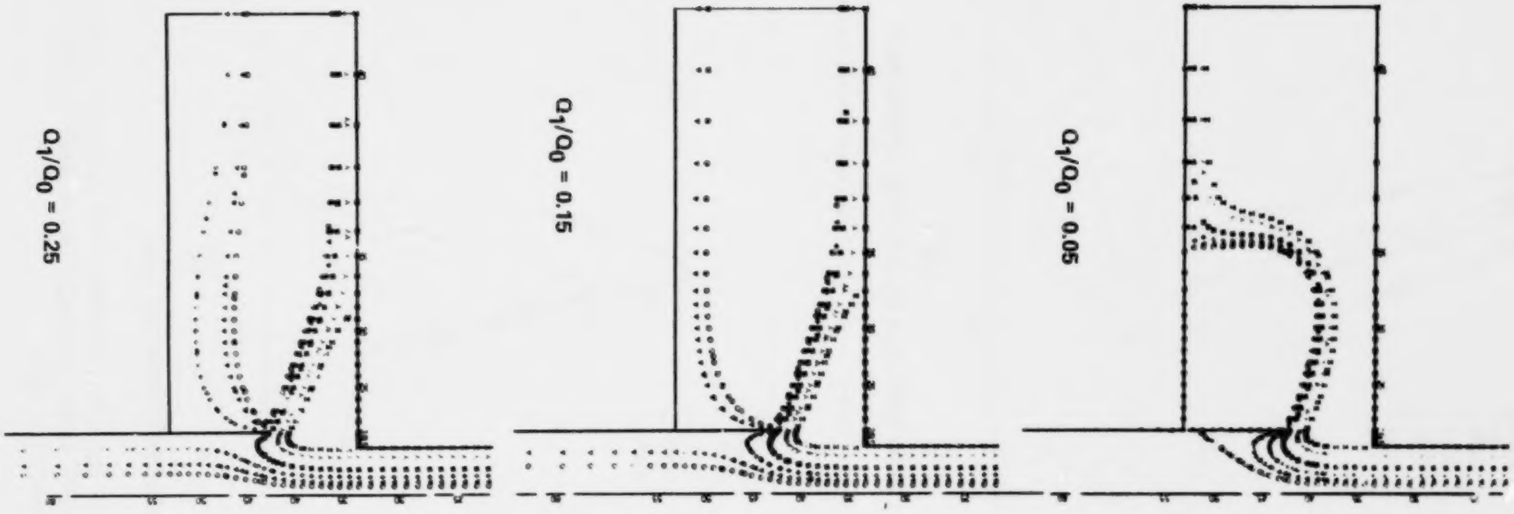

Figure 9. Theoretical streamlines at the specified values of Q_1/Q_0 ($Re = 5000$, $D_1/D_0 = 1.33$, $L_0/D_0 = 2.5$, $S/D_0 = 1$, and $\theta_0 = 45°$).

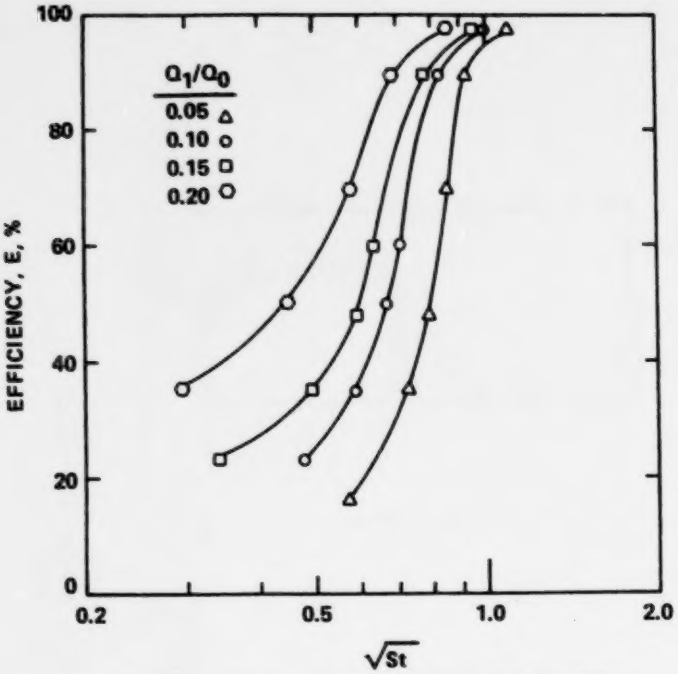

(a) LARGE PARTICLE COLLECTION EFFICIENCY

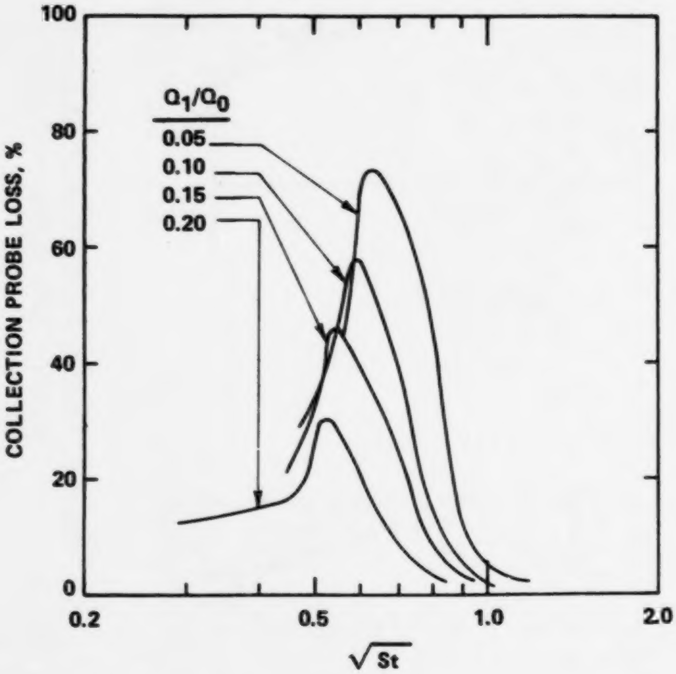

(b) COLLECTION PROBE LOSS

Figure 10. Large particle collection efficiency and collection probe loss curves at the specified values of Q_1/Q_0 (Re = 5000, D_1/D_0 = 1.33, L_0/D_0 = 2.5, S/D_0 = 1, and θ_0 = 45°).

large particles collected and those which are not is obtained for smaller values of Q_1/Q_0. Also, the cut-off size increases as Q_1/Q_0 decreases. This is expected, since particles must pass through more air to enter the minor flow stream when Q_1/Q_0 is small.

The loss curves show more losses associated with the lower Q_1/Q_0 values. This would be due to the larger percentage of the flow being exposed to the inlet of the collection probe where the losses generally occur, and should be decreased with proper inlet design.

Effect of D_1/D_0

Besides D_1/D_0 being equal to the base value of 1.33 (Figure 2b), D_1/D_0 was also set at 1.16 and 1.49 (Figure 11). Although, as shown in Figure 12, this parameter had only a small effect on the large particle collection efficiency and loss curves, there are substantial differences in the flow fields for these three cases. For example, the flow field attaches close to the nozzle exit when $D_1/D_0 = 1.49$ but does not attach when $D_1/D_0 = 1.16$. Experiments (personal communication from B.W. Loo, Lawrence Berkeley Laboratories) have shown that for values of D_1/D_0 on the order of 1.49, the reattaching flow does cause particles to impact on the nozzle exit plane surface, increasing the losses in the virtual impactor. Therefore, it is recommended that the value of D_1/D_0 be kept less than 1.49 and preferably near 1.33.

Effect of L_0/D_0

To investigate the effect of L_0/D_0, the results of a case where L_0/D_0 is small ($L_0/D_0 = 0.013$) is compared to the base case. Although the streamlines issuing from the nozzle are not parallel to the nozzle axis when $L_0/D_0 = 0.013$ (Figure 13) as they were when $L_0/D_0 = 2.5$ (Figure 2b), the effects on the large particle collection efficiency and the loss curves are negligible, as shown in Figure 14. Similar insensitivity to this parameter was found for real impactors.

Influence of S/D_0

The influence of S/D_0 was determined by using values of $S/D_0 = 0.25$, 1 (base), and 2. The flow fields shown in Figures 15 and 2b appear to be quite different. However, in the region in the collection probe where the 10% streamline attaches to the probe wall, the flow fields are similar. Thus, as expected, the resulting large particle collection efficiency curves shown in Figure 16 are nearly identical. Again, this is different from the effect found for real impactors[4] where small values of S/D_0 have a large effect on collection efficiency.

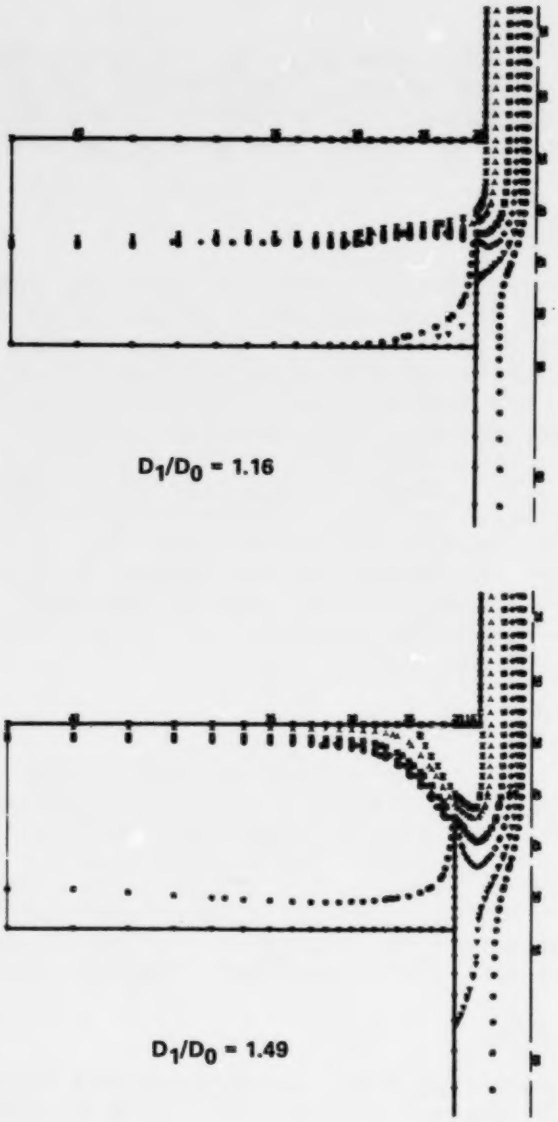

Figure 11. Theoretical streamlines at the specified values of D_1/D_0 ($Re = 5000$, $Q_1/Q_0 = 0.1$, $L_0/D_0 = 2.5$, $S/D_0 = 1$, and $\theta_0 = 45^\circ$).

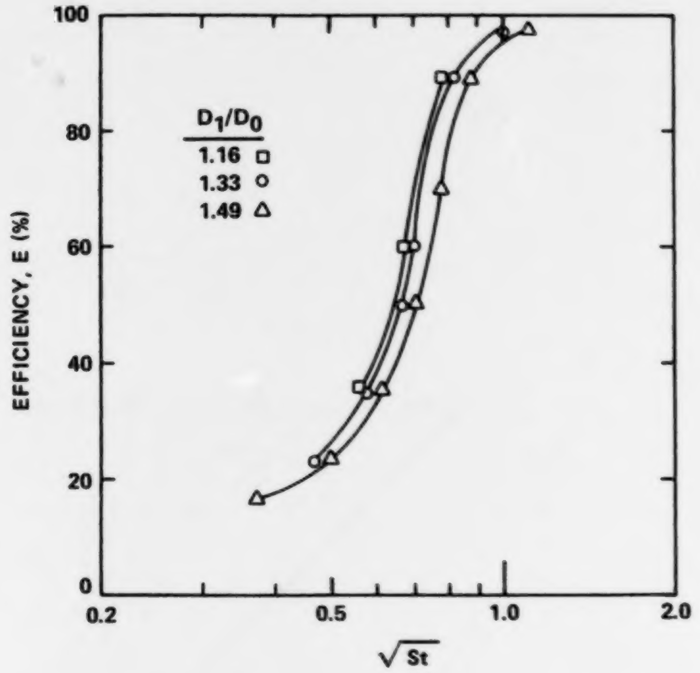

(a) LARGE PARTICLE COLLECTION EFFICIENCY

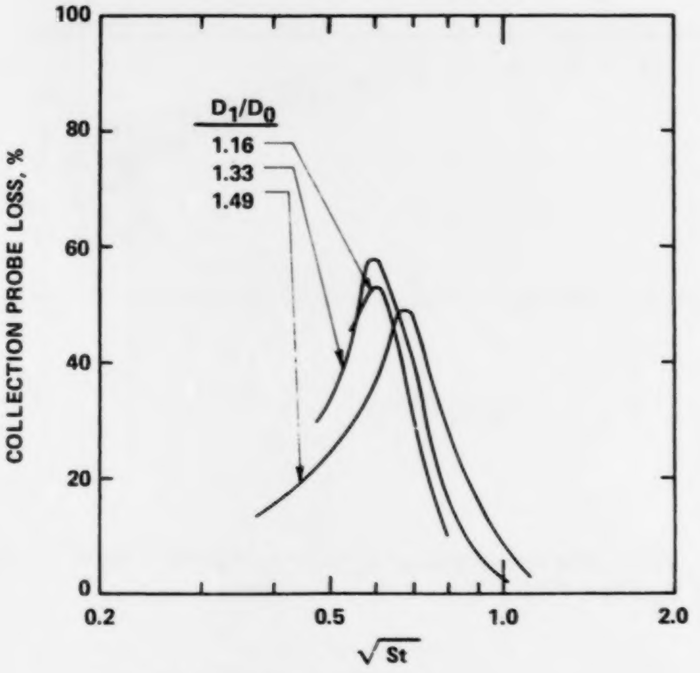

(b) COLLECTION PROBE LOSS

Figure 12. *Large particle collection efficiency and collection probe loss curves at the specific values of D_1/D_0 (Re = 5000, $Q_1/Q_0 = 0.1$, $L_0/D_0 = 2.5$, $S/D_0 = 1$, and $\theta_0 = 45^o$).*

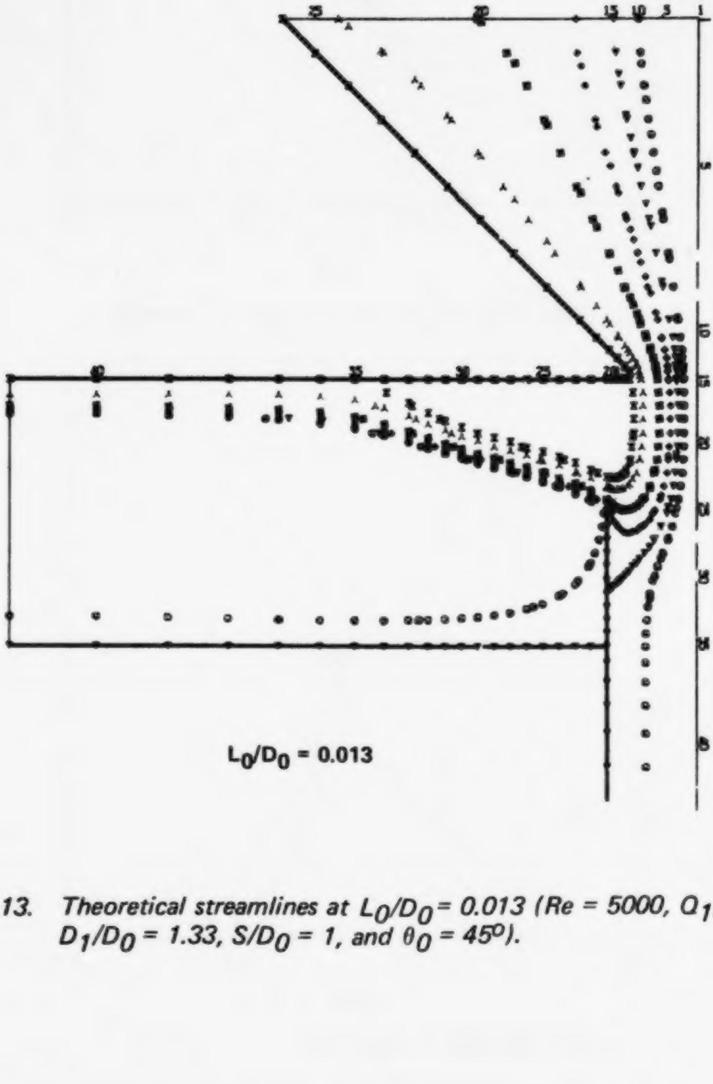

Figure 13. *Theoretical streamlines at $L_0/D_0 = 0.013$ ($Re = 5000$, $Q_1/Q_0 = 0.1$, $D_1/D_0 = 1.33$, $S/D_0 = 1$, and $\theta_0 = 45^\circ$).*

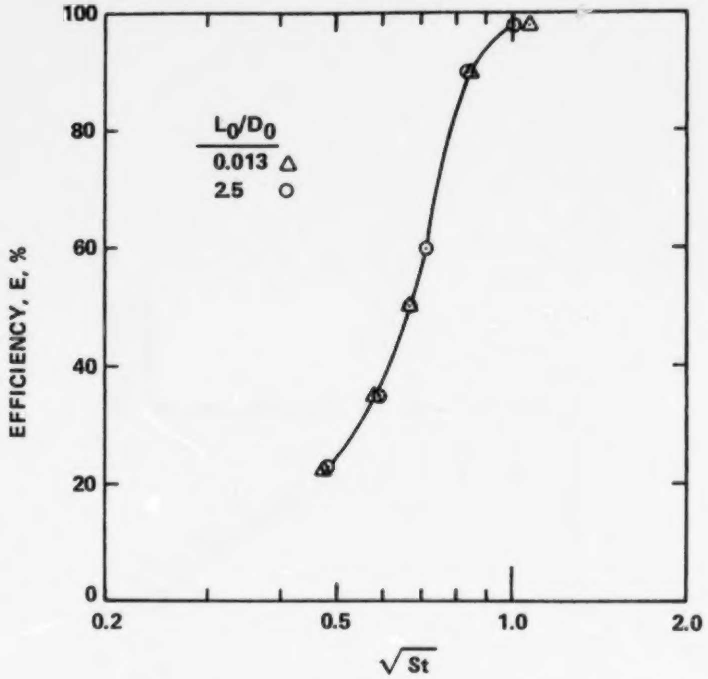

(a) LARGE PARTICLE COLLECTION EFFICIENCY

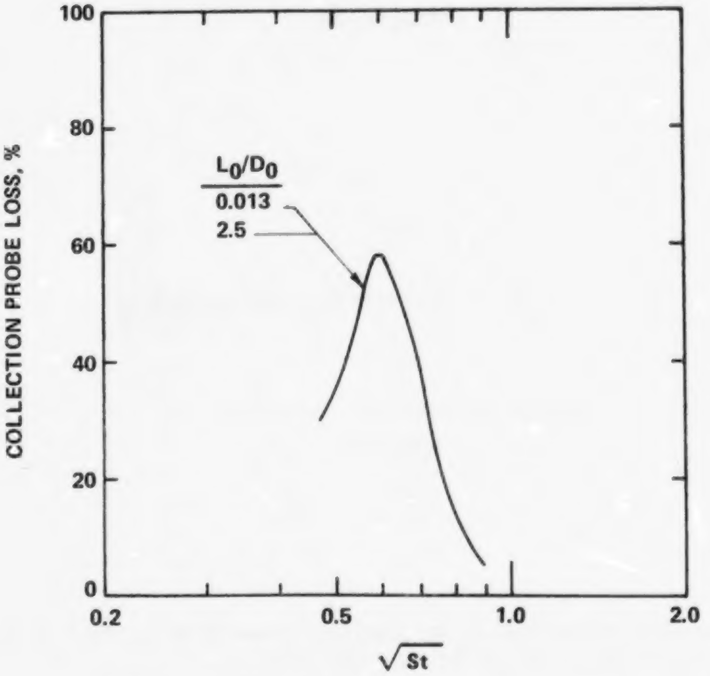

(b) COLLECTION PROBE LOSS

Figure 14. Large particle collection efficiency and collection probe loss curves at the specified values of L_0/D_0 ($Re = 5000$, $Q_1/Q_0 = 0.1$, $D_1/D_0 = 1.33$, $S/D_0 = 1$, and $\theta_0 = 45^o$).

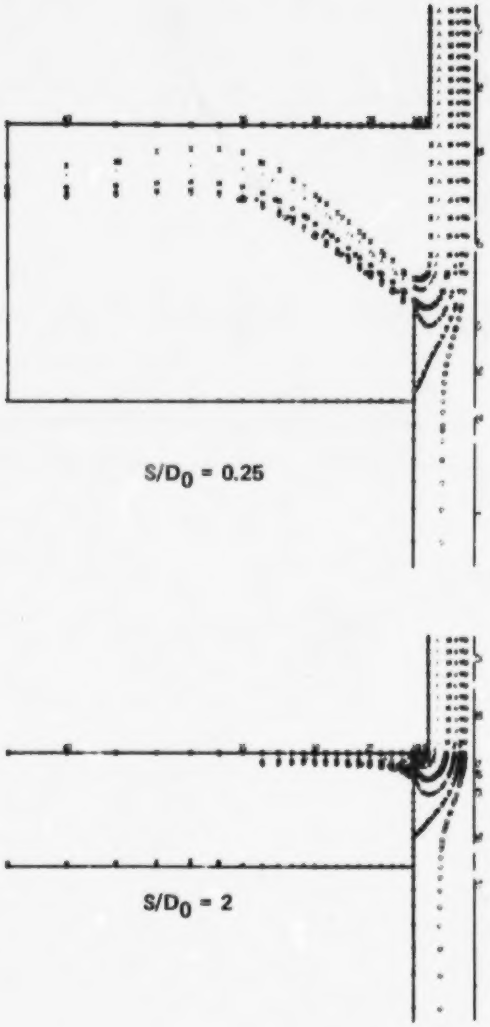

$S/D_0 = 0.25$

$S/D_0 = 2$

Figure 15. Theoretical streamlines at the specified values of S/D_0 ($Re = 5000$, $Q_1/Q_0 = 0.1$, $D_1/D_0 = 1.33$, $L_0/D_0 = 2.5$, and $\theta_0 = 45°$).

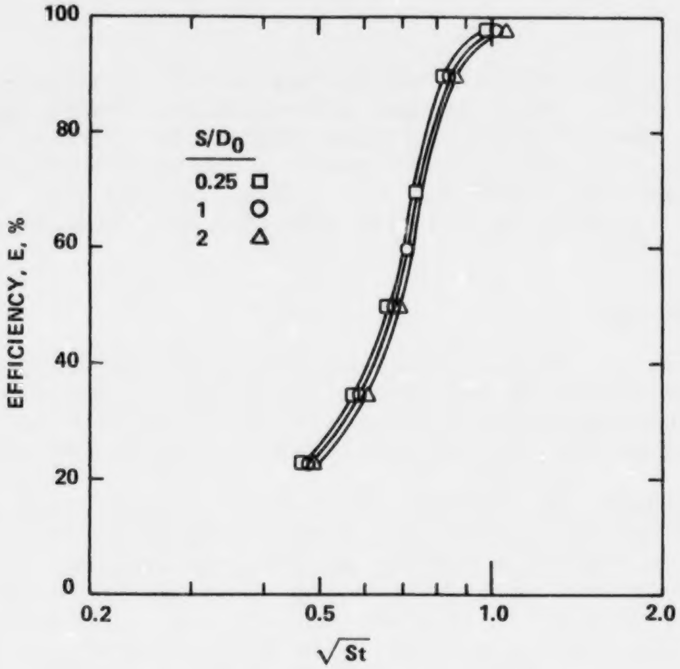

(a) LARGE PARTICLE COLLECTION EFFICIENCY

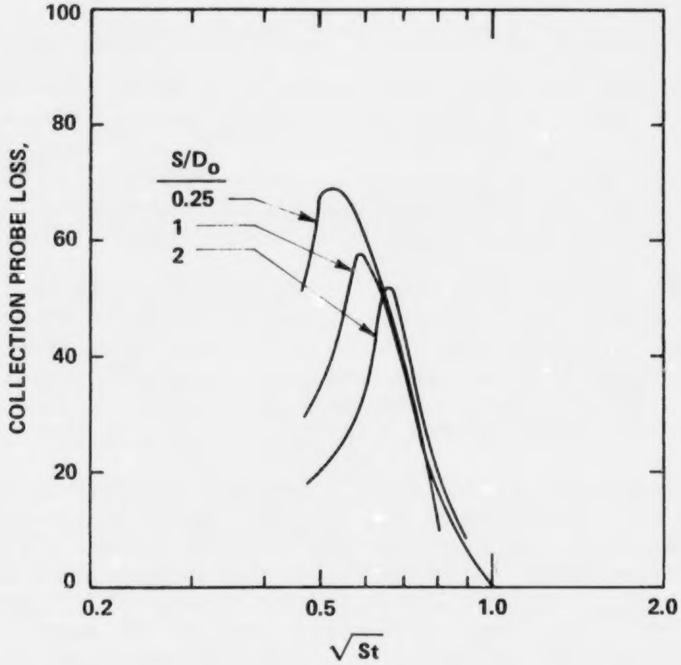

(b) COLLECTION PROBE LOSS

Figure 16. *Large particle collection efficiency and collection probe loss curves at the specified values of* S/D_0 *(*$Re = 5000$, $Q_1/Q_0 = 0.1$, $D_1/D_0 = 1.33$, $L_0/D_0 = 2.5$, *and* $\theta_0 = 45^o$*).*

However, the probe loss curves shown in Figure 16 are influenced by S/D_0, with larger losses being found with small S/D_0 values. It may be expected that additional losses will be experienced on the nozzle exit plane surface and on the backside of the collection probe for small S/D_0 values due to turbulence in the restricted area between the collection probe and nozzle exit plane.

Influence of Θ_0

The effects of the entrance angle on the large particle collection efficiency and probe loss curves are shown in Figure 17. Since the streamlines are very similar to the base case shown in Figure 2b, the streamlines for $\Theta_0 = 30°$ are not shown.

From Figure 17, it can be seen that the large particle collection efficiency curves are similar in shape for both angles, but the curve for $\Theta_0 = 45°$ is shifted to smaller particle sizes. This is due to the particles being thrown closer to the centerline for the larger Θ_0 values, making the collection of particles in the probe slightly easier. The losses shown in Figure 17 indicate less loss for $\Theta_0 = 45°$ than for $\Theta_0 = 30°$. Thus, it appears that Θ_0 should be at least 45°.

Influence of the Collection Probe Inlet Design

Four receiving tube configurations were tested as shown in Figures 2b and 18. The base design was a thin wall shown as configuration A. In configuration B, the wall was infinite in width, and in configuration C, the wall had a finite thickness. In configuration D, the wall thickness was also finite, but the inner surface was tapered in an attempt to reduce losses.

The flow fields for these configurations are shown in Figure 18, and the resulting large particle collection efficiency and probe loss curves are shown in Figure 19. Since configuration B is essentially a real impactor impaction plate with a hole in its center, particles are collected on the plate, and thus losses are meaningless for this case and are not shown.

It is interesting to note that the configuration of the entrance to the collection probe had essentially no effect on the large particle collection efficiency curve. This would be expected, since this curve defines the separation of particles which impact upon the probe wall and those which pass through with the minor flow, and since the region of importance for this curve is inside the collection probe rather than at its entrance.

The losses, however, are influenced by the collection probe configuration. For configurations where there is a sharp edge at the upper entrance, such as configurations A and C, the probe losses are quite large and the loss curves are similar.

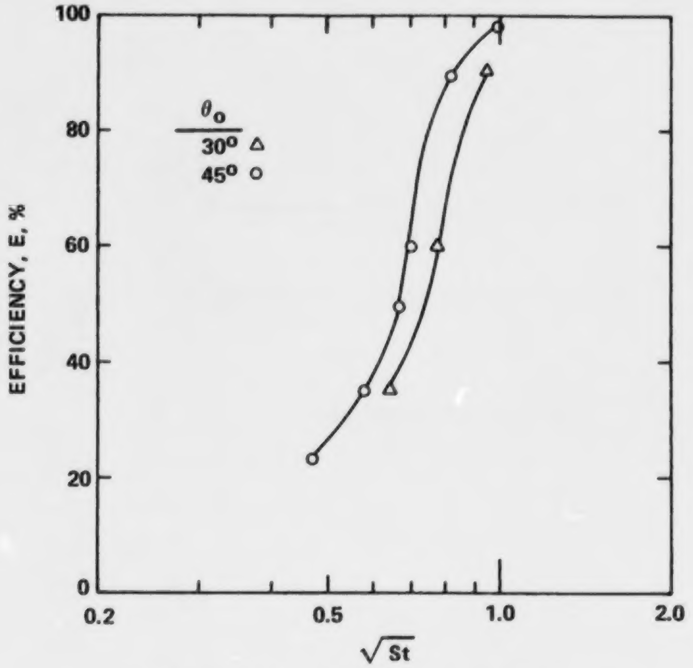

(a) LARGE PARTICLE COLLECTION EFFICIENCY

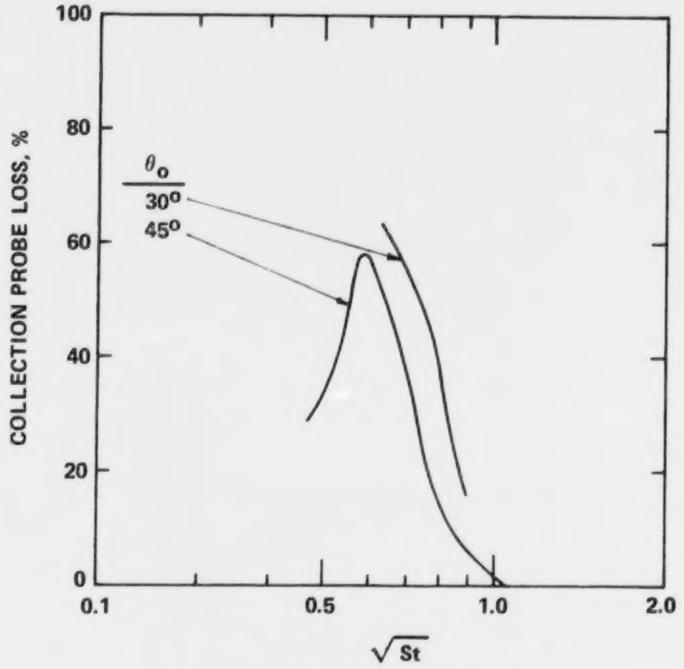

(b) COLLECTION PROBE LOSS

Figure 17. *Large particle collection efficiency and collection probe loss curves at the specified values of θ_0 ($Re = 5000$, $Q_1/Q_0 = 0.1$, $D_1/D_0 = 1.33$, $L_0/D_0 = 2.5$, and $S/D_0 = 1$.*

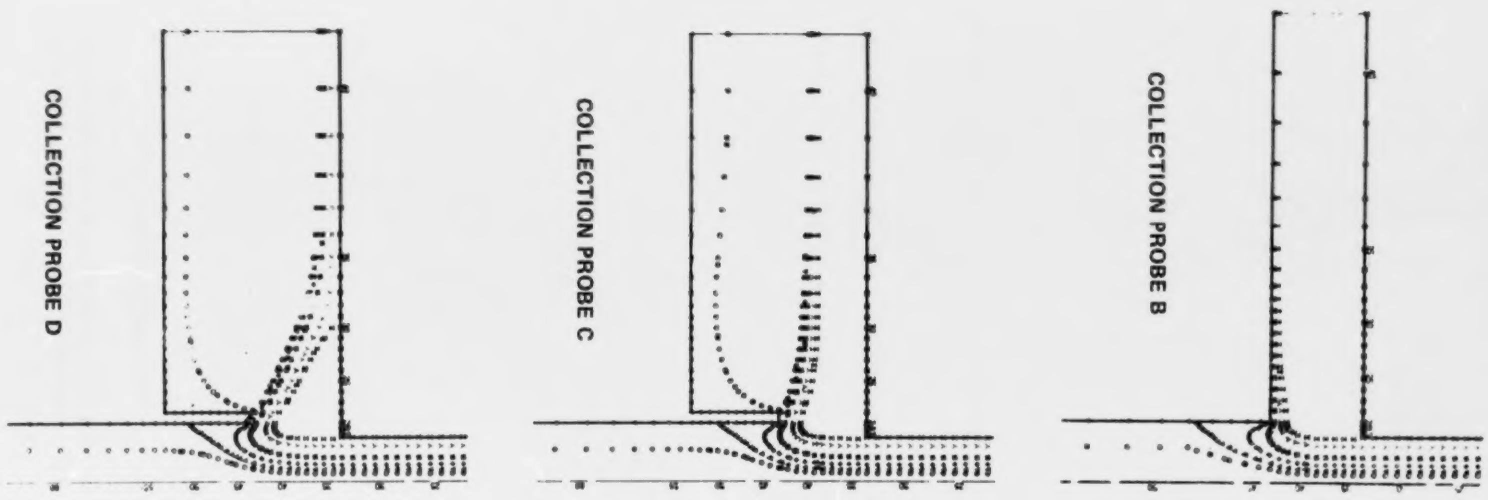

Figure 18. Theoretical streamlines for various collection probe designs ($Re = 5000$, $Q_1/Q_0 = 0.1$, $D_1/D_0 = 1.33$, $L_0/D_0 = 2.5$, $S/D_0 = 1$, and $\theta_0 = 45^o$).

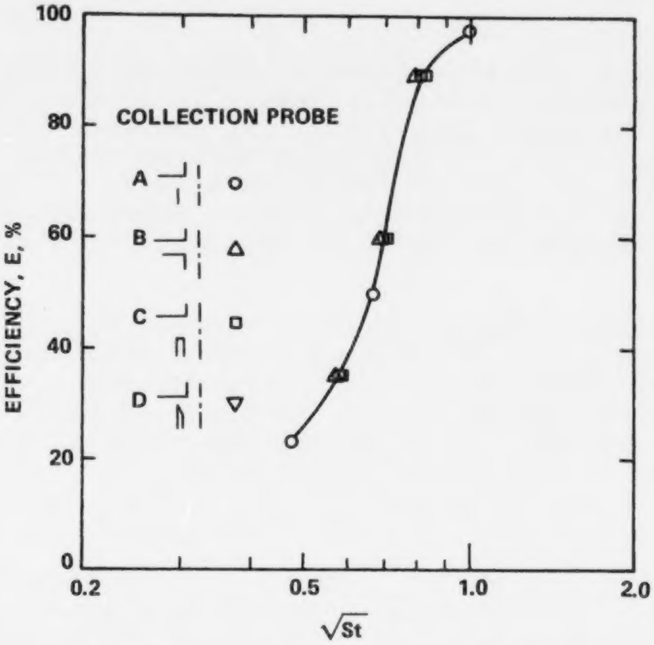

(a) LARGE PARTICLE COLLECTION EFFICIENCY

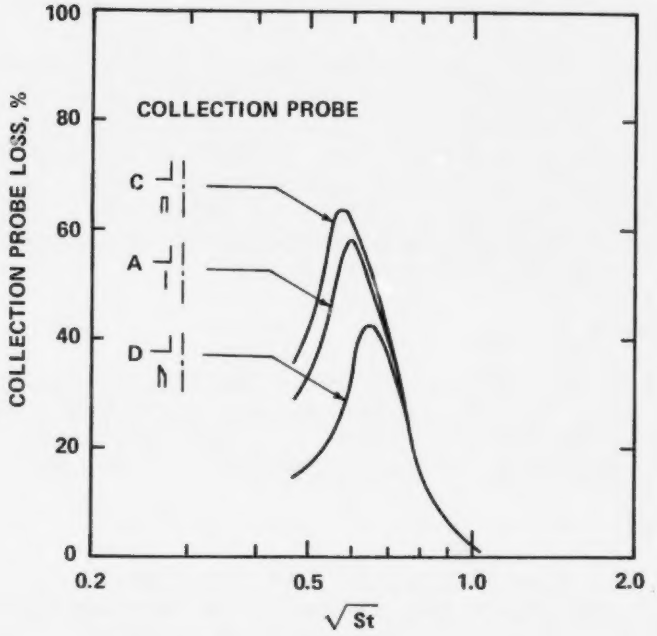

(b) COLLECTION PROBE LOSS

Figure 19. Large particle collection efficiency and collection probe loss curves for various collection probe designs ($Re = 5000$, $Q_1/Q_0 = 0.1$, $D_1/D_0 = 1.33$, $L_0/D_0 = 2.5$, $S/D_0 = 1$, and $\theta_0 = 45^o$).

The losses that were found in these cases are from particles which are traveling vertically upward along the collection probe wall toward the major flow exit. The boundary layer in this region is very thin, and particles passing within one particle radius of this wall are collected as a loss. If there were some mechanism, such as aerodynamic forces, which would keep the particle from touching the wall, it would not be collected as a lost particle.

In addition, losses should be reduced by replacing the sharp corner in configuration C with a tapered entrance (configuration D) so that the particles could not be collected as easily at the upper corner of the probe. As shown in Figure 19b, the losses were reduced. By replacing the taper with a radius, the losses should be reduced even farther.

CONCLUSIONS

An examination of the large particle collection efficiency curves reveals that they all have essentially the same shape and are not greatly influenced by any of the parameters. The only parameter which appears to influence the shape is Q_1/Q_0, because the collection efficiency curves are asymptotic to the different values of Q_1/Q_0 at low values of $\sqrt{St}$.

The reason none of the parameters has a large effect on the large particle collection efficiency curve is that this efficiency is governed by the flow field within the collection probe. The losses, however, are governed by the flow conditions at the tip of the collection probe inlet, and thus are influenced by many of the parameters. This is especially true for the case of the collection probe inlet design, where losses were reduced by adding a taper to the probe inlet.

ACKNOWLEDGEMENT

This work was supported under Bureau of Mines Contract HO177026 through the Twin Cities Mining Research Center. The financial support of the Bureau is gratefully acknowledged. This report is Particle Technology Laboratory Publication No. 378.

REFERENCES

1. Loo, B.W., J.M. Jaklevic, and F.S. Goulding. Dichotomous Virtual Impactors for Large-Scale Monitoring of Airborne Particulate Matter. In: Fine Particles: Aerosol Generation, Measurement, Sampling, and Analysis, B.Y.H. Liu, ed. Academic Press, New York, 1976. pp. 311-350.

2. Dzubay, T.G., and R.K. Stevens. Ambient Air Analysis with Dichotomous Sampler and X-Ray Fluorescence Spectrometer. Environ. Sci. Technol. 9:663-8, 1975.

3. Marple, V.A. A Fundamental Study of Inertial Impactors. Ph.D. Thesis, University of Minnesota, Mechanical Engineering Department, Particle Technology Laboratory Publication 144, 1970.

4. Marple, V.A., and B.Y.H. Liu. Characteristics of Laminar Jet Impactors. Environ. Sci. Technol. 8:648-654, 1974.

5. Jaenicke, R., and I.H. Blifford. The Influence of Aerosol Characteristics on the Calibration of Impactors. J. Aerosol Sci. 5:457-464, 1974.

6. Willeke, K., and J.J. McFeters. The Influence of Flow Entry and Collecting Surface on the Impaction Efficiency of Inertial Impactors. J. Colloid Interface Sci. 53:121-7, 1975.

7. Schott, J.H. Jet-Cone Impactors as Aerosol Particle Separators. M.S. Thesis, University of Minnesota, 1973.

8. Willeke, K. Performance of the Slotted Impactor. Am. Ind. Hyg. Assoc. J. 36:683-691, 1975.

9. Marple, V.A., B.Y.H. Liu, and K.T. Whitby. On the Flow Fields of Inertial Impactors. J. Fluids Eng. 96:394-400, 1974.

10. Fuchs, N.A. The Mechanics of Aerosols, Pergamon Press, New York, 1964. p. 154.

11. Loo, B.W., and C.C. Cork. High Efficiency Virtual Impactor for Collecting Airborne Particulate Matter. Lawrence Berkeley Laboratory Report LBL-8204, 1978.

12. McFarland, A.R., C.A. Ortiz, and R.W. Bertch, Jr. Particle Collection Characteristics of a Single-Stage Dichotomous Sampler. Environ. Sci. Technol. 12:679-682, 1978.

APPENDIX

The values of $\sqrt{St}$ for the large particle and small particle collection efficiency curves are tabulated in Tables A-1 and A-2, respectively. The cases are the same as those listed in Table 1. The base case is presented first and subsequent cases are labeled by the value of the changed variable. For example, for the case Re = 1, all variables except Re are at the base values.

The large particle collection efficiency curves are presented in the appropriate figures. The small particle collection efficiency curves are not presented, but were used to determine the collection probe loss curves as described in Figure 4. The collection probe loss curves are then presented in this paper.

TABLE A-1. VALUES OF $\sqrt{St}$ FOR THE LARGE PARTICLE COLLECTION EFFICIENCY CURVES

	Large particle collection efficiency							
Case	16%	23%	35%	50%	60%	70%	90%	98%
Base		0.48	0.59	0.67	0.71		0.84	1.01
Re = 1		.42	.53	.62	.67		.88	1.22
10		.40	.51	.60	.66		.86	
100		.54	.67	.76	.82		1.02	1.34
500		.56	.70	.80	.85		1.03	1.41
1,000		.51	.64	.73	.77		.94	1.23
15,000		.48	.59	.67	.71		.83	1.00
Q_1/Q_0 = 0.05	0.57		.73	.79		0.85	.93	1.11
.15		.34	.49	.59	.64		.78	.96
.25			.29	.45		.57	.69	.86
D_1/D_0 = 1.16			.57		.69		.80	
1.49	.37	.51	.62	.71		.80	.89	1.13
L_0/D_0 = 0.013		.48	.58	.67			.85	1.06
S/D_0 = 0.25		.47	.58	.65		.73	.87	.98
2		.49	.60	.69			.87	1.07
θ_0 = 30°			.65		.78		.96	
Collection Probes[a]								
(B)			.57		.69		.80	
(C)			.59		.71		.83	
(D)			.59		.71		.84	

[a] Collection probe A - thin wall
Collection probe B - infinite wall thickness
Collection probe C - finite wall thickness
Collection probe D - finite wall thickness with taper
(Collection probe designs are shown in Figure 18.)

TABLE A-2. VALUES OF $\sqrt{St}$ FOR THE SMALL PARTICLE COLLECTION EFFICIENCY CURVES

	Small particle collection efficiency							
Case	84%	77%	65%	50%	40%	30%	10%	2%
Base		0.23	0.39	0.47	0.51		0.58	0.64
Re = 1		.35	.46	.55	.60		.79	1.00
10		.35	.47	.56	.61		.79	
100		.41	.57	.68	.75		.96	1.23
500		.34	.54	.66	.72		.92	1.13
1,000		.28	.45	.55	.59		.71	
15,000		.24	.39	.47	.51		.58	.64
Q_1/Q_0 = 0.05	0.23		.46	.53		0.58	.60	.66
.15			.32	.43	.48		.56	.63
.25			.08	.32	.39	.45	.53	.60
D_1/D_0 = 1.16			.40		.51		.59	
1.49		.23	.43	.52		.61	.67	.74
L_0/D_0 = 0.013		.23	.38	.46		.53	.56	.63
S/D_0 = 0.25		.10	.31	.40		.46	.49	.55
2		.29	.44	.53		.60	.64	.69
Θ_0 = 30°			.43		.55		.62	
Collection Probes[a]								
(B)			---		---		---	
(C)			.34		.47		.54	
(D)			.45		.57		.65	

[a] Collection probe A - thin wall
Collection probe B - infinite wall thickness
Collection probe C - finite wall thickness
Collection probe D - finite wall thickness with taper
(Collection probe designs are shown in Figure 18.)

PAPER 3

A HEAVY GRAIN-LOADING IMPACTOR

DALE A. LUNDGREN
ERNEST R. CERINI
UNIVERSITY OF FLORIDA
DEPARTMENT OF ENVIRONMENTAL ENGINEERING SCIENCES

AND

MICHAEL L. SMITH
ANDERSEN SAMPLERS, INC.

ABSTRACT

This paper discusses a heavy grain-loading impactor (Andersen Model HCSS) which was designed for use in high grain loading applications, where standard impactors cannot be used because of collection surface overloading. The HCSS consists of two impaction chambers followed by a cyclone and glass fiber thimble. Construction of stainless steel allows its use in the high temperature, corrosive gas atmosphere encountered in industrial stack gas sampling.

Descriptive information on the HCSS is presented together with particle size collection characteristics. Data on the mass loading characteristics for a mineral dust aerosol are presented. Application areas are cited.

INTRODUCTION

The Andersen Model HCSS is a special application in-stack size-fractionating sampler developed specifically for particle size distribution measurement in high aerosol mass concentration gas streams (2 to 200 grams/m^3 or 1 to 100 grains/ft^3). Other commercially available in-stack impactors typically have mass deposit limitations on the order of 1 to 10 milligrams per stage, for mineral type aerosols, to avoid particle reentrainment problems. Therefore, these conventional impactors, when operating at 14 ℓpm (0.5 cfm) flow rates for 1 to 100 minute sampling times, are best suited to sampling in aerosol concentrations ranging from 0.002 to 2 grams/m^3 (0.001 to 1 grain/ft^3), giving total particulate matter collections of 3.5 to 35 mg. In this new sampler the particle fractionating stage surfaces are not coated with grease or filter media, making the recovery of collected material easier and chemical analysis simpler because analysis coating reactions and analysis interferences are eliminated. Because of stainless steel construction, sampling at high temperatures is possible (a unit has been successfully field tested at 1520°F) without the particle reentrainment problem often encountered when conventional impactors operate at high temperatures without collection surface coatings. This unit will fit through a 3-inch or larger sampling port and will operate in both the vertical and horizontal positions. The long length of the HCSS makes it less convenient to use in small diameter stacks and the difficulty of accurate recovery of small mass quantities makes it undesirable for use when sampling gas streams with aerosol concentrations less than 0.2 grams/m^3 (0.1 grain/ft^3).

Sampling of liquid aerosols is also possible if the final filter does not become overloaded. The glass fiber thimble provides a very large collection surface area; therefore overloading is unlikely with most aerosols. When sampling in very high temperature environments the glass fiber thimble is replaced by an alundum thimble. Because only three size fractionating stages are used, with a last stage classification at 1.5 μm (or optional 2.5 μm), the HCSS is not superior to, nor does it replace, conventional impactors. As stated, the HCSS is a special application size fractionating sampler, capable of giving good particle size distribution data in high aerosol mass concentration gas streams (where conventional impactors will overload and produce incorrect particle size distribution data).

SAMPLER DESCRIPTION

The Andersen HCSS consists of two impaction stages followed by a cyclone stage and a glass fiber thimble filter. This unit is shown schematically in Figure 1.

In use, an appropriate nozzle size is selected to enable isokinetic sampling within the approximate flow rate range from 8 to 20 ℓpm (0.3 to 0.7 cfm). The first impactor stage has a nominal cutpoint of 11 μm aerodynamic diameter at a 14 ℓpm (0.5 cfm) flow rate. The aerosol passing Stage 1 flows out through a set of three outlet tubes (only one of which is shown in Figure 1) and into the second stage impaction nozzle. Stage 2 is similar in design to Stage 1 but has a nominal cutpoint of 6 μm at the design flow rate. Aerosol exiting Stage 2, through a set of three equally spaced outlet tubes, next passes through a small cyclone of the Southern Research Institute design.[1] A standard 1.5 μm cutpoint cyclone is used, with a 2.5 μm cyclone available as an option. A high-efficiency glass fiber thimble filter removes all remaining particle matter.

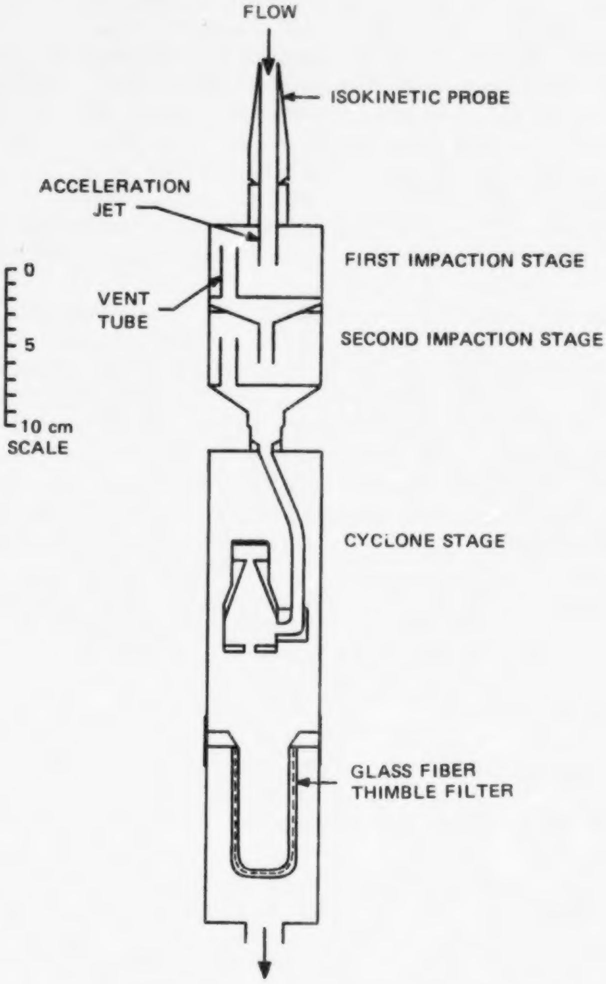
FLOW
ISOKINETIC PROBE
ACCELERATION JET
FIRST IMPACTION STAGE
VENT TUBE
SECOND IMPACTION STAGE
0
5
10 cm
SCALE
CYCLONE STAGE
GLASS FIBER THIMBLE FILTER

Figure 1. Schematic of the Andersen Model HCSS High Grain-Loading Impactor (from McFarland[3]).

Both impaction stages are scaled versions of the Andersen preseparators shown in detail in Figure 2. The model HCSS first stage has the same internal dimensions and collection characteristics as the previously tested preseparator.[2] A particle size-collection efficiency curve for a 14.2 ℓpm (0.5 cfm) flow rate, from McFarland, Ortiz and Bertch,[2] is reproduced as Figure 3. Extensive tests were run on this first stage separator using a monodisperse liquid oleic acid aerosol and a polydisperse dry fly ash aerosol. Data on the effect of flow rate upon cutpoint and mass loading characteristics are shown in Figures 4 and 5 respectively (from McFarland, Ortiz and Bertch[2]).

Stage 2 is similar to Stage 1 except for the jet dimensions. This modification changes the cutpoint as shown in unpublished data of McFarland[3] who determined the cutpoint of both stages and both optional cyclones, as shown in Figure 6. Loading characteristics of Stage 2 and the Southern Research Institute design cyclone were not previously reported; therefore the following performance tests were run.

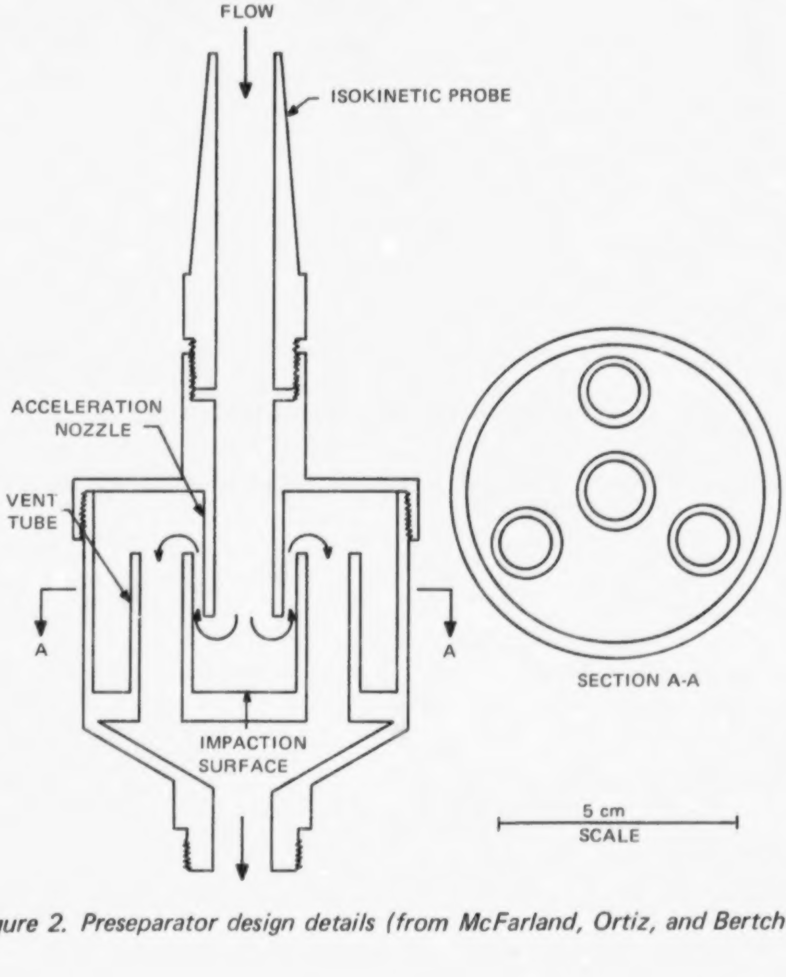

Figure 2. Preseparator design details (from McFarland, Ortiz, and Bertch[2]).

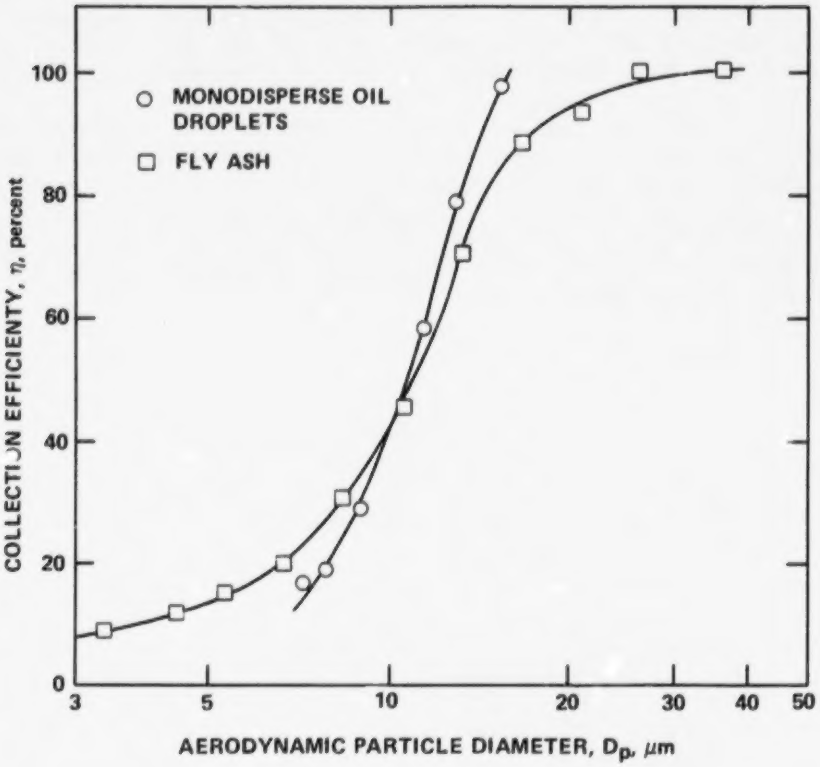

Figure 3. Preseparator particle size versus collection efficiency (from McFarland, Ortiz, and Bertch[2]).

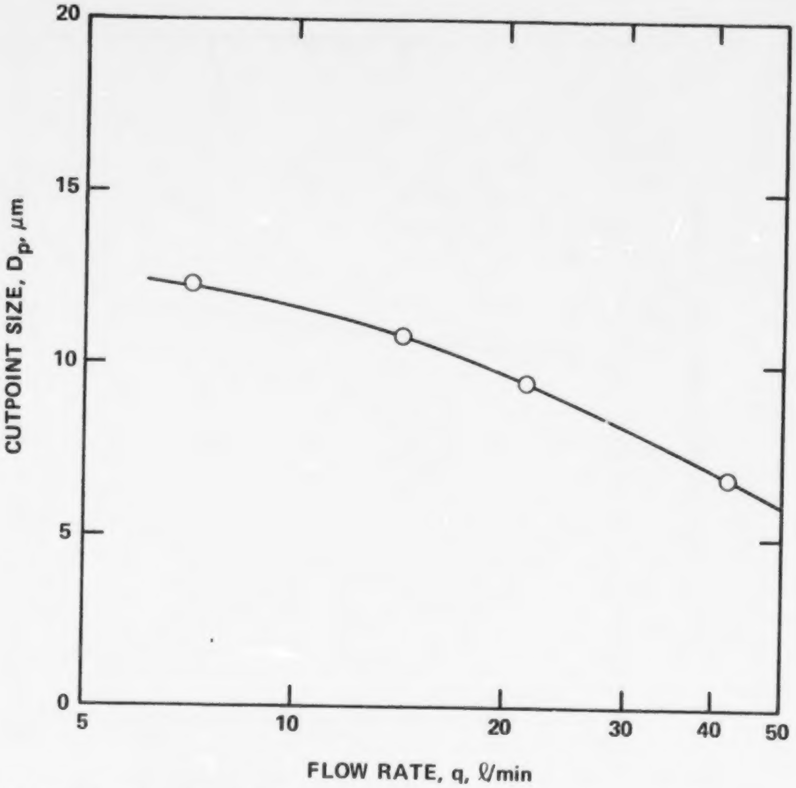

Figure 4. Effect of flow rate upon preseparator cutpoint (from McFarland, Ortiz, and Bertch[2]).

PERFORMANCE TESTS

The loading characteristics of the HCSS second stage (6 μm cut-size impactor) and third stage (1.5 μm cut-size cyclone) were evaluated using dry mineral dusts: AC Fine Test Dust and AC Coarse Test Dust (sometimes referred to as Arizona Road Dust). These are standard polydisperse mineral dusts of fairly well-known size distribution. Both dusts were dispersed into dry air with a Wright Dust Feed Mechanism.[4] Size distribution and concentration of the generated aerosol were determined by means of a standard multi-stage impactor using grease coated stainless steel collection surfaces conditioned at 200°F for one hour. Sampling time and flow rate were selected to produce near optimum stage collection deposits.

After the test aerosol concentration and size distribution were determined, the aerosol was sampled through the first two (impactor) stages of a clean HCSS and the penetrating aerosol concentration and size distribution were again determined using a standard multi-stage impactor. This initial two-minute aerosol penetration test was run on the clean HCSS sampler operating

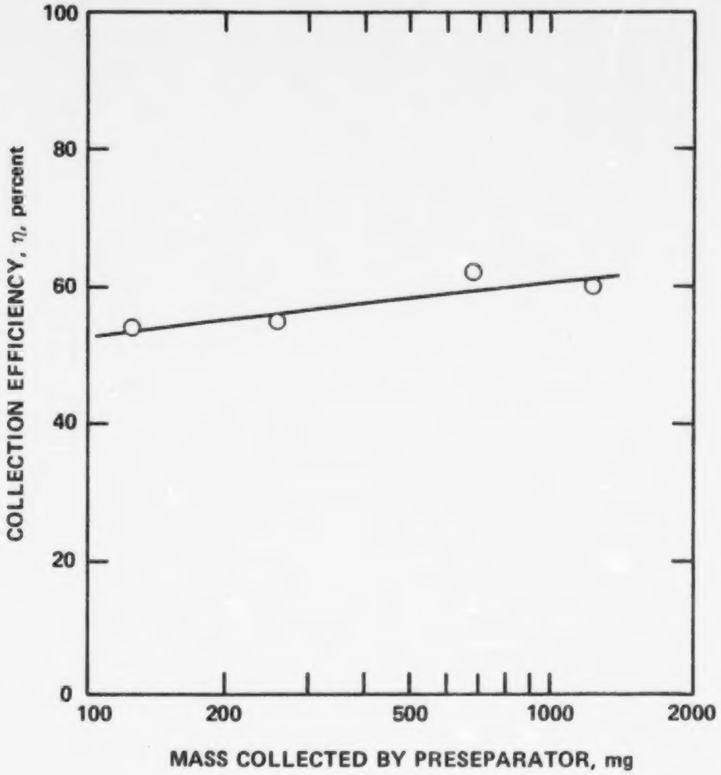

Figure 5. Preseparator mass loading characteristics (from McFarland, Ortiz, and Bertch[2]).

at the design flow rate of 14.2 ℓpm (0.50 cfm). After this initial penetration test, the first two stages were connected to the third or cyclone stage. Concentration and size distribution of the aerosol penetrating the clean cyclone were then determined using a standard multi-stage impactor. The three size fractionating stages were then connected to the glass fiber thimble and the complete HCSS unit was used to continue sampling the test aerosol for an additional 60 to 100 minutes.

After this loading period, the final filter was disconnected and a second two-minute standard multi-stage impactor test was run to determine aerosol concentration and size distribution penetrating the dust loaded cyclone. After removing the cyclone, aerosol concentration and size distribution penetrating the dust loaded second stage were likewise determined. Finally, the test aerosol concentration and size distribution were again determined with the multi-stage impactor. All stages of the HCSS were carefully cleaned and the mass of collected particulate matter determined.

This same sequence of tests were run using both AC Coarse and AC Fine Test Dust. Aerosol size distribution data, plotted

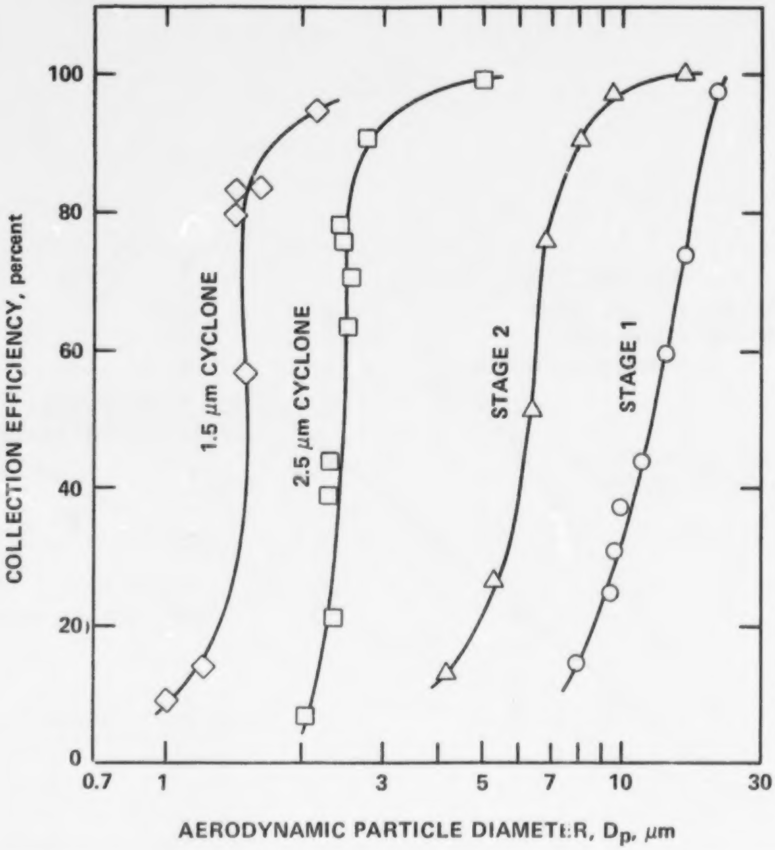

Figure 6. Particle size versus collection efficiency data for all stages of the Andersen Model HCSS sampler (from McFarland[3]).

on log normal paper, are shown for both the clean HCSS (noted as initial tests) and the dust-loaded HCSS (noted as final tests) in Figure 7 for the AC Fine Test Dust and in Figure 8 for the AC Coarse Test Dust. Actual dust quantities collected by each stage of the Model HCSS are also noted. Percent of dust penetrating the second and third stage, based on the initial two-minute test, the final two-minute test and the overall average for the 60- to 100-minute loading test did not significantly change for either stage.

Size classified mass fractions collected during the standard multi-stage impactor test using AC Fine Test Dust were used to determine the particle size/collection efficiency of both the second (impactor) and third (cyclone) stages of the HCSS. Mass concentration, before and after each respective stage, was ratioed for each particle size fraction (to determine the fractional penetration) and then used to calculate the stage fractional efficiency. Percent efficiency versus particle size (as particle

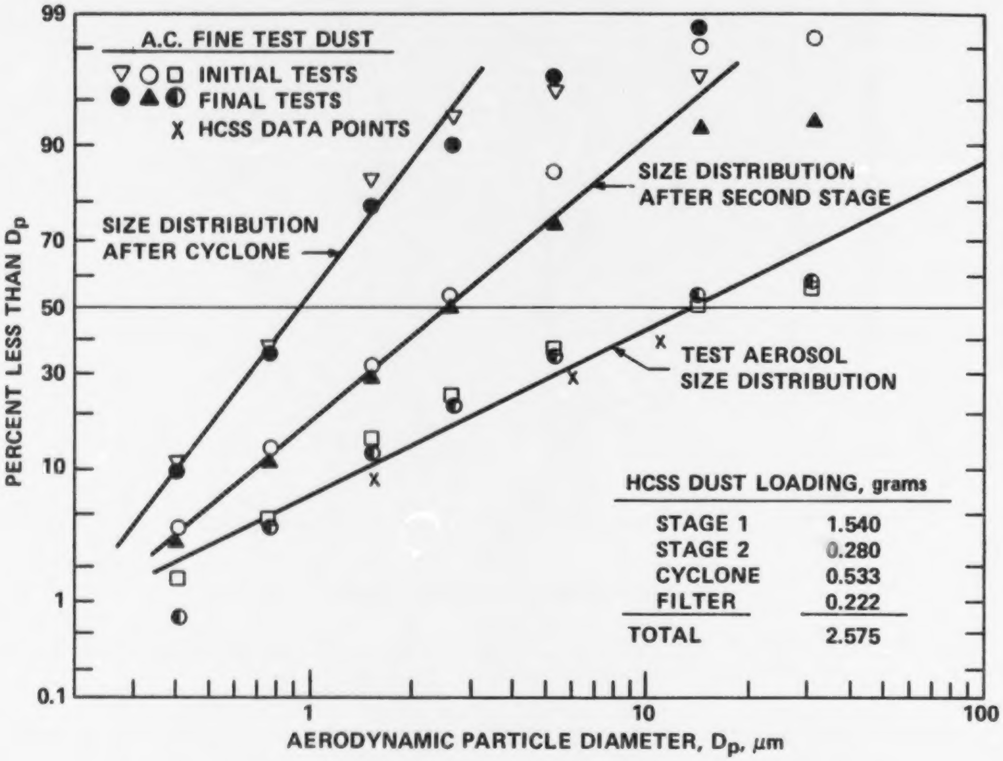

Figure 7. Inlet and outlet size distribution measurements using AC fine test dust.

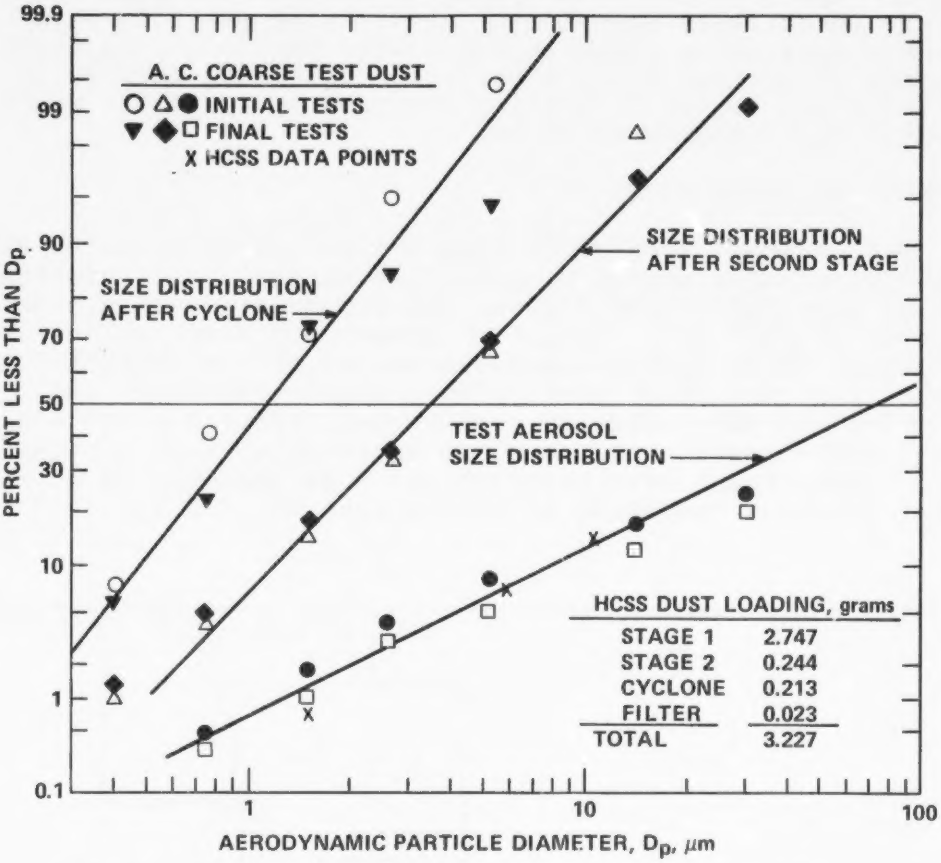

Figure 8. Inlet and outlet size distribution measurements using AC coarse test dust.

aerodynamic diameter) is shown in Figure 9. Monodisperse aerosol test data obtained by McFarland[3] is also shown. Similar data for the AC Coarse Test Dust is shown in Figure 10.

The explanation for the apparent difference in the cyclone particle size/collection efficiency curves for the two test dusts is poor experimental accuracy due to low stage weight gain. As many researchers have found, determining particle size/efficiency data using impactor classified particle size fractions, obtained before and after a particle collection device, is very difficult and serves to justify the need to run tests using known diameter monodisperse aerosols.

SUMMARY AND CONCLUSIONS

The Andersen Model HCSS high grain-loading impactor was tested with polydisperse mineral dust aerosols. If reentrainment of dust had occurred after the accumulation of a significant quantity of dust by a collection stage, the stage collection efficiency would decrease and the amount of coarse particles penetrating that stage would significantly increase. Size distribution and concentration measurements after a clean and dust-loaded HCSS impactor indicated no measurable reentrainment of dust. These tests were run with the HCSS impactor in a horizontal position operating at a flow rate of 14.2 ℓpm (0.5 cfm),

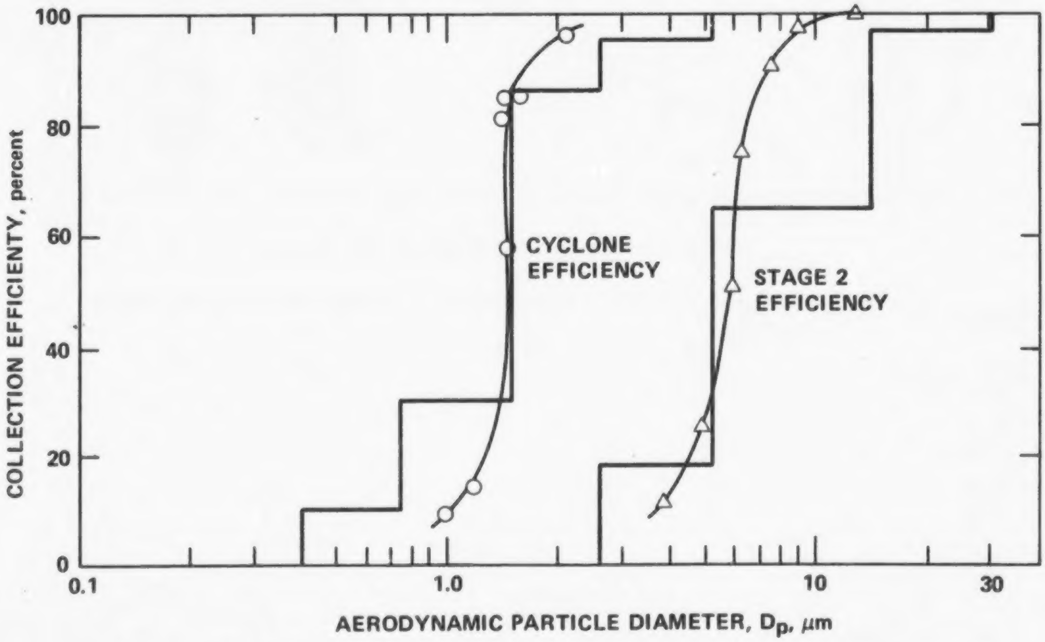

Figure 9. Particle size versus collection efficiency calculated from conventional impactor measurements using AC fine test dust (from McFarland[3]).

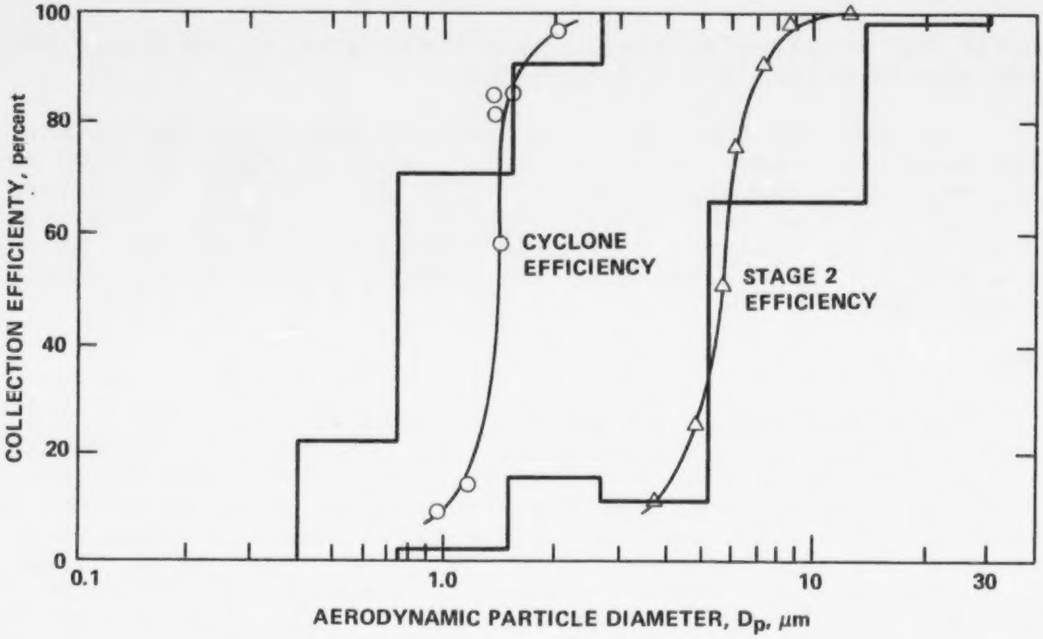

Figure 10. Particle size versus collection efficiency calculated from conventional impactor measurements using AC coarse test dust (from McFarland[3]).

sampling isokinetically through a straight sampling inlet. This is considered to be a realistic test and certainly indicates that the unit performed as intended. Aerosol size distribution plots determined using the HCSS collected particulate matter were essentially the same as determined by the standard multistage impactor, which used grease coated collection surfaces (see Figures 7 and 8). Tests run with the unit in a vertical position and with downward flow gave results comparable to the horizontal position. Tests run with upward flow through a vertical unit show somewhat higher measured penetrations.

The HCSS is recommended for aerosol size distribution measurement if the aerosol mass concentration is in the range from 2 to 200 grams/m^3 (1 to 100 grains/ft^3); with a gas stream of almost any gas composition compatible with type 316 stainless steel; at any gas temperature up to 1500°F; and at any reasonable gas pressure. For long time sampling (2 to 24 hours) the HCSS can be used for sampling aerosol mass concentrations as low as 0.2 grams/m^3 (0.1 grains/ft^3).

Particle reentrainment may be a problem for certain aerosols at flow rates of 28 ℓpm (1 cfm) or higher, although field tests with a non-bouncy aerosol did not indicate a problem. McFarland, Ortiz and Bertch[2] reported that gravitational settling within the HCSS first stage will cause a shift in collection characteristics at flow rates below 7 ℓpm (0.25 cfm). The unit may be useful for sampling at these lower flow rates if the stage collection characteristics are determined.

The HCSS has the ability to fill an important gap in the size selective sampling of aerosols: that of sampling high aerosol mass concentration streams. Inlets to particulate collection devices, fugitive dust sources, pneumatic conveying lines, particulate process streams, long time sampling applications, or use as a particle size classifier are example areas for application of the HCSS.

NOTE

Since this report was prepared, several additional field tests have been run on a very high concentration, large particle size (∿1 to 500 μm diameter) industrial aerosol. The larger particles were sintered spheres with minimum adhesion properties. Extremely high mass loadings in the first impactor stage were obtained and a carryover of about 7% of the first stage catch to the second stage was determined by a subsequent analysis. The carryover was fairly constant with first stage loading (from 5 to 25 grams) and particle size (over the 10 to 500 μm size range). This is an extreme sampling condition and represents a worst case example. Because ∿80% of the aerosol was caught on the first stage, a 7% carryover to the second stage about doubled the second stage catch and would have caused a significant error. Some carryover from the second impactor stage was also determined but was not considered significant. If appreciable quantities of 100+ μm particles of a solid, spherical shape exist in the sampled gas stream, it is recommended that the second stage catch be checked for reentrainment and a suitable correction made.

REFERENCES

1. Smith, W.B., and R.R. Wilson, Jr. Development and Laboratory Evaluation of a Five-Stage Cyclone System. EPA-600/7-78-008, U.S. Environmental Protection Agency, Research Triangle Park, NC, 1978.

2. McFarland, A.R., C.A. Ortiz, and R.W. Bertch, Jr. A High Capacity Preseparator for Collecting Large Particles. Atmos. Environ. 13:761, 1979.

3. McFarland, A.R. Laboratory Evaluation of Andersen Hi-Capacity Stack Sampler. Unpublished engineering report prepared for Andersen Samplers, Inc., December, 1978.

4. Wright, B.M. A New Dust Feed Mechanism. J. Sci. Instrum. 27:12, 1950.

PAPER 4

VELOCIMETRIC DETERMINATION OF AERODYNAMIC DIAMETER IN THE RANGE FROM 0.1 μm TO 15 μm

JAMES C. WILSON
BENJAMIN Y.H. LIU
PARTICLE TECHNOLOGY LABORATORY
MECHANICAL ENGINEERING DEPARTMENT
UNIVERSITY OF MINNESOTA

ABSTRACT

A technique for determining the aerodynamic diameter of aerosol particles is described. Particles are accelerated in a nozzle, and their velocity is measured near the nozzle exit. Careful choice of nozzle geometry and flow rate permits aerodynamic diameter to be determined from the particle velocity.

Experimental tests are reported in which velocity is measured with a laser-Doppler velocimeter. Theoretical analysis of the experimental tests shows that particle velocity can be accurately predicted.

Theoretical study of particle dynamics in the nozzle shows that both aerodynamic diameter and density affect particle velocity if the motion is ultra-Stokesian. This introduces uncertainty in determination of aerodynamic diameter for such particles and provides an incentive for minimizing the particle Reynolds number.

Nozzle configurations and flow rates are proposed which should permit determination of aerodynamic diameter in the following ranges: 0.1 μm to 1.5 μm, 0.5 μm to 10 μm, 1.5 μm to 15 μm, and 1 μm to 15 μm.

NOMENCLATURE

a	Radius of the nozzle at the exit
C	Slip correction
C_D	Drag coefficient
d	Distance from nozzle exit to point of measurement

d_f	Fringe spacing
D_a	Aerodynamic diameter
D_p	Particle diameter
ΔD_p	Diameter interval
f_D	Doppler frequency
F_b	Body force acting on a particle
F_d	Drag force acting on a particle
g	Gravitational acceleration
m	Particle mass
P	Pressure upstream of the nozzle
ΔP	Pressure drop across the nozzle
r	Radius of trajectory of particle executing curved motion
R	Radius of nozzle at position x
Re	Reynolds number, based on D_p
Re_p	Particle Reynolds number
St	Stokes number
t	Time
U_e	Gas velocity at exit of the nozzle
U_g	Gas velocity
$U_g{}^*$	Dimensionless gas velocity
U_p	Particle velocity
$U_p{}^*$	Dimensionless particle velocity
U_{pg}	Geometric mean particle velocity
U_t	Terminal velocity of particle settling under gravity
x	Position along centerline of nozzle axis
α	Angle of convergence of the nozzle

λ	Wavelength of laser radiation
μ	Viscosity of gas
ρ	Density of the gas
ρ_p	Density of the particle
σ_{gs}	Geometric standard deviation of size distribution
σ_{gv}	Geometric standard deviation of velocity distribution
τ	Period of Doppler signal
ω	Angular velocity of a particle in curved motion

INTRODUCTION

Aerodynamic diameter is an important measure of the size of aerosol particles. It is a single parameter combining particle density, diameter, shape factor, and slip correction, and is used to predict the motion of particles in settling, impaction, or in a centrifugal force field. These motions frequently cause particle deposition in the respiratory tract and particle collection in gas cleaning devices such as cyclones and settling chambers. Consequently, it is often desirable to make accurate measurements of aerodynamic diameter in order to study and predict these phenomena.

The popularity of cascade impactors, cyclones, and impingers is due in part to the fact that they measure aerodynamic diameter. However, these devices separate the particles from the suspending gas, and their use often involves time-consuming analysis of the collected particles.

This paper describes a new instrument which allows rapid, in-situ measurement of aerodynamic diameter. The instrument makes use of a nozzle to accelerate the particles and a laser-Doppler velocimeter to measure the particle velocity near the nozzle exit, as shown in Figure 1.

Small particles are able to follow the flow as it accelerates rapidly in the nozzle. Such particles emerge from the nozzle with velocities near that of the gas. Large particles lag behind the gas flow and emerge with lower velocities. The velocity of individual particles emerging from the nozzle can be measured by a laser-Doppler velocimeter. In this system, the laser beam is split and the two coherent beams are focused by the transmitting optics to a crossover point where they form interference fringes. A particle passing through the fringes scatters light, and the scattered intensity rises and falls as

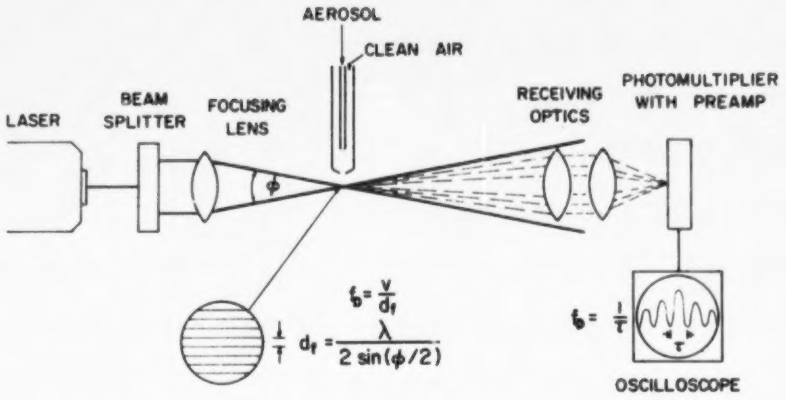
AEROSOL
CLEAN AIR
LASER
BEAM SPLITTER
FOCUSING LENS
RECEIVING OPTICS
PHOTOMULTIPLIER WITH PREAMP
ϕ
$f_D = \frac{v}{d_f}$
$d_f = \frac{\lambda}{2\sin(\phi/2)}$
$f_D = \frac{1}{\tau}$
τ
OSCILLOSCOPE

Figure 1. Schematic of the laser-Doppler velocimeter system.

the particle passes through the bright and dark bands. The scattered light is collected and focused on a photomultiplier tube (PMT), and the frequency of the intensity modulation is counted. The particle velocity perpendicular to the fringes equals this Doppler frequency, f_D, multiplied by the fringe spacing, d_f, which is calculated from the wavelength of the laser radiation and the angle between the beams. By choosing appropriate nozzle parameters and flow rates, the aerodynamic diameter can be determined from the measured particle velocity.

Other methods of determining particle size from particle velocity are reviewed elsewhere.[1]

THEORETICAL CONSIDERATIONS

Aerodynamic Diameter

The definition of aerodynamic diameter and its role in determining particle motion strongly affect the design of this instrument. Aerodynamic diameter is often defined as the diameter of a unit density sphere with the same settling velocity as the particle in question.[2] The usual mathematical expression for aerodynamic diameter is derived here by considering the motion of particles which settle with small values of the particle Reynolds number.

Equation 1 is the equation of particle motion and Equation 2 is Stokes law.

$$m \frac{d\vec{U}_p}{dt} = \vec{F}_d + \vec{F}_b \qquad (1)$$

$$F_d = \frac{(\vec{U}_g - \vec{U}_p)\, 3\, \pi\, \mu\, D_p}{C} \qquad (2)$$

Stokes law accurately describes the drag force on a spherical particle moving with a Reynolds number, Re_p, less than about 0.5, where

$$Re_p = \frac{|\vec{U}_g - \vec{U}_p| \rho D_p}{\mu} . \qquad (3)$$

In the case of a particle settling in still air under gravity, $U_g = 0$ and $F_b = mg$. The terminal velocity, U_t, is reached when the drag force equals the weight. Thus, for a particle settling in Stokes regime (i.e., $Re_p < 0.5$),

$$U_t = \frac{C D_p^2 \rho g}{18\mu} \qquad (4)$$

Since D_a, the aerodynamic diameter, is the diameter of the unit density sphere having the same U_t as the particle in question, D_a can be calculated as follows:

$$[C(D_a)]^{\frac{1}{2}} D_a = [C(D_p)\rho_p]^{\frac{1}{2}} D_p . \qquad (5)$$

Non-spherical particles are treated by including the dynamic shape factor.[3,4]

Equation 5 does not follow from the settling velocity definition if the settling occurs outside of Stokes regime, as is often the case for large particles. However, even in such cases, Equation 5 is taken as the definition of aerodynamic diameter because D_a is useful in predicting other motions of the particle which may occur in Stokes regime. For example, consider impaction ($F_b = 0$) and centrifugal motion ($F_b = mr\omega^2$). Combining Equations 1 and 2 with the appropriate expression for F_b results in an equation which can be written in terms of D_a and solved for the particle trajectory. Thus, for given flow field and initial conditions, the particle trajectory in an impactor or cyclone is determined by D_a if the motion is Stokesian. This is true whether or not the particle settles in Stokes regime.

The Present Technique

In the method described here, D_a is determined by accelerating the particle in a converging nozzle and measuring its velocity near the nozzle exit. Appropriate flow conditions must be chosen if D_a is to be accurately determined from the particle velocity. Dimensional analysis of the equations of motion indicates the factors involved in the choice.

Consider a particle on the axis of the nozzle shown in Figure 1. Equation 1 describes the motion of the particle where F_b equals zero and F_d is expressed in Equation 6.

$$F_d = \frac{\pi \rho (U_g - U_p)^2 D_p^2 C_D}{8C} \qquad (6)$$

C_D is the drag coefficient. For Rep <0.5, Stokes' law is expressed as

$$C_D = 24/Re_p \ . \qquad (7)$$

For $0.5 < Re_p < 100$, Fuchs[3] suggests the following expression for C_D:

$$C_D = \frac{24}{Re_p} + \frac{4}{(Re_p)^{1/3}} \qquad (8)$$

Equations 1 and 6 are combined and written in dimensionless form to produce Equation 9,

$$\frac{dU_p^*}{dx^*} = \frac{Re\ (U_g^* - U_p^*)^2 C_D}{24(St)U_p^*} \qquad (9)$$

where St is the Stokes number

$$St = C\ D_p^2\ \rho_p\ U_e/18\ \mu\ a \qquad (10)$$

and

$$Re = U_e\ D_p\ \rho/\mu \ . \qquad (11)$$

U_e is the centerline gas velocity at the nozzle exit and a is the nozzle exit radius. Also,

$$U_g^* = U_g/U_e \qquad (12)$$

$$U_p^* = U_p/U_e \qquad (13)$$

$$x^* = x/a \qquad (14)$$

and

$$Re_p = Re\ (U_g^* - U_p^*) \ . \qquad (15)$$

Substitution of Equations 7 and 15 into 9 shows that $U_p{}^*$ at a given point depends upon St for motion in which $Re_p < 0.5$. Thus, for motion in Stokes regime, St, and hence, D_a, can be determined from $U_p{}^*$. In cases where $Re_p > 0.5$, the use of Equation 8 implies that $U_p{}^*$ depends upon Re_p as well as St. Thus, particle velocity depends upon the product of $\rho_p C$, as well as D_a, when Re_p is large. Therefore, particles with the same velocity may have different values of D_a if they have different densities. This introduces an uncertainty in the determination of D_a from $U_p{}^*$ when ρ' is unknown and Re_p is large. This uncertainty is minimized in this method by minimizing gas velocity, and hence, Re_p. This distinguishes the present method from those which employ nozzles operating at large values of pressure drop.

EXPERIMENTAL TEST

Measurements were made of the velocity of particles emerging from a nozzle. Particle size and flow through the nozzle were varied. The experimental system is diagrammed in Figure 2. The actual test nozzle was 1.77 cm in length and had entrance and exit diameters of 1.05 cm and 0.106 cm, respectively. A short throat was found near the nozzle exit. The pressure across the nozzle was varied between 2.54 cm H_2O and 691 cm H_2O. Sheath air was used to confine the aerosol near to the center streamline.

Monodisperse aerosols were generated from PSL and PVT suspensions, as well as with a vibrating orifice aerosol generator. The velocity of individual particles was measured with a laser-Doppler velocimeter using a He-Ne laser. A fringe spacing of

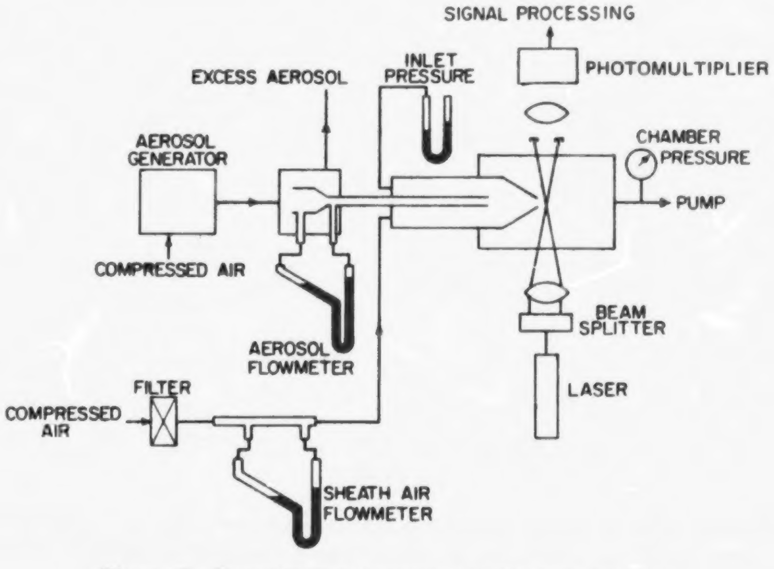
SIGNAL PROCESSING
PHOTOMULTIPLIER
EXCESS AEROSOL
INLET PRESSURE
AEROSOL GENERATOR
CHAMBER PRESSURE
PUMP
COMPRESSED AIR
BEAM SPLITTER
AEROSOL FLOWMETER
LASER
FILTER
COMPRESSED AIR
SHEATH AIR FLOWMETER

Figure 2. Experimental system for the test nozzle.

15.9 μm was used for particles larger than 3 μm, and a 15 mw He-Ne laser and 7.13 μm fringe spacing was used for smaller particles. The center of the measuring volume was approximately 145 μm from the exit of the nozzle and extended four fringes on either side of this point. Details of the experimental procedure and results are described in detail elsewhere.[1,5]

Each experimental trial resulted in a frequency distribution of velocities which is characterized by a geometric mean velocity, U_{pg}, and a geometric standard deviation, σ_{gv}. The geometric mean velocities are plotted as a function of particle size and for two values of nozzle pressure drop in Figure 3.

The resolution which could be expected from this system can be estimated from the values of σ_{gv} and the particle velocity vs. diameter curve. σ_{gv} indicates the width of the measured velocity distribution. For example, a value of 1.02 implies that approximately 67% of the measured velocities fell within 2% of the geometric mean value. An interval in diameter, ΔD_p, corresponding to σ_{gv} can be deduced from the slope of the velocity vs. diameter curve and σ_{gv}. Table 1 lists measured values of σ_{gv} and corresponding values of ΔD_p.

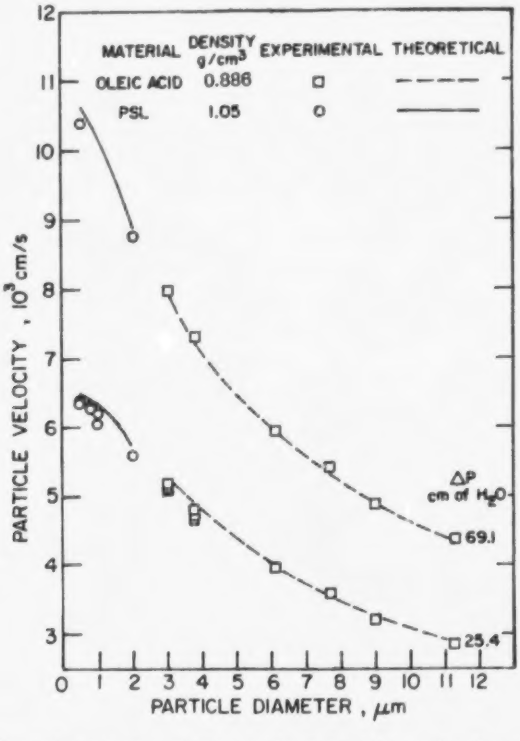

Figure 3. Experimental and theoretical particle velocity at a distance of 145 μm from the nozzle exit as a function of particle diameter and pressure drop across the test nozzle.

TABLE 1. SELECTED VALUES OF σ_{gv} AND CORRESPONDING DIAMETER INTERVALS FOR THE TEST NOZZLE

	ΔP = 25.4 cm H_2O		ΔP = 69.1 cm H_2O	
D_p, μm	σ_{gv}	ΔD_p, μm	σ_{gv}	ΔD_p, μm
0.5	1.007	±0.25	1.02	±0.19
3.04	1.005	±0.05	1.006	±0.06
9	1.007	±0.15	1.008	±0.13

If the test aerosols were truly monodisperse, ΔD_p would provide a good estimate of the resolution of the system. In the present case, the system resolution for larger particles is smaller than ΔD_p, since the actual width of the test aerosol size distribution is significant compared to ΔD_p. For the submicron particles, the slope of the velocity vs. diameter curve limits resolution for small values of pressure drop, and the increase in σ_{gv}, perhaps due to turbulence, limits resolution at large values of pressure drop.

TEST OF THE THEORY

Theoretical calculations were made of particle velocity in the test nozzle. These values were compared with the experimental results as a check on the theory. The first step in the calculation was to calculate the air velocity in the nozzle from the pressure drop and the nozzle dimensions. Some asymmetries in the nozzle shape required that average values of radius be determined at positions along the axis to allow an axisymmetric representation of the nozzle. The axisymmetric representation of the nozzle exit region is outlined in Figure 4.

The velocity of the air in the nozzle was calculated using two methods. Boundary layer calculations[6,7] were used to determine the velocity at every point in the nozzle, and Bernoulli's law applied to plug flow was used to calculate only centerline velocities. Both calculations were made for the constant property fluid case. (See reference 5 for details.) The two methods agreed quite well on the centerline velocity, as is shown in Figure 4. The boundary layer calculations also provided information on the flow profile in the test nozzle. The calculated flow profiles suggest that even for the lowest pressure drop, a sheath air flow equal to one-half of the total flow is adequate to insure that all particles experience nearly the same flow field. Therefore, only the centerline velocities are used in the calculations of particle velocity.

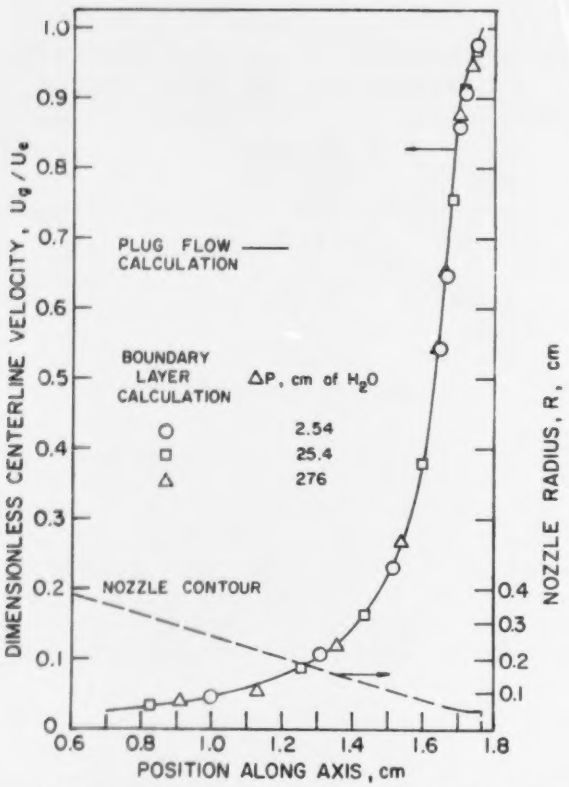

Figure 4. Air velocity on the centerline of the test nozzle calculated using the boundary-layer approximation and Bernoulli's law applied to plug flow. The axisymmetric representation of the nozzle exit region is also shown.

The particle velocity was calculated using a Runge-Kutta technique to solve Equation 1 with the drag force described by Equation 6 and the drag coefficients described by Equations 7 and 8. The particle velocity measurements were made approximately 145 μm downstream of the nozzle exit; therefore, the integration was continued to this point. The gas velocity was assumed constant over this distance. The particle and gas velocities were assumed identical at the entrance to the nozzle. The results of the calculations are shown in Figure 3.

Comparison of the experimental and theoretical values of particle velocity shows good agreement. The percent mean deviation between the measured and calculated values is on the order of 1.1% for $\Delta P = 61.9$ cm of H_2O. At a $\Delta P = 276$ cm of H_2O, the incompressible flow assumption should begin to fail, yet the mean deviation between measured and calculated velocities is only about 3%.

MEASUREMENT OF AERODYNAMIC DIAMETER

Measurement of aerodynamic diameter by this technique requires careful choice of nozzle and flow parameters. These parameters determine the resolution of the systems (particularly for smaller particles), the uncertainty introduced by uncertain density and the aerosol sample rate. General solutions to the dimensionless equation of motion were obtained to facilitate these choices. Figure 5 shows the generalized nozzle geometry used in the investigation. Three angles, $\alpha = 15°$, $30°$, and $45°$, were selected, and the dimensionless gas velocity on the centerline of each nozzle was calculated using Bernoulli's law for ideal, one-dimensional flow. The gas velocity was assumed to be constant over the distance d from the nozzle exit to the point of measurement.

Equation 9 was then solved numerically to find the dimensionless particle velocity, U_p*, for each nozzle as a function of St, Re, and d. Figure 6 shows results for $\alpha = 45°$ and $d = 0.2a$. Solution sets were obtained for $\alpha = 15°$, $30°$, and $45°$, with $d = 0$, $0.2a$, $0.4a$, and $0.6a$.[5] In the case shown in Figure 6, the principal change in dimensionless velocity occurs between $(St)^{1/2} = 0.4$ and $(St)^{1/2} = 4$. This geometry, then, should allow approximately one decade in D_a to be measured for a given flow rate. To determine a calibration curve, the smallest aerodynamic diameter to be measured with this system is assigned a value of $(St)^{1/2}$ equal to about 0.4. This fixes the ratio of U_e/a. Choosing the total flow in the nozzle then determines U_e and a. The curves are calculated for incompressible flow in the nozzle; therefore, the pressure drop across the nozzle must be small compared to the upstream pressure. Once U_e and a are chosen, values of St, Re, and D_a are determined from Equations 10, 11, and 5 for particles with the desired densities. Then U_p* is determined from the curves in Figure 6 and is plotted against D_a.

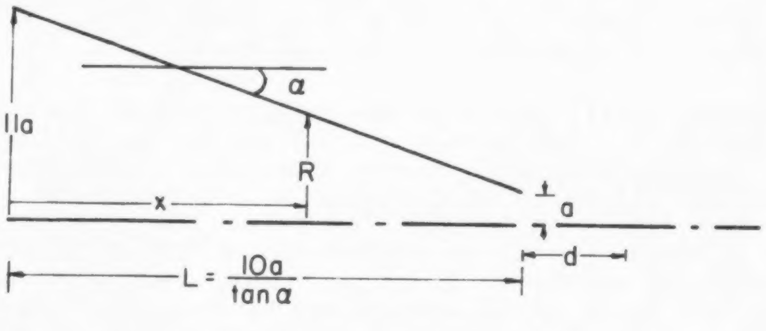

Figure 5. Nozzle shape and parameters used in the theoretical analysis.

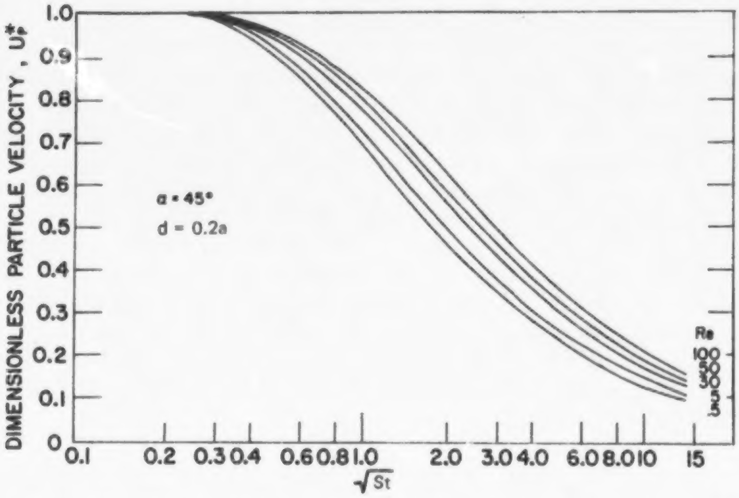

Figure 6. Dimensionless particle velocity as a function of Re and $(St)^{1/2}$ for a nozzle having $\alpha = 45°$ and $d = 0.2a$.

Figures 7 and 8 show curves of U_p* vs. D_a obtained from Figure 6. In both cases, $\alpha = 45°$, $a = 0.05$ cm, and $d/a = 0.2$. However, $U_e = 9500$ cm/s in the first case, and $U_e = 1200$ cm/s in the second.

The system shown in Figure 7 should permit the measurement of D_a for atmospheric aerosols in the range from 0.5 µm to 10 µm. For particles having D_a larger than about 2 µm, an uncertainty is introduced into the determination of D_a from U_p* if particle density is unknown. This uncertainty increases with D_a and can be reduced by reducing U_e, as is done in Figure 8. Here, resolution is lost for submicron particles, and the sample rate is reduced to a level unsuitable for atmospheric sampling; however, an even wider range of densities results in a smaller uncertainty in D_a. Experimental tests are required to determine the resolution for small particles and the maximum suitable sample flow rate. However, sample flow rates near 37 cm^3/s and 4.7 cm^3/s, respectively, are expected for the two cases.

Different nozzle and flow parameters result in the curves shown in Figure 9. The nozzle exit diameter is sufficiently large so that velocity measurement can take place very near the exit, although the value of $d = 0$ is an exaggeration. Reducing d/a moves the curves in Figure 6 to the left. The aerosol sample flow rate in this case is estimated to be 500 cm^3/s and should be sufficient to permit sampling of coarse particles in the atmosphere. The uncertainty introduced by density variations between 1 and 4.5 g/cm^3 is limited to about ±5% if $\rho_p = 2$ g/cm^3 is chosen as the reference curve.

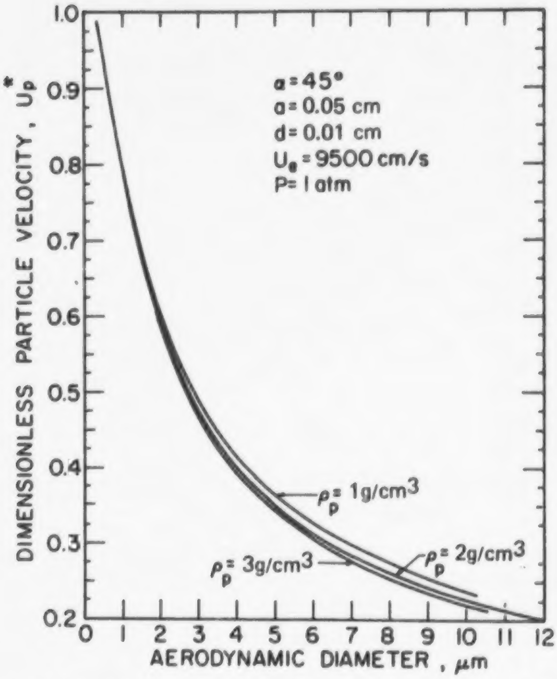

Figure 7. Calibration curve for a nozzle whose parameters were chosen to permit measurement of atmospheric aerosols in the 0.5 μm to 10 μm range. The sample flow rate would be approximately 37 cm^3/s.

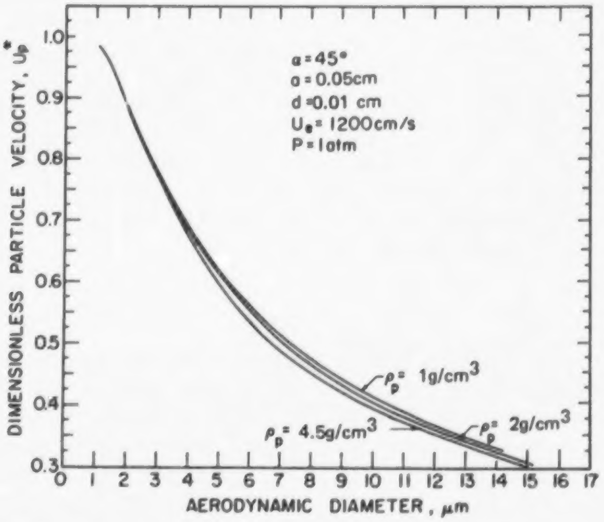

Figure 8. Calibration curve for a nozzle whose parameters were chosen to permit measurement of aerosols in the 1.5 μm to 15 μm range. The sample flow rate would be approximately 4.7 cm^3/s.

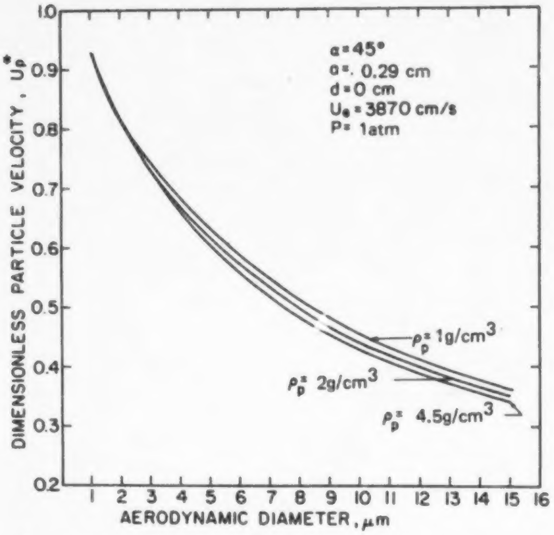

Figure 9. Calibration curve for a nozzle whose parameters were chosen to permit measurement of particles in the range from 1.5 μm to 15 μm. The sample flow rate should be adequate to permit convenient sampling of coarse particles in the atmosphere.

Measurement of D_a between 0.1 and 1.5 μm may be accomplished with a nozzle operating at reduced pressure. In the case shown in Figure 10, the pressure upstream of the nozzle is assumed to be 0.5 atm. This may be accomplished by passing the aerosol through a critical orifice upstream of the nozzle. The pressure drop in the nozzle itself is about 0.16 of the upstream pressure. The values of aerodynamic diameter shown in Figure 10 were calculated for 1 atm pressure. Experimental tests will be required to determine the effect of turbulence on the resolution and the suitable aerosol sample flow rate. Aerodynamic diameter is not often useful in predicting the motion of particles having diameters of a few tenths of a micron. For such particles, diffusion is often more important than impaction. However, measurements of D_a may be as informative in this size range as the conventional measurements of optical diameter.

CONCLUSIONS

A velocimetric technique for measuring aerodynamic diameter has been described. The method involves accelerating particles in a nozzle and measuring their velocity near the nozzle exit. Nozzle geometries and flow rates have been proposed for measurement of aerodynamic diameter in the following ranges: 0.1 μm to 1.5 μm, 0.5 μm to 10 μm, 1.5 μm to 15 μm, and 1 μm to 15 μm. Uncertain particle density introduces uncertainty in the measurement for the larger particles in each range, and the smallest

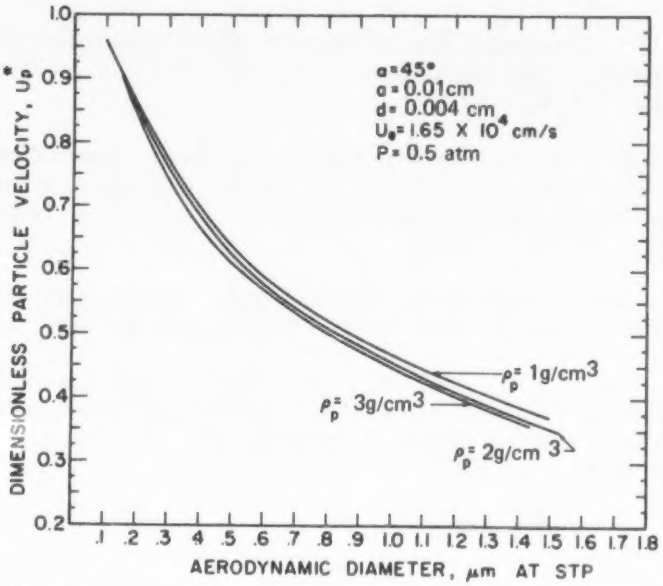

Figure 10. Calibration curve for a nozzle whose parameters were chosen to permit measurement of particles in the 0.1 μm to 1.5 μm range. Pressure upstream of the nozzle is assumed to be 0.5 atm.

particles in each range may be affected by turbulence which degrades resolution. This approach allows aerodynamic diameter to be accurately measured rapidly and in situ.

ACKNOWLEDGEMENTS

This work was completed under a contract, No. EY-76-S-02-1248, from the U.S. Energy Research and Development Administration. The laser-Doppler velocimeter was loaned by TSI, Inc., St. Paul, Minnesota. This report is Particle Technology Laboratory Publication No. 398.

REFERENCES

1. Wilson, J.C., and B.Y.H. Liu. Aerodynamic Particle Size Measurement by Laser-Doppler Velocimetry. To be published in J. Aerosol Sci.

2. International Commission on Radiological Protection Task Group on Lung Dynamics. Deposition and Retention Models for Internal Dosimetry of Human Respiratory Tract. Health Phys. 12:173-207, 1966.

3. Fuchs, N.A. The Mechanics of Aerosols. Pergamon Press, New York, 1964.

4. Raabe, O.G. Aerosol Aerodynamic Size Conventions for Inertial Sampler Calibration. J. Air Pollut. Control Assoc. 26:856-860, 1976.

5. Wilson, J.C. Aerodynamic Particle Size Measurement by Laser-Doppler Velocimetry. Ph.D. Thesis, University of Minnesota, Mechanical Engineering Department, Particle Technology Laboratory, 1978.

6. Patankar, S.V., and B.D. Spaulding. Heat and Mass Transfer in Boundary Layers, 2nd Ed. Intertext Books, London, 1970.

7. Sparrow, E.M., B.R. Baliga, and S.V. Patankar. Heat Transfer and Fluid Flow Analysis of Interrupted-Wall Channels, with Application of Heat Exchangers. J. Heat Transfer, 99 Series C:4-11, 1977.

PAPER 5

A PROTOTYPE PARTICULATE STACK SAMPLER WITH SINGLE-CUT NOZZLE AND MICROCOMPUTER CALCULATING/DISPLAY SYSTEM

JOHN C. ELDER
LARRY G. LITTLEFIELD
MARVIN I. TILLERY
LOS ALAMOS SCIENTIFIC LABORATORY
UNIVERSITY OF CALIFORNIA

ABSTRACT

A prototype particulate stack sampler (PPSS) has been developed to improve on the existing EPA Method 5 sampling apparatus. Its primary features are (1) higher sampling rate (56 ℓ/min); (2) display (on demand) of all required variables and calculated values by a microcomputer-based calculating and display system; (3) continuous stack gas moisture determination; (4) a virtual impactor nozzle with 3 μm mass median diameter cutpoint which collects fine and coarse particle fractions on separate glass fiber filters; (5) a variable-area inlet to maintain isokinetic sampling conditions; and (6) conversion to stainless steel components from the glass specified by EPA Method 5. The basic sampling techniques of EPA Method 5 have been retained; however, versatility in the form of optional in-stack filters and general modernization of the stack sampler have been provided in the prototype design. Laboratory testing with monodisperse dye aerosols has shown the present variable inlet, virtual impactor nozzle to have a collection efficiency which is less than 77% and significant wall losses. This is primarily due to lack of symmetry in this rectangular jet impactor and short transition lengths dictated by physical design constraints (required passage of the nozzle through a 7.6 cm (3 in) diameter stack port). Electronic components have shown acceptable service in laboratory testing although no field testing of the prototype under a broad range of temperature, humidity, and SO_2 concentration has been undertaken.

INTRODUCTION

The standard manual stack sampling method for particulates, EPA Method 5,[1] was reviewed to identify needed improvements.[2] A prototype particulate stack sampler (PPSS) incorporating the more desirable improvements into a general purpose particulate stack sampler has been developed. Increasing the flow rate (double the 28 ℓ/min of most Method 5 samplers commercially available) permits shorter sampling time, collection of a larger sample, or greater sensitivity. Other major improvements include: electronic calculating/display of calculated variables such as stack velocity, sample volume, and per cent of isokinetic sampling conditions; electronic continuous readout instrumentation for temperature, pressure, flow, and humidity; reduced weight in individual packages; stainless steel surfaces contacting the gas stream; improved structural strength to reduce breakage; single-point particle size classification (3 μm aerodynamic diameter) in the nozzle; and optional in-stack particulate filter sampler to simplify sampling at low stack moisture conditions. Development of a null-probe device that would greatly simplify stack sampling was discontinued due to technical problems.

It was not our intention to provide an all-purpose sampler capable of particulate sampling under all environmental conditions. Design specifications that the PPSS will meet are compared with typical Method 5 capabilities in Table 1. Our experience in the early stages of the study and experience of others has shown that not all the conditions encountered in particulate stack sampling can be accommodated by a single sampler. It was therefore decided that the design specifications should accommodate the most common ranges of stack temperatures, pressures, and humidities found in actual use. Several options could also be provided to allow sampling under special conditions outside these design limits. The PPSS will not, for example, be applicable to high-temperature conditions in the typical incinerator stack, or to the high-temperature, nearly saturated conditions of the power plant stack at the outlet of a scrubber where droplets interfere with particle size classification in the nozzle.

SI or metric units have been incorporated into the PPSS to replace the British system of engineering units commonly used in existing samplers. Consistency of units is observed within the PPSS, and external data, such as barometric pressure, are entered into the calculating/display system in the proper units.

PROTOTYPE PARTICULATE STACK SAMPLER (PPSS) COMPONENTS

The PPSS is shown schematically in Figure 1 and photographically in Figure 2. The primary components are (1) an in-stack variable-inlet, virtual impactor nozzle capable of inertially separating the particle size distribution into two fractions

TABLE 1. EPA METHOD 5 AND THE PPSS COMPARED

Feature	Method 5	PPSS
Nozzle cutpoint	None	2.5-3.5 μm
Maximum port diameter	7.6 cm (3 in.)	7.6 cm (3 in.)
Maximum weight/package	Approximately 27 kg	24 kg[a]
Sample flowrate	28 ℓ/min	56 ℓ/min
Material	Pyrex glass	Stainless steel
Stack velocity measurement	S-type pitot	S-type pitot
Maximum stack temperature		
with cooling	1000°C	Not applicable
without cooling	320°C	320°C
Maximum stack diameter	9 m (30 ft)	6 m (20 ft)
Maximum stack gas velocity	>22 m/s	22 m/s
Maximum stack gas humidity	Saturated	Nearly saturated
Particulate filters	Note b	Note b
Number of samples	5[c]	3[c]
Calculation/display	Nomograph calculation; display by dials, inclined gauge	Digital display on demand (by microcomputer)
Probe washing	Required	Not required after nozzle characteristics are known.

Notes

a. Production model weight can probably be reduced approximately 20%.

b. Both methods can be provided with either in-stack or out-of-stack particulate filters.

c. Number includes samples requiring preweighing, handling, and analysis by some method; i.e., filter containing solid material washed from probe, main gas filter, bleed gas filter, impinger volume, or desiccant weight.

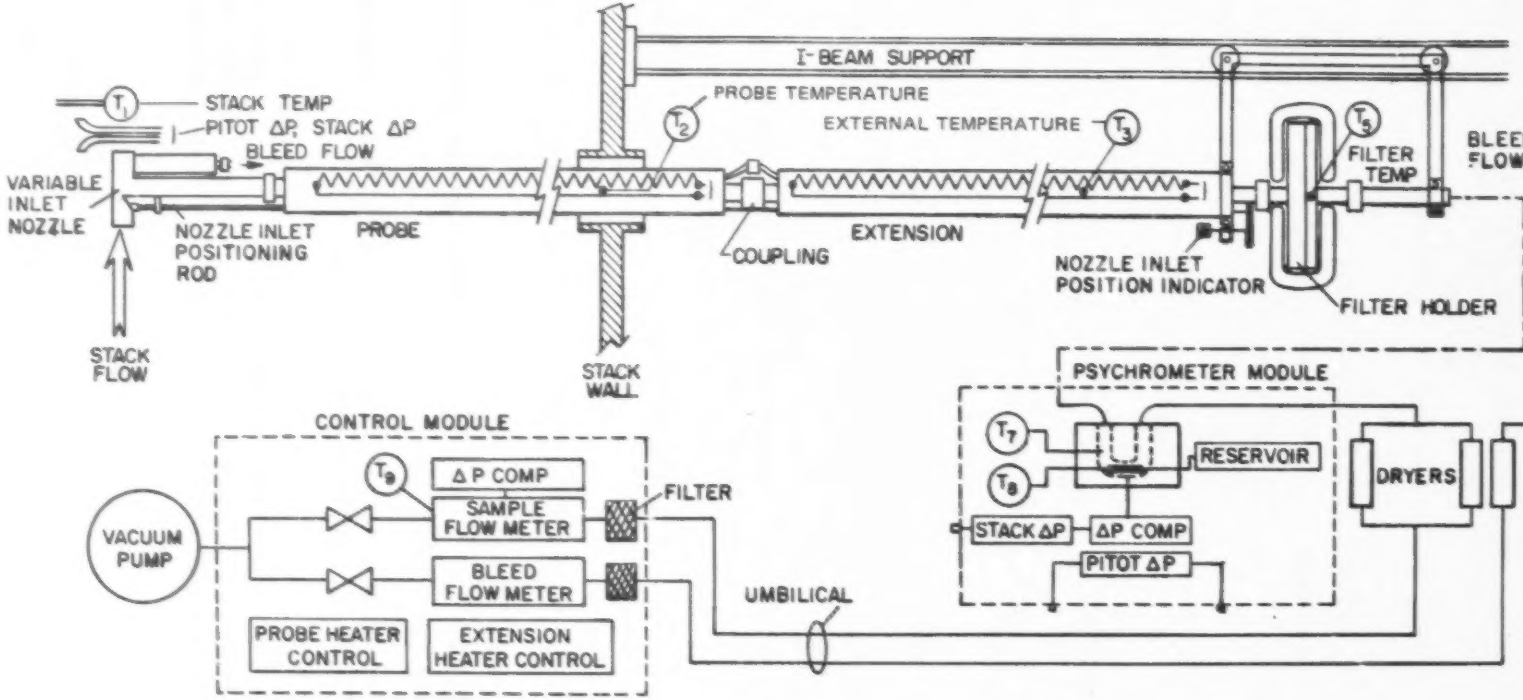
I-BEAM SUPPORT
T_1
STACK TEMP
PITOT ΔP, STACK ΔP
BLEED FLOW
VARIABLE INLET NOZZLE
NOZZLE INLET POSITIONING ROD
PROBE
STACK FLOW
STACK WALL
T_2
PROBE TEMPERATURE
COUPLING
EXTENSION
EXTERNAL TEMPERATURE
T_3
NOZZLE INLET POSITION INDICATOR
T_5
FILTER TEMP
FILTER HOLDER
BLEED FLOW
PSYCHROMETER MODULE
T_7
T_8
RESERVOIR
STACK ΔP
ΔP COMP
PITOT ΔP
DRYERS
CONTROL MODULE
T_9
Δ P COMP
SAMPLE FLOW METER
BLEED FLOW METER
FILTER
VACUUM PUMP
PROBE HEATER CONTROL
EXTENSION HEATER CONTROL
UMBILICAL

Figure 1. Schematic diagram of the PPSS.

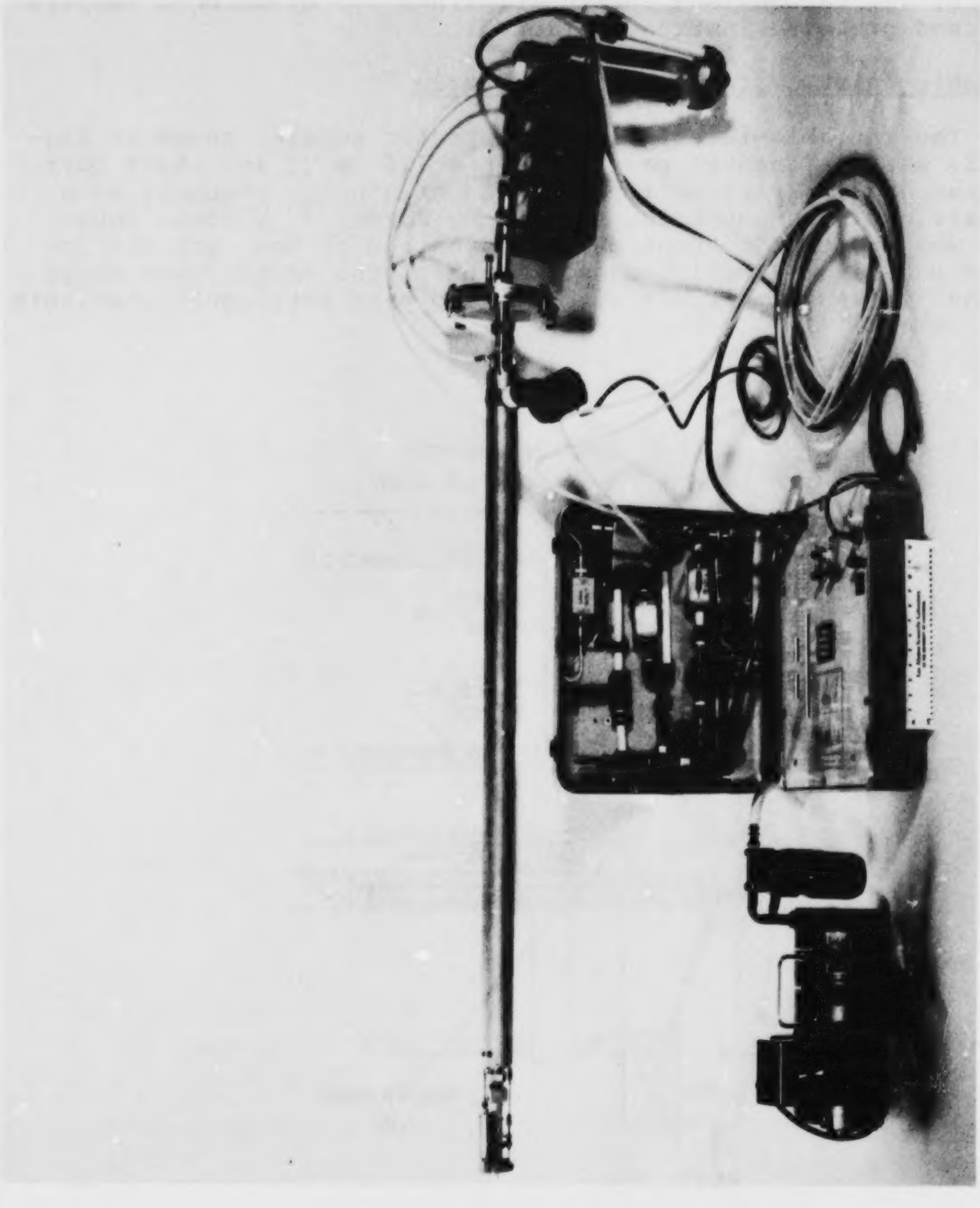

Figure 2. Overall arrangement of the PPSS modules.

(single cut-point capability), (2) a straight, heated, stainless steel probe with smooth internal surfaces and an extension to provide up to 3-m inside-stack length, (3) an insulated 200-mm-diameter filter holder, (4) a wet-bulb, dry-bulb psychrometer, (5) air-cooled or water-cooled desiccant dryer, (6) electronic flow meters, (7) carbon vane rotary pump, and (8) electronic temperature and pressure instrumentation.

Variable-Inlet, Virtual Impactor Nozzle

The variable-inlet, virtual impactor nozzle, shown in Figure 3, was designed to pass through a 7.6 cm (3 in) stack port. The rectangular virtual impactor was originally proposed as a versatile single cut-point sampler by Forney.[3] Virtual impaction was expected to provide the advantage of low particle rebound and minimal wall losses. Further, the rectangular shape of the jet was compatible with the proposed rectangular variable area inlet.

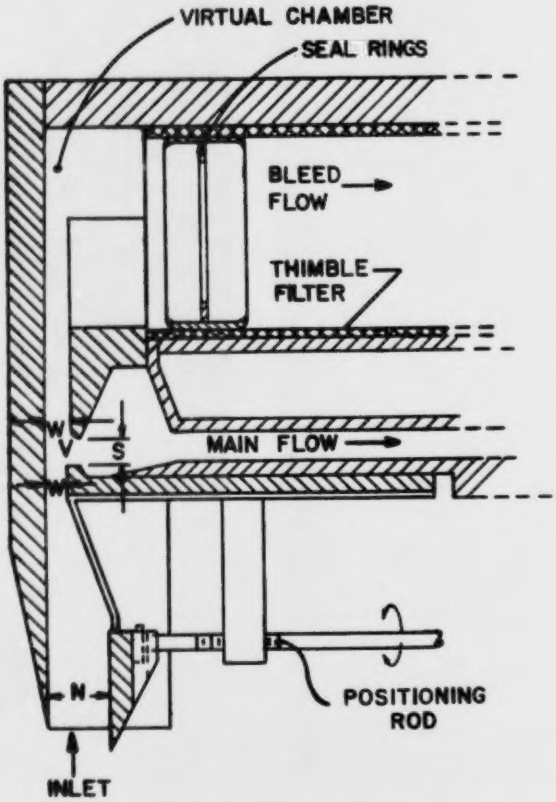

Figure 3. Section of variable-inlet, virtual impactor nozzle (Mod. 3).

The nozzle was designed to separate gas borne particles as follows: the larger particles in the gas stream intrude into a volume of relatively stagnant air and, being unable to negotiate a sharp turn at that point, proceed to a collection filter within the nozzle; the smaller particles successfully negotiate the turn and proceed along the probe to the main sample filter. By selection of appropriate length of the jet (L), width of the jet (W), separation between jet and virtual surface (S), virtual chamber width (H), main flow (Q_m) and bleed flow (Q_b), the nozzle should provide separation of particles at the desired aerodynamic diameter cutpoint. The dimensions L, W, and S and the two flowrates are maintained constant during a sampling run. Isokinetic conditions are maintained by adjusting the nozzle opening N during the run by mechanical linkage from outside the stack.

Four versions of the variable-inlet, virtual impactor nozzle were tested by sampling monodisperse dye aerosol produced using the Berglund-Liu vibrating orifice aerosol generator. The version shown in Figure 3 was the final version. Although it was adjusted to optimum ratios of S/W and H/W recommended by Forney et al.,[4] the nozzle displayed the relatively low collection efficiencies and high wall losses, as shown in Figure 4. Peak efficiency did not exceed 77% and exhibited an even lower efficiency for aerosols as large as 14 µm mass median diameter. This efficiency is total aerosol mass collected in the virtual chamber (thimble filter plus chamber wall losses) as a per cent of total aerosol mass entering the nozzle. Wall losses in the nozzle, probe, and filter holder ranged from 34-72% with particles near the cutpoint size showing the highest losses. Figure 4 shows, in less detail, the designs of the previous three virtual impactor nozzles and the performance characteristics of each of these designs. Mod 2 displayed performance characteristics comparable to those previously noted for Mod 3. Figure 5 shows a photograph, provided by Professors Ravenhall and Forney, detailing flow patterns within a water model geometrically similar to our Mod 3 nozzle. Breakup of streamlines starting before the exit of the jet illustrates nonuniformity of flow which would promote loss to the walls, particularly at a point opposite the small particle exit. Further work on this particular version is not anticipated at this time. However, if additional work is planned, it is recommended that a symmetrical nozzle (circular or annular in shape) without the constraint of fitting through a 7.6 cm port be considered. Larger port clearance will allow adequate length for smooth transitions within the inlet and nozzle and greater separation between the inlet and the flow disturbances caused by the broad body of the nozzle. Symmetry will allow the main flow stream to exit in all directions, thereby eliminating crossover and end effects inherent in rectangular impactors.

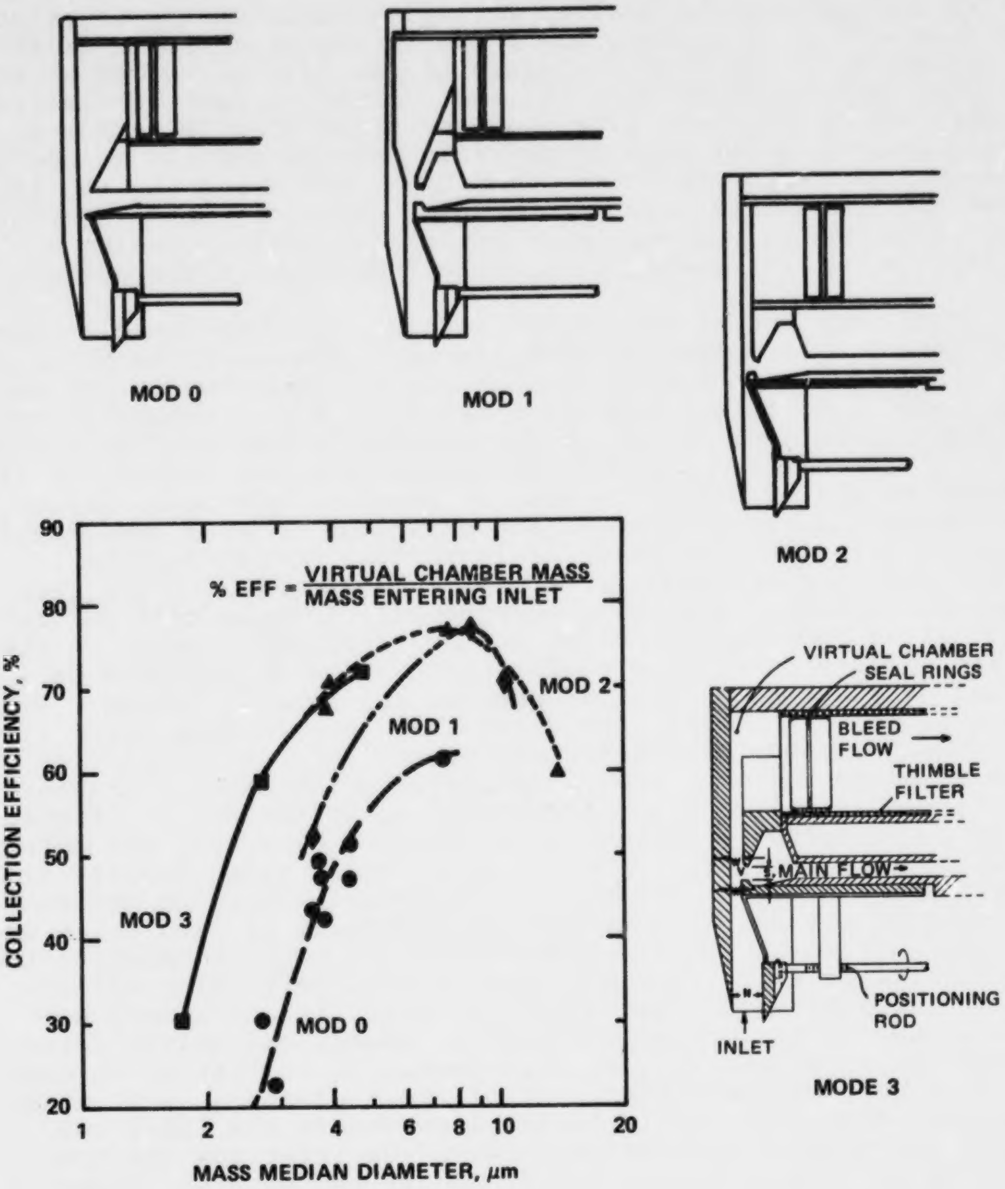
MOD 0
MOD 1
MOD 2
90
80
70
60
50
40
30
20
COLLECTION EFFICIENCY, %
% EFF = VIRTUAL CHAMBER MASS / MASS ENTERING INLET
MOD 2
MOD 1
MOD 3
MOD 0
1
2
4
6
8
10
20
MASS MEDIAN DIAMETER, μm
VIRTUAL CHAMBER
SEAL RINGS
BLEED FLOW
THIMBLE FILTER
MAIN FLOW
POSITIONING ROD
INLET
MODE 3

Figure 4. Test results of virtual impactor nozzle.

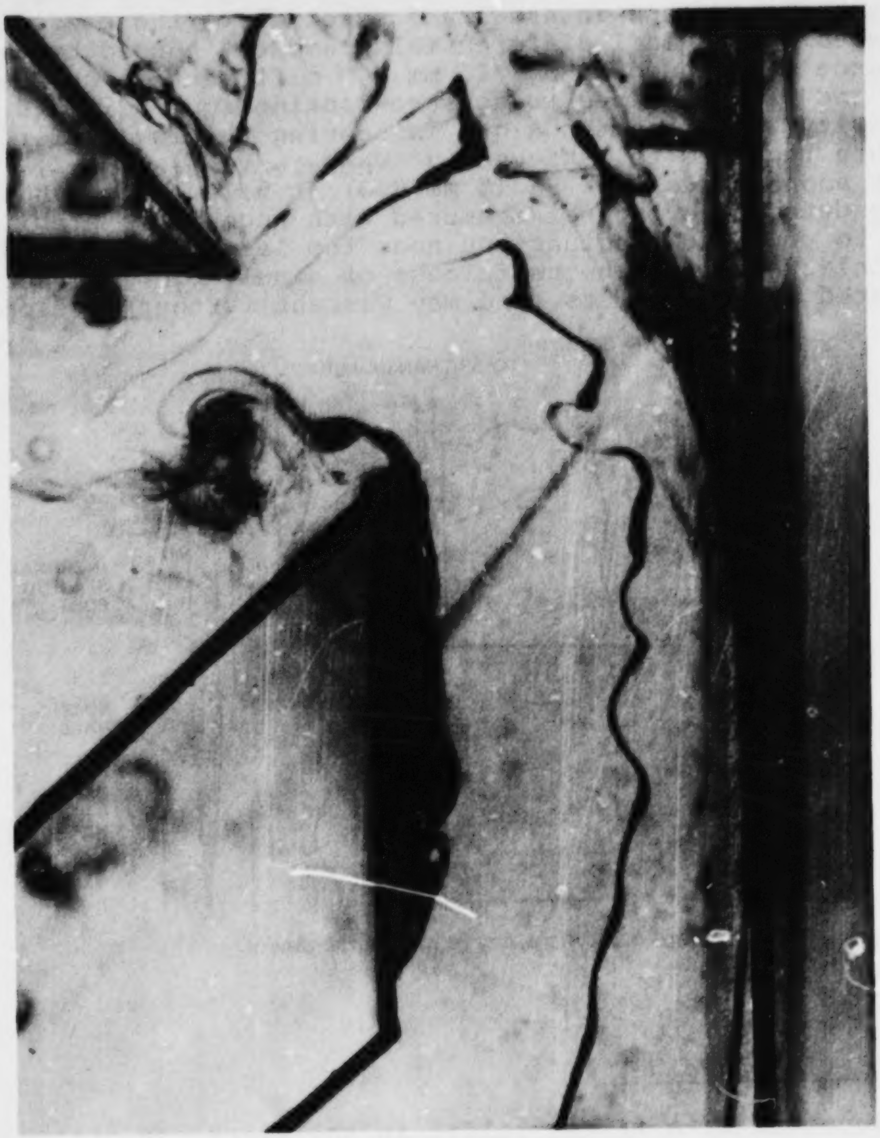

Figure 5. Dye trace in water model of nozzle (inlet at bottom).

Stack Velocity Measurement

Stack velocity is determined from S-type pitot differential pressure as measured by an electronic pressure transducer with ± 25 mm H_2O range. A null-probe device (Figure 6) which provided static pressure taps internal and external to the nozzle was evaluated. The small differential pressure induced by velocity imbalance was sensed by a ± 25 mm H_2O differential pressure transducer and was minimized to achieve isokinetic conditions. The difficulty with this technique is sensing the low differential pressure required to achieve $0.9 < V_{nozzle}/V_{stack} < 1.1$. This ΔP was approximately 50 Pa (5 mm H_2O) at 9.1 m/s, which was easily detectable but not measured with acceptable stability owing to pressure fluctuations near the large body of the variable inlet nozzle. The usefulness of a null-probe sensor was suggested by these tests, and may warrant further development.

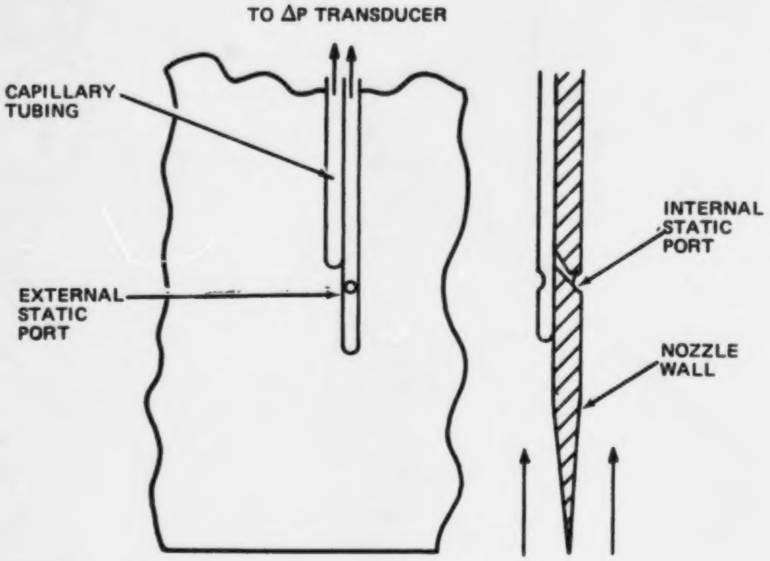

Figure 6. Static pressure null probe device.

In-Stack Filter Holder

Placement of a filter holder in the stack gas stream is not novel and is an EPA-approved procedure (Method 17).[5] The advantages of an in-stack filter are reduced deposition on extraneous surfaces and no further need for probe and filter heating. A major disadvantage appears when entrained droplets in the stack gas stream blind the filter. The PPSS provides optional capability for sampling with an in-stack filter connected to the variable-slit nozzle.

Instrumentation to Monitor Sampling Conditions

Instrumentation in the PPSS is capable of transmitting continuous voltage signals for calculating and display purposes, which replace the mechanical and manual methods of flow, pressure, and moisture measurement now part of Method 5. These instruments were selected to perform with accuracy and precision at least equivalent to that provided by Method 5 instrumentation. Field testing to establish their ruggedness has not been accomplished. Instrumentation channels are listed in Table 2 and discussed in the following sections.

Flow metering--Since the particulate mass concentration is desired in terms of dry gas volume at standard temperature and pressure, dry gas volume is measured and automatically converted to standard conditions according to perfect gas laws. The gas stream is dried and filtered prior to entering the flow meter. Additional correction is required if constituents of the gas change from the calibration gas or if temperature or pressure of the gas stream varies from calibration conditions. Gas analysis prior to each particulate sampling run is required to provide gas constants to determine mass flow meter correction.

Two flow meter types, hot-wire and turbine, were included in the prototype to permit evaluation under field conditions since laboratory testing did not show a clear advantage of one type over the other. Datametrics hot-wire mass flow meter Model 1000.5B was used to meter the bleed flow. It is compact and lightweight and has been used successfully in other areas of our laboratory. The instrument is supplied with linearizing signal conditioning. A turbine flowmeter (Flow Technology Model FTC-8) was used to meter sample flowrate. The advantage of the turbine flowmeter over a hot-wire flow sensor is its direct indication of flow volume in the presence of gases other than the components of air. Its output does, however, require compensation for temperature and pressure changes.

Flow control is performed by manual adjustment of needle valves in the main flow stream and the bleed flow stream. This adjustment is made infrequently since normal operation with the virtual impactor nozzle requires constant flow.

Moisture measurement--The PPSS contains a wet-bulb, dry-bulb psychrometer for measuring water vapor content of the sample gas stream. Total moisture can also be determined by measuring total weight change in the dryers. The volume occupied by water vapor is required in the isokinetic calculation to correct nozzle inlet velocity, which is volumetric flowrate of wet gas divided by probe nozzle cross-sectional area. The psychrometer, shown

TABLE 2. PPSS INSTRUMENTATION CHANNELS

Sensors	Range or Max	Type	Signal	Overall Precision
Stack temperature	20-325°C	RTD[a]	0-5 Vdc	±5°C
Probe temperature	20-325°C	RTD	0-5 Vdc	±5°C
Extension temperature	20-150°C	RTD	0-5 Vdc	±5°C
Holder temperature	20-150°C	Thermistor	0-5 Vdc	±1°C
Dry-bulb temperature	20-150°C	Thermistor	0-5 Vdc	±0.5°C
Wet-bulb temperature	20-150°C	Thermistor	0-5 Vdc	±0.5°C
Sample flow temperature compensation	20-150°C	Thermistor	0-5 Vdc	±1°C
Stack velocity (pitot)	±34 mb	Variable reluctance	±5 Vdc	±0.5 mb
Flow meter pressure corrected	±340 mb	Variable reluctance	±5 Vdc	±5 mb
Psychrometer pressure corrected	±340 mb	Variable reluctance	±5 Vdc	±5 mb
Sample flow rate	$7\text{-}12\times10^{-4}\,m^3/s$	Turbine	0-5 Vdc	$\pm0.2\times10^{-4}\,m^3/s$
Bleed flow rate	$1\text{-}3\times10^{-4}\,m^3/s$	Hot-wire	0-5 Vdc	$\pm0.1\times10^{-4}\,m^3/s$
Elapsed time	0-99 min: 0-60 s	Digital		
Interval time	0-99 min: 0-60 s	Digital		

[a] Resistance temperature detector.

in Figure 7, is located immediately behind the sample filter where temperature of the gas stream is maintained above dew point. The wick material is polyester, which is resistant to the acids (primarily dilute sulfuric acid) encountered in some sampling situations. The wick is fed from a water reservoir through a stainless steel tube approaching within 3 mm of the thermistor thermometer from the downstream side. Covering the feed tube with the wick adjusts the temperature of the feedwater to approximately that of the wet bulb and prevents cooling or heating of the wet-bulb thermistor by the feedwater.

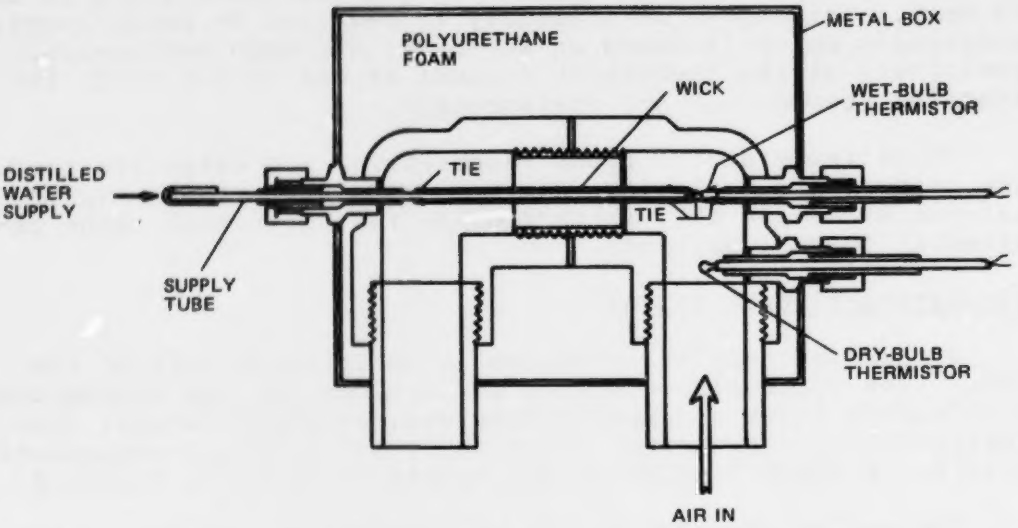

Figure 7. Arrangement of wet-bulb, dry-bulb psychrometer.

The wet-bulb, dry-bulb psychrometer may be used up to dew points of 100°C with reasonable accuracy (less than 5% maximum error). Other methods of moisture measurement such as cooled-mirror dew-point devices, hygroscopic salt devices, and semiconductor devices are limited by maximum ambient temperature, usually about 50°C.

Pressure measurement--Three pressure channels are required in the PPSS: pitot tube differential pressure (stack gas velocity); pressure at the psychrometer; and pressure at the flow measurement section to allow pressure compensation of flowrates. Pressure within the stack to allow calculation of total stack volumetric or mass discharge is measured occasionally by connecting one leg of the pitot tube to one of the existing transducers. The operating ranges of these instruments are listed in Table 2. Datametrics variable-reluctance, differential-pressure transducers with miniaturized carrier demodulators which supply dc voltage to the calculating/display system were used to monitor pressure. These transducers are lightweight and have displayed good stability.

Temperature measurement--All temperatures except stack temperature, probe temperature, and extension temperature are sensed by Yellow Springs Thermilinear thermistors which show good linearity and response. They are delicate and must be potted with epoxy to make them more rugged and resistant to acid. The accuracy of the measuring circuit is generally within ±0.2°C over the range 0-93°C. Stability appears adequate, showing standard deviation of 0.05°C on the difference between two thermistors in an oil bath. This order of stability is required by psychrometric calculation which is based on wet-bulb, dry-bulb depression. Sensitivity of the thermistor circuit is set at 0.1 V/°C, far exceeding response of any thermocouple.

Stack temperature, probe temperature, and extension temperature sensors are resistance thermometers (RTD) (Yellow Springs Platinum RTD 0-138 AX), which provide the additional range required at these locations.

Calculating/Display System

A calculating/display system is an integral part of the PPSS.[6] The system incorporates a microcomputer and microprocessor to calculate stack volumetric flowrate, sample flowrate, isokinetic ratio, and various temperature and pressure compensation factors. A block diagram of the system is shown in Figure 8.

The system operates on 115-Vac, 60-Hz line power and retains read-only (program) memory in the event of power loss. It displays data in large (1.3-cm) liquid crystal displays (LCD) visible in strong sunlight. Isokinetic ratio is updated and displayed whenever other values are not demanded. All other variables are displayed on demand through the keyboard. Separate clocks provide elapsed time and interval time capability (interval time prompts move to new sampling location).

The National Semiconductor MM 57109 MOS/LSI number-oriented microprocessor performs the number processing/calculation. This 28-pin dual in-line package provides scientific calculator instructions (key level language) with reverse polish notation entry. The capabilities of this device include all of the functions available on the Hewlett Packard HP-21 hand calculator. The Intel ASM 48 single-component microcomputer performs data sequencing computation processing and display updating.

The microcomputer is programmed in assembly language and allows operation in the following selected modes:

a. Load constants - allows loading of all constants specific to the run (i.e., barometric pressure, gas constants, etc.);

b. Profile - allows velocity traverse across the stack while calculating stack velocity;

c. Static pressure - allows stack pressure to be measured using the transducer usually assigned to monitoring psychrometer pressure;

d. Main - starts the clocks and updating of all calculated variables;

e. Main pause - allows temporary interruption of the run to relocate the sampler to another port; also accommodates mid-run delays for any other reason.

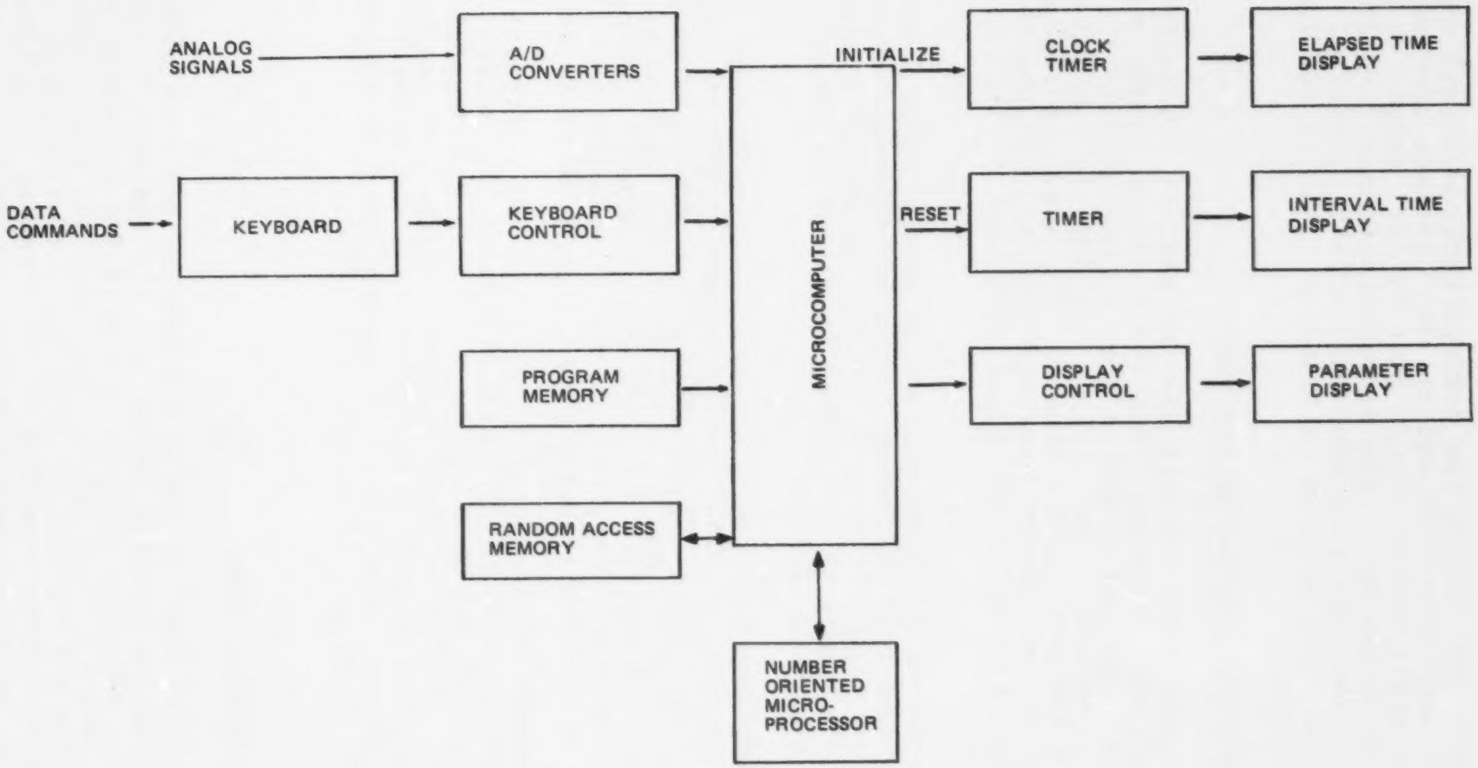
ANALOG SIGNALS
DATA COMMANDS
KEYBOARD
A/D CONVERTERS
KEYBOARD CONTROL
PROGRAM MEMORY
RANDOM ACCESS MEMORY
MICROCOMPUTER
NUMBER ORIENTED MICRO-PROCESSOR
INITIALIZE
RESET
CLOCK TIMER
TIMER
DISPLAY CONTROL
ELAPSED TIME DISPLAY
INTERVAL TIME DISPLAY
PARAMETER DISPLAY

Figure 8. Block diagram of PPSS calculating/display system.

Although interfacing the microcomputer with all analog signals has been completed and all calculations checked for accuracy, overall system errors over typical ranges of operation remain to be determined. The microcomputer has functioned without failure since original debugging of its software. Its operation is rapid, with maximum calculating time 7.5 sec for updating stack velocity.

Equipment and Structural Arrangement

The vacuum pump selected for the PPSS is a Gast 1022 carbon vane rotary pump, which provides 280 ℓ/min at 0 mmHg and 68 ℓ/min at -500 mmHg. Maximum pressure drop in the PPSS is 415 mmHg (100 mmHg occurring in the nozzle, 115 mmHg in the 200-mm filter holder, and 200 mmHg in the dryer). The Model 1022 pump weighs 23.6 kg (52 lb) and is the heaviest component in the PPSS. In general, weight of any other major component is limited to about 14 kg (31 lb).

The probe of the PPSS will be supported by an I-beam cantilevered outward from the stack. This arrangement, shown in its basic form in Figure 1, will be similar to Method 5 arrangement. The probe is clamped in two places by a trolley device which straddles the filter holder.

The sampling probe is a straight 2.32 cm ID tube of type 304 stainless steel. Total heated length is 130 cm. The probe is heated in the manner of EPA Method 5, controlled by separate automatic controller, and is provided with a cooling air blower for temperature reduction to 120°C when sampling intermediate temperature stacks. The probe extension is about the same weight and length as the sampling probe and allows 3m total length.

Lightweight dryers containing silica gel desiccant are provided for both the main and bleed streams. The dryer is designed for either air or ice bath cooling. Silica gel crystals are packed within stainless steel bellows tubing. A change in mass of the dryer can be used as a measure of total moisture in the sample gas stream. Recharging is accomplished by replacement of desiccant or drying in a warm oven (70°C).

SUMMARY AND CONCLUSIONS

A prototype particulate stack sampler has been developed with the following primary features: (1) nominal 56 ℓ/min sampling flowrate, (2) electronic transducers for pressure, temperature, flow, and humidity ratio, (3) stainless steel surfaces and components not subject to breakage, (4) electronic calculating/display system providing direct display of updated data such as stack velocity, sample volume, and isokinetic ratio,

(5) single-point particle size classification in the nozzle, (6) continuous adjustability of nozzle inlet area, and (7) manageable weight of individual components. A wet-bulb, dry-bulb psychrometer provides continuous indication of moisture content of the gas stream. The psychrometer is a particularly promising device in the severe conditions of high temperature (95 to 100°C) and high humidity in which the device must operate.

The variable inlet, virtual impactor nozzle has potential for well-characterized separation of fine and coarse particulate, although versions tested to date have shown collection efficiencies which do not exceed 77%, and high wall losses. A new design with symmetry in flow passages and less dimensional constraint is recommended.

In general, the PPSS has the operating capability of the existing Method 5 sampling train, has modernized its design, and has eliminated the obvious problem areas. However, field demonstration of the prototype might reveal other problems in the novel areas of the PPSS design. The effect of acid on the psychrometer wick and of presence of CO_2, SO_2, and other contaminants on behavior of the psychrometer is not known. Also, stainless steel surfaces in the PPSS may provide greater potential for formation of sulfate aerosols than in the glass components of the Method 5 train. Component ruggedness remains to be proven by field testing.

ACKNOWLEDGEMENTS

We would like to acknowledge the assistance of the following personnel in developing the PPSS design: Dwayne C. Ethridge, LASL, and Professors Forney and Ravenhall of the University of Illinois, Urbana-Champaign.

This work was supported by the Environmental Protection Agency and performed at the Los Alamos Scientific Laboratory operated under the auspices of the U.S. Department of Energy, Contract No. W-7405-ENG-36.

Reference to a company or product name in this paper does not imply approval or recommendation of the product by the University of California or the U.S. Department of Energy to the exclusion of others that may be suitable.

REFERENCES

1. Federal Register 36(247)(December 23, 1971).

2. Elder, J.C., M.I. Tillery, and H.J. Ettinger. Evaluation of EPA Method 5 Probe Deposition and Filter Media Efficiency. Los Alamos Scientific Laboratory Report LA-6899 PR, August, 1977.

3. Forney, L.J. Aerosol Fractionator for Large-Scale Sampling. Rev. Sci. Instrum. 47(10):1264-1269, October 1976.

4. Forney, L.J., D.G. Ravenhall, and D.S. Winn. Aerosol Impactors: A Study of a Fluid Jet Impinging on a Void. J. Appl. Phys. 49(4):2339-2345, April 1978.

5. Federal Register 41(187) (September 24, 1976).

6. Ethridge, C.D., and L.G. Littlefield. Microcontroller for Exhaust-Stack Environmental Measurements. Los Alamos Scientific Laboratory Report LA-UR-79-968, June 1979.

PAPER 6

THE EFFECTS OF NOZZLE LOSSES ON IMPACTOR SAMPLING

KENNETH T. KNAPP
ENVIRONMENTAL SCIENCES RESEARCH LABORATORY
U.S. ENVIRONMENTAL PROTECTION AGENCY-RTP

When measuring the mass, size distribution, and other properties of aerosols, getting a representative sample to the measuring device system is an absolute must for obtaining good data. The retention of particles by any part of the sampling system can greatly bias the results. With impactors and other particle sizing devices, the retention by the nozzle may be particle dependent and, therefore, completely change the size distribution obtained. This problem has been addressed by Marple and Willeke[1] and others[2-4] but few data have been given.

The retention in the nozzle and the probe in the standard stationary source standard particulate emission measurement methods such as EPA Methods 5 and 17 does not cause a problem since the nozzle and probe catches are included in the sample. However, this is not the case with the proposed inhalable particulate matter (IP) measurement method. The IP standard is to include all particulate material with an aerodynamic size at ambient conditions of 15 µm or less. The stationary source IP emission measurement method must contain a 15 µm particle size cut system. The general approach is to use a 15 µm cut point preseparator on the nozzle end of the probes used in the particulate mass measurement methods such as EPA Method 5. The preseparator would remove the particles larger than 15 µm aerodynamic size and allow the remaining particles to pass into the collection system.

Experiments were designed to test such a separation system. The first set-up tested was the preseparator with a button-hook nozzle, the nozzle type most often used with EPA Method 5 and other types of source sampling trains, since these nozzles will fit into the 3 or 4-inch ports most commonly available. A back-up filter was used for the collection of the various size and type aerosols. The efficiency of the preseparators was determined by comparing the amount of aerosol retained in the preseparator including the nozzle to the total amount of aerosol collected. After overcoming problems in generating monodisperse aerosols with aerodynamic diameters greater than 15 μm, testing began. On the first test runs with monodisperse aerosols of about 10 μm, the button-hook nozzles were found to collect more material than the preseparators. If these nozzles retained a large amount of material in the size range less than 15 μm, then they cannot be used with the preseparators without introducing serious errors in the IP measurement. Before a decision on whether the button-hook nozzles could be used with the IP method, the extent of the retention of the aerosols smaller than 15 μm by these nozzles needed to be studied. Such a study was undertaken with 3/16, 1/4, and 5/16-inch button-hook nozzles. These were chosen for the tests since they are the size nozzles most often used in stationary source testing. In addition, a 90° bend 1/4-inch nozzle was used in some tests.

Tests with laboratory generated monodisperse aerosols and re-dispersed sized coal-fired power plant fly ash were made. The monodisperse aerosols were methylene blue particles generated by a vibrating orifice (Berglund-Liu) aerosol generator. The aerodynamic size range covered with these aerosols was from about 3 μm to about 27 μm. The coal-fired fly ash used was separated into five narrow size range fractions which had mass median diameters (MMD) of 3.5, 5.8, 8, 16.5, and 26.7 μm. The sized fly ash fractions were re-dispersed by the aerosol generator of the Stationary Source Simulator Facility (SSSF) in which the nozzles were tested.

The results from several test runs with the ¼-inch button-hook nozzle and the monodisperse aerosols are given in Table 1.

TABLE 1. RETENTION OF MONODISPERSE AEROSOLS BY 1/4-INCH BUTTON-HOOK NOZZLE

Aerosol diameter, μm	% in ¼-inch nozzle
3.3	27 ± 2[a]
5.5	53 ± 3[a]
9.3	79 ± 6[a]
10.5	90[b]
11.6	13[b]
15.1	8[b]
16.3	6 ± 1[a]
26.7	4 ± 1[a]

[a] Average and range of 3 runs

[b] Single runs

The results of runs with the three nozzle sizes on various aerosols are given in Table 2.

TABLE 2. COMPARISON OF RETENTION OF MONODISPERSE AEROSOLS BY THREE NOZZLE SIZES

Aerosol diameter, µm	3/16	1/4	5/16
6.4	21	48	0
9.3	53	79	46
10.5	22	90	54
11.6	2	12.7	59
12.8	1	12	75
13.9	4	22	68
15.1	5	8	47
18.6	11	3	51
21	6	4	45
24	2	3	22

Figure 1 is a plot of the data given in Table 2.

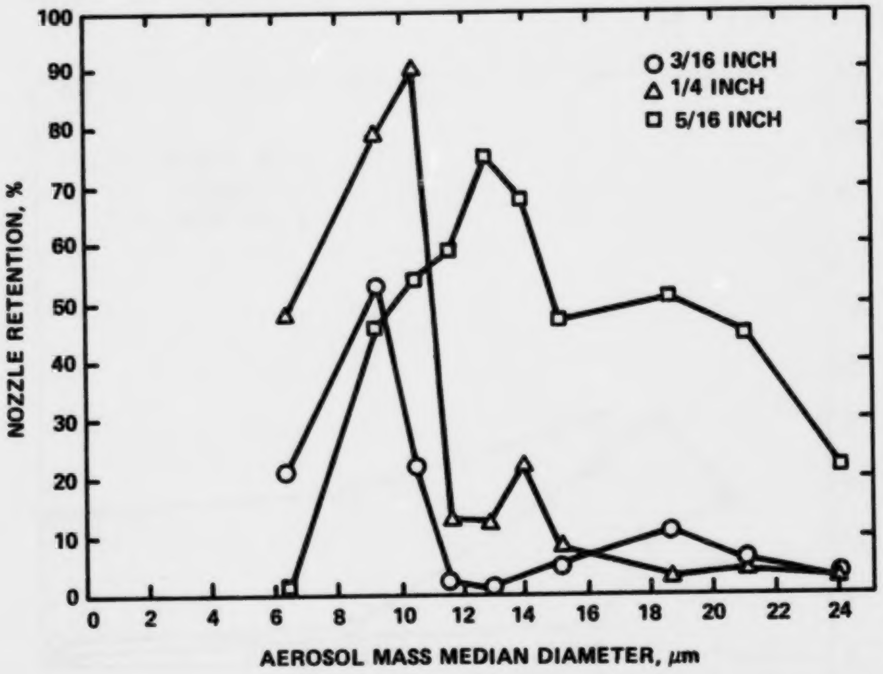

Figure 1. Retention of mondisperse aerosols by nozzles of three sizes.

A comparison of the ¼-inch button-hook with a 90° bend ¼-inch nozzle was made with monodisperse aerosols of 13.9 μm diameter. The results were 22% retained in the button-hook and 24% in the 90° bend nozzle thus indicating no difference.

The results from the fly ash study are given in Table 3 and Figure 2.

TABLE 3. RETENTION OF FLY ASH BY NOZZLES OF THREE SIZES

	% in nozzle		
Aerosol MMD, μm	3/16	1/4	5/16
3.5	28	27	16
5.8	22	42	14
8	6	33	41
16.5	4	6	29
26.7	2	4	26

The tests were for collection periods of 10 minutes. The question whether the nozzle collection would reach an equilibrium was considered and runs of different collection times were made with the ¼-inch button-hook nozzles. The results of these tests are shown in Table 4.

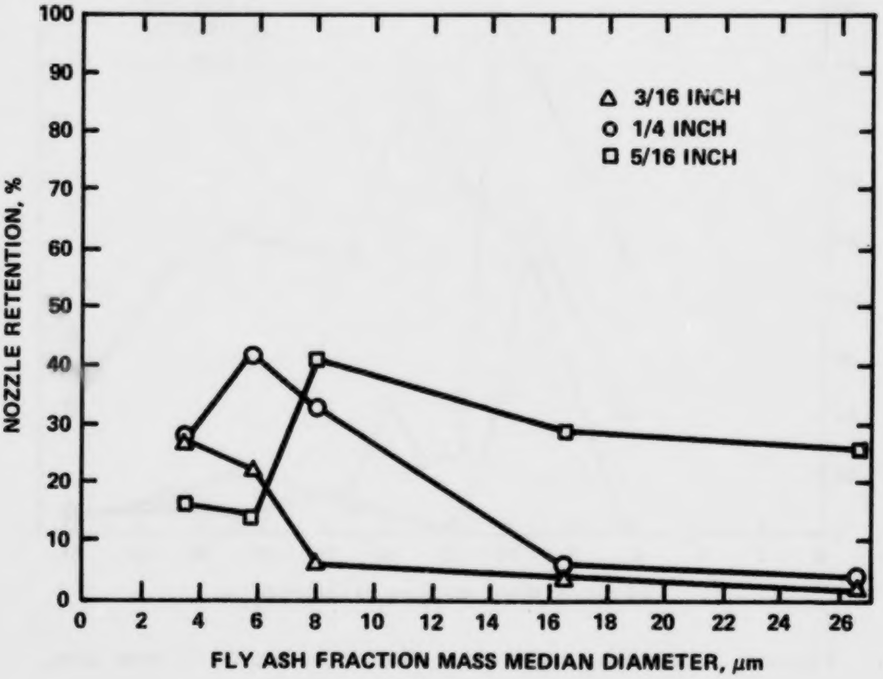

Figure 2. Retention of fly ash by nozzles of three sizes.

TABLE 4. EFFECT OF COLLECTION TIME ON RETENTION OF FLY ASH BY 1/4-INCH NOZZLE

Collection time, min	% in nozzle
5	44
10	33
20	48
30	32

No major difference over the period tested was found.

All of the above data are from runs where the flow rate was about 0.014 m^3/min (0.5 CFM). This is the flow rate at which the preseparators and impactors operate most efficiently. However, since some tests will be made at different flow rates, a study of the effects of flow rate on nozzle retention was carried out with the ¼-inch button-hook nozzles. Three flow rates were chosen for the test: the optimum flow rate for the preseparators and impactors being tested (0.5 CFM); the upper limit of efficient operation of the preseparators (0.75 CFM); and a flow rate commonly used with EPA Method 5 (1 CFM). The 1 CFM flow rate is not recommended for the preseparators because at this flow rate severe re-entrainment occurs resulting in the preseparator passing large amounts of particles greater than 15 μm. The results for tests at the three flow rates with an aerosol of about 11 μm are given in Table 5.

TABLE 5. FLOW RATES VS RETENTION OF FLY ASH BY 1/4-INCH NOZZLE

Flow rate, m^3/min	% in nozzle
0.014 (0.5 CFM)	20
0.021 (0.75 CFM)	4
0.028 (0.99 CFM)	1

The results of these tests have shown that the button-hook and 90° bend nozzles retain various amounts of the aerosols that are drawn through them. The amount retained depends on the nozzle size, the aerosol size, and the flow rate. The percent collected in the nozzle remained fairly constant over a time period up to 30 minutes and, therefore, the collection does not appear to reach an equilibrium. Thus, the possible use of preconditioning is eliminated.

Because much of the aerosols retained in the nozzles should be passed on through the preseparator and onto the filter or other collection devices, the use of the button-hook or 90° nozzle with the IP method will cause large and varied errors. The nozzle retention does not cause a problem with the standard stationary source standard particulate emission measurement methods, such as EPA Methods 5 and 17, since the nozzle catch is included in the total catch. However, particle size measurements with these types of nozzles will have serious errors.

ACKNOWLEDGEMENTS

The author wishes to acknowledge the assistance given by Donald Duke and Raymond Steward for the aerosol generation studies and Thomas Ward for separating the fly ash.

REFERENCES

1. Marple, V.A., and K. Willeke. Impactor Design. Atmos. Environ. 10:891-896, 1976.

2. Lundgren. D., and S. Calvert. Aerosol Sampling with a Side Port Probe. Am. Ind. Hygiene Assoc. J. 28:208-215, 1967.

3. Cheng, Y., and C. Wang. Inertial Deposition of Particles in a Bend. J. Aerosol Sci. 6:139-145, 1975.

4. Crane, R.I., and R.L. Evans. Inertial Deposition of Particles in a Bent Pipe. J. Aerosol Sci. 8:161-170, 1977.

PAPER 7

DILUTION SOURCE SAMPLING SYSTEM

ROBERT J. HEINSOHN
JOHN W. DAVIS
CENTER FOR AIR ENVIRONMENT STUDIES
THE PENNSYLVANIA STATE UNIVERSITY

AND

KENNETH T. KNAPP
NATIONAL ENVIRONMENTAL RESEARCH LABORATORY-RTP
U.S. ENVIRONMENTAL PROTECTION AGENCY

ABSTRACT

A source sampling system has been designed and tested that is lighter and easier to use than the conventional EPA Method 5 sampling systems. The heart of the system is an ejector pump that uses dry air to simultaneously pump, cool, and dilute a sample of a process gas stream. The sample is treated as a miniscule plume and the particles are removed from the sample after it has been cooled and diluted with dry air.

Simultaneous, full-scale source certification tests were run with the dilution sampling system and a conventional EPA Method 5 system. The emission from a coal-fired steam boiler, a glass melt tank equipped with an electrostatic precipitator, and a lime kiln equipped with a fabric filter were tested. Test results reveal that:

(a) the dilution system was considerably easier to use;

(b) the particle mass concentrations obtained with the dilution system were larger than those obtained with an EPA Method 5 system;

(c) the size distribution obtained with the dilution system contained submicron particles not observed at stack conditions as measured with an in-stack impactor;

(d) the relative abundance of elements in particles obtained by the dilution sampling system was considerably different from that in comparably sized particles obtained by the EPA Method 5 system. No consistent trends could be determined.

NOMENCLATURE

a, b	constants
$c_{m,o}$	apparent concentration of a material per unit mass of particle at any time zero
c_s	concentration of a material per unit surface area of particle
c_v, $c_{v,e}$	mass concentration of a material per unit volume of the carrier gas at any time t, or at such time when no further transport occurs, i.e., its equilibrium value
D	diffusion coefficient
D_p	particle diameter
g	acceleration of gravity
h_{fg}	enthalpy of vaporization
H	effective stack height
m_d, m_s	mass flow rate of dilution air, sample
M_a, M_s	molecular weight of air and sample
n	number of particles per unit volume of carrier gas
Pr, Pr'	Prandtl number
P_i, P_m, P_o, P_{sat}	pressure of supply air, diluted sample, control pressure, vapor saturation pressure
ΔP_s	pressure difference across the sample orifice
Q	emission source strength
Q_d, Q_s	volumetric flow rate of dilution air and gas sample
R	gas constant
r	dilution ratio (Q_d/Q_s), each corrected to standard conditions
Re	Reynolds number
s	atmospheric stability parameter

S	degree of saturation
T_d, T_m, T_s	temperature of dilution air, diluted sample, sample
T_b	boiling temperature of a liquid
t	time
u	wind speed
X	mole fraction
x,y,z	spatial coordinates
α,β	constants
θ	potential temperature
κ	thermal conductivity
ρ_v, ρ_ℓ	density of vapor and of the liquid
σ_y, σ_z	atmospheric dispersion coefficients
τ	time constant

INTRODUCTION

An inherent limitation in all contemporary source sampling systems is their inability to obtain particles in the state they will have when the plume mixes with the atmosphere. In-stack devices capture particles at stack gas temperature and gas composition and EPA Method 5 systems capture particles on filters at 121°C and in impingers at 0°C. In these cases condensation, adsorption, and agglomeration that occur in the plume do not occur in a similar fashion in the sample. The need for a sampling system that will enable operators to capture particles that represent those a plume transfers to the atmosphere has long been recognized and is the basis for a novel source sampling system reported in this paper.

A source sampling system with dilution (hereafter abbreviated SSD) has been designed that treats the sampled gas as a miniscule plume and removes particles after the sample has been diluted with clean dry air.[1-4] The purposes of this paper are to:

(1) describe the design and operation of the SSD system;

(2) analyze simultaneous samples taken with the SSD system and a conventional EPA Method 5 system; and

(3) compare the processes of adsorption, condensation, and agglomeration in the SSD system and plume.

DESIGN OF SSD SYSTEM

The SSD system is shown schematically in Figure 1; it consists of six components.

1. Probe: (length 2.07 m; mass 4.14 kg) null reading isokinetic nozzle, impactor preseparator, heated probe, 1.27 cm (½-inch) inside diameter, 1.83 m (6 ft) long.

2. Pump and Filter Assembly: (length 0.68 m; mass 7.26 kg) ball valve, sample orifice, heated enclosure, Dilution Ejector Pump (DEP), filter holder.

3. Umbilical Cord: dilution air line, 120 VAC control cable, null nozzle pressure lines, sample orifice pressure lines, thermocouple leads.

4. Control Unit: (0.46 m x 0.33 m x 0.23 m; mass 20.3 kg) pressure transducer, pressure regulator, pressure gauges, temperature controller, critical flow orifice, dilution air filter.

5. Flow Measurement Unit: (0.38 m x 0.30 m x 0.23 m; mass 7.3 kg) electronics for indicating elapsed time, volumetric flow rate, and volume of sample.

6. Dilution Air Cleaner and Dryer: (0.79 m, 0.41 m, 0.40 m; mass 25.7 kg) filters to remove oil and foreign matter, regenerative dryer to remove water vapor.

Units 1 and 2 are fitted with a taper fitting and mounted on a tripod for insertion into the stack. The Control Unit houses all the necessary meters and valves for controlling the flow of dilution air. The Flow Measurement Unit consists of power supplies and digital logic system for conditioning, integrating, and storing the signals related to the sample volumetric flow rate and elapsed time. The Dilution Air Cleaner and Dryer cleans and dries air to operate the system. The unit is located on the ground, and the air is supplied to it by plant air service or a portable air compressor. The unit is composed of commercially available equipment and will not be discussed.

Performance specifications for the SSD system are as follows:

1) Sample flow rate: 0.236 to 0.708 liter/s (0.5 to 1.5 scfm) and is adjustable so that isokinetic sampling conditions can be achieved at the nozzle inlet.

2) Sampling nozzles: 0.318 cm, 0.635 cm, 0.953 cm, and 1.270 cm (1/8 in., 1/4 in., 3/8 in., 1/2 in.).

3) The gas sample and dilution air are completely mixed before the particles are removed by a filter; the temperature of the mixture is within 5°C of the atmospheric temperature.

4) The entire apparatus is easily cleaned.

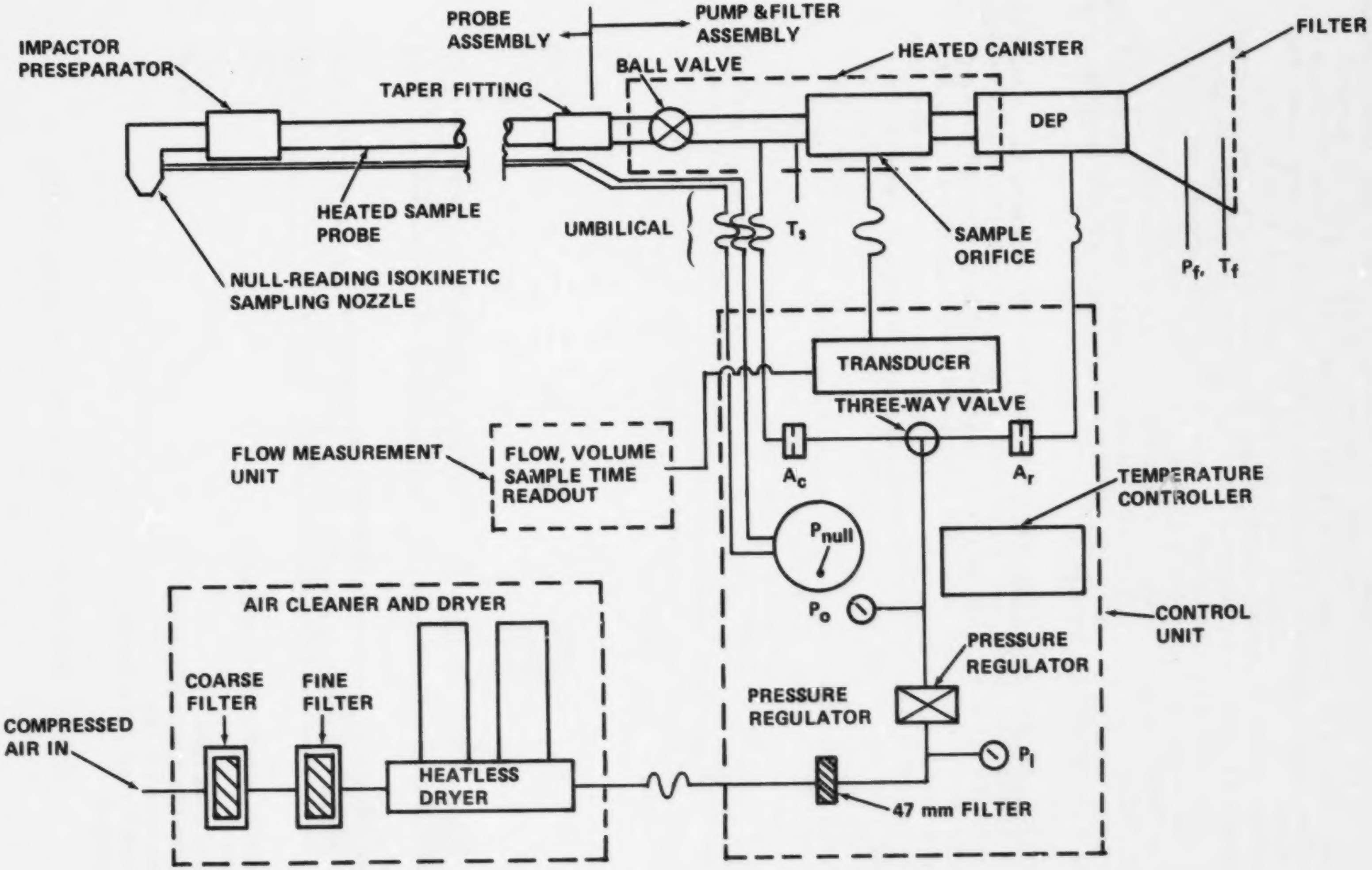
IMPACTOR PRESEPARATOR
PROBE ASSEMBLY
PUMP & FILTER ASSEMBLY
FILTER
BALL VALVE
HEATED CANISTER
TAPER FITTING
DEP
HEATED SAMPLE PROBE
UMBILICAL
T_s
SAMPLE ORIFICE
P_f, T_f
NULL-READING ISOKINETIC SAMPLING NOZZLE
TRANSDUCER
THREE-WAY VALVE
FLOW MEASUREMENT UNIT
FLOW, VOLUME SAMPLE TIME READOUT
A_c
A_r
TEMPERATURE CONTROLLER
P_{null}
AIR CLEANER AND DRYER
P_o
CONTROL UNIT
PRESSURE REGULATOR
COARSE FILTER
FINE FILTER
PRESSURE REGULATOR
COMPRESSED AIR IN
HEATLESS DRYER
P_l
47 mm FILTER

Figure 1. Schematic diagram of sampling system.

Dilution Ejector Pump--The Dilution Ejector Pump (DEP) shown in Figure 2 is the heart of the system. Sample gas is pumped by a high velocity stream of dry dilution air passing through the annular space around the sample tube, transferring momentum to the slower moving sample gas stream. The two streams mix and achieve uniform conditions$^{5-8}$ at the end of the mixing tube. The diluted stream then passes through a filter to remove particles. The DEP was designed to use a minimum amount of air to cool the sample yet keep it above the dew point. Figure 3 shows the "well mixed" sample temperature as a function of the dilution ratio (on the basis of volume), inlet sample temperature, and moisture content. The SSD system was designed to accommodate dilution ratios of 10 to 15.

Control of sample flow rate--Dilution air enters the Control Unit, is regulated to a set pressure (P_o), passes through a three-way ball valve and an orifice and into the DEP. The dilution air filter assures that all the particles collected on the DEP filter are from the sample gas. The pressure, P_o, controls the sample flow rate and is controlled by the pressure regulator. The supply pressure is P_i. A three-way ball valve is used to pass the dilution air to the DEP (as shown) or to a separate calibration system. The sample mass flow rate (m_s) is controlled by the mass flow rate of the dilution air, m_d. Since the geometry of the DEP is constant, the mass flow rate of the dilution air is a function of the regulated pressure, P_o. The pressure of the mixed gas before the filter (P_m) affects the sample mass flow rate, but as this pressure changes only slightly as particles are collected on the filter, the pressure, P_o, is the principal factor controlling the sample flow rate.

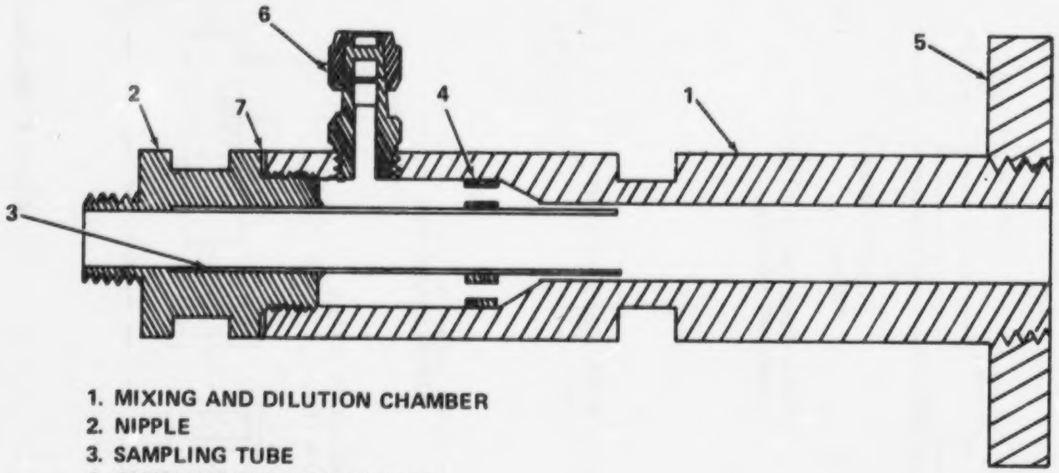

1. MIXING AND DILUTION CHAMBER
2. NIPPLE
3. SAMPLING TUBE
4. SAMPLING TUBE POSITIONER
5. MOUNTING PLATE
6. TUBE TO MALE PIPE FITTING
7. GASKET

Figure 2. Scale drawing of the dilution ejector pump (DEP).

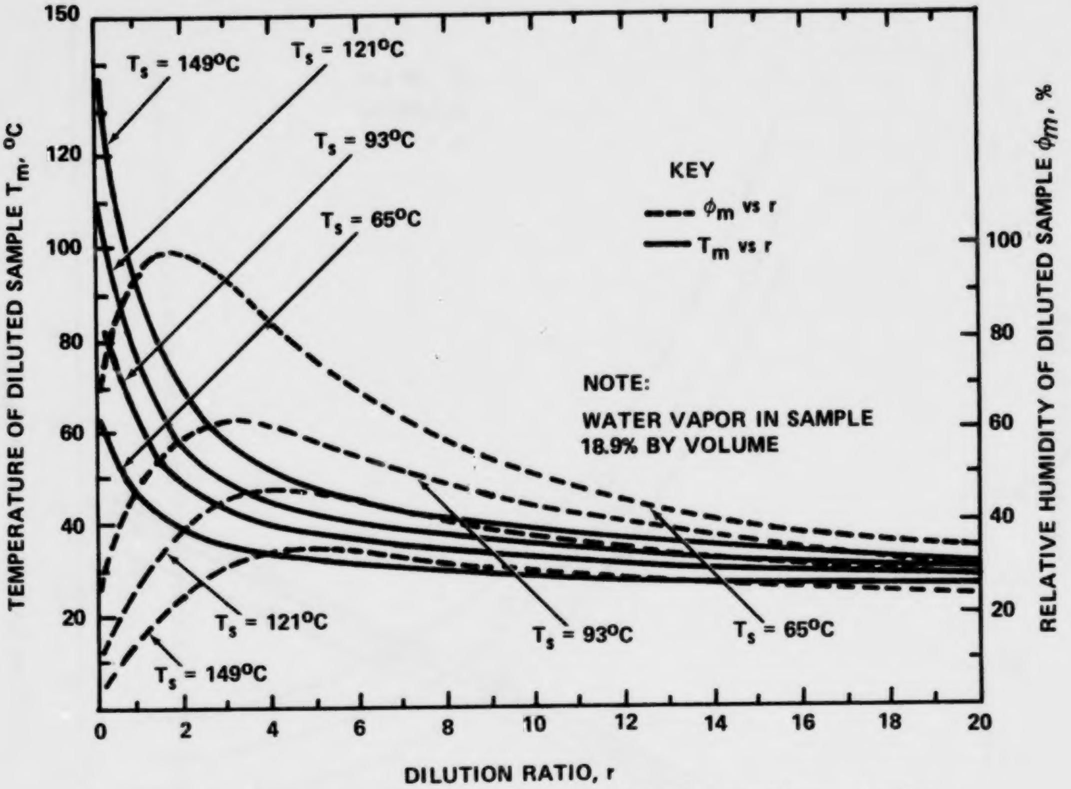

Figure 3. Temperature and relative humidity of diluted sample vs. dilution ratio for dilution air at 27°C and relative humidity less than 10%.

The sample flow rate also depends on the size of the nozzle and the length of the probe. Figure 4 is a graph of sample volumetric flow rate (Q_s) and the dilution ratio (Q_d/Q_s) versus the control pressure P_o. For the SSD system, accurate measurement of dilution volumetric flow rate is not needed since the operator adjusts it to achieve isokinetic sampling conditions and a diluted sample temperature within 5°C of atmospheric temperature. It is essential that the sample volumetric flow rate be measured accurately.

Measurement of volumetric flow rate and total volume of sample--An electronic system is used for measuring the total volume of the sample and the sample volumetric flow rate, and in displaying these values. An orifice (0.635 cm diameter) mounted upstream of the DEP was used to measure the sample volumetric flow rate. The temperatures of the orifice housing and probe were held at 93.3°C (200°F). The electronic signal is generated by a pressure transducer (located in Control Unit) that senses the difference in pressure across the orifice (ΔP_s). The transducer output is a 0.5 to 5.5 volt signal that is linearly proportional to the differential pressure of 0.0 to 38.1 cm H_2O (0.0 to 15 inches H_2O).

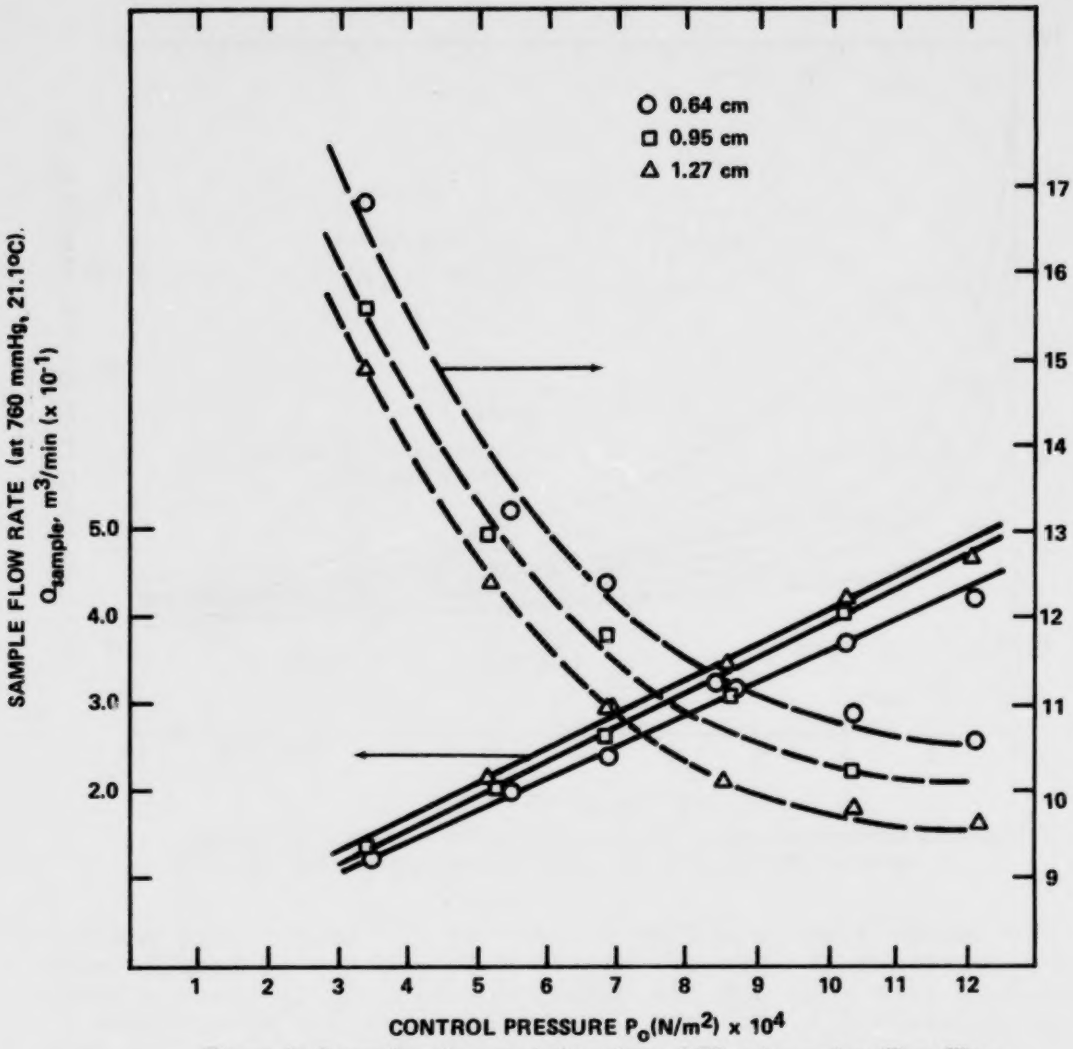

Figure 4. Operating characteristics of the DEP using a glass fiber filter and different inlet nozzles.

The volumetric flow rate of the sample, Q_S, is proportional to the square root of ΔP_S, which is obtained by passing the transducer output through a square root extractor. The output voltage from the square root extractor indicates the volumetric flow rate that is needed in the computation of sampling velocity at the nozzle. Integrated with time this signal determines the total gas volume of the sample. The integration is achieved by converting the output voltage from the square root extractor to a series of pulses with an analog-to-frequency converter, and then summing these pulses with respect to time. The total number of pulses is counted, and displayed as the total volume of the sampled gas. In addition, the elapsed time is also displayed. The display is a set of light emitting diodes (LED's). Figure 5 is a schematic diagram of the entire electronic system.

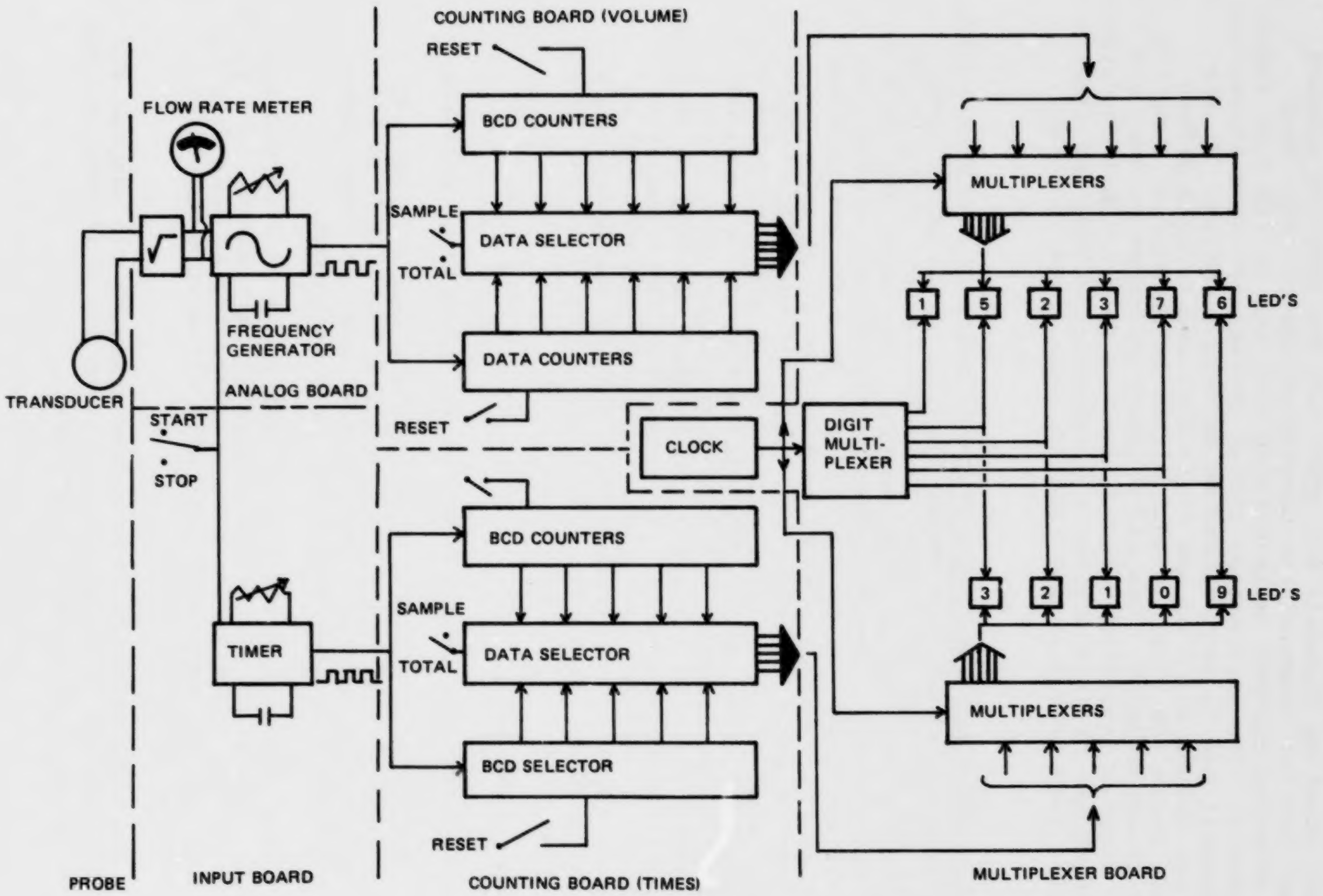
COUNTING BOARD (VOLUME)
RESET
BCD COUNTERS
FLOW RATE METER
MULTIPLEXERS
SAMPLE
DATA SELECTOR
TOTAL
FREQUENCY
GENERATOR
DATA COUNTERS
1
5
2
3
7
6
LED'S
TRANSDUCER
ANALOG BOARD
START
RESET
CLOCK
DIGIT
MULTI-
PLEXER
STOP
BCD COUNTERS
3
2
1
0
9
LED'S
SAMPLE
TIMER
DATA SELECTOR
TOTAL
MULTIPLEXERS
BCD SELECTOR
RESET
PROBE
INPUT BOARD
COUNTING BOARD (TIMES)
MULTIPLEXER BOARD

Figure 5. Block diagram electronic circuit.

Four counting channels are used, two for counting elapsed time, and two for counting the sampled volume of gas. Each volume counting channel is associated with one of the time counting channels. The information stored in each set (one volume/one time channel) can be initialized to zero by a button. In the field, one volume and time set is initialized to zero before the test, while the other is initialized to zero after sampling at each traverse point. One LED display indicates volume, and one LED display indicates elapsed time. A selector switch determines which set of information is displayed: volume and time for entire test or volume and time for that traverse point.

Calibration and cleaning system--By means of two ball valves, the operator can withdraw a sample from the stack or can pass clean dry air through the system at a desired rate so as to remove particles from the orifice and DEP or to check the calibration of the orifice. The dislodged particles pass through the system and are deposited on the filter. Thus no particles are lost during the cleaning and calibration operation which can be performed without removing the probe from the stack. The numerical value of the sampled gas volume is electronically stored prior to cleaning and calibration and can be recalled once sampling has resumed. If particles collect around the orifice and change its discharge coefficient, it will be detected by the calibration procedure. To compensate for a change in calibration, a "calibration adjust" potentiometer mounted on the face of the flow measurement unit enables the operator to adjust the recorded flow rate and to set it equal to the calibration flow rate.

OPERATION IN THE FIELD

In the field the sampling system is operated as follows:

1. A nozzle is selected such that the sample flow rate will be between 0.0140 and 0.0425 normal m^3/min. (0.5 to 1.5 scfm). (If a null-reading nozzle is not used, an independent S-type pitot must be attached to the sampling probe.)

2. With the ball valve closed, the probe is inserted in the stack. The stack gas velocity then is determined. The three-way valve is set and dilution pressure adjusted to pass dilution air through the DEP at a rate that will withdraw a sample at the isokinetic sampling rate.

3. The ball valve is then opened allowing the sampled gas to flow through the orifice. The dilution air flow rate is readjusted to maintain isokinetic sampling.

COMPARISON TESTS

Several samples were taken simultaneously with the SSD system and an EPA Method 5 sampling train from the following sources:

1) Coal-fired, traveling grate stoker, boiler (tests 1-5);
2) Glass melting tank (tests 6-11);
3) Lime kiln (tests 12-14).

In tests 1, 6, 7, and 12-14, simultaneous full-scale source certification tests were conducted. Tests 2-5 and 8-11 were conducted to determine the size distribution and elemental analysis of the particles. In tests 2-5 particle size measurements were made with an Andersen-2000, 8-stage, in-stack impactor and the SSD system. In tests 8-11 the size distributions were determined by scanning electron microscopy. Table 1 shows the mass concentrations that were obtained, Table 2 shows the size distribution, and Table 3 shows the results of elemental analysis performed by a scanning electron microscope and an X-ray spectrograph. Since the scanning electron microscope has poor accuracy, the ratio of the amount of the element in the SSD sample to that in the in-stack sample was computed.

TABLE 1. COMPARISON OF THE MASS CONCENTRATION DETERMINED BY THE SSD SYSTEM WITH THAT DETERMINED BY METHOD 5 SYSTEM

		Loading (mg/ncm)		
Source	Test	SSD	EPA Method 5 with impingers	EPA Method 5 without impingers
Coal fired boiler	1	495.6	462.1	407.6
Glass melt tank	6	71.7	45.8	38.9
	7	351.7	331.8	323.6
Lime kiln	12	116.2	126.6	111.0
	13	99.4	83.8	70.0
	14	139.0	140.3	123.6

TABLE 2. MEAN DIAMETERS AND GEOMETRIC STANDARD DEVIATIONS OF PARTICLES OBTAINED WITH THE SSD SYSTEM AND AN IN-STACK IMPACTOR

Source	Test	Sampling train	Dry gas volume (ncm)	Mean diameter (μm)	Geometric standard deviation
Coal fired boiler	2	In-stack	0.335	7.2	3.1
		SSD	1.902	0.4	6.6
	3	In-stack	0.262	10.2	2.4
		SSD	1.376	3.0	5.4
	4	In-stack	0.295	9.6	3.9
		SSD	1.351	0.3	1.7
	5	In-stack	0.312	4.1	4.6
		SSD	1.389	0.4	5.3
Glass melt tank	8	In-stack	0.192	0.4	2.2
		SSD	1.000	0.4	2.2

DISCUSSION OF RESULTS

Apparatus--One of the primary assets of the SSD system is its size and ease of operation. The DEP is considerably lighter and smaller than the mechanical pump in an EPA Method 5 system. The SSD has no glassware, impingers, ice, or impinger box to be carried to the sampling site. With no impinger box, the SSD system is also easier to install on a support mechanism, such as a monorail. The dilution air cleaner and dryer can be left unattended on the ground. The ball valve located after the probe and before the sample flow orifice is a positive shut-off. When a large probe is used the ball valve may be beyond the catwalk or roof and require the operator to reach over the railing. If the valve cannot be reached, the system can be shut off by bringing the dilution air pressure to zero. This, however, is not a positive shut-off.

Deposition of particles in the sampling system--Deposition of particles in the sampling system (probe, orifice and DEP) proved to be less than what occurs in an EPA Method 5 system. A "scalping cyclone" (Andersen-2000 preseparator) was mounted between the sampling nozzle and upstream end of the heated probe and removed particles greater than approximately 10 μm. Table 4 shows the percentage deposition in parts of the SSD system for a number of tests.

TABLE 3. RELATIVE ABUNDANCE OF ELEMENTS IN THE PARTICLES OBTAINED BY THE SSD SYSTEM TO THAT ON THE PARTICLES WITHIN THE STACK

Test No. 2 Coal-Fired Boiler with Aluminum as Reference Element

Impactor stage	Cut size µm SSD/In-stack	Element							
		Na	Al	Si	S	K	Ca	Fe	Zn
3	6.95/6.65	1.09	1.0	1.14	1.34	1.02	1.59	0.88	-
4	4.80/4.50	0.39	1.0	0.63	0.96	0.80	0.49	0.69	-
5	3.10/3.00	0.15	1.0	0.69	2.02	1.62	0.98	2.41	-
6	2.05/1.98	2.18	1.0	1.47	1.46	1.02	1.57	0.77	-
7	1.05/0.96	1.65	1.0	0.96	0.35	0.45	1.59	0.40	0.0
8	0.61/0.60	4.76	1.0	0.80	0.30	1.79	0.50	0.08	0.0
Back Up	0.42/0.40	1.44	1.0	0.95	0.24	0.90	2.00	0.67	4.51

Test No. 9 Glass Melt Tank

D_p (µm)	Background	Element						
		Al	Si	S	K	Ca	Fe	Ti
6.30	1.00	0.77	0.62	-	0.58	0.67	0.92	0.72
4.00	1.00	0.88	0.94	1.38	0.83	0.92	0.93	0.99
2.50	1.00	0.97	1.01	1.16	0.88	0.97	1.03	1.03
1.60	1.00	0.89	1.00	0.96	0.91	0.84	0.97	1.08
1.00	1.00	0.99	1.02	0.88	0.83	0.95	1.02	0.94
0.63	1.00	1.00	0.92	0.66	0.87	0.74	0.99	0.81

Test No. 10 Glass Melt Tank

D_p (µm)	Background	Element						
		Al	Si	S	K	Ca	Fe	Ti
10.00	1.00	0.50	1.71	1.50	0.71	0.79	0.78	0.75
6.30	1.00	0.73	0.18	2.70	0.82	1.14	1.01	0.96
4.00	1.00	1.06	1.22	0.59	1.10	1.06	1.48	1.14
2.50	1.00	1.18	1.16	0.50	1.34	1.38	1.50	1.27
1.60	1.00	1.00	1.02	0.68	0.98	0.96	1.10	1.07
1.00	1.00	1.10	1.00	1.02	1.09	1.07	0.94	1.00
0.63	1.00	1.09	1.10	1.30	0.95	0.93	1.15	1.16

Test No. 11 Glass Melt Tank

D_p (µm)	Background	Element						
		Al	Si	S	K	Ca	Fe	Ti
10.00	1.00	1.02	1.18	1.49	0.60	0.20	1.02	0.96
6.30	1.00	0.88	0.82	0.46	0.57	0.80	0.82	1.51
4.00	1.00	1.26	1.60	1.50	0.91	1.14	1.35	4.20
2.50	1.00	1.27	0.65	0.73	0.88	1.86	0.35	0.87
1.60	1.00	0.79	1.17	1.04	0.80	2.29	0.14	1.02
1.00	-	-	-	-	-	-	-	-
0.63	1.00	0.50	0.47	0.37	0.51	1.77	0.24	0.56
0.40	1.00	0.64	0.83	0.32	0.78	6.53	0.22	1.03

TABLE 4. DEPOSITION IN SSD SYSTEM (IN PERCENT)

Test No.	Source	Filter and filter housing	DEP and orifice	Nozzle preseparator and probe
1	Power plant	35.1	18.2	46.7
6	Glass melt tank	16.7	41.5	41.8
7	Glass melt tank	79.0	7.0	14.0
12	Lime kiln	36.6	18.7	44.7
13	Lime kiln	48.0	21.5	30.5
14	Lime kiln	36.5	16.5	47.0

In laboratory experiments a monodisperse aerosol of uranine dye was drawn through the sampling system at a volumetric flow rate of 28.32 normal liters per minute (1 scfm). It was shown that

(a) the scalping cyclone has a cut size of approximately 5 μm and is capable of removing particles above 10 μm,

(b) deposition in the sampling nozzle and orifice meter is never more than 10% of the sampled aerosol,

(c) deposition in the DEP is never more than 20% of the sampled aerosol,

(d) the final filter is the principal agent removing particles that leave the scalping cyclone.

Water content of samples--One important difference between the SSD system and an EPA Method 5 system is the procedure to calculate the water content of the sample gas. EPA Method 5 trains condense the water vapor and measure the remaining volume of gas in a positive displacement meter. The water content of the sample gas is easily determined by measuring the water in the impingers. The SSD system measures the total volume of sampled stack gas including the water vapor. The SSD system thus requires a separate procedure (such as EPA Method 4) to determine the water content.

Isokineticity is inherently easier to achieve in the SSD system. An EPA Method 5 train uses a pitot tube to measure the stack gas velocity and the sample flow rate is adjusted to achieve isokinetic conditions. To calculate the sample volumetric flow rate to achieve isokinetic conditions, the temperature and water content of the gas entering the nozzle must be known. Since the sample gas flow rate is measured after the water vapor has been condensed, the water content must be assumed to calculate the velocity. The SSD system measures the actual volumetric flow rate before condensation of water vapor and the above assumption does not have to be made.

Particle size distribution, mass concentration and elemental analysis--The mass concentration obtained by the SSD system was on the average larger than that obtained by the EPA Method 5 system when the impinger catch was included and even larger than when the impinger catch was not included. From the coal-fired boiler exhaust, the size distribution obtained by the SSD system contained a peak at 0.5 μm that was not present in the sample obtained at stack gas temperature. Figure 6 is typical of the data taken for tests 2-5. The results of the elemental analysis show no consistent pattern.

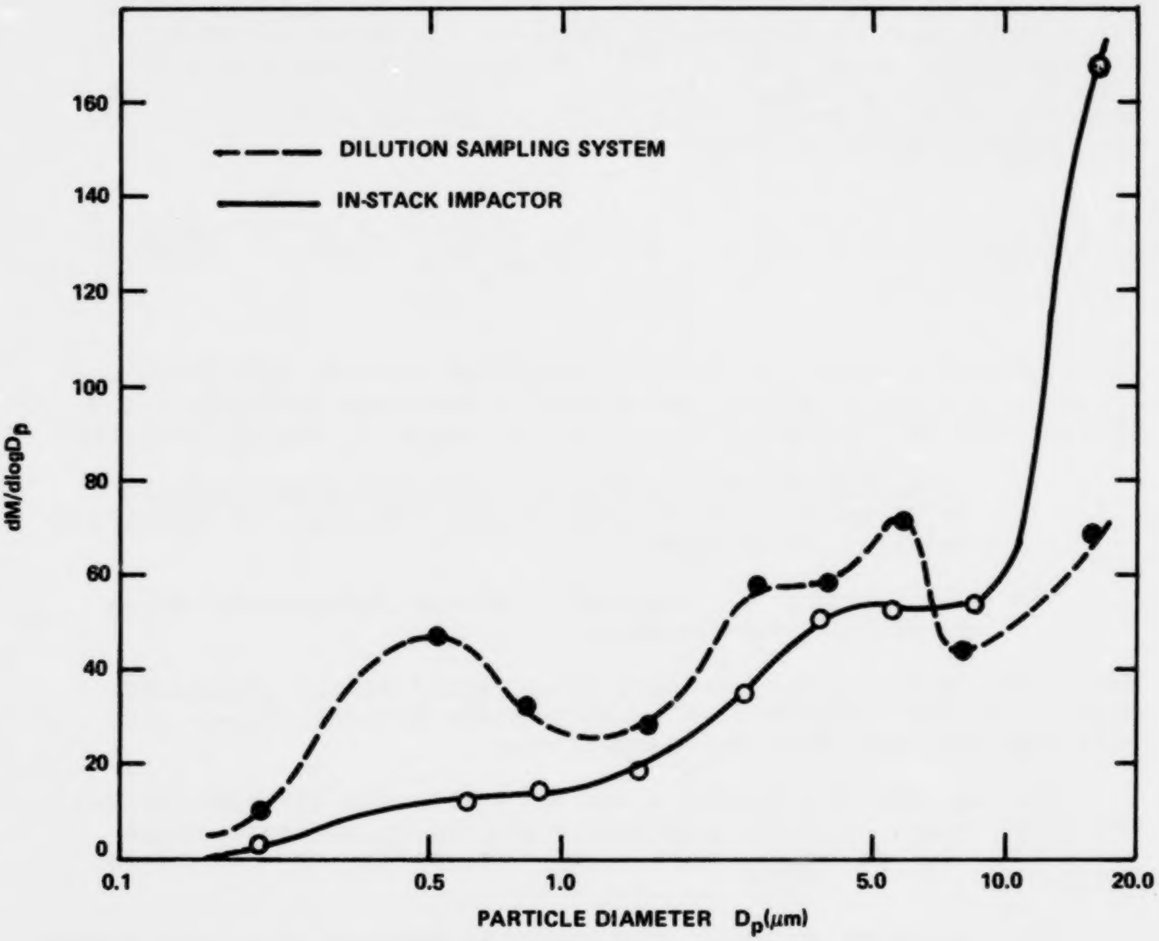

Figure 6. Particle size distribution, Test No. 3.

It is believed that the mass concentration, size distribution, and elemental analysis are affected by condensation, adsorption, and agglomeration that occur when the process gas stream mixes with air. The processes of adsorption, condensation, and agglomeration were not modeled in this research so that predictions of the mass concentration, size distribution, and the particle composition cannot be made. Rather, these processes will be examined in the plume and for samples obtained with the SSD system and an EPA Method 5 system. The purpose of this examination is to show that while the behavior of the diluted sample and the plume differ in a number of respects, samples obtained with the SSD system are more representative of the plume than samples obtained by either EPA Method 5 or Method 17 systems.

A plume rises because of its momentum and buoyancy. In plumes from combustion processes buoyancy is dominant. The plume rises until its density equals that of the surrounding atmosphere. Since plumes from fossil fuel burners have molecular weights that are approximately the same as air, the plume rises until its temperature is essentially equal to the surrounding air, whereupon the wind then carries the plume downwind where it expands laterally and vertically by turbulent diffusion. The concentration of species within the plume can be expressed by the Gaussian plume equation,

$$c_v = \frac{Q}{2\pi u\sigma_y\sigma_z}\left[\exp - \left(\frac{y^2}{2\sigma_y{}^2}\right)\right]\left\{\exp\left[-\frac{(z-H)^2}{2\sigma_z{}^2}\right] + \exp\left[-\frac{(z+H)^2}{2\sigma_z{}^2}\right]\right\} \quad (1)$$

The critical parameters in the expression are the diffusion coefficients σ_y, σ_z, which increase with downwind distance x and the atmospheric instability. From the above it can be seen that:

(a) at any downwind distance the species concentration is Gaussian with respect to the vertical (z) and transverse (y) distances

(b) with respect to downwind distance the concentration decreases exponentially.

Particles in the plume that are transferred to the atmosphere need to be characterized in terms of mass concentration, size distribution, and chemical composition.

The way the SSD sample mixes with dilution air and the way the plume mixes with the atmosphere differ in at least three respects: (a) Reynolds number, (b) time scale, and (c) mixing mechanism.

(a) Reynolds number. The Reynolds numbers of plumes depend on the installation but values of 10,000 or larger can be expected. The Reynolds number of the sample as it enters the DEP is 1000 or less. Thus not only are the Reynolds numbers different, but the plume is turbulent while the sample is laminar.

(b) Time scale. The rates at which the sample and plume mix with air are also different. The sample mixes with dilution air with a time scale given by:

time = DEP volume/volumetric flow rate ≈ 0.5 sec.

The plume mixes with the atmosphere over a time period that is difficult to estimate. Bosanquet[9] suggested that the time for a buoyant plume to rise is 2.16 s^{-1} where s is related to the potential temperature gradient $\frac{\partial\theta}{\partial z}$ by

$$s = (\frac{g}{T}) \frac{\partial\theta}{\partial z} \tag{2}$$

For a weakly stable atmosphere, t is approximately 200 seconds. Once the plume ceases to rise it spreads and mixes slowly with a time scale of the order of hours or days. Assuming a plume enters the atmosphere at 300°C and that the atmospheric temperature is 25°C, the cooling rate of the plume and SSD sample are,

plume: (300 - 25)/200 = 1.83°C/sec

SSD sample: (93.5 - 25)/0.5 = 137°C/sec

Thus the cooling rate for a plume is considerably slower than the cooling rate for the SSD sample. The mixing of the plume with the atmosphere is characterized by large scale turbulent eddies and a slow rate of change toward equilibrium, while for the SSD sample mixing is characterized by small scale turbulent eddies and rapid changes toward equilibrium.

(c) Mixing mechanism. After the plume rises, it is transported downwind. All during this time it expands and mixes with the atmosphere. Momentum transfer with the atmosphere is small and the plume spreads by lateral diffusion. The concentration of species within the plume can be expressed by Equation 1. The sample on the other hand mixes with dilution air all the while the two streams are confined within the DEP. The sample and the coaxial stream of air mix by the transfer of momentum. The concentration of species within the two streams can be estimated by various expressions obtained from the literature of ducted turbulent jets.[5-7] The thermodynamic path followed by the species within the plume is different from the path followed within the sample. The SSD sample quickly mixes with dilution air and is nearly uniform in temperature and concentration as it enters the filter. The plume remains distinct for a considerable time and mixing is gradual.

The significance of these differences must be judged by examining how particles in a process gas stream change when the stream is cooled and diluted with air. Particles within the plume or sample change by any one or combination of three processes: (a) particles may combine by coagulation, or their surfaces may act as sites for (b) condensation or (c) adsorption. To study how well a sample obtained with an SSD system simulates conditions within the plume it is necessary to determine if these three processes are affected by the differences above.

Coagulation. The rate at which the concentration (n) of particles of a particular size decreases by coagulation is given below. (Similar expressions should also be written for smaller particles that combine to form a new particle of the particular size in question. The net change in concentration will then be the difference between the two rates.) For a first estimate, simply consider the rate of removal of particles of a certain size,

$$\frac{dn}{dt} = -kn^2 \tag{3}$$

The coefficient k depends on the size of the particles but it is of the order of 10^{-10} cm^{3}sec^{-1}. Because k is small, and n is of the order of 10^3 cm^{-3}, coagulation is unimportant within the sample or during the buoyant rise of the plume. During the long period the plume spreads and mixes with atmosphere there is time for coagulation but this is somewhat compensated for by the low values of (n) brought on by dilution.

Condensation. An indication of the likelihood that condensation occurs is the degree of saturation for condensable species. The degree of saturation (S) is defined as

$$S = \frac{\text{species partial pressure at a temperature } T_m}{\text{species saturation partial pressure at a temperature } T_m}$$

$$S = \frac{X\ P_m}{P_{sat}}$$

If the value of S is equal to or above unity then condensation can be expected.

The mole fraction of species j in the diluted sample is

$$X_{j,m} = \frac{X_{j,s}}{1 + r\left(\frac{M_s}{M_a}\right)} \tag{4}$$

where r is the dilution ratio and M_s and M_a the sample and air molecular weight. The saturation partial pressure at a temperature T_m can be computed from the Clausius-Clapeyron equation, assuming Trouton's rule

$$h_{fg} = 10.5\ R\ T_b \tag{5}$$

in which the heat of vaporization (h_{fg}) is assumed constant and estimated at the boiling temperature (T_b) at one atmosphere and assuming that the vapor behaves as an ideal gas and R is the gas constant. The relationship between the saturation pressure at T_m and the boiling temperature T_b at one atmosphere can be expressed as

$$\ln\ (1/P_{sat}) = \frac{h_{fg}}{R}\left[\frac{1}{T_m} - \frac{1}{T_b}\right] \tag{6}$$

If the sample and the dilution air are ideal gases with constant specific heats and mixing is adiabatic, the temperature of the diluted sample T_m leaving the DEP can be written as

$$T_m = \frac{T_s + r\ T_d}{(r + 1)} \tag{7}$$

Thus the degree of saturation of species j is

$$S_j = \frac{X_{j,s}}{1+r\left(\frac{M_s}{M_a}\right)} \exp\left[\frac{h_{fg}}{R}\left[\frac{(r + 1)}{T_s + rT_d} - \frac{1}{T_d}\right]\right] \tag{8}$$

The saturation ratio is not easily computed for the plume. During the plume's buoyant rise there is little mixing but considerable cooling and during the downwind dispersion of the plume the reverse is true. In addition, there are distinct concentration gradients in the spreading plume and hence the saturation ratio will vary with respect to x, y, and z. For these reasons a direct comparison of the saturation ratio of the SSD sample and the plume is not possible.

The rate at which condensation increases the diameter of a single drop is given by Fletcher[10] as,

$$\frac{D_p}{4}\frac{dD_p}{dt} = G\ [S-1-\frac{a}{D_p} + \frac{b}{D_p^3}]\ f\ (Re,\ Pr')$$

$$G = \frac{D\rho_v}{\rho_L}\left[1 + \frac{Dh_{fg}^{\ 2}\ \rho_v\ M_a}{RT^2\ \kappa}\ \frac{f(Re,\ Pr')}{f(Re, Pr)}\right]^{-1} \tag{9}$$

The constants a and b relate to the effect of surface tension and presence of a solute and the function f (Re, Pr) accounts for convection heat transfer. The numerical value of the function is close to unity. Each particle in a population of small particles grows in a similar manner, but as the condensing material is removed from the vapor phase the degree of saturation (S) decreases. It will also change because of cooling and dilution. To model condensation for a population of particles requires one to know the rate of cooling, and the original particle size distribution, mass concentration, and saturation ratio. The computation is complex and was not performed for either the plume or the SSD sample. The solution is doubly difficult for the plume since the degree of saturation (S) and temperature vary with respect to x, y, and z.

While the rates of cooling and dilution in the SSD sample and plume are not identical, the SSD system more closely approximates the plume than the EPA Method 5 system in which there is no dilution and the EPA Method 17 system in which there is neither cooling nor dilution.

Adsorption. If the diameter of the particle does not change rapidly, the rate of change of the mass of an adsorbed species is equal to the rate at which material diffuses from the gas phase, viz.

$$\frac{d}{dt}\left[\rho_p \frac{\pi D_p^3}{6} c_{m,o} + c_s \pi D_p^2\right] = K\,[c_v - c_{v,e}]\,\pi D_p^2$$

$$\frac{dc_s}{dt} = K\,[c_v - c_{v,e}] \qquad (10)$$

where $c_{m,o}$ and c_s are the concentrations of a material per unit mass and surface area of the particle and where c_v refers to the concentration of the material per unit volume of gas. The constant K is the mass transfer coefficient. From the theory of adsorption, equilibrium conditions can be described by the Freundlich equation, in which $c_{v,e}$ is the concentration of the material in the gas phase at equilibrium.

$$c_{v,e} = \rho_p\,\alpha\,c_s^{\beta} \qquad (11)$$

The values of α and β depend on the molecular species in question and the units that are chosen. The quantity α is proportional to the temperature while β depends on the nature of the van der Waals forces on the particle's surface.

While the above expression was not solved for the plume or the SSD sample, it is possible to determine whether adsorption in the SSD sample is comparable to that which occurs in the plume. Values of β are in general integers larger than unity. Assume for discussion purposes that β=2.0. If the particle does not initially contain any of the adsorbate, the surface concentration at any time t can be expressed as

$$\frac{c_{s,e} - c_s(t)}{c_{s,e} + c_s(t)} = \exp(-t/\tau) \qquad (12)$$

where

$$\tau = \left[2K\ (c_v\alpha/\rho_p)^{\frac{1}{2}}\right]^{-1} \qquad (13)$$

The parameter τ is a time constant, such that if the elapsed time is equal to τ the surface concentration will be 47% of its equilibrium value, or if equal to 2 τ the surface concentration will be equal to 75% of its equilibrium value. The numerical value of τ depends on the mass transfer coefficient K, and the absorbate mass concentration c_v. The value of τ is not easy to compute since it depends on the fluid mechanics of mixing within the DEP and the plume. If τ is considerably smaller than the residence time of the SSD system, then the surface concentration will achieve its equilibrium value by the time the sample leaves the SSD system.

Filter accumulation error--Inherent in any filtration system is the constant exposure of the collected particles to the gas stream. Particles collected early in the sampling period will be exposed to the gas stream longer than those collected at the end of the sampling period. Errors which may occur will be called accumulation errors. If the processes of adsorption and condensation are completed before the sample passes through the filter, then there will be no accumulation error and the collected particles will represent those in the sample stream. If however this is not true, and the particles continue to adsorb and, or condense gas phase species, then the collected particles will not be representative of those in the sample stream.

An accumulation error may seriously affect studies in which condensation in the source is being investigated, if the degree of saturation at the filter is near unity. Under such conditions condensable vapors in the gas will continually condense on all particles collected up to that constant. Such an integrative effect will suggest condensation that greatly exaggerates what actually occurs in the plume.

CONCLUSIONS

A new source sampling system has been designed that is easier to use than a conventional EPA Method 5 system. The heart of the system is a Dilution Ejector Pump (DEP) that uses dry atmospheric air to withdraw a sample from a process gas stream and simultaneously dilute and cool it with atmospheric air. Within the DEP the sample reaches equilibrium with the dilution air in a way that replicates the way actual plumes reach equilibrium with the atmosphere. The particles in the sample are cooled to approximately ambient temperature and are deposited on a filter for analysis.

Tests have been conducted in which source samples were simultaneously withdrawn by the dilution sampling system and an EPA Method 5 system; tests were also made with the dilution sampling system and an in-stack system. Comparison of the particles obtained by the three systems reveals the following.

(1) The dilution sampling system records larger particle mass concentrations than an EPA Method 5 system.

(2) The size distribution of the particles obtained with the dilution sampling system is different from that obtained with an in-stack impactor. Depending on the combustion process, the sample obtained with the dilution system indicates the presence of submicron particles emitted to the atmosphere that are not present at stack gas temperature.

(3) The presence of various elements on, or in, the particles is significantly affected by the techniques with which the sample is obtained.

ACKNOWLEDGEMENT

This research was supported by Grant No. R803560 from the Environmental Protection Agency administered through the Center for Air Environment Studies of The Pennsylvania State University (CAES No. 521-78).

REFERENCES

1. Heinsohn, R.J., J.W. Davis, G.W. Anderson, and E.A. Kopetz, Jr. The Design and Performance of a Stack Sampling System with Dilution. Paper No. 76-37.3, Annual Meeting, Air Pollution Control Association, 1976.

2. Heinsohn, R.J., J.G. Wehrman, J.W. Davis, and G.W. Anderson. A Comparison of the Particulate Matter Obtained Using a Dilution Sampling System and a Method 5 Sampling System. Paper No. 77-12.1, Annual Meeting, Air Pollution Control Association, 1977.

3. Heinsohn, R.J., and J.W. Davis. Design of Stack Sampling System with Dilution. Center for Air Environment Studies, Pennsylvania State University, Report No. 494-78, 1978.

4. Wehrman, J.G., R.J. Heinsohn, J.W. Davis, and G.W. Anderson. Instruction Manual for a Stack Sampler with Dilution. Center for Air Environment Studies, Pennsylvania State University, Report No. 477-77, 1978.

5. Hedges, K.R., and P.G. Hill. Compressible Flow Ejectors. Part I-Development of a Finite Difference Flow Model. Paper No. 74-FE-1, Annual Meeting, American Society of Mechanical Engineers, 1974.

6. Hedges, K.R., and P.G. Hill. Compressible Flow Ejectors. Part II-Flow Measurements and Analysis. Paper No. 74-FE-2, Annual Meeting, American Society of Mechanical Engineers, 1974.

7. Razinsky, E., and J.A. Brighton. Confined Jet Mixing for Nonseparating Conditions. J. Basic Eng., Trans. ASME 93(4): 333-347, 1971.

8. Hidy, G.M., and S.K. Friedlander. Vapor Condensation in the Mixing Zone of a Jet. AIChE J. 10(1):115-124, 1964.

9. Slade, D.H., ed. Meteorology and Atomic Energy, 1968. TID-24190, Environmental Science Services Administration, Silver Spring, MD, July, 1968. p 192.

10. Fletcher, N.J. The Physics of Rainclouds. Cambridge University Press, New York, 1969. pp 122-136.

PAPER 8

AEROSOL CHARACTERIZATION WITH A QUARTZ CRYSTAL MICROBALANCE CASCADE IMPACTOR

DAVID C. WOODS
NASA LANGLEY RESEARCH CENTER

AND

RAYMOND L. CHUAN
BRUNSWICK CORPORATION

ABSTRACT

A Quartz Crystal Microbalance (QCM) cascade impactor, developed by Chuan,[1] has been used by NASA to obtain in-situ data on size distribution, elemental composition, and morphology of aerosol particles. Aerosols in rocket exhaust plumes have been characterized using the QCM, in which the data are used for developing dispersion models for predicting plume behavior as a function of meteorology and for assessing the environmental impact of the effluents. Volcanic effluents have been measured in the troposphere and characterized with the instrument to support studies leading to an understanding of the volcano's geology and its contribution to atmospheric aerosols. NASA has more recently utilized the QCM to measure both upper tropospheric and stratospheric aerosols. In this paper a description of the QCM is presented, including its integration with several aircraft which have served as platforms. Also a review of the above measurement efforts is given and selected data are presented and discussed.

INTRODUCTION

An aerosol sensor, designed by Chuan,[1] has been used extensively in research at the NASA Langley Research Center for obtaining data on a variety of aerosols. The sensor, referred to as a Quartz Crystal Microbalance (QCM) cascade impactor, measures aerosol concentration and size distribution (mass concentration as a function of particle diameter) in-situ. It combines the use of piezoelectric crystal microbalances for sensing mass in real time with the technique of inertial impaction, with a cascade of impactors for classifying aerosols by aerodynamic size. Other methods that have been used for measuring size distributions and concentrations of aerosols in-situ include collection by impaction with later laboratory analysis such as weighing, counting, etc., and single particle light scattering. All methods, while providing valuable information, have uncertainties associated with their measuring techniques. For example, the aerosols collected by the impaction methods may undergo changes and/or evaporation between the time and location of collection and the time and location of analysis. Thus, this is not a truly in-situ method. On the other hand, size information obtained from light scattering measurements involves uncertainties in the knowledge of refractive index and particle geometry. Since the QCM cascade impactor senses mass in real time, the problems associated with aerosol changes or evaporation are avoided and since the size is determined by inertial classification, refractive index is not a factor. It should be appreciated, however, that the aerodynamic size of a particle depends on its geometry and mass density. In some cases these factors may be assumed with reasonable accuracy or may be determined by post-sampling analysis. Thus, the QCM offers a complementary approach to obtaining aerosol data while avoiding some of the problems encountered with commonly used techniques.

In addition to the size distribution and mass concentration data, the size separated aerosol collections can be further analyzed in the laboratory using scanning electron microscopy (SEM) with energy dispersive x-ray analysis to determine elemental composition and particle morphology. These data are of particular interest to researchers involved in the studies of plumes from power plants, rocket motors, volcanic eruptions, etc. They are also important to the understanding of the interplay between the earth's aerosol layer and solar radiation, through scattering and absorption, which affects visibility and the earth's radiation budget and thereby may affect global climate.

We have used the QCM as an airborne sensor on several different aircraft to characterize aerosols in rocket exhaust plumes, in volcanic eruption plumes and in the upper troposphere and lower stratosphere at several global locations. Size distribution data and data on elemental composition and morphology were obtained from each set of measurements. We present herein a brief description of the QCM sensor and its use on various aircraft. Some typical data are presented.

Instrument Description and Operation

The airborne QCM sensor (shown in the photograph in Figure 1) consists of ten impaction stages. Starting with stage 1, the particle diameters for which the impaction efficiency is 50% (50% cut points) are: 25, 12.5, 6.4, 3.2, 1.6, 0.8, 0.4,

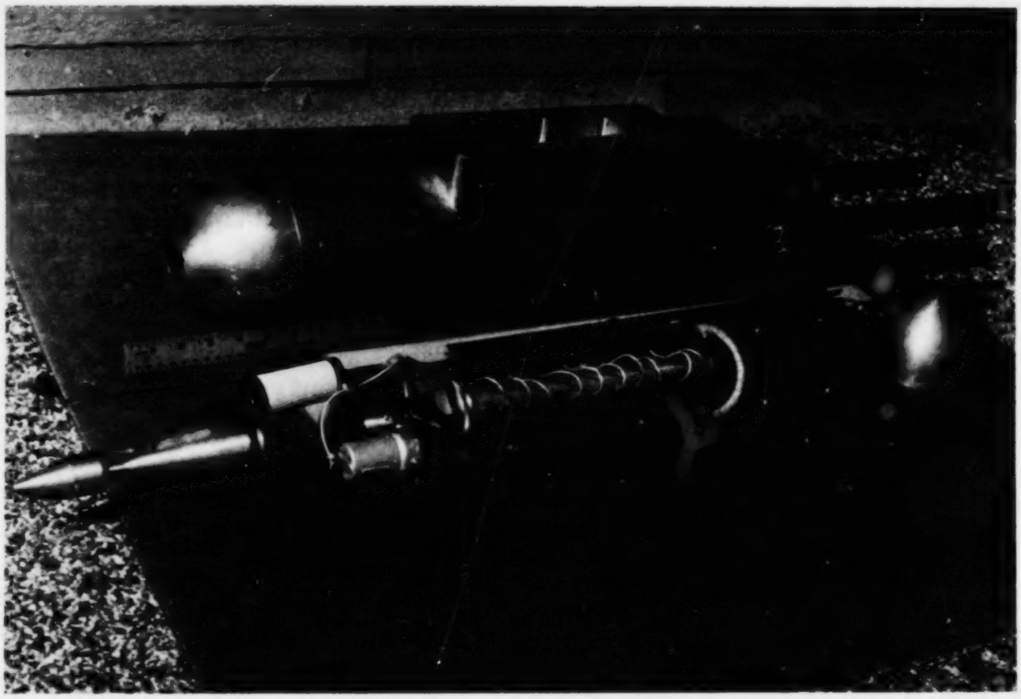

Figure 1. The 10-stage QCM cascade impactor for airborne measurements.

0.2, 0.1, and 0.05 micrometers (μm) for equivalent spherical particles with a mass density of 2 g/cm^3. The impaction surface in each stage, instead of being an inactive collector such as a glass plate, a microscope grid, or filter paper, as is used with conventional impactors, is an active piezoelectric crystal. The crystal, usually coated with a thin layer of grease to impede particle bounce, is a part of an oscillating circuit which senses the mass of the impacted aerosol by the associated change in frequency. Therefore, by continuously monitoring the oscillator frequency in each stage, one can determine the aerosol mass collected as a function of particle size.

Because of the very high sensitivity of the piezoelectric microbalance (of the order of 10^9 Hz/g) a volume flow rate of only 240 mℓ/min is used for sampling at altitudes below 3 km where the total mass concentration is on the order of 10 to 100 μg/m^3. At altitudes above 3 km where the mass concentration is on the order of 1 μg/m^3 the volume flow rate is 2 ℓ/min. When sampling in ambient air a sampling time of the order of a few minutes is usually required for a sensible signal while a sampling time of only several seconds is required when sampling in highly concentrated plumes such as rocket exhaust plumes or volcanic plumes.

When the sensor is flown external to the aircraft (e.g., under the wing of the Sabreliner and Queenaire, or on the side of the P-3), it is placed in an aerodynamically-shaped housing (shown in Figure 1) which protects the sensor and allows air to flow around the cascade maintaining the sensor at ambient temperature. Isokinetic sampling at the required flow rate is obtained by a specially designed inlet probe. It consists of two diffusers in series, as shown schematically in Figure 2. The object is to decelerate the air which enters the probe at the aircraft speed U_o (approximately 40 m/sec to 200 m/sec depending on aircraft and altitude) to a speed U_s which matches the air speed entering the impactor. U_s is equal to V/A, where V is the volume flow rate into the impactor and A is the area of its inlet. Since A is not very large (typically about 0.3 cm^2), to decelerate the air from U_o to U_s in a single duct would require that the probe inlet area be too small and it would be impractical to handle. The solution is to start with a practical probe inlet area, A_o, of the order of 0.1 cm^2 (equivalent diameter of about 0.3 cm); decelerate by a factor of 10 to 20 along a small divergence angle diffuser (included angle 15°, to assure no flow separation); skim the core of the decelerated flow with a sharp-lipped "skimmer" of area A_2, which is a small fraction of the plenum area A_1, and deliver it to the second diffuser. The excess flow in the plenum of the first diffuser is vented out to the atmosphere at the truncated base of the diffuser where the base pressure, p_b, is sub-atmospheric.

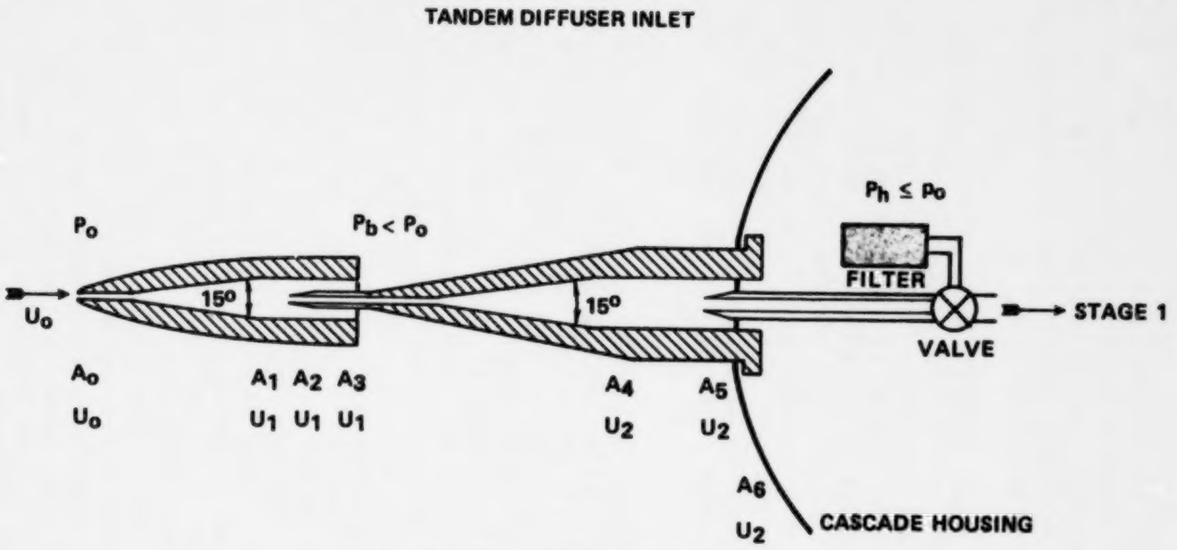
TANDEM DIFFUSER INLET
P_o
U_o
15°
$P_b < P_o$
15°
$P_h \leq P_o$
FILTER
VALVE
STAGE 1
A_o
U_o
A_1 A_2 A_3
U_1 U_1 U_1
A_4
U_2
A_5
U_2
A_6
U_2
CASCADE HOUSING

$$U_s = \text{CASCADE INLET FLOW SPEED}$$
$$= \frac{V}{A_5}$$
$$V = (U_o A_o) \frac{A_2}{A_1} \frac{A_5}{A_4}$$

Figure 2. A schematic of the airborne QCM inlet.

In the second diffuser the velocity U_1 is again decelerated by a factor of about 10, to match the impactor inlet velocity, U_s, which for the case of V = 2000 mℓ/min and inlet area of 0.3 cm^2 is about 100 cm/s (as compared to the airplane speed of 200 m/s, a factor of 200). The QCM inlet acts as the core "skimmer" in the plenum of the second diffuser. The excess flow is vented out of the base of the second diffuser into the housing which is in turn vented through its base, at base pressure, p_h, less than ambient, into the atmosphere.

The flow relationship through various stations along the tandem diffuser is shown below the schematic in Figure 2. By judicious selection of the various areas it will be found that the impactor inlet can be readily matched to any specified flight speed.

In a typical sampling flight the instrument is placed in its standby mode, in which ambient air is taken through the impactor through a total filter while en route to the sampling site. Just before a plume is entered, the sampling valve is moved from the standby position to the sampling position and the air flows directly into the impactor, bypassing the absolute filter. When the airplane leaves the plume (or when sufficient signal is obtained in case one is flying along a long plume) the valve is returned to standby. The frequency change in each stage and the time in the plume yields the aerosol mass concentration in each stage. These frequencies are recorded by a printer in the instrument control unit, so that the raw data can be analyzed after the flight.

Table 1 summarizes the measurement efforts in which the QCM cascade impactor has been utilized by the Langley Research Center. The geographical locations, the types of aerosols measured, and the aircraft used for the measurements are listed in chronological order. The following will include discussions on portions of selected experiments from this table. These discussions are intended to illustrate the kinds of experiments in which the QCM may provide useful information and the results that may be expected.

Solid Propellant Rocket Exhaust

Our initial use of the QCM as an airborne sensor was for sampling and characterizing particulates in the exhaust plumes from solid propellant rocket motors (Deltas and Titans) at Kennedy Space Center starting in 1974. For the earlier measurements we used a single stage QCM impactor[2] which was a modification of one previously used as a ground sampling instrument. It was mounted in the forward baggage compartment of a Cessna 402 with protruding isokinetic inlet probes supplying the sample to the sensor. The single stage impactor provided mass concentration data and no real-time particle size data. It was replaced in 1977 by a 10-stage impactor which was flown in a rocket plume.[3]

TABLE 1. APPLICATIONS OF THE QCM CASCADE IMPACTOR AT LANGLEY RESEARCH CENTER

Date	Location	Type of Measurement	Aircraft	Approximate Altitude (km)
May 77	Fairbanks, Alaska	Stratospheric Aerosol	NCAR Sabreliner	10-13
May 77	KSC	Rocket Effluents	Cessna 402	0.3-2.0
Aug. 77	KSC	Rocket Effluents	Cessna 402	0.3-2.0
Sept. 77	KSC	Rocket Effluents	Cessna 402	0.3-2.0
Feb. 78	Guatemala	Volcanic Effluents	NCAR Queenaire	~5
Sept. 78	Laramie, Wyoming	Tropospheric Aerosol	NASA Wallops P-3	3-7.6
Nov. 78	Sondrestrom, Greenland	Stratospheric Aerosol	NCAR Sabreliner	10-13
Dec. 78	KSC	Rocket Effluents	Cessna 402	0.3-2.0
Mar. 79	Dallas, Texas	Tropospheric Aerosol	NASA Wallops P-3	3-7.6
Apr. 79	Natal, Brazil	Tropospheric Aerosol	NASA Wallops P-3	3-7.6
Apr. 79	St. Vincent Island	Volcanic Effluents (Soufriere)	NASA Wallops P-3	3-7.6
May 79	St. Vincent Island	Volcanic Effluents (Soufriere)	NASA Wallops P-3	3-5

During a typical sampling flight the aircraft made a series of passes through the center of the visible plume flying in a figure eight pattern while at the same time changing altitude between passes. Figure 3 (from data taken in December 1978) shows a size distribution plot of $\Delta C/\Delta \log D$ as a function of D, where C is the mass concentration in units of $\mu g/m^3$, and D is the particle diameter in micrometers. The bimodal distribution, typical of rocket exhaust plumes, has a sub-micron peak at 0.1-μm diameter and a second peak between 3.2 and 6.4 μm.

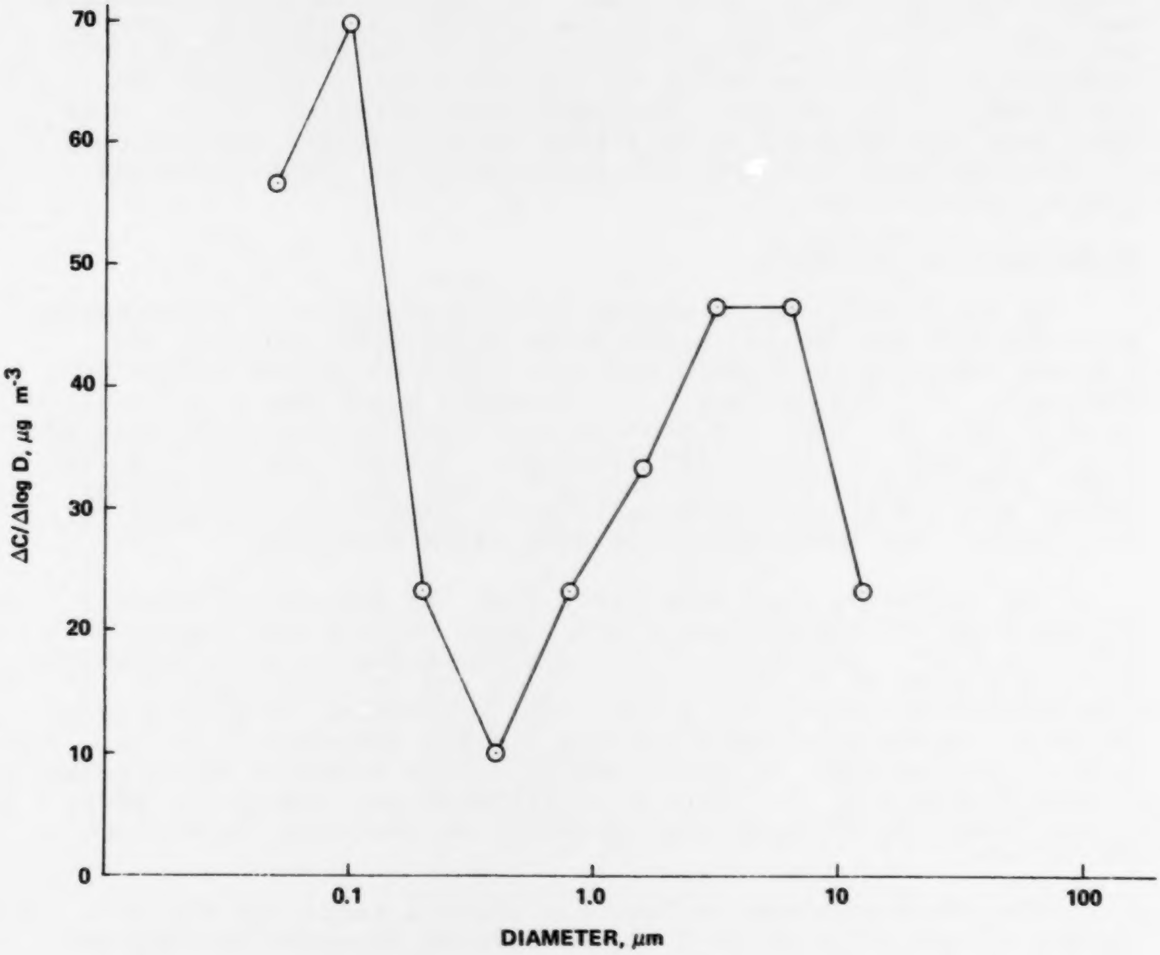

Figure 3. Particle size distribution in the exhaust plume from a Titan III rocket launched at Kennedy Space Center on December 13, 1978.

Aluminum oxide (Al_2O_3) spheres, formed by combustion of the rocket propellant, have been found to make up the major portion of the particulates in the large size mode[3] as illustrated in Figures 4a and 4b. Figure 4a shows an SEM photograph of particles collected in stage 5 of the cascade impactor corresponding to 1.6-μm diameter. Figure 4b shows an x-ray energy mapping for aluminum (Al), where the bright spots indicate the presence of Al. These spots map into the particles in Figure 4a indicating that they do contain Al. Since they are spherical in shape and show no other elements in the x-ray energy spectrum they are presumed to be Al_2O_3 particles. In general, the particles in the 0.1-μm size mode are more complex, consisting of single spherical Al_2O_3 particles, and agglomerates which contain sodium, aluminum, sulfur, chlorine, potassium, calcium, iron and zinc.[3] It is suspected that the Al_2O_3 particles formed in the exhaust cloud are formed by two processes thus producing the bimodal distribution. The spherical particles in the large size mode are believed to be formed molten alumina and the ones in the submicron size mode are believed to be formed from gas phase condensation.

Stratospheric Aerosols

In preparation for a series of intercomparative experiments with the QCM and several other types of aerosol sensors, the QCM was recently integrated and test flown on the NASA Ames U-2 aircraft. The U-2 is capable of reaching altitudes of greater than 20 km. The QCM, its control unit, and printer were mounted inside an area on top of the fuselage. A stainless steel inlet probe protruding through a cover plate was used to provide the sample air. A single three-way control switch was provided in the cockpit for the pilot to perform all operations.

The following data were taken with the QCM aboard the U-2 during a photographic mission over south central California on June 11, 1979. The measurements were made during level flight at an altitude of 19.8 km. Figures 5a and 5b show plots of $\Delta C/\Delta \log D$ as a function of D, for two consecutive 10-minute intervals. These plots show again a bimodal characteristic in mass concentration: a weaker one at 0.2-μm diameter and a relatively strong mode for the 1.6-μm diameter particles. In addition, Figure 5a shows an indication of an increase in $\Delta C/\Delta \log D$ at 0.6 μm.

The SEM photograph in Figure 6 shows a sample of the particles collected in stage 8 of the cascade impactor corresponding to the peak in the small size range of the bimodal distribution. The majority of the particles appear to be nearly spherical in shape and are on the order of about 0.2 μm in diameter, which is the 50% cut point for stage 8. There are quite a few irregularly shaped larger particles, on the order of 0.5 to 1.0 micrometers. These particles apparently have mass densities lower than 2.0 g/cm^3, the density for which the 50% collection

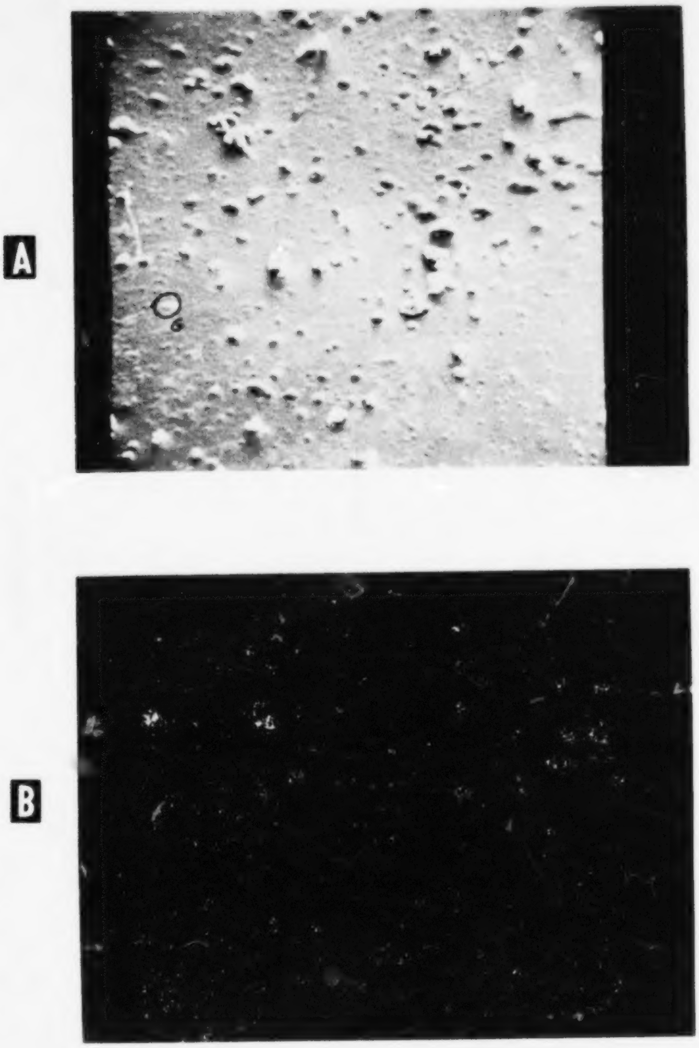

Figure 4. (a) Scanning electron microscope photograph of particles collected in stage 5 of the QCM cascade impactor for a Titan rocket exhaust plume. (b) X-ray energy mapping of particles in Figure 4a.

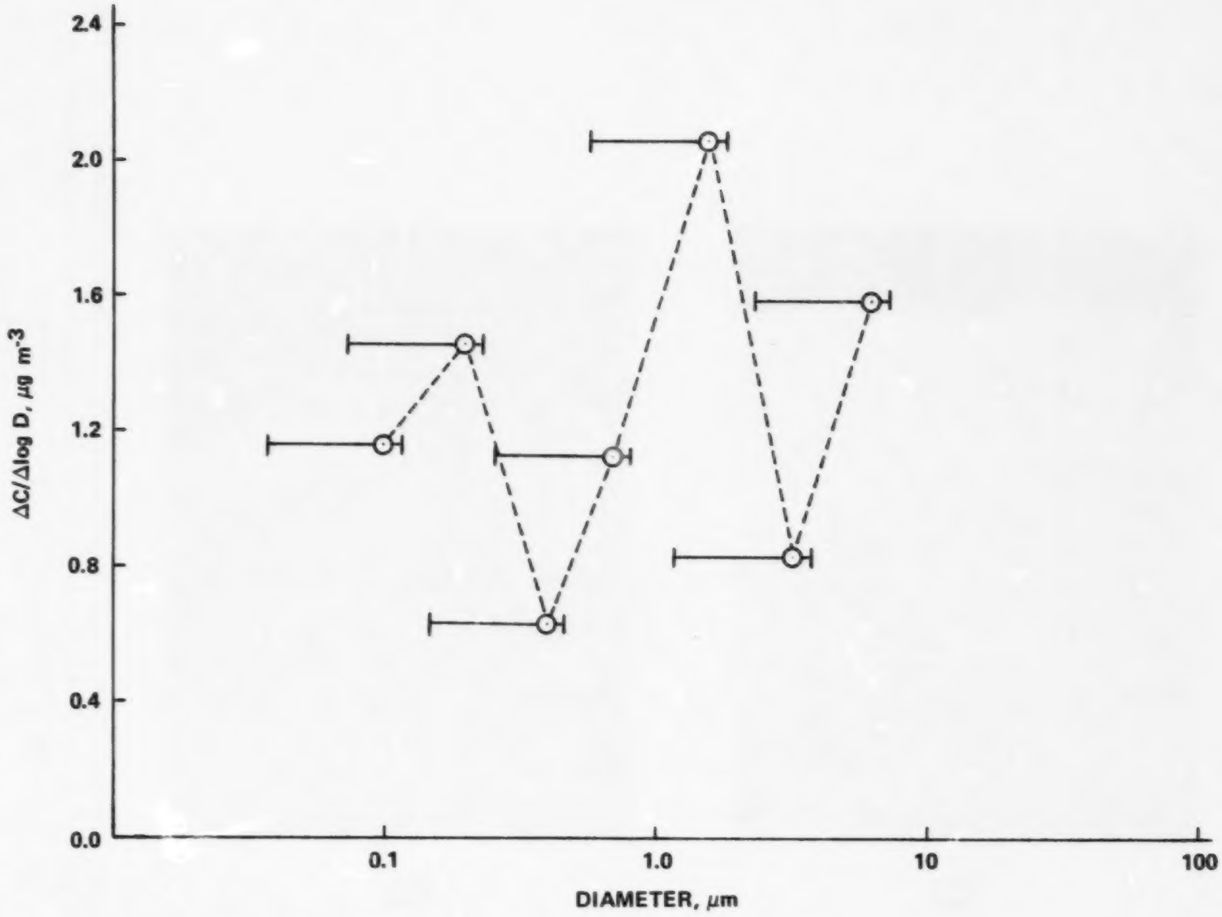

Figure 5a. *Size distribution plots of stratospheric aerosol particles measured with the QCM in the NASA Ames U-2 aircraft at 19.8 km over south central California.*

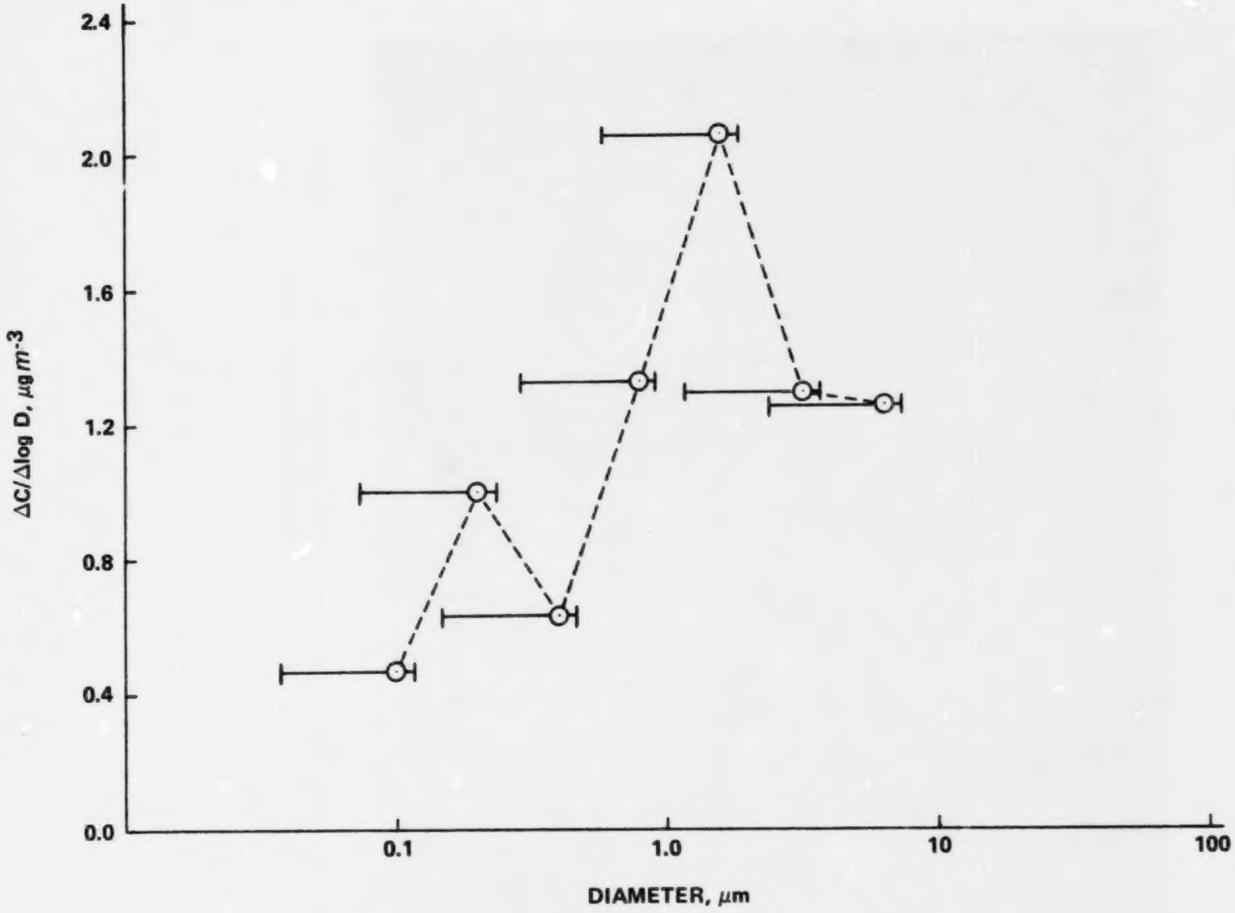

Figure 5b. *Size distribution plots of stratospheric aerosol particles measured with the QCM in the NASA Ames U-2 aircraft at 19.8 km over south central California.*

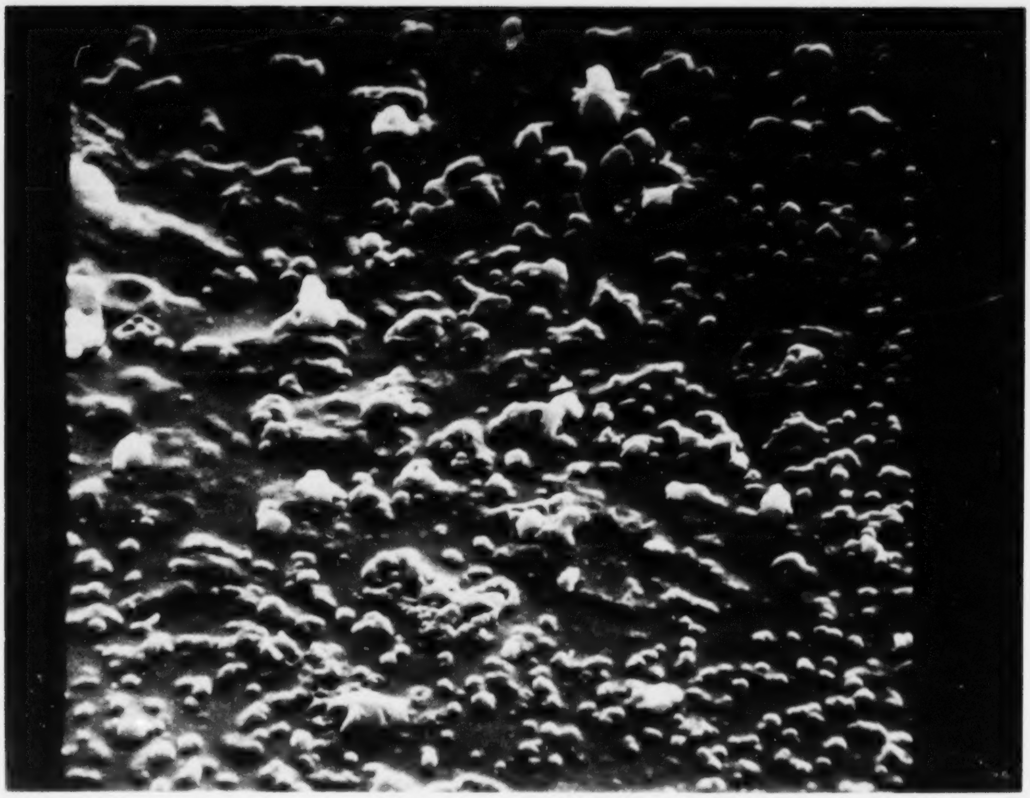

Figure 6. Scanning electron microscope photographs of stratospheric particles collected in stage 8 of the QCM cascade impactor over south central California at 19.8 km.

efficiencies are determined. The combination of density and shape causes these particles to behave aerodynamically as if they are 0.2-micrometer diameter spheres with a mass density of 2 g/cm^3.

Three of the particles in Figure 6 were selected for energy dispersive x-ray analysis, particles A, B, and C. Particle A is approximately spherical but is greater than 0.5 μm in diameter. B appears to have more of a cubic shape and is on the order of about the same size as A. C, on the other hand, is much smaller than A and B, being on the order of about 0.2 μm and spherical in shape. The type C particles are much more abundant than the other types. The x-ray energy spectra for the three particles are shown in Figure 7 along with a background spectrum. A and B show the same elements while C shows no x-ray spectrum at all, either because of its small size or because there are no elements present that can be detected by this x-ray method. In general, it was found that the morphology of the particles as well as the composition differed for the various impaction stages, indicating that the various types of particles are size dependent.

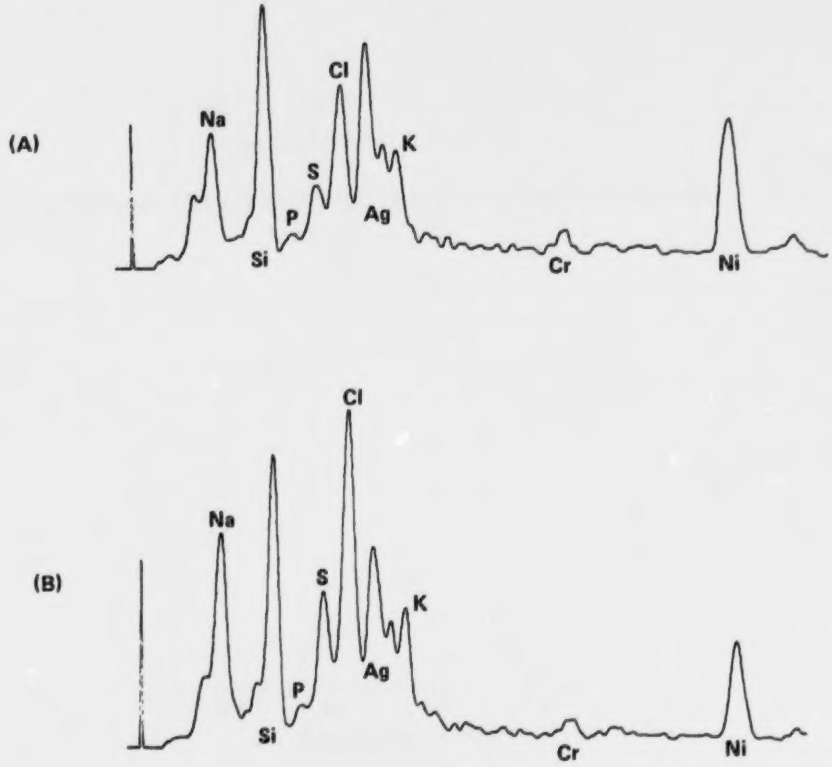

Figure 7. X-ray energy spectra for particles A, B, and C in Figure 6.

Volcanic Plumes

The QCM was aboard the NCAR Queenaire when it made a series of sampling flights over the active volcanoes, Fuego and Santiaguito in Guatemala, during February and March 1978.[4] During the sampling period, Santiaguito was producing several large ash-laden eruption clouds per day, some rising to higher than 5 km above sea level. The aircraft started sampling downwind of the visible plume and made several passes through the plume as it approached the volcano. Figure 8 shows two size distributions obtained from QCM data taken on February 28, 1978, (A) 9 miles downwind and (B) 18 miles downwind. In these plots,

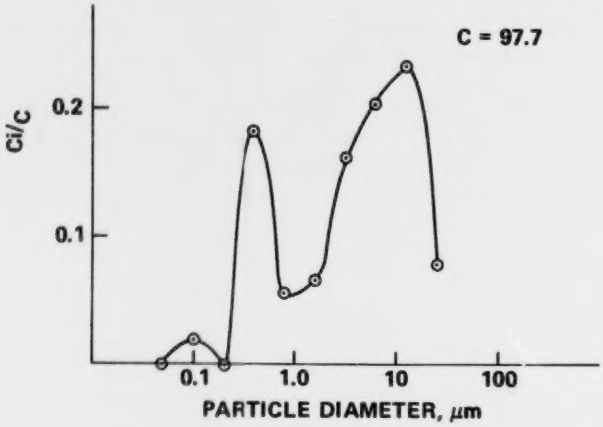

(A) SANTIAGUITO FEBRUARY 28, 1978 - 9 MILES DOWNWIND

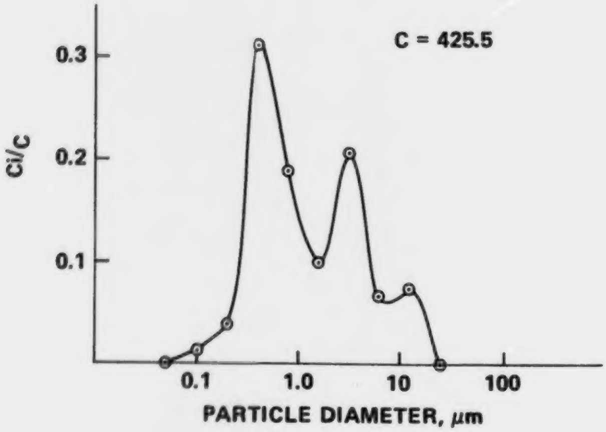

(B) SANTIAGUITO FEBRUARY 28, 1978 - 18 MILES DOWNWIND

Figure 8. Aerosol size distribution in the active plume of Volcano Santiaguito, February 28, 1978.

the mass concentration C_i in stage i of the cascade impactor was normalized to the total mass concentration C, where $C = \Sigma C_i$. The C_i/C vs. D plots may be compared with the $\Delta C/\Delta \log D$ vs. D plots by multiplying C_i/C by $C/\Delta \log D$ where C_i is the same as ΔC. These particular plots in Figure 8 show three modes in the size distribution. Many of the distributions, however, showed only two modes. The plumes were not very uniform and the size distributions tended to depend on the spatial position through which the aircraft made its pass. The particles collected from the plume were observed with an SEM. They exhibit the character of a crystal-rich volcanic magma consisting of crystal fragments of plagioclase and magnetite. It is believed that the sub-micron mode in the size distribution is caused by fragmentation caused by collisions among the particles. Since the large particles are crystalline, they can easily be broken into sub-micron size fragments by collision.

CONCLUSIONS

The basic operating principles of a ten-stage quartz crystal microbalance cascade impactor have been described. It is designed to obtain real time in-situ data on aerosol size distribution and to collect aerosols for post-sampling analysis of their elemental composition and morphology as a function of size. Examples of data have been presented which demonstrate the satisfactory performance of the instrument. These data were not obtainable in the past with previously existing sensors. There are many potential applications of this instrument for both tropospheric and stratospheric studies and it is anticipated that additional atmospheric measurements will continue to be made using this sensor.

REFERENCES

1. Chuan, R.L. Rapid Measurement of Particulate Size Distribution in the Atmosphere. In: Fine Particles, Aerosol Generation, Measurement, Sampling, and Analysis. Benjamin Y.H. Liu, ed. Academic Press, New York, 1976.

2. Woods, D.C. Measurement of Particulate Aerosol Mass Concentration Using a Piezoelectric Crystal Microbalance. In: Aerosol Measurements, D.A. Lundgren, et al., eds. University Presses of Florida, 1979.

3. Woods, D.C. Rocket Effluent Size Distributions Made With a Cascade Quartz Crystal Microbalance. In: Proceedings, 4th Joint Conference on Sensing Environmental Pollutants, 1977.

4. Rose, W.I., Jr., R.L. Chuan, R.D. Cadle, and D.C. Woods. Small Particles in Volcanic Eruption Clouds. Am. J. Sci., in press.

PAPER 9

EXTENDING PRECISION IN A COMPUTER-BASED CASCADE IMPACTOR DATA REDUCTION SYSTEM

JEAN W. JOHNSON
B.E. PYLE
WALLACE B. SMITH
SOUTHERN RESEARCH INSTITUTE

ABSTRACT

Due to the increased interest in the health effects of particulates up to 15.0 μm diameter, it has become necessary to accurately extrapolate the cumulative mass concentration beyond the effective limit of the first stage D_{50} (approximately 10.0 μm) of a cascade impactor. A first order osculating polynomial is proposed in conjunction with the Computer Impactor Data Reduction System (CIDRS, EPA 600/7-78-042) for fitting the cumulative mass curve between the first stage D_{50} and the maximum particle size. The function is a third degree polynomial which uses the known characteristics of the cumulative mass curve for its solution over this range of particle sizes. Testing this technique on a number of theoretical unimodal and bimodal size distributions demonstrates a high degree of accuracy in recovering the true, cumulative, particle concentration <15.0 μm. The technique described is proposed for recovering inhalable particulate from existing data and until such time that a cascade impactor is designed with a stage cut of 15.0 μm or greater.

BACKGROUND: THE COMPUTER-BASED IMPACTOR DATA REDUCTION SYSTEM

In March of 1978, the EPA report entitled "A Computer-Based Impactor Data Reduction System" was released.[1] The report describes a series of five computer programs, known by the acronym CIDRS, which are designed to reduce the field data taken by commercially available round jet cascade impactors. An outline of the CIDRS programs is illustrated in Table 1 with a listing of the program names and their functions.

TABLE 1. CIDRS PROGRAMS AND OUTPUT

MPROG

Cumulative mass concentration<D_{50}
Cumulative % mass concentration<D_{50}
$\Delta M/\Delta \log D$ vs. GMD
$\Delta N/\Delta \log D$ vs. GMD

SPLIN1

Fitting coefficients to generated set
of cumulative mass concentration points

GRAPH

Cumulative mass concentration
Cumulative % mass concentration
Mass vs. particle-size distribution
Number vs. particle-size distribution

STATIS

Averages with confidence bars	Cumulative mass concentration Cumulative % mass concentration Mass vs. particle-size distribution Number vs. particle-size distribution

PENTRA or PENLOG

Percent penetration-efficiency vs.
particle size with confidence bars

In brief, the sampling hardware information, sampling conditions, and particulate catch information are used as input to CIDRS to determine effective cut sizes of the various impactor stages and the particle concentration at each of these stages. This cumulative mass concentration < D_{50} vs. D_{50} is fitted by a set of continuous, modified spline curves. The mass and number size distributions may also be found from the derivative of this cumulative mass concentration curve. Since both the cumulative mass concentration curve and its first derivative are continuous, averaging of cumulative mass concentrations and mass size distributions over many runs is possible. This is done independently of stage D_{50} and stage geometric mean diameters. The averaged mass size distribution values, respective particle sizes, and upper and lower 50% confidence limits are stored in files. A separate file for inlet and outlet data is kept in this manner so that, on the final program execution, penetration-efficiency fractions and confidence limits are calculated at the various particle sizes. Both tabular and graphical outputs are produced at each of the data reduction levels described.

The curve fit to the cumulative mass distribution is a critical point in this data reduction system. After the fit is made in program SPLIN1, the stage by stage values of cumulative mass, the D_{50}'s, the stage by stage values of $\Delta M/\Delta \log D$, and the geometric mean diameters are ignored. Averaging and penetration-efficiency calculations are based strictly on the fitting coefficients as stored by SPLIN1 execution.

The method of fitting used in SPLIN1 is a graphical technique, or a "programmed French curve". The $\log_{10}$ (cumulative mass concentration) vs. $\log_{10}$ (D_{50}) points are input to SPLIN1 as illustrated in Figure 1a. Then a parabola is fitted to each set of three consecutive cumulative mass points. As shown in Figures 1b through 1d, interpolated points are defined at equal log diameter intervals between the first two of each set of three D_{50}'s. (A parabola having a negative first derivative in this interpolation area is overridden by a straight line between the two D_{50}'s to ensure a continuously increasing cumulative mass curve.) The final interpolation parabola (Figure 1e) is fitted through the second D_{50}, first D_{50}, and maximum particle size DMAX.

In the original version of SPLIN1, a hyperbolic function of the form

$$M = a_1 + \frac{a_2}{\log D} \tag{1}$$

is used to define the interpolation points between the first D_{50} and DMAX, where M is the mass concentration (mg/acm) less than particle diameter D(μm) and a_1 and a_2 are constants. Seven equally log-spaced interpolated points are defined over this broad particle range. The hyperbolic function as used for point interpolation is illustrated in Figure 1f.

The function which is proposed to replace the hyperbola, a third-degree polynomial of first order osculation, is the subject of the remainder of this paper. Such a function, used to interpolate points between the first stage D_{50} and the maximum particle diameter, is illustrated in Figure 2. Note that as the osculating polynomial approaches the total mass loading, its first derivative goes to zero. For log-diameters greater than this zero slope point (ZSPT) the cumulative mass loading is at its total value. The functional form of the osculating polynomial is discussed below. Its importance lies in the fact that it is a better suited function than the hyperbola for recovering the inhalable particulate concentration, i.e., the cumulative mass concentration < 15.0 μm, which lies in this fitting region beyond the first stage D_{50} ($\sim$10.0 μm).

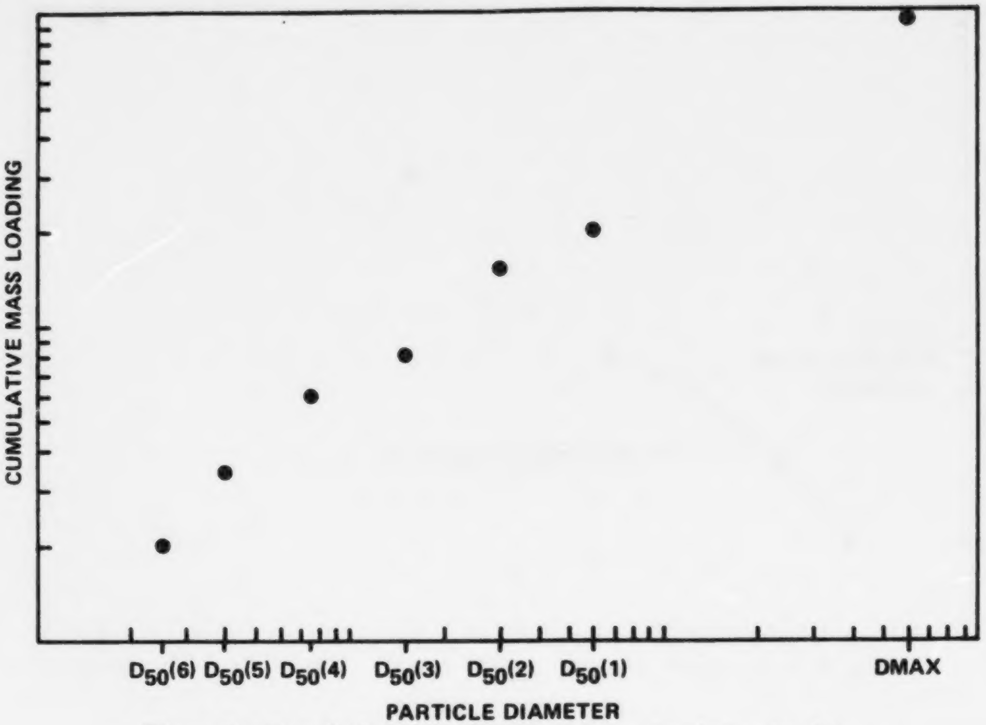

Figure 1a. Cumulative size distribution from raw impactor data.

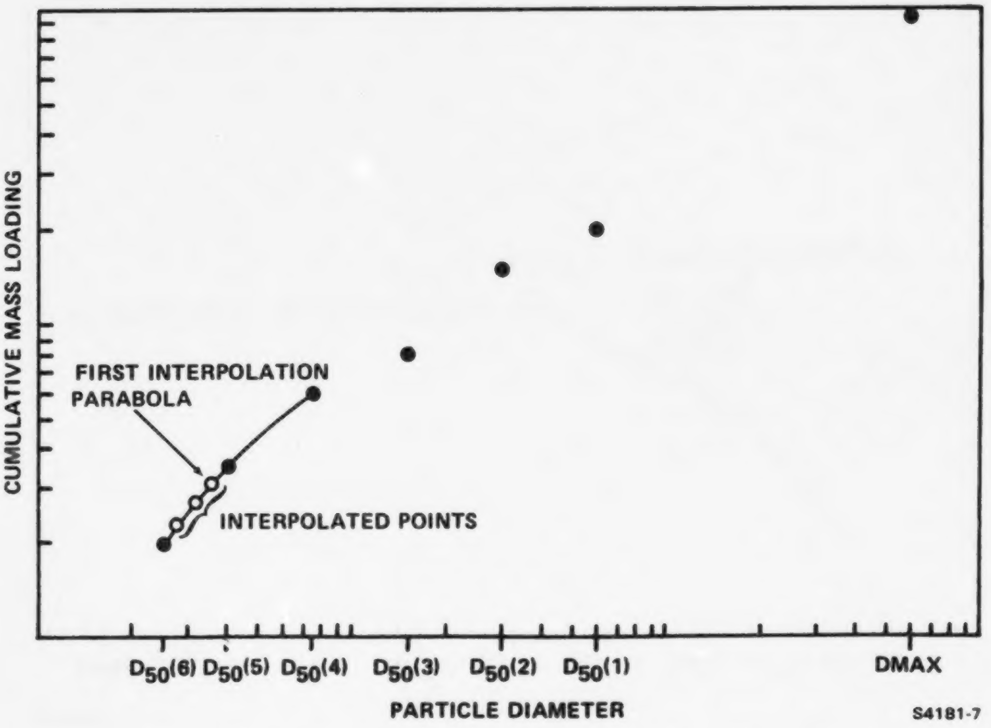

Figure 1b. Start of development of interpolated points between first and last D_{50}.

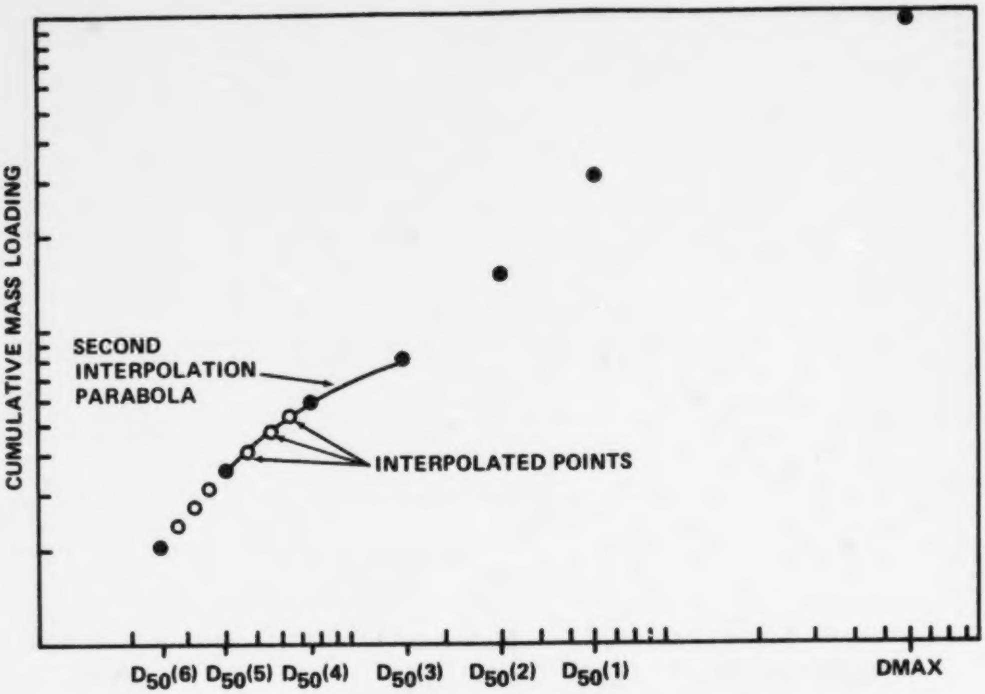

Figure 1c. Continued generation of interpolated points

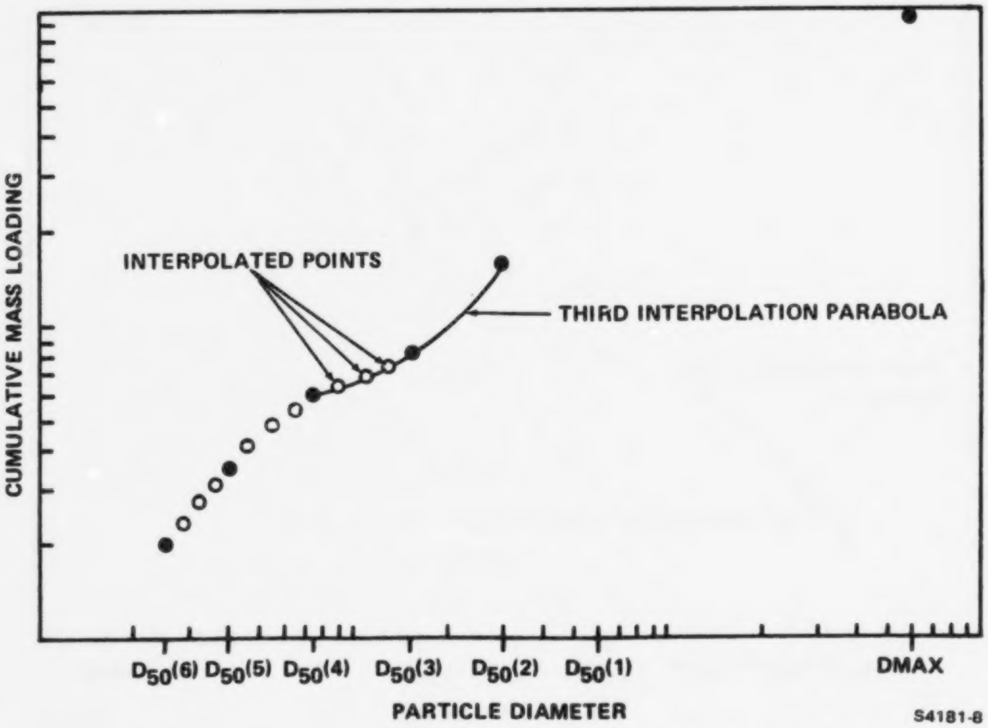

Figure 1d. Continued generation of interpolated points

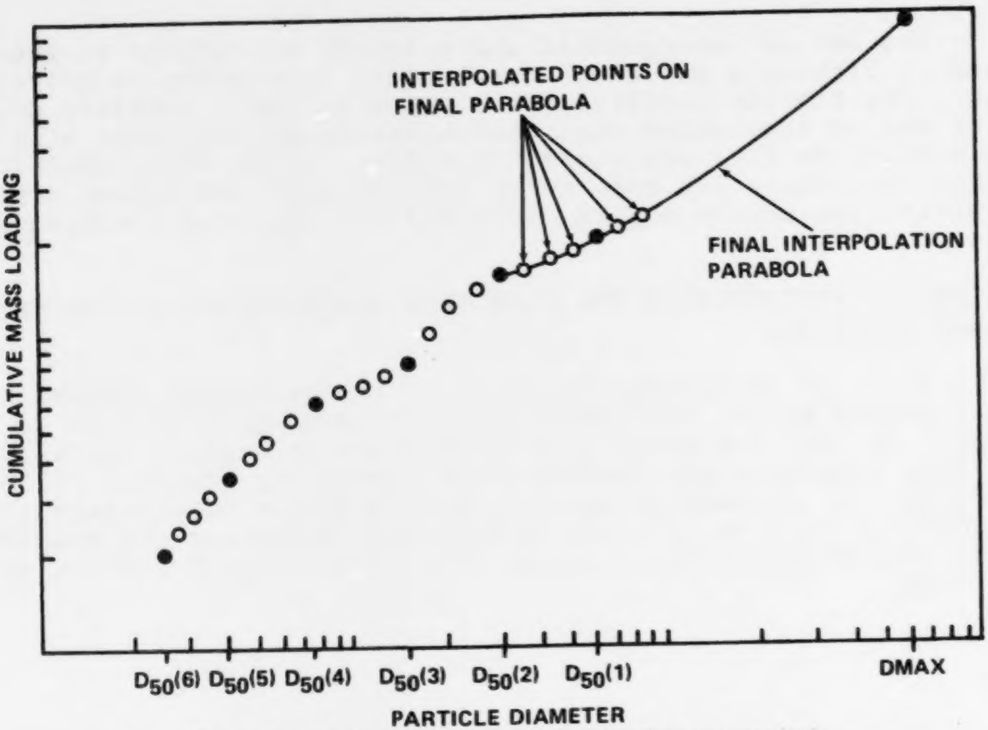

Figure 1e. Generation of interpolated points on parabola which includes DMAX.

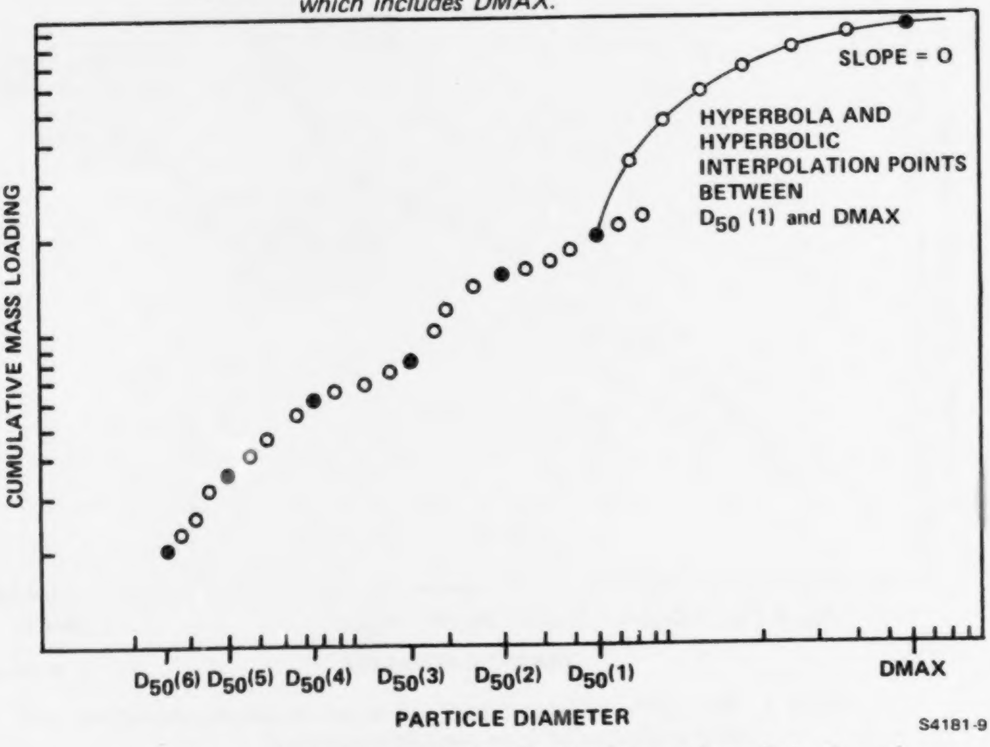

Figure 1f. Generation of interpolated points on hyperbola through $D_{50}(1)$ and DMAX

The set of interpolated and original D_{50} points is then used in fitting a series of continuous, second-degree polynomials. The fitting coefficients along with their boundary points (the set of cumulative mass concentration vs. particle size used in making the fit) are stored in files. Using these coefficients, the cumulative mass curve and the mass and number size distribution curves may be recovered for use in any subsequent program.

EXTENDING PRECISION IN THE MASS SIZE DISTRIBUTION BEYOND THE FIRST STAGE D_{50}

There is an increasing interest in the health effects of particulate matter consisting of particles up to 15.0 μm in diameter. The EPA has begun a large program to measure the emissions of this inhalable particulate from stationary sources. Also, efforts will be made to recover the inhalable particulate (IP) concentration from existing data by extrapolating the cumulative mass concentration curve beyond the first stage D_{50} limit to 15.0 μm.

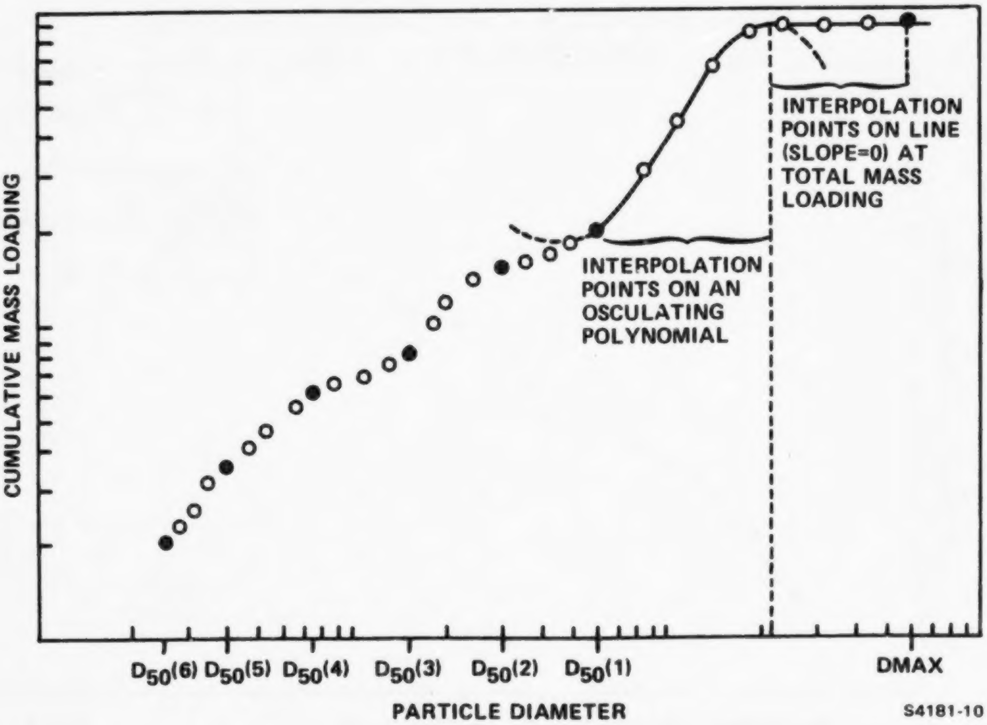

Figure 2. Generation of interpolated points on osculating polynomial and zero slope line at total mass concentration.

CIDRS has proven to be an accurate and time saving tool for impactor data reduction for the size region of approximately 0.25 μm up to 10.0 μm or the first stage D_{50}.[2] Because of the present construction of cascade impactors, there is a large span of particle sizes from the first stage cut point up to the largest particle size in the distribution. Due to the lack of information, it is difficult to describe the size distribution in this range of particle sizes. Since an extrapolation to 15.0 μm extends the data only slightly beyond the first stage D_{50}, extraction of IP mass concentration appears feasible if proper extrapolation techniques are used.

In view of this an extrapolation method that uses only the known parameters would seem ideal. The known or obtainable properties of the distribution are:

1. The first (largest) D_{50} is known.
2. The cumulative mass at the first D_{50} is known.
3. The slope of the cumulative mass curve at this D_{50} can be calculated.
4. The largest particle diameter is known or can be estimated.
5. The total cumulative mass at the largest particle diameter is known.
6. The slope of the cumulative mass curve at the largest particle diameter is known (=0.0).
7. The slope of the cumulative mass distribution is non-negative.

Until now the function used in CIDRS for fitting data beyond the first stage D_{50} has been a hyperbola of the form given in Equation 1.

Properties 1, 2, 4, and 5 are automatically satisfied by this two point fit (Equation 1). In addition, the form of the hyperbolic function generates a close approximation to properties 6 and 7 in that the slope of this function for real data is never negative and approaches zero at large D.

However, the hyperbolic function has drawbacks which limit its usefulness for extrapolation to inhalable particle sizes above the first stage D_{50}. First, property 6 is never rigorously satisfied. While the slope of the hyperbolic function approaches zero for large values of the maximum particle size, it will not be zero for a finite maximum particle size as is required. More seriously, there is no correlation between the slope of the hyperbola at the first stage D_{50} and the slope determined by the spline fitting routine. This discontinuity in slope violates property 3 of the true cumulative mass distribution and thus the hyperbolic function will not define proper mass concentrations for diameters slightly above the first stage D_{50}.

THE OSCULATING POLYNOMIAL

The new technique employs a polynomial of first order osculation to fit cumulative mass concentration from the first stage D_{50} to the maximum particle size. It not only passes through the two end points, but also may be constructed to have zero slope at the maximum particle size and have a slope at the first stage D_{50} equal to that of the spline fit through the first stage D_{50}. The osculating polynomial may also be constrained to have a non-negative slope over the specified range of particle sizes. In other words, all seven of the known or obtainable properties of the mass distribution in this particle range (as listed in the preceding section) can be satisfied by the proposed technique.

A polynomial of first order osculation is used as an approximation to a given function. By definition it matches both the function and its first derivatives at a finite number of points.[3] In general, there exists a unique (2n-1) degree polynomial fit to a set of n points. For the case of impactor data, let particle diameter be represented by the variable D, the cumulative mass loading by M(D), and the osculating polynomial approximation of this function by P(D); then properties 1-6 require

$$P(D_i) = M(D_i), \text{ and } P'(D_i) = M'(D_i) \qquad (2)$$

for i = 0,1 where the first point corresponds to the first stage D_{50} and the second to the maximum particle diameter. For the approximating equation to be physically realistic it is also necessary that property 7 be satisfied; therefore

$$P'(D) \geq 0 \text{ for } D_0 \leq D \leq D_1. \qquad (3)$$

To first order osculation, the polynomial P(D) can be described by Hermite's formula,

$$P(D) = \sum_{i=0}^{n} U_i(D)M(D_i) + \sum_{i=0}^{n} V_i(D)M'(D_i) \qquad (4)$$

where $M(D_i)$ and $M'(D_i)$ are the known values of mass concentration and its derivatives at D_0 and D_1; thus n has values of 0 and 1 only. The functions $U_i(D)$ and $V_i(D)$ can be expressed in terms of the Lagrange multipliers $L_i(D)$ and their derivatives $L_i'(D)$ such that

$$U_i(D) = \left[1-2L_i'(D_i)\ (D-D_i)\right]\left[L_i(D)\right]^2 \qquad (5)$$

$$V_i(D) = (D-D_i)\ \left[L_i(D)\right]^2 \qquad (6)$$

where

$$L_i(D) = \prod_{\substack{j=0 \\ j\neq i}}^{n} \frac{(D-D_j)}{(D_i-D_j)} \tag{7}$$

$$i = 0,1,2,----,n.$$

For the two points i = 0, i = 1 we have from Equation 7

$$L_0(D) = \frac{D - D_1}{D_0 - D_1} \tag{8}$$

$$L_1(D) = \frac{D - D_0}{D_1 - D_0} \tag{9}$$

and their derivatives are

$$L_0'(D) = \frac{1}{D_0 - D_1} \tag{10}$$

$$L_1'(D) = \frac{1}{D_1 - D_0} . \tag{11}$$

For the points i = 0, i = 1 Equation 4 becomes

$$P(D) = U_0(D)M(D_0) + U_1(D)M(D_1) + V_0(D)M'(D_0) + V_1(D)M'(D_1). \tag{12}$$

Combining Equations 5 and 6 with 8, 9, 10, and 11, the osculating polynomial then becomes

$$\begin{aligned} P(D) = &\left[1 - \frac{2(D - D_0)}{(D_0 - D_1)}\right]\left[\frac{D - D_1}{D_0 - D_1}\right]^2 M(D_0) \\ &+ \left[1 - \frac{2(D - D_1)}{(D_1 - D_0)}\right]\left[\frac{D - D_0}{D_1 - D_0}\right]^2 M(D_1) \\ &+ \left[\frac{(D - D_0)\ (D - D_1)^2\ M'(D_0)}{(D_0 - D_1)^2}\right] \\ &+ \left[\frac{(D - D_1)\ (D - D_0)^2\ M'(D_1)}{(D_1 - D_0)^2}\right]. \end{aligned} \tag{13}$$

Equation 13 can be put into a simpler form by defining the following constants:

$$k_1 = \frac{M(D_0)}{(D_0 - D_1)^2},\ k_2 = -\frac{2M(D_0)}{(D_0 - D_1)^3},\ k_3 = \frac{M(D_1)}{(D_1 - D_0)^2}$$

$$k_4 = -\frac{2M(D_1)}{(D_1 - D_0)^3},\ k_5 = \frac{M'(D_0)}{(D_0 - D_1)^2},\ k_6 = \frac{M'(D_1)}{(D_1 - D_0)^2} \tag{14}$$

$$a_1 = k_2 + k_4 + k_5 + k_6$$

$$a_2 = [k_1 + k_3 - (2\,D_1 + D_0)\,(k_2 + k_5) - (2D_0 + D_1)\,(k_4 + k_6)]$$

$$a_3 = [(k_2 + k_5)\,(D_1^2 + 2\,D_0D_1) + (k_4 + k_6)\,(D_0^2 + 2D_0D_1) - 2k_1D_1 - 2k_3D_0]$$

$$a_4 = [k_1D_1^2 + k_3D_0^2 - D_0D_1^2(k_2 + k_5) - D_0^2D_1\,(k_4 + k_6)].$$

In terms of these constants, the first order osculating polynomial can be written as a cubic equation in particle diameter D such that

$$P(D) = a_1D^3 + a_2D^2 + a_3D + a_4, \tag{15}$$

and its first derivative is

$$P'(D) = 3a_1D^2 + 2a_2D + a_3. \tag{16}$$

Property 7 above for impactor data limits the acceptable solutions 15 and 16 to those for which

$$P'(D) \geq 0,\ D_0 \leq D \leq D_1. \tag{17}$$

For some combinations of impactor data, particularly those for which the slope $M'(D_0)$ of the cumulative mass distribution at the first D_{50} is large, property 7 places an upper limit on the range (D_0 to D_1) of permissible particle diameters. For those cases, physically acceptable solutions can be found for a reduced range of particle diameters wherein the maximum size is somewhat smaller than the original D_1 or assumed maximum particle size. Figure 3 illustrates this. The first fitting osculating polynomial has the proper cumulative mass loading value at the first D_{50} and at the maximum particle diameter. The first derivative of the function at these two particle sizes is also correct, i.e., the first derivative of the osculating polynomial with respect to log diameter is the same as that for the spline fit at the first D_{50} and is zero at the maximum particle size. However, since the osculating polynomial does have negative first derivative values for $D_0<D<D_1$ (where D_1 here equals DMAX), the D_1 is "stepped" to a smaller value, and a second osculating polynomial is fitted. This second osculating polynomial is then

tested for negative first derivative values for $D_0 \le D \le D_1$. The particle size D_1 continues to be redefined at smaller values, and the osculating polynomial is fit between D_0 and D_1 until D_1 is defined at a critical value such that there are no negative derivatives over the tested particle size range for the osculating polynomial. D_1, renamed "zero slope point", ZSPT, marks

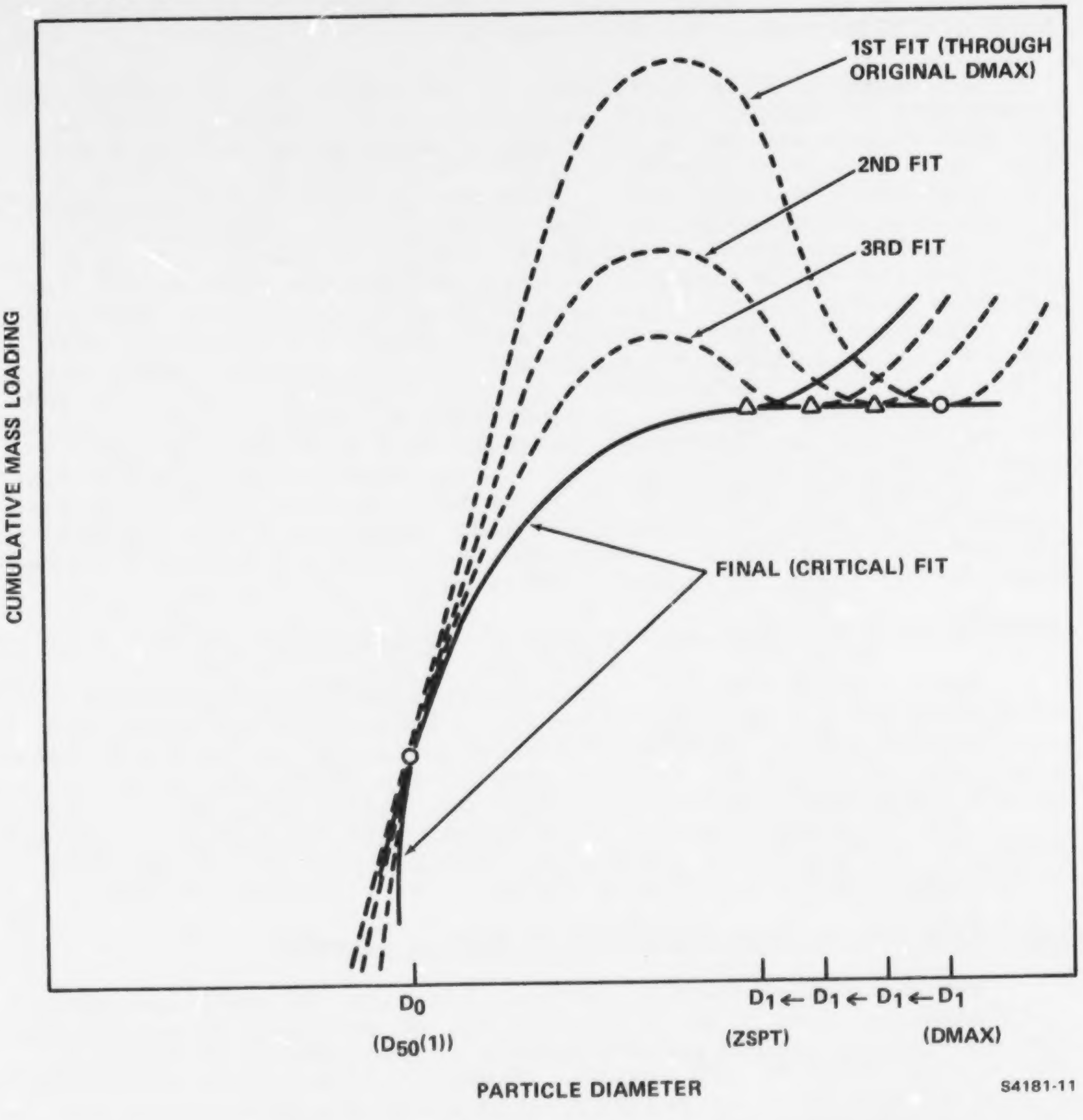
1ST FIT (THROUGH ORIGINAL DMAX)
2ND FIT
3RD FIT
FINAL (CRITICAL) FIT
CUMULATIVE MASS LOADING
D0
(D50(1))
D1 ← D1 ← D1 ← D1
(ZSPT)
(DMAX)
PARTICLE DIAMETER
S4181-11

Figure 3. Fitting the cumulative mass distribution for $D_{50}(1) \le D \le DMAX$ using a polynomial of first order osculation $P(D)$. The maximum diameter of the fitting function, D_1, is decreased until a critical fit is obtained with $P'(D) \ge 0$ for $D_0 < D < D_1$.

the maximum of the osculating polynomial at the total cumulative mass loading. As illustrated in Figure 2, interpolation points for the cumulative mass distribution are then defined along the osculating polynomial for $D_{50}(1) \le D \le ZSPT$ and are defined as the total cumulative mass loading for $\overline{Z}SPT \le D \le DMAX$.

RECOVERY OF THE INHALABLE PARTICULATE CONCENTRATION FOR LOG-NORMAL MASS DISTRIBUTIONS - ACCURACY TESTING

In order to have confidence in the value of the particulate concentration consisting of particles smaller than 15.0 μm as derived from a set of impactor data, one must be assured that the curve fitted to impactor data is a correct fit and that any extrapolation is reasonable. In order to test the "applicability" of the osculating polynomial for generating a cumulative mass distribution beyond approximately 10.0 μm, a theoretical mass distribution was assumed. The distribution was fitted with the proposed technique, and the recovered distribution was examined. For this purpose, both unimodal and bimodal distributions were theoretically sampled and the resulting data reduced using the CIDRS programs. The recovered distributions were then compared to the original, theoretical distribution. The characteristics of the particulate distribution which were individually varied were the mass median diameter MMD, the geometric standard deviation σ_g, and for bimodal size distributions, the fractional distribution of mass in each mode. Also varied were the assumed largest particle diameter DMAX and the geometric standard deviation of the stage efficiency curves σ_{gs}.

TESTING WITH UNIMODAL PARTICLE-SIZE DISTRIBUTIONS

For unimodal testing a log-normal size distribution was used with MMD = 5.0 μm and σ_g = 2.5 unless otherwise specified in the text. Also, unless otherwise specified in the text, DMAX was input as 100.0 μm, and the masses were collected using log-normal stage efficiency curves with σ_{gs} values of both 1.06 and 1.3. The data were reduced with σ_{gs} of 1.06 to simulate impactor behavior using greased substrates, while a σ_{gs} of 1.3 was used to simulate impactor behavior using glass fiber substrates.

Variation of the Particulate Mass Median Diameter

The polynomial used in conjunction with the modified spline technique in CIDRS shows a high degree of accuracy in recovering the cumulative inhalable particulate concentration (< 15.0 μm) for a wide range of MMD values. Figure 4 illustrates this with a plot of the ratio of the recovered inhalable particulate to the true inhalable particulate, IP_R/IP_T, vs. MMD for stage efficiency curves with σ_{gs} values of 1.3 and 1.06. For MMD's of 1.0, 2.0, 5.0, 10.0, and 20.0 μm, the recovery is near a perfect 1.00 except at one point. For σ_{gs} of 1.3 the IP_R/IP_T ratio is at its highest value of 1.06 at an MMD of 20.0 μm. This greater error in IP recovery may be caused by assuming a largest particle diameter (100.0 μm here) which is too small with respect to the 20.0 μm MMD.

Variation of the Geometric Standard Deviation of the Particulate Mass Distribution

To test the sensitivity of this fitting technique to different values of the aerosol geometric standard deviation, σ_g, unimodal particle-size distributions having σ_g values of 1.5 to 3.5 were tested. Figure 5 shows the ratio of recovered to true inhalable particulate IP_R/IP_T vs. these values of σ_g for stages having collection curves with geometric standard deviations of 1.3 and 1.06. The technique shows good accuracy in recovering the true IP concentration. The highest ratio value here is 1.04 for a relatively sharp mass distribution with standard deviation of 1.5. The accuracy increases as the particle-size distribution broadens.

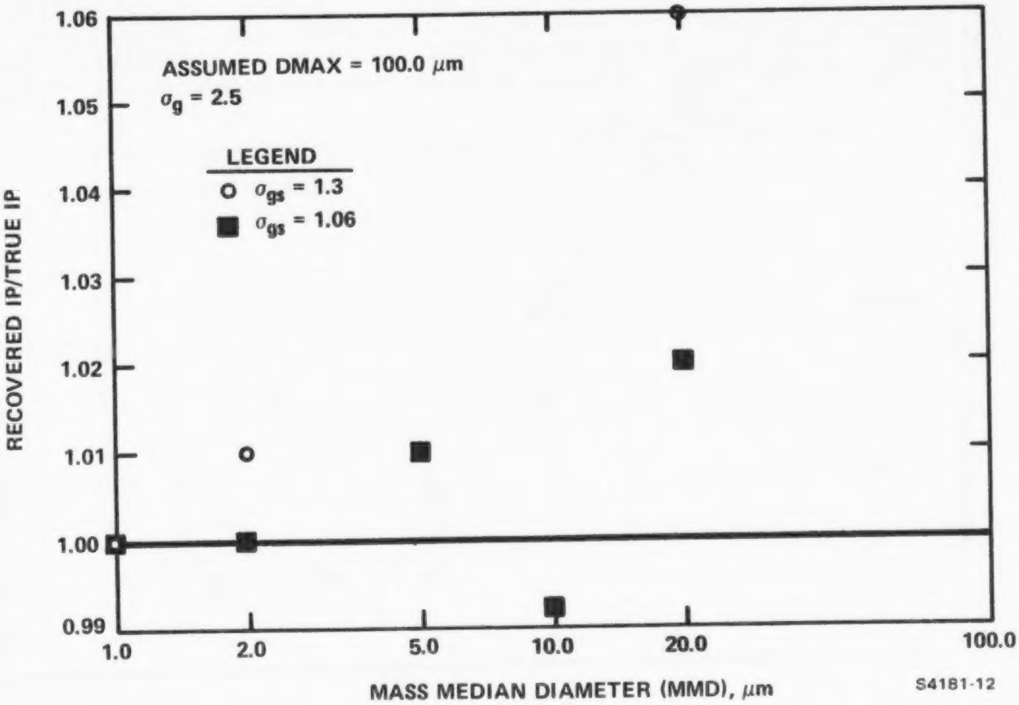

Figure 4. Ratio of recovered to true inhalable particle concentration versus mass median diameter of a unimodal log-normal particle size distribution

Variation of the Geometric Standard Deviation (Slope) of the Collection Efficiency Curve

The geometric standard deviation of the collection efficiency curve of the sampler, σ_{gs}, ranges from a near perfect cut value of 1.01 to 1.7 in this test. As shown in Figure 6, the variation of σ_{gs} has little effect on an accurate recovery of the inhalable particle concentration. The maximum error for IP recovery occurs for a sampler efficiency σ_{gs} of 1.01. Here the recovered over true inhalable particulate ratio, IP_R/IP_T, is only 1.02.

Variation of the Assumed Largest Particle Diameter in the Distribution

In this test the assumed largest particle diameter, DMAX, is varied from 20.0 μm up to 999.0 μm for the same unimodal log-normal size distribution. The results, as seen in Figure 7, show that accurate IP recovery is relatively insensitive to assumed DMAX unless it is extremely undervalued. In this distribution the ratio of recovered to true inhalable particulate IP_R/IP_T has its highest values of 1.07 (for σ_{gs} = 1.06) and 1.06 (for σ_{gs} = 1.3) for an assumed DMAX of 20.0 μm. However, for this size distribution having a mass median diameter of 5.0 μm,

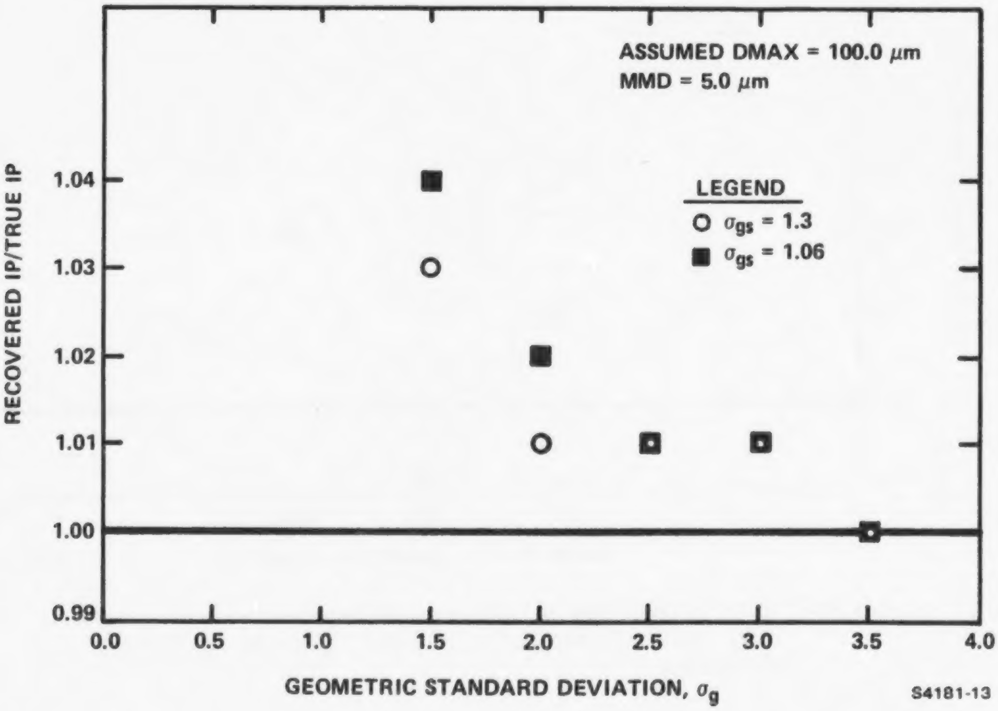

Figure 5. Ratio of recovered to true inhalable particle concentration versus aerosol geometric standard deviation of a unimodal log-normal particle size distribution.

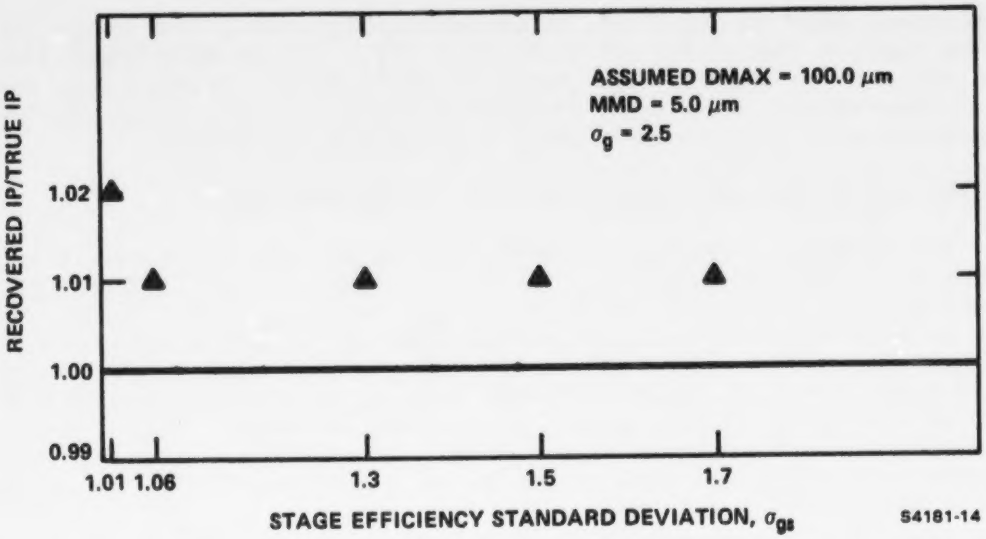

Figure 6. Ratio of recovered to true inhalable particle concentration versus stage efficiency standard deviation using a unimodal log-normal particle-size distribution.

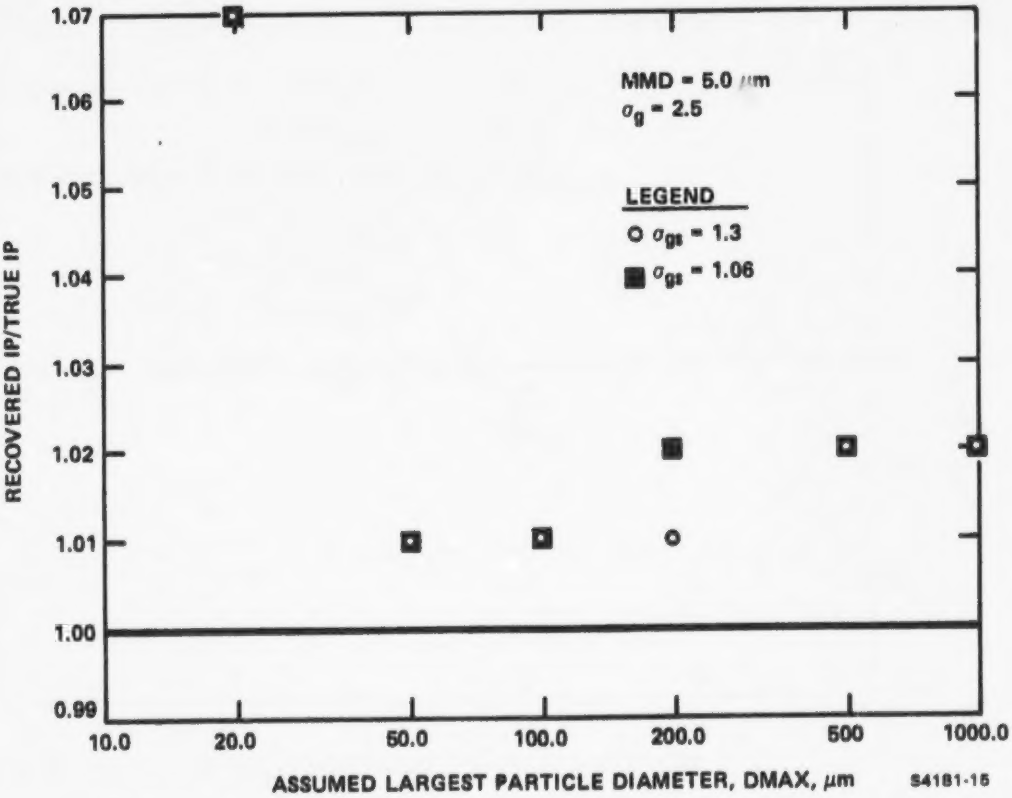

Figure 7. Ratio of recovered to true inhalable particle concentration versus assumed largest particle diameter using a unimodal log-normal particle-size distribution.

an assumed DMAX of 20.0 μm is unreasonably low. The other IP_R/IP_T values are on the order of 1.01 to 1.02. It is concluded then that only an extremely low guess of DMAX might cause large errors in IP recovery. This data reduction method still produces good IP recovery if the assumed DMAX is overapproximated.

TESTING WITH BIMODAL PARTICLE-SIZE DISTRIBUTIONS

For bimodal testing a log-normal mass distribution is used having mass median diameters of 2.0 μm (MMD_1) and 15.0 μm (MMD_2) and geometric standard deviations, σ_{g_1} and σ_{g_2}, of 2.0 for each mode unless otherwise specified in the text. As in unimodal testing the masses are collected using stage efficiency standard deviations, σ_{gs}, of both 1.06 and 1.3 to simulate greased substrates and glass fiber substrates, respectively. Also, unless otherwise specified, the assumed largest particle diameter, DMAX, is input as 100.0 μm, and there is an equal contribution of mass from each of the two modes.

Variation of Geometric Standard Deviation of the Particle-Size Distribution

In this test, the geometric standard deviations of each mode of the particle-size distribution, σ_{g_1} and σ_{g_2}, were varied from 1.5 to 3.0. As seen in Figure 8, the recovery of inhalable

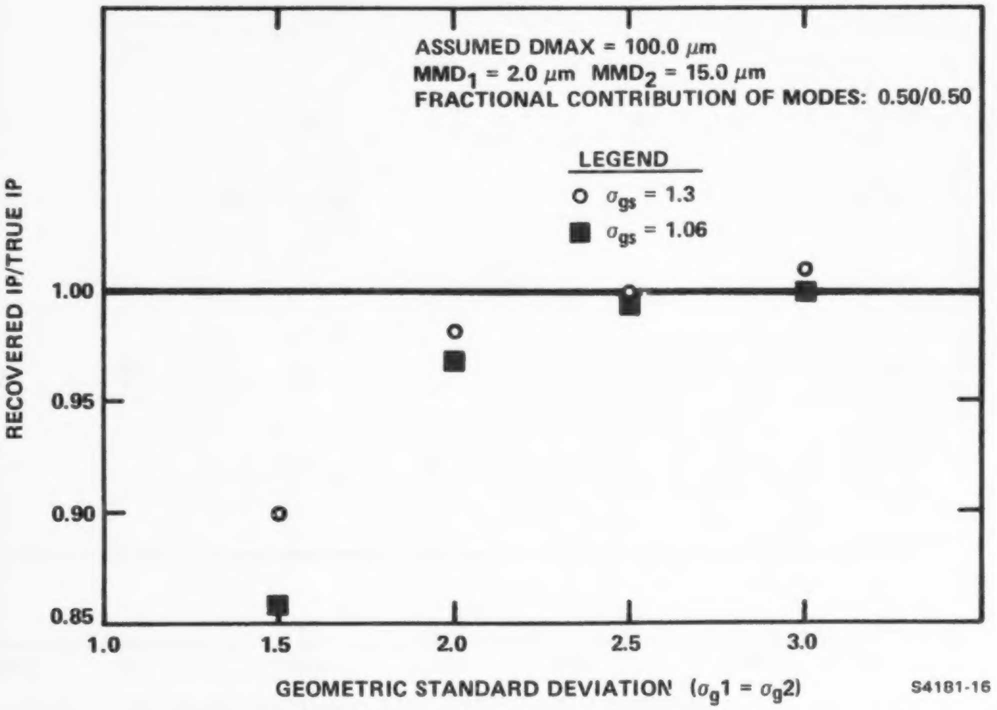

Figure 8. Ratio of recovered to true inhalable particle concentration versus aerosol geometric standard deviation of a bimodal log-normal particle-size distribution.

particulate appears more sensitive to this change of parameter than any other test. For a stage efficiency σ_{gs} of 1.06, the recovered IP is as much as 14% low for a distinctly bimodal distribution where geometric standard deviations $\sigma g_1 = \sigma g_2 = 1.5$. As the modes broaden, the recovered to true inhalable particulate ratio IP_R/IP_T approaches 1.0. This should be expected since the degree of curvature decreases in the cumulative mass distribution as these modes broaden; i.e., the distribution becomes more unimodal and the spline fitting technique must make less drastic attempts to adjust to curvature.

Variation of the Mass Median Diameter of the Second Mode

As seen in Figure 9, variation of the mass median diameter of the second mode, MMD_2, has little effect on the accuracy of IP recovery. The recovered to true inhalable particulate ratio, IP_R/IP_T, remains at or less than 1.05 as the MMD_2 ranges from 5.0 µm to 30.0 µm. The highest value of IP_R/IP_T of 1.05 occurs for an MMD_2 of 30.0 µm. This may be attributed to the large amount of mass in the second mode which falls beyond the first D_{50}.

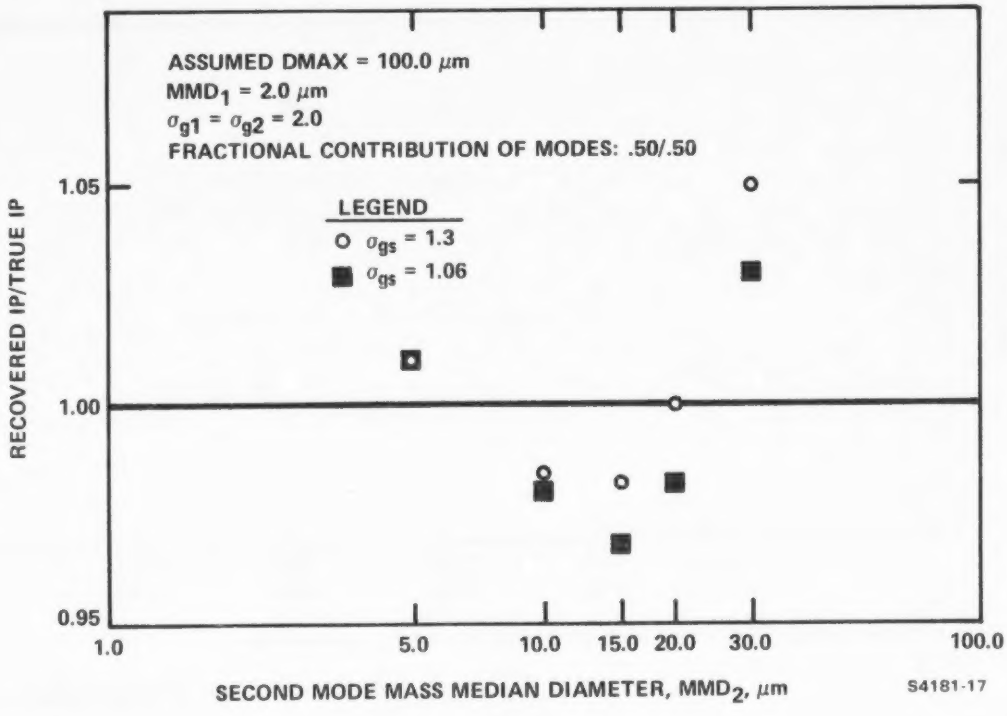

Figure 9. Ratio of recovered to true inhalable particle concentration versus second mode mass median diameter of a bimodal log-normal particle-size distribution.

Variation in Fraction of the Total Mass Contained in Each of the Modes

In this test the ratio of mass contributed by each of the two modes in the bimodal distribution was varied. Beginning with a 25% contribution of mass in the first mode and a 75% contribution of mass in the second mode, the ratio was changed on each trial with a greater fraction of mass being contributed by the first mode in each successive trial. Figure 10 shows that the recovery of inhalable particulate less than 15.0 μm of this bimodal distribution is acceptable regardless of the ratio of modes. The ratio of recovered to true inhalable particulate IP_R/IP_T is at its lowest value of 0.931 for glass fiber substrates, where the ratio of first mode mass to second mode mass is 0.25/0.75. As mass becomes less concentrated at sizes greater than the first stage D_{50}, i.e., as the mass mode ratio approaches 0.75/0.25, IP_R/IP_T approaches a perfect 1.00.

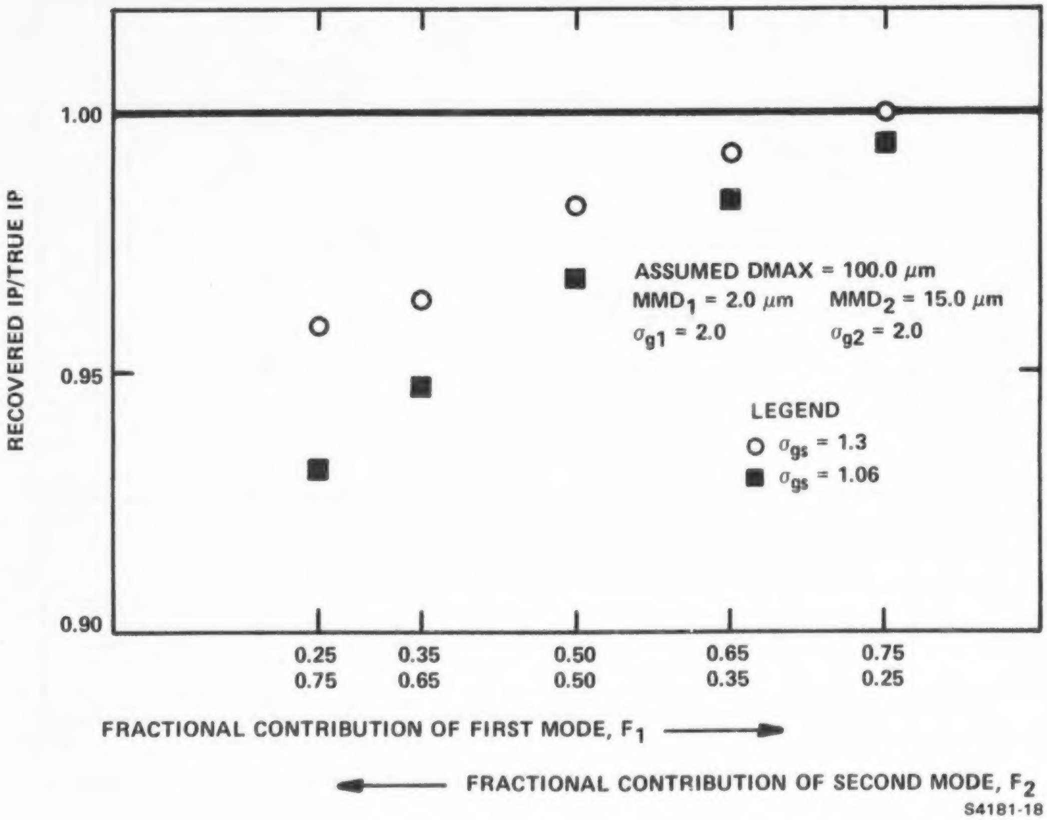

Figure 10. Ratio of recovered to true inhalable particle concentration versus fractional contribution of mass from each mode of a bimodal log-normal particle-size distribution.

CONCLUSIONS

It is concluded from the test results discussed in this paper that, for data taken by a round jet cascade impactor, a polynomial of first order osculation may be used for fitting the cumulative mass concentration curve between the first stage D_{50} and some maximum sampled particle size. This function used in conjunction with the "Computer-Based Cascade Impactor Data Reduction System"[1] provides a method for accurately determining the inhalable particulate (IP) concentration, i.e., the cumulative mass concentration of particles $\leq$15.0 μm in diameter. The method does not require the use of a 15.0 μm cut diameter sampling device. It therefore may be used for determining IP concentration in gas effluents sampled to date by conventional impactors.

To test the accuracy of the osculating polynomial for determining IP concentration, a number of unimodal and bimodal log-normal size distributions were theoretically sampled according to the impactor's stage efficiency curves and the resulting IP concentration was compared to the original values. Variations of the mass median diameter and geometric standard deviation of the size distributions, the assumed largest particle diameter, stage efficiency standard deviation, and fractional contribution of mass per mode (in the case of bimodal distributions) were studied as to their effect on recoverable IP concentration parameters.

Good recovery of the IP concentration was obtained for all "sampling runs", within approximately ± 7%, except in the case of sampling a bimodal distribution where the modes are very sharply defined and with well separated mass median diameters. Specifically, in sampling a bimodal distribution with mass median diameters of 2.0 μm and 15.0 μm with aerosol geometric standard deviations of 1.5 for each mode, the recovered IP concentration was 14% below the true IP concentration. The greater degree of error here is attributed to the sharp changes in curvature of the cumulative mass concentration curve to which the modified spline fitting procedure must adjust. It can reasonably be assumed that actual field data would fall into size distribution modes such that the dispersion of each mode could be described by a geometric standard deviation value of 1.5 μm or larger. Therefore, the degree of error in recovering IP concentration using this curve fitting procedure may be expected to be within the limits of ± 14%.

ACKNOWLEDGEMENTS

This research was supported by the U.S. Environmental Protection Agency under Contract No. 68-02-3118, D.Bruce Harris, Project Officer. Joseph D. McCain and Dr. Ashley D. Williamson, at Southern Research Institute, provided information and helpful criticism of the paper.

REFERENCES

1. Johnson, J.W., G.I. Clinard, L.G. Felix, and J.D. McCain. A Computer-Based Cascade Impactor Data Reduction System. EPA-600/7-78-042, U.S. Environmental Protection Agency, Research Triangle Park, NC, 1978. 592 pp.

2. McCain, J.D. A Data Reduction System for Cascade Impactors. EPA-600/7-78-132a, U.S. Environmental Protection Agency, Research Triangle Park, NC, July 1978.

3. Scheid, Francis. Numerical Analysis. Schaum's Outline Series, McGraw Hill, New York, 1968. p. 65.

PAPER 10

IMPLEMENTING CIDRS - A PROGRAMMER'S PERSPECTIVE

CLINTON E. TATSCH
RESEARCH TRIANGLE INSTITUTE

QUALITY ASSURANCE: THE TOTAL PERSPECTIVE

As we work with research quality assurance, it is clear that investigators in various disciplines are becoming aware that an appropriate quality assurance program is not an add-on or a separate function that can be neatly applied to existing programs. It is increasingly clear that quality assurance can only be planned and performed in any adequate sense by individuals who are personally committed to producing high-quality data. This commitment is demonstrated by a concern, in the early planning stages of a project, that estimates of precision and accuracy be obtained for each measurement or observation. By characterizing data quality as the data are collected, it becomes possible to estimate the quality of the final results. The most simple to estimate are relatively straightforward measurements such as length or weight. These measurements can be made repeatedly and carefully on everyday objects using physically "comfortable" procedures. At the other end of the scale, the assessment of computer software quality, by its very nature, is difficult to thoroughly check. The purpose of the computerized cascade impactor data reduction system (CIDRS) is to perform a series of lengthy calculations that cannot be done manually due to time constraints. Additionally, as a result of having this capability of performing more calculations more quickly, computer programs are becoming much more intricate in their decision-making (i.e., branching) capabilities; as this occurs it becomes more difficult to thoroughly check the validity of all branching options. However, work is in progress along these lines. We believe our work with the CIDRS system in the past few months has been useful in uncovering some of the pitfalls in the area of software quality assurance.

Our objectives in implementing CIDRS are:

- Modify and implement CIDRS coding for the computer installation at Research Triangle Institute
- Execute documentation examples
- Begin sensitivity analysis
- Make changes in such a way as to be most useful to other users

The first three were in the task directive from EPA: we completed the first two, and began work on the third objective. The fourth objective, that of making changes in the fashion that we did, developed shortly after we began work, and eventually assumed a place of major importance.

IMPLEMENTATION: AN OVERVIEW

In order to make any evaluation of CIDRS, it had to be executable on our computer. CIDRS was developed on a PDP 15/76 over a period of several years; hence the goals and intent of the system have changed significantly since the early code was written. In order to execute CIDRS programs, the source code must be readable and compatible with the resident FORTRAN compiler. The control language used must also function on the local computer system.

With this in mind, we obtained a tape containing CIDRS from Southern Research Institute and began its implementation on the IBM 370/168 at the Triangle Universities Computing Center (TUCC). CIDRS is made up of six mainline programs as shown in Figure 1. These programs run independently of each other with the exception of the generated data files, which are used by various programs of the system.

As indicated in Figure 1, MPPROG takes the raw impactor run data (flow rate, temperature, gas composition, stage loadings, etc.) and generates data file KMC001, which contains cumulative mass distribution data. For each impactor run, these data are used in the curve-fitting program SPLIN1 to generate FILSPL, which contains the fitting coefficients discussed earlier. These two physical files may contain data for up to 50 impactor runs with the only stipulation being that the same type of impactor must have been used for each run on the file. These two files, KMC001 and FILSPL, then serve input to GRAPH, which produces plotter output for visual checks on the individual or combined runs, or as input to STATIS, which then averages the series as into one set of interpolated points with confidence limits corresponding to all the runs on the file. The stipula-

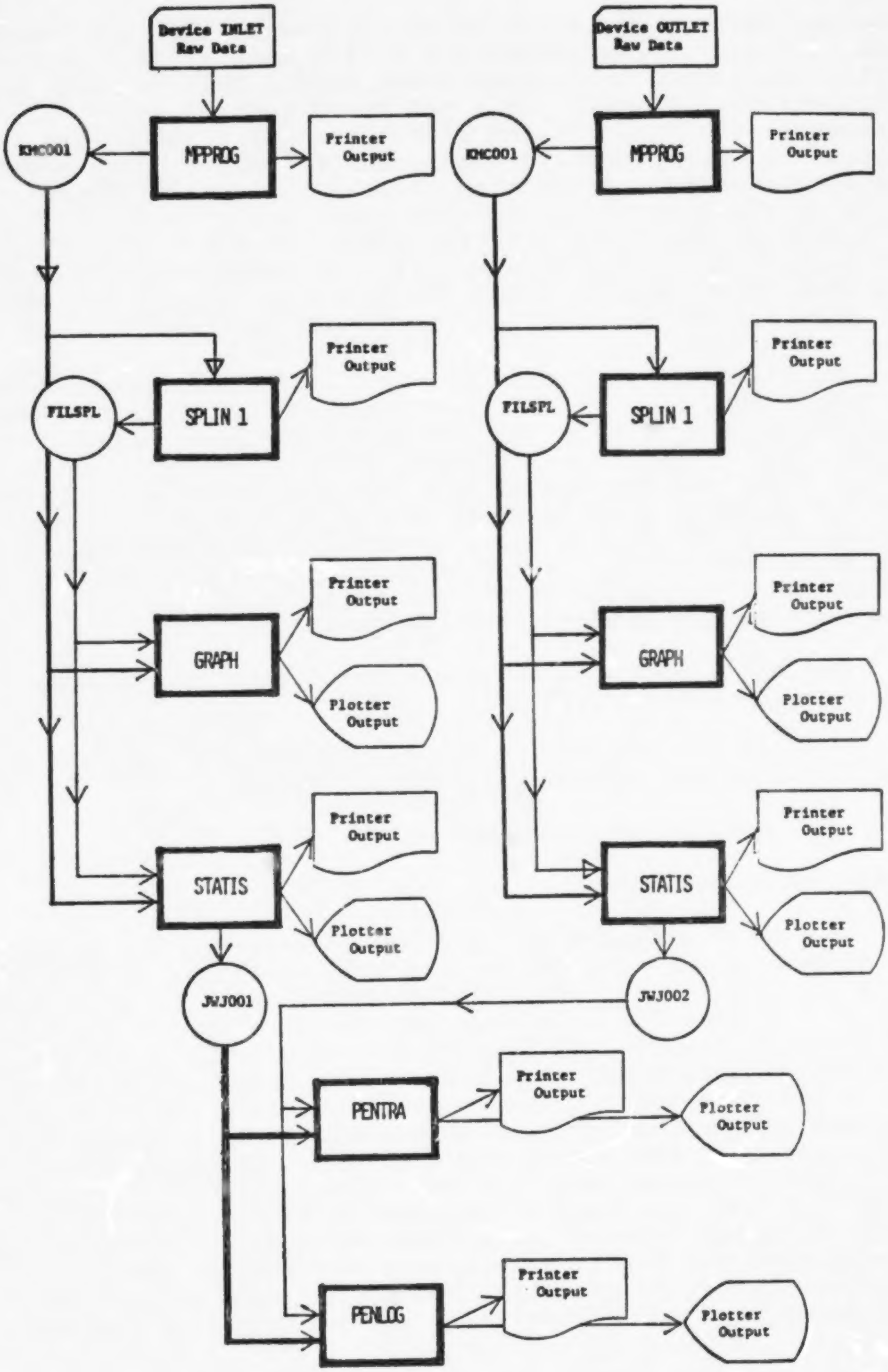
Device INLET Raw Data
Device OUTLET Raw Data
KMC001
MPPROG
Printer Output
FILSPL
SPLIN 1
GRAPH
Plotter Output
STATIS
JWJ001
JWJ002
PENTRA
PENLOG

Figure 1. CIDRS program relationships.

tion embedded in the logic of the system is that all the impactor runs included in the KMC001 and FILSPL data files should be logically related to process conditions. This may conclude the calculations. However, if a pollution control device is being evaluated, the data for the associated inlet and outlet measurement series are processed independently, starting at MPPROG. One series of data files then relates to data collected at the inlet of the control device; the other series relates to data collected at the outlet of the control device. After the data are separately averaged in STATIS, the JWJ001 and JWJ002 files are used by PENTRA and PENLOG to calculate collection efficiency (or penetration) for the control device involved.

As indicated in Figure 1, the first two programs in the series, MPPROG and SPLIN1, use direct access files and the system card reader and printer, whereas the last four, GRAPH, STATIS, PENTRA, and PENLOG, use the system plotter as well as direct access files and the system printer. In the case of CIDRS, plotter usage is proving to be the major source of trouble in implementing the system. The protocols for addressing peripheral equipment from within an executing program vary not only from manufacturer to manufacturer, but from installation to installation, due to the varying local perspectives.

The basic difficulties one might expect to encounter in implementing CIDRS would be:

1. Differences in the specific version of FORTRAN used from one machine to another, and
2. Local idiosyncrasies.

CIDRS: OUR EXPERIENCE

The basic approach we took to implementing the CIDRS system was to modify the original source code as little as possible, using the IBM Utility IEBUPDTE to insert only the necessary changes for each run. In this way, we developed a set of six modification packets, as indicated in Figure 2, which are applied in a two-step fashion, thus leaving the original source code intact and consistent with the documentation. We took this approach rather than physically modifying the original source code because in most cases the same types of changes will need to be made at other installations using, for example, a Univac or CDC machine, and leaving the modifications intact will highlight necessary changes for subsequent applications programmers. We also used the WATFIV interpreter for most of the initial work, which meant that we executed from source code every time rather than going from object modules, thus getting more thorough diagnostics.

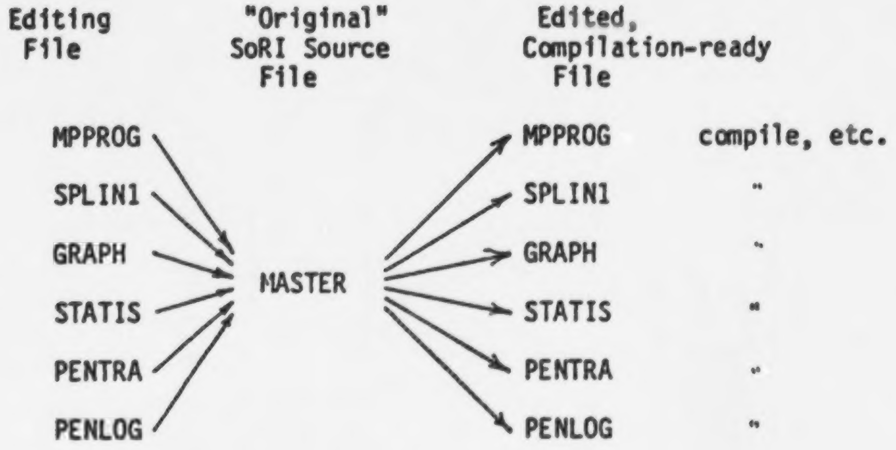

Figure 2. Structure and use of modifications to original CIDRS logic.

The difficulties we encountered in implementing CIDRS on our computer system were all installation-specific problems and for the most part could be solved in a very straightforward but laborious way. One problem we encountered was the difference between IBM and Digital Equipment protocols. A second, more frequent problem involved the I/O handlers.

The hardware-related problem that we identified was that the PDP 15/76 apparently clears core after each job, whereas the IBM 370/168 does not. This showed up in various places as uninitialized variables. Since the IBM FORTRAN-G compiler does not easily check for uninitialized variables, out-of-bounds array addresses, etc., the WATFIV file interpreter was essential to uncovering the uninitialized variables. We feel it did a thorough job.

At the outset, the FORTRAN I/O Unit numbers were converted from constants to integer variables as shown in Figure 3. The mnemonics RDR, PTR, defined as four byte variables, were used and their values supplied in a data statement at the beginning of the program as shown in Figure 4. Not only does this enhance the readability of the source code, it also means that the unit numbers for the reader and the printer may be altered by changing one or two data statements rather than by searching through the entire source listing for places that the reader and printer are used. We feel this should be done generally, not just for programs written for distribution, because it never can be anticipated when system programmers may decide to change unit numbers to upgrade or modify the system.

```
602 DO 650 L=1,NRUN
    IF(IREPET)605,615,605
605 READ(2,902)MPLOT,J1,J2,J3,J4,J5,J6
    READ(2,902)JP1,JPCNT1,JP2,JP3,JP4,JPCNT4,JP5,JP6
615 WRITE(8'L)MPLOT,J1,J2,J3,J4,J5,J6,JP1,JPCNT1,JP2,JP3,
   1JP4,JPCNT4,JP5,JP6
650 CONTINUE
```

Figure 3a. *Sample I/O statements, as received.*

```
 602 DO 650 L=1,NRUN
     IF(IREPET)605,615,605
605  READ(RDR,902)MPLOT,J1,J2,J3,J4,J5,J6
     READ(RDR,902)JP1,JPCNT1,JP2,JP3,JP4,JPCNT4,JP5,JP6
615  WRITE(GRAPHO'L)MPLOT,J1,J2,J3,J4,J5,J6,JP1,JPCNT1,JP2,JP3,
    1JP4,JPCNT4,JP5,JP6
     WRITE(PTR,904)L,MPLOT,J1,J2,J3,J4,J5,J6,JP1,JPCNT1,JP2,JP3,JP4,
    X      JPCNT4,JP5,JP6
 650 CONTINUE
```

Figure 3b. *Sample I/O statement, as modified.*

```
      INTEGER VV
      INTEGER RDR,PTR,KMC001,FILSPL,GRAPHO
      DOUBLE PRECISION XNDPEN(10),YO(10)
      DIMENSION IDALL(80),GEMAX(2),GEMIN(2),DMMAX(2),DMMIN(2),DNMAX(2)
```

Figure 4a. Specification of I/O unit mnemonics 4-byte integer variables.

```
C **************************************************************
C *                                                            *
C * => => => ASSIGN I/O UNIT NUMBERS, ETC. HERE                *
C *                                                            *
      DATA RDR/1/,PTR/3/
C *                                                            *
      DATA KMC001/10/
      DEFINE FILE 10(101,251,U,I10)
C *                                                            *
      DATA FILSPL/11/
      DEFINE FILE 11(100,507,U,I10)
C *                                                            *
      DATA GRAPHO/04/
      DEFINE FILE 04(50,15,U,I10)
C *                                                            *
C => => =>   DON'T FORGET "FILSPL" DEFINITION IN SUBROUTINE FILSPL   *
C **************************************************************
```

Figure 4b. Data definition statements for defined I/O unit variable.

The only significant difficulty we encountered had to do with the interface to the plotter; this raises an issue that has been anticipated and for which there appears to be a general solution when program systems of this nature are being developed. The actual working code can be written in such a fashion that I/O interfaces are localized into one subroutine, which clearly makes all installation-specific references to a particular device and then, in the rest of the program, all the I/O can appear symbolically. As an example of this concept, I will describe how we handled the graphics part of the last four programs of CIDRS, using modifications to GRAPH as an example.

As shown in Figure 5a, plotter commands available on Southern's PDP-15 treat the plotter as an I/O device with a unit no. 7. This way it is quite logical to have statements such as those shown in Figure 5b to either write to a device or read from the device (in the latter case it means reading the location of the pen). However, at the TUCC installation such detailed control of the plotter is not possible; it can only be accessed through high-level subroutine calls. Therefore, we went through the

---

WRITE (7) mode (followed by optional variables, depending on the value of mode).

Mode		**Additional variables**
0	**Pick up the pen**	**None**
1	**Put down the pen**	**None**
2	**Move to absolute coordinates. Address with pen up**	**IX, IY**
3	**Move to absolute coordinates. Address with pen down**	**IX, IY**
4	**Move to delta coordinates. Address with pen up**	**IX, IY**
5	**Move to delta coordinates. Address with pen down**	**IX, IY**
6	**Draw character (see note below)**	**ICNT, DATA**
7	**Set coordinate address**	**IX, IY**
8	**Move to absolute coordinate address (no pen change)**	**IX, IY**
9	**Move to delta coordinate address (no pen change)**	**IX, IY**
10	**Set character attributes**	**IXSIZ, IYSIZ, ISIN, ICOS**

Figure 5a. Plotter specifications from Reference 2.

```
WRITE(LOTS) MODE,IX,IY,JSIN,JCOS
IX=RND(SX*XB)
IY=RND(SY*YB)
MODE=2
WRITE (LOTS) MODE,IX,IY
```

Figure 5b. Sample plotter output statement, as received.

source code replacing each plotter I/O statement with a call to a newly written interface subroutine. This type of call should be valid, independent of any hardware, and the result is that the program logic now accesses a subroutine, passing along values through arguments and through common which will be of use for the plotter. The plotter interface then is written as being hardware-dependent. In this way all the necessary data are available to the interface subroutine, both physically and logically, and all changes relating to the plotter are physically isolated to the subroutine. Again, our basic approach was to design the interface subroutine PLOTTR to mimic the originally used read and write statements. This approach would probably be simplified if the I/O interface had been written at the outset as these programs were being developed. To keep things as consistent as possible with the original CIDRS programs and documentation, we elected to mimic the behavior of the PDP-15 plotter at least in the original code. In Figure 6, it may be seen how we accomplish this; at the left is the old write statement, which would move the pen to specified coordinates; to the right is the equivalent subroutine PLOTTR call. It may be noticed that the first parameter in the argument list is the "mode" of the corresponding write statement. Thus, Figure 7 shows that when PLOTTR is entered the first thing that is checked (following some initial housekeeping) is this mode value, which then determines what is to be done by the plotter. Once the branch is taken, the section of code which directly relates to hardware requirements is entered. These blocks, as illustrated in Figure 8, will need to be modified for application at other installations. These blocks are very installation-specific and one would expect that an applications programmer would go to this section of the program and make the necessary changes. Given the presumption used in making this kind of interface, and knowing the requirements of his own system then, one would expect the programmer would be capable of quickly and reliably making the changes necessary to implement each particular program on his own system. Using this approach we have exercised all six CIDRS programs and all function reliably as far as we are able to tell. We have not been able to extensively test the programs, but, to the best of our knowledge, the programs do function as they were intended.

GENERAL REMARKS

A data validation section would be useful in CIDRS as a quality assurance check, and it appears this easily could be added. For example, in MPPROG it would be appropriate to determine the type of "window" that is reasonable for each input parameter; this could be done a priori, as well as from the technical experience of the programmer. For instance, one would not anticipate that a negative weight would be a valid entry. Although a weight change less than zero may be physically observed, a negative weight would not be feasible nor would a

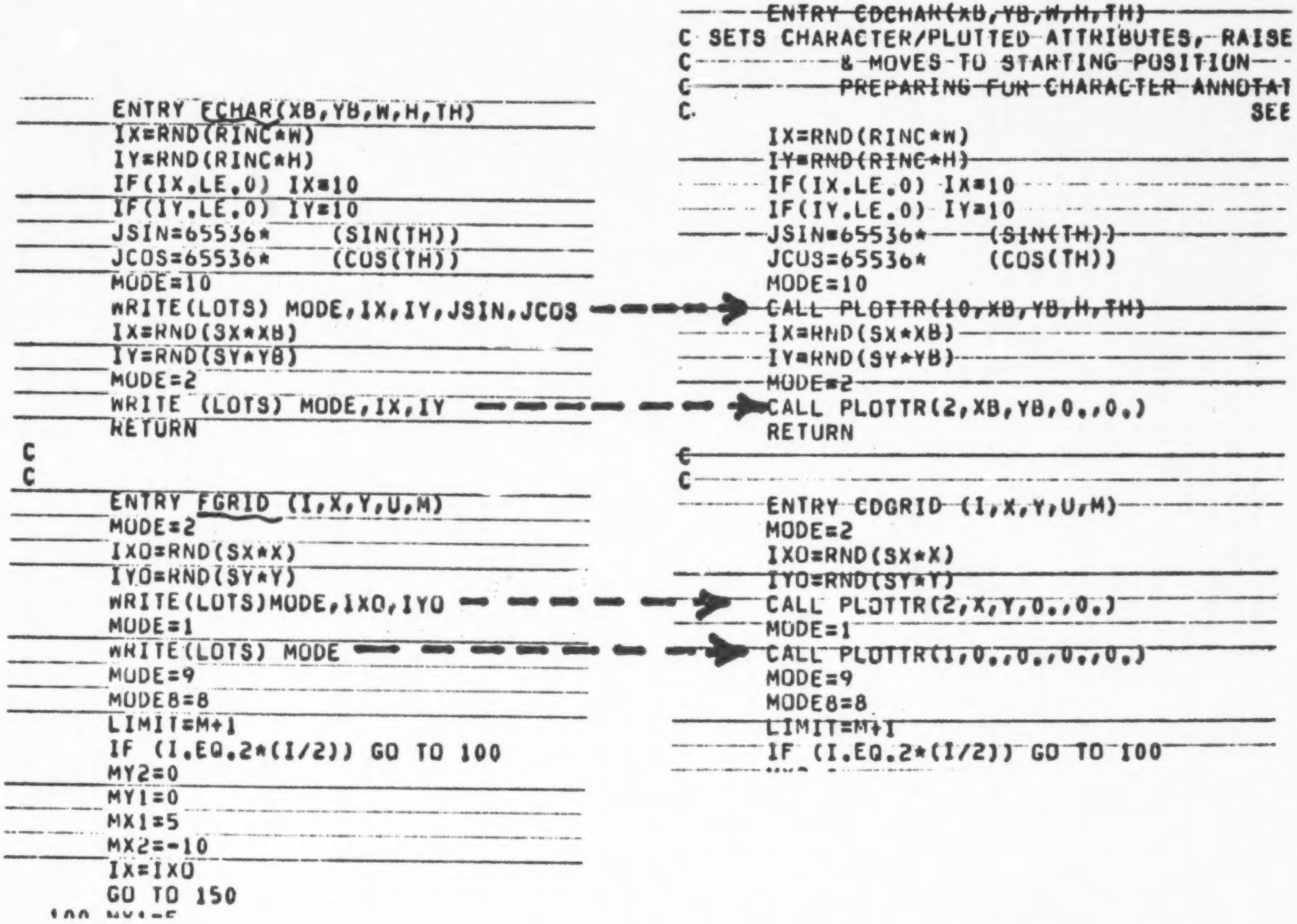

```
      ENTRY ECHAR(XB,YB,W,H,TH)
      IX=RND(RINC*W)
      IY=RND(RINC*H)
      IF(IX.LE.0) IX=10
      IF(IY.LE.0) IY=10
      JSIN=65536*     (SIN(TH))
      JCOS=65536*     (COS(TH))
      MODE=10
      WRITE(LOTS) MODE,IX,IY,JSIN,JCOS
      IX=RND(SX*XB)
      IY=RND(SY*YB)
      MODE=2
      WRITE (LOTS) MODE,IX,IY
      RETURN
C
C
      ENTRY FGRID (I,X,Y,U,M)
      MODE=2
      IXO=RND(SX*X)
      IYO=RND(SY*Y)
      WRITE(LOTS)MODE,IXO,IYO
      MODE=1
      WRITE(LOTS) MODE
      MODE=9
      MODE8=8
      LIMIT=M+1
      IF (I.EQ.2*(I/2)) GO TO 100
      MY2=0
      MY1=0
      MX1=5
      MX2=-10
      IX=IXO
      GO TO 150
```

```
      ENTRY CDCHAR(XB,YB,W,H,TH)
C SETS CHARACTER/PLOTTED ATTRIBUTES, RAISE
C           & MOVES TO STARTING POSITION
C           PREPARING FOR CHARACTER ANNOTAT
C                                         SEE
      IX=RND(RINC*W)
      IY=RND(RINC*H)
      IF(IX.LE.0) IX=10
      IF(IY.LE.0) IY=10
      JSIN=65536*     (SIN(TH))
      JCOS=65536*     (COS(TH))
      MODE=10
      CALL PLOTTR(10,XB,YB,H,TH)
      IX=RND(SX*XB)
      IY=RND(SY*YB)
      MODE=2
      CALL PLOTTR(2,XB,YB,0.,0.)
      RETURN
C
C
      ENTRY CDGRID (I,X,Y,U,M)
      MODE=2
      IXO=RND(SX*X)
      IYO=RND(SY*Y)
      CALL PLOTTR(2,X,Y,0.,0.)
      MODE=1
      CALL PLOTTR(1,0.,0.,0.,0.)
      MODE=9
      MODE8=8
      LIMIT=M+1
      IF (I.EQ.2*(I/2)) GO TO 100
```

Figure 6. Example of coding changes from original ⟶ modified code.

```
C - - - - - - - - - - - - - - - - - - - - - - - - - - -            00056057
      IF(MODE.EQ.14)GO TO 14                                          00056058
      X=XX                                                            00056059
      Y=YY                                                            00056060
      H=HH                                                            00056061
      T=TT                                                            00056062
      DX=HH                                                           00056063
      DY=TT                                                           00056064
      XS=X*XSCL                                                       00056065
      YS=Y*YSCL                                                       00056066
      DXS=DX*XSCL                                                     00056067
      DYS=DY*YSCL                                                     00056068
      IF(ICNT.EQ.1)WRITE(3,1002)ICUT                                  00056069
 1002 FORMAT(' >>>I',I5,'I',4('I',E10.2,'I'),I10)                     00056070
C     IF(ICNT.GE.ICUT)WRITE(3,1002) MODE,XX,YY,HH,TT                  00056071
      IF(MODE.EQ.0) GO TO 1010                                        00056072
      GO TO (1,2,3,4,5,6,7,8,9,10,11,12,13,14,15,16,17,18,19,         00056073
     X      20,21,22,23,24,25,26,27,28,29,30                  ),MODE  00056074
C THIS BLOCK HANDLES OUT-OF-RANGE MODES,                              00056075
C     CAUSING A TRACEABLE ABEND                                       00056076
      WRITE(PTR,1001) MODE                                            00056077
 1001 FORMAT('0>>>>>>>>>>>>> OUT-OF-RANGE MODE =',I4)                 00056078
      I=0                                                             00056079
```

Figure 7. Initial "PLOTTR" decision point, showing initial housekeeping and the branching statement for specific plotter requests.

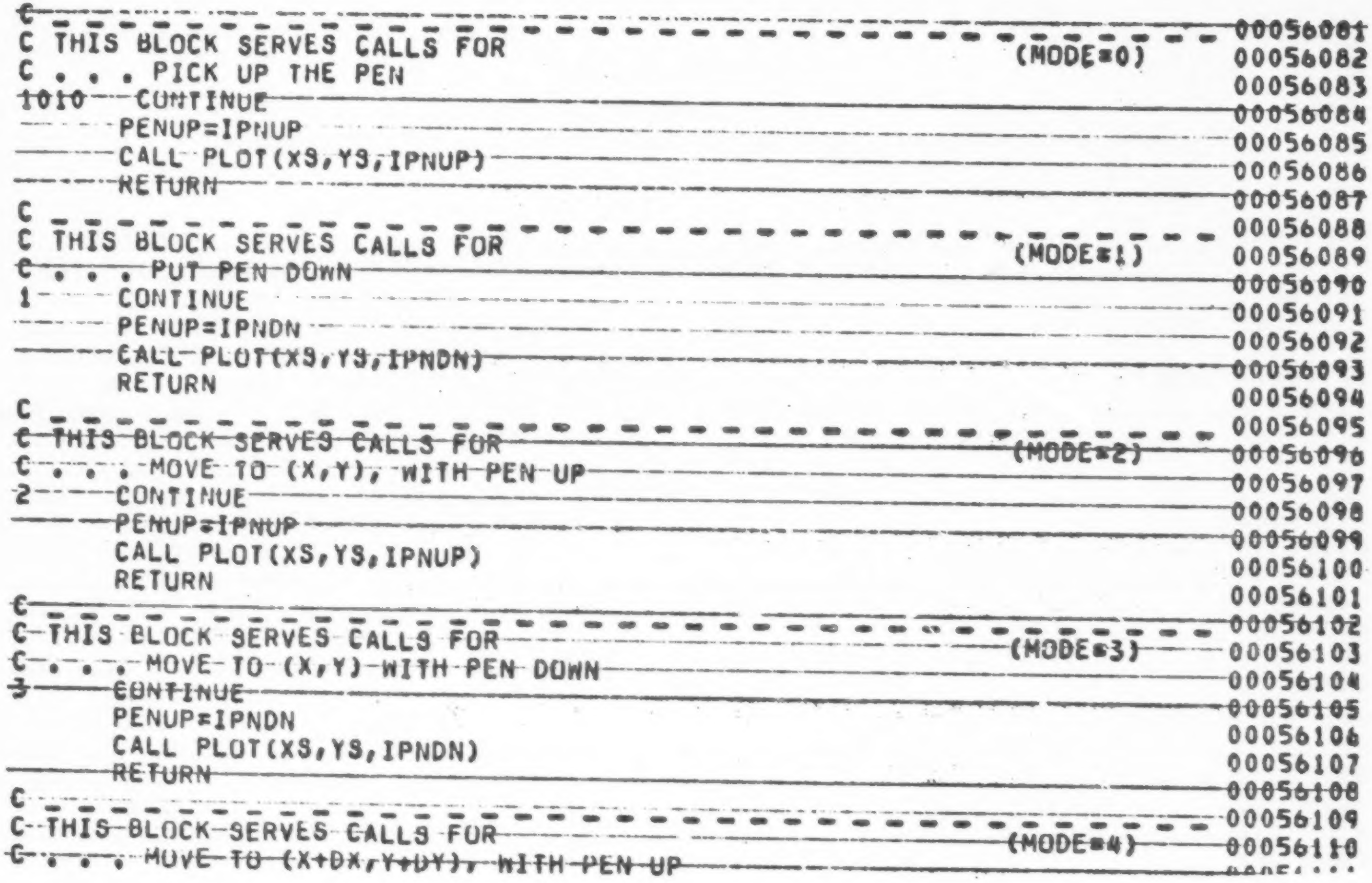

```
C - - - - - - - - - - - - - - - - - - - - - - - - - - - - - - - - - - - 00056081
C THIS BLOCK SERVES CALLS FOR                           (MODE=0)        00056082
C . . . PICK UP THE PEN                                                 00056083
1010  CONTINUE                                                          00056084
      PENUP=IPNUP                                                       00056085
      CALL PLOT(XS,YS,IPNUP)                                            00056086
      RETURN                                                            00056087
C - - - - - - - - - - - - - - - - - - - - - - - - - - - - - - - - - - - 00056088
C THIS BLOCK SERVES CALLS FOR                           (MODE=1)        00056089
C . . . PUT PEN DOWN                                                    00056090
1     CONTINUE                                                          00056091
      PENUP=IPNDN                                                       00056092
      CALL PLOT(XS,YS,IPNDN)                                            00056093
      RETURN                                                            00056094
C - - - - - - - - - - - - - - - - - - - - - - - - - - - - - - - - - - - 00056095
C THIS BLOCK SERVES CALLS FOR                           (MODE=2)        00056096
C . . . MOVE TO (X,Y), WITH PEN UP                                      00056097
2     CONTINUE                                                          00056098
      PENUP=IPNUP                                                       00056099
      CALL PLOT(XS,YS,IPNUP)                                            00056100
      RETURN                                                            00056101
C - - - - - - - - - - - - - - - - - - - - - - - - - - - - - - - - - - - 00056102
C THIS BLOCK SERVES CALLS FOR                           (MODE=3)        00056103
C . . . MOVE TO (X,Y) WITH PEN DOWN                                     00056104
3     CONTINUE                                                          00056105
      PENUP=IPNDN                                                       00056106
      CALL PLOT(XS,YS,IPNDN)                                            00056107
      RETURN                                                            00056108
C - - - - - - - - - - - - - - - - - - - - - - - - - - - - - - - - - - - 00056109
C THIS BLOCK SERVES CALLS FOR                           (MODE=4)        00056110
C . . . MOVE TO (X+DX,Y+DY), WITH PEN UP
```

Figure 8. Sample block of code that actually drives plotter from CIDRS.

weight increase of, for example, greater than 50 mg be reasonable. So, for the stage weights, a data validation section might include a check that the weight is not negative and the change is not larger than 50 mg. In terms of data quality and of being more assured of the functioning of the programs, this type of approach to screening both the input data and the control parameters is being looked into and may become part of a subsequent version.

Another aspect of data quality that is of concern is the fact that these programs will be modified to run on different operating systems. Also, depending on the user's perspective and needs, he may decide that he wants to modify some of the basic algorithms to alter the output. In this situation the program system no longer is CIDRS, but is a local modification of CIDRS and in any documentation it should be made clear just what these modifications are. Otherwise, comparing data between two operating groups will be questionable or impossible simply because a different physical meaning due to the different mathematics involved may very well have occurred.

In summary, we have obtained CIDRS as distributed by Southern Research Institute. We have implemented it in an environment different from that in which it was developed, attempting to locate and highlight identifiable problems and to design modifications that will be useful to other users installing CIDRS on their system. CIDRS appears to be a very useful and well-written set of programs, especially considering that it is the first generation package.

PAPER 11

NUMERICAL SIMULATION STUDIES AND DATA REDUCTION FOR SIZE CLASSIFYING MEASUREMENT TECHNIQUES

H. FISSAN
C. HELSPER
AEROSOLMESSTECHNIK
GESAMTHOCHSCHULE DUISBURG

ABSTRACT

Nearly all techniques that classify particles to obtain size distributions show a certain cross-sensitivity. Only a certain fraction of the particles belonging to one class of particle size is represented in that class while the rest is found in the neighboring classes.

Since generation techniques for monodisperse aerosols have been developed, it is possible to describe this non-ideal instrument behavior by rather straightforward calibration experiments. The knowledge of this systematic error makes it possible to simulate the instruments numerically for given size distributions.

The influence of the non-ideal instrument behavior on the measured distribution parameters is discussed for a wide range of possible distributions.

A data reduction program has been tested by simulation studies for various unimodal and bimodal log-normal distributions. The influence of random errors in the measured data on the results of the correction calculations is discussed. Finally the data reduction program has been applied to several real aerosols.

INTRODUCTION

For several reasons there is an increasing interest for the determination of the size distribution of aerosols. For this purpose various measurement techniques have been developed which allow classifying the particles according to their size-dependent behavior into a number of size intervals and determining a measure for the particle frequency in these intervals. The size of a particle is normally represented as the equivalent diameter of a sphere which would show the same reaction as the measured particle. So this equivalent diameter depends very much on the measurement principle used. The particle frequency is mostly determined as particle number or particle mass or as a number or mass concentration.

For all these measurement techniques the classification procedure as well as the determination of the particle concentration is not free from certain systematic errors which may cause considerable differences between the real size distribution and the one determined by the instrument. If this non-ideal instrument response is known, one can estimate the influence of these effects and can try to correct the measured data to obtain a size distribution nearer to the real one.

REAL INSTRUMENT RESPONSE OF SOME CLASSIFYING MEASUREMENT TECHNIQUES

This non-ideal instrument behavior, though predicted by theory in most cases, has often been neglected in the past, because there was nearly no possibility to describe these effects exactly. Since monodisperse aerosol standards like the vibrating orifice generator or the electrostatic classifier are available, this situation has changed and a lot of work has been done on the calibration of classifying instruments.

So the electrical aerosol analyzer (EAA) has been calibrated by Liu et al.[1] and its response to monodisperse aerosols has been represented by a calibration matrix. The cross channel interference shown by this matrix is mostly due to the mere statistical distribution of the number of elementary charges on particles of the same size.

An optical particle counter (type Gertsch HC-15) has been calibrated by DOP particles in our lab. This instrument has a very small scattering volume which allows measurement of particle concentrations up to $10^5 cm^{-3}$ with still neglectable coincidence errors. As the cross section of this scattering volume is smaller than the cross section of the sample stream, a certain number of particles cross the edge of the volume, thus scattering less light than a particle in the center of this volume. This is the reason for a considerable cross channel interference of this device. Figure 1b shows the instrument response for several monodisperse aerosols as a cumulative number distribution versus the particle diameter indicated by the instrument.

The fraction of particles measured too small increases with increasing particle size because of the increased probability for those particles to pass partially outside the scattering volume. Calibration studies in the lower particle size range are now done by means of an electrostatic classifier. For comparison the equivalent results for a Royco 225 particle counter

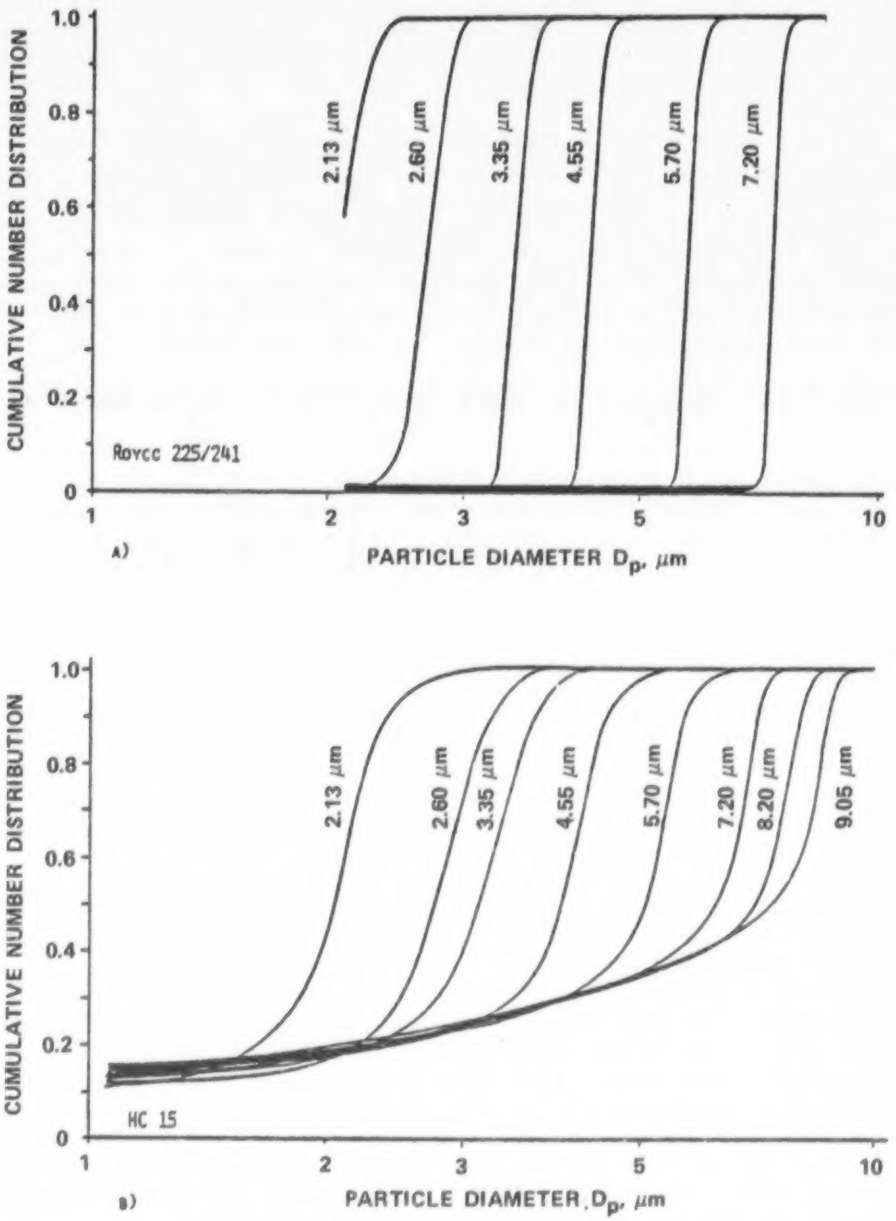

Figure 1. Calibration results of optical particle counters.

are shown in Figure 1a. The scattering volume of this instrument is limited by the sample stream so that all particles pass it with the whole cross-section. Therefore the instrument behavior is nearly ideal.

Similar calibration experiments have been done for a six-stage Andersen Stack Sampler (A.S.S.)[2] with liquid oleic acid particles to determine the collection efficiencies of the stage as well as the wall losses. In Figure 2 the percentage of total wall loss is plotted against the aerodynamic particle diameter. Results of Cushing et al.[3] for an eight stage A.S.S. and solid particles are given for comparison. Besides the fact that the number of stages was different in the two experiments, the differences between the two curves might be caused by the following reasons:

1. flow, particle density, and temperature were not the same in the two experiments,
2. the adhesion of solid and liquid particles on walls might be different,
3. in Cushing's experiments the impactor was mounted horizontally, while in ours it was mounted vertically.

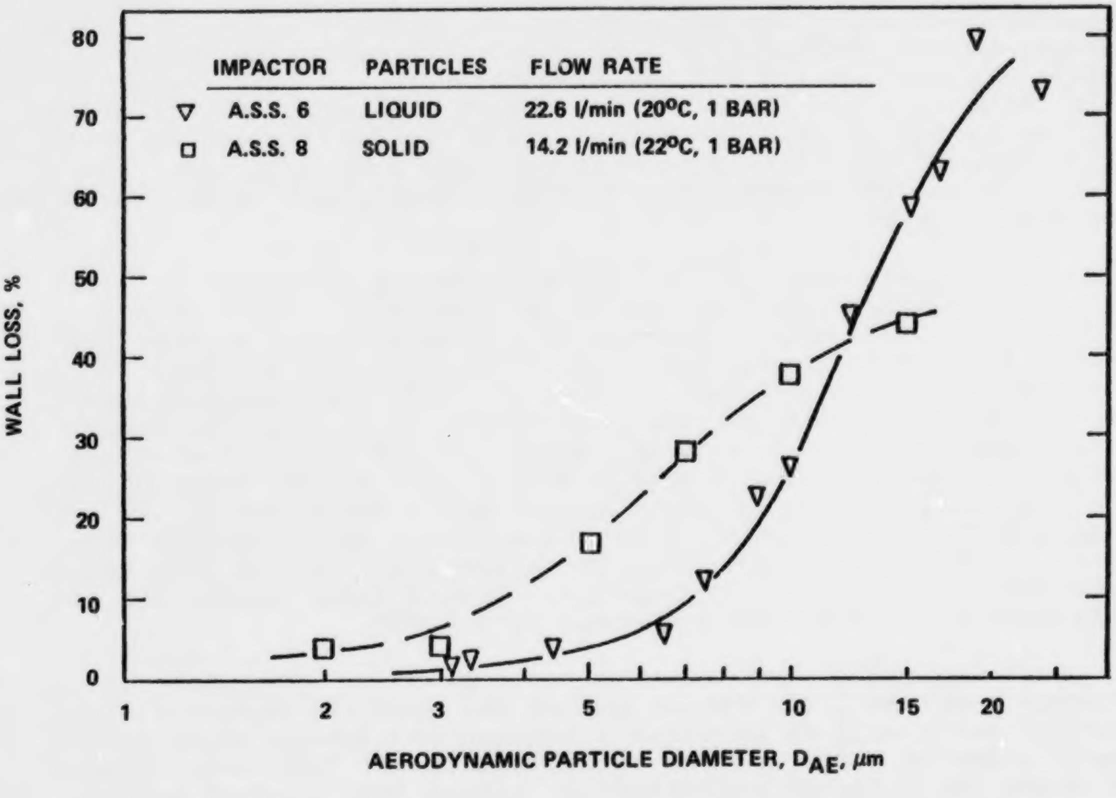

Figure 2. Total wall losses of Andersen Stack Sampler (Cushing, et al.[3]).

The collection efficiencies determined in the two experiments are compared in Figure 3. Due to bounce off and blow off the collection efficiencies for solid particles in no case reach a value of 100%. For liquid particles this extreme shape of the collection efficiency curve is only found for the first stage, where the wall losses cause this instrument response.

INFLUENCE OF NON-IDEAL INSTRUMENT RESPONSE ON THE DETERMINATION OF SIZE DISTRIBUTIONS

If one has determined the instrument's response for a set of monodisperse aerosols, it is possible to establish a response matrix to describe the instrument's overall behavior. This makes it possible to simulate the instrument numerically and to predict its response to any given size distribution for an aerosol similar to the one used in the calibration procedure. The comparison of the instrument's output with the input distribution allows estimation of the errors caused by its non-ideal behavior.

Results of a simulation of the EAA for two log-normal distributions are shown in Figure 4. The cumulative number distribution is plotted against the particle diameter. The geometric standard deviation for both input distributions which are represented by the solid lines is $\sigma_g = 2.0$; the number mean diameters are 0.03 μm and 0.3 μm, respectively. In both cases the EAA tends to shift the mean diameter of the output distributions (given by the circles and dashed lines) to smaller values while the shape of the distribution is not very much affected. The influence on the number mean diameter (NMD) seems to be dependent on the input NMD.

This dependency is shown in more detail in Figure 5. The ratio of the NMD calculated from the simulated output data to the actual input NMD is plotted as a function of the input NMD for three geometric standard deviations σ_g. For an ideal instrument this ratio should be one, at least for distributions in the middle of the covered size range, while near the upper and lower limit of this range, there are deviations due to the fact that the instrument covers only a part of the distribution. But the real instrument shows output NMD's which are by 20% too small even in the middle of its range. For NMD's smaller than 0.1 μm there are points where the effects of limited size range and non-ideal behavior compensate. Around these points the instrument will determine a correct output NMD.

If one calculates under the assumption of spherical particles a volume distribution out of the measured number distribution there will be deviations between the actual input volume mean diameter (VMD) and the calculated output VMD, too. Figure 6 shows the ratio of calculated to actual VMD, plotted against the input NMD. The deviations in this case are even more obvious, especially for large standard deviations, which is mainly

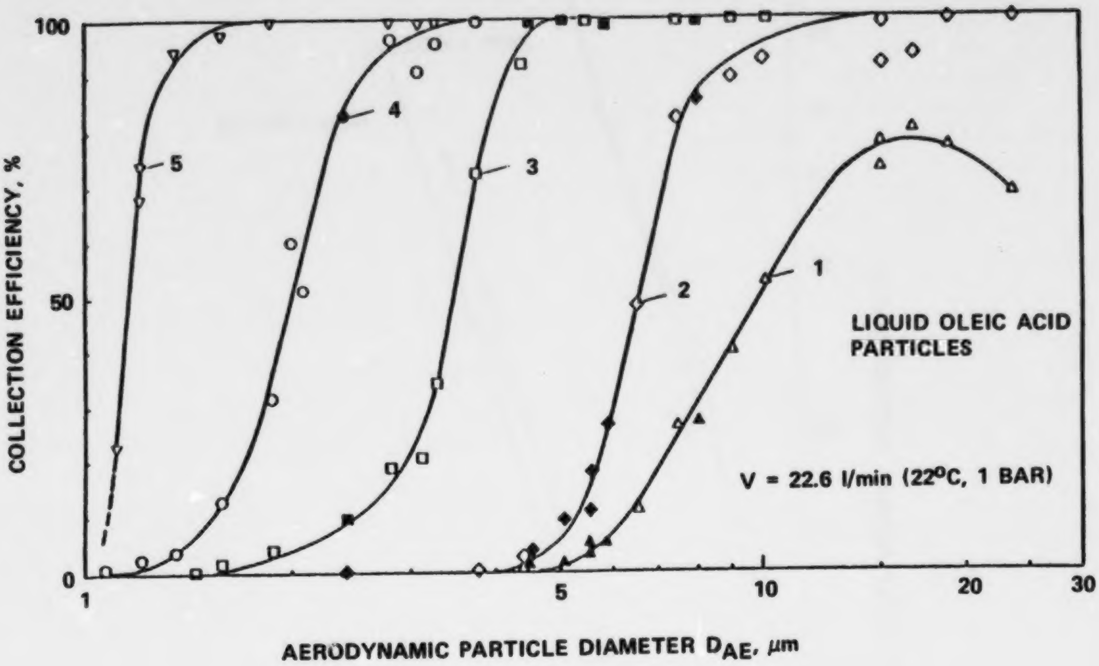

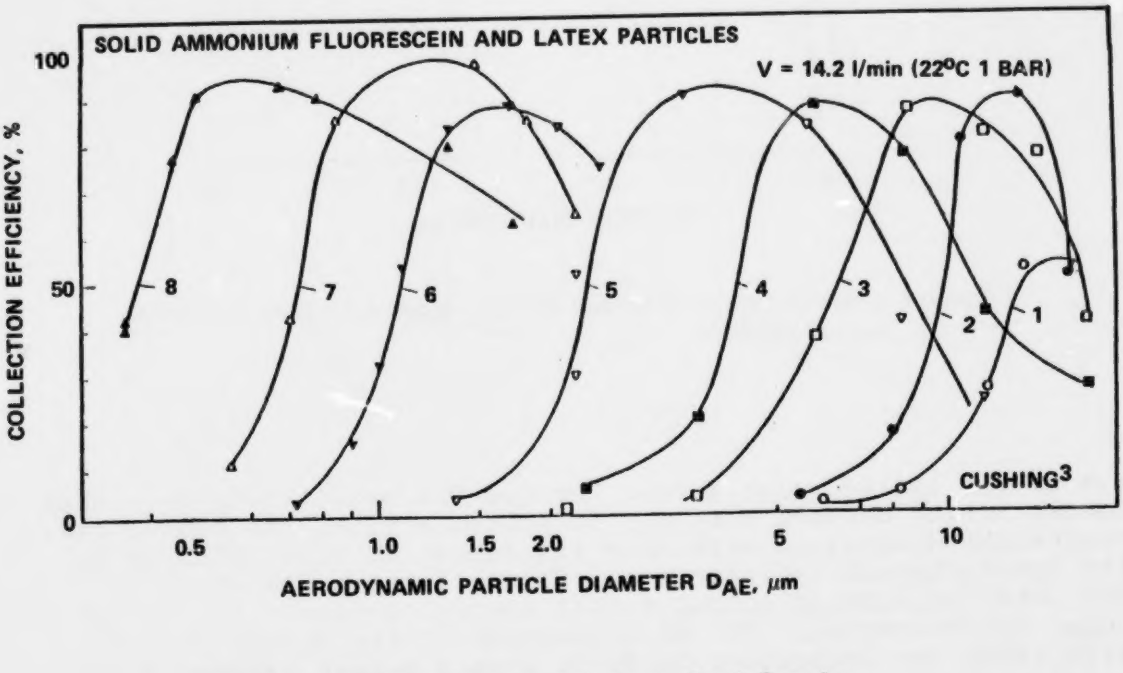

Figure 3. Collection efficiency of Andersen Stack Sampler.

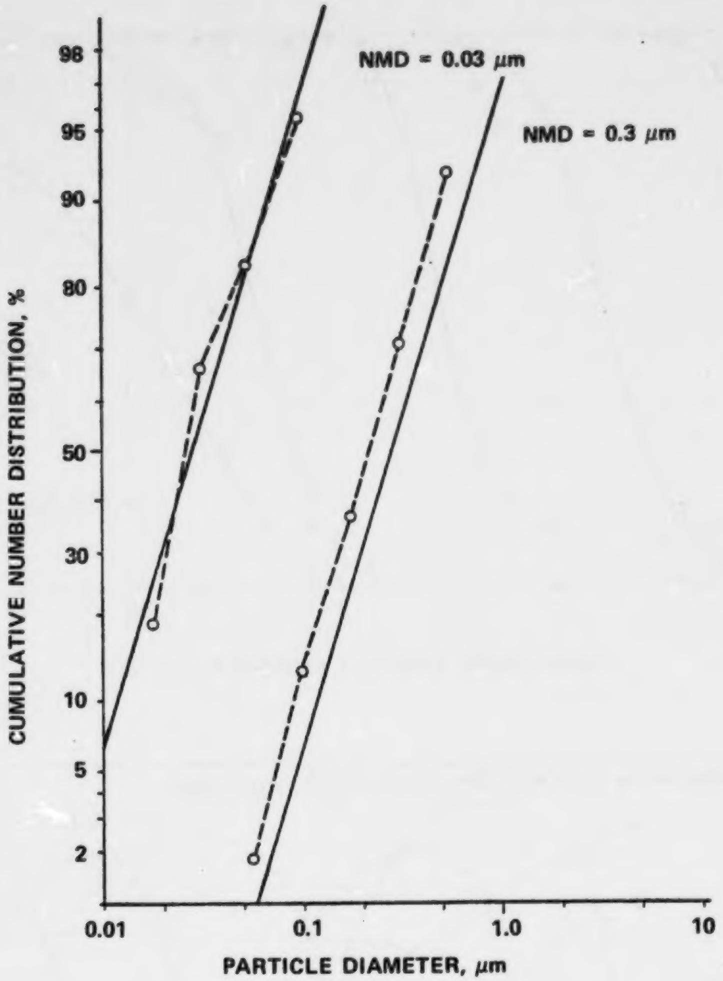

Figure 4. Calculated electrical aerosol analyzer response for given log-normal size distribution.

due to the limited size range. As the EAA sensitivity to number concentration depends strongly on particle size, the number concentration determined with this instrument is also affected by its cross-channel interference. Figure 7 shows the ratio of the total calculated output number concentration to the actual input concentration. For distributions in the middle of its size range the instrument tends to give a number concentration reading which is about 10% too high, while near the limits of the size range too small readings are caused by the fact that only a fraction of the particles is counted.

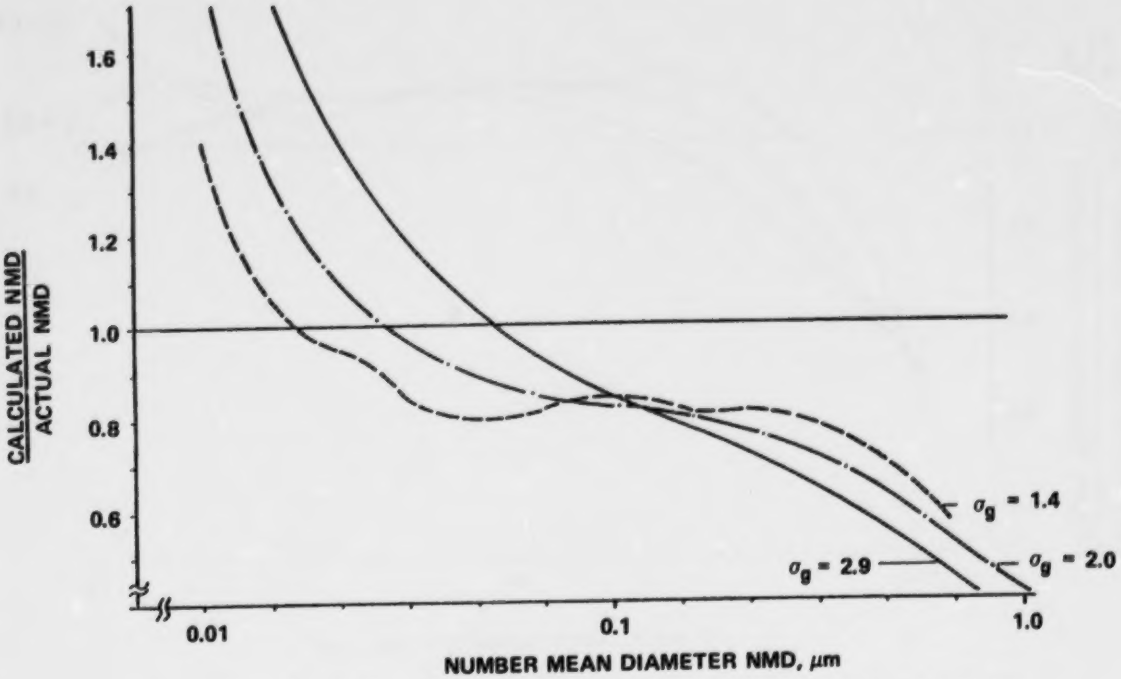

Figure 5. Ratio of calculated and actual number mean diameters for an electrical aerosol analyzer.

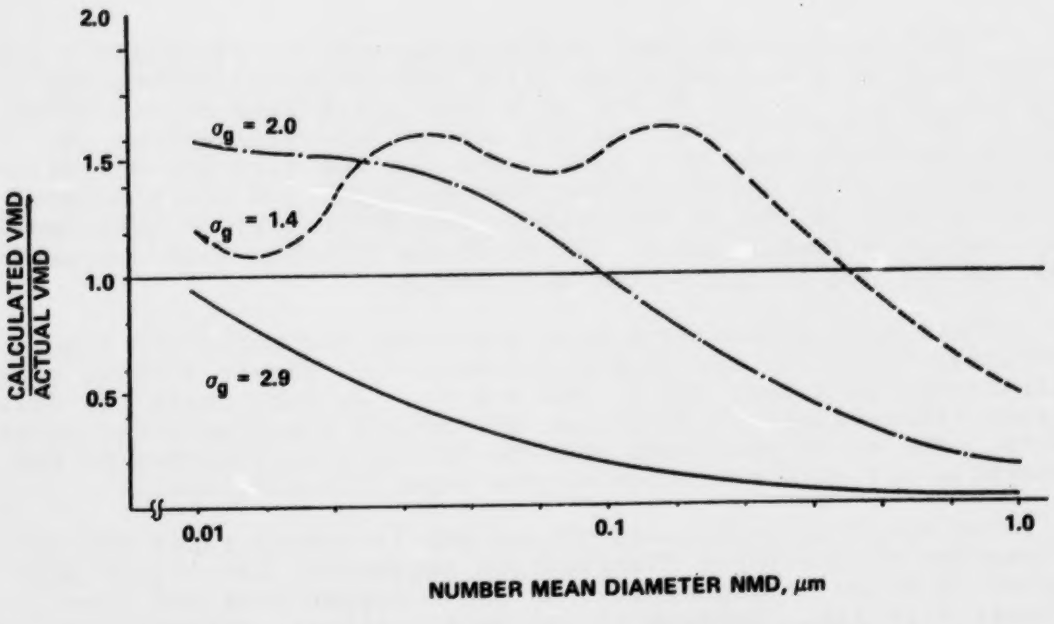

Figure 6. Ratio of calculated and actual volume mean diameters for an electrical aerosol analyzer.

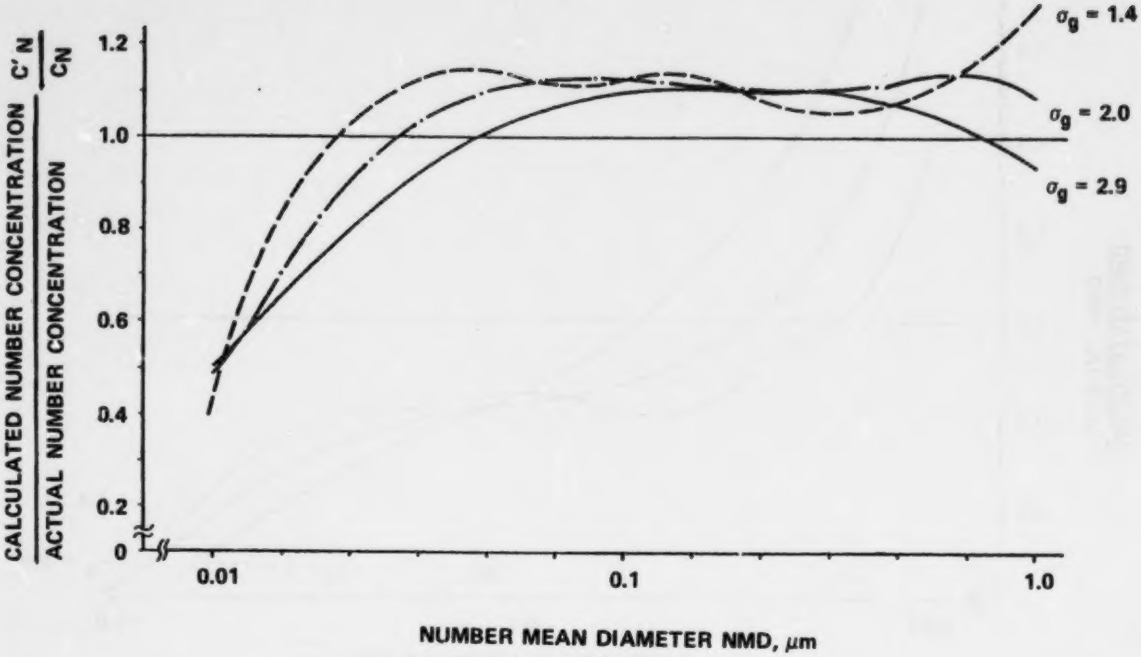

Figure 7. Ratio of calculated and actual number concentration for an electrical aerosol analyzer.

Similar calculations have been done for a six-stage A.S.S. Figure 8 shows the results for three log-normal distributions (σ_g = 3, MMD = 1.5 and 10 μm) as a cumulative mass distribution plot. For these calculations the collection efficiencies for liquid particles have been used. One can see that the deviation between the input distributions (solid lines) and the simulated measured data is nearly neglectable for distributions with small mass median diameter (MMD). It tends to increase with increasing MMD, mainly due to increasing wall losses.

These wall losses have been simulated for solid and liquid particles for a set of input distributions. Figure 9 shows these wall losses as a function of MMD and σ_g. In both cases the wall losses reach values of more than 30% of the total mass for large MMD's. For solid particles they do not very much depend on the geometric standard deviation of the input distribution.

The ratio of calculated output MMD to actual input MMD as a function of the input distribution parameters for liquid particles is shown in Figure 10. As the impactor does not have a lower size limit because of its backup filter, its behavior is nearly ideal for small MMD's. For larger MMD's and large σ_g's the output MMD is much smaller than the one for the input distribution. Besides the effect of the upper size limit, the increasing wall losses are the reason for this behavior.

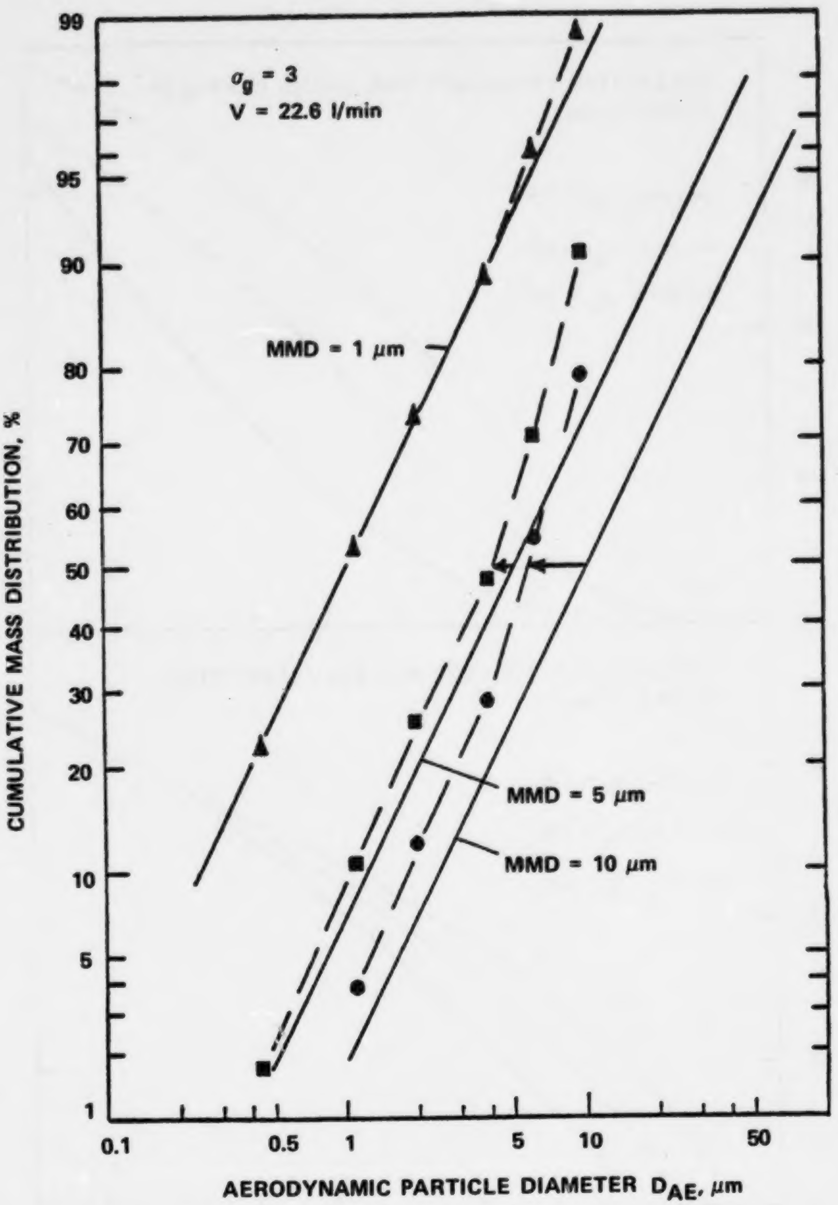

Figure 8. Calculated A.S.S. response for given log-normal size distributions (liquid particles).

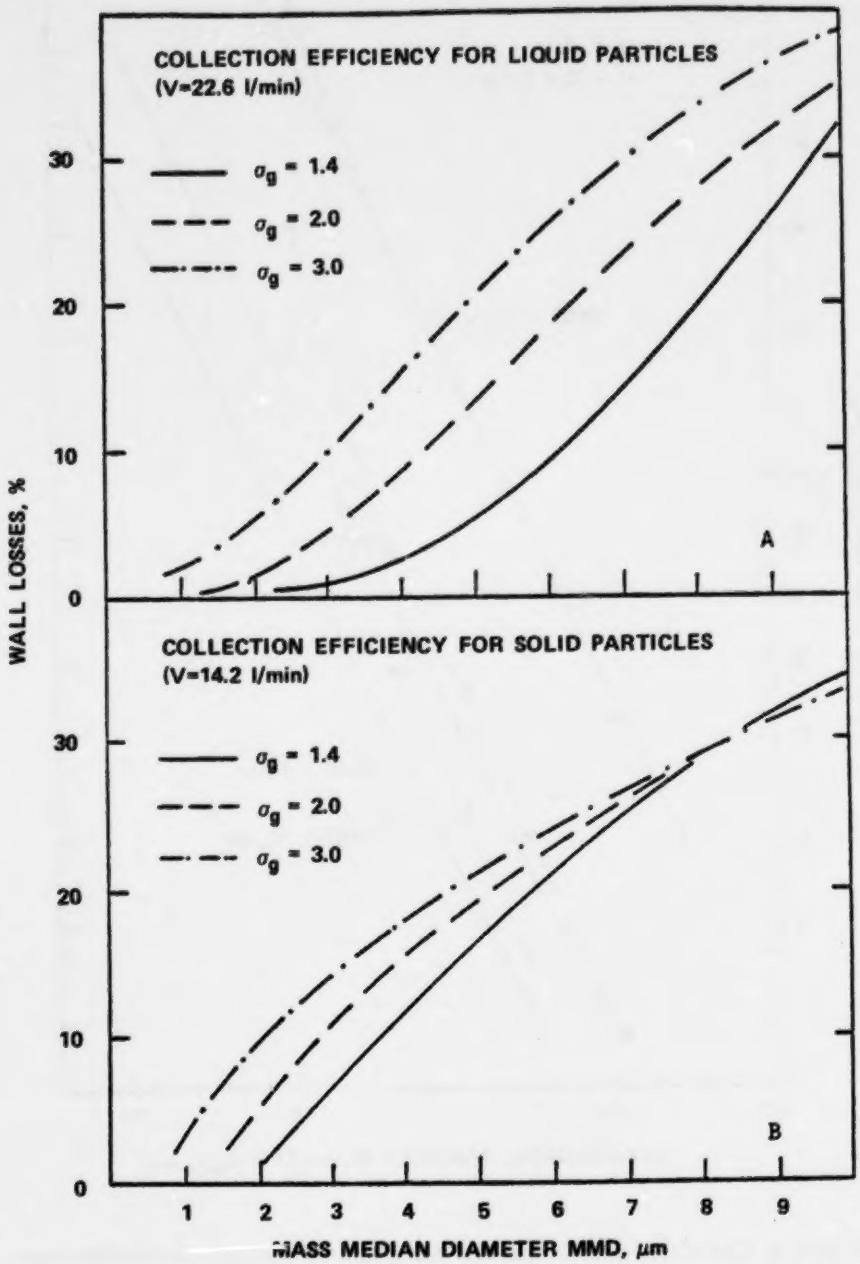

Figure 9. Calculated total wall losses for A.S.S. for log-normal size distributions.

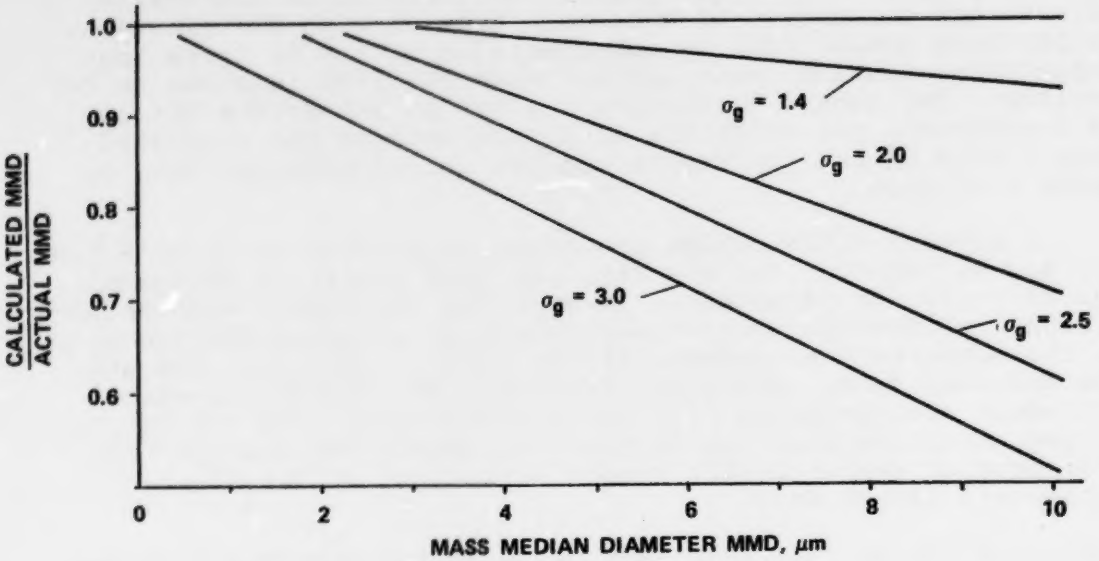

Figure 10. Ratio of calculated and actual mass median diameters for A.S.S. (collection efficiencies for liquid particles; V = 22.6 l/min).

DATA REDUCTION TAKING INTO ACCOUNT NON-IDEAL INSTRUMENT BEHAVIOR

These instrument simulation studies show that there are cases in which the errors caused by the instrument response cannot be neglected.

A data reduction procedure which would allow correction of the measured data should fulfill the following requirements:

1. It should allow correction for the instrument's systematic error even if the response matrix of the instrument is highly unstable (small errors in the measured data will give large changes in the solution).
2. It should reduce the effect of random errors in the measured data by use of physical constraints.
3. It should reduce the amount of data necessary to describe the particle size distribution.
4. It should allow a certain extrapolation of the results over the size range covered by the instrument. This would allow a comparison of different measurement techniques with only small overlapping size ranges.

To obtain these requirements, it seems to be reasonable to make the assumption of a certain type of size distribution. It has been shown[4] that by superposition of two or three log-normal distributions most aerosol size distributions can be described. For such a distribution a set of parameters has to be determined, for which the deviation between the simulated output data of the instrument and the actual measured data becomes a minimum.

A simplex minimization procedure (suggested to us by B.Y.H. Liu and A. Kapadia) for the EAA, has been chosen to optimize the distribution parameters. A modified chi-square with an additional weighting function was chosen as an objective function to characterize the goodness of fit between the simulated and the measured data. Starting parameters for the minimization procedure are estimated from the measured data. As the optimization algorithm does not necessarily detect the absolute minimum, several restarts with random variations of the starting parameters can be done.

INVESTIGATION OF THE EFFICIENCY OF THE DATA REDUCTION PROCEDURE

A lot of calculations were done to test if this data reduction procedure works satisfactorily. In a first step the program was checked with input data which were simulated from unimodal and bimodal starting parameters. The summarized results of these studies are shown in Table 1.

In test no. 1 the program used fixed starting parameters, which were not estimated from the input data. In the case of the unimodal distribution the parameters of the input distribution were recovered for all considered cases (12 sets of parameters). The parameters of the bimodal distribution were recovered only in 41% of a total of 243 sets of distribution parameters.

The calculation of estimates of the starting parameters from the simulated input data raised the success rate for bimodal distribution to 59%. In test no. 3 up to ten restarts with random variation of the estimated starting parameters in a range of ± 30% were allowed, if the goodness of fit indicated by the absolute value of the objective function was not satisfactory. This finally gave a success rate of 94% which seems to be the best that could be achieved by this method.

In some few of the successful cases the actual parameters of the input distribution were not recovered in spite of the fact that the value of the objective function indicated a very good fit. The recovered distribution was compared to the input distribution in a plot and agreed nearly exactly, which means that quite different parameters can describe nearly the same distribution. This case only occurred when the two distribution modes lay close together.

To get results which were closer to reality, in a next step the simulated input data were slightly varied to simulate random errors: 12 unimodal and 25 bimodal distributions with ten different sets of errors applied to each were investigated. In test no. 4 the errors were equally distributed between 0 and 10%, and in test no. 5 between 0 and 15%. The success rate in both cases was 100% for the unimodal and around 85% for the bimodal distributions. To test the influence of errors on the response matrix elements, which could be due to the limited accuracy of the calibration experiments, calculations were done with random errors (0 - 5%) in the matrix elements. The input data were free from errors. The success rate for the unimodal and bimodal distributions was 100%.

As a conclusion one can say that the data reduction procedure works very well in the case of unimodal distributions. For bimodal distributions several restarts with varied starting parameters are absolutely necessary to get a considerable rate of success. Even then there are cases in which no solution is found. With random errors in the input data the success rate decreases slightly.

TABLE 1. RESULTS OF TEST CALCULATIONS FOR THE EAA DATA REDUCTION PROGRAM

Test no.	Test conditions	Success rate Unimodal	 Bimodal
1	Simulated data, fixed starting parameters	100%	41%
2	Simulated data, starting parameters estimated from the input data	100%	59%
3	Like test no. 2, up to ten restarts with random variations of the estimated starting parameters	100%	94%
4	Like test no. 3, with random errors in the input data; errors equally distributed between 0 and 10%	100%	83%
5	Like test no. 4, errors equally distributed between 0 and 15%	100%	85%
6	Like test no. 3, random errors in the response matrix elements (0 - 5%)	100%	100%

When applying this data reduction method to real data, the random errors in these data will make success more difficult; the instrument behavior as determined in the calibration experiment may not be the same for particles of a shape and material different from the calibration aerosol.

To eliminate these influences, a first application check was done for a polydisperse DOP aerosol produced by an atomizer. Figure 11 shows the results of this experiment. The particle

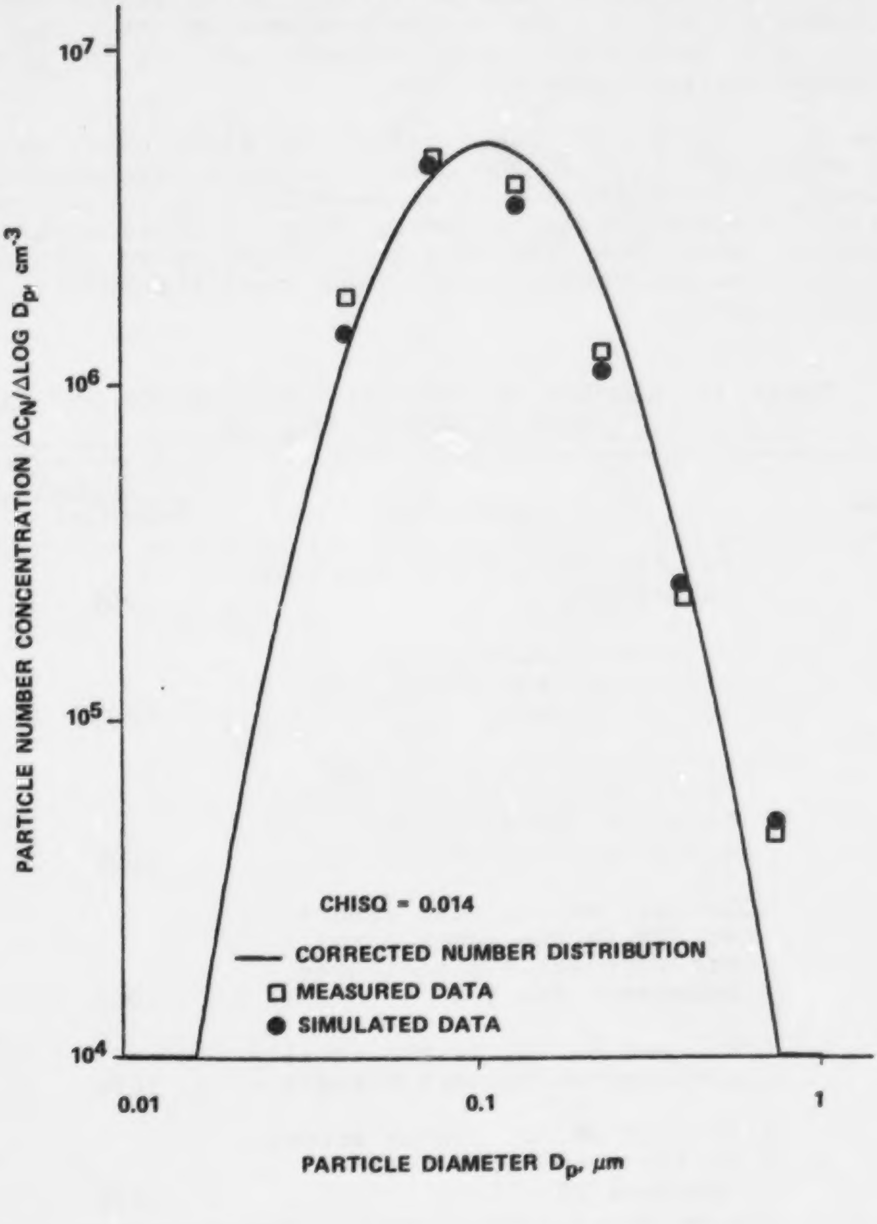

Figure 11. Atomizer aerosol (DOP).

number concentration $\Delta CN/\Delta \log D_p$ is plotted against the particle diameter D_p. The measured data are represented by squares. The corrected unimodal number distribution as determined by the data reduction program is given by the solid line. The simulated output data for this distribution, which in the case of an absolute fit had to be identical with the measured data, are given by circles. The deviations between measured and simulated data are in the range of the instrument's accuracy, which means that the corrected number distribution represents one possible solution. The value of the objective function is CHISQ = 0.014, which indicates a good fit, too.

APPLICATIONS OF THE DATA REDUCTION PROCEDURE TO REAL AEROSOLS

As mentioned above, real aerosols may differ from the calibration aerosols, as far as particle shape, particle material, and state of the gas are concerned. For any one of these reasons the response matrix of an instrument may not be valid for a certain aerosol which will cause a failure of the data reduction procedure.

In the following, several examples of applying this procedure to data of different aerosols are given.

The EAA has been used to determine the particle number distribution of the aerosol emitted by a spark ignition engine in connection with studies to characterize the content of polyaromatic hydrocarbons (PAH) in the particulate matter emitted by the engine. Figure 12 shows an example of a size distribution of this exhaust aerosol. The solid line gives the bimodal corrected number distribution and the squares represent the measured data, while the circles give the simulated data. As in the previous example, the deviations between the measured and simulated data are in the range of the instrument's accuracy, which leads to a rather small value of the objective function.

In another study the EAA has been used for the determination of the size distribution of test fire aerosols. These test fires are used to test the reaction of automatic fire detectors. In Figure 13 the particle number distribution of a smoldering wood fire aerosol is given. The fit between the measured and simulated data is very good; the value of the objective function is very low.

The next example, which is shown in Figure 14, represents the size distribution of a polyurethane fire aerosol. In this case the fit is very bad. The geometric standard deviation of the second mode has a value of $\sigma_{g2} = 1.1$, which was the lower limit for the optimization procedure. Even with this narrow distribution the simulated data are more broadly distributed than the measured data, which means that for a better fit the input distribution had to be even narrower. As it seems very unlikely that a fire will produce a monodisperse aerosol, this seems to be a case in which the instrument's calibration is not valid. This, however, makes it impossible to find an appropriate solution with a data reduction procedure based on this calibration.

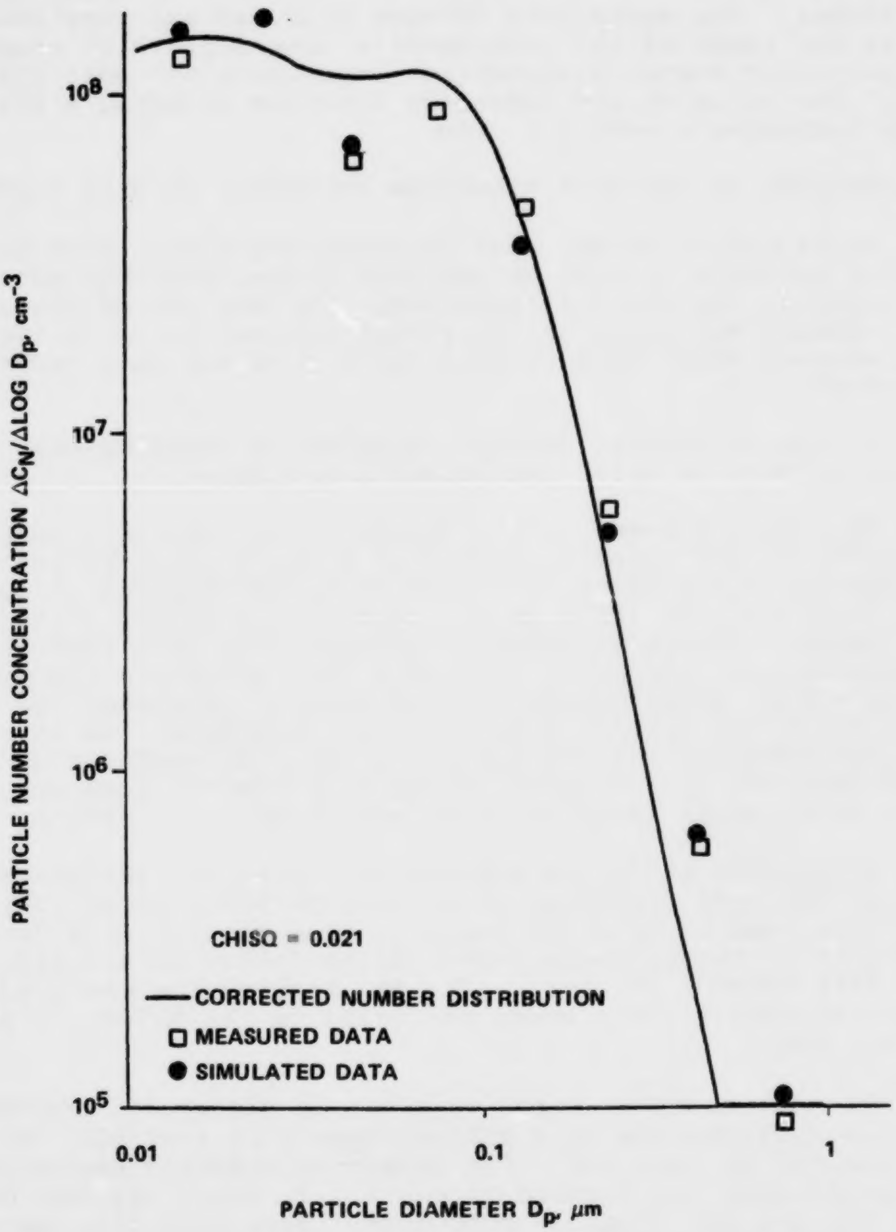

Figure 12. Spark ignition engine exhaust aerosol $n = 3000\ min^{-1}$, $\lambda = 0.92$.

In Germany, a certain type of SiO_2 aerosol is used in testing instrumentation in a dust tunnel. The particle mass distribution of this aerosol has been determined by Geipel[5] with an Andersen Stack Sampler. In Figure 15 his results are shown. In a first attempt we tried to correct his data assuming a log-normal size distribution and using the collection efficiencies for solid particles. The resulting log-normal size distribution

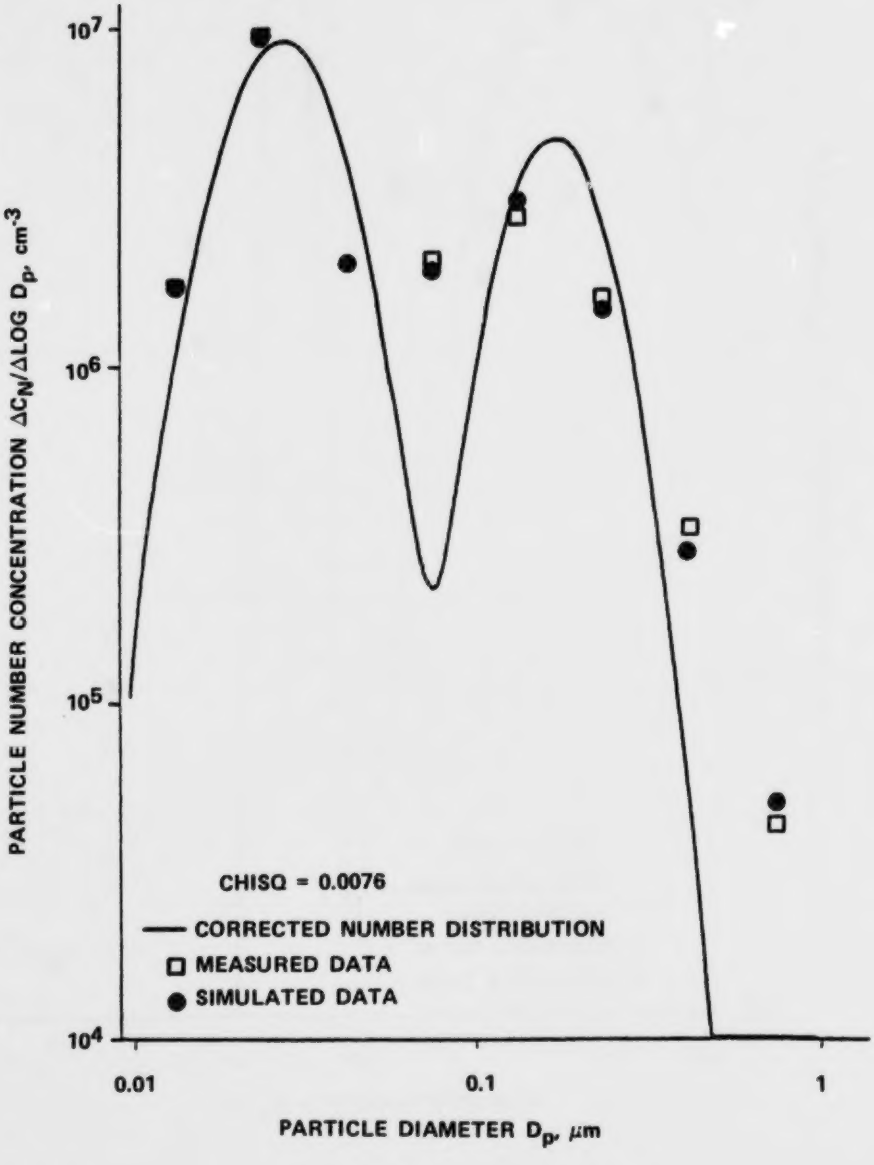

Figure 13. Smoldering wood fire aerosol.

shows rather good agreement with the distribution determined with sedimentation analysis. The calculated wall losses (36%) are also comparable with the ones measured by Geipel (38%). On the other hand the value of the objective function is rather

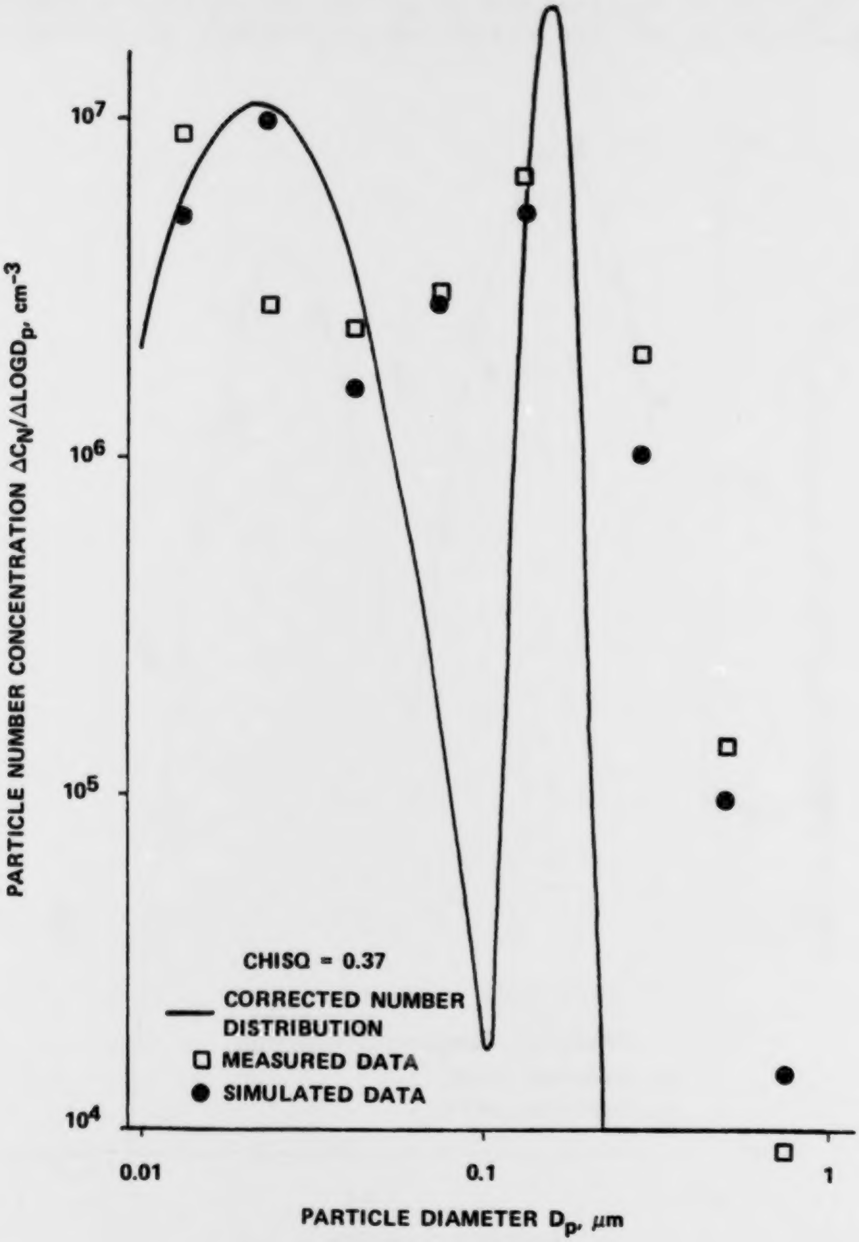

Figure 14. Polyurethane fire aerosol.

large and also the differences between measured and simulated data. Here again it hasn't been verified that one can use the collection efficiencies of the calibration experiment for this real aerosol.

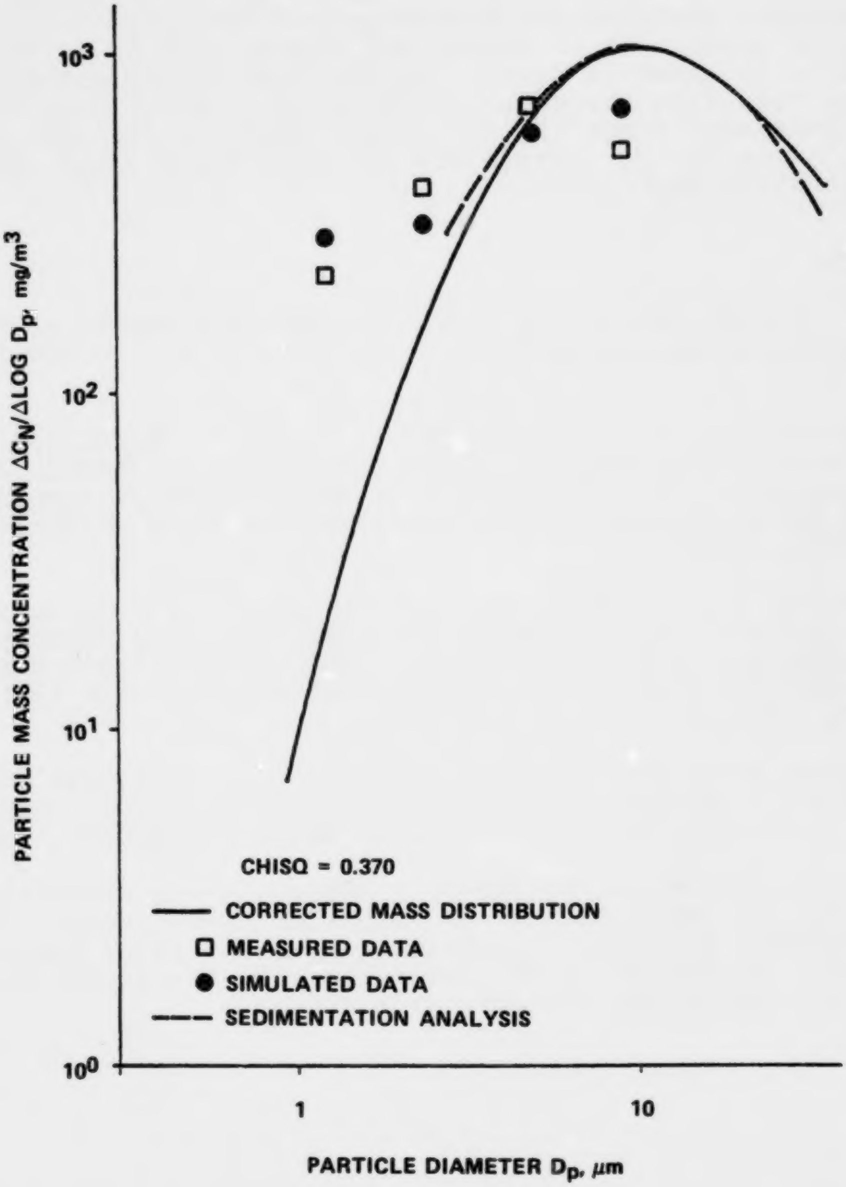

Figure 15. SiO_2 aerosol.

SUMMARY AND CONCLUSIONS

Almost all classifying instruments show a certain cross sensitivity, which can be determined by applying a monodisperse aerosol. Knowing the behavior of the instruments one can simulate the instrument numerically. These simulation studies, here shown for an Electrical Aerosol Analyzer and an Andersen Stack Sampler, allow us to judge the importance of including real behavior in the data reduction. A data reduction program based on the simplex minimization procedure has been carefully checked. It has been found that in almost all cases, even if errors are involved, a solution is found. In applying it to real aerosols this data reduction procedure finds its main limitation in the lack of knowledge about the instrument behavior for the real aerosol, which may be quite different from the aerosol used in the calibration experiment.

REFERENCES

1. Liu, B.Y.H., and D.Y.H. Pui. On the Performance of the Electrical Aerosol Analyzer. J. Aerosol Sci. 6:249-264, 1975.

2. Franzen, H., H.J. Fissan, and U. Urban. Eichung eines Andersen-Stack-Samplers unter Verwendung des Berglund-Liu-Generators. [Calibration of an Andersen Stack Sampler with the Use of a Berglund-Liu Generator.] Staub Reinhalt. Luft 38:436, 1978.

3. Cushing, K.M., G.E. Lacey, J.D. McCain, and W.B. Smith. Particulate Sizing Devices for Control Device Evaluation: Cascade Impactor Calibrations. EPA-600/2-76-280, U.S. Environmental Protection Agency, Research Triangle Park, NC, 1976. 94 pp.

4. Whitby, K.T. Modelling of Multimodal Aerosol Size Distributions. Presented at the Annual Meeting, Gesellschaft für Aerosolforschung, Bad Soden, Germany, October, 1974.

5. Geipel, W., and R. Wiedemann. Erprobung von Emissionsmessverfahren zur Feststellung von Korngrössenfraktionen. [Tests of Methods for Measuring Emissions to Determine Particle Size.] Report No. 7/79. Lehrstuhl für Thermische Kraftanlagen, Technische Universität München.

PAPER 12

NON-IDEAL BEHAVIOR IN CASCADE IMPACTORS

JOSEPH D. McCAIN
JAMES E. McCORMACK *
SOUTHERN RESEARCH INSTITUTE

INTRODUCTION

Cascade impactors have become commonly used measurement devices for the determination of size distributions of particulate emissions from industrial sources. Data obtained by means of impactors are used to characterize emissions from sources, to determine the performance of particulate control devices, and in selecting and designing control devices for specific sources.

Data provided by impactors are of relatively low resolution and do not permit the exact reconstruction of the size distribution of the aerosol being sampled, even over the limited range of sizes nominally covered by most impactors (approximately 0.5 to 15 μm). However, little has been done to estimate the magnitude of the uncertainties, or errors, which are inherent in the method insofar as they relate to industrial source emission measurements and determinations of fractional collection efficiencies of control devices. The study described here was one with the specific goals of estimating the effects of two non-ideal operating characteristics of impactors on the data obtained with them. These two non-idealities are (1) the lack of step function stage collection characteristics and (2) particle bounce. Several authors[1,2,3] have proposed various deconvolution procedures which, when applied to impactor data, would, to a large degree, correct for the effect of the finite slopes of the stage collection efficiency curves. However, little use has been made of these procedures, primarily because noise in the data frequently results in oscillatory solutions with large negative values. In any case, little quantitative information regarding the magnitude

---

*Now at the University of Minnesota

of the errors introduced by the lack of sharp size cuts in impactors commonly used for stack sampling has been published. The magnitude of errors introduced by particle bounce has not previously been quantified at all although the existence of such errors has been described in the literature.[4,5,6,7]

TECHNICAL PROCEDURES

The approach used in this study was the development of a computer model of cascade impactor performance. The model was based on actual impactor performance as measured in a calibration study of commercially available cascade impactors for stack sampling.[8] A total of four simulation models were used for both a Brink impactor in a commonly used modified configuration for stack sampling and an Andersen Mark III stack sampler. The use of glass fiber collection substrates was assumed for both impactors. Both greased substrates and glass fiber substrates are commonly used for sampling at temperatures below 150°C (300°F) but no satisfactory greases have been found for use at temperatures over 150°C. Therefore, glass fiber substrates must usually be used for collection substrates at elevated temperatures.

The first model for each impactor was one having ideal collection characteristics, i.e., step functions from 0% to 100% collection at the stage D_{50}'s. (The stage D_{50} is that particle diameter at which the stage has a collection efficiency of 50%. The D_{50} is generally used as the characteristic cut off diameter for particles collected by the stage.) This model was used as a performance standard against which the remaining three models could be compared and also provided a basis for checking the program.

The assumed operating conditions and resulting cut sizes (D_{50}'s) of the two impactors modeled in the study are given in Table 1. The models of the Brink impactor included a cyclone precollector which was assumed to have the same performance characteristics in all three of the simulations other than that of the "IDEAL Brink." The cyclone performance was based on calibration data for a cyclone in common use with the Brink impactor in a modified configuration for stack sampling. This cyclone had a collection efficiency of 100% for particles larger than about 20 μm.

The second model for each impactor utilized the actual calibration data for each stage. In this model the stage collection efficiencies increased monotonically with increasing Stokes' numbers (increasing particle size) to a maximum value of about 90% to 95%. The efficiencies then decreased for larger Stokes' numbers to a value of 35% to 40% and remained constant thereafter. A composite of the calibration data for stages two (2) through seven (7) of the Andersen impactor, which illustrates

TABLE 1. SIMULATION CONDITIONS OF THE MODELED IMPACTOR PERFORMANCE

	Brink	Andersen
Temperature, °C (°F)	177 (350)	177 (350)
Gas composition	Standard air	Standard air
Particle density, g/cm^3	2.27	2.27
Flow rate, alpm (acfm)	1.13 (0.040)	17.0 (0.600)
Barometric pressure, mm Hg	749	749
Stage/D_{50}(μm)		
1	9.60[a]	7.84
2	6.18[b]	7.40
3	3.39	4.44
4	1.85	2.87
5	1.23	1.58
6	0.905	0.855
7	0.589	0.449
8	0.198[b]	0.200

[a] Stage 1 is a cyclone precollector.

[b] Stages 2 and 8 are part of the modifications to the impactor.

the behavior described above, is shown in Figure 1. Data for stages 1 and 8 were offset from the tight grouping of the data for the remaining stages and hence were omitted in Figure 1 for purposes of clarity in illustrating the behavior trends of the stage efficiency curves. The data for the Brink impactor exhibited similar trends. This model, Model 2, is called the "Normal Bounce" model.

The third model was identical to the second except that the rollover and decline in efficiency for larger Stokes' numbers was ignored. Instead, the efficiencies were assumed to smoothly increase to 100% and remain at that value for increasingly larger Stokes' numbers. This is called the "No Bounce" model. The fourth model was also identical to Model 2 with the exception that the collection efficiencies were assumed to drop rapidly to a value of 2% for Stokes' numbers larger than that at which the collection efficiency reached a peak in the calibration data. This model was termed the "Extreme Bounce" model.

The use of the same basic collection efficiency curves for the "No Bounce", "Normal Bounce", and "Extreme Bounce" models for particle sizes smaller than those for which the collection efficiencies were maximal in the calibration data is probably a realistic representation of the actual performance of the impactors in collecting various types of particles. Rao[5] found that impactor collection characteristics for dry solid particles and oil particles were virtually identical when glass fiber substrates were used for Stokes' numbers smaller than those at which the peak efficiency was reached for the dry solid particles. Beyond this point he found that oil particles were collected with efficiencies which increased to 100% with increasing Stokes' number while the efficiencies declined for the dry particles as a result of bounce. Figure 2 shows an example of the four modeled collection efficiency characteristics of one stage of the Andersen impactor.

RESULTS AND DISCUSSION

The performance of each model of the two impactors was evaluated for aerosols having log-normal size distributions with mass median diameters (MMD) of 1.5, 2.6, 4.5, 7.8, 13.5, and 27 micrometers. Geometric standard deviations, σ_g, of 2, 3, and 4 were used at each particle size. Because of the volume of the data generated only representative results are presented in this paper.

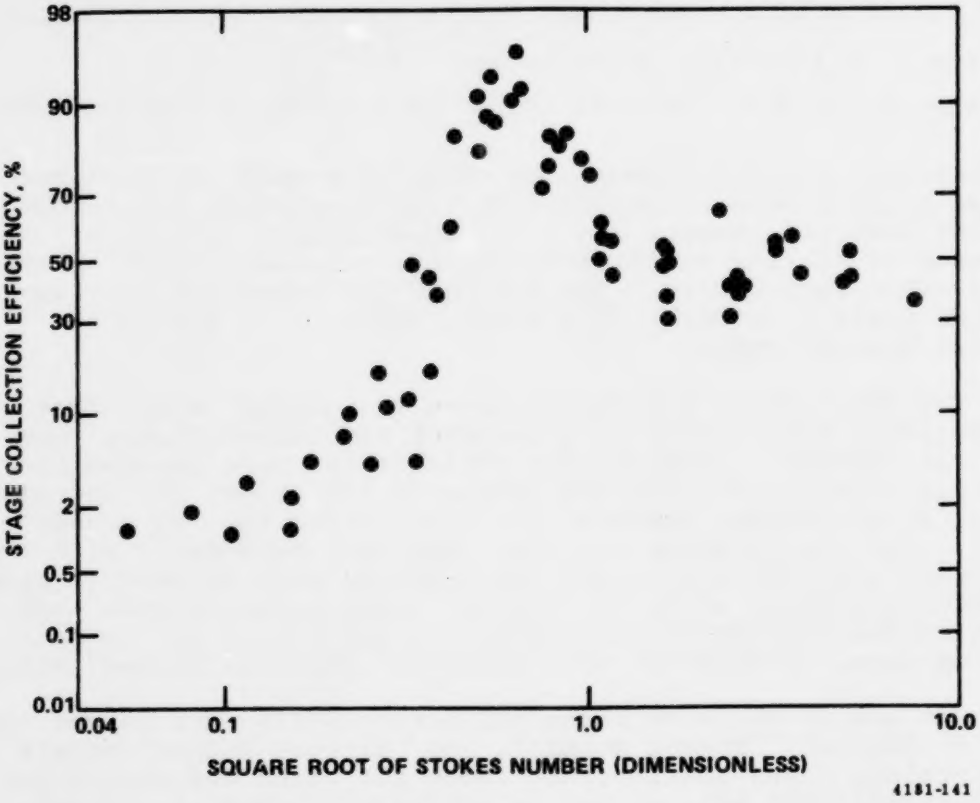

Figure 1. Composite of calibration data for the Andersen impactor, stages 2 through 7.

Figures 3 through 6 show typical results for the two impactors in a cumulative percentage presentation. It is evident from all four of these figures that particle bounce severely distorts the size distributions, especially for aerosols having large mass median diameters. Figures 3 and 4 show the results of the simulations for the same impactor and size distributions, the difference between the two being the omission of the back-up filter catch in presenting the results in Figure 4. Comparison of Figures 3 and 4 indicates that omitting the back-up filter in calculating the cumulative percentages greatly reduces the distortion resulting from bounce. Comparison of Figures 3 and 5 shows that increasing the width of the input size distribution (increasing σ_g) reduces the distortion caused by bounce although the distortion remains appreciable for the extreme bounce models at large MMD's.

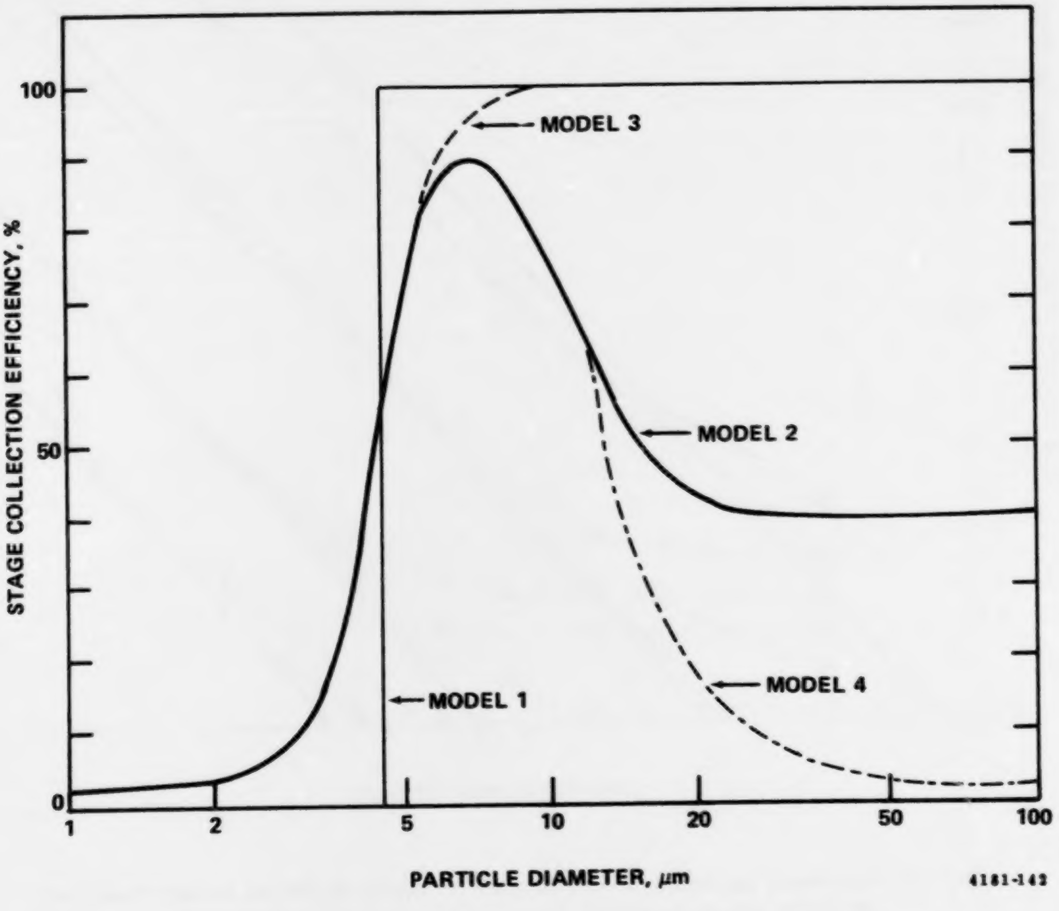

Figure 2. An illustration of the four modeled stage collection efficiency curves of a typical stage of the Andersen impactor. Model 1 is the ideal behavior model, model 2 is the normal bounce model, model 3 is the no bounce model, and model 4 is the extreme bounce model.

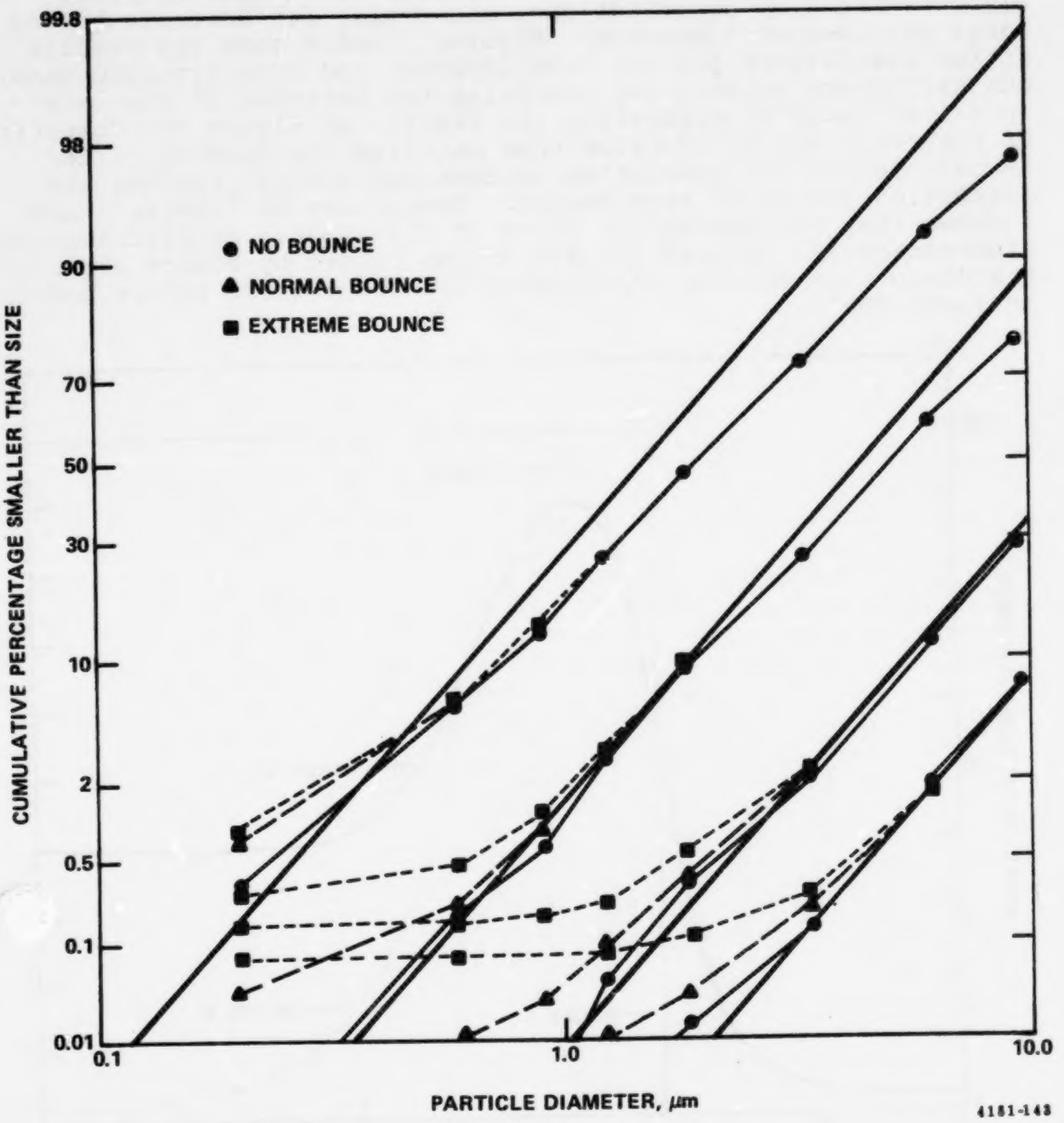

Figure 3. Recovered particle size distributions on a cumulative percentage basis from the Brink impactor models for $\sigma_g = 2.0$ and mass median diameters of 1.5, 4.5, 13.5, and 27 μm. The heavy lines represent the input distributions.

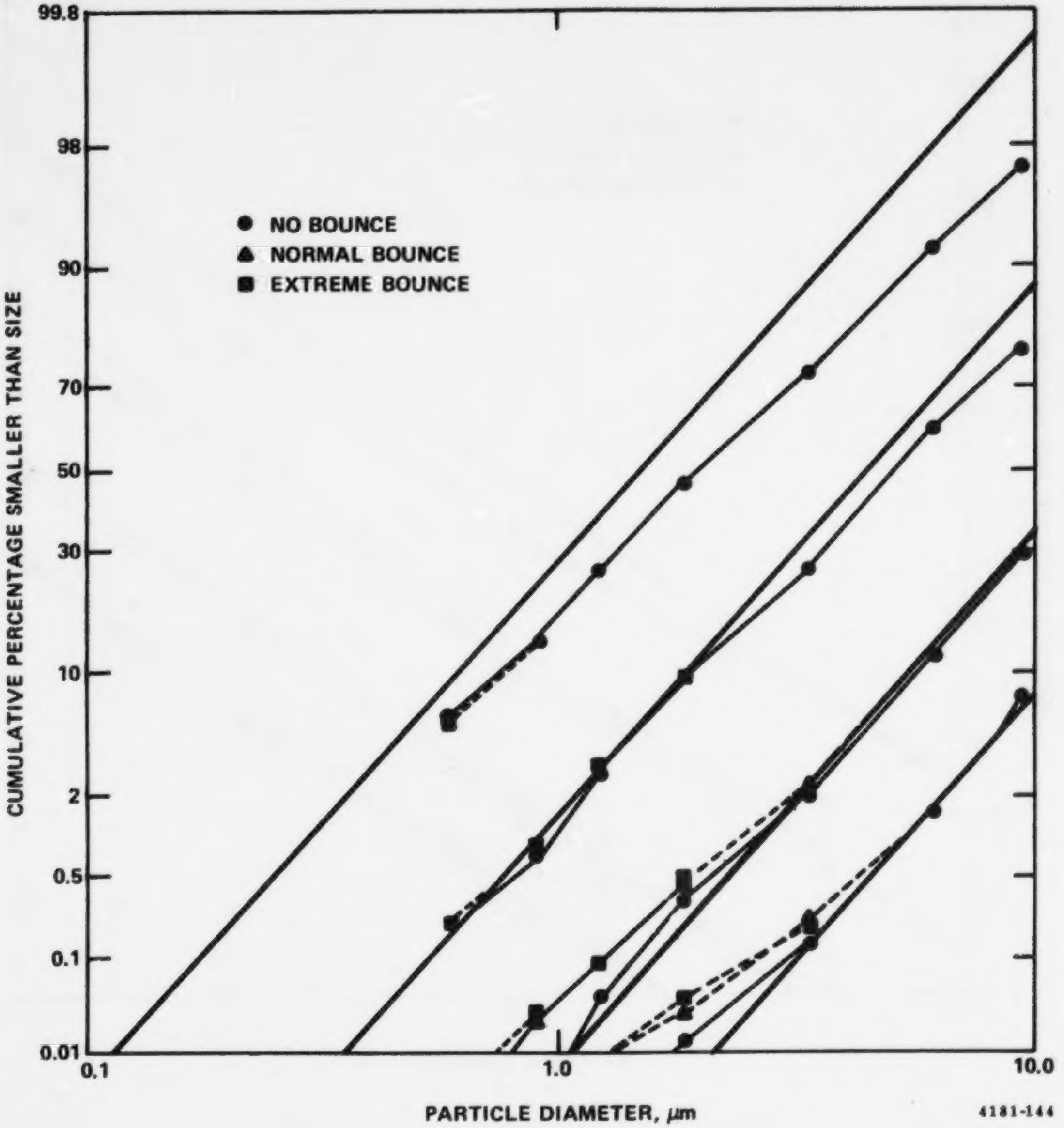

Figure 4. Recovered particle size distributions on a cumulative percentage basis from the Brink impactor models shown in Figure 3 with backup filter catches omitted from the analysis. The heavy lines represent the input distributions.

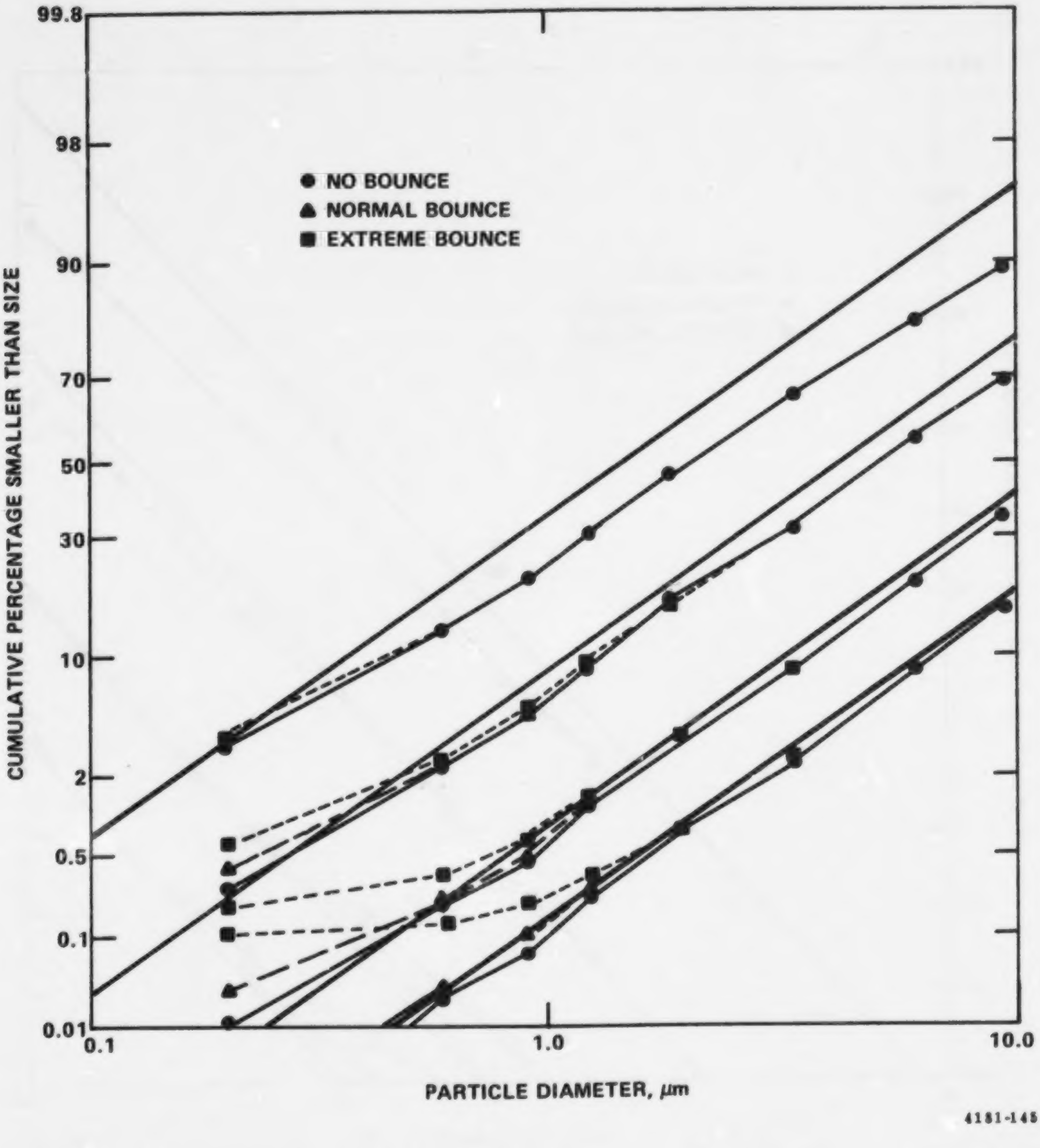

Figure 5. Recovered particle size distributions on a cumulative percentage basis from the Brink impactor models for $\sigma_g = 3.0$ and mass median diameters of 1.5, 4.5, 13.5, and 27 μm (backup filter included in the analysis). The heavy lines represent the input distributions.

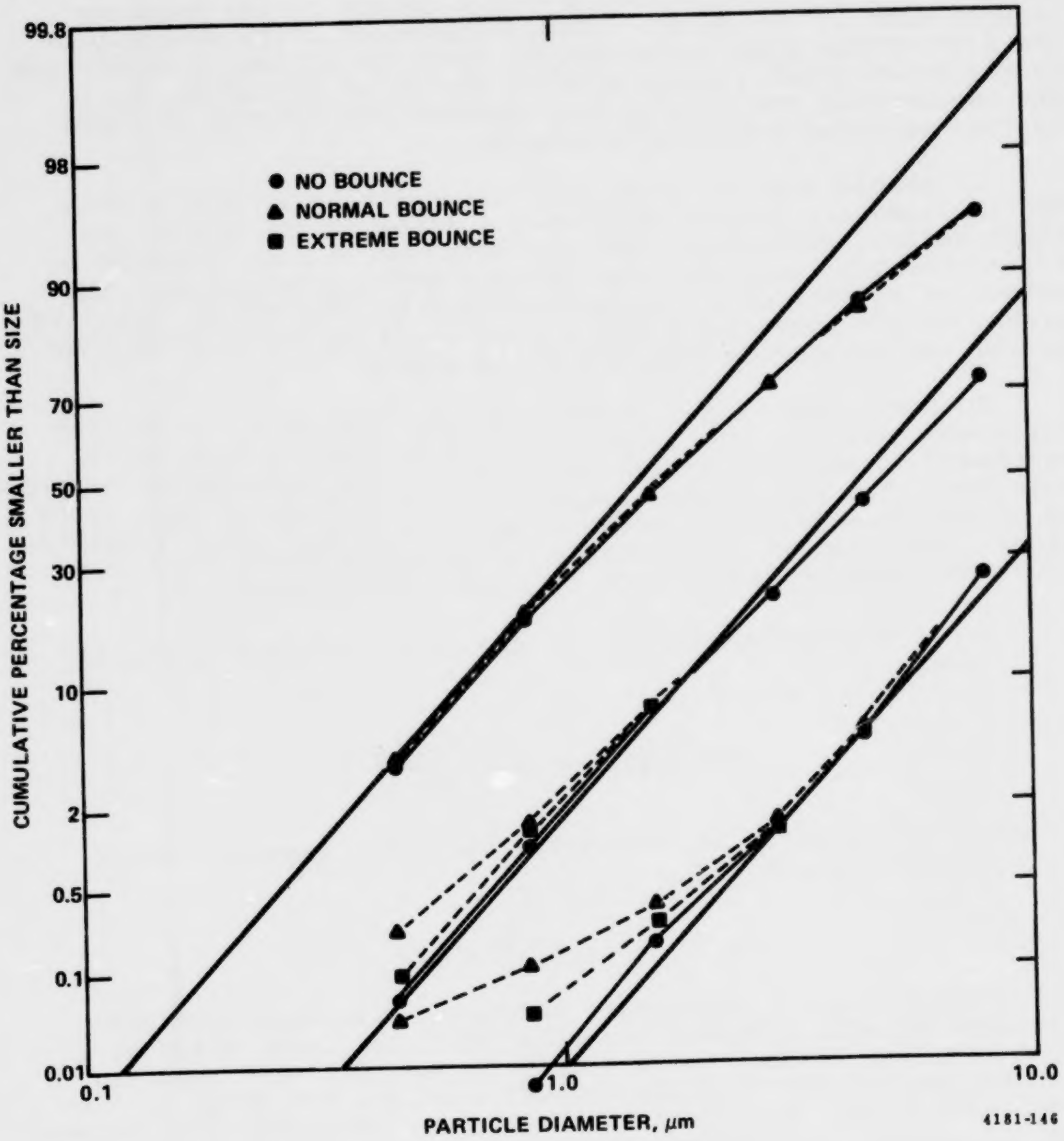

Figure 6. Recovered particle size distributions on a cumulative percentage basis for the Andersen impactor for σ_g = 2.0 and mass median diameters of 1.5, 4.5, and 13.5 µm. The backup filter was excluded from analysis in the results shown. The heavy lines represent the input distributions.

Figure 6 shows the results from the Andersen models corresponding to three of the four cases for the Brink model shown in Figure 4. Note that the deviations from the input distribution resulting from bounce are more severe in the Andersen results than in the Brink. This difference in the severity of the distortions apparently results from the cyclone precollector on the Brink which removes most of the large particles which are responsible for raising the apparent percentages of fines in the recovered size distributions.

It should also be noted that the relative errors in mass median diameters become increasingly large as the MMD of the input aerosol decreases. The recovered MMD's were found to be systematically large for test aerosol MMD's below 10 μm. The values of σ_g were also systematically high with larger relative errors at the lower values of σ_g, as would be expected because of the low resolution afforded by impactors.

In many cases (e.g., control device fractional collection efficiency studies) the slope of the size distribution curve, expressed in mass concentration units, is the quantity of greatest interest. The most common manner of presentation of this slope is of the form dm/dlogD versus diameter (units of mass concentration). The quantity dm/dlogD is often approximated directly from the impactor data, stage by stage, as $\Delta m_i/\log D_i$, where

Δm_i = mass concentration of particles retained by the ith stage

$$\text{and } \Delta \log D_i = \log \frac{(D_{50})_{i-1}}{(D_{50})_i} .$$

The particle diameter is then taken to be the geometric mean of $(D_{50})_i$ and $(D_{50})_{i-1}$ or

$$\bar{D}_g = (D_{50})_i \times (D_{50})_{i-1}$$

Figures 7 and 8 illustrate recovered size distributions presented in such a manner, together with the input distributions, for representative sets of Brink and Andersen results. The results for the "extreme bounce" case are not shown in Figures 7 and 8 but the values in those cases generally fall between the "no bounce" and "normal bounce" cases except for the back-up filters, for which the values were much higher in the "extreme bounce" case than in the other two cases. Except for the finest size fractions, represented by the back-up filter catches, and the fine fraction tails of the low σ_g distributions, the agreement between the recovered values of $(\Delta m/\Delta \log D)_i$ generally lie reasonably close to the input distributions. However, errors of up to ±35% are not infrequent.

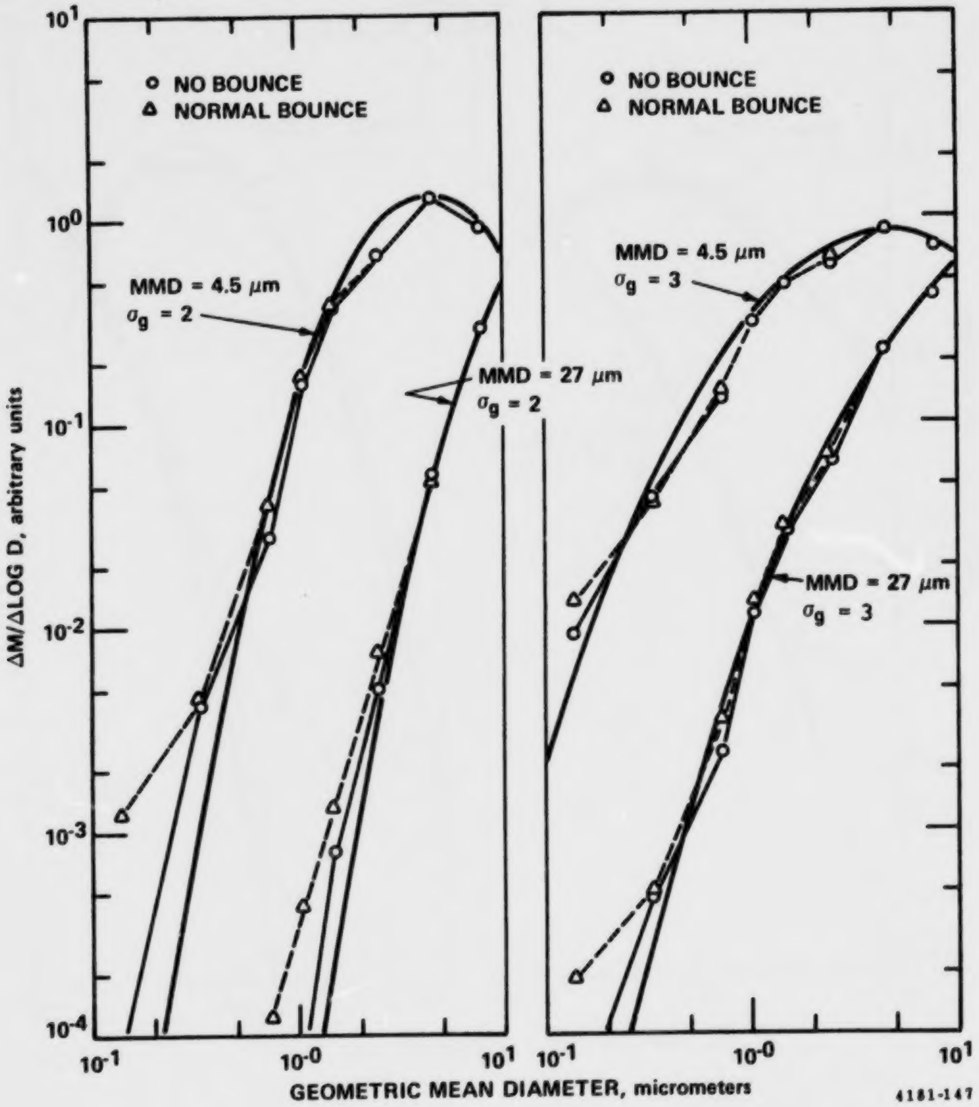

Figure 7. Recovered particle size distributions on a differential basis from the Brink impactor models for mass median diameters of 4.5 and 27 μm and σ_g's of 2 and 3. The heavy curves represent the input distributions.

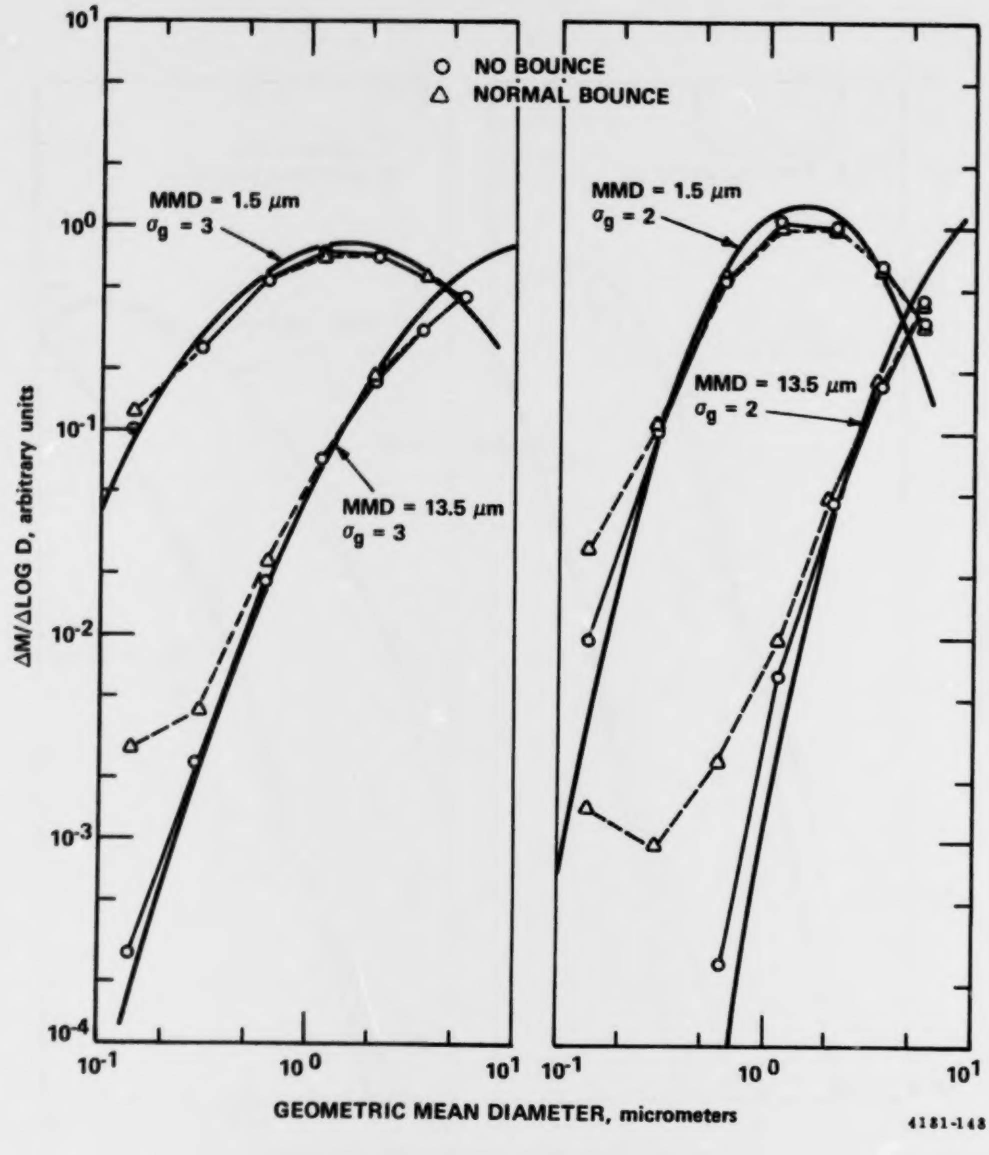

Figure 8. Recovered particle size distributions on a differential basis from the Andersen impactor models for mass median diameters of 1.5 and 13.5 μm and σ_g's of 2 and 3. The heavy curves represent the input distributions.

Tables 2 and 3 show the errors, expressed as percentages, in the recovered values of $(\Delta m/\Delta \log D)_i$ for several cases for each of the two impactors. (For the purpose of calculating log D and D for the filter catches, it was assumed that the diameter range covered by the filter was $(D_{50})_8$ down to $\frac{1}{2}(D_{50})_8$.

Although no results for $\sigma_g = 4$ have been shown, the agreement between the recovered size distributions and the input distributions was progressively better as σ_g increased and was quite good in all cases for $\sigma_g = 4$ with the exception of back-up filter catches when bounce was present.

Table 4 shows the percentages of cases in which the recovered value $(\Delta m/\Delta \log D)_i$ lay within factors of 1.2, 1.5, and 2 of the true value. From these results it appears that the concentrations of fine particles as measured with impactors can seldom be taken to be known better than to within a factor much smaller than 1.5 unless the particles are known to be adhesive or an effective adhesive coating can be applied to the substrates.

TABLE 2. PERCENT ERRORS IN $\Delta m/\Delta \log D$, ANDERSEN IMPACTOR

σ_g	2			3		
MMD	1.5	4.5	13.5	1.5	4.5	13.5
		No Bounce				
Stage/Error						
F	144			22	38	
8	9			-14	-5	
7	-8	56		-11	-4	
6	-18	13		-10	-8	4
5	-14	-19	18	-12	-17	-24
4	6	-26	-20	-7	-21	-25
3		-19	-30	10	-15	0
2		-23	-28	9	-22	-24
		Normal Bounce				
F	568	121000		44	173	1720
8	22	920		-12	8	103
7	-6	111		-11	1	37
6	-20	9	293	-12	-11	4
5	16	-18	39	-12	-16	-11
4	5	-27	-17	-7	-21	-24
3		-20	-30	9	-16	-25

NOTE: Values are omitted for stages for which the collected mass would be too small to be detected in field sampling programs.

TABLE 3. PERCENT ERRORS IN Δm/ΔlogD, BRINK IMPACTOR

σ_g	2				3			
MMD	1.5	4.5	13.5	27	1.5	4.5	13.5	27
Stage/Error								
No Bounce								
F	220				24	53		
6	-6	220			-37	-21	13	
5	-43	-35			-32	-39	-40	-37
4	-19	3			-9	-12	-5	4
3	-15	-3	84		-4	-9	-3	8
2	-1	-10	-8	33	4	-20	-23	-22
1	88	-14	-15	7	34	-3	-14	-14
Bounce								
F	550				41	123		
6	-10	238			-39	-24	12	
5	-40	-8			-29	-33	-26	-10
4	-20	10			-10	-12	0	17
3	-16	-4	107		-4	-10	-3	10
2	-1	-28	7	100	4	-18	-20	-16
1	86	-15	-18	3	33	-4	-16	-17

NOTE: Values are omitted for stages for which the collected mass would be too small to be detected in field sampling programs.

TABLE 4. PERCENTAGE OF TRIAL CASES IN WHICH RECOVERED VALUE OF (Δm/ΔlogD) IS WITHIN THE INDICATED FACTOR OF THE TRUE VALUE

	Andersen				Brink		
Factor	1.2	1.5	2.0	Factor	1.2	1.5	2.0
Stage/Percent of cases				Stage/Percent of cases			
F	0	31	38	F	0	33	56
8	57	71	79	6	35	59	82
7	65	76	82	5	11	47	100
6	65	80	90	4	80	95	100
5	75	100	100	3	74	91	91
4	30	100	100	2	42	96	100
3	40	90	90	1	71	72	100
2	(30)	(90)	(90)				

Andersen table covers all cases with MMD = 1.5, 2.6, 4.5, 7.8, 13.5 and σ_g = 2, 3 for both normal bounce and no bounce

Brink table covers all cases with MMD = 1.5, 2.6, 4.5, 7.8, 13.5, 27 and σ_g = 2, 3 for both normal bounce and no bounce

There is some evidence,[8,9] although it is not conclusive, that the use of adhesive coatings (greases) on the substrates may become ineffective as the particulate deposits build up under the impactor jets. This would result in the same type of errors due to particle bounce resulting in back-up filter contamination by oversize particles with greased substrates as has been shown to occur with glass fiber substrates.

CONCLUSIONS AND RECOMMENDATIONS

From the evidence presented here, it is suggested that back-up filter catches generally should be omitted from data presentation when dry, non-sticky particulates are sampled. Exceptions should be made only if the MMD is smaller than about 2.5 μm. In addition it is suggested that cyclone precollectors having D_{50}'s somewhat larger than the first impaction stage D_{50} be used whenever a non-sticky particulate is sampled. The use of such cyclones tends to greatly reduce errors due to particle bounce.

ACKNOWLEDGEMENT

The work reported here was done under support from the Industrial Environmental Research Laboratory of the U.S. Environmental Protection Agency; Contract No. 68-02-2131, D.B. Harris, Project Officer.

REFERENCES

1. Cooper, Douglas W., and John W. Davis. Cascade Impactors for Aerosols: Improved Data Analysis. Am. Ind. Hyg. Assoc. J. 33(2):79-89, 1972.

2. Cooper, Douglas W., and Lloyd A. Spielman. Data Inversion Using Nonlinear Programming with Physical Constraints: Aerosol Size Distribution Measurement by Impactors. Atmos. Environ. 10(9):723-729, 1976.

3. Picknett, R.G. A New Method of Determining Aerosol Size Distributions from Multistage Sampler Data. J. Aerosol Sci. 3:185-198, 1972.

4. McCain, J.D., K.M. Cushing, and W.B. Smith. Methods for Determining Particulate Mass and Size Properties: Laboratory and Field Measurements. J. Air Pollut. Control Assoc. 24(12):1172-1176, 1974.

5. Rao, A.K. An Experimental Study of Inertial Impactors. Ph.D. Dissertation, University of Minnesota, Minneapolis, 1975.

6. Dzubay, T.G., L.E. Hines, and R.K. Stevens. Particle Bounce Errors in Cascade Impactors. Atmos. Environ. 10(3):229-234, 1976.

7. Natusch, D.F.S., and J.R. Wallace. Determination of Airborne Particle Size Distributions: Calculation of Cross-Sensitivity and Discreteness Effects in Cascade Impaction. Atmos. Environ. 10(4):315-324, 1976.

8. Cushing, K.M., J.D. McCain, and W.B. Smith. Experimental Determination of Sizing Parameters and Wall Losses of Five Commercially Available Cascade Impactors. Annual Meeting, Air Pollution Control Association, Paper No. 76-37.4, 1976.

9. Lundgren, D.A. An Aerosol Sampler for Determination of Particle Concentration as a Function of Size and Time. J. Air Pollut. Control Assoc. 17(4):225-229, 1967.

PAPER 13

FIELD TESTING OF AUTOMATIC PIEZOELECTRIC MICROBALANCES FOR OUTDOOR AEROSOL MASS CONCENTRATION MEASUREMENTS

KAZUO TSURUBAYASHI
HAJIME KANO
NIHON KAGAKU KOGYO CO., LTD.

ABSTRACT

The main purpose of this paper is to describe the performance, field-testing data, and sampling technique of an automatically operated piezoelectric microbalance particle mass concentration monitor (automatic piezobalance) which has high sensitivity for particle detection. A further application, real-time particle size measurement using an Andersen cascade impactor, is also described.

Results presented here show a high correlation coefficient (greater than 0.9) between the automatic piezobalance and low volume sampling and filter weighing (LV) measurements when the sampling conditions are set up to avoid wind effects and to minimize wall losses of particles in the sampling tube.

INTRODUCTION

The Japanese law for ambient air quality standards specifies that:

1) Regulations must be established based upon the mass concentration of respirable particulate matter (defined as airborne particles smaller than approximately 10 μm).

2) The standard value of respirable particulate matter for the environment should be less than 0.1 mg/m^3, when one-hour values are averaged over a 24-hour period, and less than 0.2 mg/m^3 for each measured one-hour value.

3) Low volume sampling, using a 10 μm cut-off device and a filter weighing method, should be the standard measuring method.

Light-scattering dust meters have been accepted for measuring one-hour values only if they have been first calibrated at each local monitoring station.

Monitoring and surveillance of ambient air quality is being done by the National Air Monitoring Network and city or prefectural monitoring stations. There are more than 1000 such stations in Japan. However, ever since the law was enacted, the standard measuring method has had two main problems that still remain unsolved:

1) One-hour values of mass concentration cannot be measured by the LV method, and

2) Light-scattering measurements do not correlate well with LV measurements.

A wide range of people have requested improvement of the standard measuring method. In 1976, the automatic piezobalance (Piezobalance is a trademark registered in the USA by TSI Incorporated) was developed to solve these problems. The Japanese Environmental Agency has field tested several automatic piezobalances and several beta absorption instruments as alternative measurement methods.

PRINCIPLE AND OPERATION

The automatic piezobalance, shown schematically in Figure 1, consists of a mass-sensing/auto-cleaning system and a digital processing system. The mass-sensing/auto-cleaning system includes a vacuum pump with one ℓ/min sonic nozzle, an automatic crystal (sensor) cleaner, an analog sequence controller, a precipitator with removable precipitation needle, a detecting crystal with oscillator and mixing circuit, and an impactor. The digital processing system includes a timer-controller, LED display, and a printer that prints data, time, mass concentration, and mixed crystal frequency.

The aerosol sample is drawn into the 10-μm impactor at a flow rate of 1.0 ℓ/min by a vacuum pump. The impactor removes aerosol particles greater than 10 μm (aerodynamic particle diameter). Particles smaller than 10 μm are carried by the air to an electrostatic precipitator which deposits them onto a mass-sensing piezoelectric crystal oscillating at its natural frequency. The mass of particles on the crystal sensor causes the oscillation frequency to decrease by an amount proportional to the mass of particles. Every 10 seconds, when the instrument is operating in the check mode, the frequency change is detected by a counter and displayed on the digital readout. Every 120 seconds, when the instrument is operating in the measurement mode, the frequency change from the starting frequency is converted by a digital processor to mass concentration in units of $\mu g/m^3$ and displayed on the readout as shown in Figure 2.

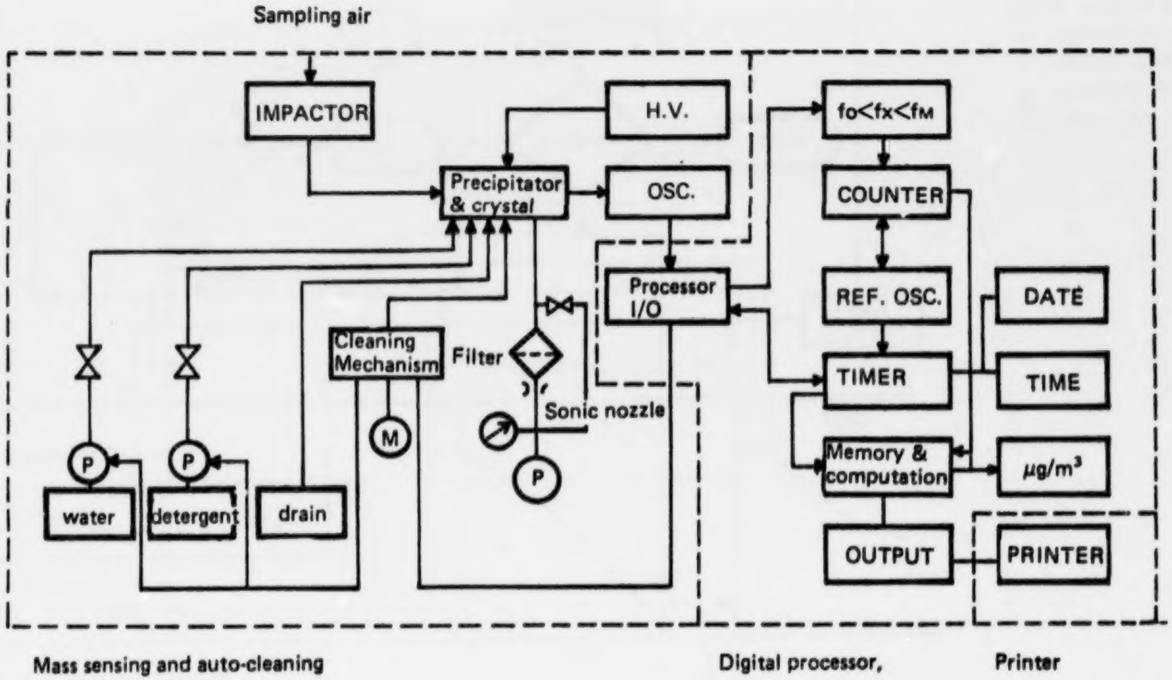
Sampling air
IMPACTOR
H.V.
Precipitator & crystal
OSC.
Processor I/O
fo<fx<fM
COUNTER
REF. OSC.
TIMER
Memory & computation
OUTPUT
DATE
TIME
μg/m³
PRINTER
Cleaning Mechanism
Filter
Sonic nozzle
M
P
water
detergent
drain
Mass sensing and auto-cleaning
Digital processor,
Printer

Figure 1. Schematic diagram of automatic Piezobalance.

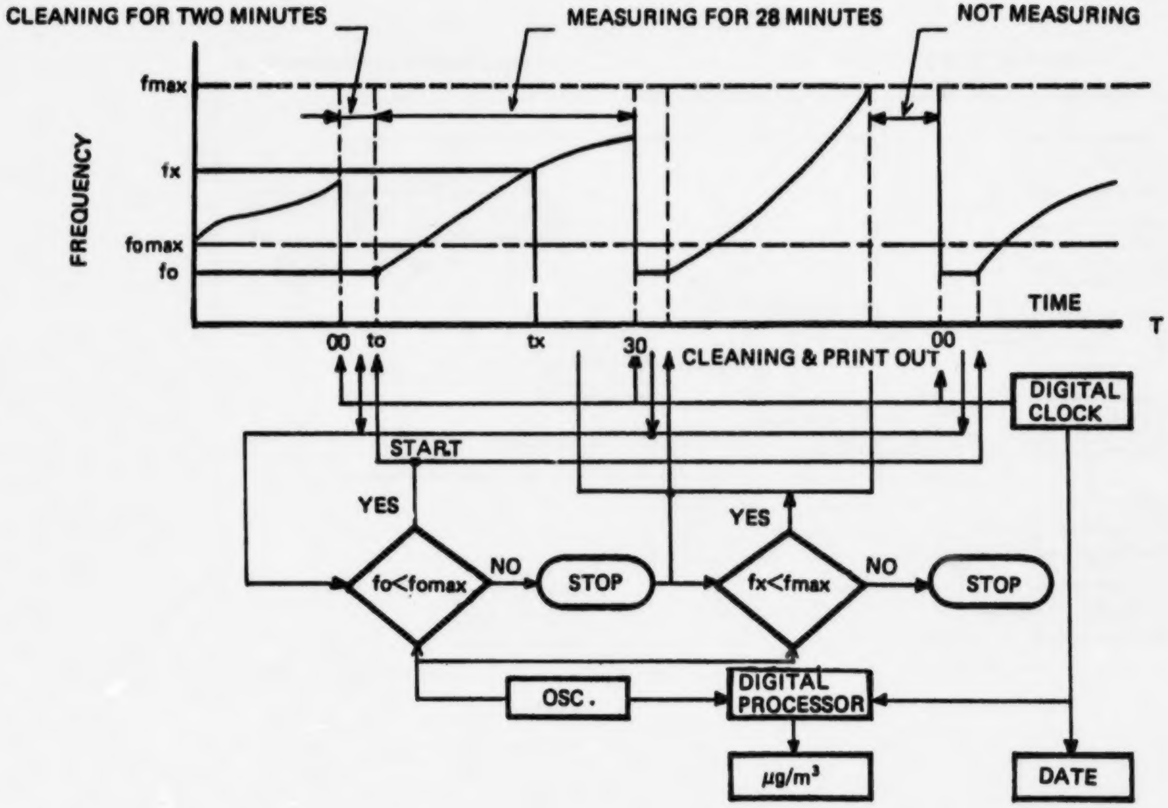
CLEANING FOR TWO MINUTES
MEASURING FOR 28 MINUTES
NOT MEASURING
FREQUENCY
fmax
fx
fomax
fo
TIME
T
00
to
tx
30
00
CLEANING & PRINT OUT
DIGITAL CLOCK
START
YES
fo<fomax
NO
STOP
YES
fx<fmax
NO
STOP
OSC.
DIGITAL PROCESSOR
μg/m³
DATE

$C_i = \alpha(fi - fo)tx$

fi: frequency shift at time tx

fo: starting frequency

α: mass concentration coefficient

$C_{1\text{-}14}$: average concentration in 0-28 min

$C_{2\text{-}14}$: average concentration in 30-58 min

$C_{hr} = (C_{1\text{-}14} + C_{2\text{-}14})/2$

C_{hr} : one hour value in 0-60 min

Figure 2. Measuring system of automatic Piezobalance.

The concentration C_i at each sampling time t_i is expressed by

$$C_i = \frac{(f_i - f_o)}{t_i} \alpha \qquad (1)$$

where

f_i is the frequency at sampling time t_i

f_o is the starting frequency

α is the mass concentration coefficient.

The displayed concentration then is the average value of all 120-second measurements from the start until the end of the sampling time.

After a sampling time of 28 min, a cleaning command signal is emitted. The last 2 min of the 30-min cycle are used for cleaning and drying the crystal sensor.

The one-hour concentration value is the average of the values obtained during the first and the second 30-min periods (28 min and 58 min after $t_i = 0$). The one-hour value is calculated automatically as defined by Equation 2:

$$C_{hr} = (C_{1-14} + C_{2-14})/2 \qquad (2)$$

C_{1-14} is the average concentration during $t_i = 0 - 28$ min

C_{2-14} is the average concentration during $t_i = 30 - 58$ min

C_{hr} is the one-hour value during $t_i = 0 - 60$ min

The time and concentration are printed every 30 minutes.

After the printout, the automatic cleaning cycle begins. The crystal is first washed with a detergent, then rinsed and dried. After 2 min, the crystal is dry and measurement begins automatically.

When something goes wrong during a measurement cycle, such as loss of precipitator current, an alarm lamp turns on and the instrument automatically stops the measurement to avoid recording erroneous values.

CALIBRATION

The crystal mass concentration coefficient, α, in Equation 1 could be calculated precisely from the basic theory of piezoelectricity if we assume ideal particle collection and sensing efficiency and if the particles are assumed to be deposited uniformly over the entire vibrating surface of the crystal.[1,2] However, the automatic piezobalance requires experimental calibration for an accurate determination of the coefficient α for the following reasons:

1) Aerosol particles are not deposited in a uniform layer over the entire electrode, making the mass sensitivity and particulate deposition profiles important.

2) Particle collection and sensing efficiencies, though repeatable, are not precisely known for each instrument, each precipitator needle, or each type of airborne particle.

3) The shape and size of the crystal electrode and the thickness of the crystal are not precisely known for a given sensor.

Therefore, we have set up a calibration procedure to experimentally determine the value of α for a standard aerosol similar to outdoor airborne particles. Figures 3 and 4 show the systems used to calibrate the automatic piezobalances with smoke, KCl, and $PbCl_2$ aerosols.[2,3] The basic technique is to adjust the piezobalance sensitivity until its concentration measurements agree with low volume filter concentration measurements while both are sampling from a common aerosol source.

The aerosol used for calibration is drawn through an impactor, usually with 10-μm cut size, and into a manifold where the aerosol is mixed and electrostatically neutralized. Several automatic piezobalances and two low-volume filter samplers, arranged nearly symmetrically around the manifold, sample simultaneously from the manifold. No significant variation has been found between sampling ports. The automatic piezobalance flow rate (1.0 ℓ/min) is maintained constant by its pump. The low-volume filter flow rate (15 ℓ/min) is continuously monitored by the operator and maintained constant by manual adjustment. The 47-mm filters in the low-volume sampling systems are either silver membrane or glass fiber filters in a tight filter holder. The filter material does not gain or lose significant weight as the relative humidity changes. Since the particles deposited on the filter usually do gain or lose moisture as relative humidity changes, the filters are weighed immediately after the sampling period at the existing relative humidity in the sampling room. The weighing uncertainty of the gravimetric microbalance is about ±5 μg. The sample period is 0.5 - 2.0 hr, collecting approximately 100 - 3000 μg of particles on each filter. The average of the automatic piezobalance measurements, made once every 2 minutes throughout each filter sample, is then compared with the corresponding low-volume filter measurements.

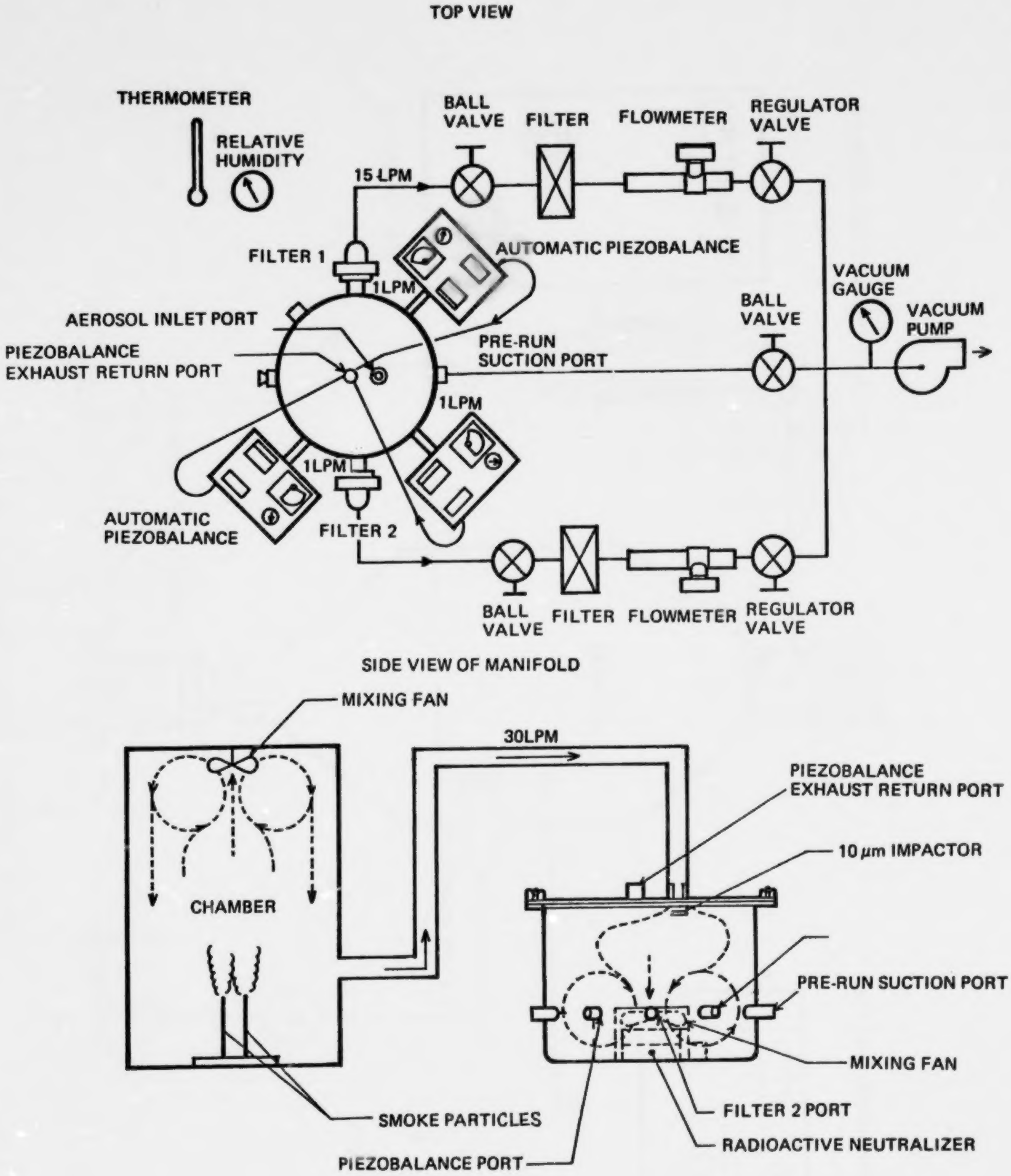
TOP VIEW
THERMOMETER
RELATIVE HUMIDITY
BALL VALVE
FILTER
FLOWMETER
REGULATOR VALVE
15 LPM
FILTER 1
AUTOMATIC PIEZOBALANCE
1LPM
VACUUM GAUGE
AEROSOL INLET PORT
BALL VALVE
VACUUM PUMP
PIEZOBALANCE EXHAUST RETURN PORT
PRE-RUN SUCTION PORT
1LPM
1LPM
AUTOMATIC PIEZOBALANCE
FILTER 2
BALL VALVE
FILTER
FLOWMETER
REGULATOR VALVE
SIDE VIEW OF MANIFOLD
MIXING FAN
30LPM
PIEZOBALANCE EXHAUST RETURN PORT
10 μm IMPACTOR
CHAMBER
PRE-RUN SUCTION PORT
MIXING FAN
FILTER 2 PORT
SMOKE PARTICLES
RADIOACTIVE NEUTRALIZER
PIEZOBALANCE PORT

Figure 3. Calibration system of Piezobalance by smoke particles.

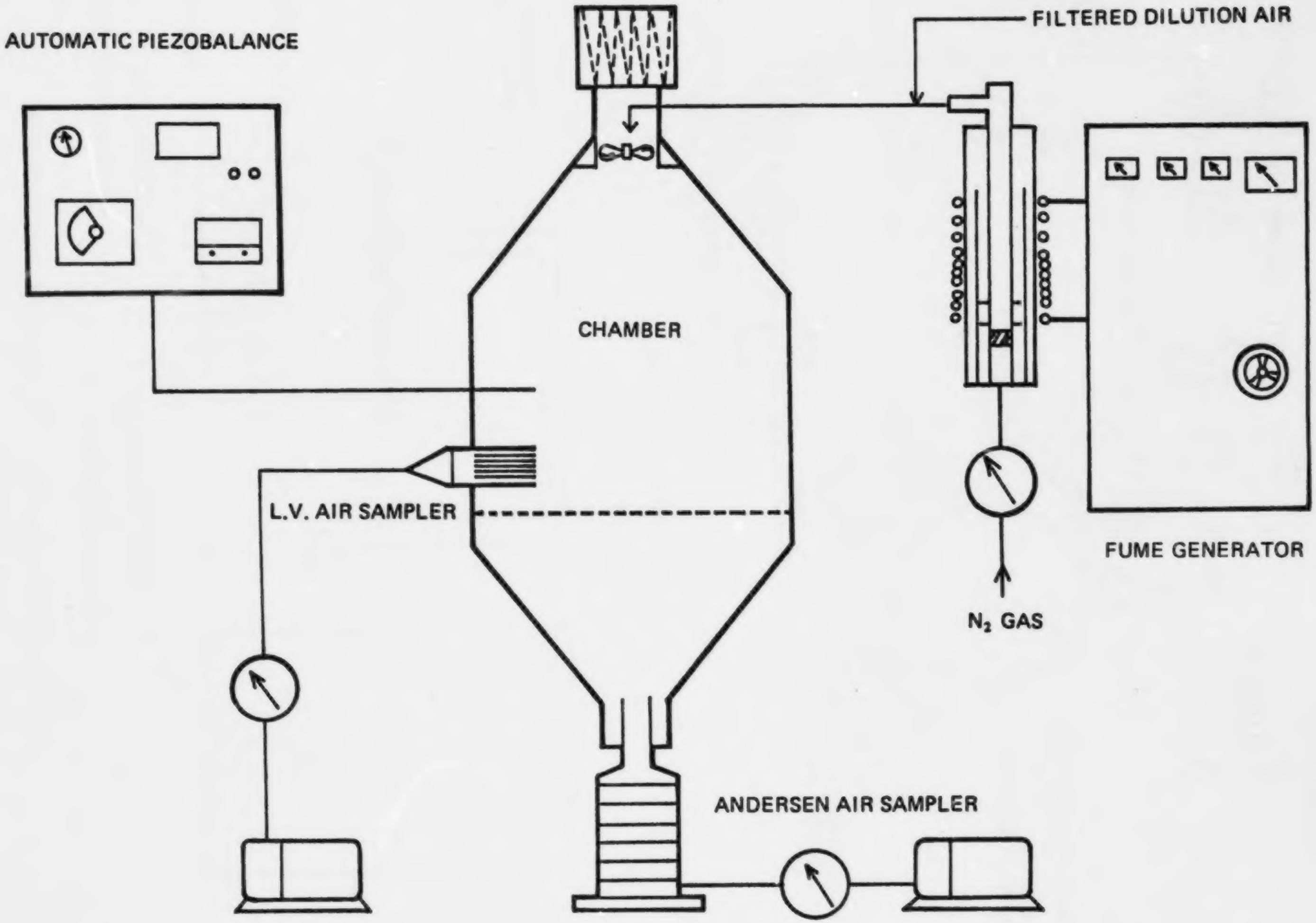
AUTOMATIC PIEZOBALANCE
FILTERED DILUTION AIR
CHAMBER
L.V. AIR SAMPLER
FUME GENERATOR
N_2 GAS
ANDERSEN AIR SAMPLER

Figure 4. Calibration system of Piezobalance by fume aerosols.

Figures 5 and 6 show the result of mass sensitivity calibrations obtained using the system shown in Figures 3 and 4.

Figures 5 and 6 show that the experimental sensitivity α for the tested aerosol is within ± 10% of the theoretical value calculated by assuming ideal particle collection, deposition, and sensing. The data also show good linearity up to concentrations at least as high as 1500 μg/m³.

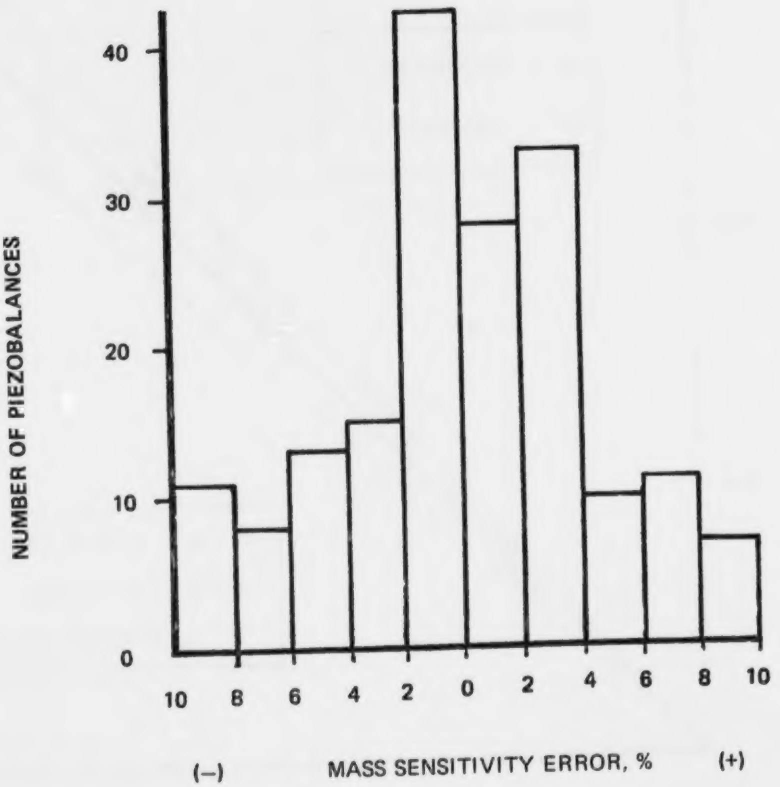

Figure 5. Experimental result of mass sensitivity test.

FIELD TESTING

After finishing the sensitivity calibrations in the laboratory, a pair of automatic piezobalances with mass concentration coefficients adjusted to the theoretical sensitivity (180 Hz/µg) were tested at two local pollution monitoring stations in Japan. The main purposes of the field test were:

1) To evaluate the variation in measurements between two automatic piezobalances for one-hour values and 24-hour averaged values.

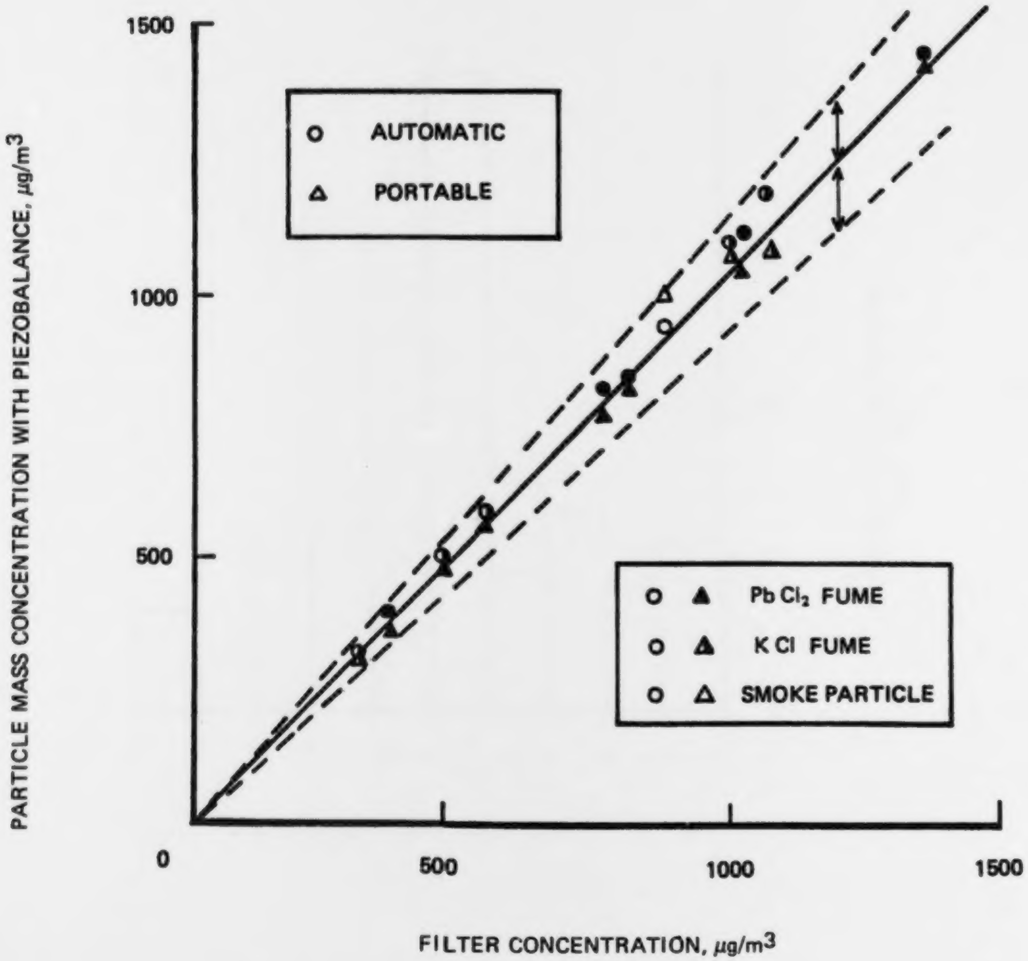

Figure 6. Experimental result of mass sensitivity calibration.

2) To evaluate the correlation between the mass concentration measured by LV method and the concentration measured by automatic piezobalances.

3) To evaluate possible variations in sensitivity for particles at each local pollution monitoring station.

4) To evaluate the resolution necessary to accurately measure mass concentration, within a one-hour period.

5) To evaluate the effects of atmospheric conditions, especially relative humidity.

Figure 7 shows the experimental setup for the automatic piezobalances at the pollution monitoring station. Two automatic piezobalances were placed in the measuring room beside other pollution measuring instruments, i.e., SO_2 monitors, NO_x monitors, light scattering dust meters, etc. Two low-volume samplers were set on the roof of the measuring room near the inlet of the air sampling manifold.

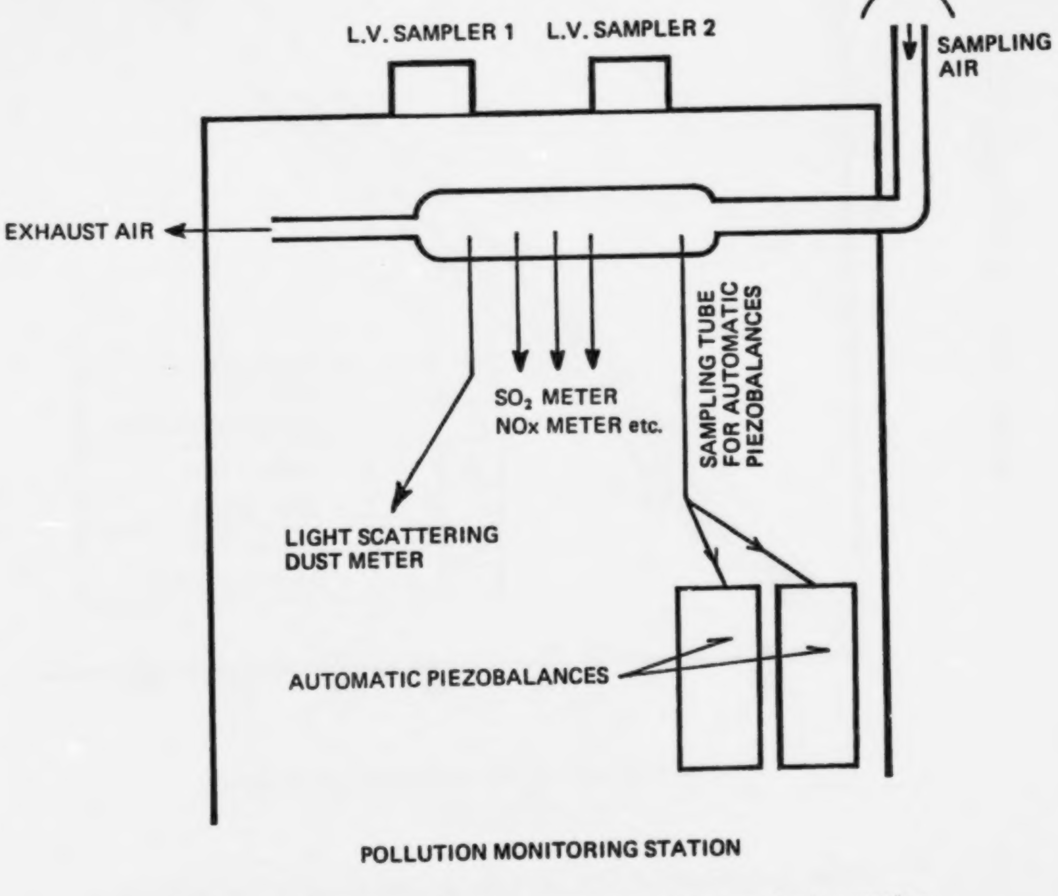
L.V. SAMPLER 1
L.V. SAMPLER 2
SAMPLING AIR
EXHAUST AIR
SAMPLING TUBE FOR AUTOMATIC PIEZOBALANCES
SO₂ METER
NOx METER etc.
LIGHT SCATTERING DUST METER
AUTOMATIC PIEZOBALANCES
POLLUTION MONITORING STATION

Figure 7. Experimental set up at the pollution monitoring station.

Airborne particles were sampled at a flow rate of approximately 150 ℓ/min. The inlet of the air sampling manifold was located more than 10 m above ground level. The air velocity at the sampling points to all the instruments was about 0.5 m/s. Polyethylene tubing with 0.375-inch I.D. carried the sampled air between the manifold and the automatic piezobalances. A branch fitting near the automatic piezobalances split the air sample to the instruments.

The experimental results are shown in Figures 8, 9, and 10. Figure 8 is the correlation between LV measurements, which sampled the air for two or three days, and the average automatic piezobalance value for the corresponding sampling time. Figure 8 shows that the correlation coefficient is greater than 0.9 at every monitoring station. It also shows that the theoretical sensitivity coefficient (180 Hz/μg) used for all instruments was valid within ± 20% at every monitoring station.

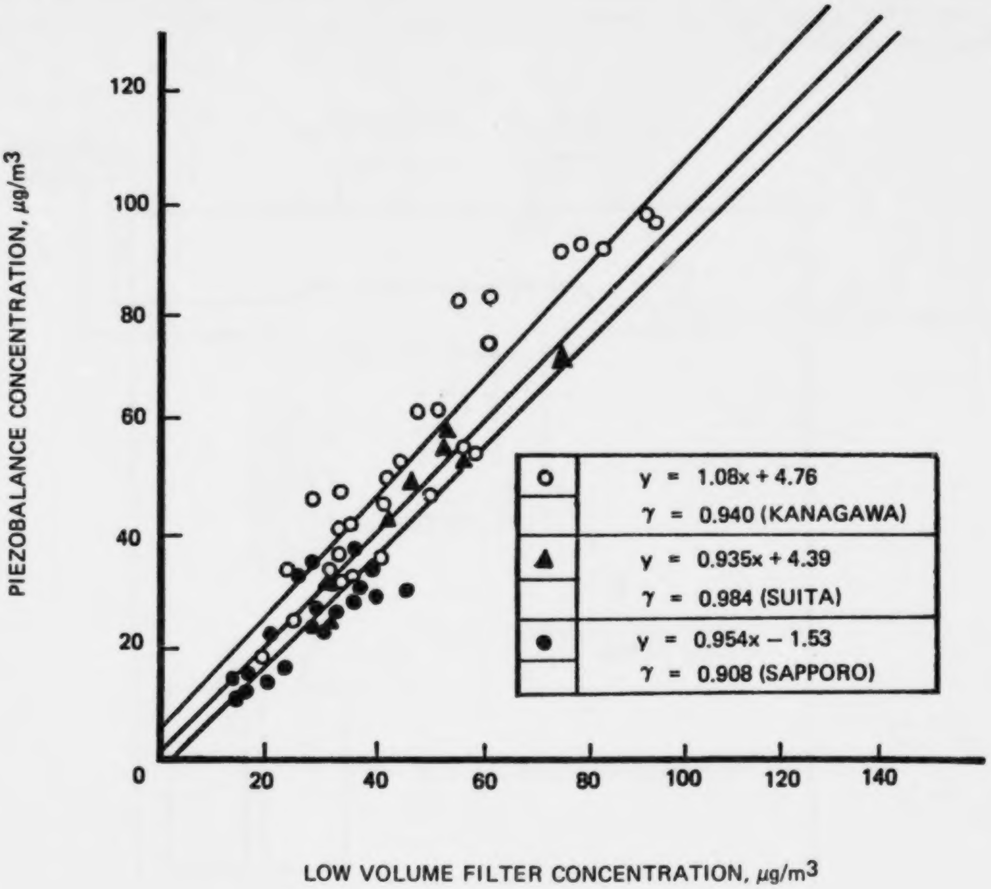

Figure 8. Comparison of L. V. filter and Piezobalance concentrations.

Figures 9 and 10 show the relationship between two automatic piezobalances for 24-hour averaged values and one-hour measurements, respectively. The indicated difference between two automatic piezobalances was ± 5 $\mu g/m^3$ ± 10% of measured value for one-hour measurements and ± 5 $\mu g/m^3$ ± 5% for 24-hour averaged values. The data also shows that the automatic piezobalance has high resolution, better than 10 $\mu g/m^3$, for one-hour mass concentration measurements of ambient atmospheric aerosol in actual field situations.

Daley et al.[4] have investigated experimentally the effect of humidity changes on the indicated mass deposit for several

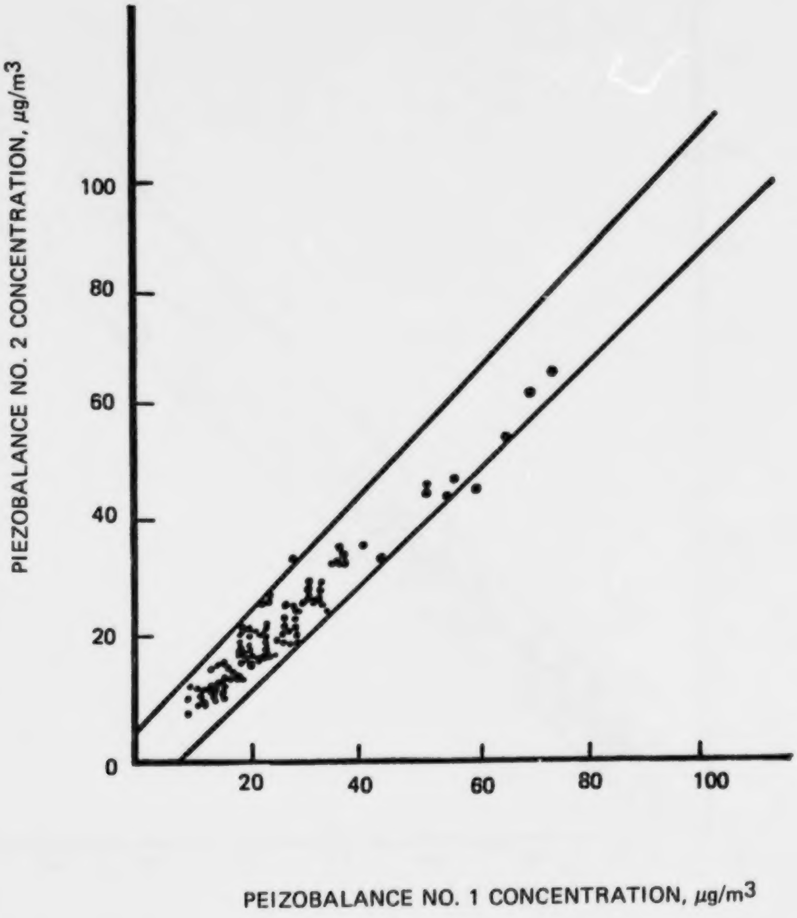

Figure 9. Comparison of two automatic Piezobalances for 24 hour averaged values.

aerosol particles. Figure 11 shows the experimental setup for measuring the humidity effects at the field testing stations. A diffusion aerosol dryer, which can reduce humidity from 80% to 40% RH, was installed at the inlet of one of the automatic piezobalances. Measurements were made at 24 to 35°C, 70 to 92% RH. The results of the experiment are plotted in Figure 12. As shown, in the concentration range below 60 μg/m³, there is no significant difference between the two automatic piezobalance indications. However, at concentrations greater than 60 μg/m³, the indication of the automatic piezobalance without the dryer increases compared with the automatic piezobalance with the dryer.

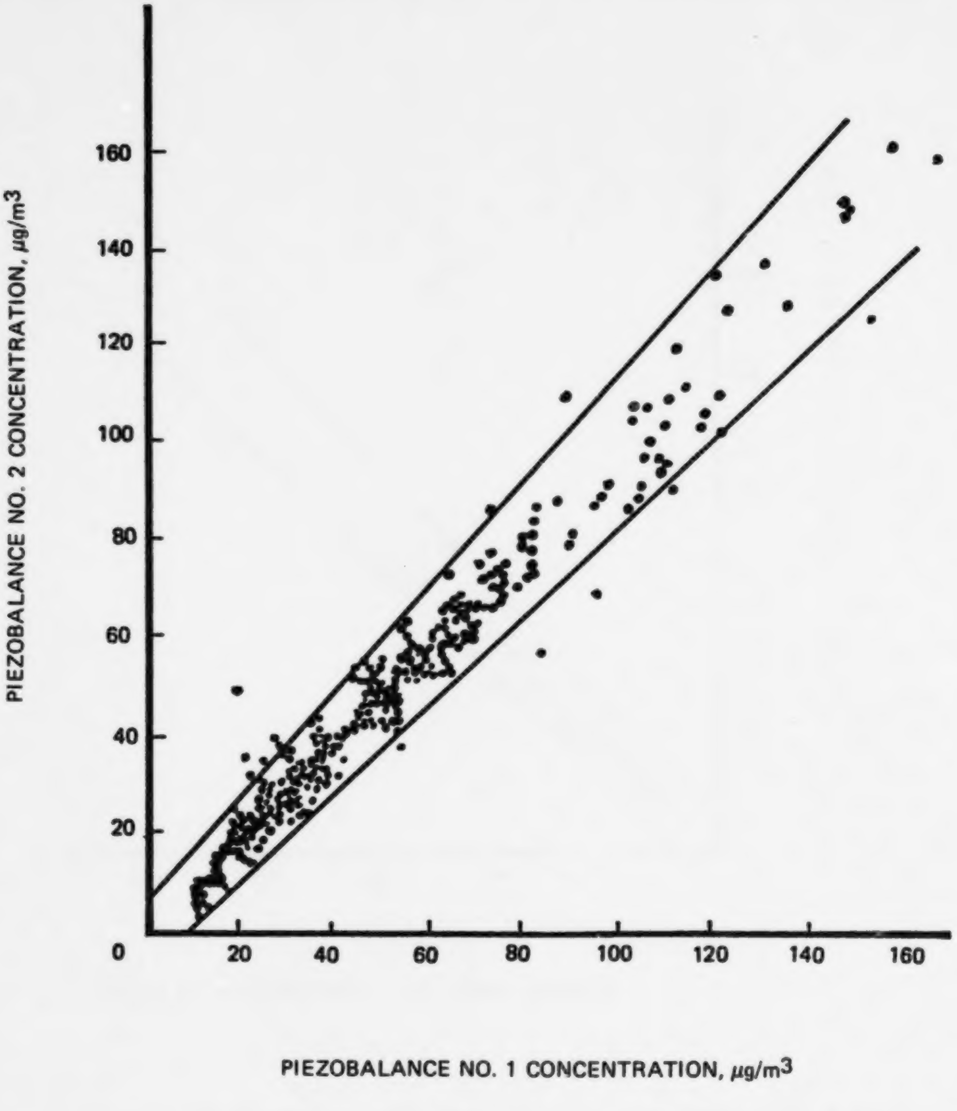

Figure 10. Comparison of two automatic Piezobalances for one hour measurements.

CONSIDERATION OF THE SAMPLING SYSTEM

The automatic piezobalance was designed for stationary operation at fixed pollution monitoring stations.[5-7] It has a sampling flow rate of 1.0 ℓ/min. For the airborne particle measurements, we must carefully design the sampling system to avoid wind-induced losses near the inlet of the sampling tube and to minimize wall losses in the sampling tube.

Figure 7 shows one of the most common sampling systems used at monitoring stations in Japan. In this case, it is necessary to use the shortest possible length of horizontal sampling tube between the sampling manifold and the instruments to avoid the above mentioned particle losses.

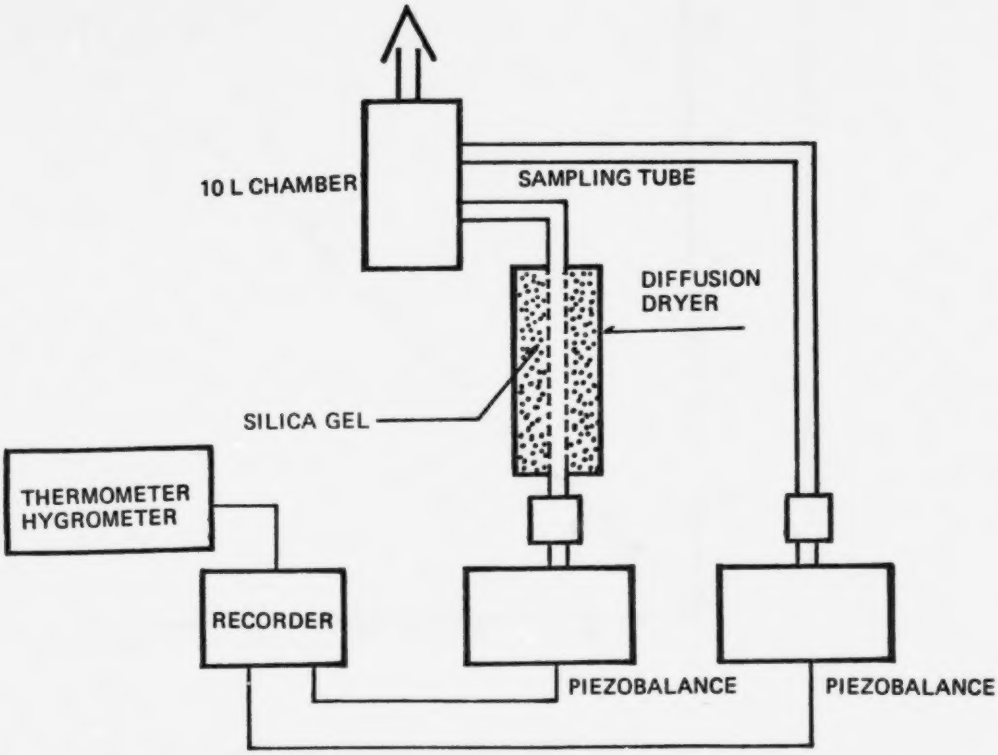
10 L CHAMBER
SAMPLING TUBE
DIFFUSION DRYER
SILICA GEL
THERMOMETER HYGROMETER
RECORDER
PIEZOBALANCE
PIEZOBALANCE

Figure 11. Experimental set-up to check the effect of humidity.

Figure 13 shows the relationship between the horizontal length of sampling tube in centimeters and the particle deposition rate in percent. The calculation was made for a flow rate of 2 ℓ/min with 1/2-in. I.D. tubing for various particle diameters (in micrometers) using an equation described by Pich.[8]

During the field tests, especially on windy days, there was a large difference between LV measurements and automatic piezobalance measurements. Deposition losses in the sampling tube can account for these observed differences.

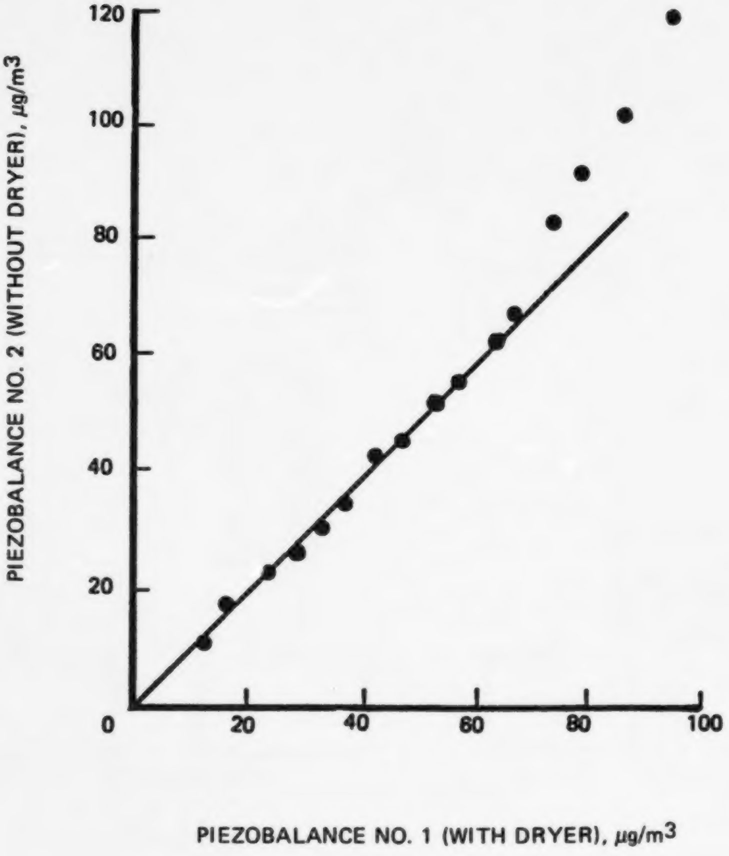

Figure 12. Effect of humidity on Piezobalance.

Figure 14 is a schematic diagram of the isokinetic total and respirable particle sampler (Isokinetic TR Sampler). This sampler was designed to avoid the losses noted above. The sampler consists of a sampling nozzle; an impactor which can deposit large particles on a filter for weighing; a filter holder with a hole in the center to allow part of the respirable particles to collect on the filter and part of the same sample to be directed to the automatic piezobalance.

This sampler can also be used for dynamic calibration to measure precisely the mass concentration coefficient for actual airborne particles at any monitoring location. Figure 15 shows a dynamic calibration setup using this sampler. As shown in the figure, one can supply test aerosol to the TR Sampler and automatic piezobalances either from a standard particle generator or from outdoor air. Figure 16 shows the data for a dynamic calibration with a particle generator. The data show a very high correlation between LV measurements and the measurements made with the automatic piezobalances.

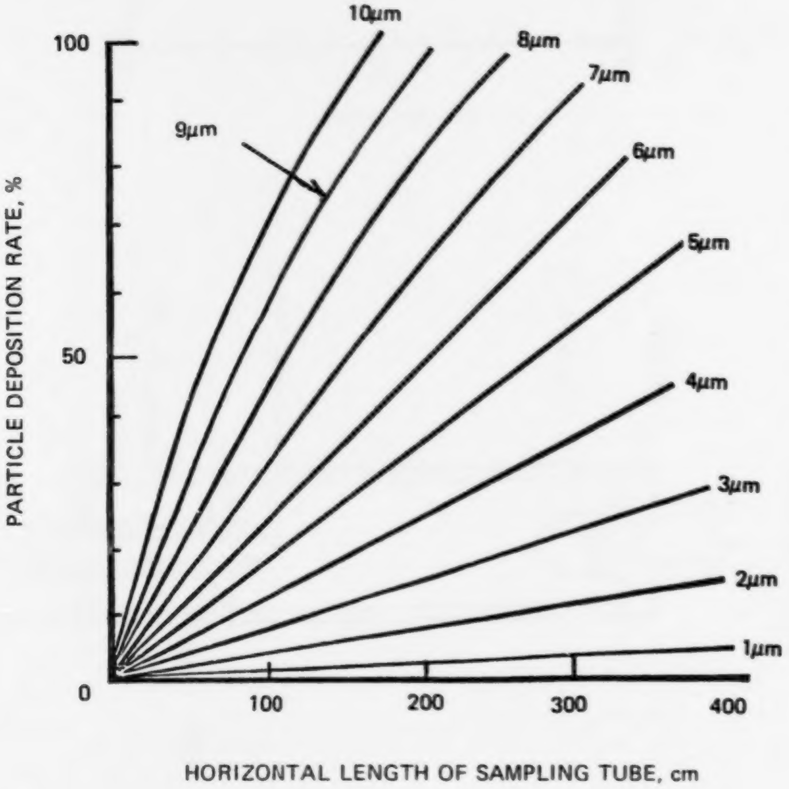

Figure 13. Relationship between tube length and particle deposition rate.

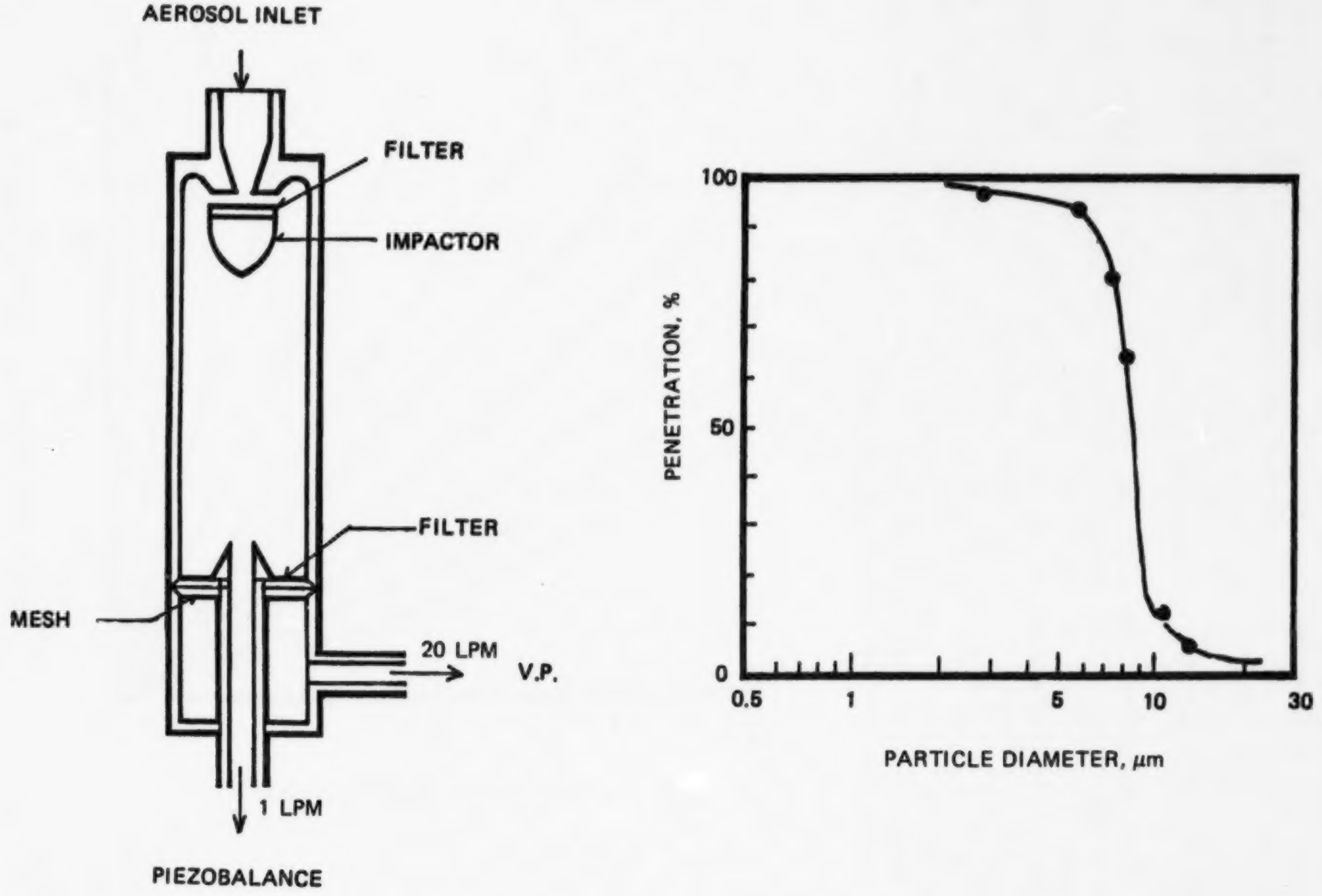
AEROSOL INLET
FILTER
IMPACTOR
FILTER
MESH
20 LPM
V.P.
1 LPM
PIEZOBALANCE
PENETRATION, %
100
50
0
0.5
1
5
10
30
PARTICLE DIAMETER, μm

Figure 14. Schematic diagram of Isokinetic TR Sampler.

OTHER APPLICATIONS

When studying hazardous effects to the human body caused by respirable particles and controlling the source of these aerosol pollutants, it is becoming more important to measure the mass concentration and size distribution of airborne particles smaller than 10 μm. At present, it takes one to two weeks to get enough samples in certain size ranges to accurately weigh using an inertial sampler such as a cascade impactor.[9]

An automatic piezobalance can make near real-time measurements of the mass concentration within size ranges determined by an inertial sampler. The experimental setup for measuring the real-time mass concentration as a function of particle size is shown in Figure 17. An Andersen ambient air sampler, modified by making a sampling hole in the side wall of each stage, was used for sizing the particles. Airborne particles were sampled by the automatic piezobalance through the side wall sampling tube at each stage of the Andersen sampler at a flow rate of 1.0 ℓ/min.

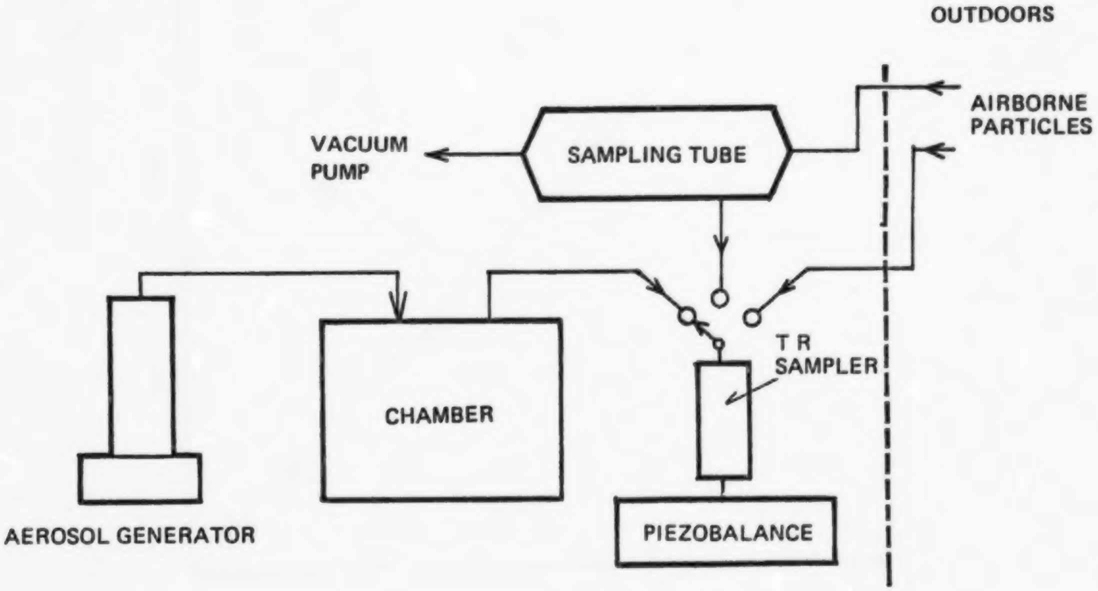

Figure 15. Dynamic calibration set-up using TR Sampler.

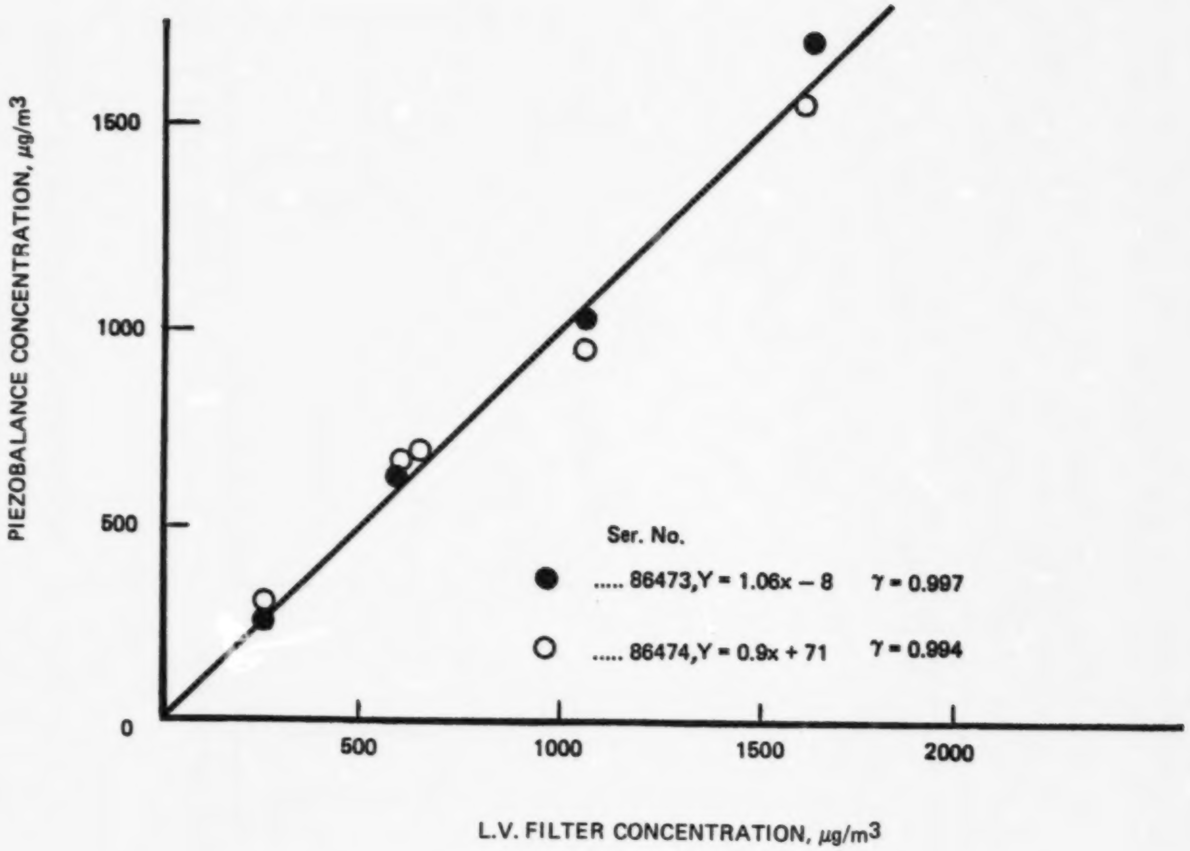

Figure 16. Dynamic calibration result with particle generator.

Before the experiment, the cut-off characteristics of each stage of the Andersen sampler were tested using 0.5 to 16 μm oleic acid particles generated by a vibrating orifice monodisperse generator and the concentration was measured using a piezobalance portable aerosol monitor. Figure 18 shows that experimental results agree well with the designed penetration characteristics.

Figure 19 shows mass concentration measurements made both by the automatic piezobalance/Andersen sampler system and by weighing the loaded filter from each stage of an Andersen sampler after one week of sampling. We did not find evidence of a bimodal size distribution in this experiment, but we did obtain similar results using the Andersen sample and the automatic piezobalance system.

The ratio of coarse to fine particles is shown in Figure 20 for a three-day period. This ratio can be very easily measured in real time by the combination of the modified Andersen sampler and automatic piezobalance.

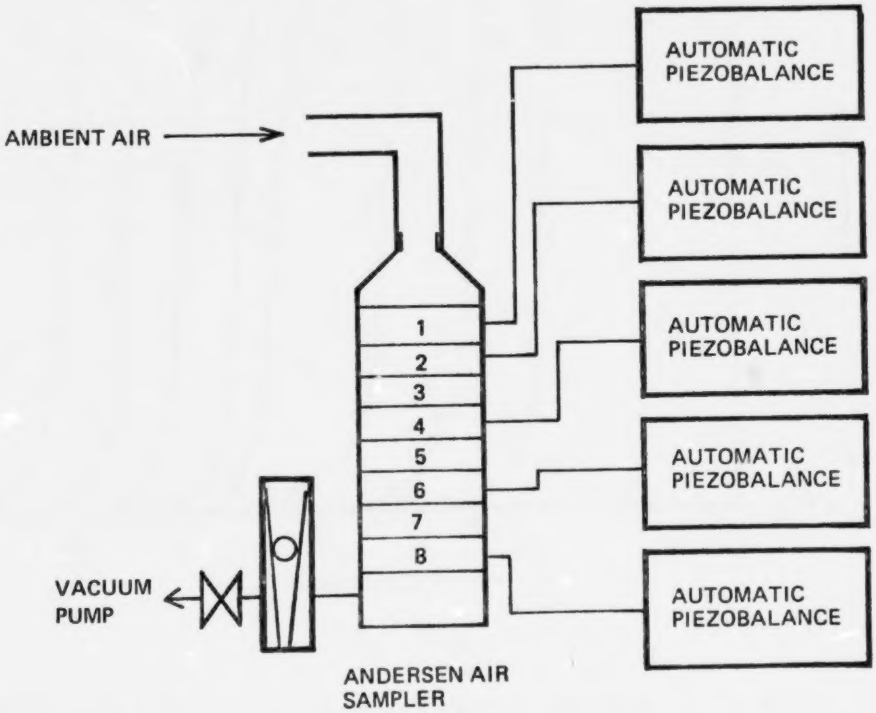
AMBIENT AIR
AUTOMATIC PIEZOBALANCE
AUTOMATIC PIEZOBALANCE
AUTOMATIC PIEZOBALANCE
AUTOMATIC PIEZOBALANCE
AUTOMATIC PIEZOBALANCE
1
2
3
4
5
6
7
8
VACUUM PUMP
ANDERSEN AIR SAMPLER

Figure 17. Experimental set-up for measuring the real-time sized particle mass concentration.

SUMMARY

Field testing data for measuring the mass concentration of airborne particles and a newly-developed application of the automatic piezobalance have been described. A summary of the results is as follows:

1) The automatic piezobalance can measure one-hour values of mass concentration within ± 20%, as compared with LV measurements.

2) The automatic piezobalance can operate for over one week without maintenance.

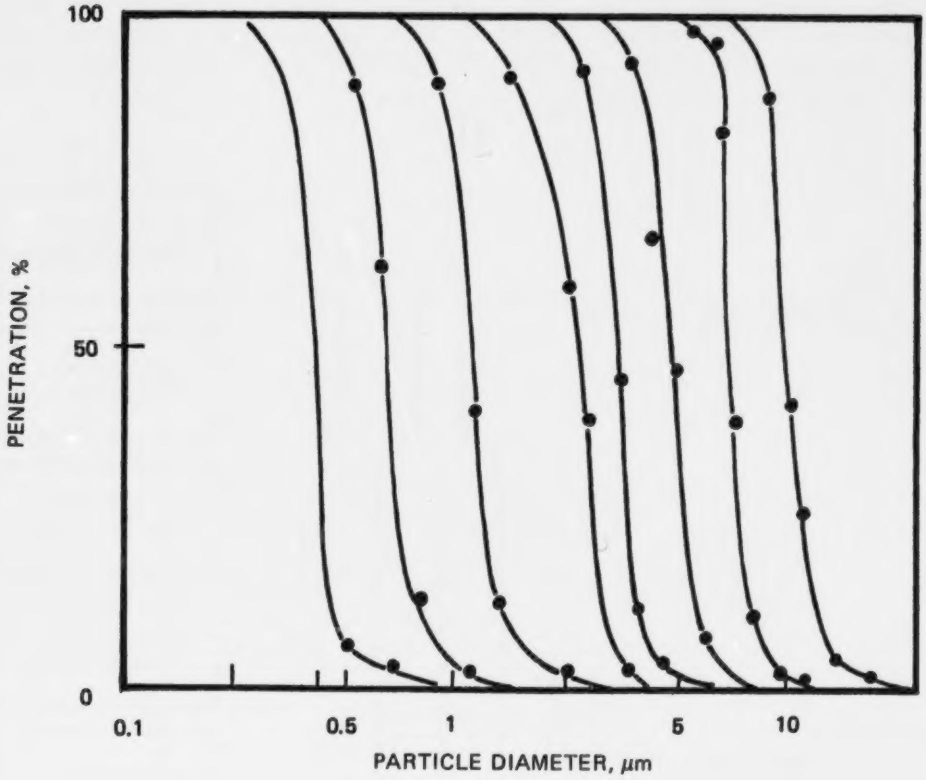

Figure 18. Penetration efficiency characteristics of Andersen air sampler.

3) A newly developed isokinetic total and respirable sampler is useful for making dynamic calibrations under field conditions and also for minimizing wind effects and wall losses of particles in sampling tubes.

4) The real-time measurement of mass concentration by size, in the 0.5 to 20 μm range, can be easily made using a modified Andersen ambient air sampler and an automatic piezobalance.

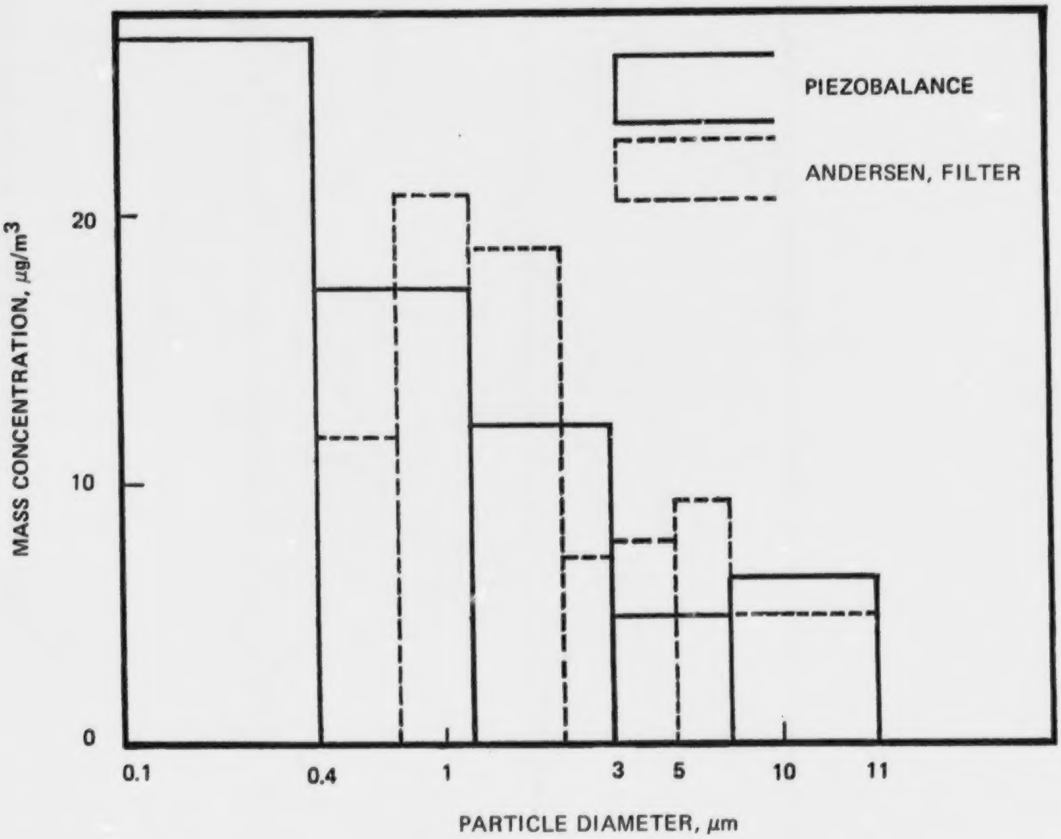

Figure 19. Size distribution measurements of airborne particles.

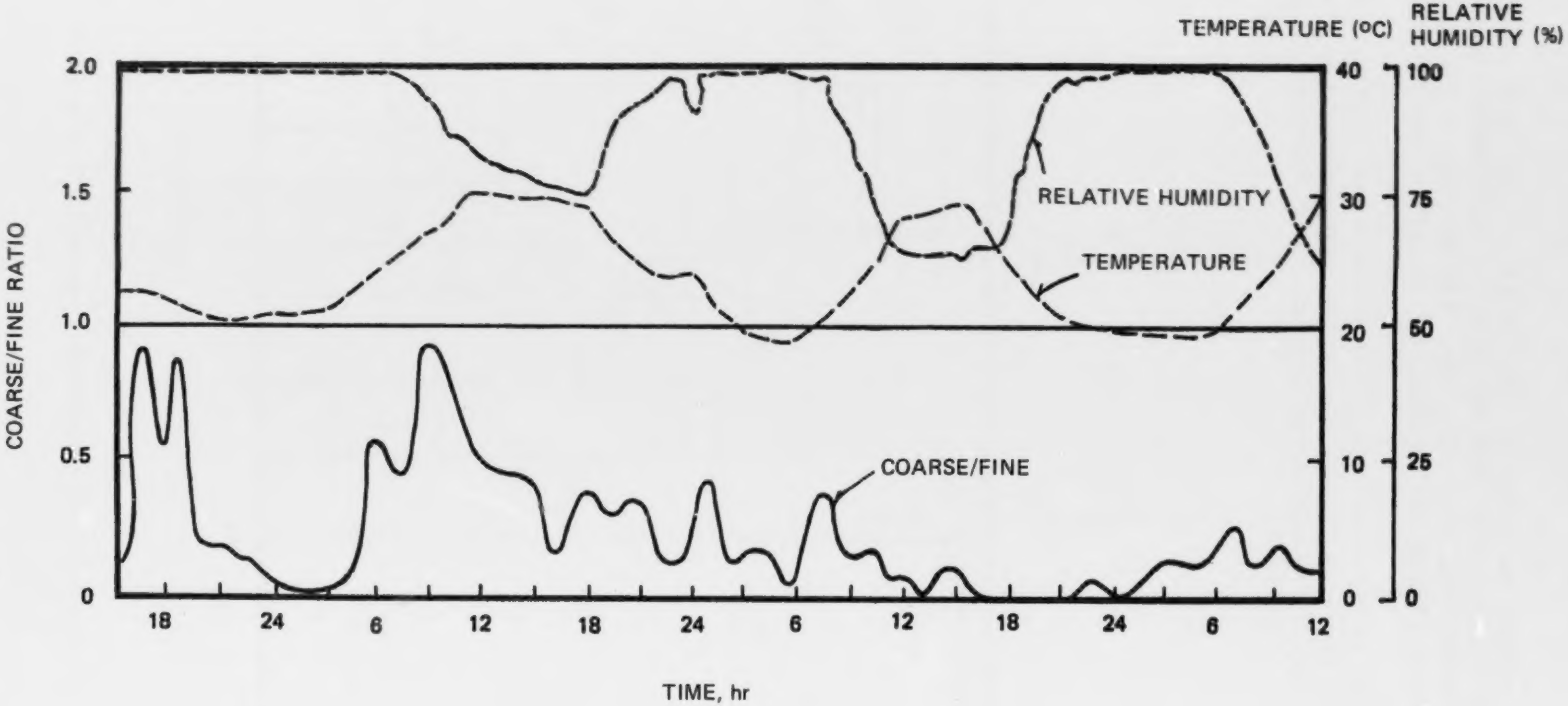

Figure 20. *Result of the real time measurements of the coarse/fine ratio by Andersen sampler and automatic Piezobalance.*

REFERENCES

1. Sem, G.J., and K. Tsurubayashi. A New Mass Sensor for Respirable Dust Measurement. Am. Ind. Hyg. Assoc. J. 36:791, 1975.

2. Sem, G.J., K. Tsurubayashi, and K. Homma. Performance of the Piezoelectric Microbalance Respirable Aerosol Sensor. Am. Ind. Hyg. Assoc. J. 38:580, 1977.

3. Homma, K. Calibration Method of Mass Sensitivity for Airborne Particle Mass Monitor. Japan Soc. Air Pollut., 1978.

4. Daley, P.S. The Use of Piezoelectric Crystals in the Determination of Particulate Mass Concentration in Air. Ph.D. Thesis, University of Florida, Gainesville, 1974.

5. Tsurubayashi, K., K. Homma, et al. On the Piezobalance Airborne Dust Meter. Japan Soc. Air Pollut., 1976.

6. Tsurubayashi, K., et al. Measurement of Airborne Particulate Mass Concentration by Automatic Piezobalance Dust Monitor. Japan Soc. Air Pollut., 1977.

7. Tsurubayashi, K. Measurement of Airborne Particulate Mass Concentration by Automatic Piezobalance. Japan Soc. Air Pollut., 1978.

8. Pich, J. Theory of Aerosol Filtration. In: Aerosol Science, C.N. Davies, ed. Academic Press, London, 1966.

9. Tsurubayashi, K. The Real-Time Measurement of Airborne Particulate Mass Concentration by Sizing. Japan Soc. Air Pollut., 1978.

PAPER 14

A NEW REAL-TIME ISOKINETIC DUST MASS MONITORING SYSTEM

JAMES C.F. WANG
COMBUSTION RESEARCH DIVISION
SANDIA LABORATORIES, LIVERMORE

ABSTRACT

A new real-time dust mass monitor is being developed by combining an automatic isokinetic sampling probe with a tapered-element oscillating microbalance (TEOM). Particulates from a stack are sampled on line through the isokinetic sampler and collected on an astroquartz mat filter of the TEOM detector. The filter is originally excited and oscillated at a low frequency (about 200 Hz). As the particulates deposit on the filter, the mass increase of the filter is reflected in a frequency reduction which is measured in real time and yields directly the collected particulate mass. The TEOM detector normally has a high mass resolution (10^{-9} g) and wide dynamic range (10^{5} - 10^{6}). It has been desensitized for high particulate loading applications. The integrated monitoring system was tested in a room-temperature wind-tunnel flow with externally injected particulates. Good agreement was obtained between the mass collected through the isokinetic sampling system and the weight loss of the dust feeder in real time.

INTRODUCTION

Particulate emission control is one of the most challenging tasks in the development of advanced fossil-fuel combustion systems. Size distribution, dust loading density, and other critical physical and chemical properties of particulates in the effluents of combustors and their associated cleanup equipment comprise the key information needed for this development.[1] However, there has been a lack of accurate and real-time particulate diagnostic techniques for the effluents from advanced power systems. This has prevented efficient evaluations of the performance of combustors and cleanup equipment and has made it difficult to develop components in the advanced power systems to meet environmental regulations and gas turbine product specifications. There is thus an urgent need for appropriate particulate diagnostic instruments, especially those with capabilities of nonintrusive, in-situ, and real-time monitoring. The difficulties which challenge the instrument designers originate from the hostile environment of most advanced fossil-fuel combustion systems.

Conventional techniques used in industry and utility companies to characterize the effluents from their boilers or furnaces require sample withdrawal by a physical probe with subsequent dilution and/or cooling. Insertion of the probe into the flow may have significant effects on the flow field in the vicinity of the probe.[2] Dilution and/or cooling of the sample during extraction may induce substantial particle size change in the sample due to agglomeration and condensation of gaseous species. Furthermore, analysis of the particulates collected is usually performed off-line and may be biased or dubious because of difficulties associated with redispersion of the particulates in the analyzer.

The physical sampling method is, however, the only means of providing samples of particulates for detailed analyses of their physical and chemical properties. The lack of reliable and unbiased physical sampling probes for high-temperature, high-pressure fossil-fuel combustion environments causes uncertainties in evaluation and modification of the combustors and cleanup equipment. An automatic, relatively nonintrusive sampling system is being developed at Sandia Laboratories as the first step toward the development of a reliable and unbiased physical sampling system. An on-line mass detector is also being developed to couple with the isokinetic probe to obtain real-time dust loading measurements.

ISOKINETIC SAMPLING SYSTEM

The process of physically extracting a sample from a flow system inherently disturbs the properties being measured. One of the major sources of error in sampling is the discrimination error of particle size due to the probe intrusion in the sampled flow (aerodynamic error). If the sampling velocity is greater than the undisturbed flow velocity due to heavy suction, smaller particles are extracted preferentially since they follow the gas stream lines more readily. On the other hand, if the flow must decelerate on entering the probe, the larger particles continue moving into the probe as a result of their inertia, thus increasing their concentration. If the sampling velocity is matched to the free-stream velocity, i.e., isokinetic sampling, the size distribution and mass loading density in the sampled stream are preserved.

The magnitude of sampling errors from anisokinetic sampling has demonstrated the necessity of well-characterized sampling conditions, especially for particles in the range of 0.5 to 100 μm in diameter.[3] In practice there can be uncertainty in obtaining true isokinetic sampling conditions. A common method of isokinetic sampling involves measuring and matching volumetric flow rates of the probe and the free stream. This necessitates measurements of pressure and temperature at the probe inlet. For fossil-fuel combustor exhaust flows, where velocity, temperature, and pressure fluctuate, it becomes difficult to follow these variations and maintain the isokinetic sampling condition. A second method is to match the static pressures at the probe inlet and in the free stream.[4] The isokinetic sampling condition can easily be achieved by nulling the difference between the two static pressures via a throttling valve which controls the sampling flow rate. An automatic isokinetic sampling system has been developed employing an electromagnetic control valve based on the "null" principle.[5] However, an automatic backflush mechanism should then be built into the sampling system to prevent the static pressure sensors from becoming plugged in the high dust loading environments commonly encountered in advanced power systems.[6]

The automatic sampling system developed at Sandia Laboratories consists of (1) a sampling probe, (2) two static pressure sensors, (3) an isokinetic sampling controller, (4) a throttling control valve, and (5) a flow meter. Figure 1 shows the schematic of the sampling system. The sampling probe is made of 6.35-mm O.D. and 4.45-mm I.D. stainless steel tubing and is shown schematically in Figure 2. The sampled-flow static pressure tap holes are located in the sampling nozzle wall at about six nozzle diameters downstream from the nozzle tip. The free-stream static pressure sensors are on a 3.175-mm O.D. stainless steel tube placed above and parallel to the sampling nozzle. This sampling nozzle and sensors configuration was demonstrated successfully in pressurized fluidized bed exhaust environments.[7] The two static sensors are connected to each side of the Validyne differential pressure transducer via 3.175-mm O.D. stainless tubes. The pressure transducer is protected by shunt tubing via a solenoid valve which is open during the backflush process. The shunt is also used to zero the pressure transducer before each sampling operation.

The isokinetic sampling controller is presently simulated by using a PDP11-34 minicomputer. A hardwired electronic controller will be built after the system response from each component is identified. As shown in Figure 1, the output from the Validyne differential pressure transducer is measured on a Validyne Model-CD12 indicator. The output from the indicator is then input to the minicomputer through an A/D converter. The computer sends a control signal to the electromagnetic throttling control valve to increase or decrease the sampling flow depending on the input from the indicator. A zero input from the indicator corresponds to the isokinetic sampling condition; thus no action is applied to the throttling valve.

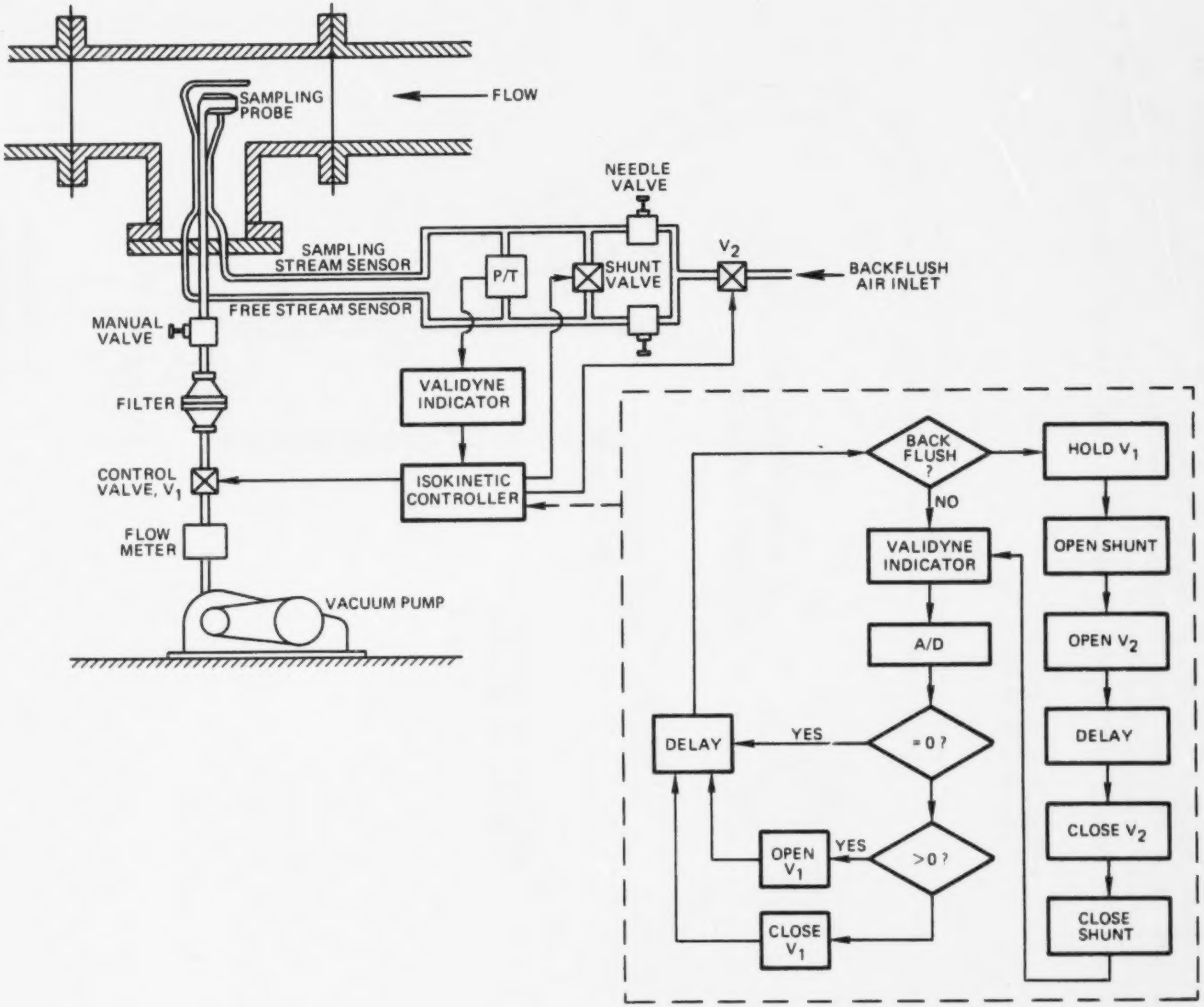
SAMPLING PROBE
FLOW
NEEDLE VALVE
SAMPLING STREAM SENSOR
FREE STREAM SENSOR
P/T
SHUNT VALVE
V_2
BACKFLUSH AIR INLET
MANUAL VALVE
FILTER
CONTROL VALVE, V_1
FLOW METER
VACUUM PUMP
VALIDYNE INDICATOR
ISOKINETIC CONTROLLER
BACK FLUSH ?
NO
HOLD V_1
OPEN SHUNT
OPEN V_2
DELAY
CLOSE V_2
CLOSE SHUNT
VALIDYNE INDICATOR
A/D
= 0 ?
YES
DELAY
> 0 ?
YES
OPEN V_1
CLOSE V_1

Figure 1. *Automatic isokinetic sampling system.*

The static pressure sensors are periodically backflushed with dry nitrogen to prevent blockage of the tap holes. During the backflush, the gas flow in the sensing line may produce an erroneous signal to the pressure transducer. Consequently, during this period, the automatic control is interrupted by an electronic "sample and hold" circuit. This circuit continuously holds the signal from the controller to the throttling valve,

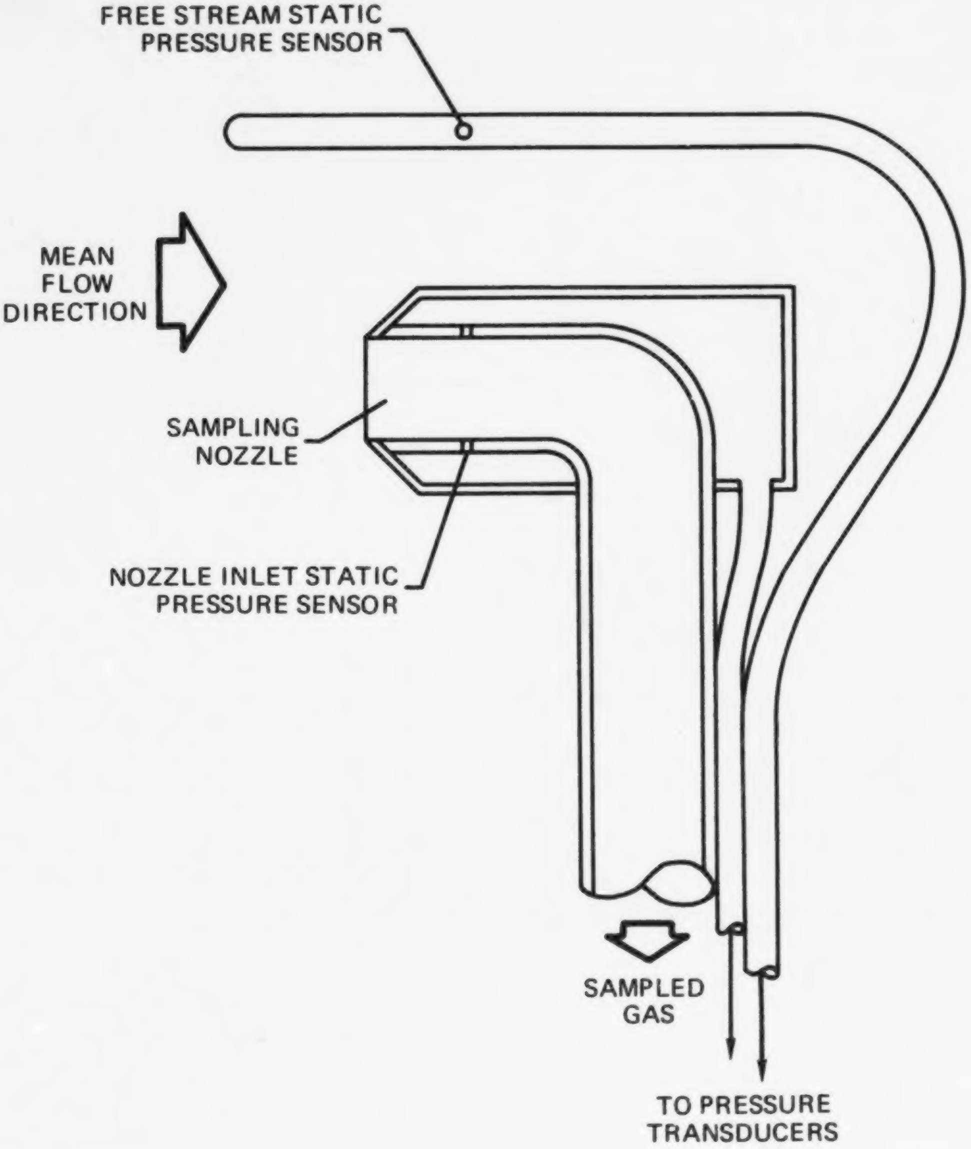
FREE STREAM STATIC PRESSURE SENSOR
MEAN FLOW DIRECTION
SAMPLING NOZZLE
NOZZLE INLET STATIC PRESSURE SENSOR
SAMPLED GAS
TO PRESSURE TRANSDUCERS

Figure 2. Schematic of the isokinetic sampling probe.

which is held, until the backflush is completed, at a value corresponding to the isokinetic flow just prior to the backflush. The periodic backflush sequence can be overridden by the operator at any time. This allows a continuous backflush mode of operation for very high dust loading environments. When the system is operated in this mode, the backflush flow must be reduced to levels which do not produce erroneous signals in the static pressure sensors.

The automatic isokinetic sampling system is also designed to permit manual operation. For a specific sampling nozzle inlet cross-section, the mass flow corresponding to isokinetic condition can be computed from the measured pressure, temperature, and velocity of the sampled flow. The sampled gas flow can then be manually adjusted via the throttling valve to match the computed isokinetic mass flow. This manual operation provides an independent backup system for automatic operation.

REAL-TIME MASS DETECTOR

A patented real-time mass measurement--a device tapered-element oscillating microbalance[8] (TEOM)--is being adapted for ambient air particulate loading density monitoring. In this work, the TEOM has been modified to provide real-time dust loading measurements for exhausts from fossil fuel combustors.

The active element of the TEOM consists of a tube constructed with high mechanical quality factor and having a special taper (Figure 3). This tube is firmly mounted at the wide end; the other end supports an exchangeable filter which can be fabricated from virtually any material. The tapered tube with the filter at the free (narrow) end is set into oscillation in a clamped-free mode between two electrostatically charged parallel-field plates. Dust-laden air is drawn through the filter and the hollow tapered tube via a vacuum pump. A feedback system maintains the oscillation, whose natural frequency will change in relation to the mass deposited on the filter. The sensitivity and frequency can be chosen at will by proper dimensioning of the oscillating tapered element.

Simplified operational details are shown in Figure 3. The tapered element is originally excited into oscillation and kept in oscillation at its natural frequency by a feedback system which consists of a light-emitting diode photo-transistor combination. The oscillation of the tapered element is converted into an electrical signal from the diode photo-transistor set via the light-blocking effect of the oscillating element. The amplified signal from the photo transistor is fed back to the conducting surface of the tapered element. The electrostatic charges on the tapered element are then modulated by this feedback signal and interact with the electrostatic field between

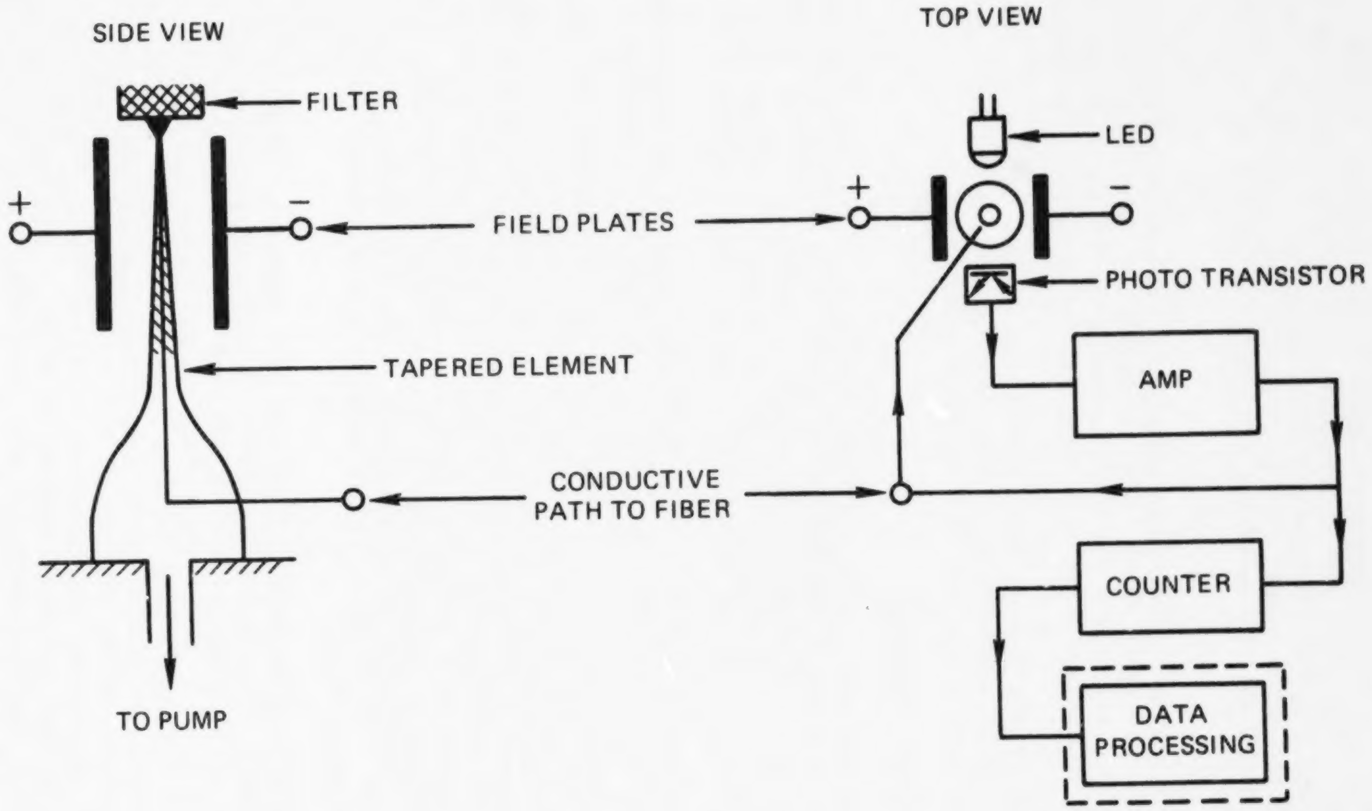
SIDE VIEW
FILTER
+
−
FIELD PLATES
TAPERED ELEMENT
CONDUCTIVE PATH TO FIBER
TO PUMP
TOP VIEW
LED
+
−
PHOTO TRANSISTOR
AMP
COUNTER
DATA PROCESSING

Figure 3. Schematic of the TEOM system.

the two parallel field plates, so that a steady-state oscillation of the tapered element at its natural frequency is established. This frequency will change as the weight of the filter increases because of the particulate deposition. A photograph of the detector assembly and the electronic controller is shown in Figure 4.

The TEOM is an oscillator whose frequency can be described with two parameters, the restoring force constant K and the effective mass m, consisting of the mass of the filter, m_F, the effective mass of the tapered elastic element, m_o, and the filter loading, Δm:

$$m = m_F + m_o + \Delta m. \tag{1}$$

The relation between these quantities is given by the expression

$$4\pi^2 f^2 = \frac{K}{m} \tag{2}$$

or

$$f^2 = \frac{K_o}{m} \text{ with } K_o = \frac{K}{4\pi^2} . \tag{3}$$

If the TEOM is initially oscillating at a frequency f_a corresponding to mass m and exhibits a frequency f_b after a mass uptake, the change in mass Δm can be obtained as a function of f_a, f_b, and K_o; namely,

$$f_a^2 = \frac{K_o}{m_a} \tag{4}$$

and

$$f_b^2 = \frac{K_o}{m_a + \Delta m} . \tag{5}$$

Elimination of m_a by combining Equations 4 and 5 leads to

$$\Delta m = K_o \ (1/f_b^2 - 1/f_a^2). \tag{6}$$

Note that Equation 6 is independent of the filter mass m_F and the effective mass m_o of the oscillating tapered element. Equation 6 is also used for calibration by measuring Δm gravimetrically, thus obtaining K_o.

In reality the frequency is not measured directly. Instead, one measures the time interval τ required for completing a certain number of cycles, N, of the TEOM's vibration. During this

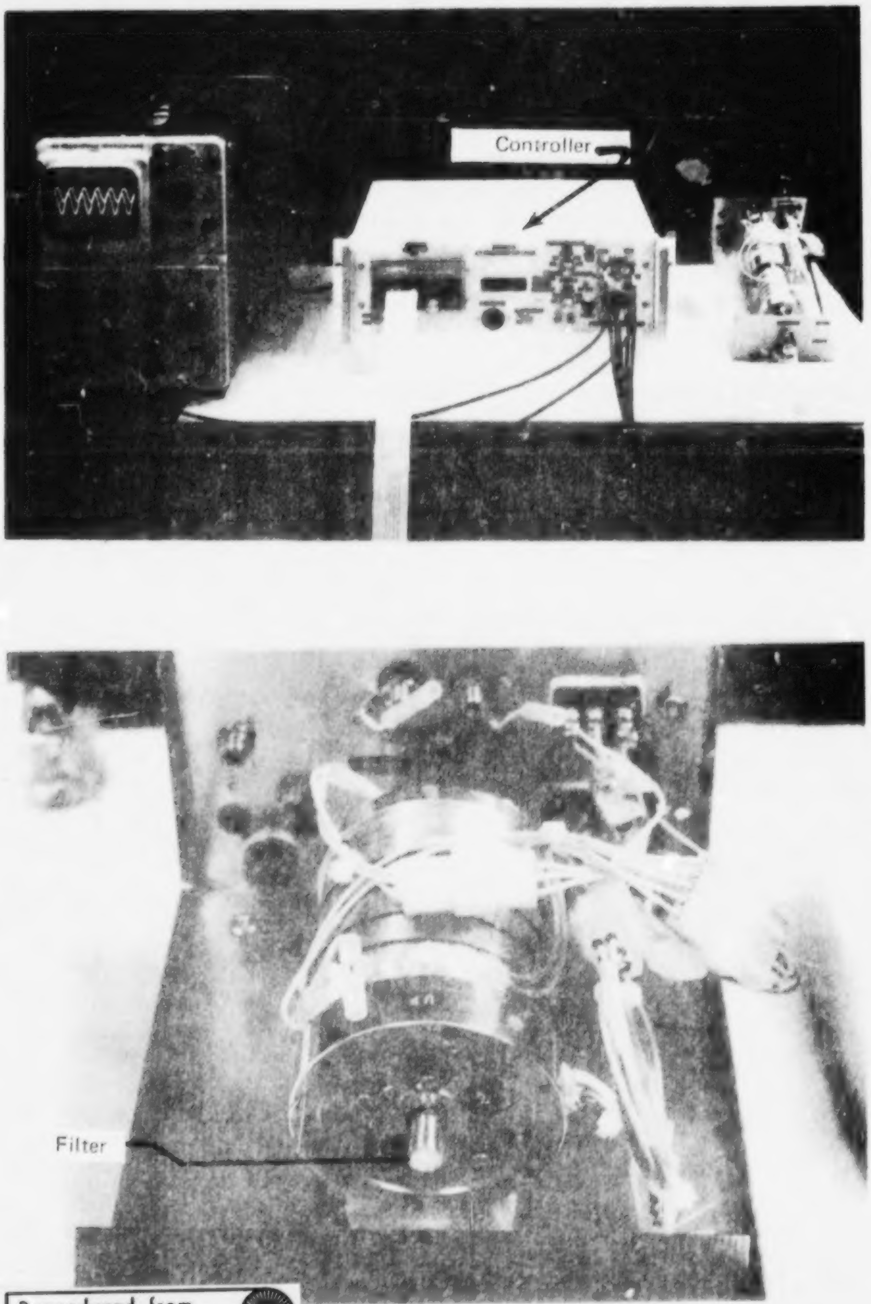
Controller
Filter

Reproduced from
best available copy.

Figure 4. TEOM detector and its controller.

gated time interval, τ, a high-frequency clock (running at a frequency f_c) registers a number of counts C. This procedure leads to measurement of the time interval with great accuracy (5 to 6 significant figures). Since

$$\tau_i = \frac{N}{f_i} \quad (i = a \text{ or } b) \tag{7}$$

and

$$C_i = \tau_i f_c \quad (i = a \text{ or } b) \tag{8}$$

Equation 6 becomes

$$\Delta m = \frac{K_o}{N^2 f_c^2} (C_b^2 - C_a^2) \ . \tag{9}$$

Thus the mass uptake Δm is determined by K_o (a property of the tapered elastic element), the chosen circuit parameters N and f_c, and the counts C_a and C_b measured before and after the mass uptake, respectively.

Unlike most other microbalances, the TEOM is mechanically strong and is easily automated with data output consisting of frequency information in the 10 to 10^2 Hz range. Mass deposition is monitored in real time. A dynamic operating range of over six orders of magnitude, from micrograms to grams, is achieved.

Although the TEOM measures mass by a frequency shift, as does a QCM (quartz crystal microbalance), there is no further similarity. Particulate collection on a QCM can only be achieved by impaction on the crystal surface. Particulate collection in this version of the TEOM is through a filter whose mass is continuously monitored by the vibration of the hollow, tapered, elastic element.

A QCM has nonuniform mass sensitivity across its surface, and its high oscillation frequency (10 MHz) produces a high surface acceleration. This necessitates strong adhesive forces for the particles; however, even if the adhesive forces are strong enough to prevent particulates from breaking loose under the surface acceleration, any mass above the immediate contact surface will fall out of phase with the crystal oscillation, leading to the well-known saturation effect of QCM's. After a buildup of a few microns in thickness, any additional mass deposition is no longer reflected in a frequency decrease, thus restricting QCM's to a low upper limit in measurable total mass deposition. QCM's can neither measure particulate depositions over a thickness of a few microns nor can they measure the mass of particles exceeding a few microns in size. Consequently, they are totally unsuitable for measuring high concentrations of relatively large particles such as are found in smokestacks.

The TEOM has none of these problems. All particles of interest are trapped in the filter and result in a frequency shift which is limited only by the capacity of the filter itself.

ROOM TEMPERATURE WIND TUNNEL

The integrated isokinetic real-time dust mass monitoring system was tested in a room temperature wind tunnel flow with externally injected particulates. A schematic of the wind tunnel facility is shown in Figure 5. The driver is a 5-hp low head air blower which is used in the suction mode. The air inlet is a 25.4-cm diameter opening through the building wall. A contraction cone reduces the air passage to a 10-cm diameter downstream from a section of honeycomb flow straightener. A T-section with a particulate injector mounted on the side flange is connected at the exit of the contraction cone. A second T-section with the isokinetic sampling probe and sensors mounted on the side flange is installed downstream from a 1.2-m-long straight Pyrex-glass pipe section after the first T-section. This straight pipe allows the injected particulates to mix with the air flow and develop into a more uniform distribution of particulates across the sampling cross section. The air flow after the sampling section is then turned 180° and exits to the inlet of the air blower. The flow rate through the wind tunnel can be adjusted between 50 and 450 SCFM via a manual butterfly valve at the exit of the blower. Downstream from the butterfly valve, at about 15 exhaust pipe diameters, a pitot-static pressure type flow meter is installed to measure the actual flow rate.

A cyclone type particulate feeder was designed, fabricated, and tested to provide continuous and uniform injection of fly ash into the wind tunnel for particulate diagnostic tests. The fly-ash feed rate can be controlled via the pressure drop across the feeder bed, and monitored on-line in real time via an electronic balance. Figure 6 shows a typical dust-feed history in terms of the weight loss of the feeder. The nearly straight line in Figure 6 demonstrates the uniformity of the dust feed rate. The dust loading density in the test section of the wind tunnel can be varied between 0.01 and 10 g/m^3 using this feeder assembly. Because of the naturally generated electrostatic charges from the fluidized fly-ash particulates inside the feeder, electrical grounding of the feeder was found necessary for optimum performance and safety.

The fly ash used in the wind-tunnel tests was obtained from cyclone catches at the exhaust cleanup system of Exxon's miniplant pressurized, fluidized-bed facility. Fly ash obtained from two cyclone catches in series was roughly preclassified at mean diameters of 1 and 5 μm, respectively. Prior to being loaded into the particulate feeder, the fly ash was sieved at 200 mesh to break up agglomerated particles and remove large particles. A typical size distribution of the fly ash from a Coulter analyzer is shown in Figure 7.

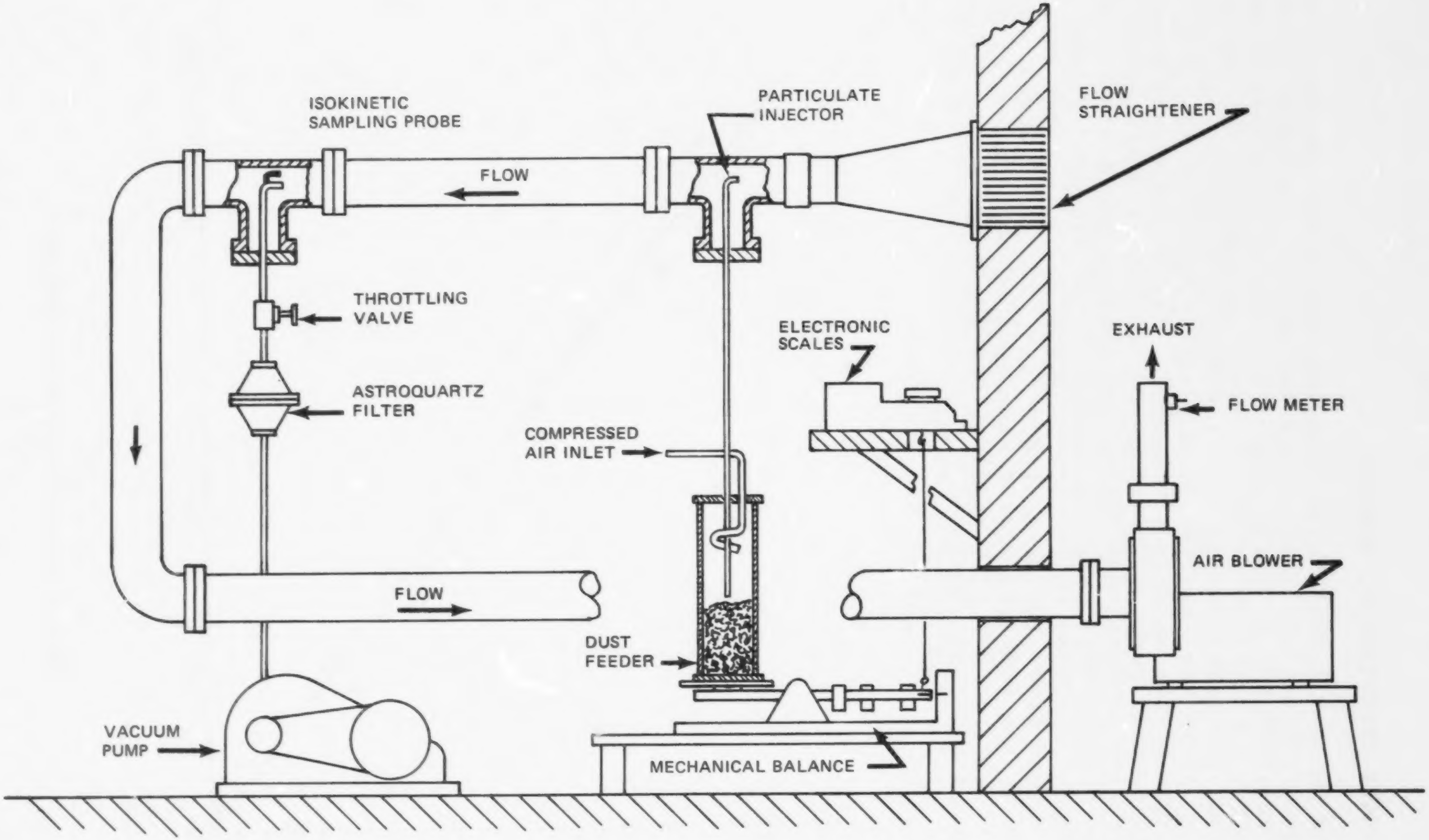
ISOKINETIC SAMPLING PROBE
PARTICULATE INJECTOR
FLOW STRAIGHTENER
FLOW
THROTTLING VALVE
ELECTRONIC SCALES
EXHAUST
ASTROQUARTZ FILTER
FLOW METER
COMPRESSED AIR INLET
AIR BLOWER
FLOW
DUST FEEDER
VACUUM PUMP
MECHANICAL BALANCE

Figure 5. Schematic of the room temperature wind tunnel.

PRELIMINARY EXPERIMENTAL RESULTS

The automatic isokinetic sampling system was tested in the room temperature wind tunnel described above. The sampling flow was established via a vacuum pump and measured by a Hasting mass flow meter. A positive filter using an astroquartz mat was used to collect the particulates from the sampling nozzle. The free stream velocity was measured by a pitot-static flow meter at the exhaust of the wind-tunnel blower. Using the signal from the differential pressure transducer, the PDP11-34 minicomputer automatically adjusted the throttling control valve on the sampling line. Isokinetic sampling condition was achieved automatically (when the differential static pressure was nulled) less than a second after the free stream flow rate was changed. The response of the sampling system was designed to be about 10 Hz, which is adequate for most applications in the combustor exhausts of advanced power systems.

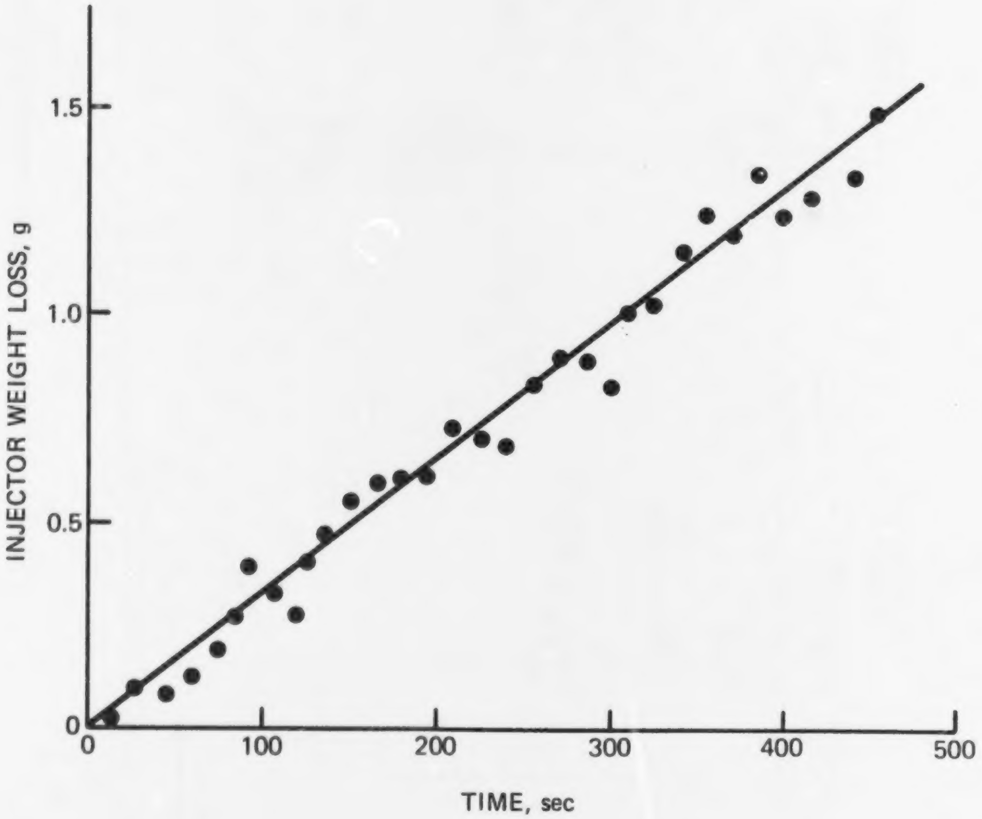

Figure 6. A typical history of dust feed rate.

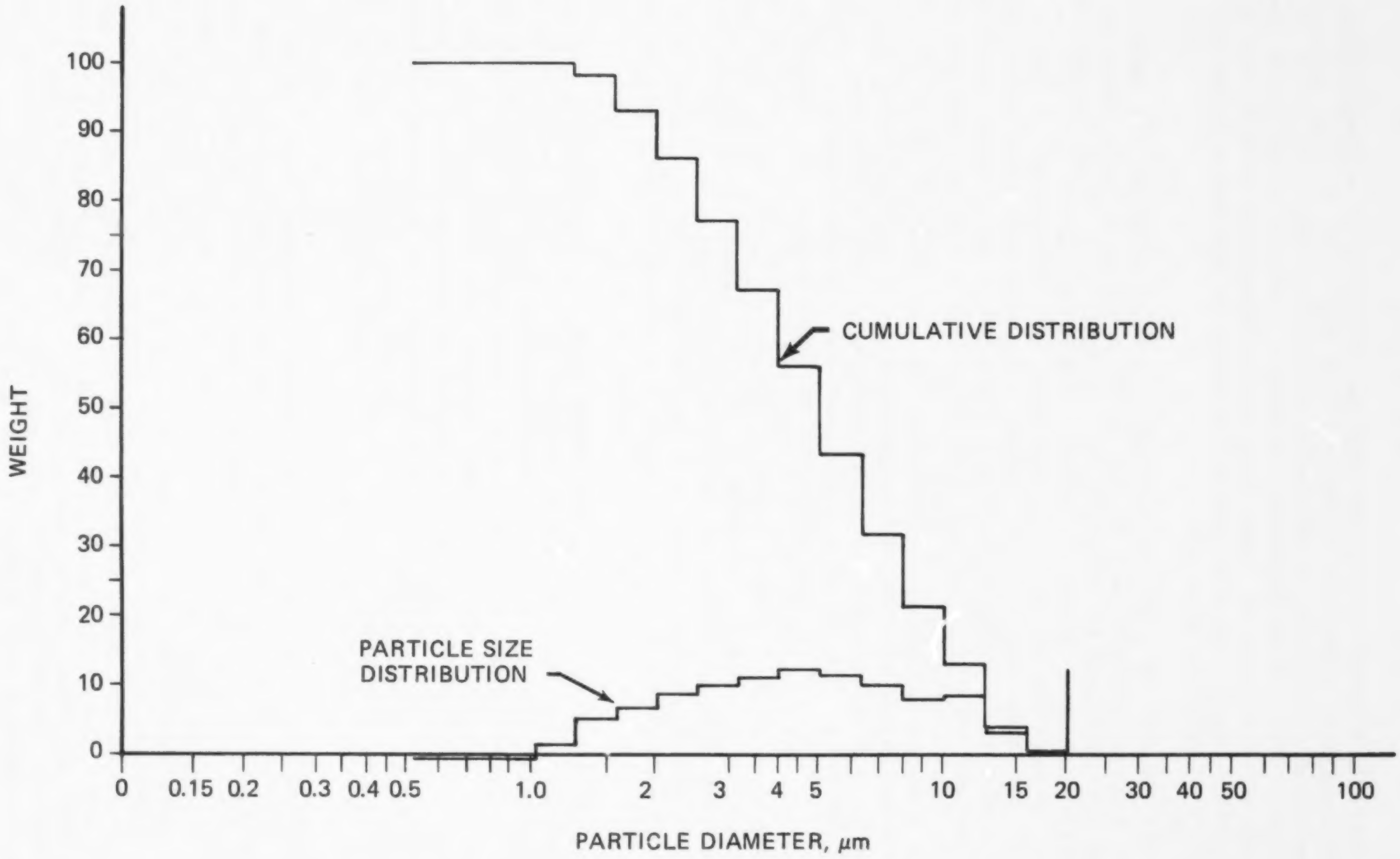

Figure 7. Size distribution of fly ash.

Figure 8 shows the experimental results of a comparison of the measured sampling velocity and the free stream velocity at the zero differential pressure condition maintained by the computer. The close agreement between the two velocities demonstrates achievement of true isokinetic sampling conditions with the present sampling configuration with an estimated overall accuracy of better than 5%.

The amount of particulate matter collected at the astroquartz filter element was found to be generally less than expected for isokinetic sampling at uniform dust loading across the test section. Several factors contributed to this discrepancy. A portion of the particulates was collected on the inside wall of the sampling probe. Clear evidence was also found via light scattering techniques that the radial dust loading density distribution at the inlet of the sampling probe was not uniform and, in fact, varied as a function of the wind-tunnel flow rate. Figure 9 shows a typical comparison of the weight of collected samples relative to what is expected from a uniform dust distribution in a free stream at isokinetic sampling conditions. At each flow rate, the weight ratio was nearly constant and reproducible. This ratio was observed to depend upon the electrostatics of the injected fly-ash particles and the potential of the sampling probe. Best results appear to occur when the sampling probe is grounded. However, the influence of electrostatic charging on dust collection needs further detailed study to optimize the isokinetic sampling processes. On the other hand, the size distribution of collected fly-ash particles appeared to be similar to that shown in Figure 7.

A preliminary test of the TEOM detector coupled to the isokinetic sampling system was performed in the room temperature wind tunnel. The history of the collected particulates was recorded in real time. At the end of each sampling test, the filter element of the TEOM detector was weighed and compared to the accumulated frequency shift displayed on the recorder. Figure 10 shows the good agreement obtained between the real-time measurements and the accumulated weights in typical calibration tests. A calibration constant of 4.62×10^{-3} g/Hz was found from a least-squares fit of the calibration data.

In Figures 11(a) and (b) are shown, respectively, photographs of the TEOM filter prior to being mounted on the TEOM's tapered element and after it had collected about 16 mg fly ash. Most of the fly ash collected was near the top of the astroquartz mat as shown in Figure 11(c). Figure 11(d) shows the back side of the same mat shown in Figure 11(c) and demonstrates that there was no trace of fly ash penetration through the astroquartz mat. The properties of light weight, ease of handling, and 100% collection efficiency for particles 1 μm and larger make the astroquartz mat an ideal filter material for the TEOM application. Furthermore, the astroquartz mat was tested at elevated temperature environments and proven to be useful up to 800°C.

Experiments on real-time dust-loading monitoring were performed using the combined system of the isokinetic sampling probe and the TEOM detector. The weight loss of the dust feeder was also monitored in real time with the combination of a mechanical balance and electronic scales (see Figure 1). A typical test result is shown in Figure 12. Output from the TEOM detector was scaled up to the total flow in the test section on the basis of the ratio of the sampled flow to the total flow and the empirical dust distribution at the inlet of the sampling probe. Thus, direct comparison of the dust collected to the weight loss of the dust feeder as a function of time could be obtained. Close agreement is shown in Figure 12 between the dust collected on TEOM and that injected into the wind tunnel. As indicated, the dust feed rate was changed twice. The TEOM output essentially matches the dust feed rate and follows, with acceptable response, changes in the feed rate. The real-time on-line dust loading monitoring capability is demonstrated.

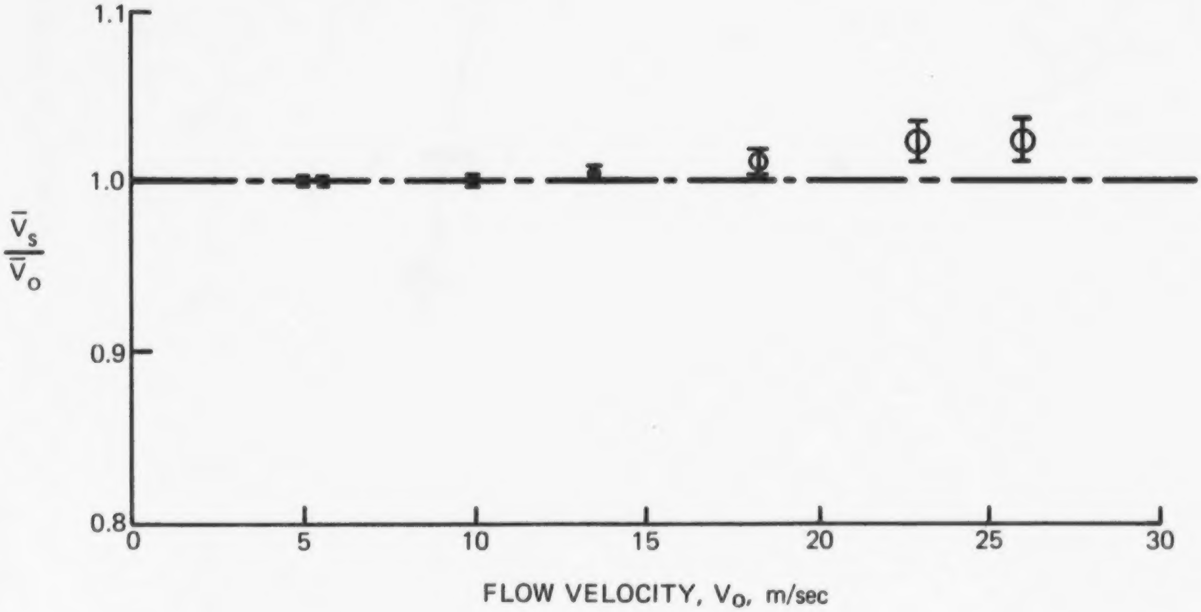

Figure 8. Test results of the isokinetic sampling system.

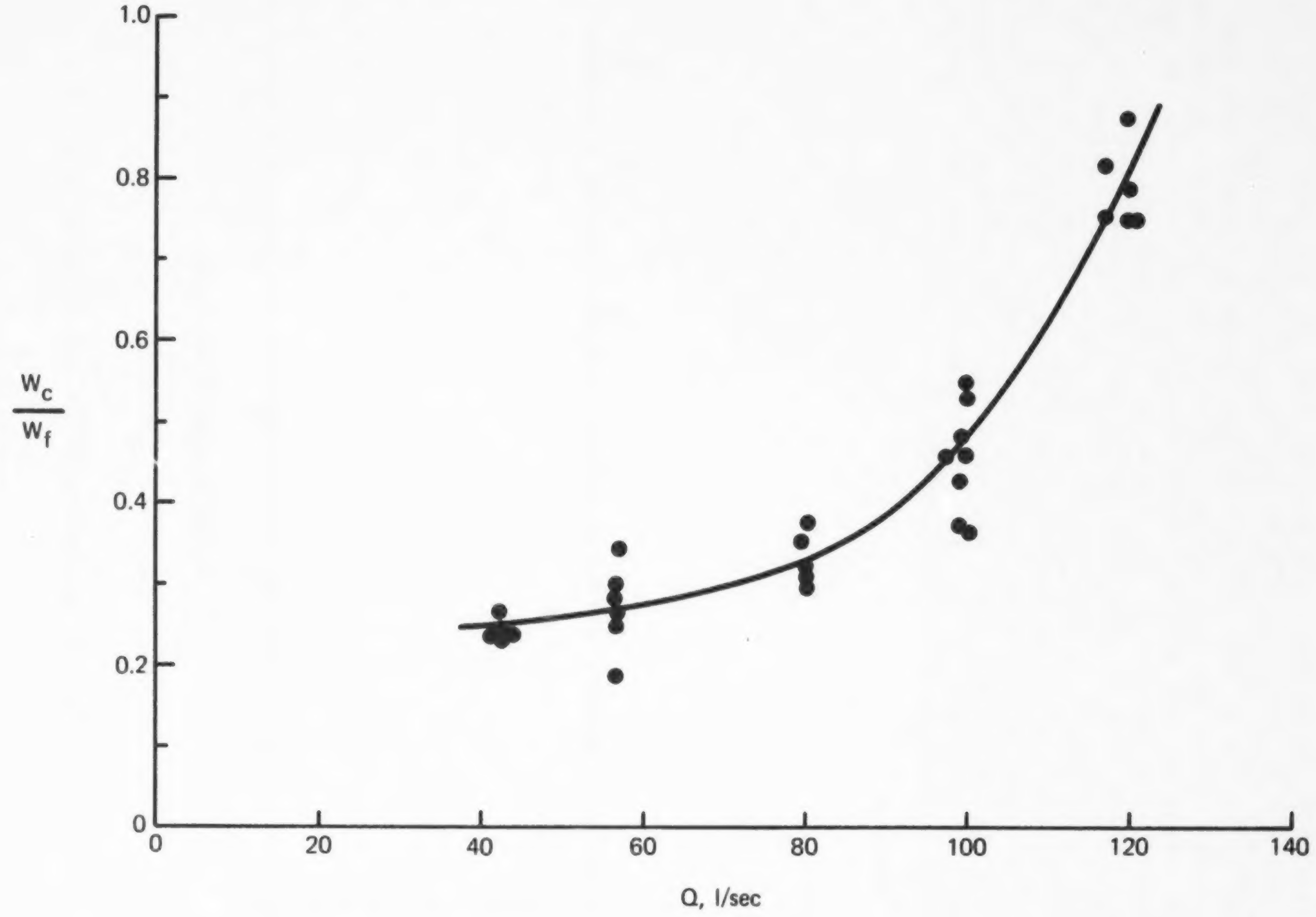

Figure 9. Dust collection test results.

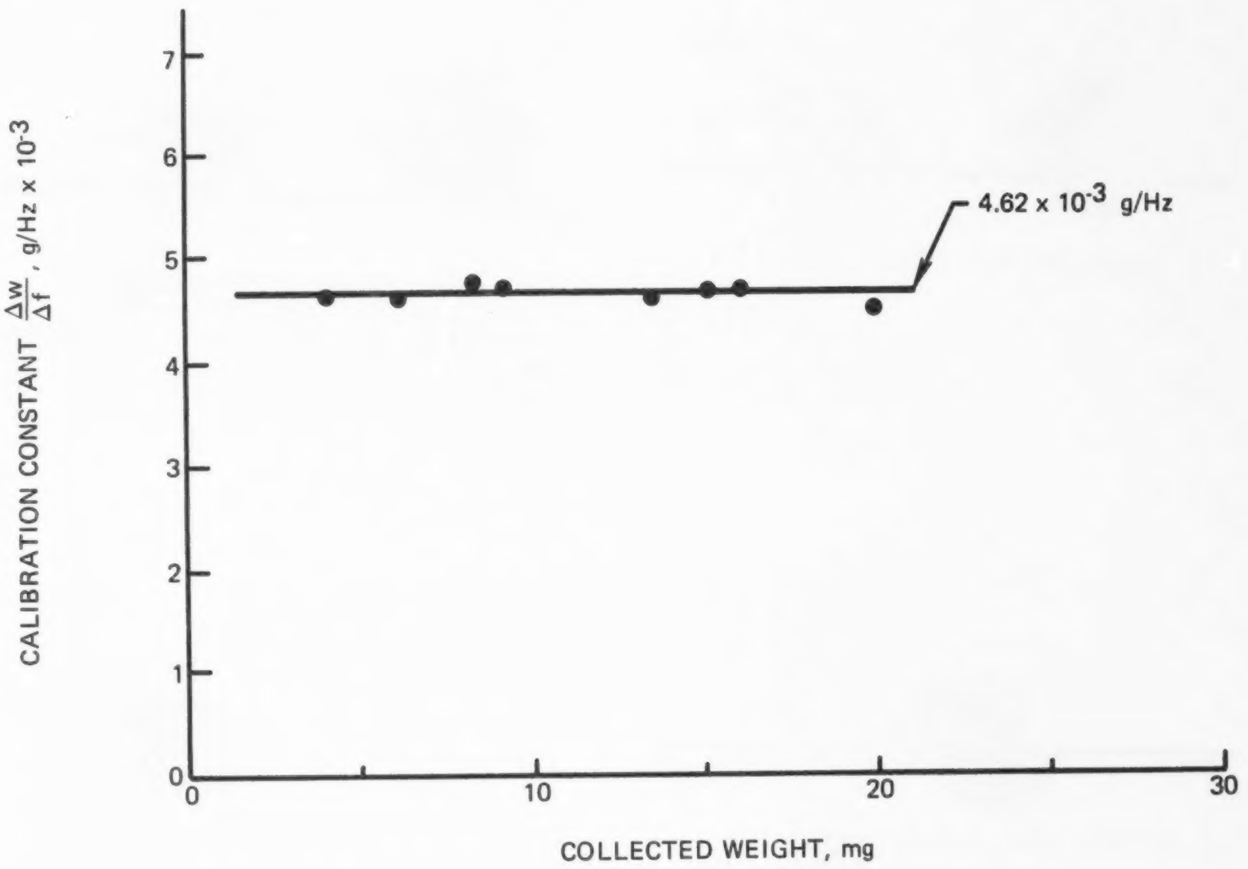

Figure 10. Calibration of TEOM detector.

Reproduced from
best available copy.

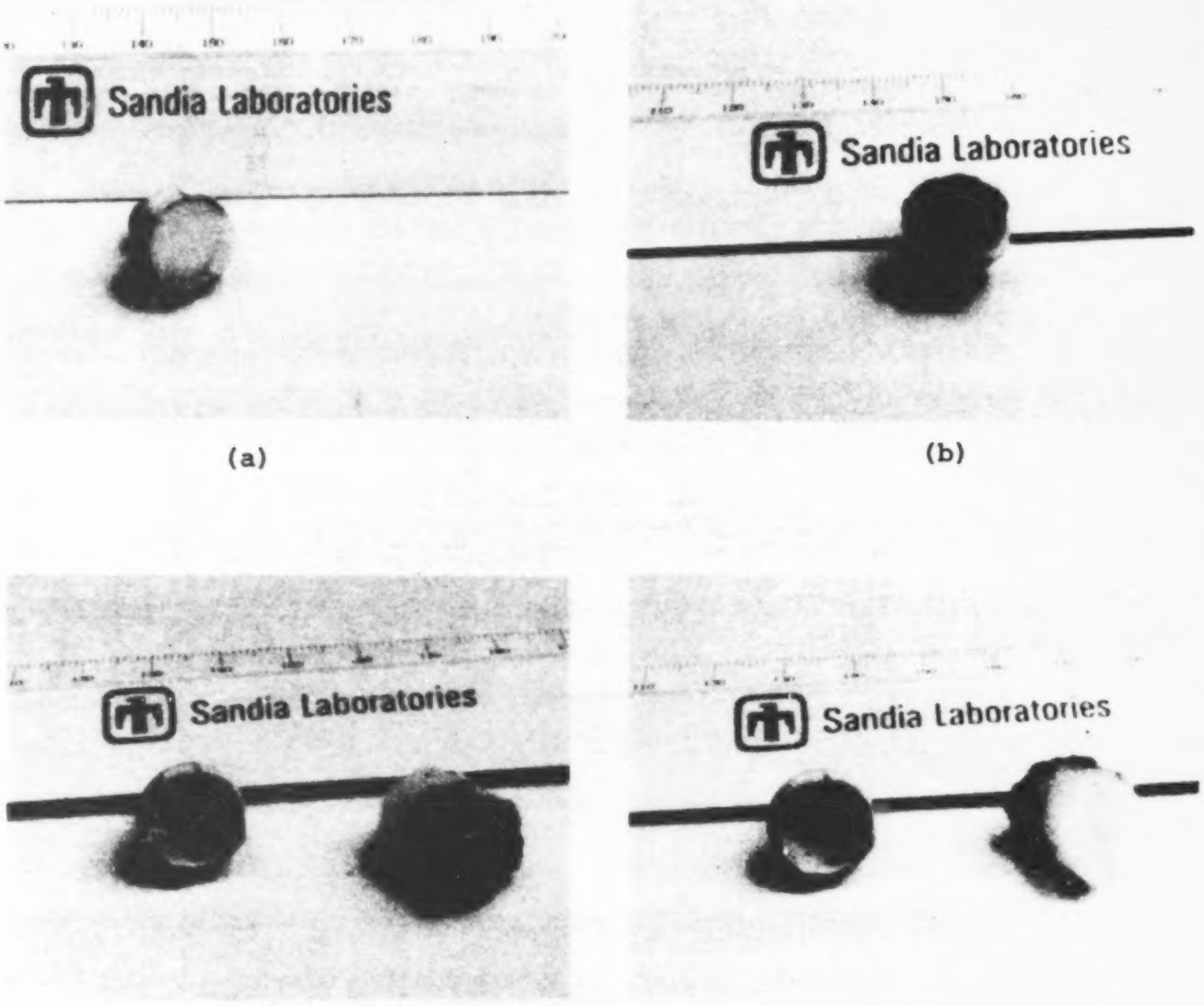
Sandia Laboratories
Sandia Laboratories
Sandia Laboratories
Sandia Laboratories

(a) (b)

(c) (d)

Figure 11. TEOM filters.

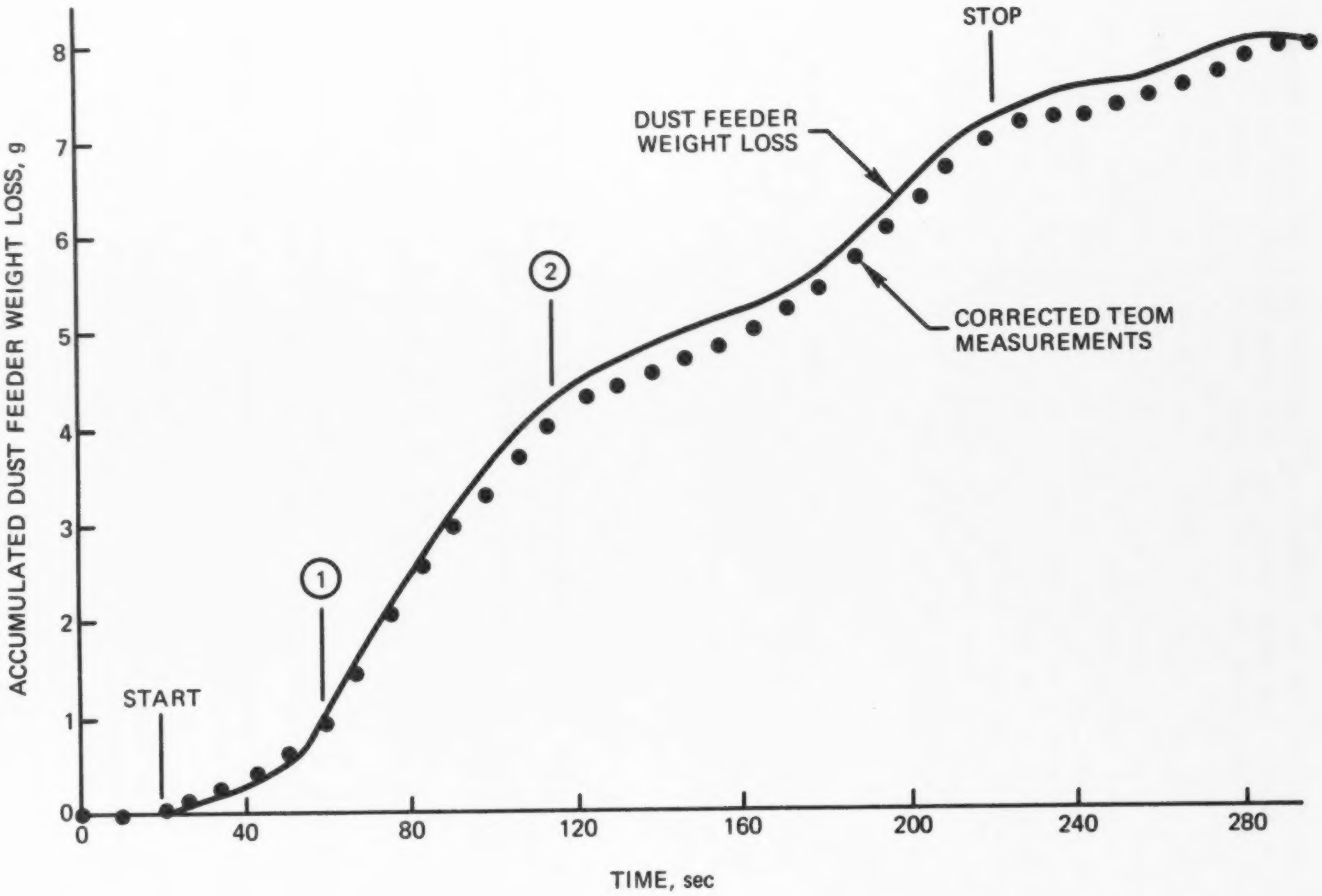

Figure 12. Test results of the integrated real-time automatic isokinetic sampling system.

SUMMARY

The combination of an automatic isokinetic sampling system and the TEOM real-time mass detector has been demonstrated to be a promising real-time particulate mass monitoring system for high dust loading environments. The bench test model described in this paper was designed for near room temperature and one atmospheric pressure condition. Additional development is underway to extend this new monitoring system to high temperature and high pressure applications. Automatic self-cleaning features and/or interchangeability for the TEOM filter during sampling processes are planned to be developed for continuous particulate mass loading monitoring applications. A particularly useful development which we are exploring is the incorporation of a TEOM detector at each dust collector of a cascade cyclone train. Such a system will permit real-time analyses of mass loading distribution according to particle size.

ACKNOWLEDGEMENTS

The author would like to thank J. Teodoro and T. Schoeppe for their help in building the test facility and performing the experiments. This work is sponsored by the Heat Engines Branch, Office of Fossil Energy, U.S. Department of Energy and is a part of the Sandia Laboratories' Diagnostic Assessment for Advanced Power Systems Program.

REFERENCES

1. Coleman, H.W., D.R. Hardesty, R.J. Cattolica, J.H. Pohl, L.A. Rahn, R.A. Hill, and D.L. Hartley. Diagnostics Assessment for Advanced Power Systems. Sandia Laboratories Report SAND79-8216, 1977.

2. Vitols, V. Theoretical Limits of Errors Due to Anisokinetic Sampling of Particulate Matter. J. Air Pollut. Control 16:79, 1966.

3. Performance and Measurements at Dust Collectors. Verein Deutscher Ingenieure, VDI-2066 Standards, 1966.

4. Branch, M.C. Sampling From High Temperature Particle Laden Flows. Sandia Laboratories Report SAND78-8253, 1978.

5. Ringwall, C.G. Compact Sampling System for Collection of Particulates from Stationary Sources. EPA-650/2-74-029, U.S. Environmental Protection Agency, Research Triangle Park, NC. 1974.

6. Wang, J.C.F., C.G. Ringwall, and C.M. Thoennes. A High-Temperature, High-Pressure Isokinetic/Isothermal Sampling System for Pressurized Fluidized Bed Application. In: Proceedings 5th International Conference on Fluidized Bed Combustion, Washington, DC, Vol III, p. 326, 1978.

7. Wand, J.C.F., R.R. Boericke, and R.A. Fuller. A High-Temperature, High-Pressure, Isokinetic/Isothermal Sampling System for Fossil Fuel Combustion Applications. In: Proceedings, Symposium on Transfer and Utilization of Particulate Control Technology. EPA-600/7-79-044d, U.S. Environmental Protection Agency, Research Triangle Park, NC, 1979. p. 310

8. Patashnick, H. U.S. Patent 3,926,271, December, 1975.

PAPER 15

A NEW REAL-TIME AEROSOL MASS MONITORING INSTRUMENT: THE TEOM

HARVEY PATASHNICK
GEORG RUPPRECHT
RUPPRECHT AND PATASHNICK COMPANY

ABSTRACT

A real-time monitoring device for airborne particulate matter has been developed on the basis of a novel mass measuring device. This new patented instrument is called a TEOM, Tapered Element Oscillating Microbalance ($\Delta m/m < 10^{-6}$, dynamic range $> 10^{6}$). Two aerosol monitoring techniques are utilized with this instrument, an impaction device (mass resolution 3×10^{-10} g) and a filter device (mass resolution 5×10^{-8} g). The TEOM filter unit uses exchangeable filter cartridges. Time resolution is 1 minute for the impactor TEOM and 30 minutes for the filter TEOM. (Time resolution: time required to measure an air pollution level of 10 $\mu g/m^3$ with an accuracy of 10%.) The impactor TEOM is used to measure the particulate content of air with high time resolution, while the filter TEOM provides an absolute measurement. The filter TEOM effectively represents a real-time absolute standard for the measurement of particulate mass concentration in the air.

DESCRIPTION OF THE TAPERED ELEMENT OSCILLATING MICROBALANCE, TEOM

It cannot be over-emphasized that the TEOM is significantly different from gravimetric and quartz crystal microbalances (QCM's). The active element of a TEOM consists of a tube constructed of a material with high mechanical quality factor and having a special taper. This tube is firmly mounted at the wide end while the other end supports a substrate (or filter cartridge) which can be composed of virtually any material. The tapered tube with the substrate at the free (narrow) end is set into oscillation in a clamped-free mode. A feedback system maintains the oscillation whose natural frequency will change in relation to the mass deposited on the substrate (or filter). The sensitivity and frequency can be chosen at will by proper dimensioning of the oscillating tapered element.

The operation of a TEOM is shown in simplified manner in Figure 1. The tapered element is kept in oscillation by a feedback system. The oscillation of the element is converted into an electrical signal by a light-emitting diode-phototransistor combination, the output of the phototransistor being modulated by the light-blocking effect of the vibrating element.

Unlike most other microbalances, the TEOM is mechanically strong and is easily automated with data output consisting of frequency information in the 10^2 to 10^3 Hz region. Mass deposition is monitored on a real-time basis.

A photograph of a typical instrument is shown in Figure 2. The unit illustrated here has a dynamic operating range over six orders of magnitude from 10^{-8} g to tens of milligrams. This is a nominal sensitivity range; greater or less sensitivity can be achieved by adjusting the dimensions of the oscillating element and the substrate.

AEROSOL MONITORING OPTIONS WITH THE TEOM

The TEOM can be used to measure aerosol mass concentrations with two different particulate collection techniques, impaction and filtration. These two methods are illustrated in Figure 3. Figure 3a shows the impaction method where particulates in the air stream are impacted against a substrate (greased or ungreased) on the TEOM. Typical mass sensitivity for an impactor TEOM is in the order of 3×10^{-10} g. Classical impaction techniques, however, have well known difficulties and as a result, a filtration TEOM unit has also been developed. The filter unit was developed to represent an absolute standard for the real-time measurements of aerosol mass concentrations. In this configuration, shown in Figure 3b, a filter cartridge is placed at the free (narrow) end of the hollow tapered element. Particulate-laden air is drawn through the filter, and the resulting filtered air is pumped down the hollow tube. Photographs of a TEOM filter unit are shown in Figure 4.

THEORY OF OPERATION

The TEOM is an oscillator whose frequency can be described with two parameters, the restoring force constant, K, and the effective mass, m, consisting of the mass of the filter (or substrate), m_F, the effective mass of the tapered elastic element, m_o, and the filter (or substrate) loading, Δm.

$$m = m_F + m_o + \Delta m \qquad (1)$$

The relation between these quantities is given by the expression:

$$4\pi^2 f^2 = \frac{K}{m} \qquad (2)$$

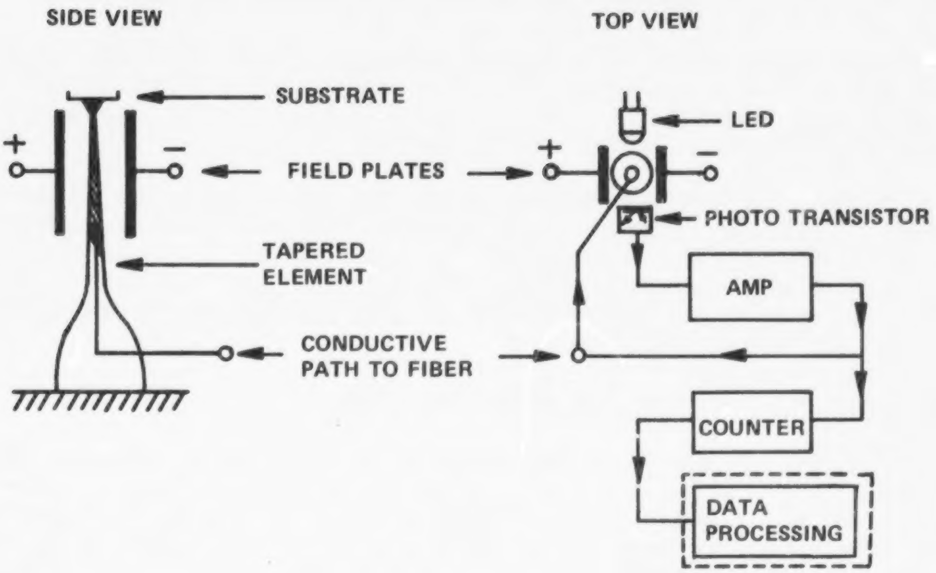
SIDE VIEW
TOP VIEW
SUBSTRATE
LED
+
−
FIELD PLATES
+
−
PHOTO TRANSISTOR
TAPERED ELEMENT
AMP
CONDUCTIVE PATH TO FIBER
COUNTER
DATA PROCESSING

Figure 1. Tapered element oscillating microbalance (TEOM) configuration (typical).

TEOM OPERATION

1. **Electric field is set up between field plates.**
2. **Image of tapered element is projected on phototransistor.**
3. **Oscillation of element initiated electrically or mechanically produces an AC voltage output from phototransistor.**
4. **AC voltage is amplified and applied to conductive path on element which maintains the oscillation due to interaction with field set up in Step 1.**
5. **Frequency of oscillation, and hence mass on substrate, is determined by frequency counter.**

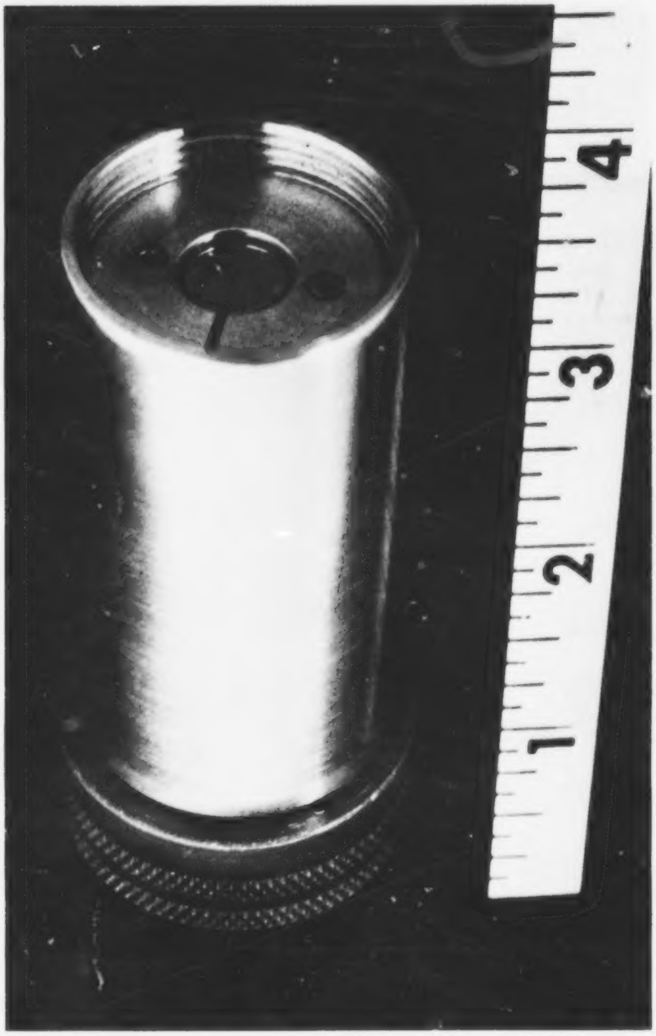

Figure 2. Typical TEOM; substrate disc is at top center.

or

$$f^2 = \frac{K_o}{m} \quad \text{with } K_o = \frac{K}{4\pi^2} \tag{3}$$

CALIBRATION PROCESS

If the mass Δm is determined gravimetrically and added to the filter, K_o can be determined from the frequencies f_1 and f_2 where f_1 is the frequency without Δm and f_2 is the frequency with the filter loading mass Δm. It is

$$f_1^2 = \frac{K_o}{m_F + m_o} \tag{4}$$

$$f_2^2 = \frac{K_o}{m_F + m_o + \Delta m} \tag{5}$$

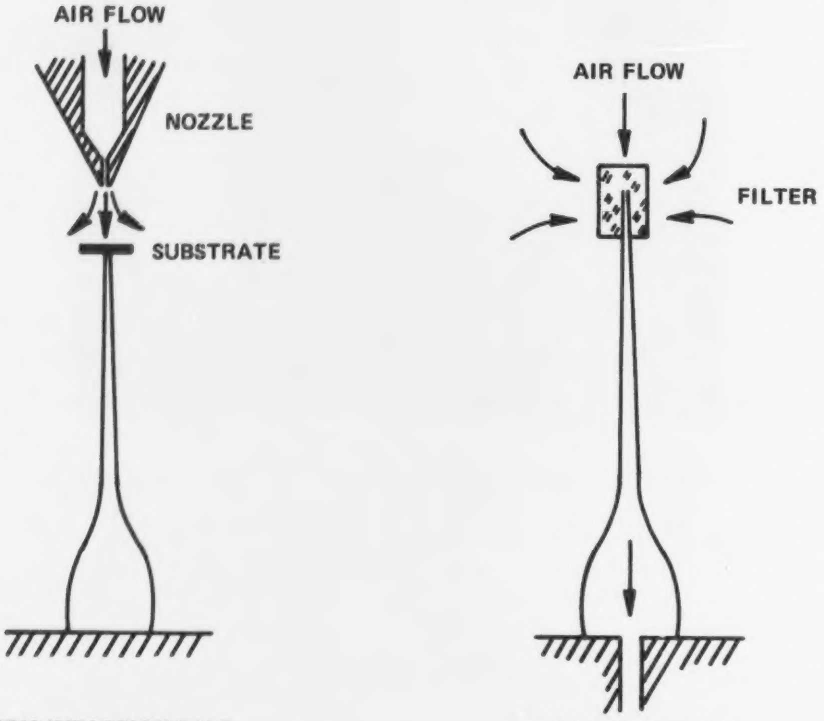

TEOM IMPACTION UNIT

3a

TEOM FILTER UNIT

3b

Figure 3. Aerosol monitoring options with the TEOM.

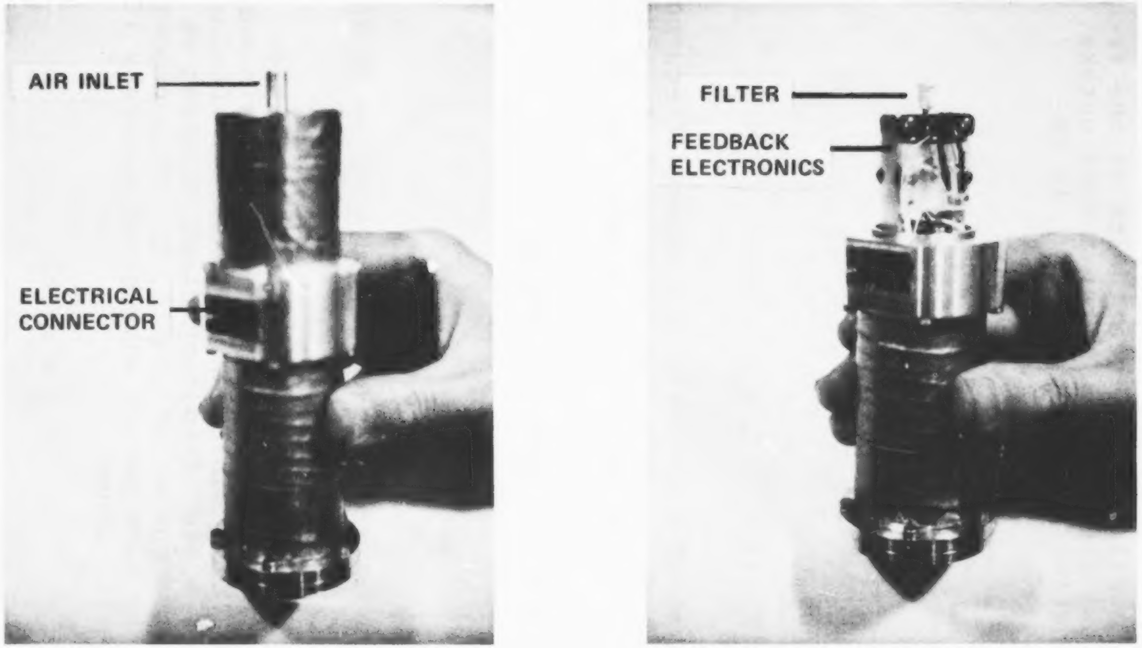
AIR INLET
ELECTRICAL CONNECTOR
FILTER
FEEDBACK ELECTRONICS

Figure 4. TEOM filter unit.

From these two equations K_o for a particular device can be calculated:

$$K_o = \frac{\Delta m}{(1/f_2^2) - (1/f_1^2)} \tag{6}$$

MASS MEASUREMENTS

If the TEOM is oscillating to start with at the frequency of f_a and exhibits the frequency f_b after a mass uptake, Δm can be obtained as a function of f_a, f_b and K_o. It is

$$f_a^2 = \frac{K_o}{m} \tag{7}$$

$$f_b^2 = \frac{K_o}{m + \Delta m} \tag{8}$$

Elimination of m leads to

$$\Delta m = K_o \; (1/f_b^2 - 1/f_a^2) \tag{9}$$

As is evident in Equation 9 the relation between frequency and mass uptake is not linear. Note that Equation 9 is independent of the filter mass, m_F, and the effective mass, m_o, of the oscillating tapered element.

For relatively small frequency changes

$$\left|\frac{\Delta f}{f_a}\right| = \left|\frac{f_b - f_a}{f_a}\right| << 1 \tag{10}$$

Equation 9 can be linearized, but this will only be an approximation.

In reality the frequency is not measured directly. Instead, the time period, τ, required for completing a certain number, N, of cycles of the TEOM's vibration is measured. During this gated time period, τ, a high frequency clock (running at a frequency f_c) registers a number of counts, C. This procedure leads to measuring the time period with great accuracy (5 to 6 significant figures). Since

$$\tau_i = \frac{N}{f_i} \qquad (i = a \text{ or } b) \tag{11}$$

and

$$C_i = \tau_i f_c \qquad (i = a \text{ or } b) \tag{12}$$

Equation 9 becomes

$$\Delta m = \frac{K_o}{N^2 f_c^2} (C_b^2 - C_a^2) \tag{13}$$

Thus the mass uptake Δm is determined by K_o (a property of the tapered elastic element), the chosen circuit parameters N and f_c and the counts C_a and C_b measured before and after the mass uptake, respectively.

COMPARISON WITH QUARTZ CRYSTAL MICROBALANCES (QCM's)

Although the TEOM measures mass by a frequency shift as does a QCM, there is no further similarity. In particular it should be obvious that the filter version of the TEOM is so vastly different from a QCM that a QCM can not physically begin to compete with a TEOM in this mode of operation. Only in the impaction mode can comparisons be made, but even here the QCM falls short.

The operation of a QCM consists of the deposition of mass on the surface of a piezoelectric crystal in a high frequency oscillator circuit (typically 10 MHz). Mass deposition onto the crystal causes a reduction of the resonant frequency. It is well known that the active area of the crystal has a bell-shaped distribution for mass sensitivity. This results in a small sample site of about 2 mm in diameter. For the measurement of a mass deposition, be it particulates or a thin film, one must either provide a uniform layer or direct the deposition to a specific well-defined section of the small active surface area. These basic characteristics of QCM's, i.e., high oscillation frequency and non-uniform mass sensitivity across the surface, result in difficulties for the measurement of particulates.

The high oscillation frequency produces a high surface acceleration. This necessitates strong adhesive forces for the particles; however, even if the adhesive forces were strong enough to prevent particulates from breaking loose under the surface acceleration, any mass above the immediate contact surface will fall out of phase with the crystal oscillation leading to the well known saturation effect of QCM's. After a build-up of a few microns in thickness, any additional mass deposition is no longer reflected in a frequency decrease, thus restricting QCM's to a low upper limit in measurable total mass deposition. QCM's can neither measure particulate depositions over a thickness of a few microns nor can they measure the mass of particles exceeding a few microns in size.

The TEOM, on the other hand, is an instrument which is inherently more suited for particulate measurements since its surface acceleration is orders of magnitude below that of a QCM.

(QCM's have oscillation frequencies in the megahertz region, whereas the TEOM oscillates around 100 Hz. Surface acceleration is proportional to f^2.) Also the TEOM is uniformly sensitive to mass across the entire substrate surface. This eliminates the need for a small sample site, rendering the total substrate surface area available for particle capture which, combined with a low surface acceleration, drastically reduces saturation effects. Additionally, even masses of particles hundreds of microns in size can be measured. The TEOM, although highly sensitive, has a sufficiently large dynamic range, due to its low susceptibility to saturation, to allow sampling for long periods of time. Furthermore, virtually any type of substrate can be used (filters, low Z materials, reactive surfaces, etc.).

AEROSOL MASS MEASUREMENTS WITH THE TEOM

Typical results of measurements with the filter TEOM unit are shown in Figure 5 which exhibits aerosol mass concentration as a function of time over one day. Data were taken in real

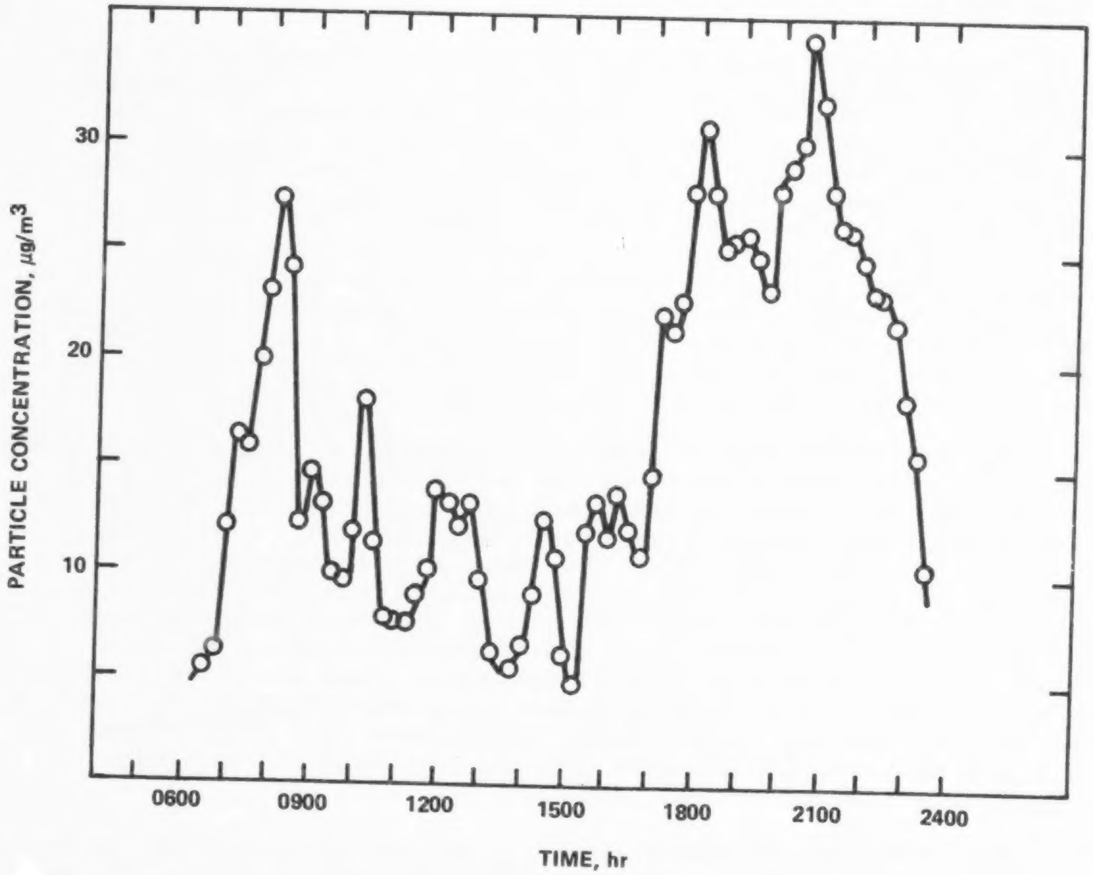

Figure 5. Air pollution in Albany on 12/11/78 (residential area) with the TEOM filter unit.

time every 15 minutes with a flow rate of 5 ℓ/min through a membrane filter cartridge with a 1 μm pore size. To eliminate the effects of humidity, a hydrophobic filter (Teflon) was used and the air stream and the instrument were maintained at 50°C. This particular unit had a mass resolution of 6.5 x 10^{-8} g. The variation of the aerosol level during the course of the day is, to a great extent, related to the traffic pattern.

Aerosol measurement results with a TEOM impaction unit are shown in Figure 6. A single stage impactor with a 50% cutpoint at 0.5 μm was used. The impaction substrate was made of titanium (ungreased) with a resulting collection efficiency of 10% calibrated against the filter unit as a standard utilizing the ambient aerosol. This efficiency will vary somewhat if there are significant changes in the aerosol size distribution compared to the ambient distribution it was calibrated against, but the purpose of using an ungreased substrate surface was to enable the instrument to operate unattended for weeks without maintenance (greased surfaces would eventually saturate). The flow rate was 3 ℓ/min

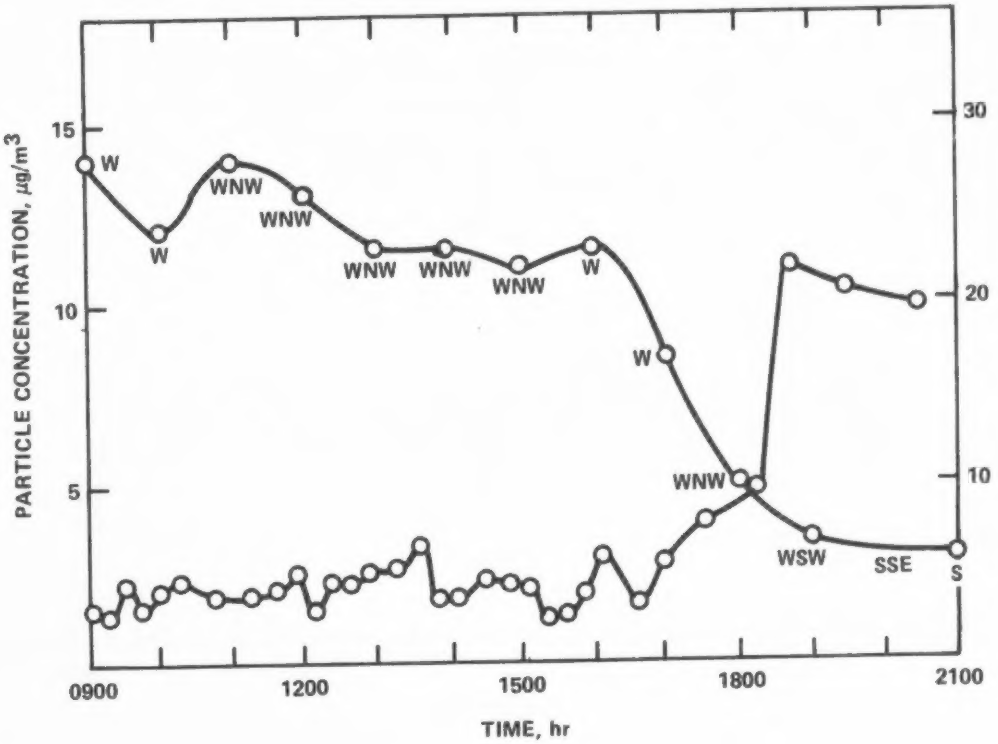

Figure 6. Air pollution on 12/14/78 versus wind condition measured with the TEOM impaction unit.

and data were taken during 3-minute sampling periods. The mass resolution was 3 x 10^{-10} g. As with the filter unit, this instrument was also run at 50°C to eliminate humidity effects. The results shown in Figure 6 depict an initially low pollution level (due to snowfall and high winds), which increased significantly as the wind direction changed and the wind speed decreased.

Results from both units as they were run side by side are shown in Figure 7. It can be seen that, with the exception of one peak near 23:10, the measurements showing aerosol variations correlate well. The peaks and valleys evident with the impactor unit are somewhat sharper due to the higher time resolution capability of that instrument.

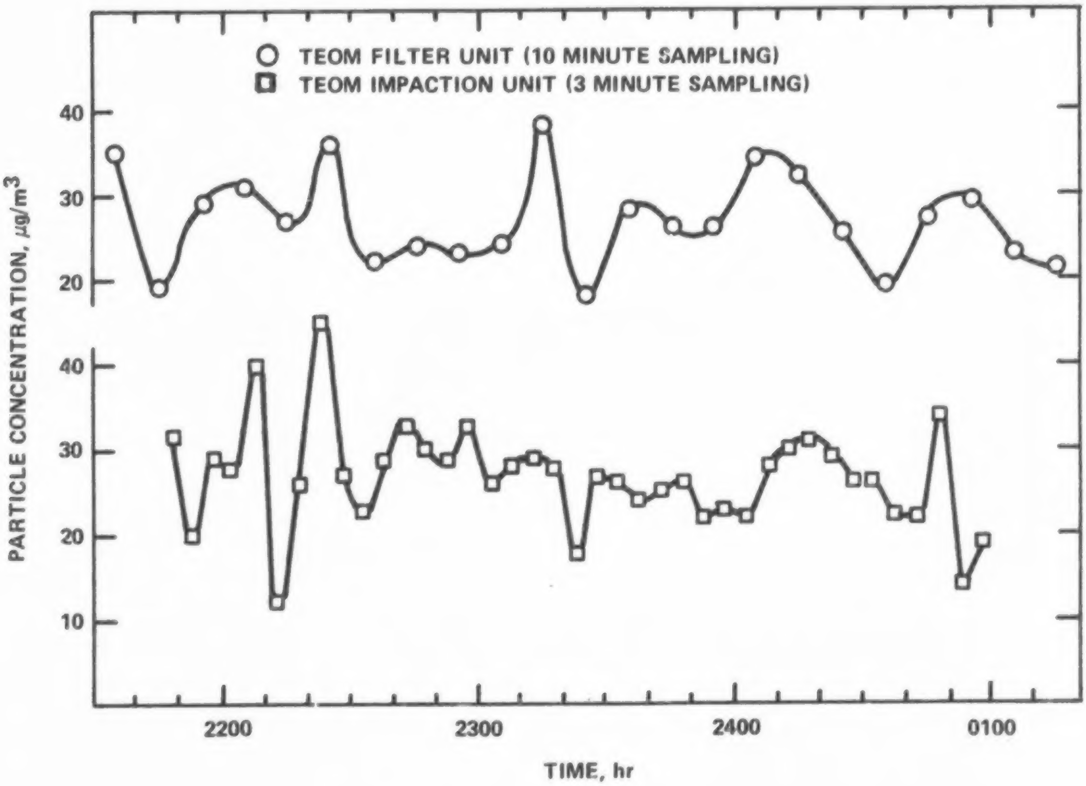

Figure 7. Simultaneous measurements with TEOM filter and impaction unit (12/12/78).

CURRENT DEVELOPMENT

The TEOM detectors are currently being mated with particle-size separators such as the dichotomous sampler and cyclones. A microprocessor is being employed to completely automate the devices. A desensitized TEOM filter unit is also being developed with an isokinetic sampler for utilization as an on-line stack sampling system.

SUMMARY

The Tapered Element Oscillating Microbalance (TEOM) represents a new, unique instrument capable of real-time aerosol mass concentration measurements utilizing two collection techniques, impaction and filtration. The impaction unit is capable of higher time resolution, but the filter unit eliminates uncertainties inherent with impaction collection techniques. The TEOM filter unit measures the mass of the collected particles and the mass, only, independent of their composition, Z values, optical properties, shapes, or any other particle property. It can be considered a detector which represents a real-time absolute standard for the measurement of particulate mass concentration in the air.

ACKNOWLEDGEMENT

The authors wish to thank the Environmental Protection Agency for partial support of this work under grant R805222020.

PAPER 16

NEW AUTOMATED DIFFUSION BATTERY/CONDENSATION NUCLEUS COUNTER SUBMICRON SIZING SYSTEM: DESCRIPTION AND COMPARISON WITH AN ELECTRICAL AEROSOL ANALYZER

GILMORE J. SEM
JUGAL K. AGARWAL
CHARLES E. McMANUS
TSI INCORPORATED

ABSTRACT

During the past several months, an automated system of instruments for measuring aerosol size distribution in the 0.005 to 0.2 μm diameter range has become commercially available. The system consists of (1) a multiple screen diffusion battery, (2) a continuous flow, non-pulsing condensation nucleus counter (CNC), and (3) a switching valve to allow the CNC to detect the concentration at each battery port. The system measures urban atmospheres continuously for several days without maintenance. It requires about 4 min to measure one distribution. The system is useful for accurate measurements in relatively dirty atmospheres ($>10^6/cm^3$) and in clean atmospheres ($<1/cm^3$), such as up- and downstream of high efficiency aerosol collectors.

This paper describes the individual instruments, recent performance data, and rapid data reduction. Some aerosol size distribution measurements are presented. Experimental data compares the new system with an electrical aerosol analyzer (EAA) while measuring sodium chloride, DOP, arc welding smoke, and propane aerosols.

INTRODUCTION

In the first symposium on Advances in Particle Sampling and Measurement at Asheville, NC, in 1978, Knutson and Sinclair[1] reported on the design and use of an automated diffusion battery particle sizing system for measuring urban aerosols. They used an automated system to measure aerosol number concentration as a function of particle diameter from 0.004 to 0.32 μm. This report describes a similar automated system made from commercially available instruments. The report also describes a computerized data reduction technique for the diffusion battery. Finally, the report describes results of several simultaneous comparisons between two commercially available techniques for making real-time submicron aerosol size distribution measurements: the multiple screen diffusion battery and the electrical aerosol analyzer.

DIFFUSION BATTERY SIZING SYSTEM

The instrumentation system used for this study included a multiple screen diffusion battery, a continuous flow condensation nucleus counter (CNC) and a valving system to switch the CNC inlet between the 11 exit ports of the diffusion battery. Figure 1 shows the system schematically. This particle sizing system is useful for diameters from 0.005 to 0.2 μm.

The multiple screen diffusion battery was first described by Sinclair and Hoopes[2] in 1975. The diffusion battery consists of 55 four-cm-diameter stainless steel screens with 250 wires

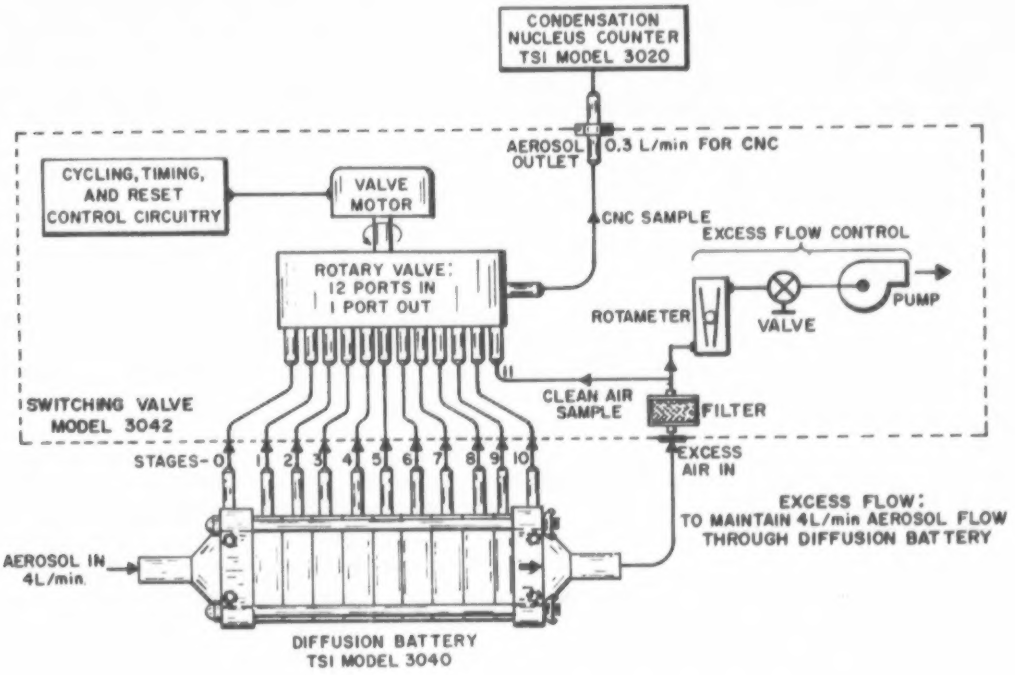
CONDENSATION NUCLEUS COUNTER TSI MODEL 3020
AEROSOL OUTLET
0.3 L/min FOR CNC
CYCLING, TIMING, AND RESET CONTROL CIRCUITRY
VALVE MOTOR
CNC SAMPLE
EXCESS FLOW CONTROL
ROTARY VALVE: 12 PORTS IN 1 PORT OUT
ROTAMETER
VALVE
PUMP
11
CLEAN AIR SAMPLE
FILTER
SWITCHING VALVE MODEL 3042
STAGES-0
1
2
3
4
5
6
7
8
9
10
EXCESS AIR IN
EXCESS FLOW: TO MAINTAIN 4L/min AEROSOL FLOW THROUGH DIFFUSION BATTERY
AEROSOL IN 4L/min
DIFFUSION BATTERY TSI MODEL 3040

Figure 1. Schematic diagram of the diffusion battery, switching valve, and condensation nucleus counter aerosol sizing system.

per cm. Normally, 4 ℓ/min of aerosol is drawn through the screens in series. The screens are mounted in 10 groups so that a condensation nucleus counter can measure the aerosol concentration upstream and downstream of each group. Sinclair and Hoopes[2] calibrated the screen diffusion battery. The screen diffusion battery must not be confused with the collimated holes structures or tubular diffusion battery also described and calibrated by Sinclair et al.[3]

The continuous flow CNC was described and calibrated by Agarwal and Sem.[4] The instrument first draws 300 cm^3/min of aerosol through a saturation chamber where the air becomes nearly saturated with butanol at 35°C. The nearly saturated aerosol then passes through a 10°C condensation tube which condenses butanol onto the particles, growing them into supermicron droplets. The droplets then pass through the sensing zone of a forward scattering optical particle detector. For concentrations below 1000/cm^3, the CNC measures particle concentration by counting individual particles as they pass through the sensing zone. The measurement in this range is a primary measurement, highly accurate, with calibration required for only the constant sample flow rate. The lowest detectable concentration is limited only by the time required to collect a statistically significant sample. Concentrations as low as 0.01/cm^3 are automatically displayed on the instrument's digital readout. For concentrations greater than 1000/cm^3, the CNC measures the light scattered in the forward direction by all particles simultaneously in the sensing zone. The photodetector output voltage is thus proportional to particle number concentration. Although accurate calibration has been performed only as high as $6 \times 10^5/cm^3$, this calibration has been extrapolated above $10^6/cm^3$.

The valving system shown in Figure 1 between the diffusion battery and the CNC has not been previously described. The purpose of the valving system is to allow a single CNC to sample, in sequence, each of the sample ports of a diffusion battery. The primary component of the valving system is a rotary valve with 12 inlet ports and one outlet port. The outlet port connects directly to the inlet of the CNC. The first inlet port samples the aerosol entering the first stage of the diffusion battery. The next 10 sample downstream of each of the 10 diffusion battery groups (or stages). The twelfth port samples air which has passed through a high-efficiency filter, serving as a check on the zero level of the system. Since the CNC requires only 0.3 ℓ/min of sample aerosol flow, an auxiliary pump and flow meter are built into the valving system to maintain 4 ℓ/min through the diffusion battery.

The valving system can operate in any of three modes: manual, one-cycle automatic, or continuous automatic. In the manual mode, the system remains on any diffusion battery port until the operator or an externally-supplied signal commands it to proceed to the next port. In the one-cycle automatic mode, the system automatically steps through all 12 ports a single time, then waits for a command to proceed through another single cycle. In the continuous automatic mode, the system steps through all 12 ports as in the one-cycle mode, but then automatically continues cycling indefinitely. The length of time on each port can be adjusted from 5 to 50 s with 25 s being a typical time required with the sizing system described here. The valving system may be set to skip all ports above any chosen port, a time saving feature when measuring very small particles. The system generates a logic level signal, one second before stepping to the next port, which can command an external recorder to accept data from the CNC. An indicator and a recordable signal indicate which port is being sampled at any given time.

The design of the rotary valve is important for determining the losses of particles passing through the system. Passages are about 4 mm diameter and 100 mm long through the rotary valve itself with no other significant obstruction. In addition, about 400 mm of 5 mm inside diameter vinyl tubing is necessary to connect the diffusion battery to the CNC. Table 1 shows the experimentally measured losses in the entire valving system. The measured size distribution can be corrected mathematically for these losses.

TABLE 1. EXPERIMENTALLY MEASURED LOSSES OF PARTICLES FLOWING THROUGH THE SWITCHING VALVE SYSTEM

Particle diameter, D_p, µm	Fractional loss, %
0.008	30.9
0.010	25.4
0.015	14.2
0.02	10.5
0.03	7.6
0.05	3.5
0.07	2.9
0.10	2.0

DIFFUSION BATTERY DATA REDUCTION

The data reduction method used for the diffusion battery was a slightly modified version of the non-linear iterative inversion suggested by Twomey[5] and adapted for use on diffusion battery data by Knutson and Sinclair.[1] The program, listed in Appendix 1, was modified for this work by Kapadia.[6] Since Knutson and Sinclair[1] describe the method in detail, this report will only mention several characteristics.

The particle size distributions in our work had a greater range of variability than those measured by Knutson and Sinclair[1] so Kapadia[6] added a test for the quality of fit of the experimental data with the computed solution. After every five iterations, the program calculates a chi squared value using the simulated raw data which would exactly result in the computed solution and the actual experimental raw data. When the chi squared value is less than 0.001, the program prints the results and stops. It will also print results and stop if 105 cycles of iteration have been completed before chi squared drops below 0.001. In the latter case, the printed value of chi squared indicates the quality of fit of the computed solution to the experimental data.

The program uses the diffusion battery calibration of Sinclair et al.[2,3] in a matrix developed by Kapadia.[6] It also corrects the CNC data for the detection efficiency using the CNC efficiency data of Agarwal and Sem.[4] The program is set up for use of an input data file so large batches of input data can be processed rapidly.

Table 2 is a typical printout of the program. The first upper column is diffusion battery port number and the second upper column is corresponding CNC experimental concentration. The third upper column is the ideal computed concentration which would exactly result in the computed distribution. The program calculates chi squared, listed at the bottom of the printout, from upper columns 2 and 3. The first lower column lists the geometric midpoint diameter, in micrometers, for each size interval. The second lower column lists corresponding number concentrations for each size interval in the form $dN/d(\log D_p)$ where N is particle number concentration (per cm^3) and D_p is particle diameter (micrometers). The third and fourth lower columns are surface and volume concentrations, respectively, calculated from number concentration assuming perfectly spherical particles and using a 45-interval size array rather than the normal 10-interval array. The bottom line of the lower columns, labeled "totals", is the total computed number, surface, and volume concentrations in units of particles/cm^3, (micrometers)^2/cm^3, and (micrometers)^3/cm^3, respectively. Notice that each of these values is the sum of the appropriate column divided by four because each decade of size contains four equal logarithmic intervals.

ELECTRICAL AEROSOL ANALYZER AND ITS DATA REDUCTION

The EAA has been used extensively during the past six years for measurements of a variety of submicron aerosol size distributions. In the remainder of this report, the diffusion battery particle sizing system is often compared with an electrical aerosol analyzer (EAA). The EAA, its performance, and its data reduction have recently been described by Sem,[7] Pui and Liu,[8] and Liu et al.[9]

TABLE 2. TYPICAL COMPUTER PRINTOUT FOR A SINGLE PARTICLE SIZING RUN OF THE DIFFUSION BATTERY AND CNC SYSTEM

```
TSI MODELS 3040 DIFF BAT AND 3020 CNC  -  TWOMEY METHOD

CNC ALCOHOL 9-10-79 RUN#2

PORT NO.      CNC DATA       CALC DATA
   0          270000.        270953.
   1          250000.        245133.
   2          207000.        202539.
   3          154000.        155325.
   4          106000.        112654.
   5           78500.         78617.
   6           55700.         53501.
   7           37000.         35829.
   8           23800.         23748.
   9           15700.         15635.
  10           10100.         10252.


MID PT. DIA    DNDLGD         DSDLGD         DVDLGD

  .0042        7.132E-03      3.982E-07      2.797E-10
  .0075        9.697E+01      1.712E-02      2.139E-05
  .0133        4.078E+04      2.277E+01      5.057E-02
  .0237        3.204E+05      5.657E+02      2.235E+00
  .0422        4.134E+05      2.308E+03      1.621E+01
  .0750        2.710E+05      4.785E+03      5.976E+01
  .1334        5.885E+04      3.286E+03      7.299E+01
  .2371        4.724E+03      8.341E+02      3.295E+01
  .4217        3.438E+02      1.920E+02      1.348E+01
  .7499        4.443E+01      7.845E+01      9.799E+00
 TOTALS        2.774E+05      3.019E+03      5.208E+01

 NO. OF ITERATIONS= 105      CHISQ=  1.610E-02
```

Several computerized procedures have been developed for reducing EAA data. The one used in this study uses the same Twomey[5] method described earlier for the diffusion battery. Appendix 2 is a listing of the program as adapted to the EAA by Kapadia.[6] Table 3 shows a typical printout of the results from the program. The printout format is the same as described earlier for the diffusion battery printout. This program is much faster than several previous EAA programs and appears to result in lower chi squared values (better fits) than most other methods.

TABLE 3. TYPICAL COMPUTER PRINTOUT FOR A SINGLE PARTICLE SIZING RUN OF THE ELECTRICAL AEROSOL ANALYZER

```
TSI MODEL 3030  EAA  -  TWOMEY METHOD

EAA ALCOHOL 9-10-79 RUN#2A

 DIA.          EAA DATA        CALC DATA

 .0032          3.310           3.308
 .0056          3.310           3.308
 .0100          3.310           3.308
 .0178          3.290           3.288
 .0316          2.790           2.788
 .0562          2.310           2.306
 .1000          1.090           1.095
 .1778           .320            .317
 .3162           .100            .090
 .5623           .020            .027
1.0000          0.000            .009

MID PT. DIA    DNDLGD          DSDLGD          DVDLGD

  .0042        0.              0.              0.
  .0075        0.              0.              0.
  .0133        1.879E+04       1.050E+01       2.333E-02
  .0237        2.166E+05       3.826E+02       1.512E+00
  .0422        2.983E+05       1.666E+03       1.171E+01
  .0750        2.980E+05       5.264E+03       6.579E+01
  .1334        9.479E+04       5.296E+03       1.177E+02
  .2371        1.357E+04       2.397E+03       9.473E+01
  .4217        1.257E+03       7.025E+02       4.937E+01
  .7499        3.636E+00       6.423E+00       8.028E-01
TOTALS         2.353E+05       3.931E+03       8.541E+01

NO. OF ITERATIONS=  20      CHISQ=  4.201E-03
```

DESCRIPTION OF THE EXPERIMENT

As with any aerosol measurement, the delivery of the sample to the diffusion battery and EAA must be done carefully. Particles larger than 0.2 μm can be lost in the sample tube by inertial impaction and gravitational settling while particles smaller than 0.03 μm can be lost or changed by diffusion to the walls or to each other. All particles can be changed drastically by evaporation or condensation of volatile components.

Figure 2 illustrates the major components of the aerosol generation and sampling system for a set of experiments involving atomized aerosols. Compressed air was regulated, dried, and filtered before entering the aerosol generator, a stable, single-jet atomizer. The output of the atomizer was a stream of droplets which could be mixed with clean dilution air before the droplet aerosol entered a diffusion dryer. The dryer consisted of a straight, 12-mm diameter tube made from stainless steel screen and surrounded by silica gel. Water or alcohol vapor diffused rapidly to the silica gel while the dried aerosol particles passed through. The dry aerosol then entered a Kr-85 electrostatic neutralizer which exposed the particles to high

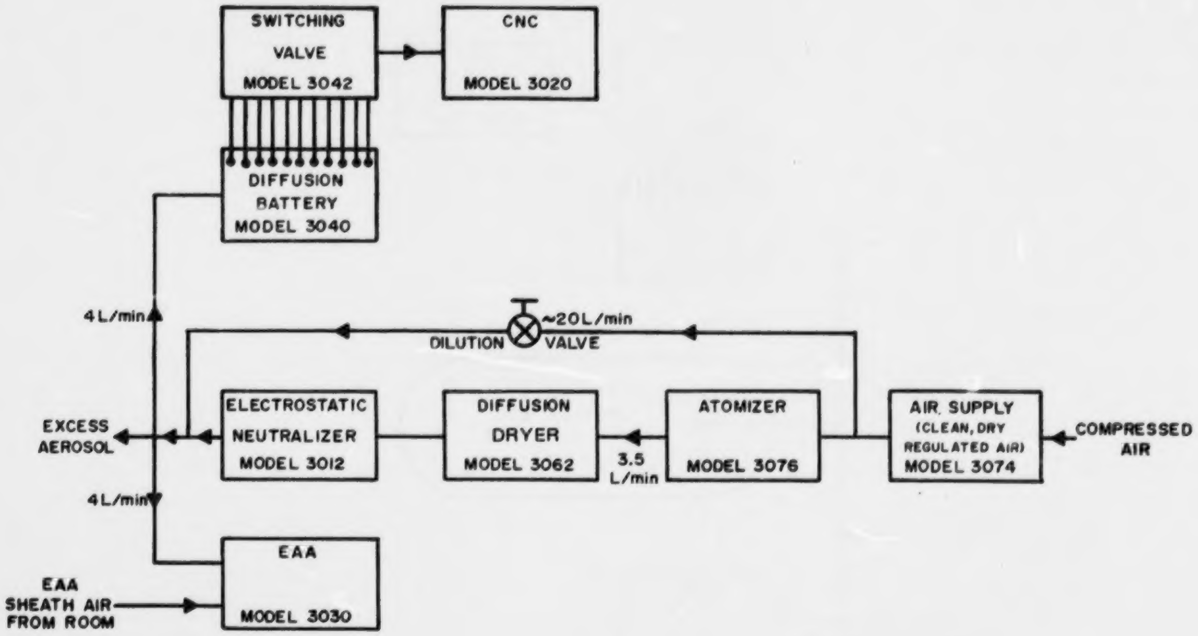
SWITCHING VALVE MODEL 3042
CNC MODEL 3020
DIFFUSION BATTERY MODEL 3040
4 L/min
~20 L/min
DILUTION VALVE
EXCESS AEROSOL
ELECTROSTATIC NEUTRALIZER MODEL 3012
DIFFUSION DRYER MODEL 3062
3.5 L/min
ATOMIZER MODEL 3076
AIR SUPPLY (CLEAN, DRY REGULATED AIR) MODEL 3074
COMPRESSED AIR
4 L/min
EAA MODEL 3030
EAA SHEATH AIR FROM ROOM

Figure 2. Schematic diagram of the aerosol generation and measurement system for the atomized aerosols.

concentrations of positive and negative ions, allowing the particles to attract neutralizing ions. The dry, neutralized aerosol then entered a mixing and damping manifold where it was available to the diffusion battery and EAA inlets. Excess aerosol was dumped from the manifold to the atmosphere.

The diffusion battery and EAA sampled simultaneously from the manifold, each at its normal 4 ℓ/min aerosol sample rate. The sample lines were less than 40 cm long, as short as possible. It was especially important to mix the aerosol well before it entered the diffusion battery so that its first sampling port sampled mixed aerosol rather than aerosol from the boundary layer with lower particle concentration. An elbow in the sample line within 10 cm of the diffusion battery inlet seems to provide sufficient mixing. The EAA drew its sheath air from the room. Data was recorded continuously on a two-pen strip chart recorder. The diffusion battery system required about 4 minutes per complete sizing run while the EAA required about 2 minutes.

Figure 3 illustrates the major components of the aerosol generation and sampling system for a set of experiments involving combustion aerosols. The major difference from the system shown in Figure 2 is the replacement of the entire generator by a 1-m^3 plastic bag. The bag was nearly filled first with either room

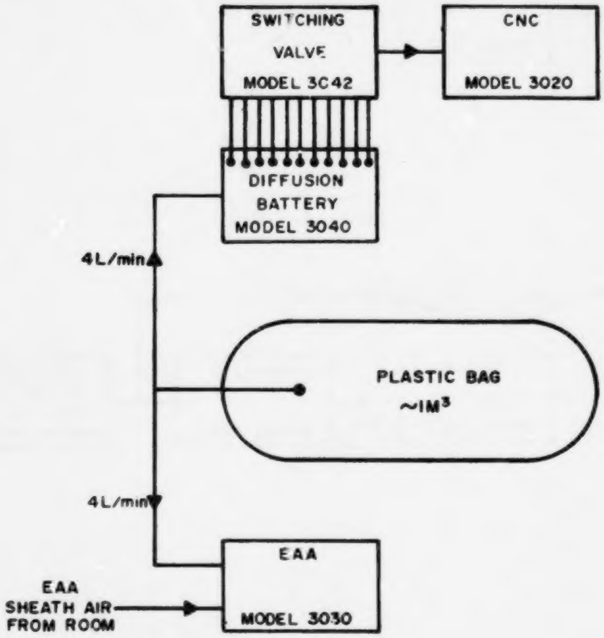

Figure 3. Schematic diagram of the aerosol generation and measurement system for the welding smoke and propane aerosols.

air or dried, filtered air. Then the combustion aerosol was introduced, in the case of welding smoke aerosol by drawing it into a large volume centrifugal blower and exhausting it into the nearly full bag, and in the case of propane aerosol by inserting the burning propane torch directly into the bag for about 10 s. The intent was not to characterize the combustion aerosol generation process, but rather to produce a representative aerosol in the bag which could challenge the diffusion battery and EAA simultaneously. By qualitatively varying the smoke introduction method, we could supply the bag with a variety of aerosol concentrations and with number median diameters in the 0.005 to 0.2 μm range.

The experimental results below are bar graphs of the measured concentration within each size range of the two measurement systems. The error bars represent the maximum range of variation observed in the experimental measurements. In some aerosol decay experiments, only one measurement was possible at a given point in time so no error bars are shown. Usually, we made two EAA size distribution measurements during a single diffusion battery measurement.

In addition to the programs listed in Appendices 1 and 2, we corrected both the diffusion battery and the EAA data to account for the exponential decay of the combustion aerosols while the sizing runs of several minutes duration were underway.

EXPERIMENTAL RESULTS AND DISCUSSION

The first aerosol we will discuss is the dry residue particles from the atomization of clean, unused, reagent grade isopropanol. Figure 4 shows the measured number of distributions. The diffusion battery measured three distributions in 12 minutes while the EAA measured six distributions during that time. Both systems measured repeatably. The diffusion battery and EAA measured similar distributions with a tendency for the EAA to measure slightly larger sizes. Figure 5 shows the same data converted to volume distributions by assuming spherical particles. If the spheres have unit density, the vertical axis is equal to mass concentration in micrograms per m^3. Figure 6 shows the same data on a log-normal plot. The measurements of both instruments were nearly log-normal with both measuring a geometric standard deviation of 1.85. The diffusion battery system measured a number median diameter of 0.041 μm and the EAA measured 0.048 μm. This aerosol spans the central portion of the size range where each measurement method is most accurate. The results indicate good agreement.

Figure 7 shows the results of the next set of comparative measurements. The atomizer system generated aerosol from a 0.1% (by volume) solution of DOP in isopropanol. Again, the results from the two measurement methods are similar. The results are

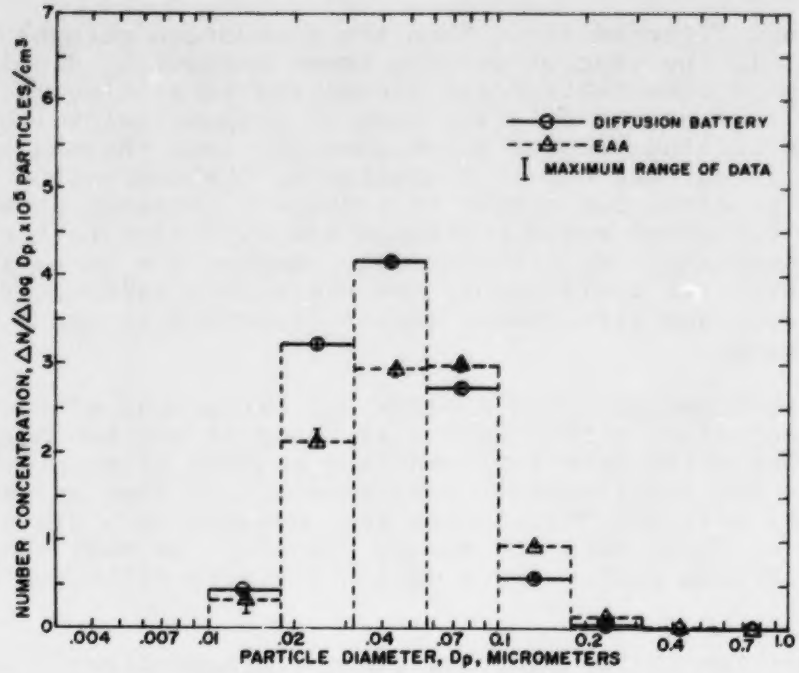

Figure 4. Number distributions measured by diffusion battery and EAA of aerosols atomized from 100% isopropanol.

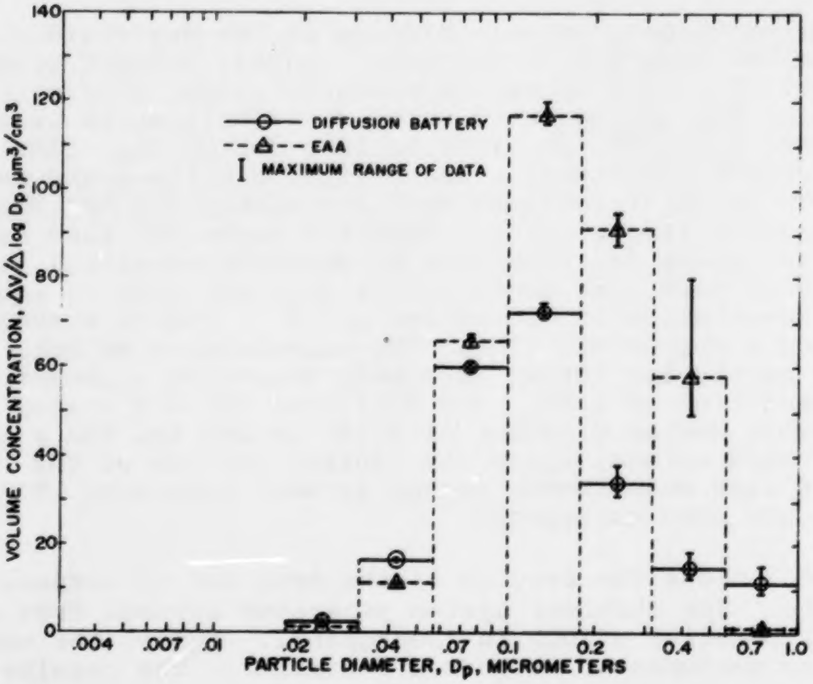

Figure 5. Volume distributions measured by diffusion battery and EAA of aerosols atomized from 100% isopropanol.

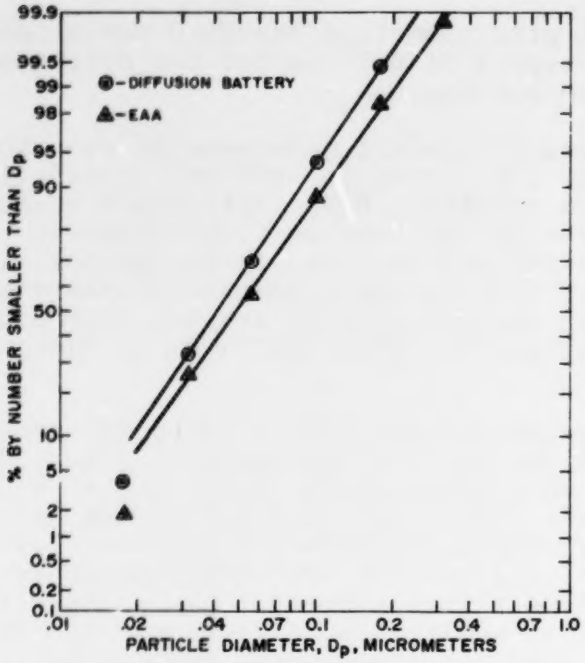

Figure 6. Cumulative number distributions measured by diffusion battery and EAA of aerosols atomized from 100% isopropanol.

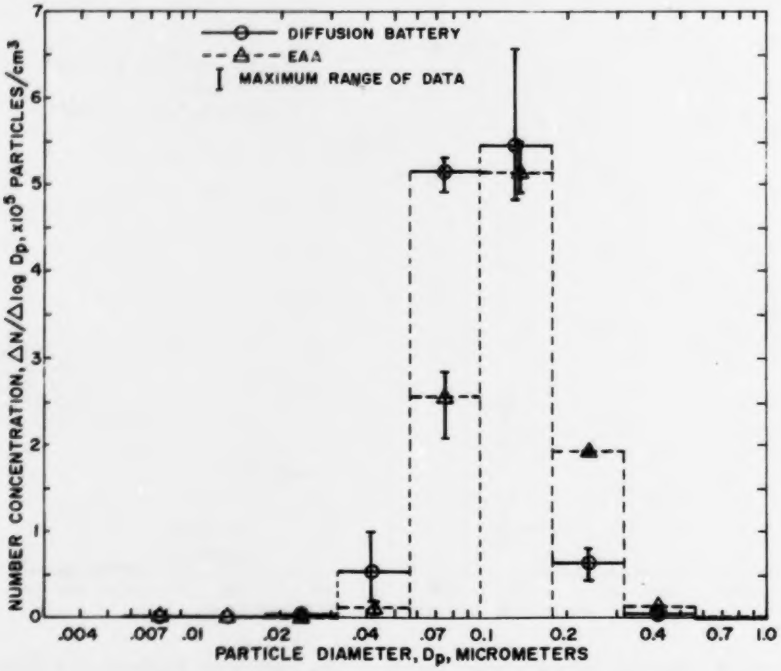

Figure 7. Number distributions measured by diffusion battery and EAA of aerosols atomized from 0.1% DOP in isopropanol.

nearly log-normal with geometric standard deviations of 1.5 and number median diameters of 0.10 μm for the diffusion battery system and 0.13 μm for the EAA .

Next, we measured aerosol generated by the atomizer system from a solution of 1.0 g NaCl in 1000 cm^3 of distilled water. Figure 8 shows the results. Both instruments measured the mode in the distribution at the same particle diameter. However, while the EAA results are very nearly log-normal with number median diameter of 0.06 μm and geometric standard deviation of 1.8, the diffusion battery results are not log-normal. The diffusion battery appears to "chop off" some of the particles above 0.2 μm.

We also measured aerosol generated by the atomizer from 10 g NaCl in 1000 cm^3 of distilled water. Figure 9 shows the results. Again, both instruments locate the mode correctly. The EAA results are nearly log-normal with number median diameter of 0.08 μm and geometric standard deviation of 1.8. The diffusion battery results are not log-normal probably because of the collection of particles above 0.2 μm by impaction and gravitational settling in addition to diffusion. The data reduction program does not consider these additional collection mechanisms.

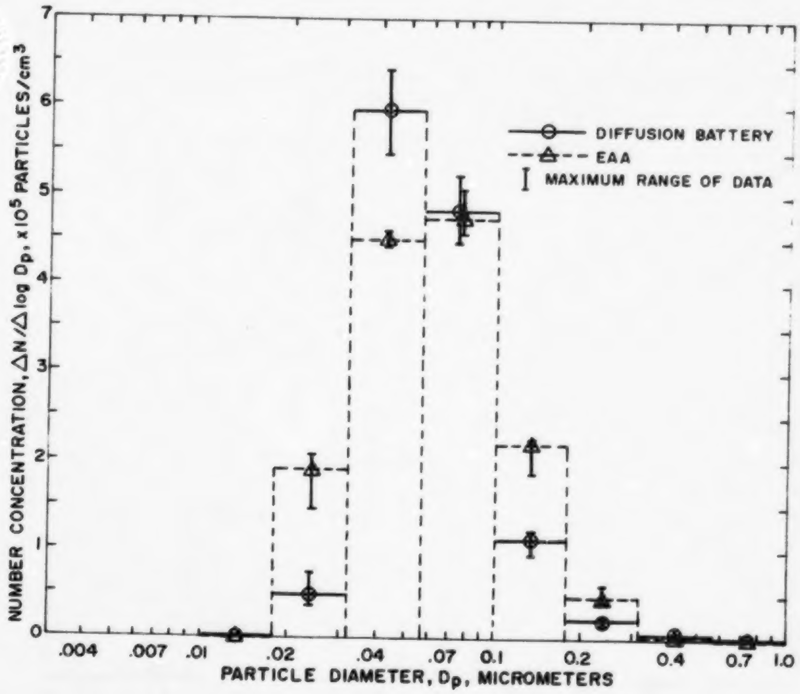

Figure 8. Number distributions measured by diffusion battery and EAA of aerosols atomized from 0.1% NaCl in distilled water.

For the next experiment, we used the bag sampling system to sample diluted smoke from an electric arc welding process. Figures 10 and 11 show the results of the diffusion battery and EAA measurements, respectively. The two runs, in each case, were 12 minutes apart. The EAA results for Run 1 show a definite bimodal shape in the number distribution with a small combustion mode near 0.03 µm and a larger mode in the accumulation range around 0.2 µm. Twelve minutes later, the smaller mode has disappeared and the accumulation mode has also decayed. However, the range around 0.075 µm shows no change, probably the result of the smaller particles colliding and growing into the intermediate range. While the diffusion battery results show a hint of similar tendencies, the data is not nearly so clear, probably because of the limited resolution of the measurement.

The final experiment reported here was the measurement of very small particles near the lower size limit of both measurement systems. We first filled the bag with clean dry air (CNC measured 200 particles/cm^3, EAA measured nothing). Then we produced a very fresh aerosol by inserting a propane torch into the bag for about 10 s. We then closed the bag and immediately began measurements. Figure 12 shows the volume distributions

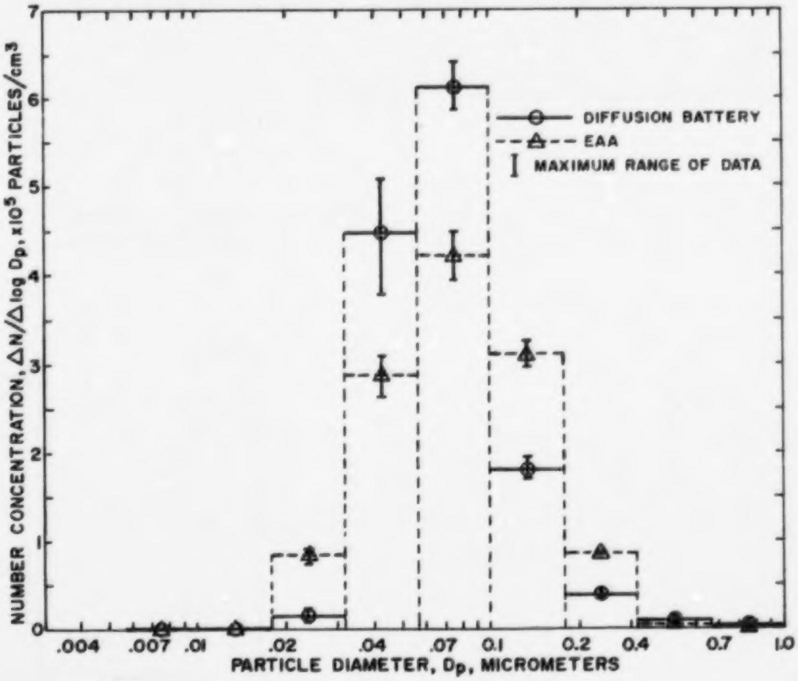

Figure 9. Number distributions measured by diffusion battery and EAA of aerosols atomized from 1% NaCl in distilled water.

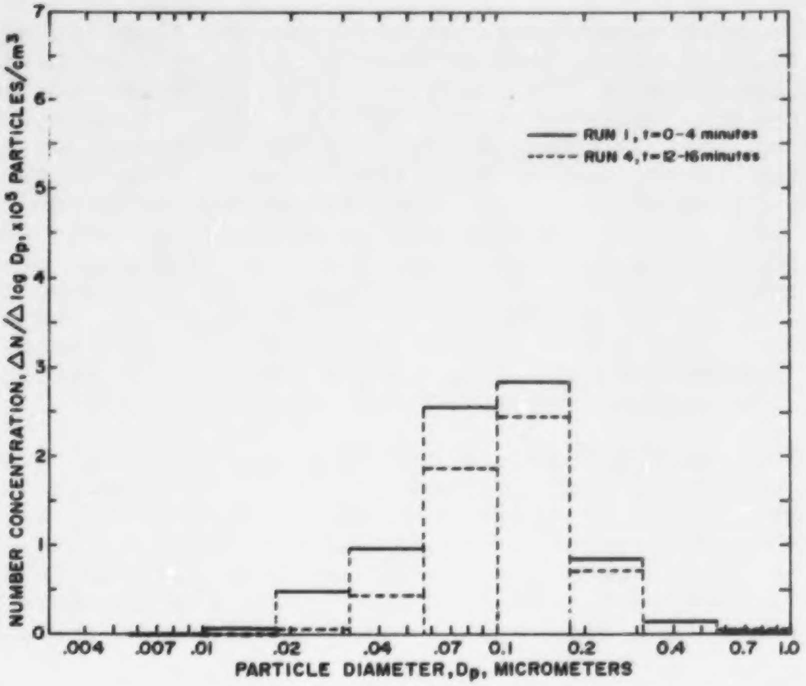

Figure 10. *Number distributions measured by diffusion battery of diluted welding smoke in a closed container as the aerosol ages.*

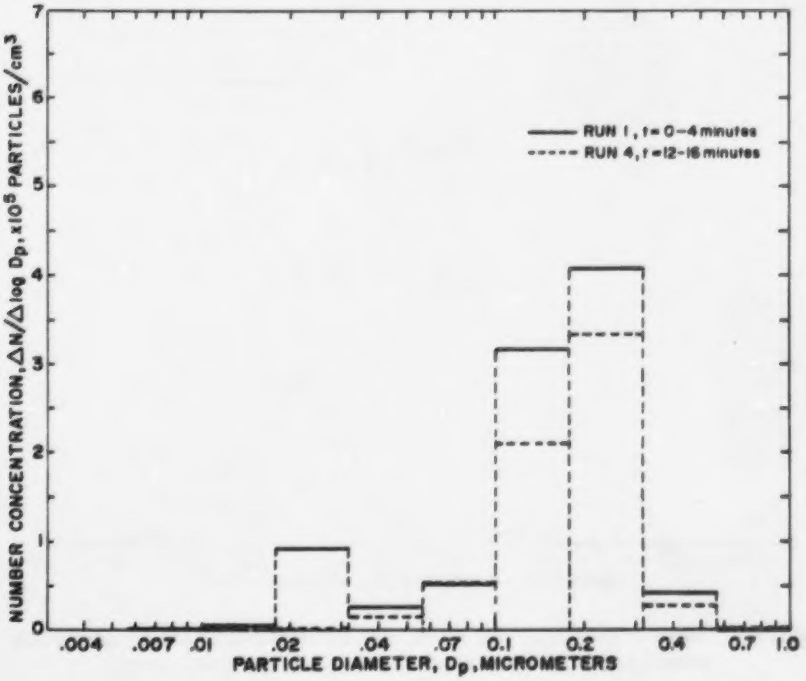

Figure 11. *Number distributions measured by EAA of diluted welding smoke in a closed container as the aerosol ages.*

measured by the EAA beginning just after the bag was filled, four minutes later, and four more minutes later. Additional measurements were made by the EAA at two-minute intervals, but are not plotted on Figure 12 for clarity. We can clearly see some interesting coagulation growth as the aerosol ages. In Figure 13, we see the volume concentration observed in three size channels of the EAA: the channels from 0.0056 to 0.01 μm, from 0.01 to 0.178 μm, and from 0.1 to 0.178 μm. The smallest channel coagulates quickly and the next smallest less quickly. The concentration in the largest channel increases as aerosol accumulates in that size range, having grown from smaller sizes. Incidentally, we extrapolated the EAA sensitivity curve of Pui and Liu[8] to obtain a number concentration in the 0.0032 to 0.0056 μm range. Although this may result in poor absolute accuracy, comparison from run to run is valid.

Figure 14 shows diffusion battery results from the propane aerosol. The decay of the aerosol is evident, but not as clear as with the EAA. The four-minute requirement for a single sizing run limits the diffusion battery in this experiment. Also, the CNC does not effectively detect particles below 0.01 μm, limiting the diffusion battery-CNC system at present to the range above 0.01 μm.

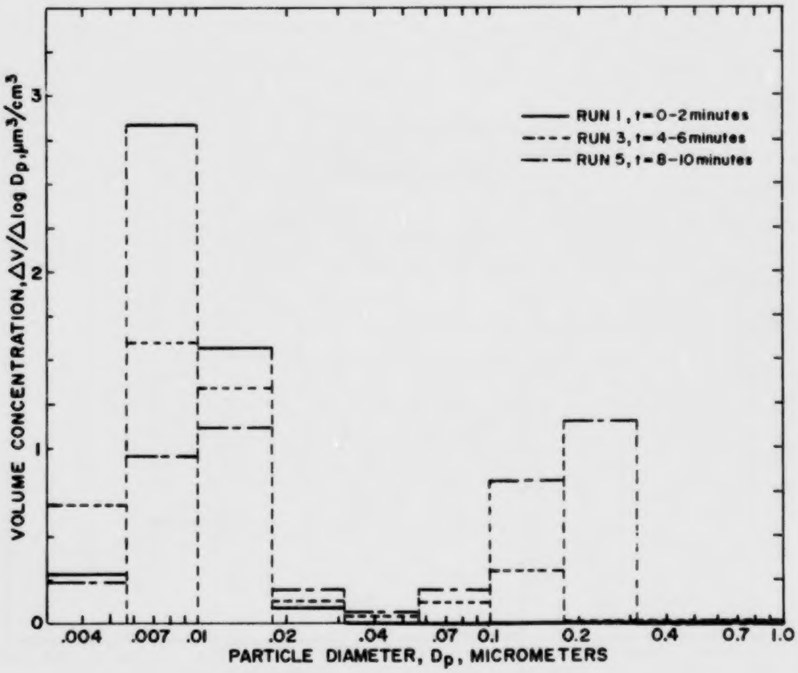

Figure 12. Volume distributions measured by EAA of fresh propane aerosol in a closed container as the aerosol ages.

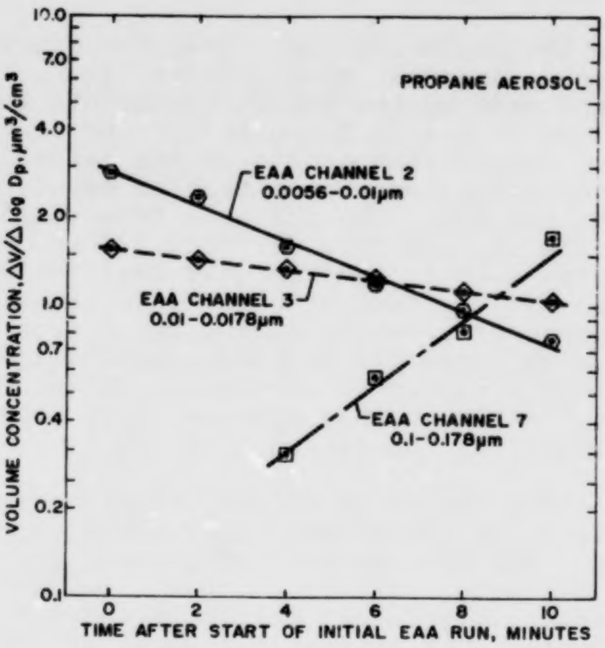

Figure 13. Decay characteristics of propane aerosol of Figure 12 as measured by EAA.

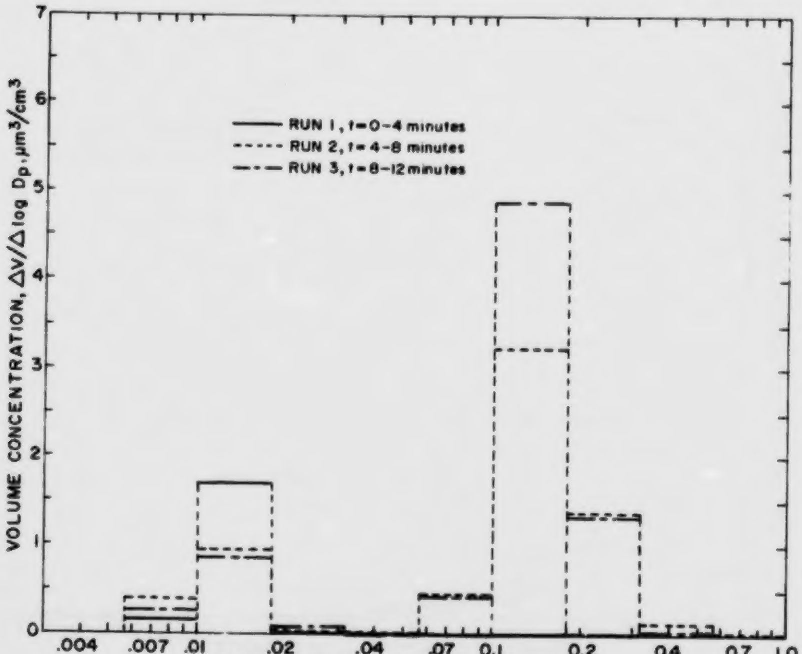

Figure 14. Volume distributions measured by diffusion battery of fresh propane aerosol in a closed container as the aerosol ages.

CONCLUSIONS

A new aerosol size measuring system has been developed consisting of a compact multiple screen diffusion battery, a continuous flow condensation nucleus counter, and an automatic rotary valve to switch the inlet of the CNC to each of the diffusion battery exit ports.

A simple computer program has been developed to convert the data from the new sizing system into submicron particle size distribution. The same approach has been used to calculate particle size distributions for the electrical aerosol analyzer.

In an experimental comparison of the new diffusion battery system with an electrical aerosol analyzer, we find good comparison in the range from 0.01 to 0.2 μm for most aerosols tested. Both systems locate the peak in the size distributions within that range. The diffusion battery system combined with the new computer program appears to cut off part of measured size distributions above 0.2 μm as evidenced by its inability to correctly measure log-normal distributions in the range around 0.2 μm. Further work is needed on data reduction methods for the diffusion battery to include the effects of inertial impaction and gravitational settling for particles greater than 0.2 μm. The diffusion battery-CNC system also needs further evaluation to determine particle losses below 0.01 μm. The current system cannot effectively measure particles below 0.01 μm because of this difficulty. On the other hand, the EAA can measure particles below 0.01 μm in circumstances where few large particles exist. The above example of the measurement of fresh propane torch aerosol demonstrates the EAA's usefulness for measuring coagulation rates for such aerosols below 0.01 μm.

ACKNOWLEDGEMENTS

We received considerable assistance with the experiment and with data reduction from Richard Remiarz. Abde Kapadia shared his computer programs with us soon after he developed them. We are grateful for this generous assistance.

REFERENCES

1. Knutson, E.O., and D. Sinclair. Experience in Sampling Urban Aerosols with the Sinclair Diffusion Battery and Nucleus Counter. In: Proceedings: Advances in Particle Sampling and Measurement. W.B. Smith, compiler. EPA-600/7-79-065, U.S. Environmental Protection Agency, Research Triangle Park, NC, 1979. pp. 98-120.

2. Sinclair, D., and G.S. Hoopes. A Novel Form of Diffusion Battery. Am. Ind. Hyg. Assoc. J. 36:39-42, 1975.

3. Sinclair, D., R.J. Countess, B.Y.H. Liu, and D.Y.H. Pui. Automatic Analysis of Submicron Aerosols. In: Aerosol Measurements, D.A. Lundgren et al., eds. University Presses of Florida, Gainesville, 1979.

4. Agarwal, J.K., and G.J. Sem. Continuous Flow, Single-Particle-Counting Condensation Nucleus Counter. Submitted to J. Aerosol Sci., 1979.

5. Twomey, S. Comparison of Constrained Linear Inversion and an Iterative Nonlinear Algorithm Applied to the Indirect Estimation of Particle Size Distributions. J. Comput. Phys. 13:188-200, 1975.

6. Kapadia, A. Ph.D. Thesis, University of Minnesota, Mechanical Engineering Department, Minneapolis, 1979.

7. Sem, G.J. Electrical Aerosol Analyzer: Operation, Maintenance, and Application. In: Aerosol Measurements, D.A. Lundgren et al., eds. University Presses of Florida, Gainesville, 1979.

8. Pui, D.Y.H., and B.Y.H. Liu. Electrical Aerosol Analyzer: Calibration and Performance. In: Aerosol Measurements, D.A. Lundgren et al., eds. University Presses of Florida, Gainesville, 1979.

9. Liu, B.Y.H., D.Y.H Pui, and A. Kapadia. Electrical Aerosol Analyzer: History, Principle, and Data Reduction. In: Aerosol Measurements, D.A. Lundgren et al., eds. University Presses of Florida, Gainesville, 1979.

APPENDIX 1

```
       PROGRAM DIFFBAT(INPUT,OUTPUT)
C      DIFFBAT USES TWOMEY'S NON-LINEAR ALGORITHM FOR REDUCING DIFFUSION
C      BATTERY DATA. THIS PROGRAM CAN BE USED FOR THE TSI SCREEN BATTERY
C      FOR 4.0 LPM FLOW RATE. THE ITERATIVE PROCEDURE IS STOPPED EITHER
C      WHEN CHI-SQUARE IS LESS THAN 0.001 OR THE NUMBER OF ITRATIONS IS
C      GREATER THAN 100, WHICHEVER OCCURS FIRST AFTER THE FIRST 20
C      ITERATIONS.
C
C      THIS PROGRAM WAS WRITTEN BY ABDE KAPADIA , A PH.D CANDIDATE AT THE
C      U OF M.
        COMMON CALIB(12,45),KDAT,DAT(12),CDAT(12),CLOSS(45),
     + ITER,FLOW,DIA(45),X,ACTDAT(11)
       DIMENSION CALDAT(11)
       DIA(1)=0.00316228
       DPMULT=1.154781985
       DO 5 J=2,45
 5     DIA(J)=DIA(J-1)*DPMULT
230    READ 20,TITLE1,TITLE2,TITLE3,TITLE4
 20    FORMAT(4A10)
C
C      SET UP THE LOSS MATRIX FOR THE TSI SCREEN BATTERY
C
        CALL TSI
C
C      ENTER DATA
C
       DO 65 J=1,11
       ACTDAT(J)=0.0
       CALDAT(J)=0.0
 65    DAT(J)=0.00
       KDAT=11
       READ  ,(ACTDAT(I),I=1,11)
       DO 80 J=1,10
       DAT(J)=ACTDAT(J)-ACTDAT(J+1)
 80    IF(DAT(J).LT.0.0) DAT(J)=0.0
       DAT(11)=ACTDAT(11)
       CALL DIFFTWO
       CALDAT(11)=CDAT(11)
       DO 73 I=1,10
 73    CALDAT(11-I)=CALDAT(12-I)+CDAT(11-I)
      PRINT 78
78    FORMAT(1X,' ',//1X,'TSI MODELS 3040 DIFF BAT AND 3020 CNC  -  TWO
     +MEY METHOD')
       PRINT 81,TITLE1,TITLE2,TITLE3,TITLE4
 81    FORMAT(/1X,4A10,//1X,'PORT NO.',5X,'CNC DATA',
     + 8X,'CALC DATA')
       DO 85 I=1,11
       J=I-1
       PRINT 83,J,ACTDAT(I),CALDAT(I)
 83    FORMAT(3X,I2,8X,F8.0,8X,F8.0)
85     CONTINUE
C
C      CALCULATE VALUES FOR OUTPUT
C
       DO 100 J=3,39,4
 100   CLOSS(J)=(0.5*CLOSS(J-2)+CLOSS(J-1)+CLOSS(J)      +
     + CLOSS(J+1)+0.5*CLOSS(J+2))*4.0
       DO 110 J=3,43,4
        CLOSS(J+1)=CLOSS(J)*3.14*(DIA(J)**2)
 110   CLOSS(J+2)=CLOSS(J)*0.523*(DIA(J)**3)
       TNUM=0.0
       TSURF=0.0
       TVOL=0.0
      DO 120 J=3,43,4
      TNUM=TNUM+CLOSS(J)
      TSURF=TSURF+CLOSS(J+1)
 120  TVOL=TVOL+CLOSS(J+2)
      PRINT 130
 130  FORMAT(//1X,'MID PT. DIA',4X,'DNDLGD',7X,'DSDLGD',7X,'DVDLGD',/)
      DO 150 J=3,39,4
 150  PRINT 160,DIA(J),CLOSS(J),CLOSS(J+1),CLOSS(J+2)
 160  FORMAT(2X,F6.4,2X,3(4X,1PE9.3))
      TNUM=TNUM/4.0
      TSURF=TSURF/4.0
      TVOL=TVOL/4.0
      PRINT 190,TNUM,TSURF,TVOL
 190  FORMAT(1X,'TOTALS',3X,3(4X,1PE9.3))
      PRINT 192,ITER,X
 192  FORMAT(//1X,'NO. OF ITERATIONS= ',I3,5X,'CHISQ= ',1PE10.3)
      DO 195 J=3,39,4
 195  CLOSS(J)=CLOSS(J)/(TNUM*4.0)
 205  READ 210,IFLAG
 210  FORMAT(I1)
      IF (IFLAG .LT. 1 .OR. IFLAG .GT. 2) GO TO 205
      GO TO (230,220) IFLAG
 220  RETURN
      END
C     DIFFTWO
C
C     THIS SUBROUTINE USES TWOMEY'S NON-LINEAR ALGORITHMF
C     FOR SOLVING THE DIFFUSION BATTERY EQUATIONS
C
C
      SUBROUTINE DIFFTWO
       COMMON CALIB(12,45),KDAT,DAT(12),CDAT(12),
     + CLOSS(45),ITER,FLOW,DIA(45),X,ACTDAT(11)
      DIMENSION CNCEFF(45)
      DATA CNCEFF/.078,.081,.093,.099,.120,.151,.29,.35,.47,.59,.69,
     + .77,.83,.90,.95,.97,29*1.0/
      KMAX=20
      JMAX=45
      DO 10 J=1,JMAX
 10   CLOSS(J)=ACTDAT(1)/JMAX
      ITER=0
 100  DO 20 K=1,KMAX
      DO 30 I=1,KDAT
      RATIO=0.0
      DO 40 J=1,JMAX
 40   RATIO=RATIO+CALIB(I,J)*CLOSS(J)*CNCEFF(J)
      IF(RATIO) 30,30,60
 60   RATIO=DAT(I)/RATIO-1.0
      DO 70 J=1,JMAX
 70   CLOSS(J)=CLOSS(J)*(1.0+(RATIO*CALIB(I,J)))
 30   CONTINUE
 20   CONTINUE
      ITER=ITER+KMAX
      IF(ITER.GT.100) GO TO 90
      DO 80 I=1,KDAT
       CDAT(I)=0.0
      DO 80 J=1,JMAX
 80   CDAT(I)=CDAT(I)+CALIB(I,J)*CLOSS(J)*CNCEFF(J)
       CALL ACHISQ
      IF(X .LT. .001) GO TO 90
      KMAX=5
      GO TO 100
90    RETURN
      END
```

APPENDIX 1 (cont)

```
C
C      THIS SUBROUTINE COMPUTES THE LOSS MATRIX FOR TSI SCREEN BATTERY
C      FOR 4.0 FLOW RATES
C
C
       SUBROUTINE TSI
        COMMON CALIB(12,45),KDAT,DAT(12),CDAT(12),
     + CLOSS(45),ITER,FLOW,DIA(45),X,ACTDAT(11)
       FLOW=4.0
 60    AK1=-1.14423
        CK1=-2.990605
 70    DO 90 J=1,45
       NSCRN=0
       SLOPE=-10.0**(AK1*ALOG10(DIA(J))+CK1)
       DO 80 I=2,11
        CALIB(I-1,J)=(10.0**(SLOPE*NSCRN))-(10.0**(SLOPE*(NSCRN+I-1)))
 80    NSCRN=NSCRN+I-1
 90    CALIB(11,J)=10.0**(SLOPE*55.)
       RETURN
       END
C
C      ACHISQ
C
C      THIS SUBROUTINE COMPUTES THE CHI-SQUARE FOR THE OBSERVED
C      AND CALCULATED DATA FOR THE DIFFUSION BATTERY.
C
C
       SUBROUTINE ACHISQ
        COMMON CALIB(12,45),KDAT,DAT(12),CDAT(12),
     + CLOSS(45),ITER,FLOW,DIA(45),X,ACTDAT(11)
       X=0.0
       TCDAT=0.0
       DO 5 J=1,KDAT
 5     TCDAT=TCDAT+CDAT(J)
       DO 10 J=1,KDAT
       AF=(CDAT(J)/TCDAT)-(DAT(J)/ACTDAT(1))
       IF(ABS(AF) .LT. .001 .AND. CDAT(J) .LT. .0001) GO TO 10
       X=X+(AF**2)/(CDAT(J)/TCDAT)
 10    CONTINUE
       RETURN
       END
*RDY*
```

APPENDIX 2

```
      PROGRAM EAATWO(INPUT,OUTPUT)
      COMMON /EAADAT/PHI(11,45),CUR1(11),CUR2(11),X,
     + ITER,DIA(45),EDN(10),EDS(10),EDV(10)
      DIMENSION COMCUR(11),SENS(45),PC1(45),PC2(45),DNI(11),
     + EAACUR(11),DNDI(10)
      DATA DIA/.00316228,.00365174,.00421697,.00486968,.00562342,
     + .00649382,.00749895,.00865965,.01000001,.01154783,.01333522,
     + .01539928,.01778281,.02053527,.02371375,.02738422,.03162280,
     + .03651744,.04216968,.04869679,.05623417,.06493821,.07498948,
     + .08659650,.10000007,.11547828,.13335224,.15399227,.17782807,
     + .20535266,.23713755,.27384217,.31622800,.36517440,.42169682,
     + .48696789,.56234175,.64938212,.74989477,.86596497,1.00000075,
     + 1.15478285,1.33352243,1.53992768,1.77828075/
      DATA DNDI/0.0;9.52E6,4.17E5,1.67E5,8.70E4,4.44E4,2.41E4,
     + 1.23E4,6.67E3,3.51E3/
      DATA JMAX,IMAX,PI/45,11,3.1416/
      DO 140 J=1,JMAX
      TMP=DIA(J)-.0125
      IF(TMP) 120,130,130
120   SENS(J)=2.351E6*(DIA(J))**6.262
      GO TO 140
130   SENS(J)=0.0004264*(DIA(J))**1.159
140   CONTINUE
145   READ 700,IOPT
700   FORMAT(I1)
      IF(IOPT.EQ.0) GO TO 300
      READ 702,TITLE1,TITLE2,TITLE3,TITLE4
702   FORMAT(4A10)
      READ ,EAACUR
      IF(IOPT.EQ.2) GO TO 230
      DO 20 J=1,JMAX
      PC2(J)=EAACUR(1)/JMAX
20    CONTINUE
      TCUR=EAACUR(1)
      IMAX1=IMAX-1
      DO 30 I=1,IMAX1
      CUR1(I)=EAACUR(I)-EAACUR(I+1)
      CUR1(I)=AMAX1(CUR1(I),0.0)
30    CONTINUE
      CUR1(IMAX)=EAACUR(IMAX)
      ITER=0
      KMAX=20
      TCUR=0.0
      DO 32 I=1,IMAX
      TCUR=TCUR+CUR1(I)
32    CONTINUE
35    DO 60 K=1,KMAX
      DO 40 J=1,JMAX
      PC1(J)=PC2(J)
40    CONTINUE
      DO 55 I=1,IMAX
      A=0.0
      DO 50 J=1,JMAX
      A=A+PHI(I,J)*PC2(J)
50    CONTINUE
      IF(A) 55,55,54
54    A=CUR1(I)/A-1.0
      DO 61 J=1,JMAX
      PC2(J)=PC2(J)*(1.0+A*PHI(I,J))
61    CONTINUE
55    CONTINUE
60    CONTINUE
      DO 70 I=1,IMAX
```

APPENDIX 2 (cont)

```
      CUR2(I)=0.0
      DO 65 J=1,JMAX
      CUR2(I)=CUR2(I)+PHI(I,J)*PC2(J)
65    CONTINUE
70    CONTINUE
      IF(ITER.GE.100) GO TO 73
      ITER=ITER+KMAX
      KMAX=5
      CALL ACHISQ
      IF(X.LT..005) GO TO 73
      GO TO 35
73    DO 80 J=1,JMAX
      PC1(J)=PC2(J)/SENS(J)
80    CONTINUE
      PC1(2)=(PC1(1)+PC1(2)+PC1(3)+.5*PC1(4))
      IF(PC1(2).LT.1E-05) PC1(2)=0.0
      DO 111 J=6,38,4
      PC1(J)=(PC1(J-2)/2.0+PC1(J-1)+PC1(J)+
     + PC1(J+1)+PC1(J+2)/2.0)
      IF(PC1(J).LT.1E-05) PC1(J)=0.0
111   CONTINUE
      PC1(42)=(.5*PC1(40)+PC1(41)+PC1(42)+
     + PC1(43)+PC1(44)+PC1(45))
      IF(PC1(42).LT.1E-05) PC1(42)=0.0
      DO 210 I=1,IMAX1
      IF(CUR1(I).LT..001) GO TO 220
      IF(CUR1(I).LT..001*TCUR) GO TO 220
      J=I*4-2
      DNI(I)=PC1(J)/CUR1(I)
      GO TO 210
220   DNI(I)=0.0
210   CONTINUE
C
C
      PRINT 704
704   FORMAT(1X,' ',//1X,'TSI MODEL 3030  EAA  -  TWOMEY METHOD')
      PRINT 705,TITLE1,TITLE2,TITLE3,TITLE4
705   FORMAT(/1X,4A10,//2X,'DIA.',8X,'EAA DATA',
     + 8X,'CALC DATA'/)
      COMCUR(11)=CUR2(11)
      DO 221 I=1,IMAX
      COMCUR(11-I)=COMCUR(12-I)+CUR2(11-I)
221   CONTINUE
      DO 222 I=1,IMAX
      PRINT 706,DIA(4*I-3),EAACUR(I),COMCUR(I)
706   FORMAT(1X,F6.4,2(8X,F6.3))
222   CONTINUE
      DO 225 I=1,IMAX1
      EDN(I)=CUR1(I)*DNI(I)*4.0
      EDS(I)=EDN(I)*PI*DIA(4*I-1)**2
      EDV(I)=EDN(I)*PI/6.*DIA(4*I-1)**3
225   CONTINUE
      CALL WRTOUT(1)
      IF(IOPT.EQ.1) GO TO 145
230   DO 250 I=1,IMAX1
      EDN(I)=CUR1(I)*DNDI(I)*4.0
      EDS(I)=EDN(I)*PI*DIA(4*I-1)**2
      EDV(I)=EDN(I)*PI/6.*DIA(4*I-1)**3
250   CONTINUE
      PRINT 707
707   FORMAT(1X,' ',//1X,'TSI MODEL 3030 EAA  -  CONSTANTS')
      PRINT 708,TITLE1,TITLE2,TITLE3,TITLE4
708   FORMAT(/1X,4A10,//2X,'DIA.',8X,'EAA DATA'/)
      DO 227 I=1,IMAX
      PRINT 706,DIA(4*I-3),EAACUR(I)
227   CONTINUE
      CALL WRTOUT(0)
      GO TO 145
300   STOP
      END
C
C
      SUBROUTINE ACHISQ
      COMMON /EAADAT/PHI(11,45),CUR1(11),CUR2(11),X,
     + ITER,DIA(45),EDN(10),EDS(10),EDV(10)
      TCUR1=0.0
      TCUR2=0.0
      IMAX=11
      X=0.0
      DO 10 I=1,IMAX
      TCUR1=TCUR1+CUR1(I)
      TCUR2=TCUR2+CUR2(I)
10    CONTINUE
      DO 20 I=1,IMAX
      ACUR2=CUR2(I)/TCUR2
      AF=(CUR1(I)/TCUR1)-ACUR2
      ABSAF=ABS(AF)
      IF(ABSAF.LT..001) GO TO 20
      X=X+(AF**2)/ACUR2
20    CONTINUE
      RETURN
      END
C
C
C
      SUBROUTINE WRTOUT(IARG)
      COMMON /EAADAT/PHI(11,45),CUR1(11),CUR2(11),X,
     + ITER,DIA(45),EDN(10),EDS(10),EDV(10)
      PRINT 710
710   FORMAT(//1X,'MID PT. DIA',4X,'DNDLGD',7X,'DSDLGD',7X,'DVDLGD',/)
      TEDN=0.0
      TEDS=0.0
      TEDV=0.0
      DO 100 I=1,10
      PRINT 711,DIA(4*I-1),EDN(I),EDS(I),EDV(I)
711   FORMAT(2X,F6.4,2X,3(4X,1PE9.3))
      TEDN=TEDN+EDN(I)
      TEDS=TEDS+EDS(I)
      TEDV=TEDV+EDV(I)
100   CONTINUE
      TEDN=TEDN/4.
      TEDS=TEDS/4.
      TEDV=TEDV/4.
      PRINT 712,TEDN,TEDS,TEDV
712   FORMAT(1X,'TOTALS',3X,3(4X,1PE9.3))
      IF(IARG.EQ.1) PRINT 713,ITER,X
713   FORMAT(//1X,'NO. OF ITERATIONS= ',I3,5X,'CHISQ= ',1PE10.3)
      RETURN
      END
C
      BLOCK DATA
      COMMON /EAADAT/PHI(11,45),CUR1(11),CUR2(11),X,
     + ITER,DIA(45),EDN(10),EDS(10),EDV(10)
      DATA PHI/
     + 1.00,.000,.000,.000,.000,.000,.000,.000,.000,.000,.000,
     + 1.00,.000,.000,.000,.000,.000,.000,.000,.000,.000,.000,
     + 1.00,.000,.000,.000,.000,.000,.000,.000,.000,.000,.000,
     + .500,.500,.000,.000,.000,.000,.000,.000,.000,.000,.000,
```

APPENDIX 2 (cont)

```
   + .000,1.00,.000,.000,.000,.000,.000,.000,.000,.000,.000,
   + .000,1.00,.000,.000,.000,.000,.000,.000,.000,.000,.000,
   + .000,1.00,.000,.000,.000,.000,.000,.000,.000,.000,.000,
   + .000,.500,.500,.000,.000,.000,.000,.000,.000,.000,.000,
   + .000,.000,1.00,.000,.000,.000,.000,.000,.000,.000,.000,
   + .000,.000,1.00,.000,.000,.000,.000,.000,.000,.000,.000,
   + .000,.000,1.00,.000,.000,.000,.000,.000,.000,.000,.000,
   + .000,.000,.480,.520,.000,.000,.000,.000,.000,.000,.000,
   + .000,.000,.050,.950,.000,.000,.000,.000,.000,.000,.000,
   + .000,.000,.080,.920,.000,.000,.000,.000,.000,.000,.000,
   + .000,.000,.000,1.00,.000,.000,.000,.000,.000,.000,.000,
   + .000,.000,.000,.510,.480,.010,.000,.000,.000,.000,.000,
   + .000,.000,.000,.440,.520,.040,.000,.000,.000,.000,.000,
   + .000,.000,.000,.490,.070,.440,.000,.000,.000,.000,.000,
   + .000,.000,.000,.150,.480,.195,.175,.000,.000,.000,.000,
   + .000,.000,.000,.145,.355,.325,.175,.000,.000,.000,.000,
   + .000,.000,.000,.035,.345,.515,.085,.020,.000,.000,.000,
   + .000,.000,.000,.000,.140,.650,.170,.020,.020,.000,.000,
   + .000,.000,.000,.000,.050,.610,.310,.030,.000,.000,.000,
   + .000,.000,.000,.000,.000,.510,.405,.085,.000,.000,.000,
   + .000,.000,.000,.000,.000,.450,.480,.070,.000,.000,.000,
   + .000,.000,.000,.000,.000,.400,.510,.090,.000,.000,.000,
   + .000,.000,.000,.000,.000,.130,.670,.170,.030,.000,.000,
   + .000,.000,.000,.000,.000,.030,.470,.380,.080,.040,.000,
   + .000,.000,.000,.000,.000,.000,.350,.460,.140,.040,.010,
   + .000,.000,.000,.000,.000,.000,.220,.480,.200,.060,.040,
   + .000,.000,.000,.000,.000,.000,.150,.450,.250,.090,.060,
   + .000,.000,.000,.000,.000,.000,.080,.420,.320,.110,.070,
   + .000,.000,.000,.000,.000,.000,.020,.320,.380,.180,.100,
   + .000,.000,.000,.000,.000,.000,.000,.310,.360,.180,.150,
   + .000,.000,.000,.000,.000,.000,.000,.200,.390,.210,.200,
   + .000,.000,.000,.000,.000,.000,.000,.195,.305,.260,.240,
   + .000,.000,.000,.000,.000,.000,.000,.130,.270,.250,.350,
   + .000,.000,.000,.000,.000,.000,.000,.110,.280,.250,.350,
   + .000,.000,.000,.000,.000,.000,.000,.070,.230,.250,.450,
   + .000,.000,.000,.000,.000,.000,.000,.040,.200,.260,.500,
   + .000,.000,.000,.000,.000,.000,.000,.040,.200,.260,.500,
   + .000,.000,.000,.000,.000,.000,.000,.040,.200,.260,.500,
   + .000,.000,.000,.000,.000,.000,.000,.040,.200,.260,.500,
   + .000,.000,.000,.000,.000,.000,.000,.040,.200,.260,.500,
   + .000,.000,.000,.000,.000,.000,.000,.040,.200,.260,.500/
     END
*RDY*
```

PAPER 17

AN IN-SITU LIQUID DROPLET SIZING SYSTEM

DANIEL E. MAGNUS
DAVID S. MAHLER
KLD ASSOCIATES, INC.

ABSTRACT

The development of an in-situ device for measuring the size and concentration of liquid droplets is described. The sensing element or probe is a hot wire approximately 5 μm in diameter and 1 mm long. When droplets impact the hot wire, the resultant electronic signal is a diagnostic for the droplet size. An electronic processing system was implemented to analyze automatically the signals and determine the droplet size distribution (number of droplets in each of 14 independent size intervals). For each sample run, the entire distribution is determined, and subsequent off-line processing is used to compute the droplet concentration and/or entrained mass.

The measuring system is called the DC-2 and was developed under the sponsorship of the EPA. The device has been used to evaluate efficiency of demisters used to remove entrained mass from various types of scrubbers. The device has also been successfully demonstrated in cooling tower studies and the measurement of oil droplet distributions and selected acid mists.

The technology to improve the performance of the probe and to interface the system with a microprocessor is discussed.

INTRODUCTION

In 1974 KLD Associates, Inc. developed and successfully demonstrated an instrument using the hot-wire principle for measuring the size and concentration of liquid droplets in a gas stream. The demonstration of the device included both laboratory and field measurements. Originally the device was designed for the droplet size range from 20 μm to 500 μm. However, the field studies showed the importance of measurements in the range from 1 μm to 100 μm, where a majority of the droplets are found. Based upon these studies, the electronics of the system was redesigned to include droplets in the size range from 1 μm to 600 μm.

Under a contract from the Environmental Protection Agency, the apparatus for the measurement of droplets was to be improved and refined to enable in-situ measurements under adverse field conditions. The desired improvements in this area of technology included:

- reducing the number of adjustments to be performed by the operator and providing for automatic data acquisition,
- providing 14 sub-intervals of droplet sizes over the range from 1 µm to 600 µm,
- building into the electronics the calibration curve for droplet size and displaying the results in digital form in engineering units, and
- improving the ruggedness of the probe to make it more suitable for field measurements.

The above design objectives were incorporated into a droplet measuring device which is designated as the DC-2. The purpose of this paper is to describe the results of this design effort and to discuss both laboratory and field results achieved with the equipment. Also presented are some recent new design activities to interface the device with on-line computers.

PRINCIPLE OF OPERATION

The operation of the heat transfer droplet sensor is based on the local cooling caused by a droplet attaching to a hot wire. The concept is schematically shown in Figure 1, where the hot wire and its longitudinal temperature distribution are shown (a) before a water droplet (cross-hatched circle) interacts with the wire. The electrical resistance of the wire in (a) is high and substantially uniform along the wire. In situation (b), the portion of the wire covered by the droplet is cooled to approximately the droplet temperature. With a constant electrical current heating the wire, a measurable voltage drop can be sensed between the wire supports. The voltage for condition (a) (before the droplet attachment) is reduced in direct proportion to the cooled length of wire, i.e., the droplet diameter (condition b). The electrical energy delivered to the wire evaporates the water, leaving the sensor dry and ready for further interactions with droplets.

The above description of the operating principle for the hot wire probe is an idealization and in actual practice the electrical signal is rather complex. A typical electrical signal obtained during a droplet-hot wire interaction is shown in Figure 2. Reduction of the voltage implies cooling of the wire. An initial fast decay of the signal is observed; it corresponds

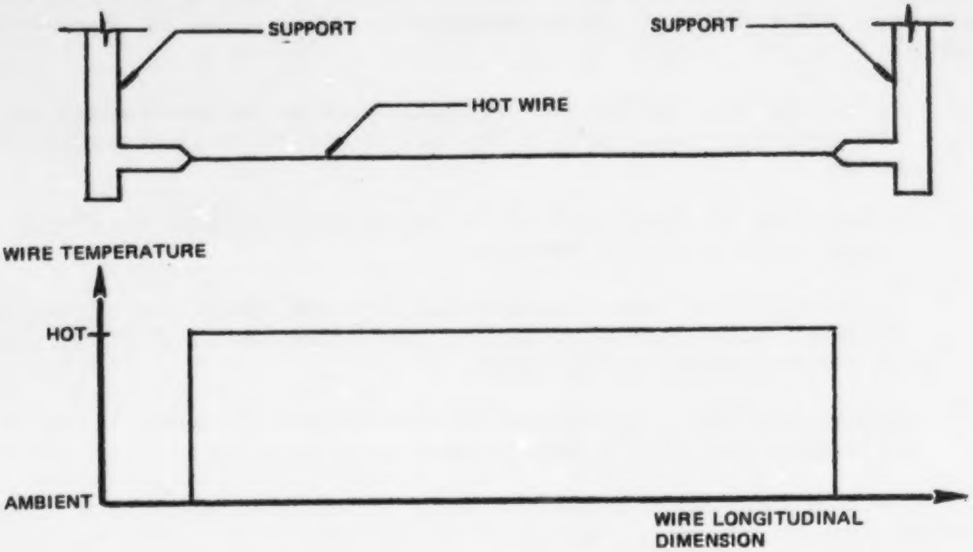
SUPPORT
SUPPORT
HOT WIRE
WIRE TEMPERATURE
HOT
AMBIENT
WIRE LONGITUDINAL DIMENSION

(a) TEMPERATURE BEFORE ATTACHMENT

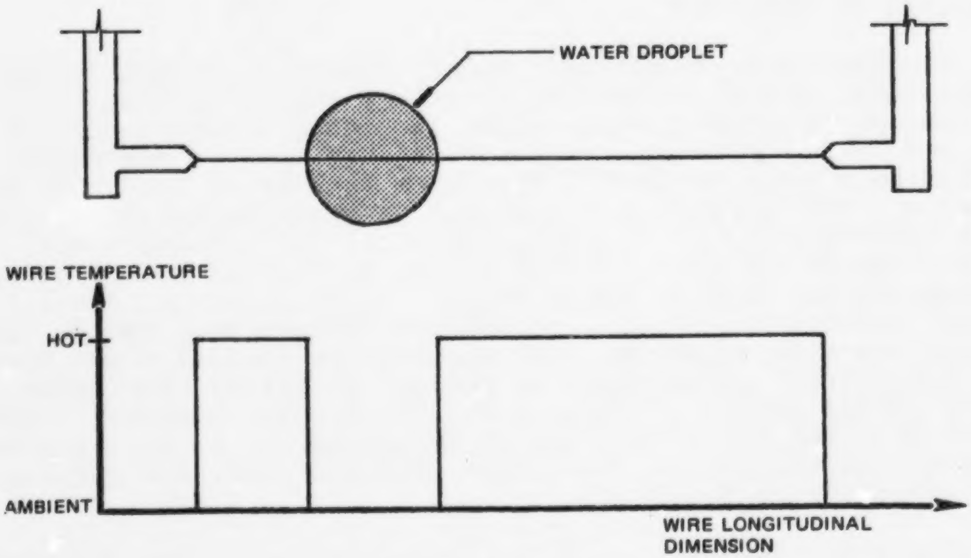
WATER DROPLET
WIRE TEMPERATURE
HOT
AMBIENT
WIRE LONGITUDINAL DIMENSION

(b) TEMPERATURE AFTER ATTACHMENT

Figure 1. Principle of operation of the sensor.

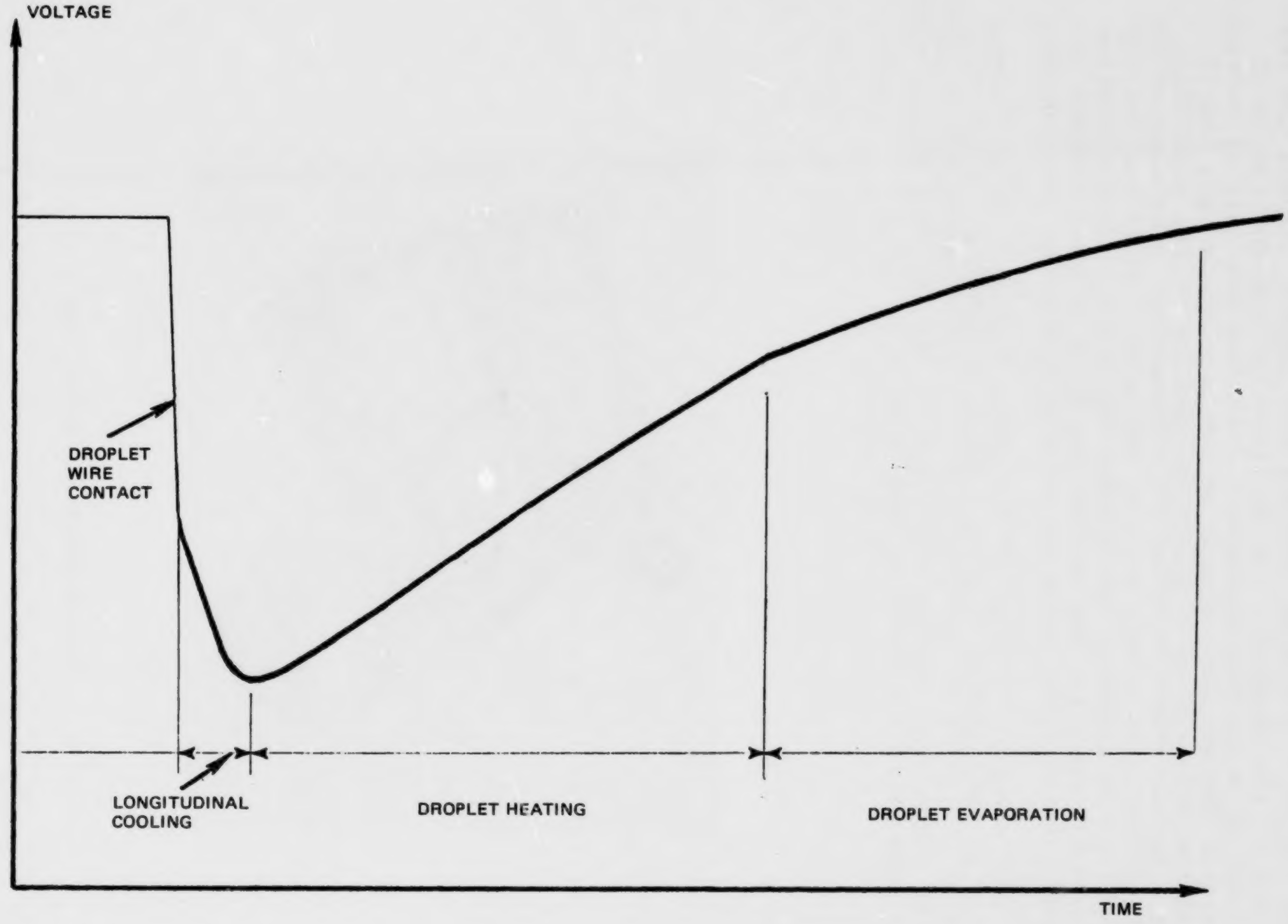

Figure 2. Electrical signal from sensor.

to the initial contact of the droplet and the wire. During this period the wire is cooled radially and rapidly assumes the temperature of the droplet. The duration of this portion is of the order of a few microseconds. Following the initial contact, the signal changes more slowly as the droplet centers itself around the wire and as longitudinal cooling of the wire takes place. During this period of the interaction, a warming of the droplet/wire takes place, raising the signal until the boiling temperature is reached; the droplet shrinks due to evaporation and then disappears. The voltage in the wire then returns to the equilibrium level prior to the interaction of the droplet.

The foregoing concept of measuring droplet size and concentration is implemented using two major components: a hot wire probe as a transducer and electronic instrumentation for analyzing the electrical signals for droplet size and storing the data. These components are shown in Figure 3.

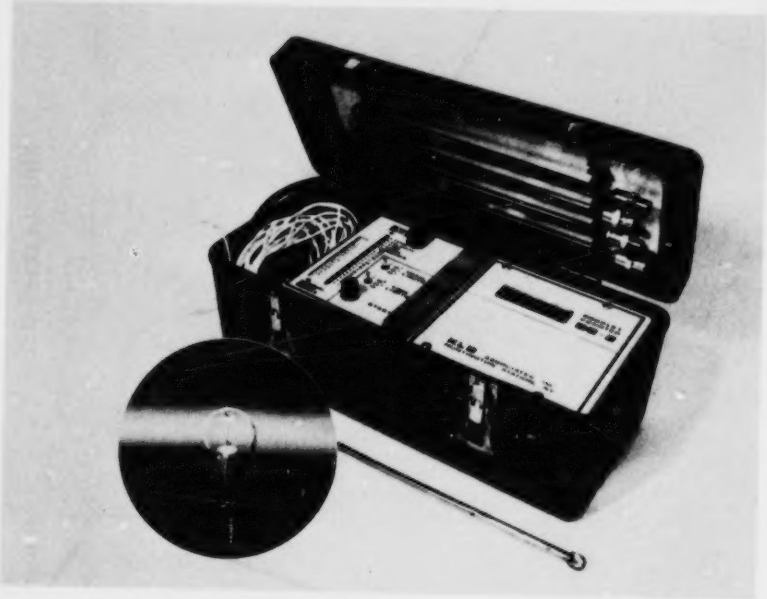

Figure 3. Droplet counter and probe.

The probe is made from platinum wire 5 µm in diameter, and the active portion of the wire is one millimeter long. With this size wire, the DC-2 can measure diameters of droplets from 1 µm to 600 µm. As shown in Figure 3, the fine wire is mounted across a ring at the top of the transducer, which is connected to the instrumentation box by a single coaxial cable. This type of probe is called an open probe since it is unprotected against breakage during handling. Other designs have been fabricated with sliding sleeves which cover the probe and successfully minimize damage from handling.

The electronics box for analyzing the signals from the probe determines the size of the interacting droplet with respect to 14 size ranges and permanently stores the count for each range. The size ranges can be adjusted by changing a plug-in ladder network. The DC-2 comes equipped with four ladder networks, and thereby allows the operators to study a variety of droplet distributions. The equipment is designed for simple operation and a single pushbutton switch (START) automatically cycles the DC-2. When the START switch is pushed, the device remains in the droplet counting mode until a preselected number of droplets (100, 1,000 or 10,000) interact with the probe or a prescribed time limit (10, 100, 1,000 seconds) is reached. After completing a measurement cycle, the system halts and the data can be read from a liquid crystal display, which was chosen for its superior performance in bright ambient light.

The electronics box has been designed to provide the field user with a light-weight and compact instrument. The box is 14½ in. long, 6 in. wide, and approximately 6 in. high and weighs approximately 10 lbs. The case and card bucket are made of drawn aluminum; the circuit cards are wire-wrapped and made of glass epoxy. The instrument is powered from 125VAC (± 15%), 60 Hz line requiring 2.5 watts of power. The electronic system is designed using low power, CMOS logic with a maximum counting rate of 500 droplets/sec. In the report by Medecki, et al., a description of the logic and circuit diagrams is presented.[1]

LABORATORY INVESTIGATIONS

Laboratory investigations with the DC-2 have emphasized three types of activity:

- droplet attachment mechanism
- calibration procedures
- comparisons with other droplet measurement techniques

For the first two types of activity, attachment mechanisms and calibration, carefully controlled procedures for generating droplets are required as well as reliable techniques for recording and verifying the droplets interacting with the hot wire probe. A variety of techniques were used to generate monodispersions and polydispersions of droplets. These techniques included: saturated steam, vibrating capillary, micropump, rotating disc, Berglund Liu generator, and various nozzles. The monodispersion generated with the Berglund Liu apparatus was most useful for developing the initial calibration curve for the device. However, the available size range was restricted and therefore other techniques were used to extend the range of calibration. Working with a polydispersion, the interacting droplets are observed under a microscope during attachment to the hot wire.

A photographic camera records the image of both the wire and the droplet, and a permanent record is obtained to study the attachment mechanism and to provide the calibration data. Since the interaction time is short, an electronic flash is used to stop the motion at the instant of droplet contact; no appreciable shrinkage due to evaporation takes place and accurate calibration data is obtained. The duration of the flash is approximately one microsecond, which is compatible with movement and shrinkage of the droplet in the diameter range of interest. Simultaneously, the electrical signal from the probe is displayed on an oscilloscope and photographed. These two photographic records provide the data for calibrating the DC-2.

With such equipment, the attachment mechanisms of droplets can be comprehensively studied. In this manner, the effects of surface tension between the droplet and the wire have been investigated. Further, the influence of eccentric collision[2] between the droplet and the wire was studied as a function of droplet size and velocity relative to the wire. Also the limitations on flow velocity were investigated[3] and an upper bound on the droplet size was designed for a flow velocity of approximately 10 m per second for droplets no larger than 600 μm. If higher flow velocities are encountered, the large droplets tend to shatter upon contact with the wire.

Using the above-mentioned equipment, a complete calibration curve has also been developed for the DC-2 and this calibration curve has been implemented into the electronics of the system. The calibration curve provides a direct relationship between the droplet size and the electronic signal generated by the probe, as droplets interact at low velocities. Under actual field conditions, the flow influences the droplets interacting with the wire. This type of flow phenomena is usually expressed in terms of a capture area which is a relationship dependent upon droplet size. Such problems have been investigated in aerosol filtration[4,5] using a two-dimensional analysis for the flow past an infinite cylinder. It can be shown that viscous conditions have a significant effect upon the capture area for small droplets. These effects are most important in the size range from 1 μm to 10 μm.

To further verify the performance of the DC-2, a series of laboratory tests were performed to validate the device with other apparatus such as the Brink impactor which is used to sample droplet and particulate distributions in industrial applications. To minimize any measurement error, a closed system with a steady flow was used in the laboratory (Figure 4). The droplets were generated using a disc rotating at a constant speed in a closed box. The entrained droplets were drawn from the box by a constant volume pump (0.03 ft^3/min) located downstream of the impactor and the flow was returned to the box. During the test, the droplet distributions upstream and downstream of the impactor were monitored by the DC-2s noted as A and B in Figure 4.

The system was operated with pure water or a 10% sodium chloride solution. Aluminum foil cups were used as targets in the impactor. The tests with pure water identified some sources of measurement errors in the impactor. For example, the DC-2 at location A indicated a stable droplet distribution, but the impactor results were erratic. The length of the sampling time has a pronounced influence on the measurements with the impactor and the scatter of data was found to be unacceptable. These problems were attributed to evaporation and/or condensation taking place at various points in the impactor. Because of these problems with the impactor, the quantitative studies with pure water were discontinued early in the research.

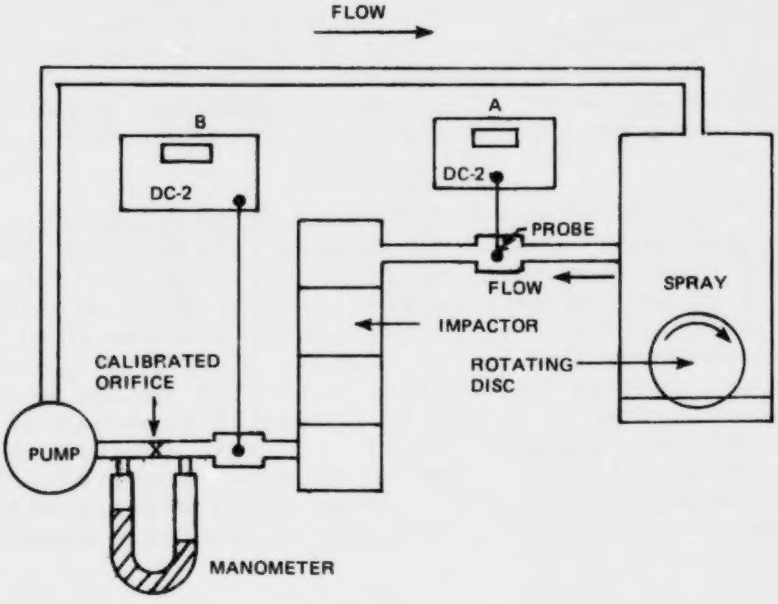

Figure 4. Laboratory apparatus.

The impactor measurements with a salt solution were more dependable, but not entirely satisfactory. Again, the impactor results tended to have excessive scatter which was more pronounced as the sampling time increased. By very careful measurement, it was determined that the salt concentration of the liquid collected at the impact target is less than 10% and often as low as 5%. This result suggests that the samples were being diluted by condensation of water vapor from the saturated flow. Another interesting observation from the impactor studies was demonstrated by the transient behavior at its output. The droplet concentration measured by the DC-2 at location B was initially very low. Approximately 10 to 60 minutes (depending on the number of impactor stages) were required for the droplet distribution to stabilize and to establish a meaningful distribution. Hence, the impactor must be conditioned to the sampled environment to achieve reliable data.

All subsequent tests were carefully designed to permit adequate time for the impactor to stabilize, but the impactor data still exhibited some scatter. In an attempt to further improve performance, the impactor was placed inside the box where the droplets are generated. After "soaking" in the test environment, tests were performed, but only minor improvements in the performance of the impactor were observed.

Based upon this experience with the impactor, some carefully selected and controlled tests were performed to provide data for comparing the DC-2 and the impactor. A typical distribution of number concentration versus droplet diameter is shown in Figure 5. The results from the DC-2 are presented as the dashed curve and include the effects of the flow field on the capture size of the wire. The results from the impactor are rather close considering the scatter associated with such measurements.

Another series of tests currently in progress utilizes a well-calibrated spray nozzle in an open system. The nozzle produces a very high concentration of droplets in the size range from 1 μm to 50 μm. A very carefully controlled uniform flow condition is established with this system and the flow is confined to a tube approximately 1 inch in diameter. Steady state conditions are readily established with this system and the mass flow is determined at a specified operating pressure by direct measurement of the consumed liquid. In this manner the entrained mass measured with the DC-2 can be directly compared with the fluid flow through the nozzle. These tests are currently in progress and initial results indicate a favorable comparison.

FIELD/LABORATORY EQUIPMENT

The basic equipment for measurements in the field and the laboratory consists of the probe and the DC-2 electronic box. The droplet distribution data acquired during each sample period can be manually read via the liquid crystal display and the results recorded on appropriate log sheets. To facilitate the collection of many data samples, a printer/controller unit was developed for controlling two DC-2s. The unit is useful when simultaneous measurements are required upstream and downstream of a device (e.g., to evaluate the efficiency of a demister). A schematic configuration of the equipment is shown in Figure 6.

Both DC-2 units, A and B, are under the direct control of the printer/controller. Samples can be taken in a continuous mode with the data from units A and B printed after the completion of each data cycle. The system can also be used for periodic sampling with units A and B. The time period can be preset to 5, 10, 15, 30, 60 or 120 minutes by the operator. In either mode, the printed data includes all the measured parameters and the real-time when the data cycle was completed. After completing a specified number of data cycles, the printer/controller automatically terminates operation.

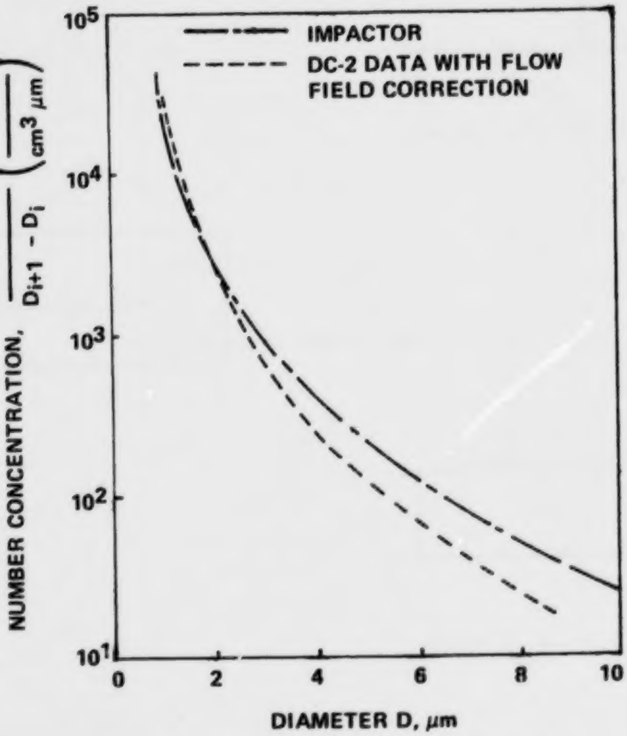

Figure 5. Number concentrations for the DC-2 and impactor. Impactor sample period equals 80 min.

More recently, KLD has interfaced the DC-2 with a microprocessor system to further facilitate the acquisition of a large number of data sample points. This type of arrangement has been very advantageous during the laboratory tests where hundreds of data samples are recorded and must be subsequently processed to analyze the results. The printer and computer for this system are too large and bulky for application to field work. However, KLD has recently designed a compact microprocessor system which is capable of data acquisition and analysis in the field environment.

For application in the field, devices to support the probe while surveying across large ducts are available. Currently a telescoping pole approximately 2 in. in diameter is used to survey across a large duct in typical power plant applications. The pole is capable of extending to 14 feet. The pole itself is supported by a support bearing attached to the sidewall of the duct. This type of equipment reduces the data activities in the field to a routine procedure after the appropriate access ports have been installed.

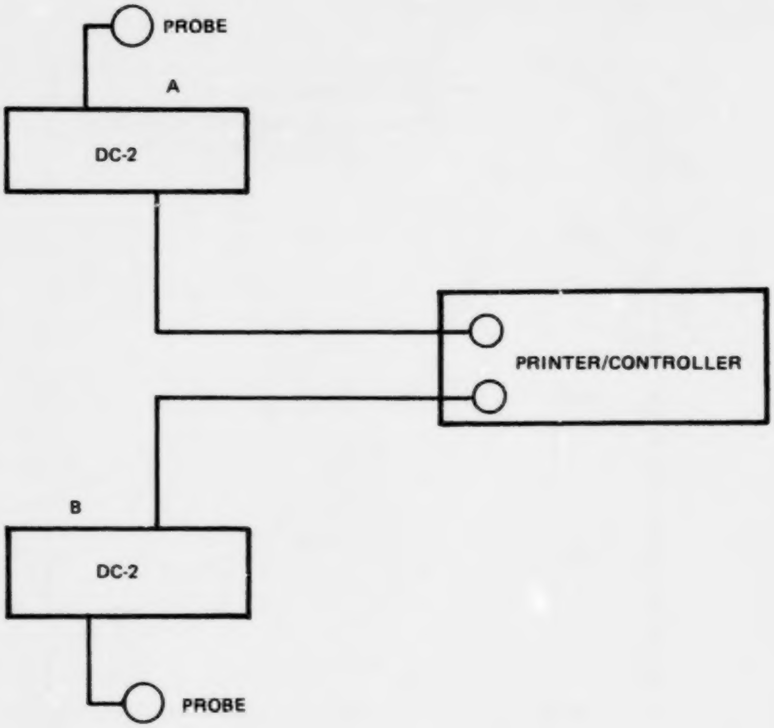

Figure 6. Printer/controller for automatic operation with two DC-2 units.

FIELD MEASUREMENTS

The measurement of droplet distributions and concentrations is important in several applications such as the evaluation of demister performance in power plants, assessment of entrained mass in quenching towers and environmental control in large manufacturing complexes where oil mist can be a problem. Some of these studies[1] have been documented in other reports.

The field studies at the limestone scrubber/demisters provided the most severe test environment because of the accumulation of limestone on the sensor. However, the contamination of the sensor is easily detected as a reduction of the droplet counting rate or by periodically inspecting the sensor. Then the contaminated sensor is cleaned with hydrochloric acid or the entire probe is replaced to expedite the work.

Field studies of limestone scrubber/demister have been performed at power plants at Shippingport, PA and Becker, MN. At Shippingport a 12-foot square section was surveyed through six ports approximately 40 feet downstream of the demister stage. At one site, the tests were performed downstream of a single demister. At the second site, two demisters were in series and measurements were taken after the second demister. For both sites the duct downstream of the demister is horizontal. Such a survey required about two hours to complete following equipment set-up. A total of 51 droplet distributions were recorded.

The average velocity measured with the DC-2 was 10 m/sec, and this value was used for computing the number concentration. Typical results are shown in Figure 7 as a function of droplet size. The upper curve is the number distribution for the site with a single demister, whereas the lower curve is for the double demisters in series.

The data for the two sites is summarized below:

	Number of Demisters	
	1	2
Volume concentration (gr/ft^3)	0.21	0.093
Droplet concentration ($no./cm^3$)	525	301
Mass mean diameter (μm)	11.9	11.0

At the Becker Power Plant the mass carry-over from the demister section was determined. In this power plant the demisters and duct work have a vertical orientation and the surveys were performed over a cross-section of approximately 15 x 21 ft. Five access ports were located along each of the longest sides of the duct. The surveys were performed by extending a pole approximately half-way into the duct and taking measurements from the mid-point of the duct to the wall. A total of 30 spatial locations were used over the entire cross-section. At each location two to four measurements were taken and averaged to obtain the distribution at each location.

A demister with two rows of chevrons is used in this power plant. During this evaluation period, one row of chevrons was removed and the tests repeated to assess the effect on the mass carry-over. The size of this coal power plant is 760 megawatts. The scrubbers remove approximately 80% of the sulfur dioxide and the liquid to gas ratio is 30 gallons/1000 ft^3.

CONCLUSIONS

The hot-wire sensor is an effective means of measuring the droplet size and concentration. The DC-2 has been successfully used in the laboratory and has provided valuable insight into the behavior and performance of impactors when used as a sampling device for droplet distributions. Also, the DC-2 has been demonstrated in the field under various adverse environments. The field studies were successful and useful measurements were obtained. Measurements can be taken rapidly with a minimum of labor and set-up time.

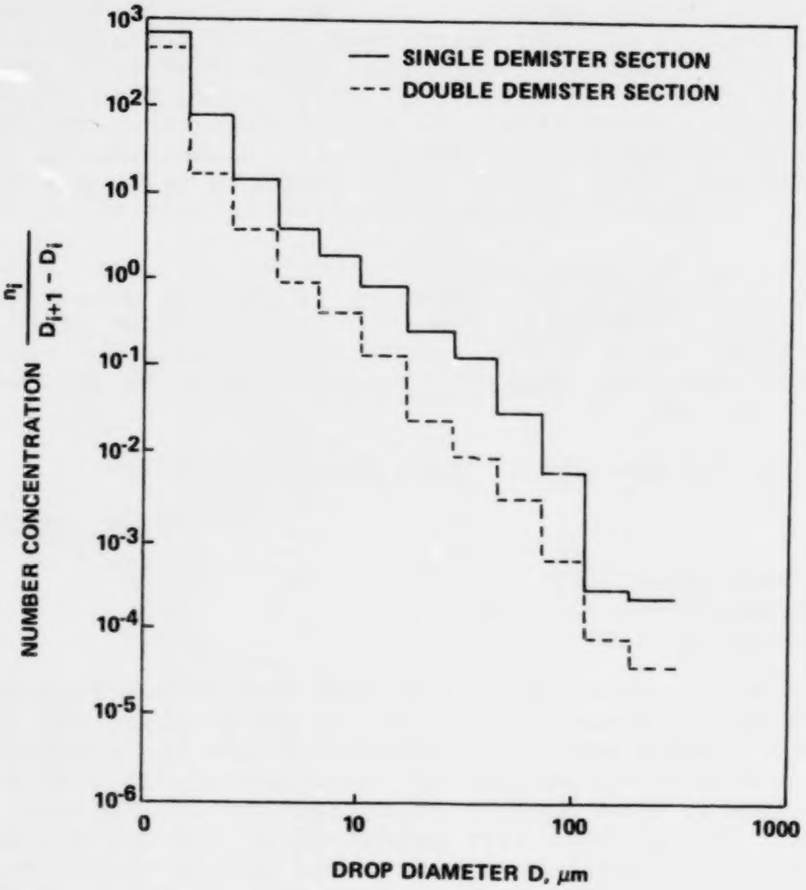

Figure 7. Number concentration vs. droplet diameter for a single and double demister.

ACKNOWLEDGEMENTS

The research and development work on hot wire technology for the detection and measurement of droplets was sponsored by the Environmental Protection Agency, Research Triangle Park, NC. Mr. Bruce Harris was the Project Officer for the EPA and his support and suggestions are gratefully acknowledged. The measurements at Shippingport were coordinated by Mr. Dennis Martin of York Research. The measurements at the Becker Power Plant were sponsored by Combustion Engineering, Inc. and were under the supervision of Mr. Kal Malki.

REFERENCES

1. Medecki, H., K. Wu, and D.E. Magnus. Development of Droplet Sizing Technique for the Evaluation of Scrubbing Systems. EPA-600/7-79-166, U.S. Environmental Protection Agency, Research Triangle Park, NC, July 1979.

2. Medecki, H., M. Kaufman, and D.E. Magnus. Design, Development, and Field Test of a Droplet Measuring Device. Environmental Protection Technology Series. EPA-650/2-75-018, U.S. Environmental Protection Agency, Research Triangle Park, NC, February 1975.

3. Medecki, H. and D. Magnus. Liquid Aerosol Detection and Measurement. Presented at 68th Annual Meeting of the Air Pollution Control Association, 1975.

4. Davies, C.N., ed. Aerosol Science. Academic Press, New York, 1966.

5. Fuchs, N.A. The Mechanics of Aerosols. Pergamon Press, New York, 1964.

PAPER 18

SOME AERODYNAMIC METHODS FOR SAMPLING INHALABLE PARTICLES

WALLACE B. SMITH
KENNETH M. CUSHING
M. CHRISTINE THOMAS
RUFUS R. WILSON, JR.
SOUTHERN RESEARCH INSTITUTE

AND

D. BRUCE HARRIS
INDUSTRIAL ENVIRONMENTAL RESEARCH LABORATORY-RTP
U.S. ENVIRONMENTAL PROTECTION AGENCY

INTRODUCTION

At present, most measurements used to characterize particulate emissions from stationary sources are made with cascade impactors, cyclone trains, and filters. However, these methods do not distinguish between the inhalable and non-inhalable fractions of the suspended particles. The objective of the investigation described in this paper was the development of equipment and procedures for measuring the concentration of inhalable particles, either by modifying existing sampling systems and procedures or by developing new ones. The systems that were developed are to be used for establishing emission factors for stationary sources by measuring the concentrations of inhalable particles in stacks and in fugitive emissions. The systems were designed to have a second cut point at 2.5 ± 0.5 µm aerodynamic diameter. This requirement ensures that the systems used to measure the emission factors will yield data comparable to that measured in the ambient atmosphere using the EPA dichotomous samplers.

The devices considered as candidates for inhalable particulate samplers were impactors, cyclones, and horizontal elutriators.

Impactors are compact and the theory describing their operation is well developed. However, impactors of conventional designs are inefficient collectors for particles with diameters larger than the cut point values of the impactor stages.[1-3] Particle bounce resulting in reentrainment is evidently responsible for much of the inefficiency.

Cyclone collectors are not subject to this problem, and they also have the advantage that the inlet is at a right angle to the axis of the cyclone and hence the sampling nozzle can be pointed directly into the gas stream in the stack without the need for a button-hook or curved nozzle. On the other hand, cyclone samplers are bulky compared to other samplers, and no adequate theory exists for their performance.

Horizontal elutriators are also somewhat bulky and they are sensitive to orientation. However, reentrainment is not a problem, and the theory describing their performance is straightforward and accurate.[4]

Four prototype systems were investigated during this study: (1) horizontal elutriators for sampling fugitive emissions and to be used as precollectors for in-stack cascade impactors and the EPA Source Assessment Sampling System (SASS), (2) a high-volume cascade impactor for fugitive emissions, (3) a precollector cyclone for use with in-stack cascade impactors, and (4) a dual-cyclone train for in-stack sampling. All of the prototype systems were evaluated under conditions of gas flow and temperature consistent with those present in actual sampling conditions.

EXPERIMENTAL INVESTIGATION AND RESULTS

Prototype systems employing horizontal elutriators, inertial impactors, and cyclones were fabricated and tested in the laboratory.

Horizontal Elutriators

Horizontal elutriators have consistently predictable collection efficiencies, as confirmed by Stein, et al.,[5] Rimberg and Thomas,[6] and Corn, et al.[7] Elutriators have been used both as particle sizing instruments and as particle collection devices.[8]

The experiments described in this section were performed to verify the theory of particle collection by settling and to develop design criteria for inlet collectors to be used in conjunction with two sampling systems developed for the Environmental Protection Agency: the Fugitive Ambient Sampling Train (FAST) and the Source Assessment Sampling System (SASS). Designs were also developed for applications with in-stack cascade impactors.

The initial concept of the horizontal elutriator was the result of studies to measure quantitatively the deposition of aerosol particles on surfaces adjacent to, or suspended in, moving gas streams flowing through laboratory apparatus. Natanson[4] and Thomas[6] independently solved this problem theoretically for a circular horizontal tube of radius a. Although the derivations are somewhat complex, the results can be summarized and simplified in terms of the collection efficiency (Eff) by the following equation:

$$\mathrm{Eff} = \frac{2}{\pi}\left[2\varepsilon\sqrt{1-\varepsilon^{2/3}} - \varepsilon^{1/3}\sqrt{1-\varepsilon^{2/3}} + \arcsin \varepsilon^{1/3}\right] \qquad (1)$$

where

$$\varepsilon = \frac{3V_s L}{8a\bar{V}}$$

V_s is the settling velocity,

L is the length of tube,

a is the radius of tube, and

$\bar{V}$ is the average velocity of the gas.

The theory describing the performance of a rectangular flat plate elutriator is considerably less complex and is re-derived here to give the reader a better understanding of the particle motion in the elutriator. The settling velocity of spheres in a gas stream is given by the equation

$$V_s = \frac{C\rho g d^2}{18\mu} \qquad (2)$$

where

V_s is the settling velocity,

g is the acceleration due to gravity,

C is the slip correction factor,

ρ is the particle density,

d is the particle diameter, and

μ is the viscosity of the gas.

In health-related studies, the aerodynamic behavior of the particles is of interest. It is therefore convenient to relate the settling velocity of all particles, whatever their shape or density, to that of spheres having unit density. The aerodynamic diameter is defined as the diameter of a unit density sphere having the same settling velocity as the particle of interest. The aerodynamic diameter is given from Equation 2 by setting $\rho = 1\ \mathrm{g/cm^3}$ (the units must be retained). Also, for particles larger than about 2 μm, the slip correction factor is approximately equal to unity. A graph of settling velocity vs. diameter is shown in Figure 1.

For fully developed flow between parallel plates, the velocity profile of a gas is parabolic with the maximum velocity equal to 1.5 times the average and with zero velocity at the plates:

$$V_x = \left(\frac{6y}{h} - \frac{6y^2}{h^2}\right) \bar{V} \qquad (3)$$

where

V_x is the velocity parallel to the plates, at a point y,

y is the displacement above the bottom plate,

h is the spacing between plates, and

$\bar{V}$ is the average velocity of the gas.

The velocity profile and a typical particle trajectory are illustrated in Figure 2.

The efficiency with which particles are collected is determined by the dimensions of the channel, the velocity of the gas, the settling velocity of the particles, and the height at which the particles enter the channel.

Consider a particle which enters the channel at position y_o as shown in Figure 3 and which has a trajectory of length L (the length of the channel). All particles of this diameter or larger entering at or below position y_o will be captured. All particles of this diameter entering the channel at positions higher than y_o will penetrate the channel.

Now, from Equation 3:

$$\frac{dx}{dt} = \left(\frac{6y}{h} - \frac{6y^2}{h^2}\right) \bar{V}$$

but dy is given by $dy = -V_s dt$; therefore

$$\int_0^L dx = \frac{\bar{V}}{V_s} \int_{y_o}^0 \left(\frac{6y}{h} - \frac{6y^2}{h^2}\right) dy; \text{ and}$$

$$V_s L = \left(\frac{3y_o^2}{h} - \frac{2y_o^3}{h^2}\right) \bar{V} \qquad (4)$$

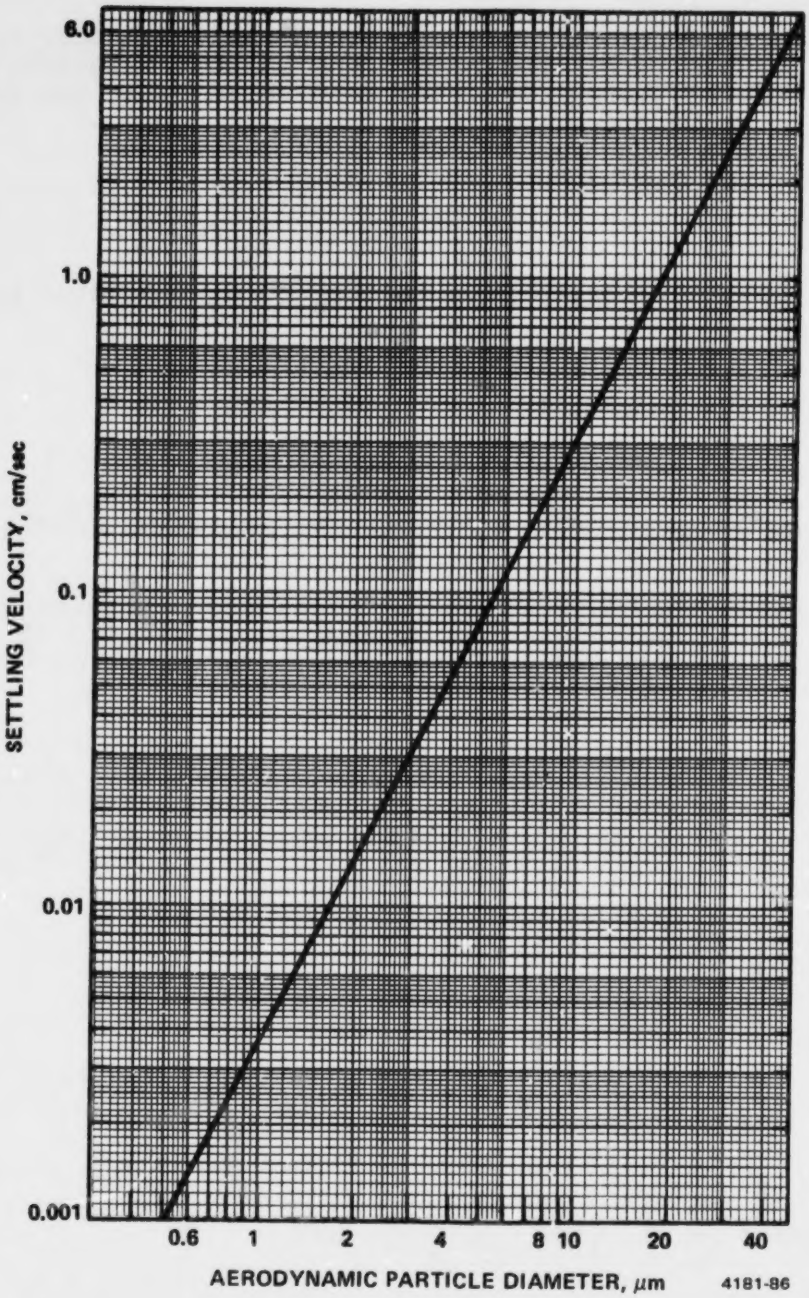

Figure 1. Settling velocity in air for unit density spheres.

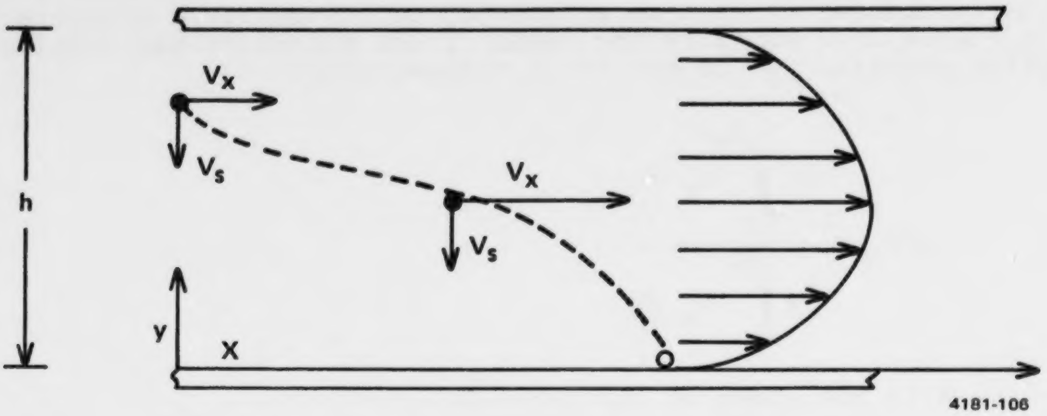
Vx
Vs
Vx
Vs
h
y
X
4181-106

Figure 2. Velocity profile and particle trajectory between parallel plates.

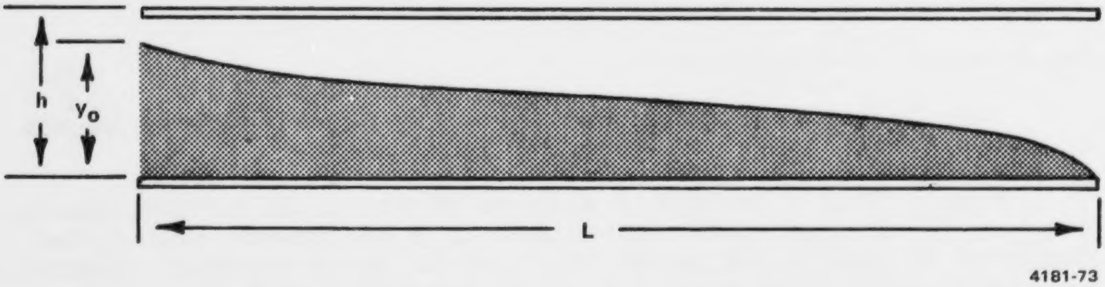
h
yo
L
4181-73

Figure 3. Zone of 100% particle collection.

from which the settling velocity of the particle may be determined.

If the particles are uniformly distributed within the gas, the fractional collection efficiency of the particle illustrated in Figure 2 is equal to the ratio of the volume of gas passing below position y_o to the total volume; thus:

$$\text{Eff.} = \frac{W \int_0^{y_o} V_x \, dy}{W \int_0^{h} V_x \, dy}$$

where W is the width of the channel.

Now, from Equation 4,

$$\text{Eff.} = \frac{V_s L}{h \bar{V}} = \frac{C \rho g d^2 L}{18 \mu h \bar{V}} \qquad (5)$$

The theoretical efficiency curves for a horizontal elutriator with a circular cross-section (from Equation 1) and for a horizontal elutriator with a rectangular cross-section (from Equation 5), both designed to have a cut point of 15 µm aerodynamic diameter, are shown for comparison in Figure 4.

The efficiency is found to be independent of the vertical velocity profile and, as Fuchs[4] observed, Equation 5 can be derived more easily assuming plug flow.

Experimental Procedures--

Experiments were conducted to verify Equation 5 and to set design parameters for the FAST and SASS inlets.

Figure 5 is a schematic diagram of the experimental apparatus used to investigate the performance of a horizontal elutriator designed to have a cut point (D_{50}) of 15 µm aerodynamic diameter. The settling chamber consists of 28 channels, each 7 mm high, 17.8 cm wide, and 38.1 or 20 cm long. A high volume blower (Model 305, Sierra Instruments) connected in series with a variable voltage transformer was used to supply the desired air flow rate through the chamber. Monodisperse particles of methylene blue were generated using a vibrating orifice aerosol generator (VOAG) for particles larger than 4 µm aerodynamic diameter. During each test, the particles were sampled and checked frequently by optical microscopy to ensure constant monodispersity.

All particles entering the horizontal elutriator were collected either by settling on the plates or on the 8 in. x 10 in. (20.3 cm x 25.4 cm) filter downstream from the plates.

Upon completion of each test, the plates and filter were washed separately with tap water. Samples from each wash were centrifuged to remove debris, and the masses of methylene blue collected on the plates and on the filter were determined by absorption spectroscopy.

The velocity distribution through the settling chamber was studied to determine the configuration necessary to obtain uniform flow. The use of two filters and an extended flared inlet was necessary to provide the desired velocity distribution. Figure 6 is a velocity profile measured using a thermal anemometer immediately upstream from the blower before the plates were in position. From these data, it was evident that the blower was pulling uniformly across the rectangular opening where the 20.3 cm x 25.4 cm filter was positioned. Figure 7 shows the velocity profile measured upstream of the collector plates.

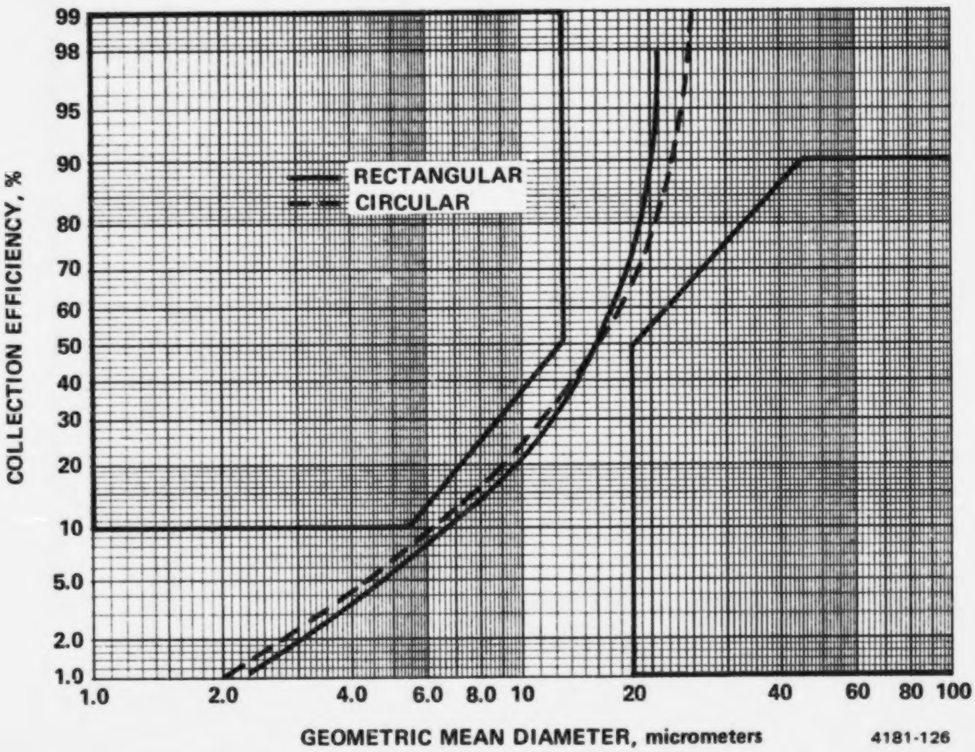

Figure 4. Theoretical collection efficiency by particle settling in rectangular and circular tubes.

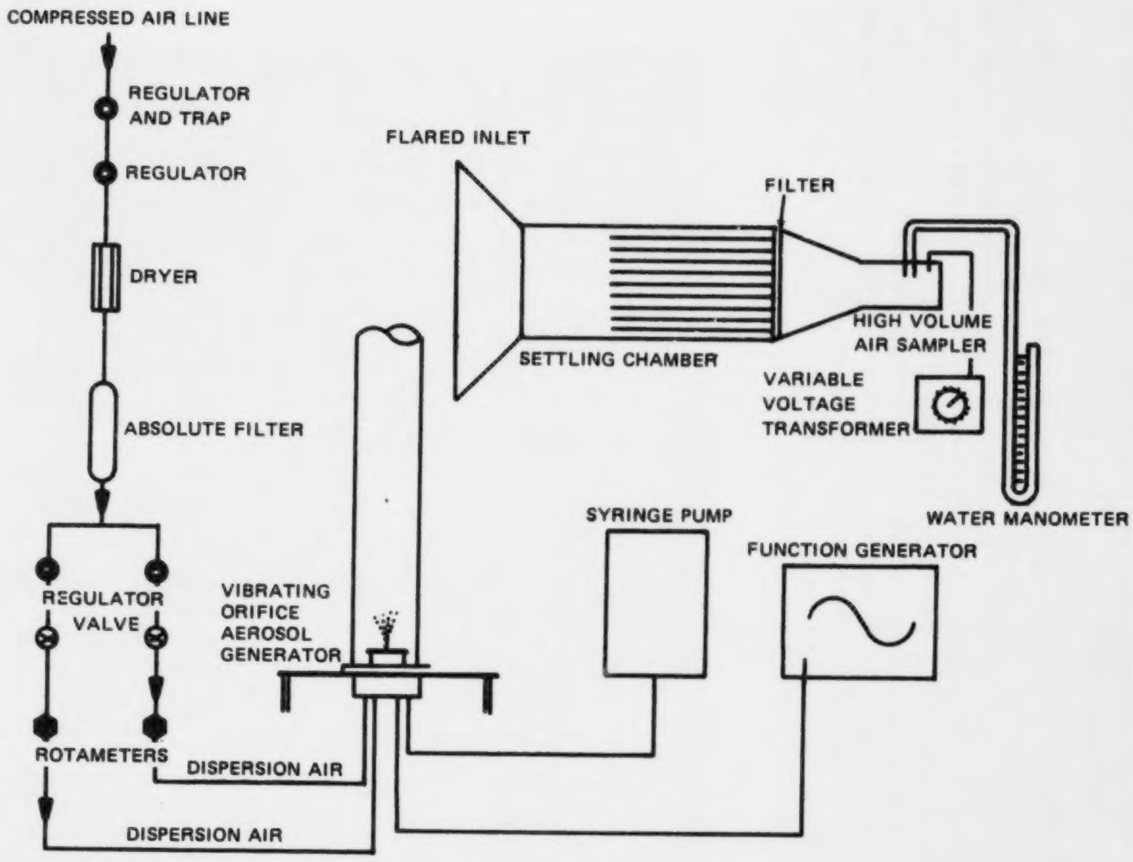
COMPRESSED AIR LINE
REGULATOR AND TRAP
REGULATOR
DRYER
ABSOLUTE FILTER
REGULATOR
VALVE
ROTAMETERS
DISPERSION AIR
DISPERSION AIR
VIBRATING ORIFICE AEROSOL GENERATOR
FLARED INLET
SETTLING CHAMBER
FILTER
HIGH VOLUME AIR SAMPLER
VARIABLE VOLTAGE TRANSFORMER
WATER MANOMETER
SYRINGE PUMP
FUNCTION GENERATOR

4181-74

Figure 5. Apparatus used to measure the collection efficiency of the settling chamber.

The velocity profiles shown in Figures 6 and 7 were considered satisfactory, and the overall average velocity was used to calculate the theoretical performance curves for the system. The average velocity through the chamber, measured using the thermal anemometer, was in agreement with previous calibration of the blower.

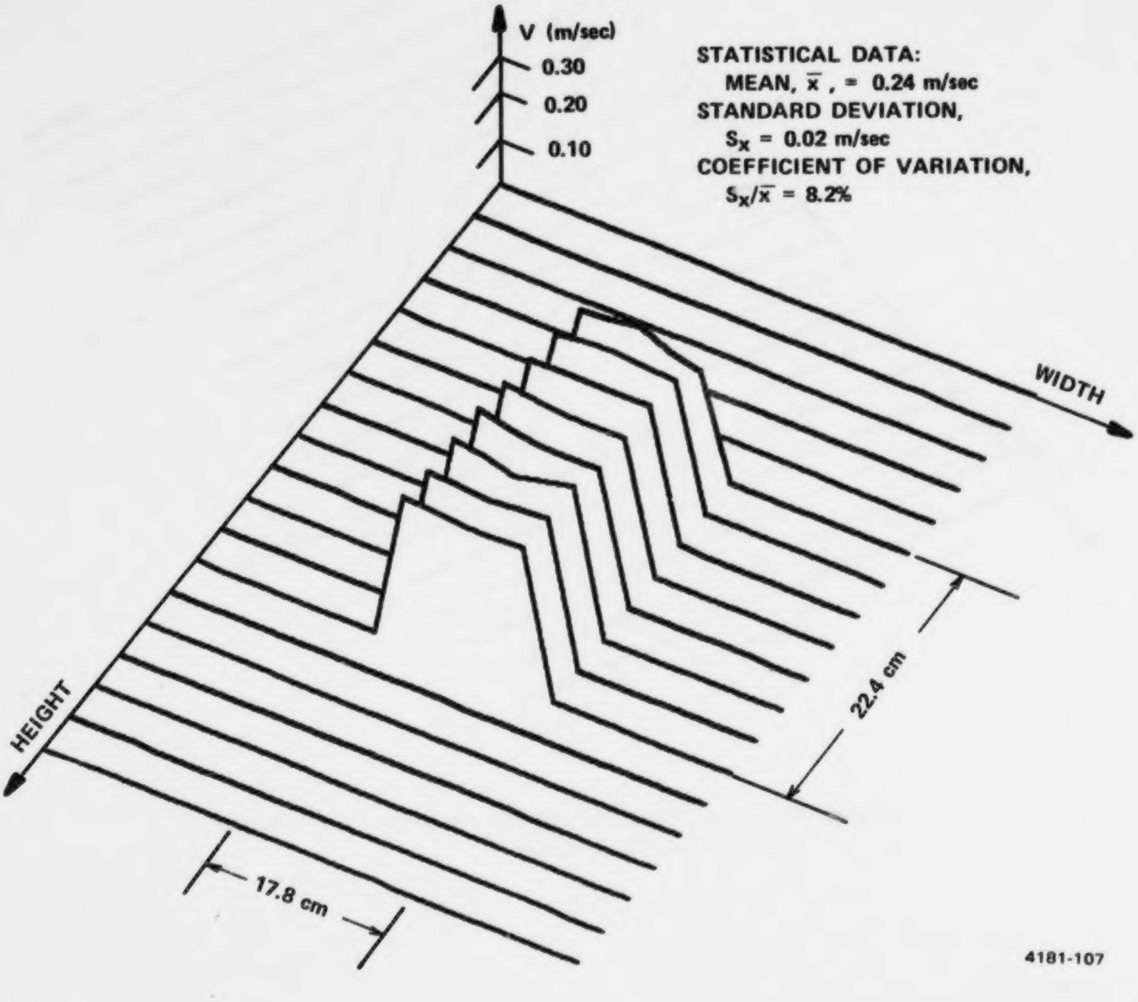

Figure 6. Profile of the air velocity immediately upstream from the blower of the settling chamber before the plates were positioned.

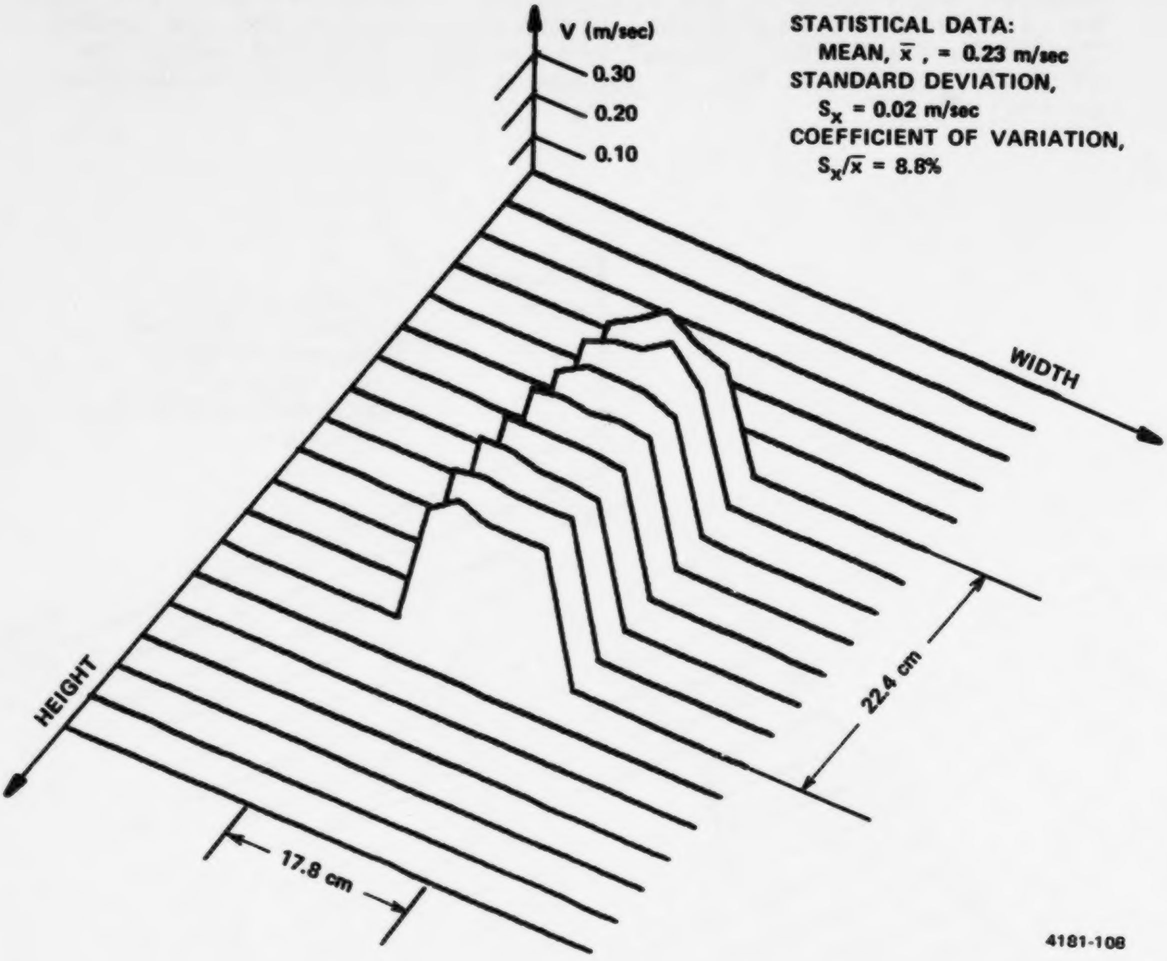

Figure 7. Profile of the air velocity upstream from the plates of the settling chamber.

Results--

Two sets of experimental data were obtained from the testing of the horizontal elutriator. The first set was acquired while operating the settling chamber at an average gas velocity of 70 cm/sec and a plate length of 38.1 cm. The second data set was obtained by operating the system at 40 cm/sec after shortening the plate length to 20 cm. The theoretical curves of the collection efficiency versus aerodynamic particle diameter shown in Figures 8 and 9 were developed from Equation 5 using the following parameter values:

Figure 8	Figure 9
ρ = 1.35 g/cm^3	ρ = 1.35 g/cm^3
g = 9.8 m/sec^2	g = 9.8 m/sec^2
L = 38.1 cm	L = 20 cm
μ = 181 micropoise	μ = 181 micropoise
h = 0.701 cm	h = 0.701 cm
$\bar{V}$ = 70 cm/sec	$\bar{V}$ = 40 cm/sec
Reynolds No. = 315	Reynolds No. = 180

The calculated values from theory for the collection efficiency were found to be in excellent agreement with the measured values. No corrections were made for end effects.

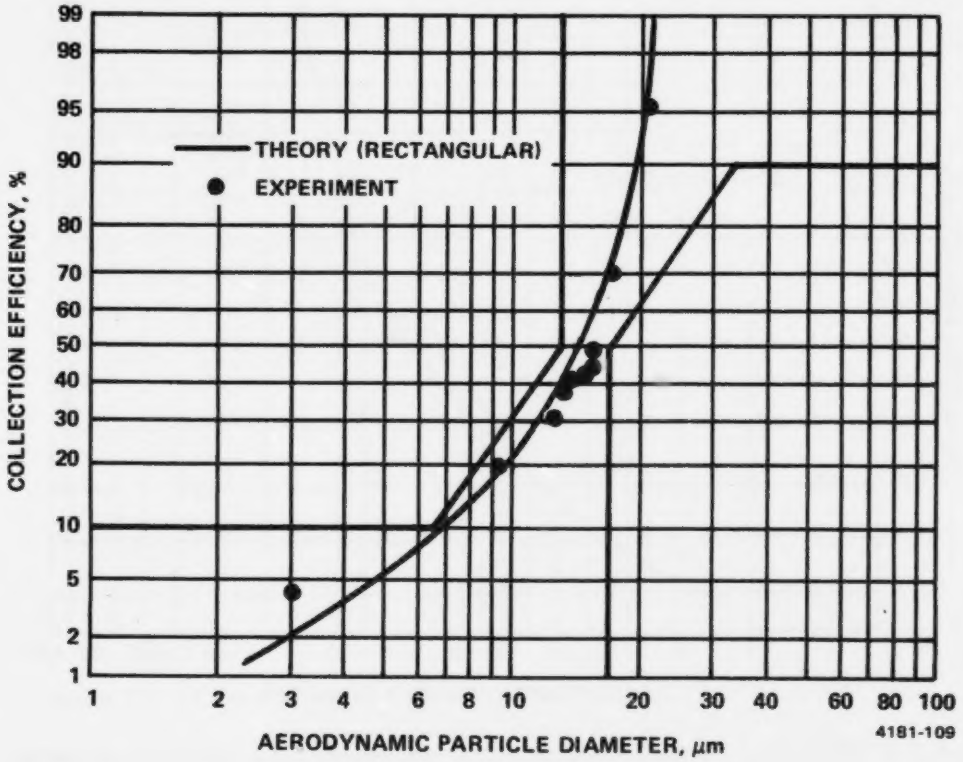

Figure 8. Theoretical and experimental collection efficiencies for a horizontal elutriator with rectangular cross-section, plate length 38.1 cm, average gas velocity 70 cm/sec.

Collector Design--

The experiments described above indicated that the theoretical equations can be used to predict particle collection by horizontal elutriators to a high degree of accuracy. Consequently, the equations were used to create design nomographs for inhalable particulate precollectors to be used in conjunction with the three systems of interest. Design parameters were calculated for horizontal elutriators to be used with: (1) cascade impactors operated at 14.2 ℓ/min and 149°C, (2) SASS trains operated at 185 ℓ/min and 204°C, and (3) FAST trains operated at 5,282 ℓ/min and 23°C.

Figures 10, 11, and 12 are the design nomographs for the three trains. On the vertical axis is the open area required, neglecting the thickness of the tube walls. The horizontal axis is the length of the elutriator required to yield the inhalable particulate performance at the specified flow rate and temperature. In constructing the graphs, it is assumed that the

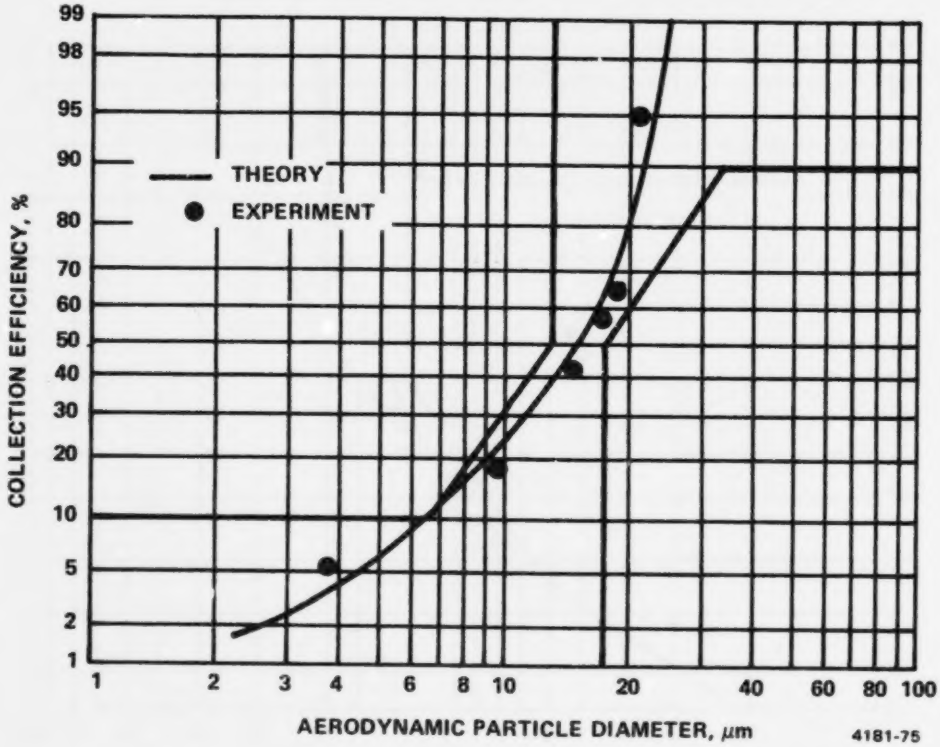

Figure 9. Theoretical and experimental collection efficiencies for a horizontal elutriator with rectangular cross-section, plate length 20 cm, average gas velocity 40 cm/sec.

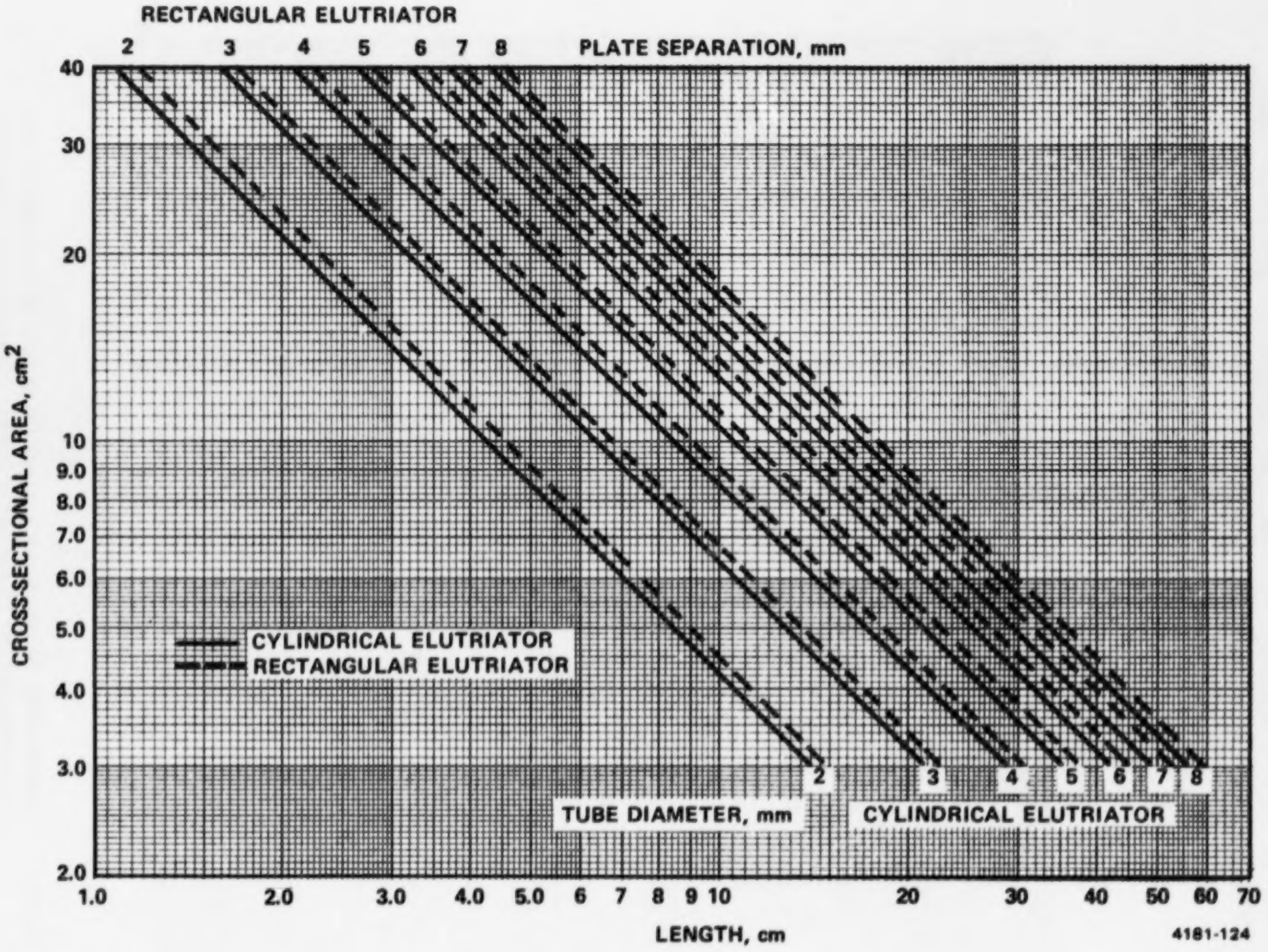

Figure 10. *Relationship of design parameters for horizontal elutriators with D_{50} cutpoints of 15 μm aerodynamic diameter used as precollectors for instack cascade impactors.*

rectangular channels have widths much greater than their heights, so that the vertical walls will not have a significant effect on the gas flow.

It can be seen from these graphs that circular tubes can be used to construct a system having the required performance with much smaller overall dimensions than rectangular tubes or channels.

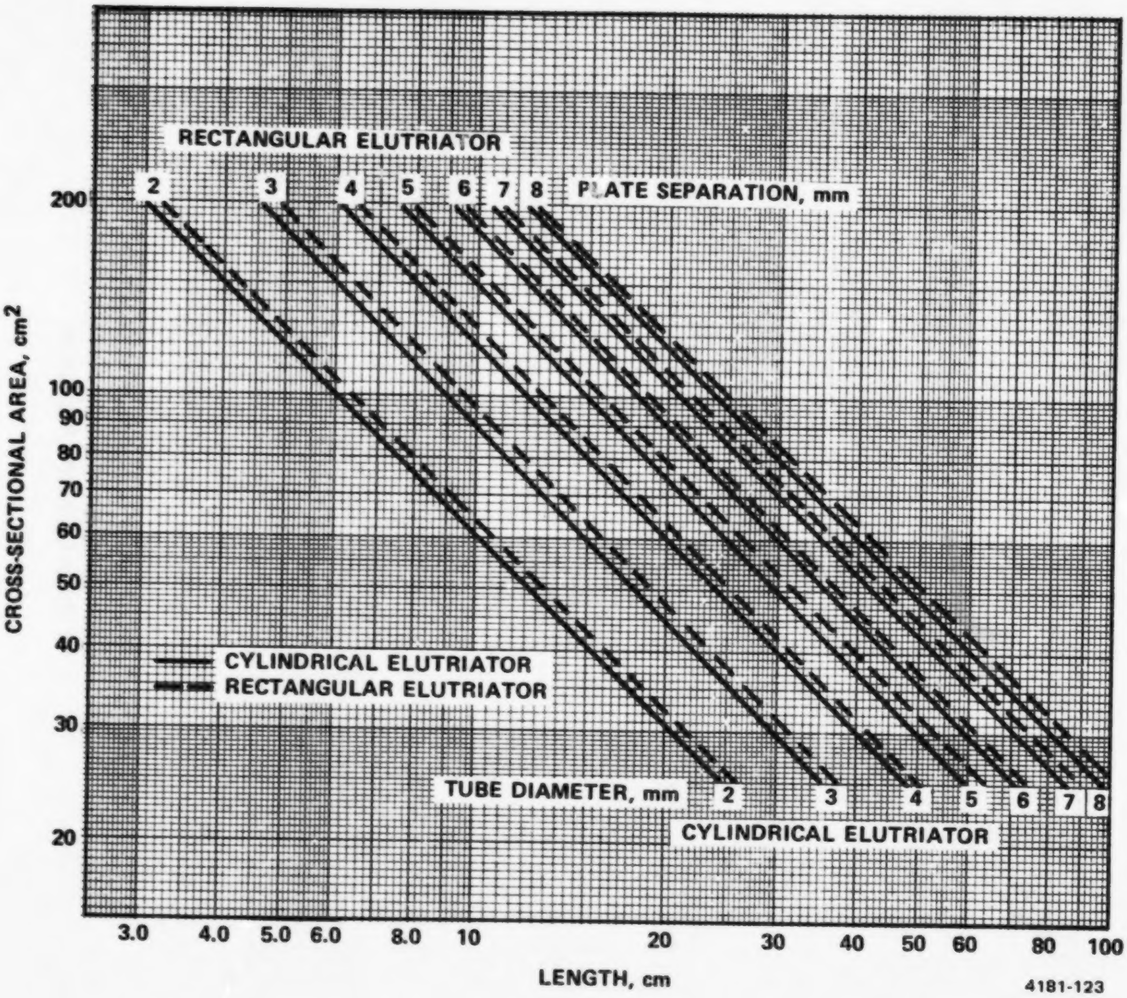

Figure 11. Relationship of design parameters for horizontal elutriators with D_{50} cutpoints of 15 μm aerodynamic diameter to be used with SASS trains.

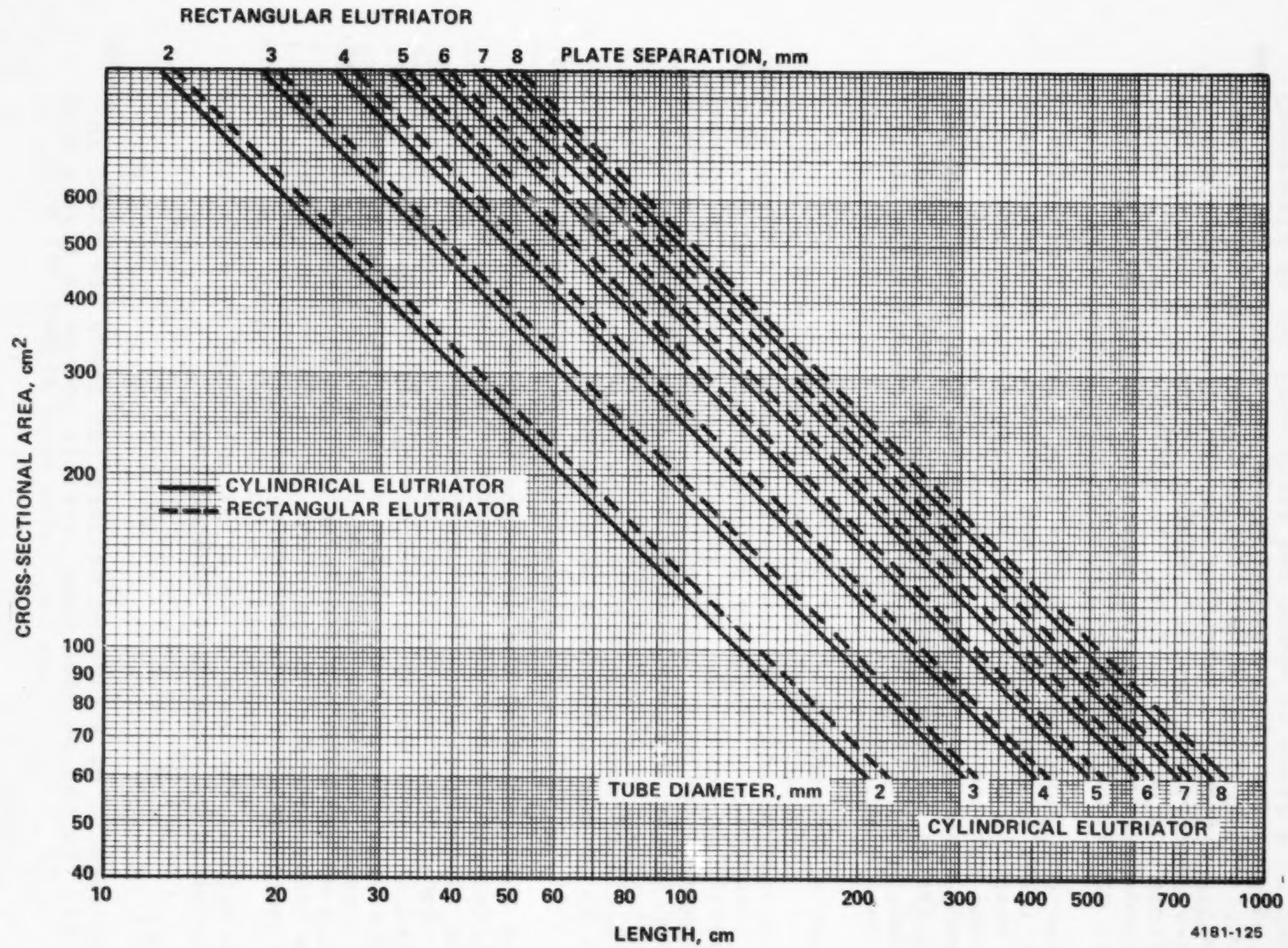

Figure 12. *Relationship of design parameters for horizontal elutriators with D_{50} cutpoints of 15 μm aerodynamic diameter to be used with FAST.*

High-Volume Impactor

The theory of particle collection by impaction has been developed to a state in which the efficiency can be reasonably well predicted for ideal conditions if the geometry of the system is known.[9,10] Critical dimensions and parameters of the system are the jet width, the length of the jet, the jet-plate spacing, the jet velocity, the Reynolds number of the jet, and the type of particle collection surface. In addition to being a well-understood system of particle separation and sizing, impactors are very compact in size.

However, impactors can suffer from a severe limitation if the particles or substrates are not adhesive. Particles much larger than the D_{50} have greater stopping distances and may strike the substrates with high velocities and rebound. This phenomenon results in an efficiency curve that rises with particle diameter to a maximum, frequently at less than 70-80 percent, and then declines to much lower efficiencies for still larger particles.[1,2,3]

Experimental Procedures--

A prototype impactor was constructed using six first stages from a commercially available cascade impactor (Model 35, Sierra Instruments) in parallel. The impactor is designed to operate at a flow rate of about 0.020 m^3/sec. In this study, which was performed before the inhalable particulate performance curve was developed, the flow rate through each impactor was approximately 0.015 m^3/sec. The reduced flow rate was selected to achieve 95 percent collection of 15-μm particles. The impactor stages were covered either with glass fiber substrates or grease.

The FAST including the prototype impactor stage is shown schematically in Figure 13. The calibration aerosols were generated using a vibrating orifice aerosol generator as described above. For these tests, however, ammonium fluorescein particles were used and the cleanup procedure was slightly different. To help ensure the recovery of the aerosol particles trapped by the grease (petroleum jelly) on the impactor collection plates, they were washed with benzene in an ultrasonic cleaner in addition to being washed with ammonium hydroxide. Glass fiber substrates were washed with ammonium hydroxide.

As before, the mass of material collected on each surface was determined by absorption spectroscopy.

Results--

The results of a limited calibration study are shown in Figure 14. It can be seen that particle bounce is severe with

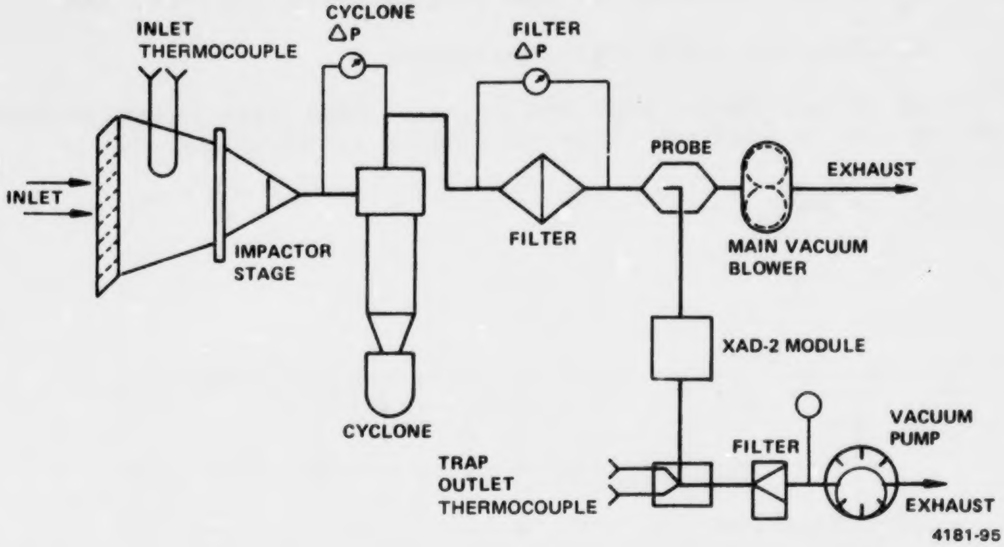
INLET
THERMOCOUPLE
CYCLONE
ΔP
FILTER
ΔP
PROBE
EXHAUST
INLET
IMPACTOR
STAGE
FILTER
MAIN VACUUM
BLOWER
XAD-2 MODULE
CYCLONE
VACUUM
PUMP
TRAP
OUTLET
THERMOCOUPLE
FILTER
EXHAUST
4181-95

Figure 13. Fugitive air sampling train (FAST) components.

both glass fiber and greased substrates. Because of these unsatisfactory results, the experiments with impactors were abandoned in favor of the horizontal elutriator. It should be noted that stages 2-5 of the same type of impactor have been calibrated by Willeke and shown to behave well with liquid particles.[11]

Cyclones

Although the flow in cyclones is more complicated than in impactors and no theory exists to adequately predict their behavior, several experimental investigations have been performed demonstrating their utility for separating and sizing small particles.[12,13,14] Smith et al.,[15] and John et al.,[16] have demonstrated that the curves of particle collection efficiency for small cyclones can be as steep as those of impactors, and significant reentrainment does not occur. Chan and Lippmann[17] have shown that experimental efficiency data for small cyclones can be fitted well using the empirical relationship:

$$\mathrm{Eff} = 0.5 + 0.5 \tanh \left[\left(\frac{D_p}{KQ^n} \right)^2 + \left(A-2B \right) \frac{D_{pn}}{KQ^n} + B - A \right], \tag{6}$$

where

Q is the sample flow rate, $\mathrm{cm}^3/\mathrm{sec}$,

D_p is the diameter of the sampled particle, cm, and

A,B,K,n are empirical constants.

Also it was shown that the D_{50} vs. flow rate relationship is given over a limited range of sampling conditions by:

$$D_{50} = KQ^n. \tag{7}$$

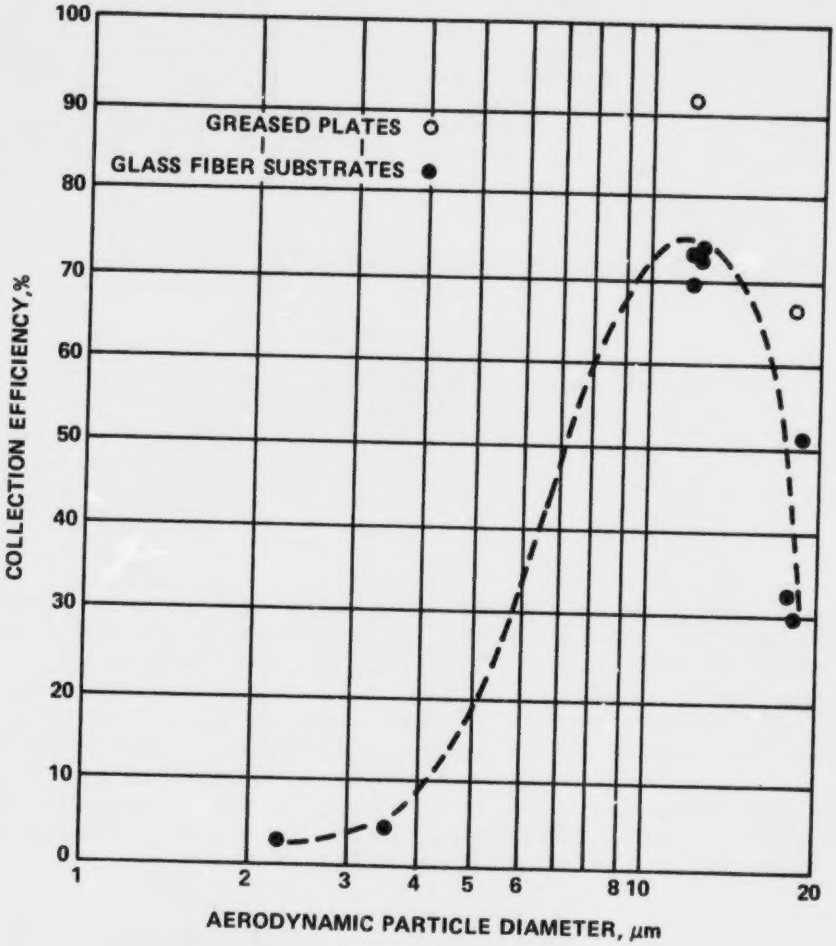

4100-13

Figure 14. Particle collection efficiency for the impactor.

From their own research and data reported by others, Chan and Lippmann reported values of K ranging from 6.17 to 4591, and values of n from -0.636 to -2.13. Smith et al. reported values of K from 14.0 to 44.6, and n from -0.63 to -1.11. Although the trend in the data is for n to have larger values for small cyclones (D_{50}'s) and K to be larger, the correlation is not consistent enough to be predicted from the cyclone geometry, and no data are reported for temperatures other than ambient. Furthermore, there are definite discontinuities and hysteresis effects in the relationship given in Equation 7, even for individual cyclones, as the flow is increased and decreased. The discontinuous and hysteresis effects are generally attributed to transitions from turbulent to laminar flow, or the reverse, in the outlet tube of the cyclone as the flow is changed.[13-17]

Smith et al. found the D_{50} of cyclones to increase linearly as the gas temperature and viscosity were increased; but again the rate of increase was not predictable from the cyclone geometry. Certainly a modification to Equation 7 would be required to predict any temperature dependence. Lacking an adequate theory for predicting the performance of cyclones before they are designed and calibrated, it was found necessary in this study, as in previous work, to extrapolate the dimensions for a new cyclone to give the desired performance from those of similar cyclones of known performance.

However, because of these difficulties, and the requirement that the inhalable particulate cyclones always be operated to yield D_{50}'s at 15 ± 2 μm, it was still considered necessary to calibrate them over a range of temperatures and flow rates similar to those expected in field operation.

Experimental Procedures--

The objective of this phase of the program to develop samplers for inhalable particles was to design and evaluate two systems: (1) a cyclone to be used as the precollector for cascade impactors, and (2) a system, consisting of two cyclones and a filter in series, to be used as the primary system for measuring the total particulate concentration, the inhalable particulate concentration, and the fine particle concentration. Both systems are to be used in process streams where the particle concentration and temperature are generally much higher than in the atmosphere. The precollector for impactors and the first cyclone in the series train must have efficiency curves satisfying the specifications for inhalable particulate samplers shown in Figure 4. The second cyclone in the series train must be designed to have a D_{50} of 2.5 ± 0.5 μm aerodynamic.

The nominal operating conditions used in designing the systems were flow rates of 14 ℓ/min and 21 ℓ/min at 150°C, respectively, for the precollector and cyclone systems. With these operating conditions as a goal, the dimensions of the cyclones were extrapolated from those previously evaluated.[15]

Figures 15 and 16 are schematic illustrations of the two new systems. The precollector cyclone is designated SRI-IX and the large cyclone in the series train, SRI-X. Cyclone SRI-III, which had been previously evaluated as part of the SRI/EPA 5-stage cyclone train, was found to be adequate for the smaller cyclone in the new system.

The critical dimensions of all three cyclones are given in Figure 17.

In order to calibrate the cyclones at elevated temperatures, the heating arrangement shown in Figure 18 was used in conjunction with the vibrating orifice aerosol generator described above. Tests were made at temperatures of 23°C, 93°C, and 150°C. Ammonium fluorescein particles were used for calibrating the cyclones. Samples were taken frequently of the heated aerosol to ensure that the calibration system was stable and that the particles were spherical and of the proper size.

In this study, the primary objective was to determine the operating conditions under which the cyclones satisfied the design criteria. For this purpose, it was sufficient to use an abbreviated calibration procedure and thus to reduce the extensive amount of testing that would be needed for complete calibration. At a specific temperature, monodisperse particles having nominal aerodynamic diameters of 15 μm were generated and sampled. Tests were made at a variety of flow rates to determine the sampling rate required to yield a D_{50} of 15 μm at the given temperature. Only limited data were taken to determine collection efficiency vs. particle diameter.

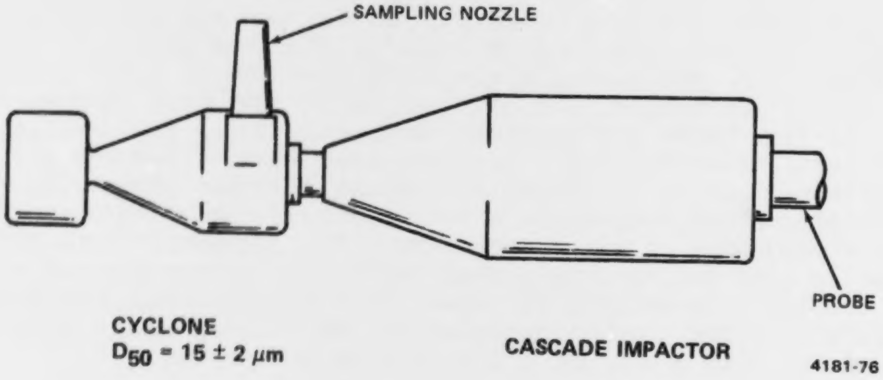

Figure 15. Schematic of a cascade impactor/precollector cyclone system.

When preparing to generate monodisperse particles using the vibrating orifice method, it is necessary to know the solution flow rate and frequency of vibration in order to calculate the concentration of solute required to yield the desired particle diameter after drying. In practice, the flow rate can be selected and the solution prepared precisely, but the frequency at which the generator is finally found to yield maximum stability is unpredictable to some extent. Therefore, as indicated in the figure captions, the actual particle diameters differed slightly from 15 µm. In these tests the particles had aerodynamic diameters of 15.0 ± 0.6 µm.

Results--

Figures 19-22 show the calibration data for the three cyclones. In Figure 19, the particle collection efficiency is plotted vs. flow rate for cyclone SRI-IX.

As indicated in the figure, data were taken at 23°C, 93°C, and 150°C. Similar data are shown in Figure 20 for cyclone SRI-X.

The settling velocity in air of 15 µm particles is 0.7 cm/sec and there was some concern that settling might influence the collection efficiency of the larger cyclones by making them sensitive to orientation. In Figure 20, which contains calibration data for cyclone SRI-X, data are shown taken with the cyclone in both vertical and horizontal orientations. It can be seen that there is little, if any, effect due to particle settling.

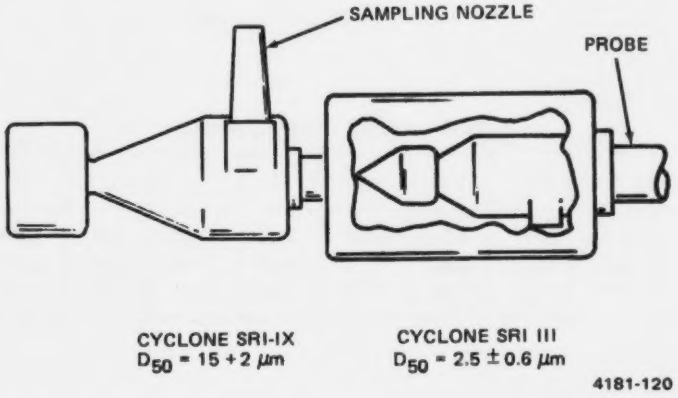

Figure 16. Schematic of two-cyclone system.

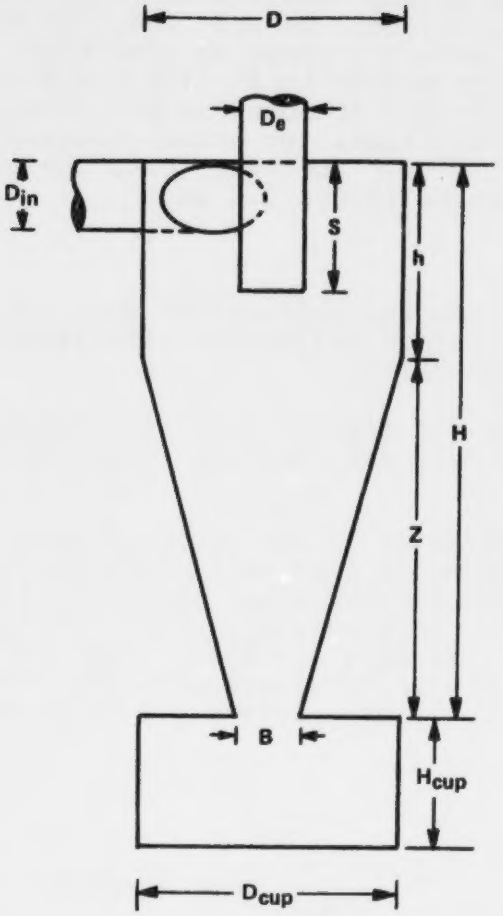

DIMENSIONS (CENTIMETERS)

CYCLONE	D	D_{in}	D_e	B	H	h	Z	S	H_{cup}	D_{cup}
SRI-X	6.14	1.83	2.17	2.92	8.47	2.82	5.65	2.40	2.635	6.14
SRI-III	3.11	0.75	0.83	0.76	4.91	1.40	3.51	1.08	2.22	3.10
SRI-IX	5.12	1.53	1.81	2.43	7.06	2.35	4.71	2.00	2.26	5.12

4181-22

Figure 17. Summary of cyclone dimensions.

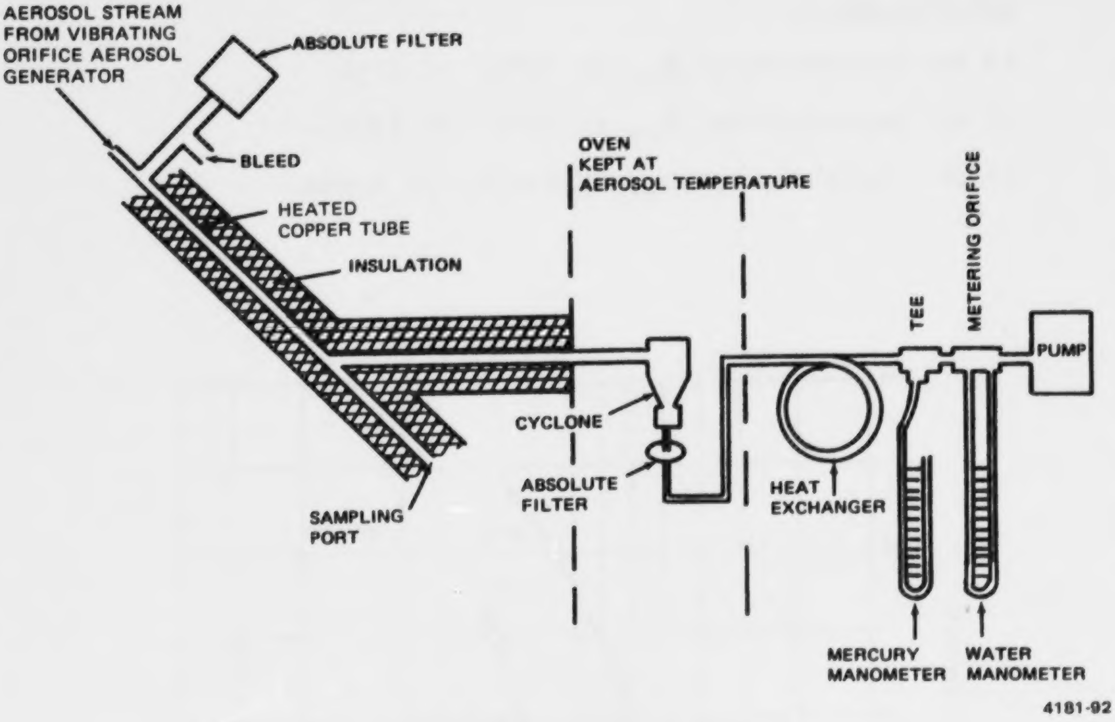
AEROSOL STREAM FROM VIBRATING ORIFICE AEROSOL GENERATOR
ABSOLUTE FILTER
BLEED
HEATED COPPER TUBE
INSULATION
OVEN KEPT AT AEROSOL TEMPERATURE
METERING ORIFICE
TEE
PUMP
CYCLONE
ABSOLUTE FILTER
HEAT EXCHANGER
SAMPLING PORT
MERCURY MANOMETER
WATER MANOMETER
4181-92

Figure 18. Calibration system for heated aerosols.

The data reported in Figures 19 and 20 will be used to select the flow rates of the new sampling trains. Since there is no adequate theory for calculating cyclone efficiency, cyclone SRI-III was calibrated at the same flow rates required for proper operation of cyclone SRI-X. These calibration data are shown in Figure 21. D_{50}'s and flow conditions for the three cyclones, as derived from the graphs, are:

Cyclone SRI-III

3.1 μm (aerodynamic) D_{50} at 23°C, 11 ℓ/min

2.6 μm (aerodynamic) D_{50} at 93°C, 20 ℓ/min

2.3 μm (aerodynamic) D_{50} at 150°C, 23 ℓ/min

Cyclone SRI-IX

15 μm (aerodynamic) D_{50} at 23°C, 6.8 ℓ/min

15 μm (aerodynamic) D_{50} at 93°C, 12 ℓ/min

15 μm (aerodynamic) D_{50} at 150°C, 14 ℓ/min

Cyclone SRI-X

15 μm (aerodynamic) D_{50} at 23°C, 11 ℓ/min

15 μm (aerodynamic) D_{50} at 93°C, 20 ℓ/min

15 μm (aerodynamic) D_{50} at 150°C, 23 ℓ/min

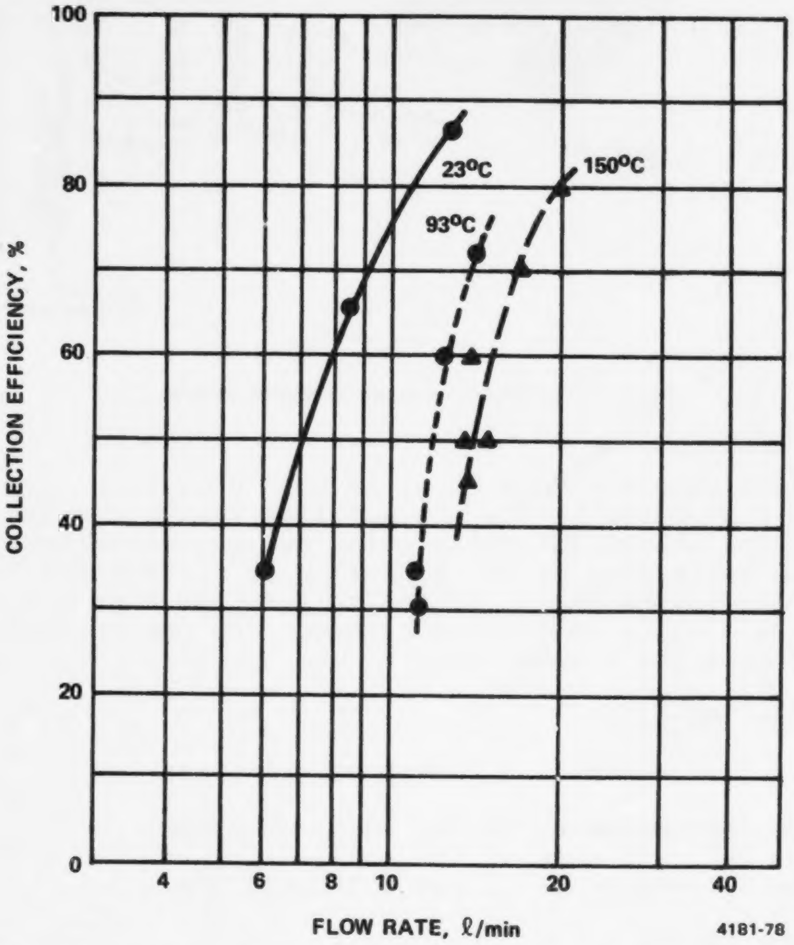

Figure 19. Collection efficiency of cyclone IX vs. flow rate for particles of 15±0.6 μm aerodynamic diameter.

Also, limited data were taken with particles with diameters other than 15 μm using cyclone IX. These are shown plotted with the inhalable particulate performance specifications in Figure 22.

The data reported above define the operating points of cyclones SRI-IX and SRI-X at three discrete values of temperature. Figure 23 shows the data plotted on semi-log coordinates with a smooth line fitted to the points. The equations of flow rate vs. viscosity are:

For cyclone SRI-X, $Q = (105 \log\mu - 225)\,\ell/\text{min}$ and for cyclone SRI-IX, $Q = (69.5 \log\mu - 150)\,\ell/\text{min}$.

It is not known at present how accurately these equations can be extrapolated to temperatures greater than 150°C.

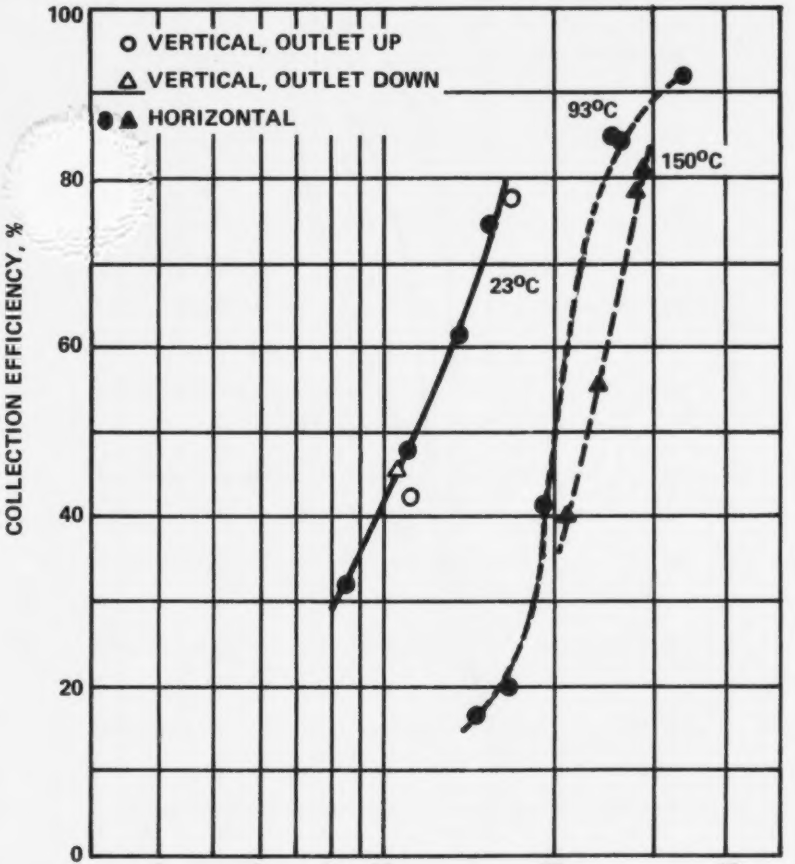

Figure 20. Collection efficiency of cyclone X vs. flow rate for particles of 15±0.6 μm aerodynamic diameter.

In order to gain a better qualitative understanding of the mechanisms governing the performance of cyclones, Table 1 was prepared summarizing some of the dimensions and operating parameters of cyclones evaluated at Southern Research Institute. The parameters of greatest interest are the Stokes number of 15 μm particles in the inlet and the ratio of the settling velocity to the centripetal velocity of 15 μm particles in the cyclone body. The latter is calculated assuming that the air flow in the cyclone body is a jet having the same velocity and diameter as in the inlet. This is obviously a crude approximation, but probably accurate enough to allow a reasonable estimate of the desired ratio.

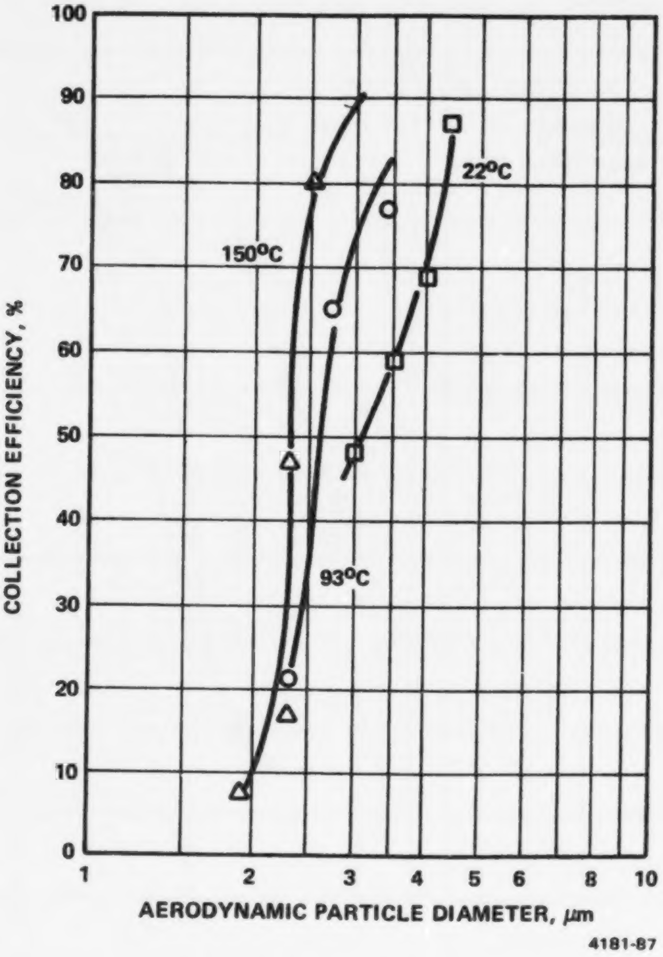

Figure 21. Collection efficiency vs. aerodynamic particle diameter for Cyclone III at 22° and 11.3 ℓ/min (□), 93°C and 19.8 ℓ/min (○), and 150°C and 22.7 ℓ/min (△).

The settling velocity V_s of unit density spheres is given by the expression (equivalent to Equation 2):

$$V_s = mg\beta \tag{8}$$

where
m is the particle mass,
β is the particle mobility, and
g is the acceleration due to gravity.

The centripetal velocity V_c is given by:

$$V_c = \frac{mV_{in}^2}{R}\beta, \tag{9}$$

where
V_{in} is the gas velocity in the inlet and
R is the cyclone radius.

The desired ratio, then, is:

$$\frac{V_s}{V_c} = \frac{gR}{V_{in}^2} \tag{10}$$

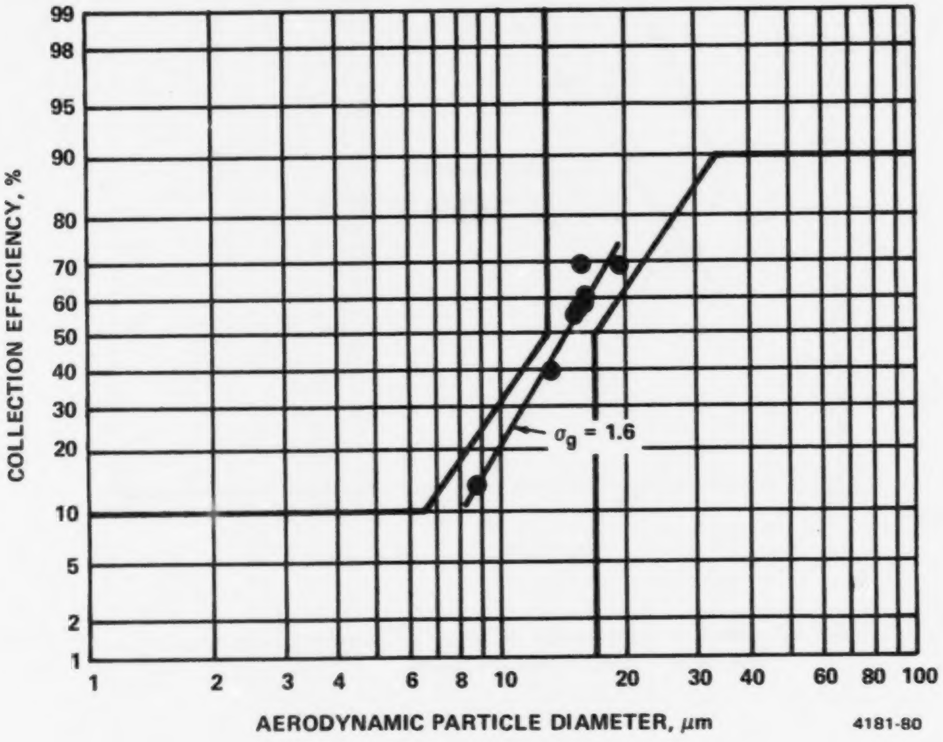

Figure 22. Calibration data for cyclone IX at 14 ℓ/min and 150°C.

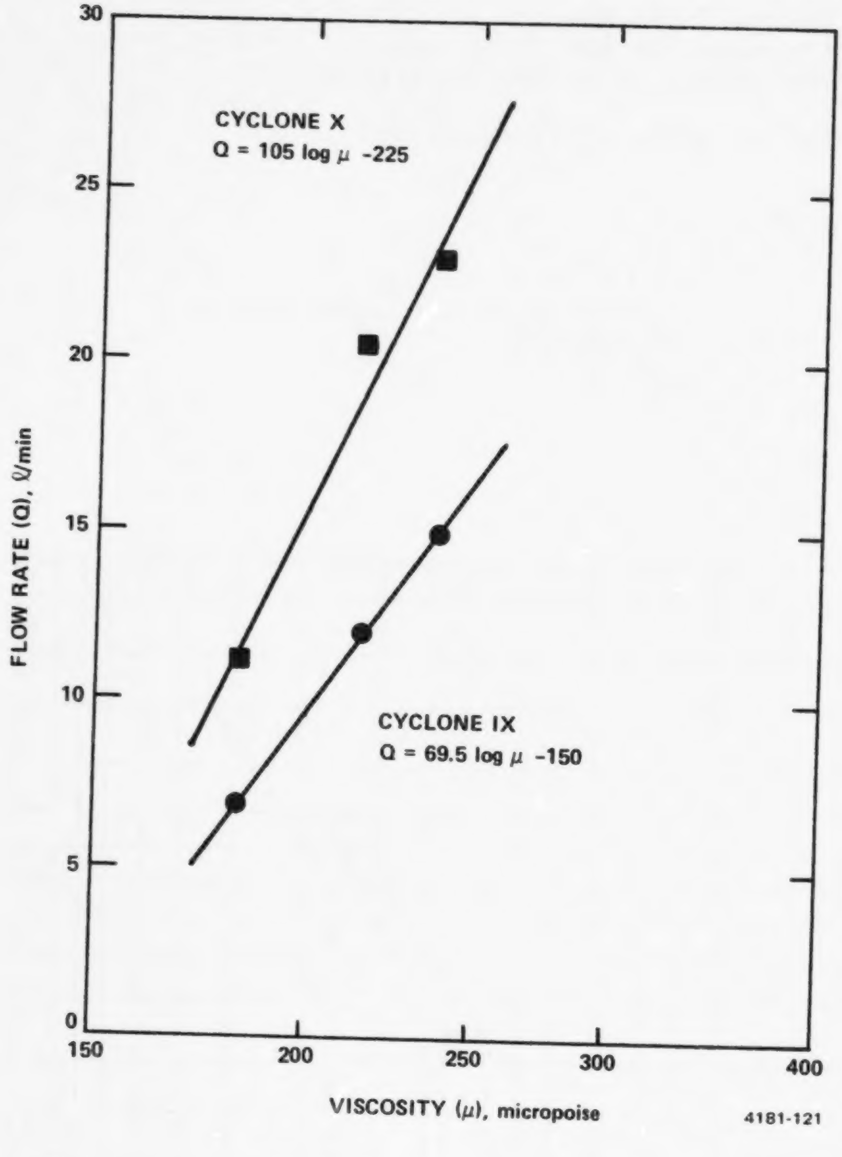

Figure 23. Gas flow rate versus viscosity at D_{50} = 15 μm aerodynamic diameter for cyclones IX andX.

TABLE 1. OPERATING PARAMETERS OF SRI CYCLONES

Cyclone Number	$Q(cm^3/sec)$	D(cm)	$D_{in}(cm)$	$V_{in}(cm/sec)$	$\Delta P(mm\ H_2O)$	$D_{50}(\mu m)$	$\sqrt{St}$	gR/V_{in}^2
V	472	1.52	0.30	6670	1800	0.32	0.1	1.6×10^{-5}
IV	472	2.54	0.57	2300	330	0.65	0.1	2.3×10^{-4}
III	472	3.11	0.75	1100	70	1.4	0.1	1.3×10^{-3}
II	472	3.66	1.01	600	40	2.1	0.1	5.0×10^{-3}
I	472	4.47	1.27	370	5	5.4	0.2	1.6×10^{-2}
BRINK	28	1.27	0.51	130	-	13	0.6	4.0×10^{-2}
IX	233(150°C)	5.11	1.53	130	-	15	0.3	0.2
X	190	6.14	1.83	70	-	15	0.2	0.6

Q is the sample flow rate
D is the diameter of the cyclone body
D_{in} is the diameter of the inlet
V_{in} is the gas velocity in the inlet
ΔP is the pressure drop across the cyclone
St is the Stokes number of the 15-μm particles in the inlet
gR/V_{in} is the ratio of the settling velocity to the centripetal velocity in the cyclone body

The values of $\sqrt{St}$ and V_S/V_C can be used to estimate whether or not impaction onto the wall opposite the inlet or particle settling is likely to play a large part in the collection efficiency of a cyclone. If $\sqrt{St}$ is less than about 0.4, then impaction is not likely to occur.[10] If V_S/V_C is very small, then settling is not likely to occur. From Table 1, it can be seen that impaction is probably very significant in the cyclone used with the Brink impactor, while settling probably contributes somewhat to the collection efficiency of cyclones SRI-IX and SRI-X.

SUMMARY AND CONCLUSIONS

Three systems have been developed and evaluated for the purpose of sampling inhalable particles without reentrainment: (1) a horizontal elutriator for sampling fugitive and ambient aerosols, (2) a cyclone precollector to be used in-stack with cascade impactors, and (3) a series-cyclone train for in-stack use. Each of the systems was calibrated under typical sampling conditions and found to perform within the range specified for samplers of inhalable particles. A fourth method, a high volume impactor, was tested and rejected because of poor performance due to particle bounce.

Second generation versions of the systems have been constructed for use in the field to determine emission factors for inhalable particles from stationary sources.

ACKNOWLEDGEMENT

This research was supported by the U.S. Environmental Protection Agency under contract 68-02-3113.

REFERENCES

1. Corn, M., and F. Stein. Re-entrainment of Particles from a Plane Surface. Am. Ind. Hyg. Assoc. J. 26:325-336, 1965.

2. Rao, A.K., and K.T. Whitby. Non-ideal Collection Characteristics of Single Stage Cascade Impactors. Am. Ind. Hyg. Assoc. J. 38:174-179, 1977.

3. Cushing, K.M., J.D. McCain, and W.B. Smith. Experimental Determination of Sizing Parameters and Wall Losses of Five Source-Test Cascade Impactors. Environ. Sci. Technol., 13:726-731, 1979.

4. Fuchs, N.A. The Mechanics of Aerosols. Pergamon Press, New York, 1964.

5. Stein, F., W.A. Esmen, and M. Corn. The Shape of Atmospheric Particles in Pittsburgh Air. Atmos. Environ. 3:443-453, 1969.

6. Rimberg, D., and J.W. Thomas. Comparison of Particle Size of Latex Aerosols by Optical and Gravity Settling Methods. J. Colloid Interface Sci. 32:101-105, 1970.

7. Corn, M., F. Stein, Y. Hammad, S. Manekshaw, W. Bell, S.J. Penkola, and R. Freedman. Physical and Chemical Characteristics of "Respirable" Coal Mine Dust. Ann. N.Y. Acad. Sci. 200:17-30, 1972.

8. Mercer, T.T. Aerosol Technology in Hazard Evaluation. Academic Press, New York, 1973. pp. 192-200.

9. Ranz, W.D., and J.B. Wang. Impaction of Dust and Smoke Particles. Ind. Eng. Chem. 44(6):1371-1380, 1952.

10. Marple, V.A. A Fundamental Study of Inertial Impactors. Ph.D. Thesis, University of Minnesota, Mechanical Engineering Department, Minneapolis. Particle Technology Laboratory Publication 144, 1970. 243 pp.

11. Willeke, K. Performance of the Slotted Impactor. Am. Ind. Hyg. Assoc. J. 36:683-691, 1975.

12. Rusanov, A.A. Determination of the Basic Properties of Dust and Gases. In: Ochistka Dymovykh Gasov v Promyshlennoy Energetike [Cleaning Stack Gases in Industrial Power Engineering], A.A. Rusanov, I.I. Urbakh, and A.P. Anastasiadi, eds. "Energiya," Moscow, 1969.

13. Hochstrasser, J.M. The Investigation and Development of Cyclone Dust Collector Theories for Application to Miniature Cyclone Presamplers. Ph.D. Thesis, University of Cincinnati, Cincinnati, 1976.

14. Lippmann, M., and T.L. Chan. Cyclone Sampler Performance. Staub Reinhalt. Luft 39:7-12, 1979.

15. Smith, W.B., R.R. Wilson, and D.B. Harris. A Five-Stage Cyclone System for In-Situ Sampling. Environ. Sci. Technol. 13(11):1387-1392, 1979.

16. John, W.G., P. Reischl, and J.J. Wesolowski. Size-Selective Monitoring Techniques for Particulate Matter in California Air. AIHL/SP-12. Final Report, California Air Resources Board Contract No. A5-00487, 1978.

17. Chan, T.L., and M. Lippmann. Particle Collection Efficiencies of Air Sampling Cyclones: An Empirical Theory. Environ. Sci. Technol. 11:377-382, 1977.

PAPER 19

DEPOSITION OF INHALED PARTICLES AND POSSIBLE SAMPLING METHODS

VITTORIO PRODI
GIUSEPPE TARRONI
CARLO MELANDRI
LABORATORIO DI FISICA SANITARIA
DIPARTIMENTO RADIAZIONI, CNEN

ABSTRACT

Inhalation is one of the most important routes of internal contamination. The efficiency of incorporation depends on aerosol properties and on fluid dynamic properties of the airways. In this paper total and regional deposition in humans will be briefly reviewed with the aim of understanding the basic mechanisms responsible for particle deposition and assessing the sensitivity of deposition to the main aerosol, physiological, and possibly pathological factors. The available data on sampling efficiency of the airways will be also reported in order to reach a detailed picture of the overall transfer efficiencies.

Two approaches to aerosol characterization for inhalation toxicology will then be presented. One is based on a direct size distribution measurement with a recently proposed aerosol spectrometer and the other is based on the simulation of the regional deposition. The first can be referred to the cut-off sizes that are being introduced by EPA, while the second, if a particular breathing pattern and individual deposition are assumed, can yield directly the amount deposited in each region.

INTRODUCTION

The atmospheric environment may contain airborne contaminants that pose serious risks of incorporation and then of toxic action. Particulate contamination is of great concern and is of challenging difficulty to a quantitative assessment of inhalation risks.

Incorporation of particulate matter is a step process that comprises inhalation of the aerosol, deposition of the inhaled aerosol, and clearance or translocation of the deposited aerosol, and the final result is the retention of the contamination with the resulting toxic action.

Each one of these steps has measured or measurable efficiencies that depend on aerosol properties, on airways configuration, and on respiration patterns. Very detailed reviews have been published by the ICRP Task Group[1] on Lung Dynamics and by Lippmann.[2] Therefore here only the most recent results will be reported, with emphasis on the parameters relevant to the risk of incorporation.

Definitions

Inhalability: is the probability for an airborne particle to enter the airways.[3]

Deposition: is the probability for an inhaled particle to touch a surface of the respiratory tract and to adhere to it.[3]

Total deposition: is such a probability referred to the entire respiratory tract.

If a more detailed picture of the contamination is needed, the respiratory tract is divided into regions, characterized by predominant deposition and, for slowly soluble particles, clearance mechanisms. There is a generally accepted definition of the regions:[1,3]

Extrathoracic airways, in which the deposition is mainly due to inertia and particles are cleared within minutes either by mechanical transport of particles or secretions.

Tracheobronchial airways, in which particles are deposited by inertia and settling and from which particles are removed within hours by mechanical transport of secretions.

Alveolar air spaces, characterized by small particle-to-wall distances, in which particles are deposited mainly by gravitational settling and brownian diffusion. The removal takes months or even years, mainly by phagocytosis, and subsequent cell transport to the mucociliary escalator or to the lymphatic system, or by dissolution.

Regional deposition is the probability for an inhaled particle to reach a surface of the given region and adhere to it. Total deposition is the sum of regional depositions.

Retention: total retention is the probability for a deposited particle to be retained in the body, while regional retention is such a probability referred to a given region of the respiratory tract.

Deposition mechanisms: particles are transported across streamlines by a number of mechanisms: if they touch a surface, they deposit there. The main mechanisms are gravitational settling, brownian diffusion, inertial impaction, and electrostatic attraction due to image forces. Experimental data are available for spherical or compact particles and here interception will not be considered. All of these mechanisms are strongly size dependent. Where aerodynamic effects prevail (settling and impaction), the

aerodynamic diameter, of a particle, defined as the diameter of a 1 g cm^{-3} density sphere having the same settling velocity as the particle, is a satisfactory and unique parameter accounting for deposition[3] and aerodynamic techniques should be preferred for characterization. Where diffusion prevails, since the diffusion coefficient is independent of density, the aerodynamic diameter is not representative and a

diffusive diameter should be introduced.[4] This could be defined as the diameter of the sphere that has the same diffusive properties as the unknown particle. It is therefore important that characterization of an aerosol in this range should be based on diffusion or on techniques that can be uniquely related to diffusion. In the case of very large densities the range of overlap of diffusion and aerodynamic effects varies and one can still have aerodynamic deposition with appreciable diffusive deposition.

AIR FLOW IN THE RESPIRATORY TRACT

Deposition depends strongly on the flow which is effective in airways, because it can affect the time-dependent mechanisms through the mean residence time, MRT, (time dependent mechanisms are settling and diffusion; electrostatic deposition is also time-dependent,[1-3] at least in the range 0.3 to 0.6 μm) and the "prompt" mechanisms (impaction) through the volumetric flow rate,[3] VFR. A detailed description of the aerodynamic properties of the respiratory tract has been given by Lippmann[2] and here will just be briefly reported.

Respiratory frequency and tidal volume rule the MRT and the VFR. Mixing between tidal and residual air has a very important role in transferring inhaled particles into the residual volume and thereby strongly increasing their residence time. Mixing can take place in the conducting airways due to turbulence and to vortices that even in laminar flow are established in the bifurcations[5] and propagate in the following branches. The mixing mechanism which is important in the whole respiratory tract is due to the non-uniformity, both geometric and dynamic, of the airways. Their diameter in each generation is considerably scattered; branching angles, also, are asymmetric; this produces a non-uniform flow in the following bifurcations which is not reversed in the exhalation.

The overall effect is a considerable mixing.[6] This has been studied theoretically and an effective coefficient can be introduced that accounts for the observed effect.[7,8,9]

This non-uniformity can be enhanced by the relatively rigid structures (blood vessels and bronchi) of the airways: during expansion and contraction geometric similarity is not preserved. The mixing effect is enhanced at lower values of the functional residual capacity and this can account for the increased deposition with decreasing expiratory reserve volume,[9] ERV.

Accurate morphometric data are not available for populations; it is not possible therefore to correlate the scatter of deposition values to any distribution of morphometric parameters, but there is little doubt that this scatter should be due to anatomical as well as physiological or pathological differences.[2]

TOTAL DEPOSITION

Total deposition has received greater attention than regional deposition, since it can be studied in vivo with relatively simple approaches. Two techniques will be considered here: one[10,11,12] is based on the measurement of inhalation and exhalation flow rates and particle concentration just at the entrance of the airways. The numbers of inhaled and exhaled particles and the volumes are then computed by multiplication and integration.

The other[13] is based on the measurement of the particle concentration averaged over several cycles with the volunteer (exhalation) and without the volunteer (inhalation) and on a separate measurement of respiratory volumes.

The two techniques have been recently compared and gave coincident results.[13]

Heyder and coworkers[3,14] have thoroughly investigated total deposition, DE, as a function of route of inhalation, particle size, and respiratory parameters.

Size

The behavior of DE as a function of size is shown in Figure 1 (from Heyder et al.[3]) for mouth breathing. The general trend shows a minimum around 0.5 µm and increases both for decreasing and for increasing size. Below 0.5 µm the increase is due to increasing diffusion coefficient. Unfortunately in the ultrafine range experimental data is scarce.[15] Above 0.5 µm deposition is due to gravitation and impaction.

MRT

Figure 1 shows also the effect of MRT on total deposition:[3] DE increases with increasing MRT because both diffusion and settling are time dependent. Impaction becomes important at higher sizes and this is shown by the smaller effect of MRT at high VFR.

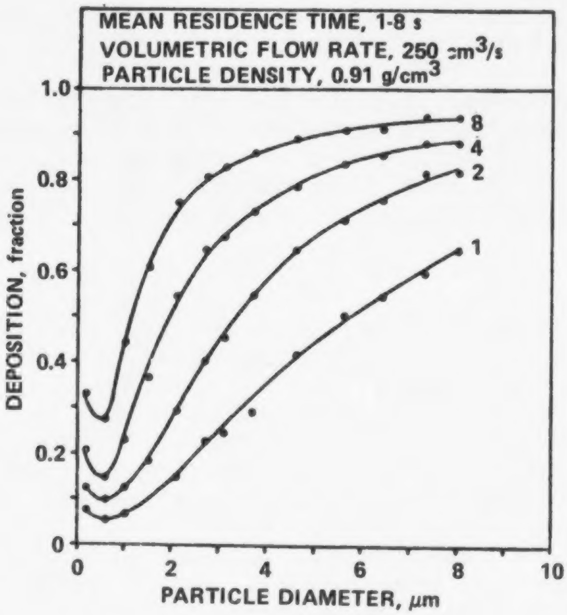

Figure 1. Effect of particle size and mean residence time on total deposition (from Heyder et al.[3]).

VFR

Total deposition is independent of VFR up to 1 ~ 1.5 μm since impaction is not effective for the range of VFR encountered. At larger sizes VFR begins playing a more and more important role, as shown in Figure 2 (from Heyder et al.[3]). The importance of impaction is depicted in Figure 3, where MRT and VFR are varied while keeping the tidal volume (TV) constant. There is a definite cross-over of the curves, which is even more dramatic for nose breathing, as shown in Figure 4 (also from Heyder et al.[3]), where it takes place around 1 μm, showing the contribution of impaction to nose deposition.

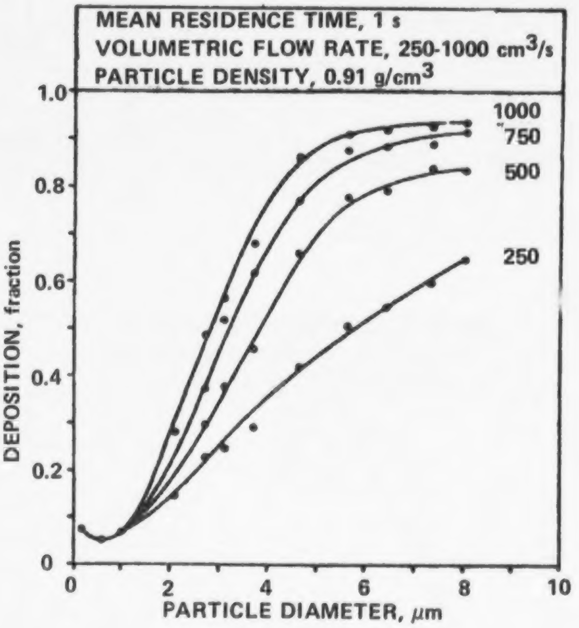

Figure 2. Effect of particle size and volumetric flow rates on total deposition (from Heyder et al.[3]).

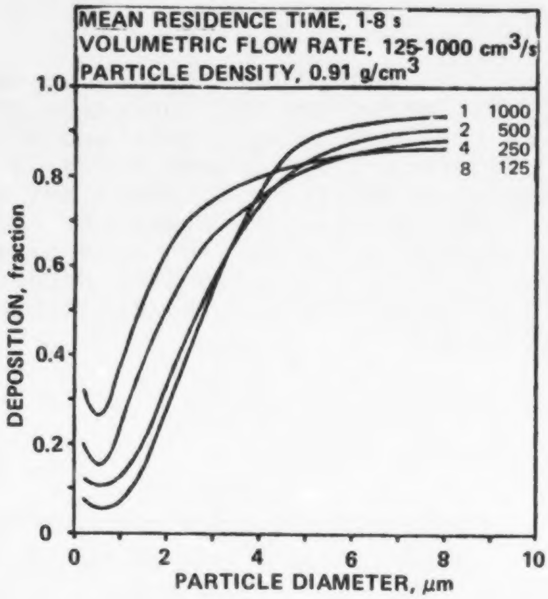

Figure 3. Effect of particle size on total deposition for mouth breathing at 1000 cm^3 tidal volume (from Heyder et al.[3]).

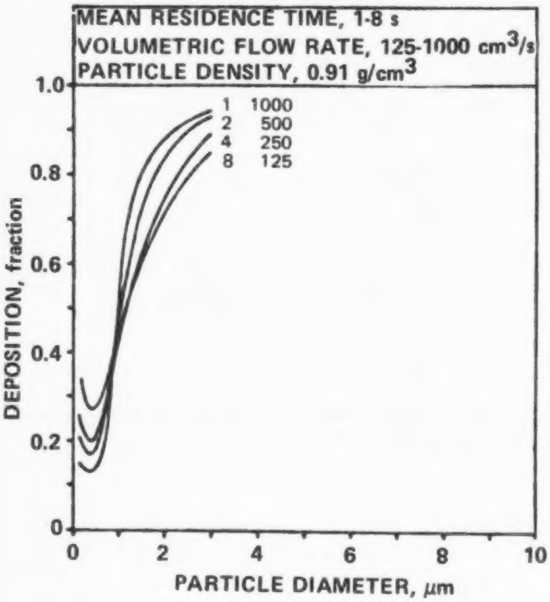

Figure 4. Effect of particle size on total deposition for nose breathing at 1000 cm^3 tidal volume (from Heyder et al.[3]).

Biological Variability

It is now generally accepted[2] that even under strictly controlled breathing conditions and residual volumes there is a definite intersubject variability of total deposition. An example of this is given[16] in Figure 5, where the DE is plotted as a function of particle size between 0.3 and 1.5 μm unit density spheres for six volunteers, breathing at 1000 cm^3 TV and 15 respiration/min, each at his own expiratory reserve volume, ERV. This is interesting since in this range total deposition is also alveolar deposition.

The scatter of data reaches a factor of 2 and cannot be explained on the basis of respiratory parameters.

For each volunteer instead, with 0.6 μm aerosols, a marked dependence on ERV is found. The relative DE can be expressed as a -1/3 power of the ERV relative to normal, probably due to a stronger mixing with smaller volumes;[9] a 10% variation of DE corresponds to a 30% variation of ERV around the normal value.[16]

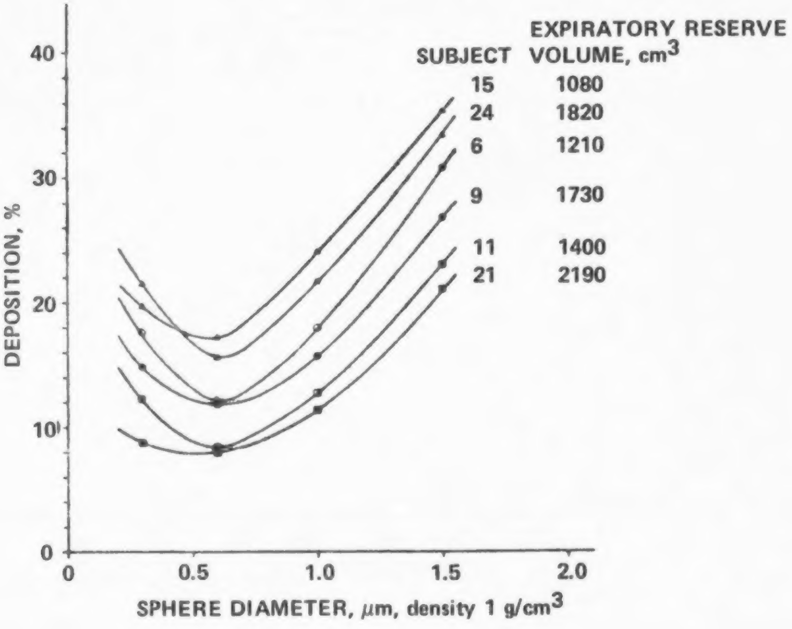

Figure 5. Total deposition for a group of 6 volunteers, at 1000 cm^3 tidal volume and 15 respirations/min (from Tarroni et al.[16]).

Electric Charges

Electric charges carried by aerosol particles have a definite effect on deposition, leading to an increased efficiency. This has been found in deposition measurements of aerosols produced by atomization; when the aerosol was not neutralized, deposition was higher and poorly reproducible.

Quantitative measurements[16,17] have been performed only with monodisperse particles charged with positive elementary charges in a narrow number distribution and in controlled breathing conditions. The electrostatic deposition, shown in Figure 6, increases monotonically with increasing charge number for 0.3 and 0.6 µm unit density spheres and is due to image forces[17] and therefore connected with the charge individually carried.

This has been confirmed theoretically[18] in the concentration range considered.

Quantitative information on charge distribution of actual aerosols is lacking; for aerosols freshly generated by disruption (grinding and atomization) the absolute charge can be very high and its contribution to total and regional deposition should be evaluated.

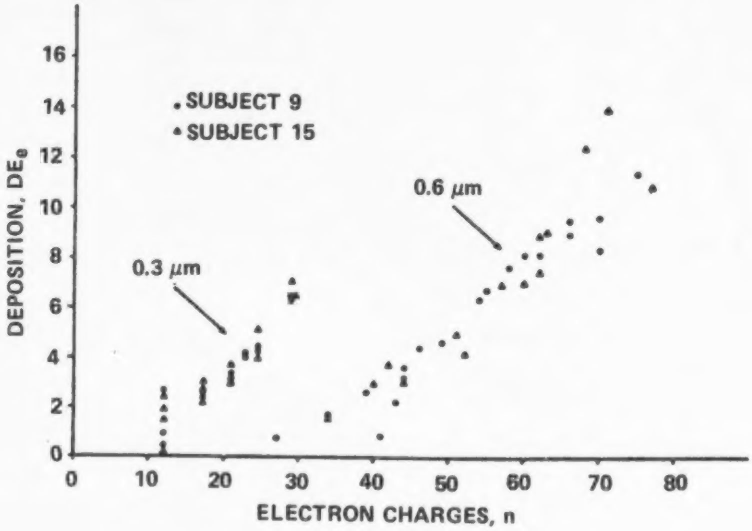

Figure 6. Contribution to total deposition from electric charges carried by 0.3 and 0.6 µm particles (from Tarroni et al.[16]).

REGIONAL DEPOSITION

Nose Deposition

Nose deposition must be treated separately since the breathing route can be to some extent a matter of choice for the subject, and has peculiar clearance pathways; this is important both for total and regional deposition.

Nose deposition data[19,20,12,21,22] have been recently summarized by Lippmann[2] and are shown in Figure 7.

The deposition is a linear function of the logarithm of the inertia parameter D^2F when F is the VFR and is practically quantitative for 9 μm particles at a flow rate of 30 liters per minute.

The results are in fairly good agreement with the ICRP Task Group deposition curve, based on Pattle's[23] data.

Heyder and Rudolf[24] have also successively studied in detail the deposition in the nose during exhalation, which is fairly close to deposition during inhalation, although this efficiency applies only to the transmitted fraction.

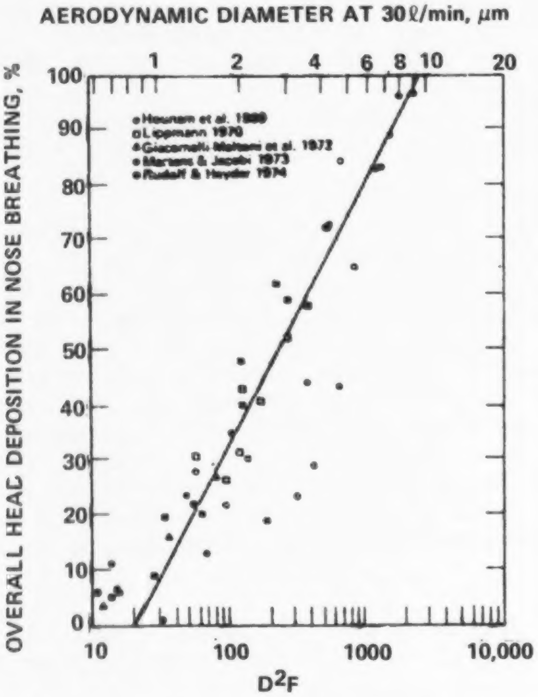

Figure 7. Head deposition during inhalation via the nose vs the impaction parameter D^2F (from Lippmann[2]). The solid line is the ICRP[1] curve based on Pattle's[23] data.

Mouth Breathing

Extrathoracic Deposition--

Regional deposition in mouth breathing has been studied by Lippman,[2] Lippmann and Albert,[25] Chan and Lippmann,[26] and by Stahlhofen et al.[27] by external counting of labeled deposited particles.

Head deposition too can be linearly fitted with the lg D^2F parameter. Lippmann's[2] data have been extrapolated to obtain the size for quantitative head deposition, which is around 17 μm for a 30 ℓ min^{-1} VFR.

Stahlhofen et al.'s[27] data show a slightly higher efficiency pointing to 100 percent deposition around 11 μm at the same flow rate.

The inertial parameter is not fully representative of deposition since the geometry of the airways may be dependent on the flow.

This should be considered in establishing effective thresholds of sampling instruments and guidelines. In Figure 8 the average extrathoracic deposition of three subjects[27] is reported for two flow rates together with Lippmann's curve.[2]

In Figure 9 the effective total and regional depositions are shown as the average of three subjects,[27] for two breathing patterns: TV = 1500 cm^3, 15 resp.min^{-1} (MTR = 2 sec, VFR = 750 $\text{cm}^3\ \text{sec}^{-1}$) and TV = 1000 cm^3, 7.5 resp.min^{-1} (MRT = 4 sec, VFR = 250 $\text{cm}^3\ \text{sec}^{-1}$). For the extrathoracic deposition the curves are derived from the same data points of Figure 8.

Tracheobronchial Deposition--

Tracheobronchial deposition has been studied in vivo by Lippmann, Albert, and Peterson,[28] on a large number of volunteers, ranging from healthy non-smoking to smoking, mild bronchitic and severe bronchitic. Lately it has been studied by Chan and Lippmann[26] both in hollow casts and in vivo and by Stahlhofen, Gebhart and Heyder[27] on three healthy subjects. In addition, detailed studies have been performed on hollow casts of human bronchial trees by Chan, Schreck, and Lippmann,[29] that have pointed out the flow pattern in the trachea, and preferential deposition sites in connection with air flow and turbulence. In addition the effect of electric charges on hollow cast deposition has been examined[30] and the dependence on image forces has been confirmed.

The studies of Chan and Lippmann[26] have shown a remarkable biological variability of deposition data even in the tracheobronchial tree.

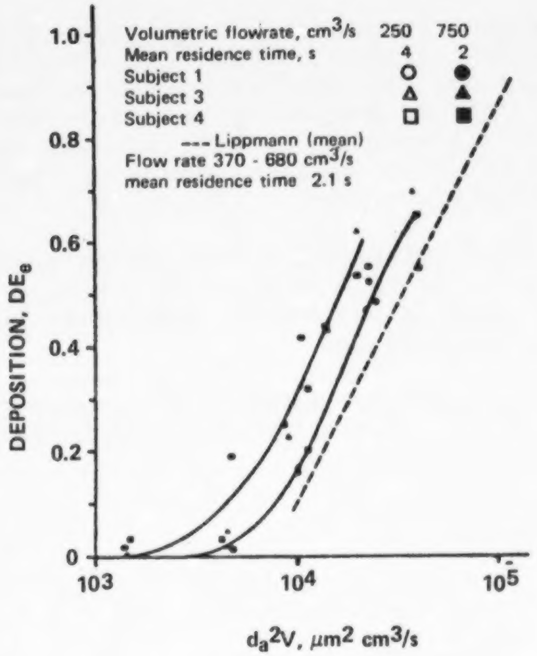

Figure 8. Head deposition during inhalation via the mouth vs. impaction parameter. The solid lines and points are for three subjects at two volumetric flow rates (from Stahlhofen et al.[27]), while the broken line is Lippmann's[2] fitted curve.

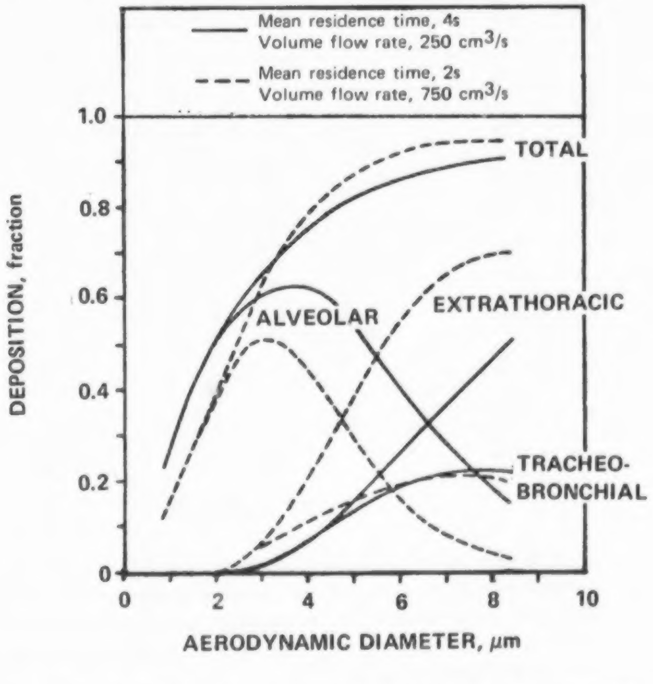

Figure 9. Average total and regional depositions for three subjects at two different respiratory patterns and for mouth breathing (based on data of Stahlhofen et al.[27]).

Figure 10 shows the TB deposition expressed as a fraction of the aerosol entering the trachea. The straight lines represent the average and the scatter of the values found by Lippmann,[2] while the data of Stahlhofen et al.[27] are shown by the points. These show a smaller scatter of data and two distinct behaviors at two rates as well as values of deposition slightly lower than Lippmann's average.

The actual tracheobronchial deposition is a bell-shaped curve that departs from zero around or slightly above 2 μm aerodynamic size and reaches a maximum, according to the flow conditions, between 6 and 10 μm.

In Figure 9 the average actual TB deposition for three subjects[27] is plotted as a function of particle size for two respiratory patterns.

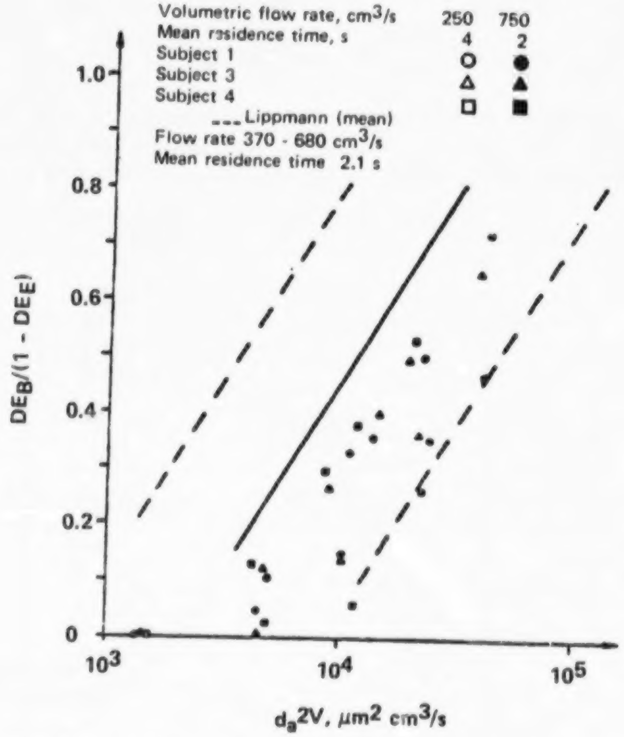

Figure 10. *Deposition in the ciliated tracheobronchial region during mouth breathing, in percent of the aerosol entering the trachea. The straight lines represent the average and the scatter of Lippmann's[2] data while the points are the values obtained by Stahlhofen et al.[27] (from Stahlhofen et al.[27]).*

It has been pointed out that deposition depends strongly on the health conditions and increases for smokers and again for bronchitic patients. Chan and Lippmann[26] have proposed a parameter, called the bronchial deposition size, BDS, derived by expressing tracheobronchial deposition as a function of the Stokes number. This was found to be 1.20 cm for healthy nonsmokers, 1.02 for smokers, 0.9 for patients under treatment for obstructive lung disease, and 0.6 for severely disabled patients.

This effect may be important when establishing sampling guidelines and in evaluating health hazards of airborne particles since it points out population groups particularly at risk in some circumstances.

Alveolar Deposition--

The gas exchange region of the airways is characterized by a very large surface area and therefore by a small average particle-to-wall distance and a large cumulative cross-section. Therefore deposition in the aerodynamic size range is practically due to gravitational settling.

The alveolar deposition therefore increases with increasing MRT at constant VFR. Because of the behavior of extrathoracic and tracheobronchial deposition, alveolar deposition also follows a bell-shaped curve: the relative maximum is around 3 μm and can be shifted to smaller sizes both for increasing MRT at constant VFR and for increasing VFR at constant MRT. In the first case the alveolar deposition values increase since the extrathoracic and tracheobronchial deposition do not vary appreciably and gravitational deposition is more effective. Figure 11, from Heyder et al.,[3] shows this effect in detail.

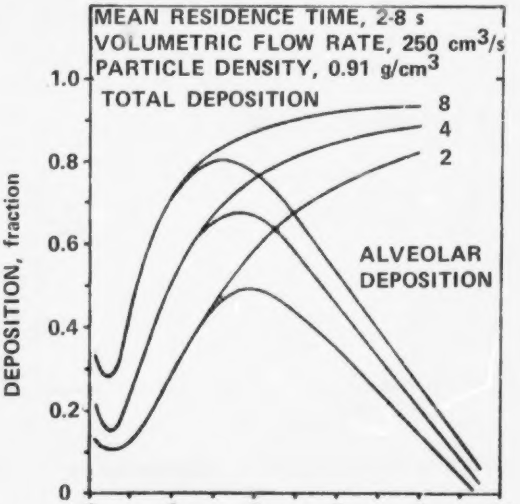

Figure 11. Effect of particle size and mean residence time on total and alveolar deposition (from Heyder et al.[3]).

Instead, the increase in VFR causes a higher deposition by impaction in the higher regions and therefore transmits a lower fraction of large particles to the alveolar region and the effect of increased VFR covers the effect of decreased MRT.

The data of Stahlhofen et al.[27] for alveolar deposition are also summarized in Figure 9 as the average of their three subjects. These are in good agreement with Lippmann and Albert's[25] and Chan and Lippmann's[26] data for comparable respiration patterns. These data are plotted together for comparison in Figure 12 (from Chan and Lippmann[26]). The scatter of these are larger probably because of the larger number of subjects. Consequently intersubject variability is more considerable and the respiration is not as strictly controlled. This, though, makes them more representative of the range of values that one can find in a population.

INHALABILITY

Very little is known on the efficiency of intake of the airways for aerosol particles as a function of particle size, respiratory conditions, wind speed, and orientation of the head. The only extended work has been done by Ogden and Birkett.[31] Experiments were run on a tailor's dummy in a wind tunnel and with wind speeds of 0.75 and 2.75 m sec^{-1} and orientations from 0° to 180°.

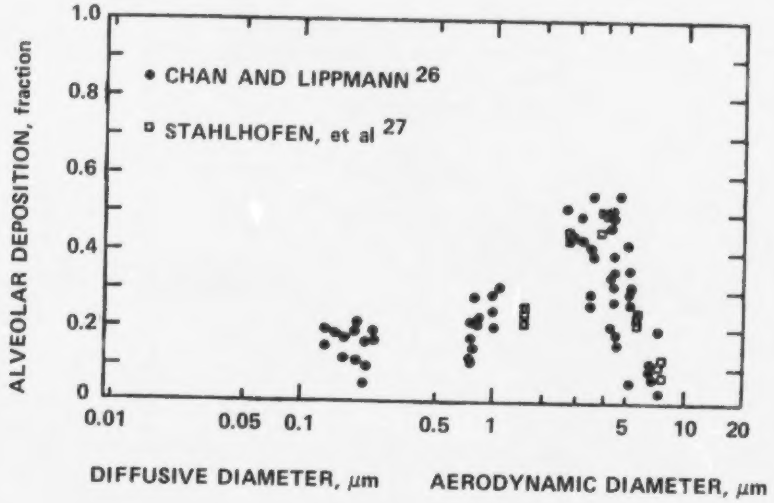

Figure 12. Alveolar deposition data of Chan and Lippmann[26] and of Stahlhofen et al.[27]

With 2.75 m sec^{-1} wind speed, already at 5 μm diameter the aerosol is strongly oversampled for nose and mouth breathing at 84 cm^3 sec^{-1} VFR, is sampled faithfully at 335 cm^3 sec^{-1}, and undersampled for higher VFR. At lower wind speed the portal of entry is not as important and the deviation of the sampled concentration from the true concentration is at most of the order of 25% above 15 - 20 μm.

Orientation between 0° and 90° is very important: with a 5 ℓ min^{-1} VFR at 90° and with a wind speed of 0.75 m sec^{-1}, the nose can sample 5 μm particles with an efficiency almost halved with respect to 0°. At a higher wind speed and at 45° the nose can strongly oversample, while the mouth samples always with a reduced efficiency.

Ogden and Birkett conclude that if the exposure is averaged for all wind directions, to simulate a worker uniformly exposed, the differences largely disappear and for winds between 0.75 and 2.75 m sec^{-1} and minute volumes between 20 and 40 ℓ for nose and mouth breathing, the efficiency ranges as functions of the aerodynamic diameter are shown in Table 1.

TABLE 1. RANGE OF ENTRY EFFICIENCIES FOR A HEAD RANDOMLY ORIENTED TO A WIND BETWEEN 0.75 AND 2.75 m sec^{-1} BREATHING WITH MINUTE VOLUME 20 - 40 LITERS[a]

Aerodynamic diameter, μm	0	5	10	15	20	25	30
Efficiency range, %	100	68-83	46-72	39-67	33-60	31-55	30-52

[a] From Ogden and Birkett[31]

SENSITIVITY CALCULATIONS

Particle deposition in the airways depends, as shown, on many parameters. Most of the measurements refer to laboratory conditions and their bearing on industrial or environmental hygiene is not straightforward. It is therefore interesting to study the sensitivity of total and regional deposition to aerosol parameters, respiration pattern, inhalation portal, and individual variability.

Total Deposition

The data used for the sensitivity calculation are:

1) total deposition curves as a function of particle size, respiratory frequency, and tidal volume for mouth and nose breathing obtained by Heyder and coworkers[14,3,27] in the range 0.3 to 9 μm;

2) intersubject variability between 0.3 and 1.5 μm and electric charge deposition values at 0.3 and 0.6 μm up to 70 elementary charges obtained at our laboratory.[16,17]

When not otherwise specified the aerosol was assumed log normally distributed with a geometric standard deviation $\sigma_g = 2$, which can be considered reasonable in many working environments; the reference breathing pattern is 1000 cm^3 tidal volume and 15 respirations min^{-1} (abbreviated 1000/15).

The sensitivity to particle size is presented in Table 2 for mouth and nose breathing, where the data is given as a percentage variation of deposition with respect to a 1 μm, $\sigma_g = 2$ aerosol. The effect of size is very strong, especially for mouth breathing, and can reach a factor of 3.

TABLE 2. TOTAL DEPOSITION: EFFECT OF MEDIAN SIZE OF PARTICLES

D, μm	Δ% Deposition, mouth breathing	Δ% Deposition, nose breathing
0.6	-28	-33
1.0	–	–
1.5	+42	+31
2	+81	+52
3	+146	+76
4	+193	+87
6	+250	+97
8	+281	+100
10	+299	+103

In Table 3 the effect of an increase of σ_g from 2 to 3 is shown, as a percentage variation of deposition with respect to the value at $\sigma_g = 2$, for mouth and nose breathing. The effect is especially remarkable again for mouth breathing. The dependence on σ_g is linear, so any σ_g can be evaluated.

In Table 4, an example of the effect of biological variability is given: it is remarkable at small sizes since the absolute value is low. At higher sizes deposition approaches 100% for all the subjects; little room is therefore left for individual variations.

TABLE 3. TOTAL DEPOSITION: EFFECT OF AN INCREASE OF σ_g FROM 2 TO 3

D, μm	Δ% Deposition, mouth breathing	Δ% Deposition, nose breathing
0.6	+35	+39
1	+40	+9
1.5	+27	-5
2	+15	-9
3	-1	-9
4	-8	-8

TABLE 4. TOTAL DEPOSITION: POSSIBLE INTERSUBJECT VARIABILITY

D, μm	Δ% Deposition
0.6	±34
1	±26
1.5	±20
2	±17
3	±12
4	±9

The effect of the respiration pattern is shown, as a percent variation in deposition with respect to 1000/15, in Table 5 for mouth breathing and Table 6 for nose breathing.

It can be remarked that 500/15 can be taken as reference for the respiration at rest, 1000/15 for moderate activity and 1000/30 for strong physical activity. The highest deposition is found in the case of moderate activity.

Nose breathing is compared to mouth breathing in Table 7; the data are the percent variation of nose breathing with respect to mouth breathing.

Table 8 summarizes the sensitivity calculations for the various parameters in the specified ranges. For the effect of electric charges, the increase is referred to the 28 elementary charges on 0.3 μm particles and 70 charges on 0.6 μm. As was observed above, unipolar charging is rare, but, since deposition is by image forces, a comparable increase in efficiency could take place with aerosols freshly produced by mechanical action and not neutralized.

TABLE 5. TOTAL DEPOSITION: EFFECT OF BREATHING PATTERN (VIA MOUTH)

	Δ% Deposition[a]	
D, μm	TV = 500 cm³, 15 respirations/min	TV = 1000 cm³, 30 respirations/min
0.6	-10%	-44%
1	-15%	-33%
1.5	-17%	-22%
2	-18%	-15%
3	-18%	-7%
4	-17%	-4%
6	-14%	-1%
8	-11%	-0
10	-9%	+1%

[a] With respect to TV = 1000 cm³, 15 respirations/min.

TABLE 6. TOTAL DEPOSITION: EFFECT OF BREATHING PATTERN (VIA NOSE)

	% Deposition[a]	
D, µm	TV = 500 cm^3, 15 respirations/min	TV = 1000 cm^3, 30 respirations/min
0.6	-30%	+2%
1.0	-30%	+5%
1.5	-26%	+5%
2	-21%	+4%
3	-15%	+2%
4	-10%	+2%
6	-5%	+1%
8	-3%	0
10	-2%	0

[a] With respect to TV = 1000 cm^3, 15 respirations/min

TABLE 7. TOTAL DEPOSITION: PERCENT VARIATION OF NOSE BREATHING WITH RESPECT TO MOUTH BREATHING

D, µm	Δ% Deposition
0.6	+100
1.0	+115
1.5	+99
2	+80
3	+53
4	+38
6	+21
8	+14
10	+9

Only two values for each parameter are given since they generally act in a different way for sizes greater or smaller than 1.5 µm.

In the range below 1.5 µm the inhalation route is the most sensitive variable, while the others have the same effect and have to be known with comparable accuracy. Above 2 µm the ruling parameter is particle size.

Aveolar Deposition

The data available at the time the calculation was performed were essentially the experimental alveolar deposition curve summarized by Lippmann[2] for mouth breathing, and, for nose breathing, the curve calculated by introducing the nose deposition. In the range below 2 µm the curves were completed with Heyder et al.'s data[14] of total deposition, since from 0.3 to 2 µm total and alveolar deposition coincide.

TABLE 8. TOTAL DEPOSITION: SUMMARIZED SENSITIVITY TO RELEVANT AEROSOL AND RESPIRATION PARAMETERS

	Particle size range, µm	Δ% Deposition
Size of particles[a]	0.6-1.5	300
	2-10	30
Geometric standard deviation[a]	0.6-1.5	40
	2-10	10
Electric charge of particles[a]	0.3	35
	0.6	65
Breathing pattern[a]	0.6-1.5	30
	2-10	15
Inhalation route, nose vs mouth	0.6-1.5	100
	2-10	80~10
Intersubject variability	0.6-1.5	30
	2-10	10

[a] Mouth breathing

In Table 9 the effect of size is shown, for mouth and nose breathing respectively; the effect of changing σ_g from 2 to 3 is shown separately for the inhalation portal in Table 10 and the percent decrease in alveolar deposition when inhaling through the nose with respect to mouth breathing is shown in Table 11.

As in the case of total deposition, the parameter sensitivity is summarized in Table 12. The alveolar region is an organ at risk for "insoluble" particles (or better, slowly transferable materials); Table 12 therefore can be taken as an indication of the uncertainties one faces as far as deposition is concerned when the aerosol is completely unknown. Alveolar deposition is less sensitive to size, standard deviation, and inhalation portal than total deposition.

Unfortunately more data is needed, especially for charged particles, for a complete assessment; nevertheless it can be stated that the uncertainties of the inhaling subject (respiration pattern, route of entry, biological variability) are comparable to the uncertainties of the aerosol characterization.

Some aspects of these will be dealt with in the following section, but it should be stressed here that, for a realistic evaluation of inhalation risks, more data is needed also on oxygen demand, minute volume, frequency, individual variability of deposition, and route of inhalation.

TABLE 9. ALVEOLAR DEPOSITION: EFFECT OF MEDIAN SIZE OF PARTICLES

D, μm	Δ% Deposition, mouth breathing	Δ% Deposition, nose breathing
0.6	-25	-12
1	-	-
1.5	+26	+11
2	+40	+13
3	+45	+3
4	+32	-13
6	0	-43
8	-33	-63
10	-54	-76

TABLE 10. ALVEOLAR DEPOSITION: EFFECT OF AN INCREASE OF σ_g FROM 2 to 3

D, μm	Δ% Deposition, mouth breathing	Δ% Deposition, nose breathing
0.6	+22	+19
1	+13	+2
1.5	-10	-16
2	-25	-27
3	-38	-32
4	-35	-22

TABLE 11. ALVEOLAR DEPOSITION: PERCENT VARIATION OF NOSE BREATHING WITH RESPECT TO MOUTH BREATHING

D, μm	Δ% Deposition
0.6	-19
1	-31
1.5	-39
2	-44
3	-51
4	-54
6	-59
8	-62
10	-64

POSSIBLE SAMPLING METHODS

At our laboratory we have essentially followed two approaches to aerosol characterization for inhalation risk assessment, besides the consolidated techniques that are generally in use.

One is based on a simplified size spectrometry that can be used in the field and the other is based on the simulation of the total and regional deposition in the human respiratory tract.

The Inertial Spectrometer

Size characterization in the field is now performed by means of cascade impactors.[32] These are simple instruments and so well known that any description is redundant here. They have been improved in recent years and have greatly profited from theoretical studies.[33,34] Nevertheless the usual drawbacks have only partially been overcome; particle bouncing and reentrainment are still problems. Vapor supersaturation across the last stages, which may increase particle mass by condensation, has also to be considered.[35] Cascade centripeters[36] and generally virtual impactors have improved the performance as far as stage loading is concerned, but the wall losses may become a problem.

Sampling cyclones have been greatly improved[37-41] with the aid of semiempirical theories. Sharp cut-offs have been obtained together with good classification performance. These are particularly useful in high concentration environments since particle bouncing and reentrainment can be avoided.

A new instrument has been recently described[42] that works as a continuous spectrometer, has no moving parts, and collects

TABLE 12. ALVEOLAR DEPOSITION: SUMMARIZED SENSITIVITY TO SOME OF THE RELEVANT PARAMETERS

	Particle size range, μm	Δ% Deposition
Size of particles[a]	0.6-1.5	25
	2-10	40
Geometric standard deviation[a]	0.6-1.5	20
	2-10	30
Inhalation route, nose vs mouth	0.6-1.5	30
	2-10	50

[a] Mouth breathing

the whole aerosol on just one filter. It is essentially composed of a 2-mm deep rectangular channel, with a 90° bend, which is flushed with clean air. A thin aerosol sheath is injected upstream of the bend; while the streamlines follow the curvature, the particles, because of their inertia, tend to persist in their initial velocity at the bend. Therefore the particles depart from the original streamlines by a distance which is a function of their aerodynamic diameter. The external wall downstream of the bend is made of a membrane filter through which air is sucked. The particles are separated according to size while airborne; the small separation is strongly magnified by the aerodynamic projection to the filter surface. The filter will then collect the whole aerosol: the particles too small to be diverted will be collected toward the end of the filter, large particles are precipitated at the beginning, and the intermediate sizes are continuously separated. The deposit can then be analyzed to yield the aerodynamic activity diameter, mass diameter, and elemental size distribution. It could also be turned into a real time aerosol spectrometer since the ceiling has no other function than flow containment and can house appropriate detectors.

The total flow rate in the present version is 7 ℓpm and the aerosol sampling rate can reach 1/10 of that, while still preserving good resolution. A high resolution run with 0.5, 1.14, and 2.01 μm latex spheres sampled separately is shown in Figure 13.

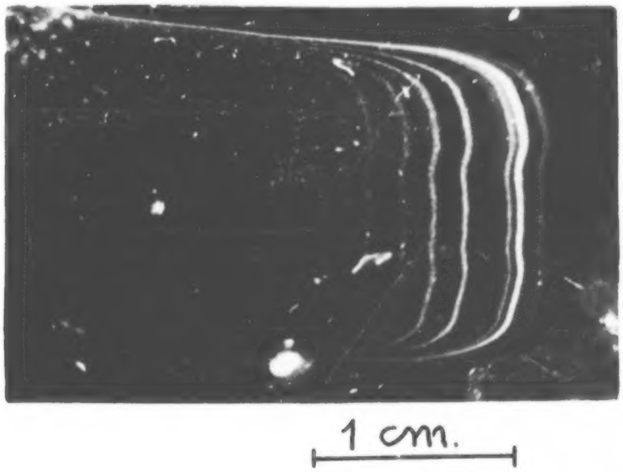

Figure 13. Deposition pattern of 0.5, 1.14, and 2.01 μm latex particles sampled separately with the inertial spectrometer. The singlet and multiplet lines of 1.14 and 2.01 spheres are clearly visible.

An example of a calibration curve is shown in Figure 14.

This spectrometer could meet the proposed sampling criteria of EPA[43] by working at a reduced flow rate. The deposit could then be cut into three sections: sizes greater than 15 μm, between 15 and 2.5 μm, and below 2.5 μm and each section could be analyzed for the quantity needed for toxicological evaluation. In fact membrane filters are of controlled composition and are an ideal means for environmental chemical analysis. The filter can be easily stored; the procedure could be greatly simplified since the filter could be evaluated only in the case, for example, when a total particulate sampling would exceed a predetermined investigation level.

For general application to size distribution measurements, the deposit can be scanned and a signal can be obtained that is a function of the amount of material contained in each size. Examples of these could be radiometric scanning in the case of radioactive materials, X-ray fluorescence scanning, or optical scanning of the diaphanized filter. Otherwise the filter can be cut, with the aid of the calibration curve, in equal logarithmic intervals and the amount of material contained in each

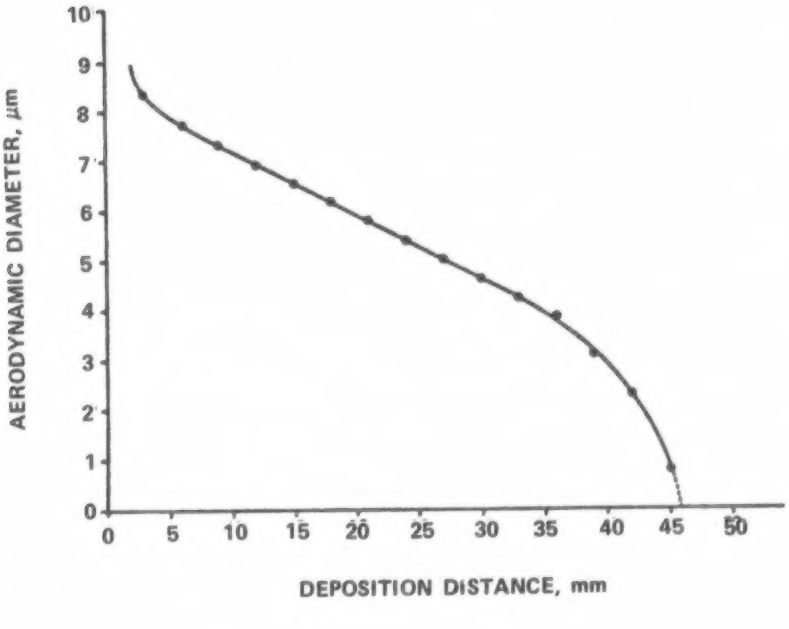

Figure 14. Calibration curve of the inertial spectrometer.

section analyzed with standard microchemical techniques. The cumulative or differential distribution can be obtained of the mass or activity and then the activity median or mass median aerodynamic diameter can be obtained. For each size fraction the inhalability and deposition can be readily computed even with a desk-top programmable microcomputer, for the particular conditions of the individual involved.

Figure 15 shows the distribution of sodium chloride particles labelled with uranine as analyzed with fluorescence techniques.

If necessary, the aerosol can be humidified in order to let the hygroscopic particles grow by water condensation. The pressure drop across the bend is too low to cause any appreciable modification of the aerosol before deposition.

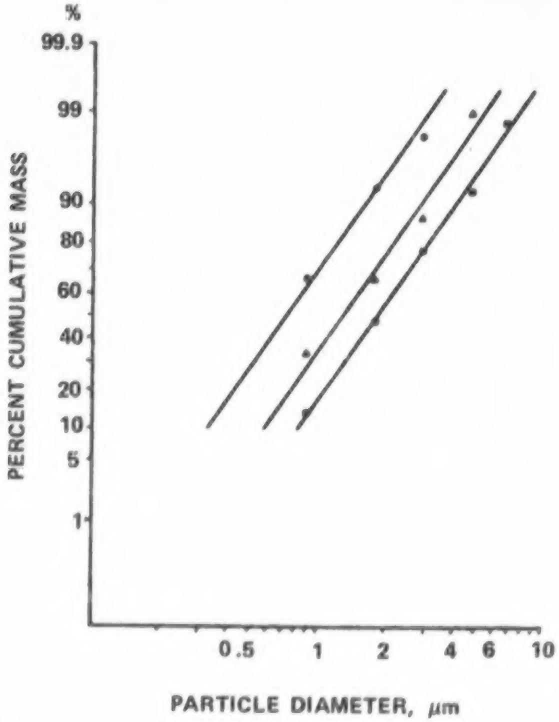

Figure 15. Cumulative mass vs. size of a uranine-tagged sodium chloride aerosol sampled with the inertial spectrometer and determined by fluorometry.

Deposition Simulating Sampler

Another approach has been already described[4] and has been recently developed into a field sampler, taking also into account the most recent data on total and regional deposition.

It is based on the simulation of the total and regional deposition of particles in the human respiratory tract.

In this way the size characterization of the aerosol is not needed; the approach is then simpler than size spectrometry but it is not as flexible in the sense that a particular respiratory pattern has to be assumed as a reference.

Bubbles of aerosols freely rising through a water column experience a particle deposition by inertia, sedimentation, and diffusion. The combination of these mechanisms produces a deposition behavior which is quite close to absolute alveolar deposition in the respiratory tract. Therefore if, before the bubbler, a stage is added with a deposition efficiency of the tracheobronchial plus extrathoracic airways, what is captured in each stage is a measure of the effective regional deposition.

In the present set-up the first stage is composed of a diffusion humidifier and a specially designed cyclone. The sum of the deposition in the two stages gives the total deposition. This approach has the advantage of inducing condensation growth of the particles where appropriate. The present set-up[44] has been checked only for particles larger than 0.5 µm, that is, only in the aerodynamic range. It has been previously shown,[4] though, that in the diffusion range particles are captured in the bubbles by a diffusion mechanism; this might be a more correct approach than pushing aerodynamic separation to sizes where aerodynamic effects play no role in particle deposition.

There are several parameters adjustable in order to vary the deposition efficiency: the height of the water column, by which the residence time of the bubble in water can be varied; the number and diameter of the bubbling nozzles, by which the bubble diameters can be to some extent adjusted and the impaction efficiency during bubble formation can be affected.

For the evaluation of the deposit there are two possibilities: either the material in each stage is recovered and measured or parallel lines can be assembled, each containing one stage more than the other and terminating with a membrane filter. The difference in the filter content would then be attributed to the capture of the missing stage or stages.

The drawback of this approach is again that it matches one particular respiratory pattern at a time and it has to be readjusted to match other conditions; this is essentially equivalent to selecting a reference condition or threshold that always causes some rigidity in the system.

In Figure 16 the deposition efficiencies obtained in the sampler are shown by the experimental points as a function of the particle size.

For comparison the deposition efficiency in humans[3] is shown with the solid lines, for 1500/15 and mouth breathing.

CONCLUSIONS

The deposition efficiency in the human respiratory tract depends strongly on respiration pattern, portal of inhalation, minute volume and individual variability besides aerosol properties, like particle size, shape, electric charge, and solubility.

Therefore, fixing particular particle sizes as a threshold has a meaning only if referred to particular breathing situations and for particular aerosols; consequently the need arises for safety factors that invariably make the evaluation of the inhalation hazard less and less realistic.

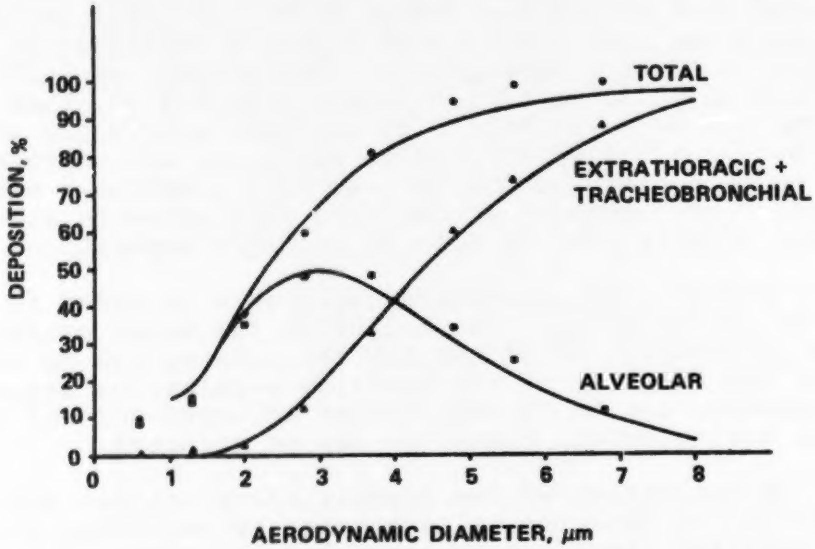

Figure 16. Deposition efficiency in the simulating sampler[44] (dots), as compared with the total alveolar deposition in humans for mouth breathing, 1500/15,[3] (solid line).

The more rigorous approach would then be a direct evaluation of particle size distribution and of other aerosol properties. These could be introduced into the appropriate inhalability and deposition functions; then the effective deposition in the realistic situation could be computed.

This approach may appear like requesting more resources than the evaluation of just two or three fractions. The amount of resources needed can be decreased if total dust is sampled together with the aerosol for size distribution. The aerosol could then be characterized only if the total dust sample exceeds a prefixed investigation level or whenever the circumstances would suggest to do so.

REFERENCES

1. Morrow, P.E., Chairman. ICRP Task Group Report on Lung Dynamics: Deposition and Retention Models for Internal Dosimetry of the Human Respiratory Tract. Health Phys. 12:173-208, 1966.

2. Lippmann, M. Regional Deposition of Particles in the Human Respiratory Tract. In: Handbook of Physiology, Section 9: Reaction to Environmental Agents. D.H.K. Lee, H.L. Falk, S.D. Murphy, and S.R. Geiger, eds. Bethesda, MD, American Physiological Society, 1977. pp. 213-232.

3. Heyder, J., J. Gebhart, and W. Stahlhofen. Inhalation of Aerosols; Particle Deposition and Retention. Presented at American Chemical Society Annual Meeting, Symposium on Aerosol Generation and Exposure Facilities, April, 1979.

4. Melandri, C., and V. Prodi. Simulation of the Regional Deposition of Aerosols in the Respiratory Tract. Am. Ind. Hyg. Assoc. J. 32:52-57, 1971.

5. Schroter, R.C., and M.F. Sudlow. Flow Patterns in Models of the Human Airways. Respir. Physiol. 7:431-455, 1969.

6. Ultman, J.S., and H.S. Blatman. Longitudinal Mixing in Pulmonary Airways. Analysis of Inert Gas Dispersion in Symmetric Tube Network Models. Respir. Physiol. 30:349-367, 1977.

7. Taulbee, D.B., and C.P. Yu. A Theory of Aerosol Deposition in the Human Respiratory Tract. J. Appl. Physiol. 38:77-85, 1975.

8. Yu, C.P., and D.B. Taulbee. A Theory for Predicting Respiratory Tract Deposition of Inhaled Particles in Man. In: Inhaled Particles IV, W.H. Walton, ed. Pergamon Press, Oxford, 1977. pp. 35-46.

9. Taulbee, D.B., and C.P. Yu. Theory of Particle Deposition in the Human Lung. Presented at Annual Meeting, Gesellschaft für Aerosolforschung, Bad Soden, Germany, 1976.

10. Muir, D.C.F., and C.N. Davies. The Deposition of 0.5 μm Diameter Aerosols in the Lungs of Man. Ann. Occup. Hyg. 10:161-174, 1967.

11. Heyder, J., J. Gebhart, G. Heigwer, C. Roth, and W. Stahlhofen. Experimental Studies of the Total Deposition of Aerosol Particles in the Human Respiratory Tract. J. Aerosol Sci. 4:191-208, 1973.

12. Giacomelli-Maltoni, G., C. Melandri, V. Prodi, and G. Tarroni. Deposition Efficiency of Monodisperse Particles in the Human Respiratory Tract. Am. Ind. Hyg. Assoc. J. 33:603-610, 1972.

13. Heyder, J., J. Gebhart, C. Roth, W. Stahlhofen, G. Tarroni, T. De Zaiacomo, M. Formignani, D. Melandri, and V. Prodi. Intercomparison of Lung Deposition Data for Aerosol Particles. J. Aerosol Sci. 9:147-155, 1978.

14. Heyder, J., L. Armbruster, J. Gebhart, E. Grein, and W. Stahlhofen. Total Deposition of Aerosol Particles in the Human Respiratory Tract for Nose and Mouth Breathing. J. Aerosol Sci. 6:311-328, 1975.

15. Swift, D.L., F. Shanty, and J.T. O'Neil. Human Respiratory Deposition Pattern of Fume-Like Particles. Presented at American Industrial Hygiene Association Conference, May, 1977.

16. Tarroni, G., C. Melandri, V. Prodi, T. De Zaiacomo, M. Formignani, and P. Bassi. An Indication on the Biological Variability of Aerosol Total Deposition in Humans. Presented at American Industrial Hygiene Association Conference, May, 1979.

17. Melandri, C., V. Prodi, G. Tarroni, M. Formignani, T. De Zaiacomo, F.G. Bompane, and G. Maestri. On the Deposition of Unipolarly Charged Particles in the Human Respiratory Tract. In: Inhaled Particles IV, W.H. Walton, ed. Pergamon Press, Oxford, 1977. pp. 193-203.

18. Yu, C.P., and K. Chandra. Precipitation of Submicron Charged Particles in Human Lung Airways. Bull. Math. Biol. 39:471, 1977.

19. Hounam, R.F., A. Black, and M. Walsh. Deposition of Aerosol Particles in the Nasopharyngeal Region of the Human Respiratory Tract. Nature 221:1254-1255, 1969.

20. Lippmann, M., and R.E. Albert. Deposition and Clearance of Inhaled Particles in the Human Nose. Ann. Otol. Rhinol. Laryngol. 79:519-528, 1970.

21. Maertens, A., and W. Jacobi. Die in vivo Bestimmung der Aerosolteilchen Deposition in Atemtrakt bei Mund-bzw-Nasen Atmung [The In-Vivo Determination of the Deposition of Aerosol Particles in the Respiratory Tract by Mouth or Nose Breathing]. Presented at Annual Meeting, Gesellschaft für Aerosolforschung, Bad Soden, Germany, October, 1973.

22. Rudolf, G., and J. Heyder. Deposition of Aerosol Particles in the Human Nose. Presented at Annual Meeting, Gesellschaft für Aerosolforschung, Bad Soden, Germany, October, 1974.

23. Pattle, R.E. The Retention of Gases and Particles in the Human Nose. In: Inhaled Particles and Vapors. C.N. Davies, ed. Pergamon Press, Oxford, 1961. pp. 302-309.

24. Heyder, J., and G. Rudolf. Deposition of Aerosol Particles in the Human Nose. In: Inhaled Particles IV, W.H. Walton, ed. Pergamon Press, Oxford, 1975. pp. 107-125.

25. Lippman, M., and R.E. Albert. The Effect of Particle Size on the Regional Deposition of Inhaled Aerosols in the Human Respiratory Tract. J. Am. Ind. Hyg. Assoc. 30:257-275, 1969.

26. Chan, T.L., and M. Lippmann. Experimental Measurements and Empirical Modelling of the Regional Deposition of Inhaled Particles in Humans. Submitted to Am. Ind. Hyg. Assoc. J.

27. Stahlhofen, W., J. Gebhart, and J. Heyder. Experimental Determination of the Regional Deposition of Aerosol Particles in the Human Respiratory Tract. Presented at American Industrial Hygiene Association Conference, May, 1979.

28. Lippmann, M., R.E. Albert, and H.T. Peterson. The Regional Deposition of Inhaled Aerosols in Man. In: Inhaled Particles III, W.H. Walton, ed. Unwin, London, 1971, pp. 105-120.

29. Chan, T.L., R.M. Schreck, and M. Lippmann. Effect of Turbulence on Particle Deposition in the Human Trachea and Bronchial Airways. Presented at Annual Meeting, American Institute of Chemical Engineers, November, 1978.

30. Chan, T.L., M. Lippmann, V.R. Cohen, and R.B. Schlesinger. Effect of Electrostatic Charges on Particle Deposition in a Hollow Cast of the Human Larynx-Tracheobronchial Tree. J. Aerosol Sci. 9:463-468, 1978.

31. Ogden, T.L., and J.L. Birkett. The Human Head as a Dust Sampler. In: Inhaled Particles IV. W.H. Walton, ed. Pergamon Press, Oxford, 1977. pp. 93-105.

32. May, K.R. The Cascade Impactor: An Instrument for Sampling Coarse Aerosols. J. Sci. Instrum. 22:187-195, 1945.

33. Marple, V.A., and B.Y.H. Liu. Characteristics of Laminar Jet Impactors. Environ. Sci. Technol. 8:648-654, 1974.

34. Marple, V.A., and K. Willeke. Inertial Impactors-Theory, Design and Use. In: Fine Particles, Aerosol Generation, Measurement, Sampling, and Analysis. B.Y.H. Liu, ed. Academic Press, New York, 1976. pp. 411-446.

35. Tarroni, G., C. Melandri, V. Prodi, M. Formignani, and T. De Zaiacomo. Taratura di una Centripeta in Cascata per Campionamenti di Aerosol in Diverse Condizioni Operative. [Calibration of a Cascade Centripeter for Sampling Aerosols under Diverse Operating Conditions.] Presented at Annual Meeting, Italian Health Physics Society, Bologna, October, 1977.

36. Hounam, R.F., and R.J. Sherwood. The Cascade Centripeter: a Device for Determining the Concentration and Size Distribution of Aerosols. Am. Ind. Hyg. Assoc. J. 26:122-131, 1965.

37. Chan, T., and M. Lippmann. Particle Collection Efficiencies of Air Sampling Cyclones: An Empirical Theory. Environ. Sci. Technol. 11:377-382, 1977.

38. Lippmann, M., and T.L. Chan. Cyclone Sampler Performance. In: Proceedings: Advances in Particle Sampling and Measurement. W.B. Smith, compiler. EPA-600/7-79-065, U.S. Environmental Protection Agency, Research Triangle Park, NC, 1979. pp. 30-51.

39. Blachman, M.W., and M. Lippmann. Performance Characteristics of the Multi-Cyclone Aerosol Sampler. Am. Ind. Hyg. Assoc. J. 35:311-316, 1974.

40. Smith, W.B., K.M. Cushing, G.E. Lacey, and J.D. McCain. Particulate Sizing Techniques for Control Device Evaluation. EPA-650/2-74-102a, U.S. Environmental Protection Agency, Research Triangle Park, NC, 1975. p. 133.

41. Smith, W.B., and R.R. Wilson. Development and Laboratory Evaluation of a Five-Stage Cyclone System. EPA-600/7-78-008, U.S. Environmental Protection Agency, Research Triangle Park, NC, 1978. p. 59.

42. Prodi, V., C. Melandri, G. Tarroni, T. De Zaiacomo, M. Formignani, and D. Hochrainer. An Inertial Spectrometer for Aerosol Particles. J. Aerosol Sci. 10:411-420, 1979.

43. Miller, F.J., D.E. Gardner, J.A. Graham, R.E. Lee, W.E. Wilson, and J.D. Bachmann. Size Considerations for Establishing a Standard for Inhaled Particles. J. Air Pollut. Control Assoc. 29:610-615, 1979.

44. Melandri, C., V. Prodi, G. Tarroni, M. Formignani, and T. De Zaiacomo. Aerosol Sampling by Simulation of the Regional Deposition in the Human Airways. Presented at Annual Meeting, Gesellschaft für Aerosolforschung, Düsseldorf, October, 1979.

PAPER 20

AEROSOL SAMPLING INLETS AND INHALABLE PARTICLES

BENJAMIN Y.H. LIU
DAVID Y.H. PUI
PARTICLE TECHNOLOGY LABORATORY
MECHANICAL ENGINEERING DEPARTMENT
UNIVERSITY OF MINNESOTA

ABSTRACT

The problem of sampling aerosols from the ambient atmosphere has been considered from a theoretical point of view. Following a review of the various samplers and inlets used in ambient sampling, the factors contributing to high sampling efficiency for large particles are discussed. It is pointed out that the major mechanisms for particle loss in sampling inlets are impaction on external surfaces, and impaction, turbulent deposition, and sedimentation on internal surfaces. Therefore, an efficient inlet is one for which these losses are minimized.

Based on these theoretical considerations, a new inlet for sampling inhalable particles (particles with aerodynamic diameter of 15 μm or less) has been designed, constructed, and tested. The inlet incorporates an inlet configuration allowing for the efficient entry of large particles into the inlet opening, followed by an impactor to remove the coarse, non-inhalable particles. The inlet has been found to have essentially wind speed independent characteristics for wind speeds of up to 9 km/hr, the maximum wind speed used in the tests. The impactor used has also been found to have sharp cut-off characteristics with a sharpness of cut parameter, σ_g, of 1.18. It is believed that this particular inlet will meet the requirements of a high efficiency inlet for sampling inhalable particles from the ambient atmosphere.

INTRODUCTION

Sampling of aerosols from the ambient atmosphere is an important and necessary first step in atmospheric aerosol measurement. To obtain accurate measurement results, a representative aerosol sample must be drawn through an inlet into the particle measuring or collecting device. The sampling inlet is an important part of any aerosol measuring system and, as such, must be designed with care. An ideal inlet should allow all particles of interest to enter and arrive at the sensing or collecting zone of the instrument while excluding rain, snow, insects, plant matter, and other airborne debris. The performance of the inlet should also be unaffected by wind up to some maximum speed.

Inhalable particulate matter (IPM) has been defined by the Environmental Protection Agency[1] as particles with aerodynamic diameters of 15 μm or less. New particulate air quality standards based upon IPM are being developed by the Agency. Unlike the conventional high-volume sampler which measures the total suspended particulates (TSP) with an uncertain cut-off size for large particles, samplers for IPM must have well-defined large particle cut size characteristics. The development of an inlet of high efficiency for particles of up to 15 μm aerodynamic diameter, therefore, is essential for the development of new IPM standards.

In this paper, we will first briefly review the various approaches to ambient aerosol sampling, with particular emphasis on the inlet designs. A new inlet for the accurate sampling of IPM will then be described, together with the criteria of design and the performance data obtained on this new inlet.

AMBIENT AEROSOL SAMPLING AND INLET DESIGNS

A principal requirement of ambient aerosol sampling is that the instrument must be protected from rain and snow. This can be accomplished by means of simple weather-proof housings or more elaborate inlet designs to achieve high inlet efficiency. The term "inlet efficiency" is used here for the total transmission efficiency of the inlet system, defined as the fraction of particles transmitted by the inlet from the ambient atmosphere to the sensing or collecting zone of the instrument. For an inlet of a specific design, the inlet efficiency is generally a function of particle size, wind speed, and sampling flow rate. High inlet efficiency can be achieved easily for small particles, viz., those with diameters of a few micrometers or less. However, for large particles, high inlet efficiency can be obtained only with careful design.

High-Volume Sampler

Figure 1 is a schematic diagram of the widely used high-volume, or hi-vol, sampler. The hi-vol sampler is the standard reference method for TSP (total suspended particulate) measurement in the ambient atmosphere, in terms of which the national ambient particulate air quality standards are defined.[2] In the standard hi-vol, a 20.3 cm x 25.4 cm (8 in. x 10 in.) filter is placed horizontally within the main sampler housing, which is about 29 cm x 36 cm (11½ in. x 14 in.) in cross-section. The clearance area between the main housing and the roof at its closest point is specified to be 580.5 ± 193.5 cm^2 (90 ± 30 $in.^2$). Recent wind tunnel tests of the hi-vol by McFarland et al.[3] showed that the D_{50} cut size (aerodynamic diameter corresponding to an inlet efficiency of 50%) is >30 μm at a wind speed of 2 km/hr, decreasing to about 30 μm at 8 km/hr and 17 μm at 24 km/hr. In addition, the inlet efficiency was found to depend on wind direction. Table 1 shows a comparison of the inlet efficiency of the hi-vol with several other ambient aerosol samplers and inlets.

Isokinetic Sampling

In principle, isokinetic sampling can be used for atmospheric sampling. Although capable of high accuracy, isokinetic sampling is seldom used because the system to achieve true isokinetic conditions in the ambient atmosphere is necessarily complicated: the inlet must be directed to face the wind and the suction speed in the inlet must also be adjusted to match the wind speed. The latter task is extremely difficult to achieve under variable wind conditions.

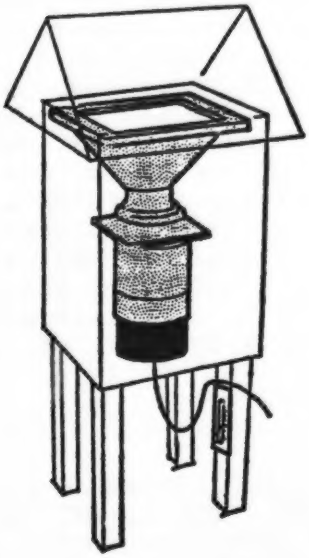

Figure 1. Schematic diagram of the high-volume, or hi-vol, sampler.

TABLE 1. CHARACTERISTICS OF AMBIENT AEROSOL SAMPLERS AND INLETS

Sampler or inlet	Reference	D_{50} or D (Efficiency)	Wind speed, km/hr
Hi-vol	McFarland, et al. (1979)[3]	>30 μm	2
		30 μm	8
		17 μm	24
Rotating cowl	Sehmel (1973)[4]		
Rockwell inlet	Willeke and McFeters (1975)[6]	25 μm	0
SRI inverted inlet	Bird, et al. (1973)[5]	5 μm (39%)	9.2
		5 μm (30%)	46
		5 μm (20%)	68
		12 μm (35%)	9.2
		12 μm (12%)	46
		12 μm (35%)	68
Beckman dichotomous sampler inlet	McFarland, et al. (1979)[3]	15.5 μm	2
		13 μm	8
		10.5 μm	24
Sierra dichotomous sampler inlet	Wedding and John (1979)	11 μm	0
		22 μm	5
		15 μm	15
		10 μm	42

In the "rotating cowl" sampler (Figure 2) developed by Sehmel,[4] a wind vane was used to direct the inlet of a 56.6 ℓ/min (20 cfm) cascade impactor against the wind. The suction speed in the inlet was kept fixed at 1.9 km/hr. Thus, the sampler operated sub-isokinetically most of the time, except near calm air conditions. The sampler was used to collect particles up to 63 μm in diameter in a study of the resuspension of soil particles by wind.

Inverted Inlet

An inverted inlet may consist of a simple open-face filter operating face down, as shown in Figure 3a, or an open-face filter attached to a cylindrical tube, as shown in Figure 3b. Figure 4 shows an inverted inlet designed and tested by Southern Research Institute.[5] The inlet efficiencies were found to be 39%, 30%, and 20%, respectively, for 5 μm diameter particles at wind speeds of 9.2, 46, and 68 km/hr. For 12 μm particles, the efficiencies were 35%, 12%, and 35%, respectively, at the same wind speeds.

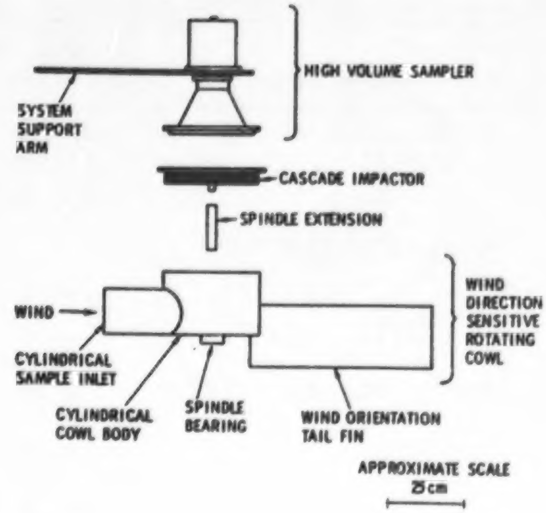
HIGH VOLUME SAMPLER
SYSTEM SUPPORT ARM
CASCADE IMPACTOR
SPINDLE EXTENSION
WIND
WIND DIRECTION SENSITIVE ROTATING COWL
CYLINDRICAL SAMPLE INLET
CYLINDRICAL COWL BODY
SPINDLE BEARING
WIND ORIENTATION TAIL FIN
APPROXIMATE SCALE
25cm

Figure 2. The "rotating cowl" sampler described by Sehmel (1973).[4]

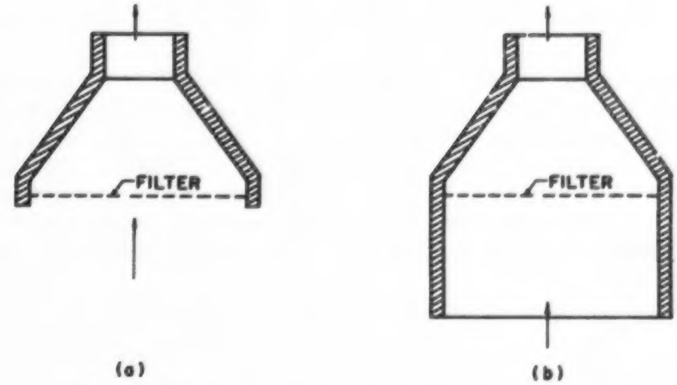
FILTER
FILTER
(a)
(b)

Figure 3. The inverted inlet.

Circumferential Side-Entrance Inlet

Figure 5 is an omni-directional inlet of the circumferential side-entrance type. The inlet, designed and built by Rockwell International Corp. at the suggestion of the author (Liu) and his colleagues (K.T. Whitby and V.A. Marple), was used in EPA's CHAMP (Community Health Air Monitoring Program) stations for ambient air monitoring. The inlet incorporates a circumferential impactor to remove coarse particles. Tests by Willeke and McFeters[6] showed that, at the sampling flow rate of 1133 ℓ/min (40 cfm), the cut-point of the circumferential impactor was 25 μm under calm air conditions. However, no data on the sampling efficiency as a function of wind speed are available.

Figure 6 shows another inlet of the circumferential, side-entrance type. The inlet, designed by McFarland et al.,[7] was intended for the virtual dichotomous sampler.[8] The same inlet design is now used in the commercial dichotomous samplers produced by Beckman Instruments, Inc. (Process Instrument Div., 2500 Harbour Blvd., Fullerton, CA 92634) and Sierra Instruments, Inc. (P.O. Box 909, Carmel Valley, CA 93924). Tests on the Beckman inlet by McFarland et al.[3] showed that the D_{50} size of the inlet was 15.5 μm at a wind speed of 2 km/hr, decreasing to 13 and 10.5 μm, respectively, at wind speeds of 8 and 24 km/hr. Similar tests by Wedding and John (personal communication) on the Sierra inlet resulted in D_{50} cut sizes of 11 μm, 22 μm, 15 μm, and 10 μm, respectively, at wind speeds of 0, 5, 15, and 42 km/hr.

Wind Shield and Baffles

The idea of using a wind shield or baffle to minimize the effect of wind on the inlet efficiency was suggested by the author (Liu) and more fully explored by Agarwal in an internal report at the University of Minnesota Particle Technology Laboratory.[9]

Consider the impaction of particles on a cylindrical object of radius, R. The impaction is governed by the Stokes number,

$$St_W = W\,\tau/R \qquad (1)$$

where W is the wind speed, and τ is the particle relaxation time given by

$$\tau = 2\,a^2\,\rho_p C/9\,\mu \qquad (2)$$

where a is the particle radius, ρ_p is the particle density, C is the slip correction, and μ is the gas viscosity. For impaction to occur, the Stokes number must be larger than some critical value. Thus, by choosing R to be sufficiently large, impaction can be prevented for particles of a certain size up to a certain maximum wind speed.

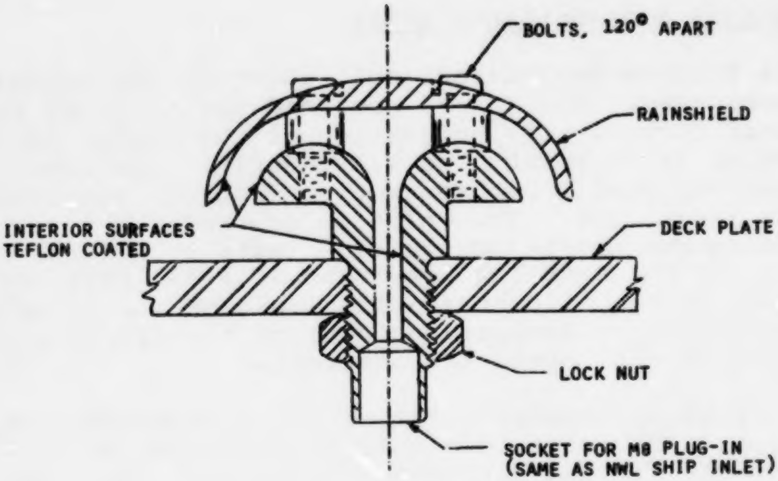
BOLTS, 120° APART
RAINSHIELD
INTERIOR SURFACES TEFLON COATED
DECK PLATE
LOCK NUT
SOCKET FOR M8 PLUG-IN (SAME AS NWL SHIP INLET)

Figure 4. The Southern Research Institute inverted inlet.[5]

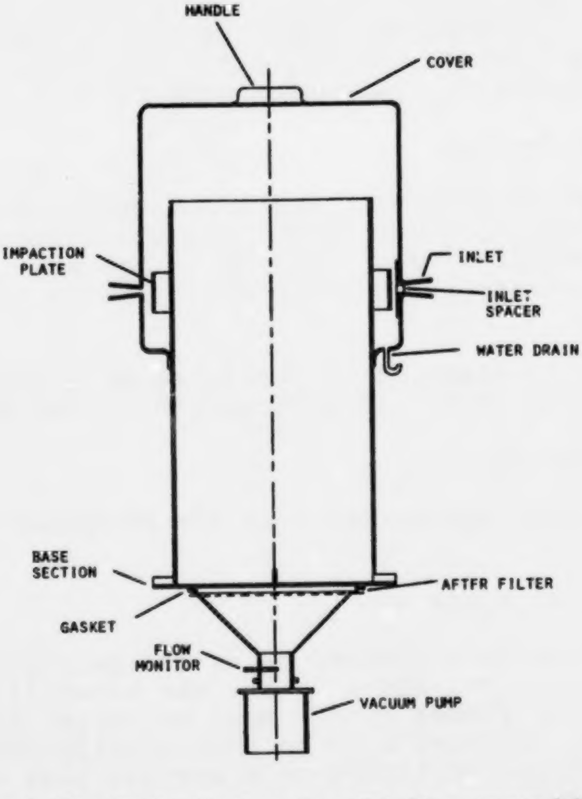
HANDLE
COVER
IMPACTION PLATE
INLET
INLET SPACER
WATER DRAIN
BASE SECTION
AFTFR FILTER
GASKET
FLOW MONITOR
VACUUM PUMP

Figure 5. The Rockwell circumferential side-entrance inlet.

If particles are to be sampled into a tube of a radius r, and the tube is placed at a right angle to the wind, particle impaction at the tube entrance will occur if r is small. However, if the tube is placed within a cylindrical wind shield or baffle of a radius R, as shown in Figure 7, and R is made sufficiently large, particle impaction on the wind shield can be prevented for particles of the same size at the same wind speed. If particle impaction does not occur on the wind shield, the aerosol concentration inside the wind shield must be the same as the concentration outside. Unbiased sampling can then take place from the relatively calm air region within the wind shield. However, no systematic study of the wind shield idea has been made, and the actual performance of the wind shield remains unknown.

Figure 8 shows the inlet of a virtual dichotomous sampler described by Dzubay et al.[10] incorporating a wind shield. In this inlet, an auxiliary blower operating at a relatively high sampling flow rate of 200 ℓ/min draws in air from around the wind shield into the annular space, forming a downward-moving jet. Large particles above 20 µm continue to travel down because of their inertia, while smaller particles are drawn in through the circumferential slit opening into the vertical sampling pipe, where they are sampled isokinetically at a rate of 14 ℓ/min into the dichotomous sampler. No performance data on this inlet were given.

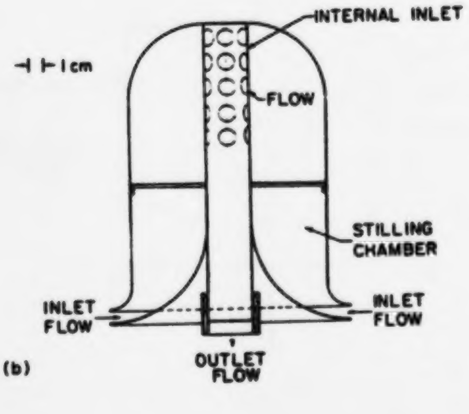

Figure 6. The McFarland et al. circumferential side-entrance inlet.[7]

THEORETICAL CONSIDERATIONS

For an aerosol inlet to be efficient, particle loss must be small. Particle loss can occur on the external surfaces of an inlet or on internal surfaces. Therefore, an efficient inlet is one for which both the external and internal particle losses are minimized.

Consider, for instance, the circumferential, side-entrance inlet shown schematically in Figure 9. With horizontal wind, particle impaction can occur on the external surfaces of the inlet because the streamlines entering the inlet must make a rather sharp turn at the entrance, and the particle trajectories can deviate from the streamlines of the flow. This is depicted in the upper half of the figure. If the inlet is placed at a distance which is not too far from the instrument housing, streamlines deflected by the instrument housing can also enter the inlet at a rather sharp angle, causing additional impaction losses to occur. This is depicted in the lower half of the figure. Therefore, in designing aerosol inlets, both the external shape of the inlet, as well as the distance between the inlet and the main instrument housing, must be considered.

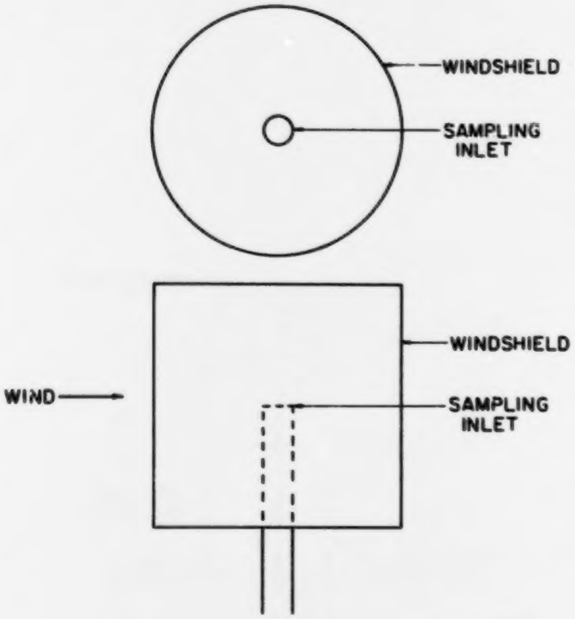

Figure 7. Wind shield or baffle.

Once the particles are brought into an inlet by the streamlines, additional loss can occur by impaction, turbulent deposition, and sedimentation. Careful consideration of all three internal particle loss mechanisms must be made in order to arrive at a satisfactory design. Loss of particles by Brownian diffusion is generally unimportant in aerosol inlets because of the large particle size involved.

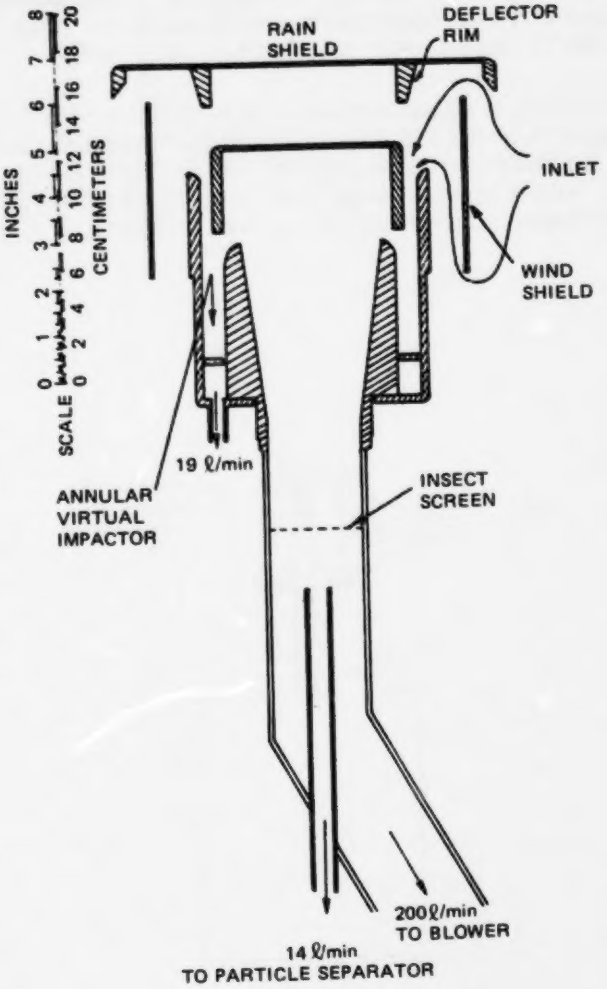
SCALE
INCHES
0 1 2 3 4 5 6 7 8
CENTIMETERS
0 2 4 6 8 10 12 14 16 18 20
RAIN SHIELD
DEFLECTOR RIM
INLET
WIND SHIELD
19 ℓ/min
ANNULAR VIRTUAL IMPACTOR
INSECT SCREEN
200ℓ/min TO BLOWER
14 ℓ/min TO PARTICLE SEPARATOR

Figure 8. The wind shield inlet for the virtual dichotomous sampler.[10]

A completely rigorous theoretical approach to inlet design does not exist at the present time. Much of the previous theoretical work on aerosol inlets was concerned with sampling under calm air conditions,[11-15] and thus was not applicable to ambient sampling under wind. Similarly, the analysis of Davies[16] and Davies and Subari[17] on the sampling efficiency of a thin-walled tube in a cross-wind, while interesting in showing the mechanics of sampling, is not particularly useful in inlet designs, since the straight tube is known to perform poorly under moderate to high wind conditions and is thus not suitable as a general purpose high efficiency inlet. Thus, instrument designers, when faced with the problem of inlet design in the past, traditionally took a rather empirical approach, and many of the resulting inlets consequently have not performed too well.

In the following discussions, we will show that it is not necessary to have a completely rigorous theoretical solution to the problem before an efficient inlet can be designed. We will show that, with a qualitative understanding of the fluid and particle mechanics involved, a satisfactory inlet can be designed.

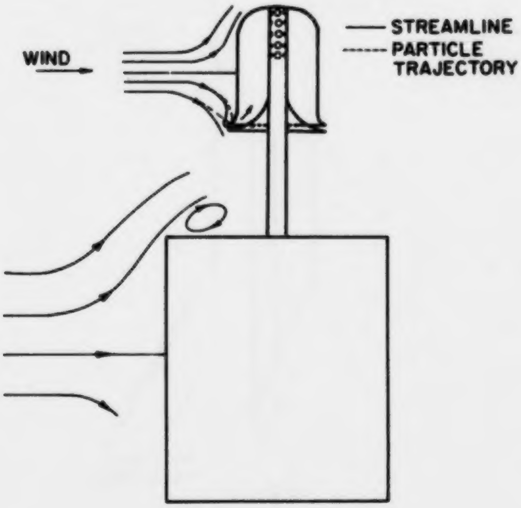

Figure 9. Streamlines and particle trajectories around an aerosol inlet.

Consider the three inlet configurations shown in Figure 10. A simple vertical tube is used to sample the ambient aerosol into the instrument. With horizontal wind, particle impaction near the upstream side of the tube can occur because of the bending of the streamlines there. In Figure 10b, a circular flange is placed over the top of the vertical tube to deflect the streamlines which would otherwise enter the tube from below. The flange keeps the streamlines straight prior to their entry into the tube, thus eliminating particle loss by external impaction. Therefore, the design of Figure 10b is inherently a more efficient design than that of Figure 10a. Similarly, in Figure 10c, the horizontal entrance near the top is enlarged compared to that in Figure 10b. This causes the streamlines to bend more gradually while entering the inlet, resulting in reduced impaction loss on the internal surfaces. Thus, of the three inlet designs shown in Figure 10, the design of Figure 10c should be the most efficient.

The inlet configuration of Figure 10b, and, by extension, that of Figure 10c, are similar to the case analyzed theoretically by Zebel.[18] Zebel showed that, for an inlet consisting of a slit or hole in an infinite wall, the aspiration efficiency can be approximated by the equation

$$E_1 = \frac{1}{1 + 1.09St_w} \tag{3}$$

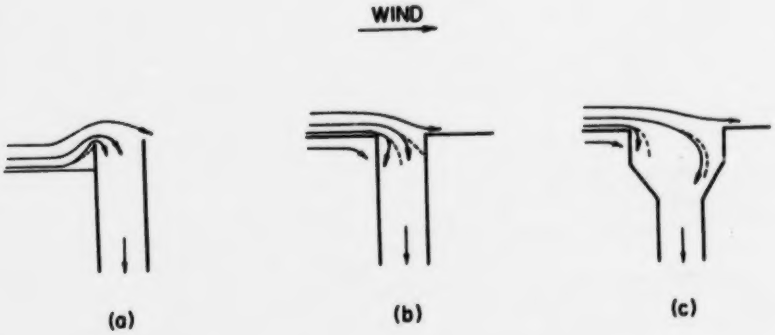

Figure 10. Comparison of three aerosol inlets.

where the aspiration efficiency is the ratio of the number of particles carried by the flow through the inlet opening to the number of particles in the original air volume in the ambient atmosphere, and St_W is the Stokes number based on wind velocity. In Zebel's calculation, potential flow was assumed. Figure 11 shows the streamlines near the entrance to the slit or hole for the case where the wind speed, W, is equal to the suction speed in the slit or hole.

Figure 12 shows the performance of a sampling inlet predicted by Zebel's equation for a circular inlet of 9.2 cm (3-5/8 in.) diameter. The result shows that, for particles of 15 μm aerodynamic diameter, the aspiration efficiency is essentially 100% at low wind speeds, decreasing to 90% at a wind speed of 25 km/hr and 80% at 57 km/hr. Thus, Zebel's results suggest that it should be possible to design an inlet to sample inhalable particles efficiently. The inlet performance can also be made reasonably independent of wind speed up to some rather high wind speeds.

A NEW IPM INLET

On the basis of the above considerations, we have designed the inlet shown in Figure 13 for sampling inhalable particles. The specific inlet has been designed for the virtual dichotomous sampler, and for a sampling flow rate of 1 m^3/hr or 16.7 ℓ/min.

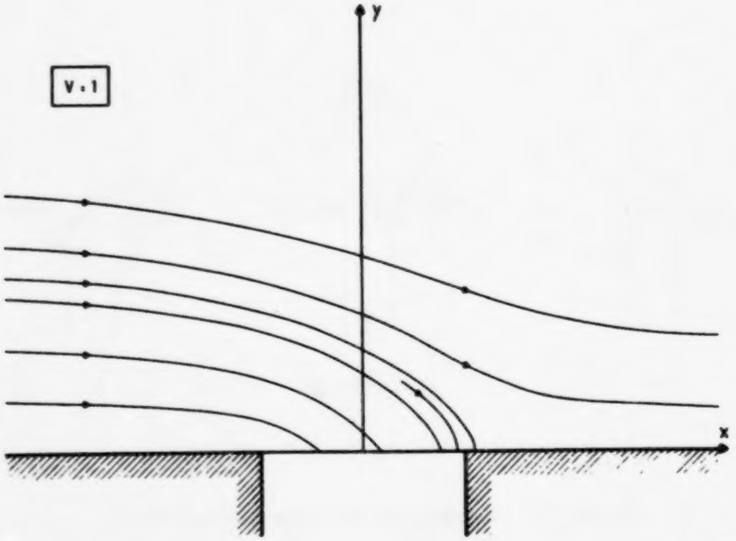

Figure 11. Streamlines over a slit or hole inlet in an infinite wall.

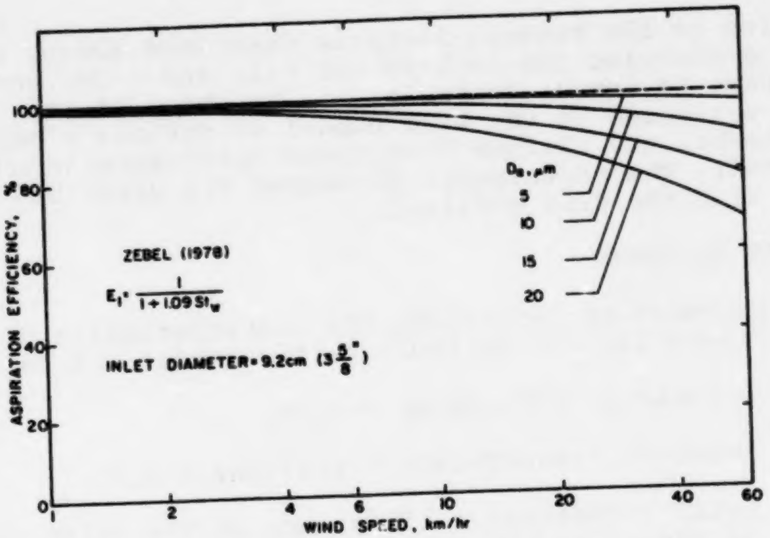

Figure 12. Efficiency of the ideal "hole in an infinite wall" inlet.

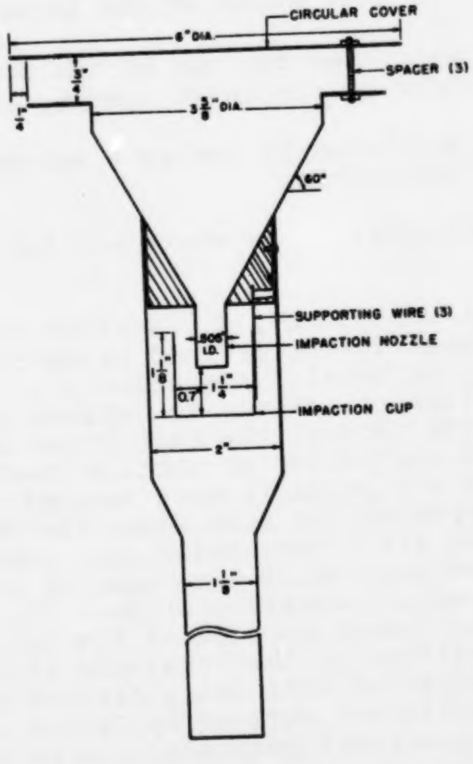
CIRCULAR COVER
6" DIA.
SPACER (3)
3/4"
1/4"
3 5/8" DIA.
60°
SUPPORTING WIRE (3)
.505" I.D.
IMPACTION NOZZLE
1 1/8"
0.7
1 1/4"
IMPACTION CUP
2"
1 1/8"

Figure 13. The University of Minnesota aerosol inlet for inhalable particles.

In addition to the several features described above, the inlet contains a circular top to keep out rain and snow, and an internal impactor to remove coarse particles above 15 µm. This inlet has been evaluated in the wind tunnel at various wind speeds up to 9 km/hr, the maximum wind speed obtainable in our present wind tunnel. The experiments performed are described below, together with the data obtained.

DEFINITION OF TERMS

For purposes of describing the characteristics of the inlet shown in Figure 13, the following efficiencies are defined:

E_1 = aspiration efficiency = m_1/m_0 (4)

E_2 = impactor transmission efficiency = m_2/m_1 (5)

E = total transmission efficiency of the inlet system, or the inlet efficiency = $m_2/m_0 = E_1E_2$ (6)

where

m_1 = mass of particles carried by a given volume of flow through the exit plane of the impactor nozzle

m_2 = mass of particles carried by the same volume of flow through the exit plane of the inlet system, and

m_0 = mass of particles in the same volume of air in the ambient atmosphere.

All particle masses referred to above are for particles of a certain size.

The aspiration efficiency, E_1, defined above, is similar to the aspiration coefficient defined by Davies[11] or the suction coefficient defined by Zebel[18] (Equation 3). The only difference is that the aspiration efficiency is defined in terms of the particle mass passing through the exit plane of the impactor nozzle, whereas the aspiration or suction coefficient is usually defined in terms of the particle mass brought in by the flow through the inlet opening, in this case, the top of the funnel. Thus, the aspiration efficiency takes into account the particle loss in the entrance portion of the impactor nozzle, whereas the aspiration or suction coefficient does not. However, since particle loss in the funnel portion of the inlet has been found to be small for particles in the inhalable size range, the difference between aspiration efficiency defined here and the aspiration or suction coefficient defined by Davies and Zebel is not large and, for all practical purposes, can be ignored.

The impactor transmission efficiency, E_2, defined by Equation 5, is usually referred to as "penetration" in impactor studies. However, in the present case, the impactor is used to remove the non-inhalable particles and to transmit the inhalable particles efficiently. The term "impactor transmission efficiency", therefore, appears appropriate. Finally, the total transmission efficiency of the inlet system, E, or the inlet efficiency for short, is the same as the "inlet effectiveness" defined by McFarland et al.[3,7] However, the term "efficiency" is believed to be appropriate, since in engineering usage, efficiency generally means, and is usually defined as, the ratio of the desired output to the input. For example, the efficiency of a power plant is defined as the ratio of the energy output of the power plant to the energy input. In the present case, the inlet system may be considered as a particle transmission device, the desired output being the aerosol transmitted or delivered to the sampling or measuring instrument, and the input, the aerosol drawn in from the ambient atmosphere. Therefore, the term "inlet transmission efficiency", or the "inlet efficiency" for short, is appropriate and should cause no confusion.

EXPERIMENTAL STUDY AND RESULTS

The preliminary tests of the inlet completed were of two main types. In one type of test, the inlet was evaluated with an optical particle counter in the wind tunnel and its performance compared with several other inlet configurations. The purpose of these experiments was to compare the relative performance of the several inlet configurations in order to see if the chosen configuration indeed had the highest aspiration efficiency. For these experiments, the absolute value of the aspiration efficiency was not needed. In the second type of test, the absolute aspiration efficiency of the inlet was measured, as well as the absolute impactor transmission efficiency and the absolute inlet efficiency. The measurement was made by sampling the particles through the inlet and through an isokinetic probe, and comparing the collected particle mass by fluorometric analysis.

The experiments were performed in the low-speed wind tunnel facility of the Particle Technology Laboratory. The wind tunnel has a 50 cm x 50 cm (20 in. x 20 in.) test section and is capable of a maximum wind speed of 9 km/hr. The projected area of the inlet in the direction of flow is about 125 cm^2. Thus, about 5% of the test section area was blocked by the inlet under test. A complete description of the wind tunnel facility has been given by Whitby et al.[19]

Figure 14 shows the test setup for measuring the relative performance of the inlets by means of an optical particle counter (OPC). Monodisperse aerosols of oleic acid were generated by the vibrating orifice monodisperse aerosol generator (Berglund and Liu[20]) and introduced into the wind tunnel. The particles were then sampled into an optical particle counter (Royco 245, Royco Instruments, Inc., 141 Jefferson Drive, Menlo Park, CA 94025) through the different test inlets. By comparing the counts registered by the OPC when different inlets were used, the relative performance of the inlets could be determined. For these experiments, the impactor was removed from the inlet shown in Figure 13, and the entire flow of 16.7 ℓ/min passing through the inlet was sampled into the Royco 245 counter. The geometrical diameter of the particle was calculated from the liquid flow rate, the solution concentration, and the vibrating frequency in accordance with the method described by Berglund and Liu.[20] The geometrical diameter was then converted to aerodynamic diameter by multiplying by the factor $\sqrt{\rho_p}$, where ρ_p = 0.894 g/cm^3 is the density of oleic acid.

The inlets tested included the UM inlet of Figure 13 with the circular top and impactor cup removed--referred to here as the reference inlet--, a funnel inlet (the UM inlet without the top, flange, and impactor cup), and two tube inlets consisting of straight 5.08 cm (2 in.) and 3.81 cm (1.5 in.) diameter tubes which were placed perpendicular to the horizontal wind in the wind tunnel. Under steady state conditions, the counts registered by the OPC over the same time interval represent the relative efficiency of the inlets tested.

The results of the above experiments are shown in Figures 15, 16, and 17. In these plots, the aspiration efficiency of the inlets relative to the reference inlet is shown plotted against wind speed for particle aerodynamic diameters of 12.8, 14.2, and 15.6 µm. In all cases, the reference inlet was found to

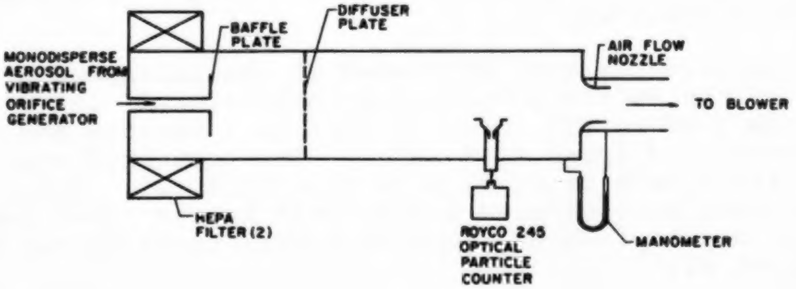
MONODISPERSE AEROSOL FROM VIBRATING ORIFICE GENERATOR
BAFFLE PLATE
DIFFUSER PLATE
AIR FLOW NOZZLE
TO BLOWER
HEPA FILTER (2)
ROYCO 245 OPTICAL PARTICLE COUNTER
MANOMETER

Figure 14. Test setup for measuring the relative efficiencies of different inlet configurations.

have the highest aspiration efficiency and to show the least dependence on wind speed. For example, comparing the reference inlet with the 3.81 cm diameter tube inlet, the aspiration efficiency of the latter for 12.8 μm diameter particles is 90% of that of the reference inlet at a wind speed of 3 km/hr. However, at a wind speed of 9 km/hr, the aspiration efficiency of the tube inlet drops to only 12% of that of the reference inlet. It was also found that the addition of the circular top to the reference inlet did not change its aspiration efficiency. Therefore, the data obtained above were, for all practical purposes, the same as the aspiration efficiency of the various test inlets relative to the complete UM inlet of Figure 13.

The absolute performance of the complete UM inlet of Figure 13 was evaluated in the wind tunnel with fluorescein-tagged DOP (dioctyl phthalate) aerosol and by comparison with an isokinetic probe. The aerosol was generated by dissolving DOP and fluorescein in isopropyl alcohol and spraying the solution through

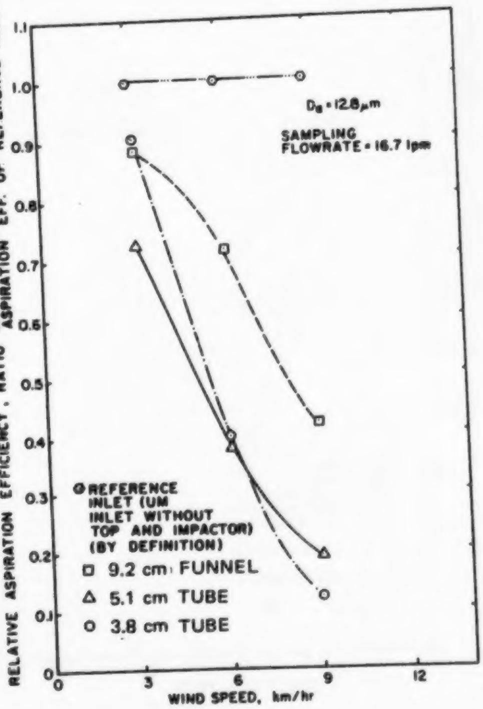

Figure 15. Relative performance of several inlet configurations for 12.8 μm diameter particles.

the vibrating orifice droplet generator. The geometrical diameter of the aerosol was similarly calculated from the droplet generator operating conditions and converted to aerodynamic diameter by multiplying by $\sqrt{\rho_p}$, where $\rho_p = 0.980$ g/cm³ is the density of DOP. Since the amount of fluorescein used was small (about 2% of the DOP mass in most cases), the slight increase in droplet density due to fluorescein addition was ignored.

In these tests with fluorescein-tagged DOP aerosol, a Millipore filter was mounted directly at the exit of the UM inlet to sample the particles passing through the inlet. Following sampling, the fluorescein was extracted from the filter by immersing the filter in 20 to 80 ml of 0.01 N aqueous solution of NaOH. The solution and filter were then agitated in an ultrasonic bath for 2 to 3 minutes. The fluorescein concentration in the solution was then measured with a fluorometer (Model 110, G.K. Turner Associates, Palo Alto, CA). The filter at the exit of the isokinetic probe was similarly analyzed. To measure the material deposited on the inside surface of the isokinetic probe,

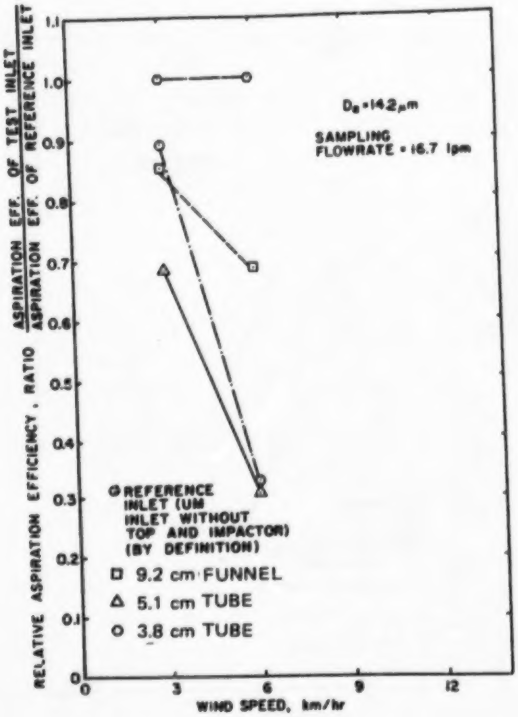

Figure 16. Relative performance of several inlet configurations for 14.2 μm diameter particles.

a wet cotton swab was used to wipe the inside surface of the probe clean. The cotton swab was then immersed in 20 ml of wash solution and similarly agitated in an ultrasonic bath for 2 to 3 minutes to extract the fluorescein from the cotton swab. Generally, very little material was found on the inside surface of the isokinetic probe.

To measure the material collected on the inside surface of the impaction cup, the outside surface was first wiped clean with a wet cotton swab and 20 ml of wash solution was added to the cup and ultrasonically agitated. The solution was then analyzed. The same cotton swab was then used to wipe the remaining surfaces in the inlet to determine the wall losses in the inlet. The cotton swab was then similarly analyzed.

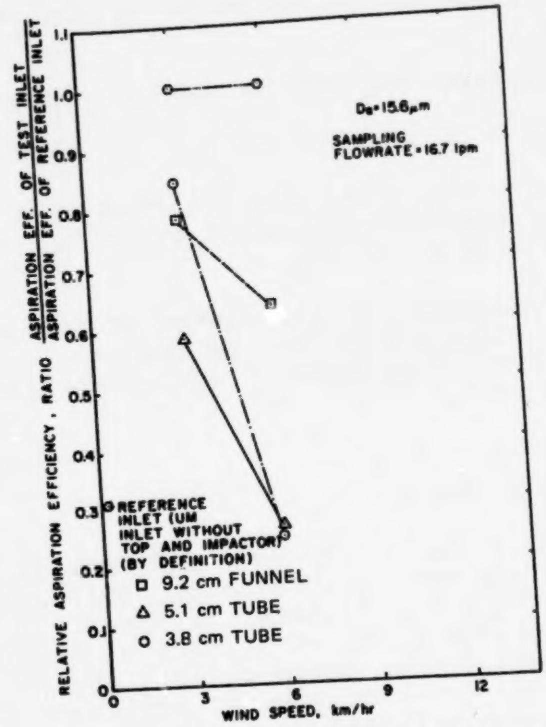

Figure 17. Relative performance of several inlet configurations for 15.6 μm diameter particles.

From these measurements, the various efficiencies were calculated as follows:

$$\text{Impactor transmission efficiency} = m_f/(m_i + m_w + m_f) \quad (7)$$

$$\text{Inlet aspiration efficiency} = (m_i + m_w + m_f)/m_o \quad (8)$$

$$\text{Inlet transmission efficiency} = m_f/m_o \quad (9)$$

$$\text{Wall loss} = m_w/(m_i + m_w + m_f) \quad (10)$$

where

m_i = mass of fluorescein deposited on the inside surface of the impaction cup

m_w = mass of fluorescein deposited on the remaining wall surfaces of the inlet downstream of the impactor nozzle

m_f = mass of fluorescein deposited on the filter at the exit of the inlet

m_o = (mass of fluorescein collected by the isokinetic probe) $\times \left(V_i/V_o\right)$

V_i = volume of flow sampled through the inlet

V_o = volume of flow sampled through the isokinetic probe

In these experiments, the inlet was operated at a sampling flow rate of 16.7 ℓ/min, and the isokinetic probe, at various flow rates depending on wind speed.

The measured transmission efficiency of the impactor is shown in Figure 18. The efficiency is seen to be independent of the wind speed. The sharpness of cut of the impactor, as measured by the parameter

$$\sigma_g = (D_{15.9}/D_{84.1})^{\frac{1}{2}} \quad (11)$$

is 1.18 where $D_{15.9}$ is the aerodynamic diameter of the particle corresponding to an impactor transmission efficiency of 15.9%, and $D_{84.1}$ is the aerodynamic diameter of the particle corresponding to an impactor transmission efficiency of 84.1%. The impactor is seen to have rather sharp cut-off characteristics which are desirable from the point of view of achieving sharp separation of inhalable and non-inhalable particles.

In Figure 19, the aspiration efficiencies of the inlet for particles of aerodynamic diameters of 8.5, 11.0, and 13.4 μm are shown as a function of wind speed. Within the limits of

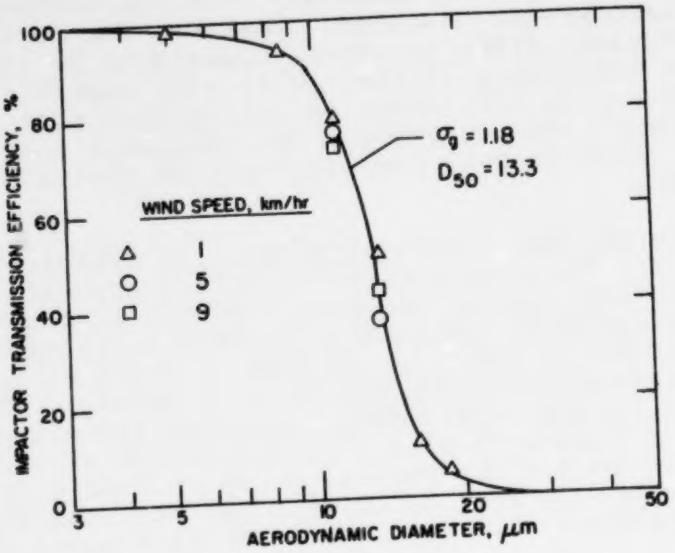

Figure 18. Experimental transmission efficiency of the impactor used in the University of Minnesota inlet.

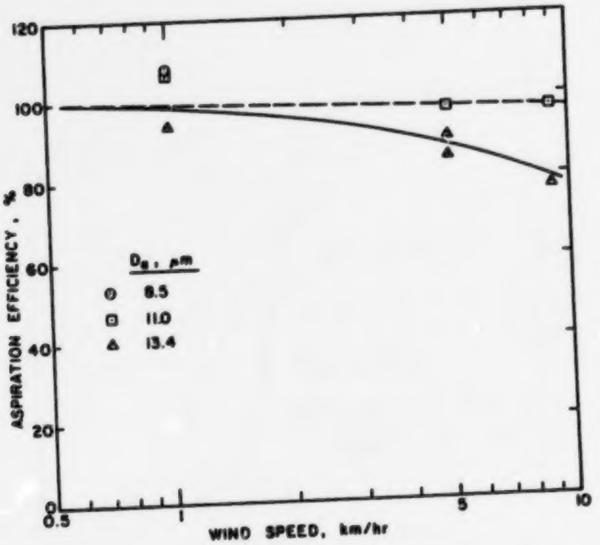

Figure 19. Experimental aspiration efficiency of the University of Minnesota inlet.

error of the measured aspiration efficiency (about ±10%), the aspiration efficiency is essentially 100% for particles of 8.5 and 11.0 μm aerodynamic diameter. However, for particles of 13.4 μm aerodynamic diameter, there appears to be some decrease in aspiration efficiency at the higher wind speeds. This decrease in aspiration efficiency is larger than that predicted by Zebel's theoretical equation. This suggests that the flow field at the inlet is more complicated than that assumed by Zebel in his analysis.

In Figure 20, the overall transmission efficiency of the inlet is shown. The change in inlet efficiency with wind speed is very slight and, for all practical purposes, negligible. Since the maximum wind speed used in these tests was 9 km/hr, it would be useful to see what changes in inlet efficiency would be expected theoretically for higher wind speeds. This can be done by combining the experimental impactor transmission efficiency curve of Figure 18 with the theoretical aspiration efficiency of Equation 3. The result, shown in Figure 20, suggests that the inlet should work quite well and not show significant wind speed dependent characteristics for wind speed of 24 km/hr.

In Figure 20, the characteristics of the present inlet are compared with those of the inlet used in the Beckman dichotomous sampler (McFarland et al.[3]). The present inlet is seen to be considerably sharper in its cut-off characteristics.

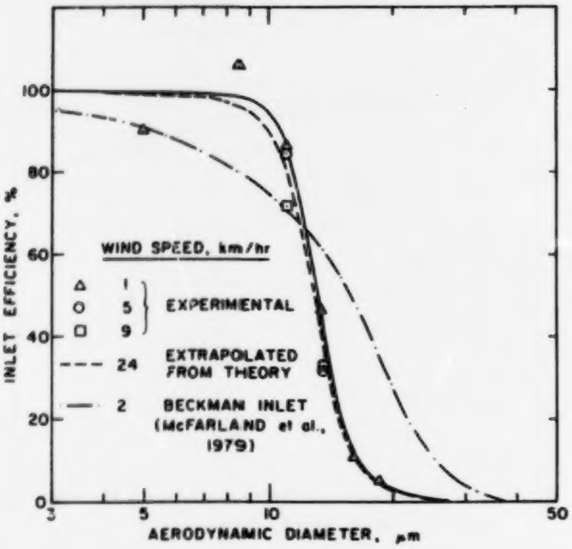

Figure 20. Experimental inlet efficiency for the University of Minnesota inlet and its comparison with the Beckman dichotomous sampler inlet.

The wall loss data for the present inlet are shown in Table 2. The maximum wall loss observed is 8.1% for particles of 11.0 μm aerodynamic diameter, and the average wall loss for all the tests combined is 1.85%.

DISCUSSIONS, CONCLUSIONS, AND FUTURE WORK

When using the inlet described above on an actual aerosol sampling instrument, the distance between the inlet and the instrument is important and must be considered. If the inlet is installed too close to the main instrument housing, the situation depicted in Figure 9 could arise where the streamline deflected upward by the housing could interfere with the operation of the inlet, thereby degrading its performance. It is recommended that the distance between the inlet and the top of the main instrument housing be kept equal to or larger than the height of the instrument housing, as shown in Figure 21(a). If it is not possible or desirable to have this minimum distance of separation between the inlet and the instrument housing, a horizontal deflection plate can be installed over the top of the instrument housing, as shown in Figure 21(b), to prevent the streamlines deflected upward by the instrument housing from interfering with the inlet operation. With these precautions, it is believed that the performance of the inlet, as determined for an isolated inlet in a wind tunnel, should be the same as the actual performance of the inlet when installed on the instrument.

TABLE 2. WALL LOSS IN UM INLET

Wind speed, km/hr	D_a, μm	Wall loss, %
1	5	0.9
	8.5	1.0
	11	8.1
	13.4	0
	16	0.1
	18.5	0.9
5	11	3.0
	13.4	0.4
9	11	3.8
	13.4	1.3

Based on the work performed so far, we believe the inlet described above will meet the basic requirement of an inlet for sampling inhalable particles from the ambient atmosphere. However, the D_{50} diameter of the present inlet is 13.3 μm, which is somewhat smaller than the 15.0 μm diameter that was intended. The D_{50} diameter can be increased by increasing the impactor nozzle diameter slightly, from the present value of 1.28 cm to 1.39 cm. This slight increase in nozzle diameter should not affect the inlet operation in other respects.

Before the present inlet is adopted for routine sampling, it is desirable that additional tests be performed. In addition to wind tunnel testing at higher wind speeds, the inlet should also be tested for its actual field performance characteristics. Some limited tests have shown that the inlet is weather-proof, at least for rain, i.e., the circular top is effective in keeping out rain. We believe that insects, plant matter and other airborne debris would, by virtue of their large size, be effectively trapped by the impaction cup. By coating the inside surface of the impaction cup with a non-volatile grease, particle bounce and re-entrainment could also be prevented. Unlike other impactors designed for size classification of small aerosol particles, the present impactor operates at a relatively low jet velocity of 8.4 km/hr, which should minimize the problem of particle bounce and re-entrainment. In addition, if coarse particles should bounce when they come in contact with the bottom of the cup, they would lose much of their momentum

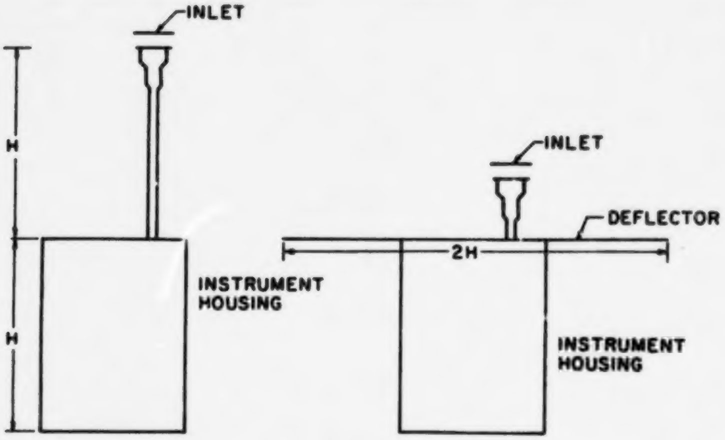

Figure 21. Two methods of installing an inlet on an aerosol sampling instrument.

and energy and be subsequently caught by the vertical surfaces in the impaction cup. Therefore, we do not believe that particle bounce and re-entrainment would be a problem for an impactor of this particular design.

In addition to the above, we have also designed an inlet which is similar to the inlet described above, except that a cyclone is used for separating the inhalable and non-inhalable particles. This new inlet will be evaluated and reported sometime in the future.

ACKNOWLEDGEMENTS

This research is supported by a grant, No. R804600, from the Environmental Protection Agency. The Agency's support is gratefully acknowledged. We also wish to thank Sandra Iverson of the University of Minnesota for her able assistance in carrying out some of the experimental measurements reported here. This report is Particle Technology Laboratory Publication No. 397.

REFERENCES

1. Miller, F.J., D.E. Gardner, J.A. Graham, R.E. Lee, Jr., W.E. Wilson, and J.D. Bachmann. Size Considerations for Establishing a Standard for Inhalable Particles. J. Air Pollut. Control Assoc. 29:610, 1979.

2. National Primary and Secondary Ambient Air Quality Standards. Federal Register 36(84) Friday, April 30, Part II, 1971.

3. McFarland, A.R., C.A. Ortiz, and C.E. Rodes. Characteristics of Aerosol Samplers Used in Ambient Air Monitoring. Presented at the 86th National Meeting of the American Institute of Chemical Engineers, 1979.

4. Sehmel, G.A. An Evaluation of High-Volume Cascade Particle Impactor Systems. Presented at the 2nd Joint Conference on Sensing of Environmental Pollutants, Instrument Society of America, 1973.

5. Bird, A.N., Jr., D.V. Brady, and J.D. McCain. Evaluation of Sampling Systems for Use of the M8 Alarm Aboard Ships. Report SRI-EAS-73-064, Southern Research Institute, Birmingham, AL, 1973.

6. Willeke, K., and J.J. McFeters. Calibration of the CHAMP Fractionator. Particle Technology Laboratory Publication No. 252, University of Minnesota, 1975.

7. McFarland, A.R., J.B. Wedding, and J.E. Cermak. Wind Tunnel Evaluation of a Modified Andersen Impactor and an All-Weather Sampler Inlet. Atmos. Environ. 11:535, 1977.

8. Dzubay, T.G., and R.K. Stevens. Ambient Air Analysis with Dichotomous Sampler and X-Ray Fluorescence Spectrometer. Environ. Sci. Technol. 9:663, 1975.

9. Agarwal, J.K. The Sampling of Aerosols. Particle Technology Laboratory Report No. 208, University of Minnesota, 1972.

10. Dzubay, T.G., R.K. Stevens, and C.M. Peterson. Application of the Dichotomous Sampler to the Characterization of Ambient Aerosols. In: X-Ray Fluorescence Analysis of Environmental Samples, T.G. Dzubay, ed. Ann Arbor Science Publishers, Ann Arbor, MI, 1977. p. 95.

11. Davies, C.N. The Entry of Aerosols into Sampling Tubes and Heads. Brit. J. Appl. Phys. Ser. 2, 1:921, 1968.

12. Kaslow, D.E., and R.J. Emrich. Aspirating Flow Pattern and Particle Inertia Effects Near a Blunt Thick-Walled Tube Entrance. Department of Physics, Lehigh University, Bethlehem, PA. Technical Report No. 23, 1973.

13. Kaslow, D.E., and R.J. Emrich. Particle Sampling Efficiencies for an Aspirating Blunt Thick-Walled Tube in Calm Air. Department of Physics, Lehigh University, Bethlehem, PA. Technical Report No. 25, 1974.

14. Kim, Y.W. An Analytical Consideration of the Particle Inertia Effect with an Application to Aerosol Sampling Efficiency Calculation. Department of Physics, Lehigh University, Bethlehem, PA. Technical Report No. 24, 1974.

15. Agarwal, J.K., and B.Y.H. Liu. A Criterion for Accurate Aerosol Sampling in Calm Air. To be published in Am. Ind. Hyg. Assoc. J.

16. Davies, C.N. Sampling Aerosols with a Thin-Walled Tube. Presented at the 12th International Colloquium on Polluted Atmospheres, Paris, May, 1976.

17. Davies, C.N., and M. Subari. Inertia Effects in Sampling Aerosols. In: Proceedings: Advances in Particle Sampling and Measurement. W.B. Smith, compiler. EPA-600-7-79-065, U.S. Environmental Protection Agency, Research Triangle Park, NC, 1979.

18. Zebel, G. Some Problems in the Sampling of Aerosols. In: Recent Developments in Aerosol Science, D.T. Shaw, ed. Wiley, New York, 1978. p. 167.

19. Whitby, K.T., A.B. Algren, R.C. Jordan, and J.C. Annis. Evaluation of Air Cleaners for Air Conditioning and Ventilation, Part I--Apparatus. ASHAE Trans. 64:401, 1958.

20. Berglund, R.N., and B.Y.H. Liu. Generation of Monodisperse Aerosol Standards. Environ. Sci. Technol. 7:141, 1973.

METRIC CONVERSION FACTORS

To convert from:	To:	Multiply by:
pounds, avoirdupois (lb)	kilograms (kg)	0.454
grains (gr)	grams (g)	0.0648
grains/cubic foot (gr/ft^3)	grams/cubic meter (g/m^3)	2.29
inches (in.)	centimeters (cm)	2.54
feet (ft)	meters (m)	3.05
feet/minute (ft/min)	meters/second (m/s)	0.508
cubic feet/minute (ft^3/min or cfm)	cubic meters/second (m^3/s)	0.000472
gallons (U.S.) (gal.)	liters (ℓ)	3.79
gallons (U.S.)/minute (gal./min)	liters/second (ℓ/s)	0.0632
gallons/1000 cubic feet (gal./1000 ft^3)	liters/cubic meter (ℓ/m^3)	0.134
inches water gauge (in. WG or H_2O)	millimeters of mercury (mm Hg)	1.87
temperature °F	temperature °C	(°F-32) x 5/9